DE GRUYTER OPEN

Acta Geophysica
vol. 63, no. 3, June 2015, pp. 601-604
DOI: 10.1515/acgeo-2015-0025

In Memoriam to Professor Andrzej Władysław Wernik

With great regret we announce that Professor Andrzej W. Wernik passed away on 24 April 2015 at the age of 76, after a long and serious illness.

Professor Andrzej W. Wernik was the founder and leader of ionospheric research in Poland, one of the pioneers of Polish space research, and world wide renowned specialist in ionospheric physics.

He was the author and co-author of approx. 160 papers published in the peer reviewed journals and conference proceedings on wave propagation in the ionosphere, wave propagation in stochastically inhomogeneous media, ionospheric physics, ionospheric plasma turbulence, acoustic-gravity waves in the upper atmosphere, and methods of data analysis.

His M.Sc. degree in astronomy was earned from the Warsaw University in 1960 with M.Sc. thesis "Extinction of the night sky light in an anisotropically scattering atmosphere".

In 1960 he started his scientific career in the Institute of Geophysics of the Polish Academy of Sciences (PAS), to move in 1977 together with his group to the newly established Space Research Center PAS where he has been working until the end of 2014.

In 1963, during his work on geomagnetic data interpretation, he became fascinated with the ionosphere. In 1966 he organized the first regular obser-

vations of Explorer 22 (Polar Beacon-B) 20 MHz radio signals to study the ionosphere using measurements of Faraday rotation and signal amplitude fluctuations. The same year he initiated the project to construct an advanced receiver for satellite radio beacons at frequencies of 20, 30, 40, 90, and 360 MHz, aiming to measure dispersive Doppler frequency at any pair of these frequencies as well as the Faraday rotation. Great accuracy of these measurements made it possible to investigate small frequency scintillations. The apparatus was used since January 1969 to receive beacon signals from Explorer 22, from a number of Intercosmos satellites, and after some modifications, from the geostationary ATS-6 satellite. In such a way for a long time he became engaged in the problem of scintillations in the satellite telecommunication. A number of his works on scintillations were made at that time in cooperation with Dr. Ludwik Liszka of Kiruna Geophysical Observatory in Sweden during several research stays in Kiruna.

His Ph.D. degree in geophysics obtained from the Institute of Geophysics PAS in 1968 was based on the thesis "Effects of non-uniform ionospheric structure on the propagation of radio signals from the Earth's artificial satellites". His Ph.D. supervisor was Prof. Stefan Manczarski, the legendary radio specialist working during the II World War for the Polish underground Home Army.

Later, during his post-doc stay (1972/1973) in the Department of Electrical Engineering of the University of Illinois he worked in cooperation with prof. K.C. Yeh and C.H. Liu on the development of scattering theory of radio scintillations, including multiple scattering and GHz signals. This work was recognized with the prestigious award of the Scientific Secretary of the Polish Academy of Sciences.

In 1978 Prof. Wernik obtained the D.Sc. habilitation degree from the Institute of Fundamental Technological Research PAS for his scientific works assembled under the title "Theory of scintillations of trans-ionospheric radio waves". The same year he was awarded with the Silver Cross of Merit by the Polish Council of State, the Medal of the Space Research Committee PAS, and the Brown Medal for the Services for State Defense.

In 1968 in Poland the cooperation with INTERCOSMOS organization started. Prof. Wernik used this opportunity to access the Intercosmos satellite ionospheric data (for his research on photoelectrons) and to launch own instruments in space. It materialized only in December 1981 aboard the Vertical-10 rocket with the Polish digital analyzer of plasma density fluctuations probing the mid-latitude ionosphere at altitudes of 200-1500 km. Observations of intense and sharp irregularities of ionospheric plasma density during this experiment allowed to modify the scintillation theory giving better agreement with observations.

As an acknowledgement of his achievements in science, education, and activity to the benefit of Polish space research the prestigious scientific title of the Professor in Physics has been awarded to him by the President of Poland in 1989.

During his career, Prof. Wernik was involved in a wide international cooperation. Between 1972 and 1988 he visited many times the Department of Electrical and Computer Engineering of the University of Illinois at Urbana-Champaign, USA. In 1984-1987, in cooperation with this University and the University of Oulu he initiated systematic studies of radio scintillations at the Polish Polar Station Hornsund at Svalbard, where HILAT (USAF HIgh LATitude Research Satellite) and Polar Bear (USAF Polar Beacon and Research satellite) radio beacon signals were received.

In 1993 he spent 6 months as a visiting scholar at the National Central University in Chung-Li, Taiwan. With the specialists from the University of Oslo he worked on ionospheric plasma turbulence, with Italian scientists from Istituto dei Sistemi Complessi and Istituto Nazionale di Geofisica e Vulcanologia – on the statistical model of scintillation and space plasma turbulence.

He participated as an expert in many international scientific and educational projects of the European Commission and ESA. Recently it was TRANSMIT project – Training Research and Applications Network to Support the Mitigation of Ionospheric Threats.

Prof. Wernik was a splendid lecturer and promotor of more than 10 Ph.D. students. His last student was Dr. Shishir Priyadarshi of India, the grantee of TRANSMIT project. Working under the supervision of Prof. Wernik he defended his Ph.D. thesis "B-splines model of ionospheric scintillation" earning Ph.D. degree in October 2014. This work was based on the last project of Prof. Wernik – scintillation data analysis from GPS receivers placed at the Polish Polar Station Hornsund at Svalbard and in Warsaw.

Prof. Wernik served scientific community in many ways during all his professional life:

- In 1990-1992 he chaired the Commission G Ionospheric Radio and Propagation of URSI.
- In 1996-1999 – Member of the Bureau of the Scientific Committee on Solar-Terrestrial Physics (SCOSTEP).
- In 1996-2000 − Associate Editor of „Radio Science" published by the American Geophysical Union.
- In 1999-2002 − Vice-President of URSI, and
- In 2002-2005 − Vice-President and Treasurer of URSI.
- In 2014-2015 – Honorary Chairman of Commission G of the National URSI Committee.

- In 2010-2013 – Member of Central Commision for Degrees and Titles.

Prof. Wernik was member of the Research Council of the Institute of Geophysics PAS, Research Council of the Space Research Center PAS, Committee of Geophysics, National URSI Committee, Committee of Polar Research, American Geophysical Union (silver pin), Polish Astronomical Society, Polish Geophysical Society, Advisory Committee of *Acta Geophysica* published by Springer.

Prof. Wernik was survived by his beloved wife Maria, his daughter Dorota, and his 2 grandchildren Zofia and Jan (Sophie and John). He will be remembered by his friends and coworkers as a nice person of positive attitude to everybody, generous and warm, of noble manners, with science passion, a splendid example of fruitful great scientist and good man. Throughout all difficult moments in the history of Poland before 1989 and the transformation later on that disturbed research work in our Institute, he was always quiet and determined to continue steadily his work, creating so needed peaceful atmosphere around.

Iwona Stanisławska and Barbara Popielawska
Space Research Center
Polish Academy of Sciences

DE GRUYTER OPEN

Acta Geophysica
vol. 63, no. 3, June 2015, pp. 605-633
DOI: 10.1515/acgeo-2015-0011

Quasi-static Planar Deformation in a Medium Composed of Elastic and Thermoelastic Solid Half Spaces Due to Seismic Sources in an Elastic Solid

Anil K. VASHISTH[1], Kavita RANI[2], and Kuldip SINGH[3]

[1]Department of Mathematics, Kurukshetra University, Kurukshetra, India
e-mail: akvashishth@kuk.ac.in (corresponding author)

[2]Department of Mathematics, Government Post Graduate College, Hisar, India
e-mail: karya4@gmail.com

[3]Department of Mathematics, Guru Jambheshwar University of Science and Technology, Hisar, India; e-mail: profkbgju@gmail.com

A b s t r a c t

A two-dimensional problem of quasi static deformation of a medium consisting of an elastic half space in welded contact with thermoelastic half space, caused due to seismic sources, is studied. Source is considered to be in the elastic half space. The basic equations, governed by the coupled theory of thermoelasticity, are used to model for thermoelastic half space. The analytical expressions for displacements, strain and stresses in the two half spaces are obtained first for line source and then for dip slip fault. The results for two particular cases, adiabatic conditions and isothermal conditions, are also obtained. Numerical results for displacements, stresses and temperature distribution have also been computed and are shown.

Key words: seismic sources, thermoelastic, quasi-static, deformation.

1. INTRODUCTION

The elasticity theory of dislocation was developed and applied by Steketee (1958), Rongved and Frasier (1958), and Maruyama (1964, 1966). The problems related to seismic sources in elastic media have been studied extensively by many researchers (Burridge and Knopoff 1964, Singh and Ben-Menahem 1969, Singh 1970, Sato 1971, Singh *et al.* 1973, Sato and Matsu'ura 1973, Jovanovich *et al.* 1974a, b; Freund and Barnett 1976, *etc*.). The detailed description about seismic sources is given in the classical texts: Aki and Richards (1980), Ben-Menahem and Singh (1981), Lay and Wallace (1995), and Stein and Wysession (2003).

Singh and Garg (1985) studied the static deformation of an isotropic multilayered half space by a normal line load and a shear line load. Singh and Garg (1986) described the representation of two-dimensional seismic sources and obtained the integral expressions for the Airy stress function in an unbounded medium due to various two-dimensional sources and represented the sources in terms of jumps across the plane through the sources. Garg and Singh (1987) extended the results of Singh and Garg (1985) by considering the multilayered half space as transversely isotropic. Pan (1989a, b) provided a unified solution of the static deformation of the transversely isotropic and layered half space by general surface loads. Rani *et al.* (1991) extended the work of Singh and Garg (1986) and obtained closed form analytical expressions for the displacements and stresses at any point of a uniform half space due to two-dimensional buried sources by applying the traction free boundary conditions at the surface of the half space.

Okada (1985, 1992) provided compact analytical expressions for the surface deformation and internal deformation due to inclined shear and tensile faults in a homogeneous isotropic half space. Heaton and Heaton (1989) obtained the deformation field induced by point forces and point force couples embedded in two Poissonian half spaces in welded contact. Singh *et al.* (1992) derived closed form expressions for displacements and stresses in two welded half spaces caused by two-dimensional sources. Many other researchers discussed source problems for different types of sources *viz*. Kumari *et al.* (1992), Singh *et al.* (1993, 2003), Garg *et al.* (1996, 2003), Tomar and Dhiman (2003), Kumar *et al.* (2005), Singh *et al.* (2005), and Madan *et al.* (2005).

Thermoelasticity deals with dynamical systems whose interactions with the surroundings include not only mechanical work and external work but also the exchange of heat. Theory of thermoelasticity studies the influence of temperature of an elastic medium on the distribution of stress and strain as well as the inverse effect of the deformation on the temperature distribution.

Attempts have been made to study source problems in thermoelasticity. However, most of such studies are attributed to internal and surface heat sources, (*e.g.*, Lanzano 1986a, b, Dziewonski and Anderson 1981, Rundle 1982, Small and Booker 1986, Abd-Alla 1995, Shevchenko and Gol'tsev 2001, Kit *et al.* 2001, Youssef 2006, 2009, 2010, Mallik and Kanoria 2008, Hou *et al.* 2008a, b, 2009, 2011, Kumar and Gupta 2009, Attetkov *et al.* 2009, *etc.*). Some authors have considered mechanical sources also; *e.g.*, Pan (1990) considered quasi-static governing equations of thermoelasticity and discussed the transient thermoelastic deformation in a transversely isotropic and layered half space by surface loads and internal sources. Kumar and Rani (2004) considered a dynamical two-dimensional problem of thermoelasticity and studied the deformation due to mechanical and thermal sources in generalized thermally conducting orthorhombic material. Ghosh and Kanoria (2007) derived analytical expressions for thermoelastic displacements and stresses in composite multi-layered media due to varying temperature and concentrated loads. Quasi-static deformation of a thermoelastic medium due to seismic sources or quasi static mechanical sources has not been studied so far.

For a realistic Earth model, it is appropriate to involve thermoelastic medium in the model. The study of quasi static deformation of a thermo- elastic medium, in welded contact with an elastic medium, due to seismic sources is important for its geophysical applications. The theory developed in this paper may find its applications in seismic faulting. When the source surface is very long in one dimension in comparison with the other, the use of two-dimensional approximations is justified and consequently calculations are simplified to a great extent and one gets a closed form of analytic solution. A very long strip source and a very long line source are the examples of such two-dimensional sources.

In this paper, quasi static deformation of a medium consisting of a homogeneous isotropic thermoelastic half space in welded contact with a homogeneous elastic half space, due to a line source and dip slip fault in an elastic half space, is studied. Numerical results for displacements, stresses and temperature distribution are presented graphically. The present problem is useful in the field of geomechanics where the interest is about the various phenomena occurring in the earthquakes and measuring of displacements, stresses, and temperature field due to the presence of certain sources.

2. FORMULATION OF THE PROBLEM

Consider a medium consisting of thermoelastic half spaces ($z \geq 0$) and an elastic half space ($z \leq 0$) which are in welded contact along the plane $z = 0$, as shown in Fig. 1. A line source parallel to the x-axis passing through the point $(0, 0, -h)$ in the elastic half space is considered.

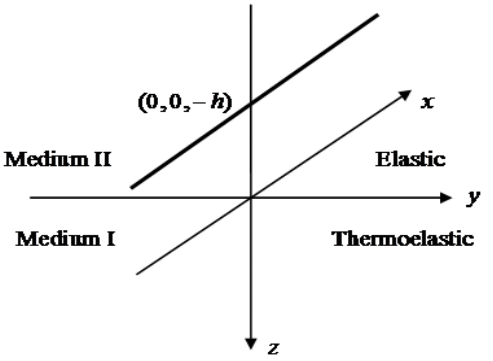

Fig. 1. A line source through the point $(0, 0, -h)$.

A two-dimensional plane strain problem in *yz*-plane is considered so that the displacement components can be written as:

$$u_i = u_i(y,z,t)\,, \quad (i = y,z)\,, \qquad u_x = 0\,. \tag{1}$$

3. BASIC EQUATIONS AND THEIR SOLUTIONS

3.1 For thermoelastic half space

The stress strain relations for a thermoelastic medium (Nowacki 1975) are given by:

$$\sigma_{ij} = \lambda\varepsilon_{kk}\delta_{ij} + 2\mu\varepsilon_{ij} - \beta\theta\delta_{ij}\,, \quad i,j,k = x,y,z\,, \tag{2}$$

where σ_{ji} and ε_{ij} are components of stress and strain tensor, respectively, λ, μ are Lame's constants, $\beta = (3\lambda + 2\mu)\alpha_t$ is the thermoelastic coupling coefficient, θ is the temperature difference, and α_t is the coefficient of linear thermal expansion.

The stress components for a plane strain problem in the *yz*-plane are given by:

$$\sigma_{yy} = \lambda\varepsilon_{kk} + 2\mu\varepsilon_{yy} - \beta\theta\,, \tag{3a}$$

$$\sigma_{zz} = \lambda\varepsilon_{kk} + 2\mu\varepsilon_{zz} - \beta\theta\,, \tag{3b}$$

$$\sigma_{yz} = 2\mu\varepsilon_{yz}\,, \tag{3c}$$

where

$$\varepsilon_{kk} = \frac{1}{2(\lambda+\mu)}\left(\sigma_{yy} + \sigma_{zz} + 2\beta\theta\right). \tag{3d}$$

The strain components can be represented as:

$$2\mu\varepsilon_{yy} = (1-\upsilon)\,\sigma_{yy} - \upsilon\sigma_{zz} + \alpha_0\theta \ , \tag{4a}$$

$$2\mu\varepsilon_{zz} = (1-\upsilon)\,\sigma_{zz} - \upsilon\sigma_{yy} + \alpha_0\theta \ , \tag{4b}$$

$$2\mu\varepsilon_{yz} = \sigma_{yz} \ , \tag{4c}$$

where $\upsilon = \dfrac{\lambda}{2(\lambda+\mu)}$ is Poisson's ratio and $\alpha_0 = (1-2\upsilon)\beta$.

The equations of equilibrium for thermoelastic medium, in the absence of body forces, are

$$\sigma_{yy,y} + \sigma_{yz,z} = 0 \ , \tag{5a}$$

$$\sigma_{zy,y} + \sigma_{zz,z} = 0 \ , \tag{5b}$$

and the compatibility equation is

$$\varepsilon_{yy,zz} + \varepsilon_{zz,yy} = 2\varepsilon_{yz,yz} \ . \tag{6}$$

Using Eqs. 4 and 5 in Eq. 6, we get

$$\nabla^2\left(\sigma_{yy} + \sigma_{zz} + 2\eta\theta\right) = 0 \ , \tag{7}$$

where

$$\eta = \frac{\alpha_0}{2(1-\upsilon)} = \frac{(1-2\upsilon)}{2(1-\upsilon)}\beta \ , \qquad \nabla^2 \equiv \frac{\partial^2}{\partial y^2} + \frac{\partial^2}{\partial z^2} \ .$$

The heat conduction equation can be written as

$$\lambda_0\theta_{,ii} - \rho C_e\dot{\theta} - \beta T_0\dot{\varepsilon}_{kk} = 0 \ , \qquad (i,k = y,z) \ , \tag{8}$$

where λ_0 is the thermal conductivity, C_e is the specific heat, ρ is the density, and T_0 is the temperature at natural state.

The stress function U is defined as:

$$\sigma_{yy} = \frac{\partial^2 U}{\partial z^2} \ , \qquad \sigma_{zz} = \frac{\partial^2 U}{\partial y^2} \ , \qquad \sigma_{yz} = -\frac{\partial^2 U}{\partial y \partial z} \ . \tag{9}$$

Using Eqs. 3d and 9 in Eqs. 7 and 8, we get

$$\nabla^2\left(\nabla^2 U + 2\eta\theta\right) = 0 \tag{10}$$

and

$$\lambda_0\nabla^2\theta - \left(\rho C_e + \frac{\beta^2 T_0}{(\lambda+\mu)}\right)\dot{\theta} - \frac{\beta T_0}{2(\lambda+\mu)}\left(\nabla^2\dot{U}\right) = 0 \ . \tag{11}$$

Equations 10 and 11 imply that

$$\left(c\nabla^2 - \frac{\partial}{\partial t}\right)\nabla^2\theta = 0 \tag{12}$$

and

$$\left(c\nabla^2 - \frac{\partial}{\partial t}\right)\nabla^4 U = 0 \ , \tag{13}$$

where

$$c = \lambda_0 \left[\rho C_e + \frac{{\alpha_0}^2 T_0}{\mu(1-2\upsilon)} - \frac{{\alpha_0}^2 T_0}{2\mu(1-\upsilon)}\right]^{-1} \ . \tag{14}$$

The general solution of Eq. 12 may be written as

$$\theta = \theta_1 + \theta_2 \ , \tag{15}$$

where

$$c\nabla^2\theta_1 = \frac{\partial\theta_1}{\partial t} \tag{16}$$

and

$$\nabla^2\theta_2 = 0 \ . \tag{17}$$

Similarly, the general solution of Eq. 13 can be expressed as:

$$U = U_1 + U_2 \ , \tag{18}$$

where

$$c\nabla^2 U_1 = \frac{\partial U_1}{\partial t} \tag{19}$$

and

$$\nabla^4 U_2 = 0 \ . \tag{20}$$

Equations 16, 17, 19, and 20, with the time dependence as $e^{-i\omega t}$, can be written as

$$\nabla^2\theta_1 + \frac{i\omega}{c}\theta_1 = 0 \ , \tag{21}$$

$$\nabla^2\theta_2 = 0 \ , \tag{22}$$

$$\nabla^2 U_1 + \frac{i\omega}{c}U_1 = 0 \ , \tag{23}$$

$$\nabla^4 U_2 = 0 \ , \tag{24}$$

where θ_1, θ_2, U_1, and U_2 are functions of y and z only.

Application of Fourier transform to Eqs. 21-24, solution of the resulting differential equations, inversion of Fourier transform and further simplification leads to

$$\theta = \int_0^\infty \left(A_1 e^{-mz} + A_2 e^{-kz}\right)\begin{pmatrix}\sin ky \\ \cos ky\end{pmatrix} dk \ , \tag{25}$$

$$U = \int_0^\infty \left(B_1 e^{-mz} + \left(B_2 + B_3 kz \right) e^{-kz} \right) \begin{pmatrix} \sin ky \\ \cos ky \end{pmatrix} dk \ , \tag{26}$$

where

$$m = \left(k^2 - \frac{i\omega}{c} \right)^{1/2}, \quad \mathrm{Re}(m) > 0$$

and A_i, B_i may be functions of k. Equation 9 gives

$$\sigma_{yy} = \int_0^\infty \left(m^2 B_1 e^{-mz} + \left(B_2 k^2 - 2B_3 k^2 + B_3 k^3 z \right) e^{-kz} \right) \begin{pmatrix} \sin ky \\ \cos ky \end{pmatrix} dk \ , \tag{27}$$

$$\sigma_{zz} = \int_0^\infty \left(B_1 e^{-mz} + \left(B_2 + B_3 kz \right) e^{-kz} \right) \begin{pmatrix} \sin ky \\ \cos ky \end{pmatrix} \left(-k^2 \right) dk \ , \tag{28}$$

$$\sigma_{yz} = \int_0^\infty \left(mB_1 e^{-mz} + \left(\left(B_2 - B_3 \right) k + B_3 k^2 z \right) e^{-kz} \right) k \begin{pmatrix} \cos ky \\ -\sin ky \end{pmatrix} dk \ . \tag{29}$$

Making use of Eqs. 25 and 26 in Eqs. 10 and 11, we get

$$A_1 = -\frac{(m^2 - k^2)}{2\eta} B_1 = \frac{i\omega}{2\eta c} B_1 \ , \tag{30}$$

$$A_2 = \frac{2(\upsilon_u - \upsilon)}{\alpha_0} k^2 B_3 \ , \tag{31}$$

where

$$\upsilon_u = \upsilon + \frac{{\alpha_0}^2 T_0}{2\mu \left(\rho C_e + \dfrac{{\alpha_0}^2 T_0}{\mu(1-2\upsilon)} \right)} \ . \tag{32}$$

The displacement components can now be written as:

$$2\mu u_y = -\int_0^\infty \left(B_1 e^{-mz} + \left(B_2 + B_3 (2\upsilon_u - 2 + kz) \right) e^{-kz} \right) k \begin{pmatrix} \cos ky \\ -\sin ky \end{pmatrix} dk \tag{33}$$

and

$$2\mu u_z = \int_0^\infty \left(mB_1 e^{-mz} + \left(B_2 + B_3 (1 - 2\upsilon_u + kz) \right) k e^{-kz} \right) \begin{pmatrix} \sin ky \\ \cos ky \end{pmatrix} dk \ . \tag{34}$$

The heat flux in z-direction is found as

$$q_z = -\lambda_0 \theta_{,z} = \lambda_0 \int_0^\infty \left(mA_1 e^{-mz} + kA_2 e^{-kz} \right) \begin{pmatrix} \sin ky \\ \cos ky \end{pmatrix} dk \ . \tag{35}$$

3.2 For elastic half space

A homogeneous isotropic elastic medium can be characterized by the shear modulus (μ') and the Poisson's ratio (υ'). The plane strain problem for an isotropic elastic medium can be solved in terms of the Airy stress function Φ such that

$$\sigma'_{yy} = \frac{\partial^2 \Phi}{\partial z^2}, \quad \sigma'_{zz} = \frac{\partial^2 \Phi}{\partial y^2}, \quad \sigma'_{yz} = -\frac{\partial^2 \Phi}{\partial y \partial z}, \tag{36}$$

where Φ satisfies the biharmonic equation

$$\nabla^2 \nabla^2 \Phi = 0 \tag{37}$$

and σ'_{ij} are the components of stress tensor.

Let there be a line source parallel to the x-axis passing through the point $(0, 0, -h)$ of the elastic half space ($z < 0$). The Airy stress function for a line source parallel to the x-axis passing through the point $(0, 0, -h)$ in an unbounded isotropic elastic medium (Singh and Garg 1986), can be expressed in the form

$$\Phi_0 = \int_0^\infty \left(S_1 + S_2 k \left|z + h\right|\right) e^{-k|z+h|} \begin{pmatrix} \sin ky \\ \cos ky \end{pmatrix} \frac{dk}{k}. \tag{38}$$

The source coefficients S_1 and S_2 are independent of k.

The source coefficients for different types of sources, as given in Singh and Garg (1986), are given in Table 1. In this table, the upper sign is for $z > -h$, the lower sign is for $z < -h$ and

$$\alpha' = \frac{1}{2(1-\upsilon')}.$$

The Airy stress function for the elastic half space can now be written as

$$\Phi = \Phi_0 + \int_0^\infty \left(C_1 + C_2 kz\right) e^{kz} \begin{pmatrix} \sin ky \\ \cos ky \end{pmatrix} dk, \tag{39}$$

where the unknowns C_1, C_2 are to be determined from the boundary conditions.

Using Eqs. 36, 38, and 39, the stresses are obtained as

$$\sigma'_{yy} = \int_0^\infty \left\{ \left[S_1 + S_2 \left(-2 + k\left|z + h\right|\right) \right] e^{-k|z+h|} + \left[C_1 + C_2 \left(kz + 2\right) \right] k e^{kz} \right\} \begin{pmatrix} \sin ky \\ \cos ky \end{pmatrix} k dk, \tag{40}$$

$$\sigma'_{zz} = -\int_0^\infty \left[\left(S_1 + S_2 k \left|z + h\right|\right) e^{-k|z+h|} + \left(C_1 + C_2 kz\right) k e^{kz} \right] \begin{pmatrix} \sin ky \\ \cos ky \end{pmatrix} k dk, \tag{41}$$

Table 1

Values of coefficients for different types of sources

Source	S_1	S_2	Upper or lower solution
Single couple (yz)	$\mp\dfrac{F_{yz}}{2\pi}$	$\pm\alpha'\dfrac{F_{yz}}{2\pi}$	upper
Single couple (zy)	$\pm\dfrac{F_{zy}}{2\pi}$	$\pm\alpha'\dfrac{F_{zy}}{2\pi}$	upper
Double couple (yz) + (zy) $F_{yz}=F_{zy}=D_{yz}$	0	$\pm\alpha'\dfrac{D_{yz}}{\pi}$	upper
Centre of rotation $F_{yz}=F_{zy}=R_{yz}$	$\pm\dfrac{R_{yz}}{\pi}$	0	upper
Dipole (yy)	$(1-\alpha')\dfrac{F_{yy}}{2\pi}$	$-\alpha'\dfrac{F_{yy}}{2\pi}$	lower
Dipole (zz)	$(1-\alpha')\dfrac{F_{zz}}{2\pi}$	$\alpha'\dfrac{F_{zz}}{2\pi}$	lower
Centre of dilatation (yy) + (zz) $(F_{yy}=F_{zz}=C_0)$	$(1-\alpha')\dfrac{C_0}{\pi}$	0	lower
Double couple (zz) – (yy) $(F_{yy}=F_{zz}=D'_{yz})$	0	$\alpha'\dfrac{D'_{yz}}{\pi}$	lower

$$\sigma'_{yz}=\int_0^\infty\left\{\pm\left[S_1-S_2\left(1-k\left|z+h\right|\right)\right]e^{-k|z+h|}-\left[C_1+C_2\left(1+kz\right)\right]ke^{kz}\right\}\begin{pmatrix}\cos ky\\-\sin ky\end{pmatrix}kdk\ . \quad (42)$$

The corresponding displacement components are

$$2\mu' u'_y=\int_0^\infty\begin{bmatrix}\left\{-S_1+S_2\left(2-2\upsilon'-k\left|z+h\right|\right)\right\}e^{-k|z+h|}\\-\left\{C_1+C_2\left(2-2\upsilon'+kz\right)\right\}ke^{kz}\end{bmatrix}\begin{pmatrix}\cos ky\\-\sin ky\end{pmatrix}dk \quad (43)$$

and

$$2\mu' u'_z=\int_0^\infty\begin{bmatrix}\pm\left\{S_1+S_2\left(1-2\upsilon'+k\left|z+h\right|\right)\right\}e^{-k|z+h|}\\+\left\{-C_1+C_2\left(1-2\upsilon'-kz\right)\right\}ke^{kz}\end{bmatrix}\begin{pmatrix}\sin ky\\\cos ky\end{pmatrix}dk\ . \quad (44)$$

4. BOUNDARY CONDITIONS

The boundary conditions at the plane $z=0$ are

$$\sigma_{yz}=\sigma'_{yz}\ ,\quad \sigma_{zz}=\sigma'_{zz}\ ,\quad u_y=u'_y\ ,\quad \text{and}\quad u_z=u'_z\ . \quad (45)$$

Further, if the heat flux is not exchanged at the interface, then

$$q_z = 0 \ , \quad \text{at} \quad z = 0 \ . \tag{46}$$

It is noticed from Table 1 that the source coefficients S_1 and S_2 have different values according to $z > -h$ and $z < -h$. Let $S_1'$and S_2' be the values of S_1 and S_2 respectively, for $z > -h$. The boundary conditions 45 and 46 yield the system

$$mB_1 + kB_2 - kB_3 + kC_1 + kC_2 = \left(S_1' - S_2' + S_2' kh\right) e^{-kh} \ , \tag{47}$$

$$kB_1 + kB_2 - kC_1 = \left(S_1' + S_2' kh\right) e^{-kh} \ , \tag{48}$$

$$kB_1 + kB_2 + 2k\left(\upsilon_u - 1\right) B_3 - \mu_r kC_1 - 2\mu_r k\left(1 - \upsilon'\right) C_2 = \mu_r \left(S_1' + S_2' kh - 2S_2' + 2S_2' \upsilon'\right) e^{-kh} \ , \tag{49}$$

$$mB_1 + kB_2 + k\left(1 - 2\upsilon_u\right) B_3 + \mu_r kC_1 - \mu_r k\left(1 - 2\upsilon'\right) C_2 = \mu_r \left(S_1' + S_2' kh + S_2' - 2S_2' \upsilon'\right) e^{-kh} \ , \tag{50}$$

$$mA_1 + kA_2 = 0 \ , \tag{51}$$

where $\mu_r = \mu/\mu'$.

On solving these equations, we have

$$\begin{gathered}
A_1 = \frac{\Omega}{2\eta} Q(k+m) S_2' e^{-kh} \ , \quad A_2 = -\frac{m}{k} A_1 \ , \\
B_1 = \frac{\Omega}{k-m} Q S_2' e^{-kh}, \ B_2 = \left[-\frac{P_2}{k}\left(S_1' - \frac{S_2'}{2} + S_2' kh \right) + \frac{Q S_2'}{2k}\left(1 - \frac{k+m}{k-m}\Omega \right) \right] e^{-kh}, \ B_3 = \frac{Q}{k} S_2' e^{-kh}, \\
C_1 = \left[-\frac{P_1}{k}\left(S_1' + S_2' kh \right) + \frac{S_2'}{2k}\left(P_2 + (1+\Omega) Q \right) \right] e^{-kh}, \quad C_2 = \frac{P_1}{k}\left(2S_1' - S_2' + 2S_2' kh \right) e^{-kh},
\end{gathered} \tag{52}$$

where

$$\begin{gathered}
P_1 = \frac{1-\mu_r}{1+3\mu_r - 4\mu_r \upsilon'} \ , \quad P_2 = P_1 - 1 \ , \quad P_3 = \frac{4\upsilon_u - 3 - \mu_r}{1-\mu_r} \ , \\
Q = \frac{P_2}{P_1 (P_3 + \Omega)} \ , \quad \Omega = \frac{k^2 \gamma}{m(m+k)} \ , \quad \gamma = \frac{2(\upsilon - \upsilon_u)}{1-\upsilon} \ .
\end{gathered} \tag{53}$$

Substituting the values of A_i, B_i, C_i's from Eqs. 52 in Eqs. 27-29, 33-34, 40-44, and 25, we get the integral expressions for the stress components and displacement components in Medium I and II, and the temperature difference in Medium I in terms of the source coefficients S_1' and S_2'.

These integrals can be solved numerically for arbitrary values of ω. However, analytical solutions can be found for two particular cases:

Case (i) $\omega \to \infty$ which further implies that no net flow of heat takes place, *i.e.*, the adiabatic condition.

Case (ii) $\omega \to 0$ which further implies that $\theta \to 0$, *i.e.*, the isothermal condition.

5. VERTICAL DIP SLIP DISLOCATION

Following Maruyama (1966), the double couple $(yz) + (zy)$ is equivalent to a vertical dip slip dislocation so that its moment can be represented as

$$D_{yz} = \mu' b\, ds \ , \tag{54}$$

where b is the slip and ds is the width of the line dislocation.

From Table 1, we have

$$S_1' = 0 \, , \quad S_2' = \alpha' \frac{D_{yz}}{\pi} = \frac{D_{yz}}{2\pi(1-\upsilon')} \ , \tag{55}$$

with the stipulation that in the representation of integrals, the upper sign is to be selected.

The results for the two limiting cases, $\omega \to \infty$ and $\omega \to 0$, are obtained in analytical form as follows:

Case (i) Adiabatic case

$$U = \alpha' \frac{D_{yz}}{\pi} \left[\frac{1}{2} \left(P_2 + Q_2 \right) \tan^{-1} \left(\frac{y}{z+h} \right) + \left(-P_2 h + Q_2 z \right) \frac{y}{R_1^2} \right] , \tag{56}$$

$$\sigma_{yy} = \frac{\alpha' D_{yz}}{\pi} \frac{y}{R_1^4} \left[P_2 \left(z + 3h \right) - Q_2 \left(5z + 3h \right) + 8 \left(Q_2 z - P_2 h \right) \frac{(z+h)^2}{R_1^2} \right] , \tag{57}$$

$$\sigma_{yz} = \frac{\alpha' D_{yz}}{\pi} \frac{1}{R_1^2} \left[\frac{1}{2} (Q_2 - P_2) + \left\{ P_2 (z + 7h) - Q_2 (7z + h) \right\} \frac{(z+h)}{R_1^2} + \frac{8 (Q_2 z - P_2 h)(z+h)^3}{R_1^4} \right] , \tag{58}$$

$$\sigma_{zz} = -\frac{\alpha' D_{yz}}{\pi} \frac{y}{R_1^4} \left[P_2 (z + 3h) - Q_2 (z - h) + 8 \left(Q_2 z - P_2 h \right) \frac{(z+h)^2}{R_1^2} \right] , \tag{59}$$

$$\varepsilon_{yy} = \frac{\alpha' D_{yz}}{2\mu\pi} \frac{y}{R_1^4} \left[P_2 (z+3h) - Q_2 \left(5z+3h + \left(\frac{\alpha_0 \gamma}{\eta} - 4\upsilon \right) (z+h) \right) + 8 \left(Q_2 z - P_2 h \right) \frac{(z+h)^2}{R_1^2} \right] , \tag{60}$$

$$\varepsilon_{yz}=\frac{\alpha' D_{yz}}{2\mu\pi}\frac{1}{R_1^2}\left[\frac{1}{2}(Q_2-P_2)+\{P_2(z+7h)-Q_2(7z+h)\}\frac{(z+h)}{R_1^2}+\frac{8(Q_2z-P_2h)(z+h)^3}{R_1^4}\right], \tag{61}$$

$$\varepsilon_{zz}=-\frac{\alpha' D_{yz}}{2\mu\pi}\frac{y}{R_1^4}\left[P_2(z+3h)-Q_2\left((z-h)+\left(4\upsilon-\frac{\alpha_0\gamma}{\eta}\right)(z+h)\right)+8\left(Q_2z-P_2h\right)\frac{(z+h)^2}{R_1^2}\right], \tag{62}$$

$$u_y=\frac{\alpha' D_{yz}}{2\mu\pi}\frac{1}{R_1^2}\left[-\frac{1}{2}\left[P_2(z+3h)+Q_2(h-z)-4Q_4(z+h)\right]-2\left(Q_2z-P_2h\right)\frac{(z+h)^2}{R_1^2}\right], \tag{63}$$

$$u_z=\frac{\alpha' D_{yz}}{2\mu\pi}\frac{y}{R_1^2}\left[\frac{1}{2}\left(P_2-Q_2+4Q_4\right)+2\left(Q_2z-P_2h\right)\frac{(z+h)}{R_1^2}\right], \tag{64}$$

$$\theta=-\frac{\alpha' D_{yz}}{\pi}\left(\frac{\gamma}{\eta}\right)Q_2\frac{y(z+h)}{R_1^4}, \tag{65}$$

where $R_1^2=y^2+(z+h)^2$, $Q_2=P_2/P_1P_3$, and $Q_4=Q_2(1-\upsilon_u)$.

For the above limiting case, the solutions for the elastic half space are obtained as follows:

$$\Phi=\frac{\alpha' D_{yz}}{\pi}\left[y(z+h)\frac{1}{R_1^2}+\frac{1}{2}\left(P_2+Q_2\right)\tan^{-1}\left(\frac{y}{h-z}\right)-P_1\frac{y(z+h)}{R_2^2}+4P_1h\frac{yz(h-z)}{R_2^4}\right], \tag{66}$$

$$\sigma'_{yy}=\frac{\alpha' D_{yz}y}{\pi}\left[2\left(-3+4\frac{(z+h)^2}{R_1^2}\right)\frac{(z+h)}{R_1^4}+\left(P_2+Q_2\right)\frac{(h-z)}{R_2^4}-2P_1(5h-3z)\frac{1}{R_2^4}\right.$$
$$\left.+8P_1\left(h-z\right)\left(z^2+3h^2-10hz\right)\frac{1}{R_2^6}+96P_1hz\frac{(h-z)^3}{R_2^8}\right], \tag{67}$$

$$\sigma'_{zz}=\frac{\alpha' D_{yz}y}{\pi}\left[2\left(1-4\frac{(z+h)^2}{R_1^2}\right)\frac{(z+h)}{R_1^4}-\left(2P_1(z+h)+(P_2+Q_2)(h-z)\right.\right.$$
$$\left.\left.-8P_1(h-z)(h^2-z^2+6hz)\frac{1}{R_2^2}+96P_1hz\frac{(h-z)^3}{R_2^4}\right)\frac{1}{R_2^4}\right], \tag{68}$$

$$\sigma'_{yz}=\frac{\alpha' D_{yz}}{\pi}\left[\left(1-8\left(\frac{z+h}{R_1}\right)^2+8\left(\frac{z+h}{R_1}\right)^4\right)\frac{1}{R_1^2}+\left(\frac{1}{2}\left(P_2+Q_2-2P_1\right)+\left(8P_1-P_2-Q_2\right)\frac{(h-z)^2}{R_2^2}\right.\right.$$
$$\left.\left.-12P_1hz\frac{1}{R_2^2}-8P_1\frac{(h-z)^4}{R_2^4}\right)\frac{1}{R_2^2}+96P_1hz\frac{(h-z)^2}{R_2^6}\left(1-\left(\frac{h-z}{R_2}\right)^2\right)\right], \tag{69}$$

$$\varepsilon'_{yy} = \frac{\alpha' D_{yz} y}{2\mu'\pi}\left[2\left(-3 + 2\upsilon + 4\frac{(z+h)^2}{R_1^2}\right)\frac{(z+h)}{R_1^4} + (P_2 + Q_2)\frac{(h-z)}{R_2^4} \right.$$
$$- 2P_1\left(5h - 3z - \upsilon(6\mathrm{h} - 2z)\right)\frac{1}{R_2^4}$$
$$\left. + 8P_1(h-z)\left(z^2 + 3h^2 - 10hz - 4\upsilon h(\mathrm{h}-\mathrm{z})\right)\frac{1}{R_2^6} + 96P_1 hz\frac{(h-z)^3}{R_2^8}\right], \quad (70)$$

$$\varepsilon'_{zz} = \frac{\alpha' D_{yz} y}{2\mu'\pi}\left[2\left(1 + 2\upsilon - 4\frac{(z+h)^2}{R_1^2}\right)\frac{(z+h)}{R_1^4} - \left\{ 2P_1\left((z+h) - \upsilon(6h - 2z)\right) + (P_2 + Q_2)(h-z)\right.\right.$$
$$\left.\left. - 8P_1(h-z)\left(h^2 - z^2 + 6hz - 4\upsilon(h-z)\right)\frac{1}{R_2^2} + 96P_1 hz\frac{(h-z)^3}{R_2^4}\right\}\frac{1}{R_2^4}\right], \quad (71)$$

$$\varepsilon'_{yz} = \frac{\alpha' D_{yz}}{2\mu'\pi}\left[\left(1 - 8\left(\frac{z+h}{R_1}\right)^2 + 8\left(\frac{z+h}{R_1}\right)^4\right)\frac{1}{R_1^2} + \left(\frac{1}{2}\left(P_2 + Q_2 - 2P_1\right) + \left(8P_1 - P_2 - Q_2\right)\frac{(h-z)^2}{R_2^2}\right.\right.$$
$$\left.\left. - 12P_1 hz\frac{1}{R_2^2} - 8P_1\frac{(h-z)^4}{R_2^4}\right)\frac{1}{R_2^2} + 96P_1 hz\frac{(h-z)^2}{R_2^6}\left(1 - \left(\frac{h-z}{R_2}\right)^2\right)\right], \quad (72)$$

$$u'_y = \frac{\alpha' D_{yz}}{2\mu'\pi}\left[\left(3 - 2\upsilon' - 2\frac{(z+h)^2}{R_1^2}\right)\frac{(z+h)}{R_1^2} - \left(\frac{1}{2}(P_2 + Q_2)(h-z) + P_1(h+z)\right.\right.$$
$$\left. + 2(1-\upsilon')\ P_1(z-3h)\right)\frac{1}{R_2^2}$$
$$\left. + 2P_1\left(h^2 - z^2 + 6hz - 4(1-\upsilon')h(h-z)\right)\frac{(h-z)}{R_2^4} - 16P_1 hz\frac{(h-z)^3}{R_2^6}\right], \quad (73)$$

$$u'_z = \frac{\alpha' D_{yz} y}{2\mu'\pi}\left[\left((1 - 2\upsilon') + 2\frac{(z+h)^2}{R_1^2}\right)\frac{1}{R_1^2} - \left(\frac{1}{2}(P_2 + Q_2) + P_1(1-2\upsilon')\right)\frac{1}{R_2^2}\right.$$
$$\left. + 2P_1\left(3h^2 - z^2 - 4\upsilon' h(h-z)\right)\frac{1}{R_2^4} - 16P_1 hz\frac{(h-z)^2}{R_2^6}\right], \quad (74)$$

where $R_2^2 = y^2 + (z-h)^2$.

Case (ii) Isothermal case

To obtain the results for this particular case, we define

$$P_4 = \frac{4\upsilon - 3 - \mu_r}{1 - \mu_r} \quad Q_1 = \frac{P_2}{P_1 P_4} \quad \text{and} \quad Q_3 = (1-\upsilon)Q_1\ . \quad (75)$$

The expressions for stress components and displacement components for the present case of isothermal are similar to that for the Case (i) if we replace Q_2 by Q_1 and Q_4 by Q_3. These results coincide with the corresponding expressions for a source in an elastic half space in welded contact with another elastic half space (Singh *et al.* 1992).

6. NUMERICAL RESULTS AND DISCUSSION

Equations 57-64 and 67-74 can be used for computing the stresses, strain and displacements in the two half spaces under adiabatic (thermal equilibrium) conditions. The temperature difference is given by Eq. 65. To obtain the results for the stresses, strain, and displacements under isothermal conditions, Q_2 and Q_4 are changed to Q_1 and Q_3 respectively, in Eqs. 57-64 and 67-74. Following Aki and Richards (1980) and Ahrens (1995), the parameters for thermoelastic medium (Pyrope rich garnet) are taken as

$$\mu = 8.51514\times(10)^{10}\,\mathrm{kg\,m^{-1}s^{-2}},\ \lambda = 11.4508\times(10)^{10}\,\mathrm{kg\,m^{-1}s^{-2}},\ \alpha_t = 3.11\times(10)^{-5}\,\mathrm{K^{-1}},$$
$$\rho = 3620\ \mathrm{kg\,m^{-3}},\ T_0 = 1000\ \mathrm{K},\ C_e = 1076\ \mathrm{m^2K^{-1}s^{-2}},\ \beta = (3\lambda + 2\mu)\alpha_t . \tag{76}$$

For the elastic half space, the Poisson ratio (υ') is taken as 0.25. To make the quantities dimensionless, the followings are defined

$$Y = \frac{y}{h},\quad Z = \frac{z}{h},\quad T = \frac{2ct}{h^2},\quad U_i' = \frac{h}{bds}u_i ,$$
$$\Theta = \frac{h^2}{\mu' bds}\theta,\quad \Sigma_{ij} = \frac{h^2}{\mu' bds}\sigma_{ij},\quad \Sigma_{ij}' = \frac{h^2}{\mu' bds}\sigma_{ij}' . \tag{77}$$

The displacements, strain and stresses generated by a vertical dip-slip dislocation located at a point $(0, 0, -h)$ of the elastic half space are computed.

For $z = 0$, the displacement components for both the limiting cases, adiabatic and isothermal, are computed and shown in Fig. 2 for $\mu_r = 0.5$. Here μ_r is the ratio of rigidity of thermoelastic and elastic half spaces. For $\mu_r = 2$, the displacement components are compared in Fig. 3. It is noticed that the difference between adiabatic and isothermal deformations is more significant when the thermoelastic half space is more rigid than the elastic half space. The more rigid the elastic half space, the larger the horizontal and vertical displacements are.

Assuming that $\mu_r = 2$, the variation of the dimensionless stresses (Σ_{yy}, Σ_{zz}, and Σ_{yz}) with dimensionless horizontal distance (Y) from the fault is shown in Figs. 4a, 5a, and 6a for $z = 0$ and that for $z = h$ is shown in Figs. 4b, 5b, and 6b. At the interface $z = 0$, the stresses Σ_{zz} and Σ_{yz} first decrease with Y and then increase steadily when horizontal distance is a little

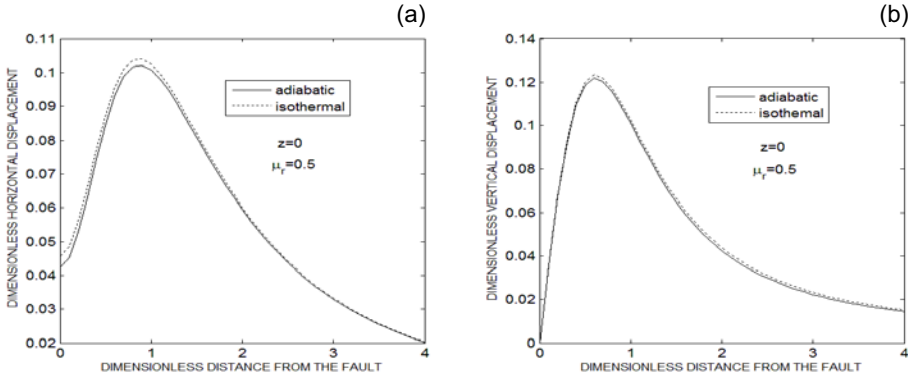

Fig. 2. Variation of horizontal and vertical displacements at the interface $z = 0$ with horizontal distance from the fault for $\mu_r = 0.5$.

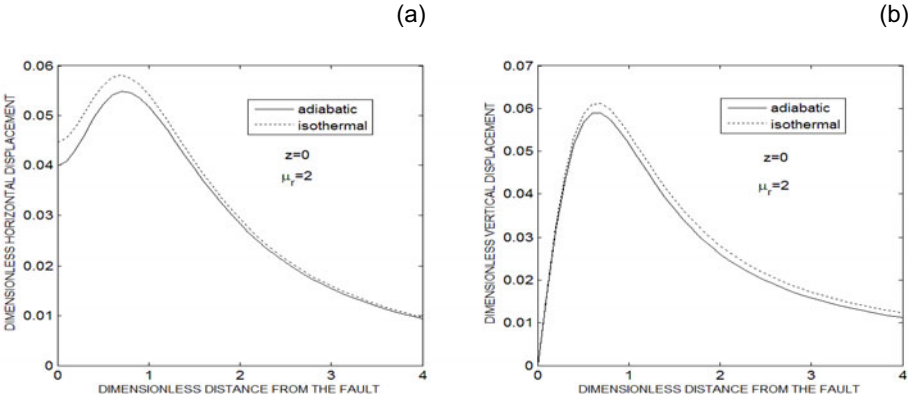

Fig. 3. Variation of horizontal and vertical displacements at the interface $z = 0$ with horizontal distance from the fault for $\mu_r = 2$.

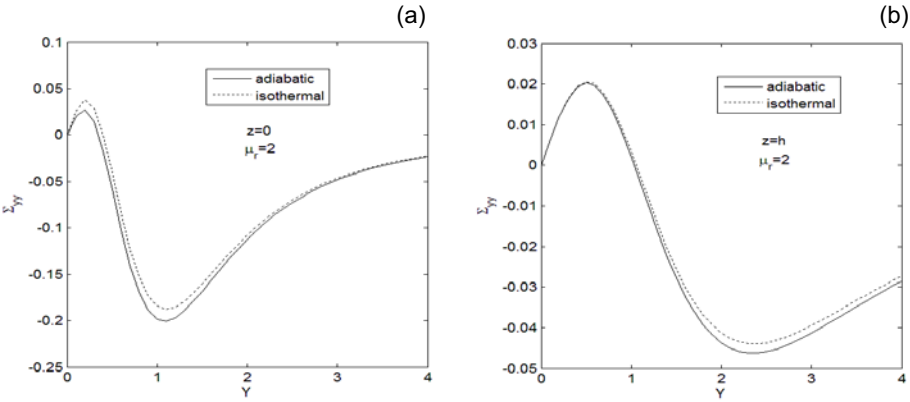

Fig. 4. Variation in dimensionless stress Σ_{yy} in the thermoelastic half space with horizontal distance from the fault $z = 0$ (a), and $z = h$ (b).

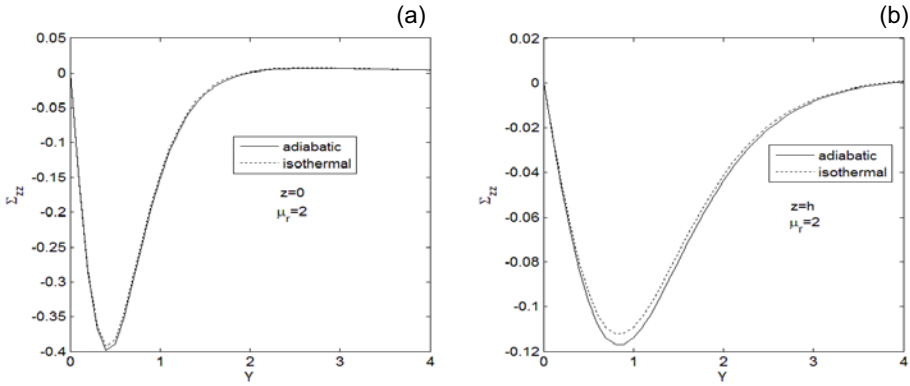

Fig. 5. Variation in dimensionless stress Σ_{zz} in the thermoelastic half space with horizontal distance from the fault $z = 0$ (a), and $z = h$ (b).

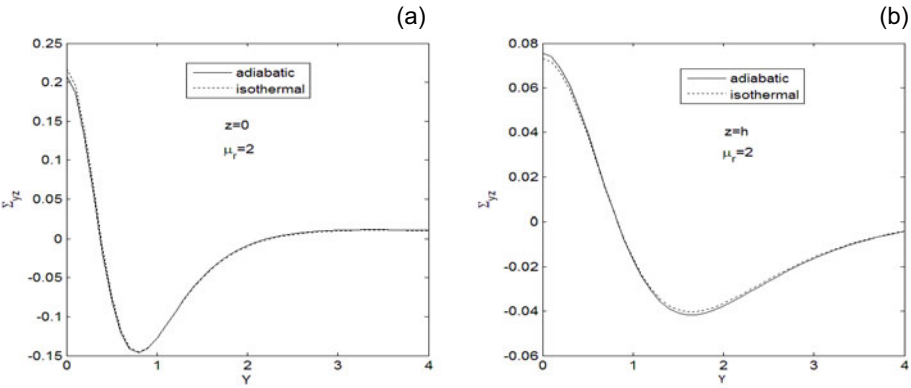

Fig. 6. Variation in dimensionless stress Σ_{yz} in the thermoelastic half space with horizontal distance from the fault $z = 0$ (a), and $z = h$ (b).

less than the depth of the source. As the horizontal distance increases further, *i.e.*, more than twice of the source depth, Σ_{zz} and Σ_{yz} approach to zero. However, Σ_{yy} first increases then decreases and then again increases with Y. The variation pattern of Σ_{yy}, Σ_{zz}, and Σ_{yz} gets smoother for $z = h$, as evident from Figs. 4b-6b. In Figure 7, depth profiles of the stresses Σ_{yy}, Σ_{zz}, and Σ_{yz} are exhibited for $y = h$, $\mu_r = 2$. The stress Σ_{yy} has a maximum value near the plane of source, *i.e.*, $z = -h$. As it goes away from the plane of source towards the interface, it firstly decreases and then increases. It experiences a discontinuity at the interface. Below the plane $z = h$ and above the plane $z = -3h$, the stress Σ_{yy} becomes stable and approaches to zero. In the case of Σ_{yz} and Σ_{zz}, the stresses are continuous at the interface, as expected from the boundary conditions. As we move away from the interface in the elastic medium, Σ_{zz} increases up to a little before the source plane $z = -h$, decreases and

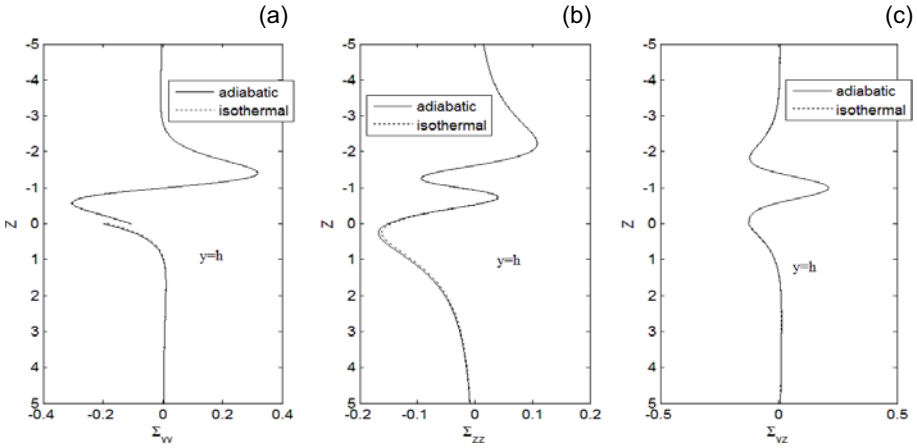

Fig. 7. Variation in dimensionless stresses Σ_{yy} (a), Σ_{zz} (b), and Σ_{yz} (c) with distance from the interface for $y = h$.

increases rapidly up to $z = -2h$, then smoothly decreases and approaches to zero. Similarly, in the thermoelastic half space, it increases smoothly and approaches to zero. The stress Σ_{yz} is greatest on the plane of source, decreases up to a distance h and then increases and approach to zero which is a physically plausible situation also. It is symmetric about the plane of source. No major difference in the variation of the stresses for the two limiting cases is noticed.

From the Eqs. 25, 27-29, 33-34, and 40-44, we get the integral expressions for the temperature, displacements, and stresses at any point in each of the two half spaces caused by a vertical dip slip dislocation located at the point $(0, 0, -h)$ of the elastic half space in $k - \omega$ domain. On replacing $(-i\omega)$ by s, we get the solutions in Fourier–Laplace transform domain, where s is the Laplace transforming variable. Two integrations are required to be performed to get the solution in the space time domain. Schapery (1962) proposed a very simple and efficient approximate formula for finding Laplace inversion numerically. Accordingly, it can be written as

$$\theta(t) \approx [s\bar{\theta}(s)]_{s=1/(2t)} \ , \tag{78}$$

where $\bar{\theta}(s)$ is the Laplace transform of $\theta(t)$.

Inverse Fourier transform is computed numerically. Due to exponential decay, the integrands decrease very rapidly with k.

Figure 8 demonstrates the variation of temperature with time at different depths. It is noticed that the deviation is significant near the interface and the temperature difference approaches to zero as time increases at all depth.

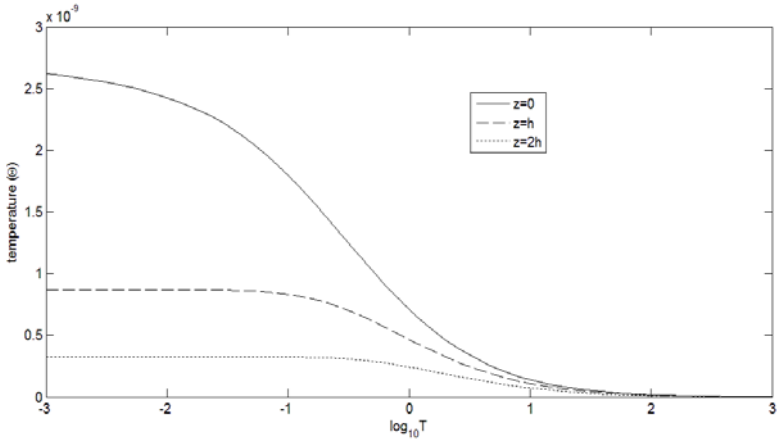

Fig. 8. Diffusion of the temperature difference Θ with T for $y = h$ and $z = 0$, h, $2h$.

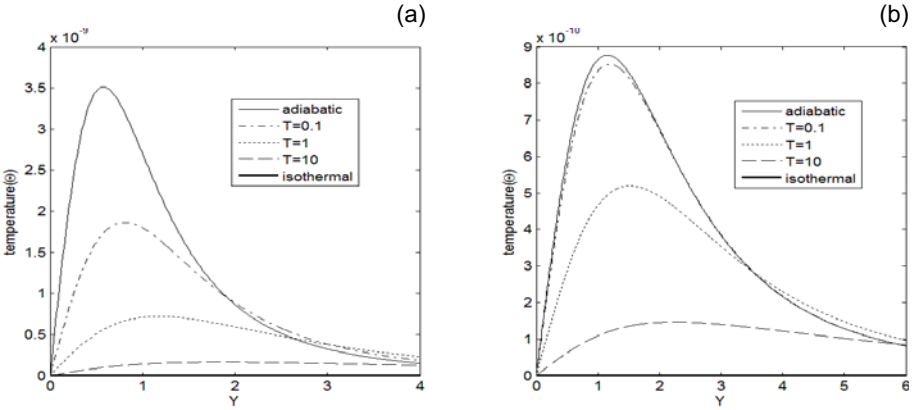

Fig. 9. Variation of the temperature difference Θ with the horizontal distance Y from the fault for $y = h$ at five times $T = 0$, 0.1, 1, 10, ∞ for $z = 0$ (a), and $z = h$ (b).

Temperature difference's variation with Y for different times $T = 0$ (adiabatic), 0.1, 1, 10, ∞ (isothermal), for $z = 0$ and $z = h$ is shown in Fig. 9. As expected, the temperature difference is found zero in the isothermal state. The point of maxima of the temperature difference moves away from the source with time. The temperature difference at different times is more significant on the interface. For all the times, the curves tend to merge for large Y. As T increases, maximum value of temperature difference decreases and maxima travels rightwards with Y.

Figure 10 depicts the depth profile of temperature difference at different times: $T = 0$ (adiabatic), 0.1, 1, 10, ∞ (isothermal). Temperature difference is greatest on the interface and strongly depends on time. As the distance from the interface increases, the temperature difference diffuses rapidly.

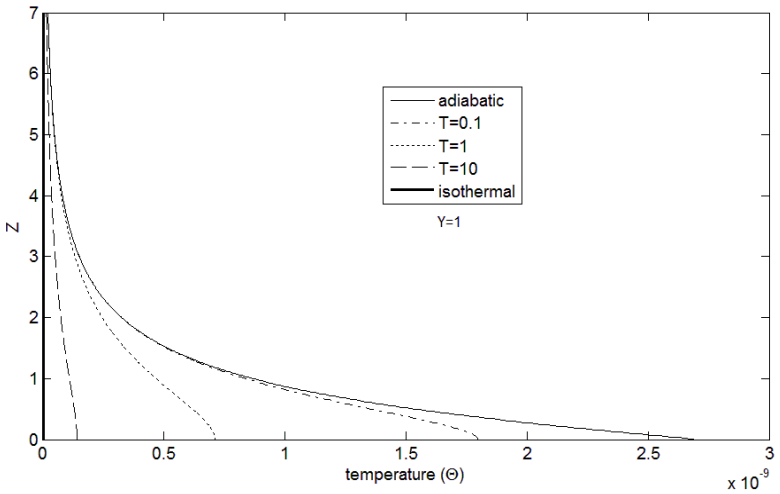

Fig. 10. Variation of the temperature difference Θ with the distance from the interface for $y = h$ at $T = 0, 0.1, 1, 10, \infty$.

Figures 11-15 exhibit time history of dimensionless displacements and stresses for $y = h$: (a) $z = 0$, and (b) $z = 2h$. It is noticed that, at the interface, horizontal displacement and Σ_{yz} decrease slowly with T and then increase, but the vertical displacement and stresses Σ_{yy} and Σ_{zz} increase with time. At $z = 2h$, the horizontal displacement and Σ_{zz} increase with time but the vertical displacement, stresses Σ_{yy} and Σ_{yz} firstly decrease then increase. It is noticed that as the distance from the interface increases, the point of minima of the displacements and stresses move rightward along the time. Also, the variation in displacements and stresses is significant in the range $T = 0.01$ to $T = 100$.

The stress Σ_{yy}'s variation with temperature and with horizontal distance from the fault is shown in Fig. 16. Similarly, the stresses profiles of Σ_{zz} and Σ_{yz} are shown in the Figs. 17 and 18. It can be concluded from these graphs that temperature distribution does not have a major role in the determination of stresses in the thermoelastic half space except in the vicinity of the fault plane. In Fig. 19, the stress profiles with temperature and distance from the interface are depicted. These graphs also confirm the observations about stress variation with Z made earlier.

Deformation in elastic medium is presented in Figs. 20-23.Variation of horizontal and vertical displacements at $z = -1.5h$ with horizontal distance from the fault are presented in Fig. 20 and that at $z = -5h$ are presented in Fig. 21. Horizontal displacement first decreases and then increases and approaches to zero. Vertical displacement first increases, then deceases and

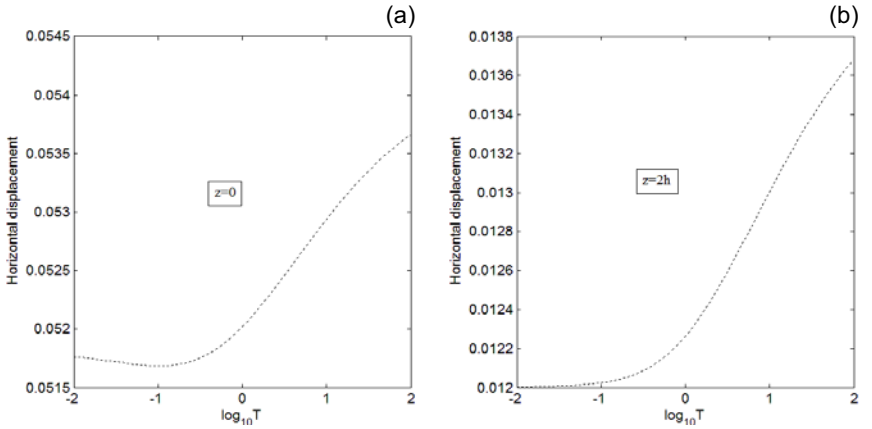

Fig. 11. Variation of horizontal displacement with time T: (a) $z = 0$, and (b) $z = 2h$.

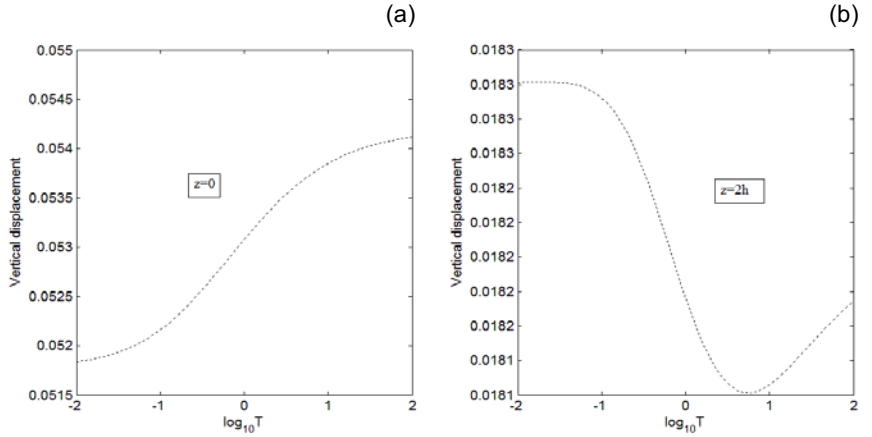

Fig. 12. Variation of vertical displacement with time T: (a) $z = 0$, and (b) $z = 2h$.

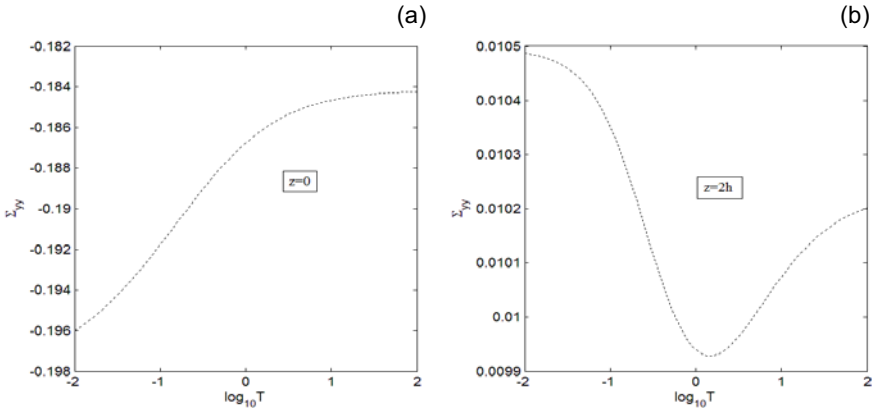

Fig. 13. Variation of stress Σ_{yy} with time T: (a) $z = 0$, and (b) $z = 2h$.

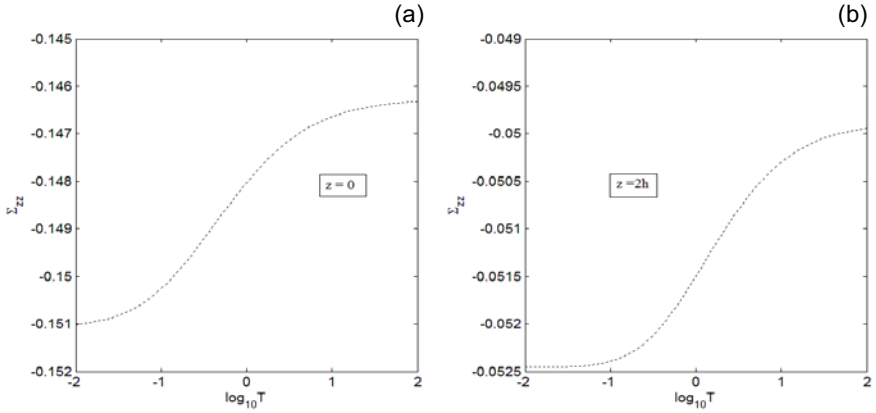

Fig. 14. Variation of stress Σ_{zz} with time T: (a) $z = 0$, and (b) $z = 2h$.

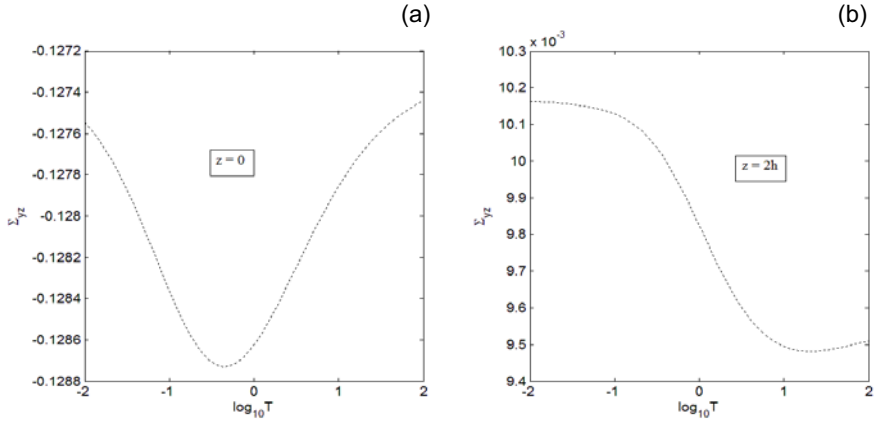

Fig. 15. Variation of stress Σ_{yz} with time T: (a) $z = 0$, and (b) $z = 2h$.

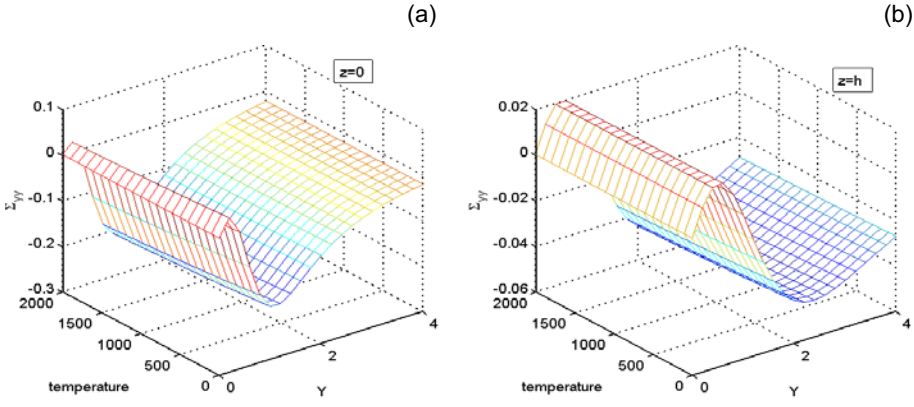

Fig. 16. Variation of stresses Σ_{yy} with temperature and distance from fault $z = 0$ (a), and $z = h$ (b).

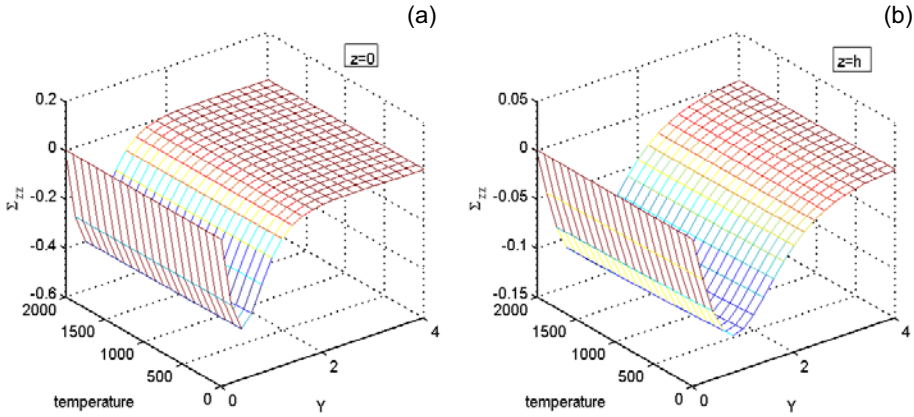

Fig. 17. Variation of stresses Σ_{zz} with temperature and distance from fault $z = 0$ (a), and $z = h$ (b).

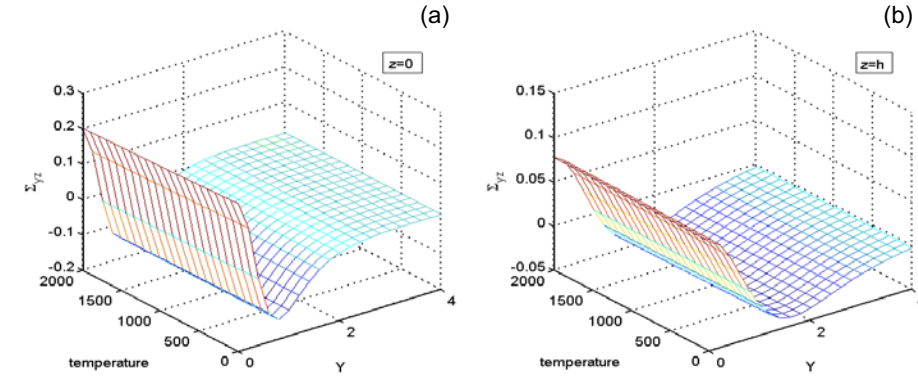

Fig. 18. Variation of stresses Σ_{yz} with temperature and distance from fault $z = 0$ (a), and $z = h$ (b).

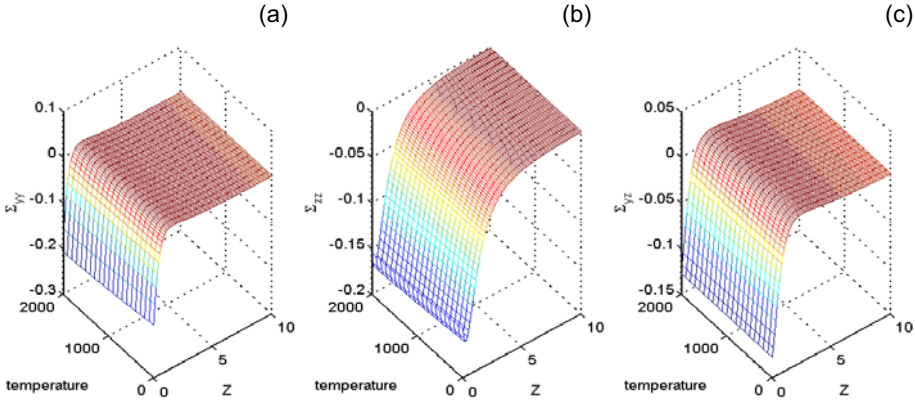

Fig. 19. Variation of stresses Σ_{yy} (a), Σ_{zz} (b), and Σ_{yz} (c) with temperature and distance from interface for $y = h$.

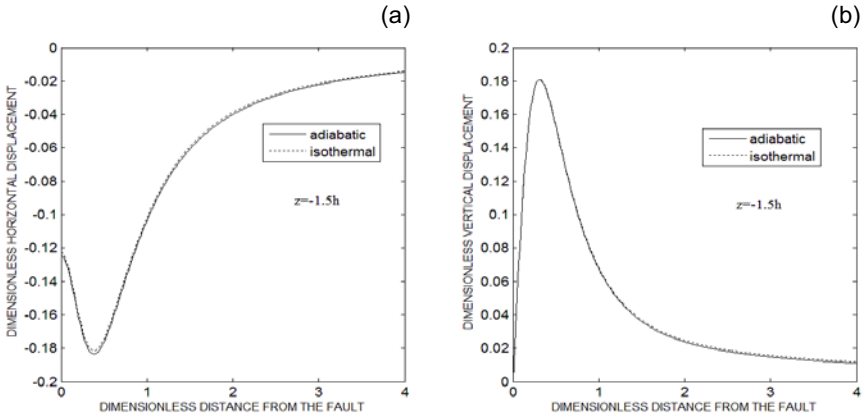

Fig. 20. Variation of horizontal and vertical displacements at $z = -1.5h$ with horizontal distance from the fault.

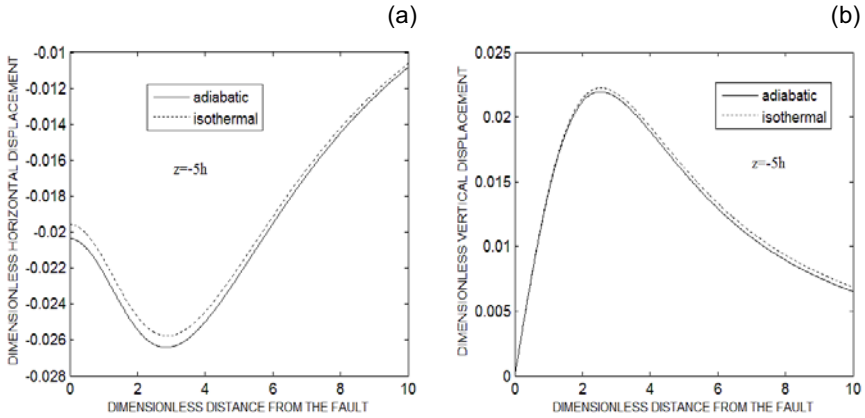

Fig. 21. Variation of horizontal and vertical displacements at $z = -5h$ with horizontal distance from the fault.

approaches to zero. It is noticed that difference in the two extreme cases (adiabatic and isothermal) is more significant at $z = -5h$ than $z = -1.5h$ but the displacements are more significant near the plane of source (*i.e.*, $z = -1.5h$).

Variation of the stresses $\Sigma'_{yy}, \Sigma'_{zz}, \Sigma'_{yz}$ at $z = -1.5h$ with horizontal distance from the fault are presented in Fig. 22a, b and that at $z = -5h$ are presented in Fig. 23a, b. The difference in the limiting cases is significant at far distance from the source. There is a sharp stress drop in elastic half space, *i.e.*, the region containing the fault in comparison to the other half space. At a sufficient distance from the source, the shear displacement increases steadily and the longitudinal displacement decreases steadily.

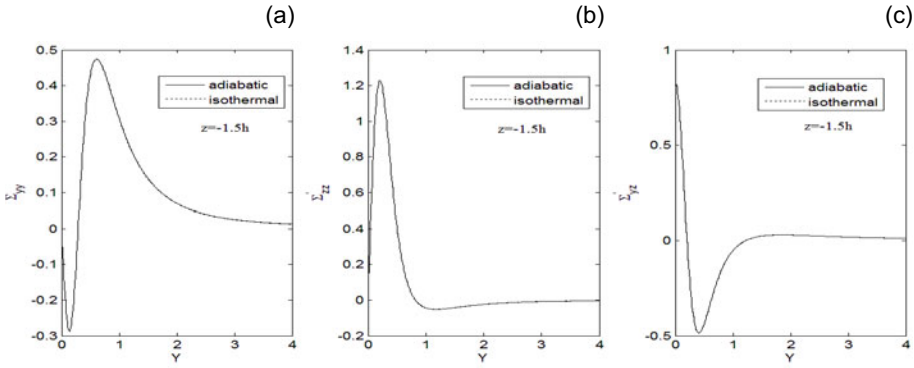

Fig. 22. Variation of stresses Σ'_{yy} (a), Σ'_{zz} (b), and Σ'_{yz} (c) at $z = -1.5h$ with horizontal distance from the fault.

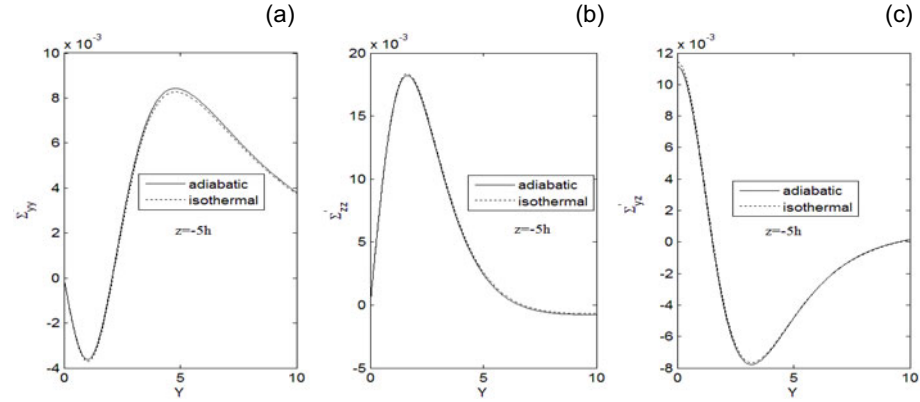

Fig. 23. Variation of the stresses Σ'_{yy} (a), Σ'_{zz} (b), and Σ'_{yz} (c) at $z = -5h$ with horizontal distance from the fault.

The effect of thermoelasticity in the deformation of elastic medium is more significant when the source is nearer to the interface $z = 0$. If the elastic medium is considered as the crustal layer of the Earth and mantle layer is modeled as thermoelastic medium, then due to the fault occurring in the crust near the mantle, the effect of thermoelasticity is significant on the Earth's surface.

List of parameters

Symbol	Description
x, y, z	Cartesian coordinates
t	time
u_i	displacement components of thermoelastic medium
h	distance of the source from interface
σ_{ij}	stress tensor of thermoelastic medium
ε_{ij}	strain tensor of thermoelastic medium
δ_{ij}	Kronecker delta
λ, μ	Lame's constants of thermoelastic medium
α_t	coefficient of linear thermal expansion
$\beta = (3\lambda + 2\mu)\alpha_t$	thermoelastic coupling coefficient
θ	difference between absolute temperature and temperature at the natural state
υ	Poisson's ratio of thermoelastic medium
λ_0	thermal conductivity
C_e	specific heat
ρ	density
T_0	temperature of the medium at natural state
q_i	components of heat flux
ω	frequency
u_i'	displacement components of elastic medium
μ'	shear modulus of elastic medium
υ'	Poisson's ratio of elastic medium
σ_{ij}'	stress tensor of elastic medium
μ_r	ratio of rigidity of thermoelastic and elastic mediums
Y, Z	dimensionless Cartesian coordinates
T	dimensionless time
U_i'	dimensionless displacement components
Θ	dimensionless temperature difference
Σ_{ij}	dimensionless stress tensor of thermoelastic medium
Σ_{ij}'	dimensionless stress tensor of elastic medium

References

Abd-Alla, A.M. (1995), Thermal stress in a transversely isotropic circular cylinder due to an instantaneous heat source, *Appl. Math. Comput.* **68**, 2-3, 113-124, DOI: 10.1016/0096-3003(94)00085-I.

Ahrens, T.J. (ed.) (1995), *Mineral Physics and Crystallography: A Handbook of Physical Constants*, American Geophysical Union, Washington, D.C.

Aki, K., and P.G. Richards (1980), *Quantitative Seismology: Theory and Methods*, Vol. I and II, W.H. Freeman & Co., San Francisco.

Attetkov, A.V., I.K. Volkov, and S.S. Pilyavskii (2009), Temperature field of a solid body containing a spherical heating source with a uniformly moving boundary, *J. Eng. Phys. Thermophys.* **82**, 2, 368-375, DOI: 10.1007/s10891-009-0185-x.

Ben-Menahem, A., and S.J. Singh (1981), *Seismic Waves and Sources*, 2nd ed., Springer Verlag, New York.

Burridge, R., and L. Knopoff (1964), Body force equivalents for seismic dislocations, *Bull. Seismol. Soc. Am.* **54**, 6a, 1875-1888.

Dziewonski, A.M., and D.L. Anderson (1981), Preliminary reference Earth model, *Phys. Earth Planet. In.* **25**, 4, 297-356, DOI: 10.1016/0031-9201(81)90046-7.

Freund, L.B., and D.M. Barnett (1976), A two-dimensional analysis of surface deformation due to dip-slip faulting, *Bull. Seismol. Soc. Am.* **66**, 3, 667-675.

Garg, N.R., and S.J. Singh (1987), 2-D static response of a transversely isotropic multilayered half-space to surface loads, *Indian J. Pure Appl. Math.* **18**, 8, 763-777.

Garg, N.R., D.K. Madan, and R.K. Sharma (1996), Two-dimensional deformation of an orthotropic elastic medium due to seismic sources, *Phys. Earth Planet. In.* **94**, 1-2, 43-62, DOI: 10.1016/0031-9201(95)03095-6.

Garg, N.R., R. Kumar, A. Goel, and A. Miglani (2003), Plane strain deformation of an orthotropic elastic medium using an eigenvalue approach, *Earth Planets Space* **55**, 1, 3-9, DOI: 10.1186/BF03352457.

Ghosh, M.K., and M. Kanoria (2007), Displacements and stresses in composite multi-layered media due to varying temperature and concentrated load, *Appl. Math. Mech.* **28**, 6, 811-822, DOI: 10.1007/s10483-007-0611-5.

Heaton, T.H., and R.E. Heaton (1989), Static deformations from point forces and force couples located in welded elastic Poissonian half-spaces: Implications for seismic moment tensors, *Bull. Seismol. Soc. Am.* **79**, 3, 813-841.

Hou, P.-F., A.Y.T. Leung, and C.-P. Chen (2008a), Fundamental solution for transversely isotropic thermoelastic materials, *Int. J. Solids Struct.* **45**, 2, 392-408, DOI: 10.1016/j.ijsolstr.2007.08.024.

Hou, P.-F., A.Y.T. Leung, and C.-P. Chen (2008b), Green's functions for semi-infinite transversely isotropic thermoelastic materials, *ZAMM J. Appl. Math. Mech*. **88**, 1, 33-41, DOI: 10.1002/zamm.200710355.

Hou, P.-F., L. Wang, and T. Yi (2009), 2D Green's functions for semi-infinite orthotropic thermoelastic plane, *Appl Math. Model.* **33**, 3, 1674-1682, DOI: 10.1016/j.apm.2008.03.004.

Hou, P.-F., S. He, and C.-P. Chen (2011), 2D general solution and fundamental solution for orthotropic thermoelastic materials, *Eng. Anal. Bound. Elem.* **35**, 1, 56-60, DOI: 10.1016/j.enganabound.2010.04.007.

Jovanovich, D.B., M.I. Husseini, and M.A. Chinnery (1974a), Elastic dislocations in a layered half-space – I. Basic theory and numerical methods, *Geophys. J. Int.* **39**, 2, 205-217, DOI: 10.1111/j.1365-246X.1974.tb05451.x.

Jovanovich, D.B., M.I. Husseini, and M.A. Chinnery (1974b), Elastic dislocations in a layered half-space – II. The point source, *Geophys. J. Int.* **39**, 2, 219-239, DOI: 10.1111/j.1365-246X.1974.tb05452.x.

Kit, H.S., B.E. Monastyrs'kyi, and O.P. Sushko (2001), Thermoelastic state of a semiinfinite body with plane surface crack under the action of heat sources, *Mater. Sci.* **37**, 4, 610-614, DOI: 10.1023/A:1013272721094.

Kumar, A., S.J. Singh, and J. Singh (2005), Deformation of two welded elastic half-spaces due to a long inclined tensile fault, *J. Earth Syst. Sci.* **114**, 1, 97-103, DOI: 10.1007/BF02702012.

Kumar, R., and R.R. Gupta (2009), Plane strain deformation in an orthotropic micropolar thermoelastic solid with a heat source, *J. Eng. Phys. Thermophys.* **82**, 3, 556-565, DOI: 10.1007/s10891-009-0220-y.

Kumar, R., and L. Rani (2004), Deformation due to mechanical and thermal sources in generalised orthorhombic thermoelastic material, *Sadhana* **29**, 5, 429-447, DOI: 10.1007/BF02703254.

Kumari, G., S.J. Singh, and K. Singh (1992), Static deformation of two welded elastic half-spaces caused by a point dislocation source, *Phys. Earth Planet. In.* **73**, 1-2, 53-76, DOI: 10.1016/0031-9201(92)90107-7.

Lanzano, P. (1986a), Thermoelastic deformations of Earth's lithosphere: A mathematical model, *Earth Moon Planets* **34**, 3, 283-304, DOI: 10.1007/BF00145087.

Lanzano, P. (1986b), Heat conduction within an elastic Earth, *Earth Moon Planets* **36**, 2, 157-166, DOI: 10.1007/BF00057608.

Lay, T., and T.C. Wallace (1995), *Modern Global Seismology*, Academic Press, San Diego.

Madan, D.K., K. Singh, R. Aggarwal, and A. Gupta (2005), Displacements and stresses in an anisotropic medium due to non-uniform slip along a very long strike-slip fault, *ISET J. Earthq. Technol.* **42**, 1, 1-11.

Mallik, S.H., and M. Kanoria (2008), A two dimensional problem for a transversely isotropic generalized thermoelastic thick plate with spatially varying heat source, *Eur. J. Mech. A* **27**, 4, 607-621, DOI: 10.1016/j.euromechsol.2007.09.002.

Maruyama, T. (1964), Statical elastic dislocations in an infinite and semi-infinite medium, *Bull. Earthq. Res. Inst. Univ. Tokyo* **42**, 2, 289-368.

Maruyama, T. (1966), On two-dimensional elastic dislocations in an infinite and semi-infinite medium, *Bull. Earthq. Res. Inst. Univ. Tokyo* **44**, 811-871.

Nowacki, W. (1975), *Dynamical Problems of Thermoelasticity*, PWN Polish Sci. Publ., Warszawa, Noordhoff Int. Publ., Leyden.

Okada, Y. (1985), Surface deformation due to shear and tensile faults in a half-space, *Bull. Seismol. Soc. Am.* **75**, 4, 1135-1154.

Okada, Y. (1992), Internal deformation due to shear and tensile faults in a half-space, *Bull. Seismol. Soc. Am.* **82**, 2, 1018-1040.

Pan, E. (1989a), Static response of a transversely isotropic and layered half-space to general surface loads, *Phys. Earth Planet. In.* **54**, 3-4, 353-363, DOI: 10.1016/0031-9201(89)90252-5.

Pan, E. (1989b), Static response of a transversely isotropic and layered half-space to general dislocation sources, *Phys. Earth Planet. In.* **58**, 2-3, 103-117, DOI: 10.1016/0031-9201(89)90046-0.

Pan, E. (1990), Thermoelastic deformation of a transversely isotropic and layered half-space by surface loads and internal sources, *Phys. Earth Planet. Int.* **60**, 1-4, 254-264, DOI: 10.1016/0031-9201(90)90266-Z.

Rani, S., S.J. Singh, and N.R. Garg (1991), Displacements and stresses at any point of a uniform half-space due to two-dimensional buried sources, *Phys. Earth Planet. Int.* **65**, 3-5, 276-282, DOI: 10.1016/0031-9201(91)90134-4.

Rongved, L., and J.T. Frasier (1958), Displacement discontinuity in the elastic half-space, *J. Appl. Mech*. **25**, 125-128.

Rundle, J.B. (1982), Some solutions for static and pseudo-static deformation in layered, nonisothermal, porous media, *J. Phys. Earth* **30**, 5, 421-440, DOI: 10.4294/jpe1952.30.421.

Sato, R. (1971), Crustal deformation due to dislocation in a multi-layered medium, *J. Phys. Earth* **19**, 1, 31-46, DOI: 10.4294/jpe1952.19.31.

Sato, R., and M. Matsu'ura (1973), Static deformations due to the fault spreading over several layers in a multi-layered medium. Part I: Displacement, *J. Phys. Earth* **21**, 3, 227-249, DOI: 10.4294/jpe1952.21.227.

Schapery, R.A. (1962), Approximate methods of transform inversion for viscoelastic stress analysis. **In:** *Proc. 4th U.S. National Congress of Applied Mechanics, 18-21 June 1962, Berkeley USA*, Vol. 2, 1075-1085, American Society of Mechanical Engineers, New York.

Shevchenko, V.P., and A.S. Gol'tsev (2001), The thermoelastic state of orthotropic shells heated by concentrated heat sources, *Int. Appl. Mech.* **37**, 5, 654-661, DOI: 10.1023/A:1012364530719.

Singh, K., D.K. Madan, A. Goel, and N.R. Garg (2005), Two-dimensional static deformation of an anisotropic medium, *Sadhana* **30**, 4, 565-583, DOI: 10.1007/BF02703280.

Singh, S.J. (1970), Static deformation of a multilayered half-space by internal sources, *J. Geophys. Res.* **75**, 17, 3257-3263, DOI: 10.1029/JB075i017p03257.

Singh, S.J., and A. Ben-Menahem (1969), Displacement and strain fields due to faulting in a sphere, *Phys. Earth Planet. In.* **2**, 2, 77-87, DOI: 10.1016/0031-9201(69)90003-X.

Singh, S.J., and N.R Garg (1985), On two-dimensional elastic dislocations in a multilayered half-space, *Phys. Earth Planet. In.* **40**, 2, 135-145, DOI: 10.1016/0031-9201(85)90067-6.

Singh, S.J., and N.R. Garg (1986), On the representation of two-dimensional seismic sources, *Acta Geophys. Pol.* **34**, 1, 1-12.

Singh, S.J., A. Ben-Menahem, and M. Vered (1973), A unified approach to the representation of seismic sources, *Proc. Roy. Soc. London A* **331**, 1587, 525-551, DOI: 10.1098/rspa.1973.0006.

Singh, S.J., S. Rani, and N.R. Garg (1992), Displacements and stresses in two welded half-spaces caused by two-dimensional sources, *Phys. Earth Planet. In.* **70**, 1, 90-101, DOI: 10.1016/0031-9201(92)90164-Q.

Singh, S.J., G. Kumari, and K. Singh (1993), Static deformation of two welded elastic half-spaces caused by a finite rectangular fault, *Phys. Earth Planet. In.* **79**, 3, 313-333, DOI: 10.1016/0031-9201(93)90112-M.

Singh, S.J., A. Kumar, and J. Singh (2003), Deformation of a monoclinic elastic half-space by a long inclined strike-slip fault, *ISET J. Earthq. Technol.* **40**, 1, 51-59.

Small, J.C., and J.R. Booker (1986), The behaviour of layered soil or rock containing a decaying heat source, *Int. J. Numer. Anal. Meth. Geomech.* **10**, 5, 501-519, DOI: 10.1002/nag.1610100504.

Stein, S., and M. Wysession (2003), *An Introduction to Seismology, Earthquakes, and Earth Structure*, Blackwell Publishing, Oxford.

Steketee, J.A. (1958), On Volterra's dislocations in a semi-infinite elastic medium, *Can. J. Phys*. **36**, 2, 192-205, DOI: 10.1139/p58-024.

Tomar, S.K., and N.K. Dhiman (2003), 2-D deformation analysis of a half-space due to a long dip-slip fault at finite depth, *J. Earth Syst. Sci.* **112**, 4, 587-596, DOI: 10.1007/BF02709782.

Youssef, H.M. (2006), Problem of generalized thermoelastic infinite medium with cylindrical cavity subjected to a ramp-type heating and loading, *Arch. Appl. Mech*. **75**, 8-9, 553-565, DOI: 10.1007/s00419-005-0440-3.

Youssef, H.M. (2009), Generalized thermoelastic infinite medium with cylindrical cavity subjected to moving heat source, *Mech. Res. Commun.* **36**, 4, 487-496, DOI: 10.1016/j.mechrescom.2008.12.004.

Youssef, H.M. (2010), Two-temperature generalized thermoelastic infinite medium with cylindrical cavity subjected to moving heat source, *Arch. Appl. Mech.* **80**, 11, 1213-1224, DOI: 10.1007/s00419-009-0359-1.

Received 7 January 2014
Received in revised form 10 June 2014
Accepted 13 June 2014

DE GRUYTER OPEN

Acta Geophysica
vol. 63, no. 3, June 2015, pp. 634-651
DOI: 10.1515/acgeo-2015-0002

Imaging the Underground Coal Gasification Zone with Microgravity Surveys

Andrzej KOTYRBA, Łukasz KORTAS,
and Krzysztof STAŃCZYK

Central Mining Institute (GIG), Katowice, Poland
e-mails: a.kotyrba@gig.eu, l.kortas@gig.eu (corresponding author),
k.stanczyk@gig.eu

A b s t r a c t

The paper describes results of microgravity measurements made on the surface over an underground geo reactor where experimental coal gasification was performed in a shallow seam of coal. The aim of the research was to determine whether, and to what extent, the microgravity method can be used to detect and image a coal gasification zone, especially caverns where the coal was burnt out. In theory, the effects of coal gasification process create caverns and cracks, *e.g.*, zones of altered bulk density. Before the measurements, theoretical density models of completely and partially gasified coal were analysed. Results of the calculations of gravity field response showed that in both cases on the surface over the gasification zone there should be local gravimetric anomalies. Over the geo reactor, two series of gravimetric measurements prior to and after gasification were conducted. Comparison of the results of two measurement series revealed the presence of gravimetric anomalies that could be related to the cavern formation process. Data from these measurements were used to verify theoretical models. After the experiment, a small cavern was detected at the depth of the coal seam by the test borehole drilled in one of the anomalous areas.

Key words: microgravity, time lapse data, coal, gasification, control.

1. INTRODUCTION

Underground coal gasification (UCG) is a process of converting a solid body into an energy fuel in gas form, which occurs in a seam (Gregg and Edgar 1978, Burton *et al*. 2005, Shafirovich and Varma 2009). The very essence of the technology is to ignite coal in a seam, then maintaining the gasification process, and extracting the obtained gases to the surface, to some power devices, or a chemical processing installation. To gasify the coal, it is necessary to supply oxygen to the gasification area. It may be supplied either in the pure form as O_2 or in a jet of air. Additionally, steam can be also used as a gasifying factor. Depending on the type of medium introduced to the coal, output gas of different composition is obtained. The components of gas of energy value are: methane CH_4, hydrogen H_2, and carbon oxide CO. The processes occurring in a coal seam during underground gasification cause transformation and loss of its mass. The transformation may be complete and then a cavern formation is observed in the area where the coal had been gasified. It may be also a partial process, and then a zone of structurally and chemically transformed coal together with solid products such as char and ash remains in the coal seam. The combustion process is a dynamic phenomena accompanied by cracking of a coal block. Therefore, in some laboratory trials performed in Japan a seismoacoustic method was applied to observe and monitor the fissures creation and development (Itakura *et al.* 2010, Su *et al.* 2013). Recently, many articles dealing with UCG aspects are published. The current state of knowledge was summarized last year in a paper published in the journal *Progress in Energy and Combustion Science* (Bhutto *et al.* 2013). Among 123 references to this paper only one provides brief information concerning practical application of ground penetrating radar for imaging and monitoring the UCG process (Stańczyk *et al.* 2010).

Shape and structure of the coal transformation zone are crucial for assessing influence of underground coal gasification process on the geological environment. That is why, to use the technology, the methods which enable remote imaging of a gasification zone and controlling its development in a coal seam are so important, which in fact means testing the area with geophysical methods. One of them is the gravimetric method, because the results of measurements made with the method reflect density differentiation of geological formations adjacent to the surface (Jacoby and Smilde 2009). The method was successfully used in detecting underground caverns (Fajklewicz 1989, Styles *et al.* 2005). The process of underground coal gasification leads to mass loss in the volume of a seam where the process takes place. It increases differentiation of average bulk density of a layer of rock mass between the surface, where the measurement is made, and the area of the seam undergoing gasification.

Efficiency of the microgravity method in detecting caverns and zones of locally decreased density in relation to the surrounding rocks, *e.g.*, fracture zone, is limited by the depth of a seam and the size of the zones of locally altered density, caused by the coal gasification process. Hitherto applications of the gravimetric method show that it should be effective in case of shallow coal seams, located up to a few dozen meters deep, depending on the dimensions of the gasification zone. In the case of seams located deeper, the method may be also useful to record secondary effects of the gasification process which may occur in overlying rocks, *i.e.*, deformations of rock layers, changes in humidity resulting from heat propagation, *etc*. Information on the lack of such effects is also very important to assess the impact on the environment.

The tests were conducted during a gasification experiment on a block of coal in a seam called "geo reactor" limited by roadways at a depth of approx. 16 m, in Barbara experimental colliery. Location of a colliery on the map of Poland is shown in Fig. 1a. Their scope was to make two series of gravimetric measurements on the surface, above the place where gasification experiment took place. The first series of measurements was made before initiating the gasification process at the end of July 2013. The second series was made after finishing the gasification process in late August 2013.

2. GEOLOGICAL AND MINING CONDITIONS AT THE SITE OF EXPERIMENT

In the area of the underground coal gasification experiment, Carboniferous strata are covered with a thin layer of Quaternary sediments of a thickness of approximately 1-2 m. Carboniferous formations show regular stratification and appear in form of beds of sandstones, mudstones, and shales. Between the lithologic layers there are numerous coal seams of variable thickness, between a few centimeters and a few meters. The shallowest at the site is coal seam 310 which lies approx. 16 m below ground level of thickness ranging between 1.3 and 2.0 m. According to the mining plan shown in Fig. 1b the seam is oriented almost horizontally and not faulted. The nearest fault in coal deposit was encountered about 3 km to the east from the site of experiment. Seam 310 is accessible with two shafts and is cut with numerous roadways which are currently used for research and development purposes. The part of the seam where the gasification experiment was conducted is limited by roadways with a leak-tight concrete lining.

The geological structure of the overburden at the site of experiment was examined by a borehole B1, performed after experiment termination. Its lithological log is shown in Fig. 1c. According to the borehole data, the shale layer acts as the proximate roof of a coal seam. The shale beds dominate also

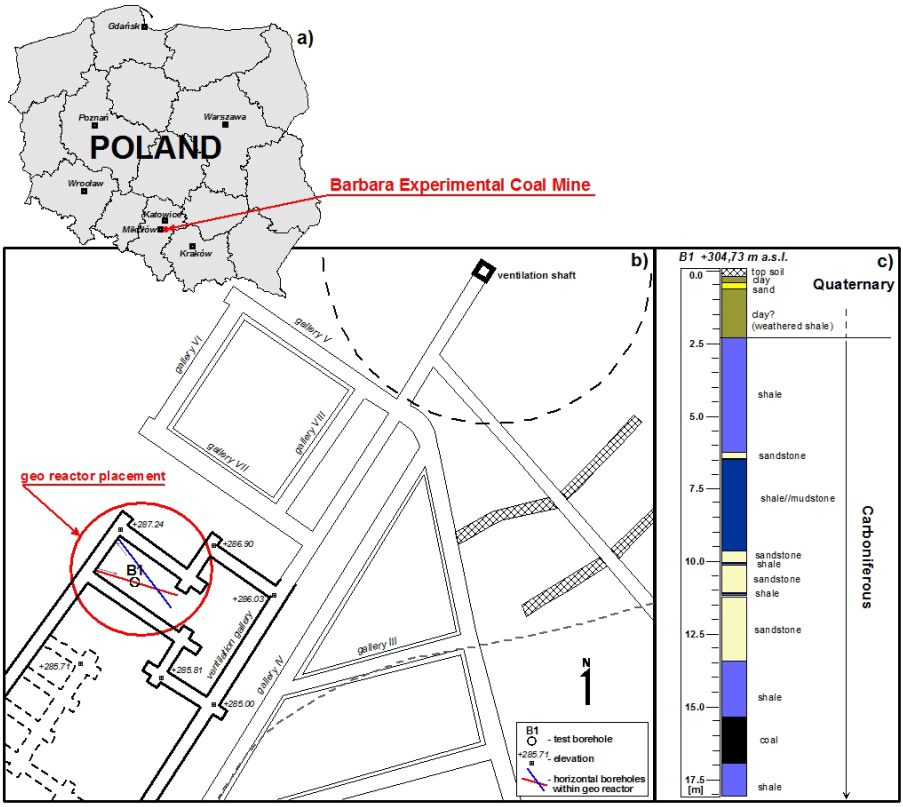

Fig. 1. Location of coal gasification experiment and its geological and mining conditions: (a) location of Barbara experimental mine on the map of Poland, (b) mining plan of the coal seam 310, and (c) geological log of the borehole B1.

in upper parts of the overburden. The water table in Quaternary sands was not detected in the borehole. Therefore, it can be assumed that it occurs in sand layer periodically. No water was also met in carboniferous beds. During the drilling a flush disappeared just when the coal seam was reached. The borehole data allow to assess that the overburden of a seam 310 was impermeable in a close vicinity of the gasification panel. It does not exclude the possibility of fissures presence in the strata surrounding the gasification panel.

3. COAL GASIFICATION TECHNOLOGY

In the seam, two horizontal boreholes were drilled crossing approximately in the axis of symmetry of the coal seam. In one of the boreholes, coal was ignited with an explosive charge and then oxygen was supplied to borehole by pipes connected with surface installation. The borehole is marked red in

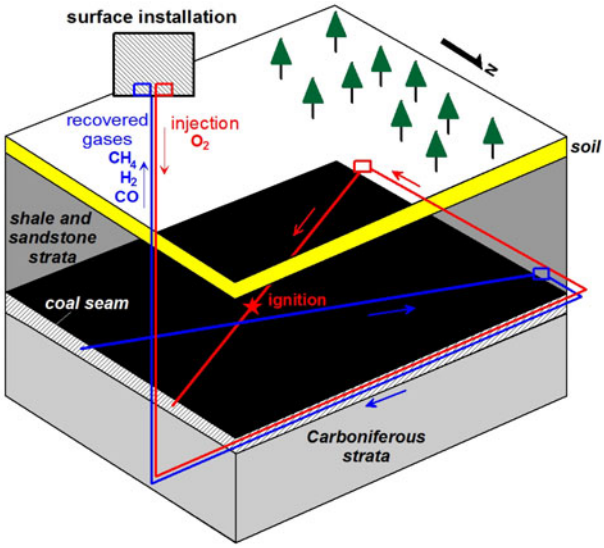

Fig. 2. Schematic diagram of a coal gasification system in an underground seam, Barbara experimental coal mine.

Fig. 2. The other borehole marked in blue color was used to receive gases produced in the process and then transport them to the surface with pipes.

The coal gasification process in the seam lasted for 142 hours. For the initial 101 hours the process was stable and the composition of the flue gases was stable too. Then, as a result of leakages, in the geo reactor there was a gradual decrease in the quality of flue gases, *i.e.*, much higher concentration of nitrogen in flue gases and lower concentration of hydrogen and carbon oxide. The chemical composition of the obtained products is presented in Table 1. Temperature of the process changed within the range of between 800 and 1500°C. After finishing the gasification process, with the borehole which was used to supply oxygen (blue in Fig. 2), the pumping of gaseous nitrogen commenced. The operation lasted for approximately four weeks and finally resulted in extinguishing fire in the coal seam.

Table 1

Average concentration of gaseous components

	Average concentration [% volume]							
Stage	H_2	CO	CH_4	C_2H_6	H_2S	CO_2	N_2	O_2
I. 0-101 hrs	42.17	37.74	2.50	0.07	0.27	15.53	1.34	0.38
II. 101-142 hrs	21.87	17.41	2.34	0.14	0.05	14.39	41.27	2.53
Total (0-142 hrs)	36.30	31.87	2.45	0.09	0.21	15.20	12.88	1.00

Analysis of the composition of gas evolved in a UCG together with other parameters of the process enable to balance the mass of burnt coal and its products. This theoretical thermo-dynamical approach is applied in estimation of combustion cavern shape and size by numerical modelling (Perkins and Sahajwalla 2006, Bhutto *et al*. 2013). In view of possible negative effects on the environment, theoretical models of the process have to be verified by the *in situ* measurement methods. They can be used also for the control of process in real time. The microgravity seems to be one of the methods suitable for this task.

4. FIELD MEASUREMENTS

The test site where gravimetric measurements were made is located in Mikołów within former Barbara coal mine which at present is used for research and development purposes. The area where the gasification experiment was conducted is shown in Fig. 3.

Fig. 3. Location of gravimetric measurements in the test site, Barbara experimental mine. In red – gravimetric points, in green – surveying benchmarks.

Observations of microgravity in the test area were made with CG-5 Autograv gravimeter produced by Scintrex, Canada. The CG-5 gravimeter, according to its manufacturer, enables measurements with accuracy of up to 0.005 mGal and repeatability of read-outs up to ±0.001 mGal (Scintrex 2006). Boundaries of the test area are marked with surveying benchmarks nos. I, II, VII, and VIII (green in Fig. 3), which indicate the corners of the roadways in coal seam 310. The test area was roughly rectangular of 9.60 × 16.00 m. *In situ* tests were planned in such a way that the measuring points were directly above the expected caverns, *i.e.*, at the junction of the flues and around the place.

Gravimetric points (red in Fig. 3) in the test site were determined in a rectangular but irregular measuring grid. Ten rows of six points each were marked. The grid included 61 points altogether, numbered from 1 to 60, as well as a base point marked no. 100. The distances between the points were 2 m and met the assumptions of a detailed gravimetric survey. Distances between the measurement lines ranged between 1 and 5 m and were adapted to perform geophysical tests with other methods to facilitate matching and complex interpretation of the obtained results. The points were marked directly on the ground. More detailed layout of measuring points in the test site is presented in Fig. 3. Gravimetric profiles were parallel to the roadway support, *i.e.*, to the line between surveying benchmarks nos. I and VIII, where the inlet and the outlet, used in the coal gasification process, were located. According to the base map for the test area, in the western corner of the area in the ground there is a power cable, oriented NNW-SSE. The lower density of soil filling the trench could cause anomalies in records obtained in that part of the test site.

The point chosen as the base one and numbered 100 was outside the experiment influence zone, 10 m SW of the boundary of the research area. Basing on this point, additional gap-filling observations were made. The gap-filling measurements were made with the intermediate point method according to the schematics: 100, 1, 2, 3, …, n, 100, where 100 is base point, and 1, 2, 3, …, n are scattered points. Linking the series allowed eliminating short-term drifts of zero point of the gravimeter. Medium- and long term-changes of zero point of the gravimeter, caused mainly by the vertical component of lunisolar forces, were eliminated during measurements. The software installed on CG-5 gravimeter allowed calculating according to Longman's algorithm, and considering corrections for Earth tides during read-outs. The corrections may reach ±0.04 mGal/h, and during a day they may change by even ±0.3 mGal. The long-time drift correction was applied automatically during the measurements. It was taken as constant and equal to 0.51 mGal/day basing on calibration done few days before taking the measurements. The short-time drift was calculated according to changes of the

readings on the base point for each measurement cycle and was applied during the data processing.

In the tests made, it was not necessary to calculate topographic corrections for gravity, due to a generally flat surface of the tested area. Maximum amplitude of the elevation difference was 0.52 m due to the slight terrain dipping to NE. To reduce the measured values to the physical level of the Earth, it was enough to measure the height of the tripod where the device was mounted. Apart from that, a differential map was used for final interpretation. Therefore, it could be assumed that the difference in altitudes of particular stations had no influence on final image.

According to the methodology, measurements were made in one point until an identical read-out of accuracy of 0.005 mGal was observed. It resulted in approximately 200 recorded values of gravity for each of the measurement series. Such a procedure ensures high quality and accuracy of microgravity measurements. After recording the data *in situ* and uploading them on a PC, correct values of measurements were selected for all of the points. Values burdened with the biggest error, considering mainly standard deviation of a single measurement approximated from a series of 30-second read-outs, were discarded.

The measurements were conducted in two separate series. Series I was taken prior the ignition of the coal on 29 July 2013, and Series II was performed after the gasification on 21 August same year.

To determine the accuracy of measurements, in some of the points, the gravimetric observations before and after the gasification were made twice. Basing on the values obtained in the repeated measurements, mean square error (MSE) of a single measurement was obtained according to the equation:

$$\mu_0 = \pm\sqrt{\frac{\sum_{i=1}^{n} v^2}{2n}}\ , \tag{1}$$

where v is the differences between repeated measurements, and n is the number of repeated observations.

The repeated gravimetric measurements within each series allowed to calculate mean square error of a single measurement, which in the first series was ±0.0028, and in the second merely ±0.0021 mGal. The value is lower than the one which is specified by the manufacturer of CG-5 apparatus. This is most probably caused by a relatively low number of the set of repeated measurements, although similar values of measurement errors are reported by other users of the apparatus (Parseliunas *et al.* 2011). The next stage of *in situ* works was to determine XY coordinates of the points and their altitude above sea level with technical levelling method. It is an extremely important

step for the accuracy of the gravimetric measurements as the height of the point determines the value of correction in Bouguer reduction. For small anomalies, oscillating slightly above the error range, incorrect determination of the height of the measuring point may result in an incorrect image of distribution of anomalies in the area and incorrect interpretation of the data. Appropriate corrections were then made to the measurement data. Finally, we obtained relative values of gravity in the so-called Bouguer reduction.

5. DATA PROCESSING

Within the framework of the calculations, relative values of gravity for all the gap-filling measurement points were calculated. The calculations were made basing on the local value of gravity assumed in the base point. Then the value of anomaly of gravity in Bouguer reduction was calculated with the equation:

$$\delta g = g + (0.3086 - 0.04187\rho)h - \gamma_0 \ , \tag{2}$$

where g is measured value of gravity [mGal]; h – altitude above sea level of a measuring point [m] in Baltic system; ρ – density of the reduced layer [g/cm^3], in the reported tests the value of $\rho = 2.0$ g/cm^3 was assumed; 0.3086 h – free-air anomaly (Faye's anomaly) [mGal], eliminating influence of altitude of a measuring point in relation to the reference level; 0.04187 ρh – Bouguer anomaly [mGal], eliminating component of vertical attractive force of a rock complex limited with horizontal planes going through the measuring point and the reference level; γ_0 – normal value of gravity [mGal], in the documented gravimetric tests local normal gravity was assumed, with relative values increasing towards north by 0.0008 mGal.

Mean square error (MSE) of determining the value of anomaly in Bouguer reduction for density of 2.0 g/cm^3 for both measurement series was respectively:

$$\begin{aligned} \nu_0 &= \pm\sqrt{\mu_0^2 + (0.3086 - 0.0419\rho)^2 \cdot m_h^2 + m_{\gamma_0}^2} \\ &= \pm 0.0036 \text{ mGal (series I)} \\ &= \pm 0.0029 \text{ mGal (series II)} \end{aligned} \tag{3}$$

where μ_0 is error of determining value of gravity (±0.0028, ±0.0021 mGal), m_h – error of determining height (±0.005 m), m_{γ_0} – error of determining normal value (±0.0008 mGal).

Interpreting the results of tests, the value of measurement error of ±0.005 mGal, provided by the manufacturer of CG-5 gravimeter, was assumed.

6. TEORETICAL MODELS OF A GASIFICATION ZONE AND ITS INFLUENCE ON THE LOCAL GRAVITY FIELD

Earlier researches made with the radar method in a large-scale model simulating conditions in the deposit show that in a block of pure coal (without impurities of other minerals) which undergoes the gasification process, in the limited volume there are at least three areas of different structure and physicochemical properties (Kotyrba and Stańczyk 2013):

- coal in natural form,
- physically and chemically transformed coal with char of various rank,
- cavern.

Because of that, before the measurements we analysed theoretically, using a 2D modelling method, the influence of the three types of structure of a coal seam − models 1, 2, and 3 − on the local gravity field in the area where the gasification process occurs. In all the three models we assumed that the seam is 2 m thick and its roof strata are oriented horizontally at a depth of 15 m. We also assumed that gasification occurs in the whole cross-section of the seam and the occurrence of a cavern covering its whole thickness is possible. In the models, the gasification zone is a regular 9 m long rectangular. In the intermediate stage of the process, in the central part of the zone there forms a 3-meter long cavern. In the final stage of the experiment, in the area of gasified coal, there is a 12-meter long cavern.

In natural conditions, the geometry of gasification areas in a coal seam is not going to be regular due to the occurrence of other rocks in coal seams, such as thin layers of gangue. That is why a model assumption of the geometry of a gasification zone is a highly idealised one. Nevertheless, it allows assessing possibility of using the gravimetric method and formulate preliminary criteria to interpret data obtained during in situ measurements.

Such assumptions reflect the general character of changes occurring in gasified coal as the process continues. At the beginning of the experiment, a zone of degasified coal is created in a seam. The process results from the phenomenon of oxidation of carbon particles. Within the zone, an area of increased porosity, comparing with the surrounding, is created. Then, it is a cavern surrounded by areas of transformed coal and gasification products. In natural conditions, solid products of the process as ash and slag, or fragments of the surrounding rocks falling from the roof, may be collected inside the cavern. In the final stage of the process, when all the coal undergoes conversion from solid body into gas, the cavern should cover the whole gasification zone. Density parameters for coal assumed in the model are shown in Table 2.

Theoretical calculations were conducted using a module for presurvey modelling (Geotools 1999), based on 2D modelling concept (Talwani *et al.* 1959). Their results are presented in Fig. 4.

Table 2

Values of rock density assumed in computational models

Type of rock	Bulk density [g/cm^3]
coal *in situ*	1.40
degasified coal	1.00
adjacent rock	2.00

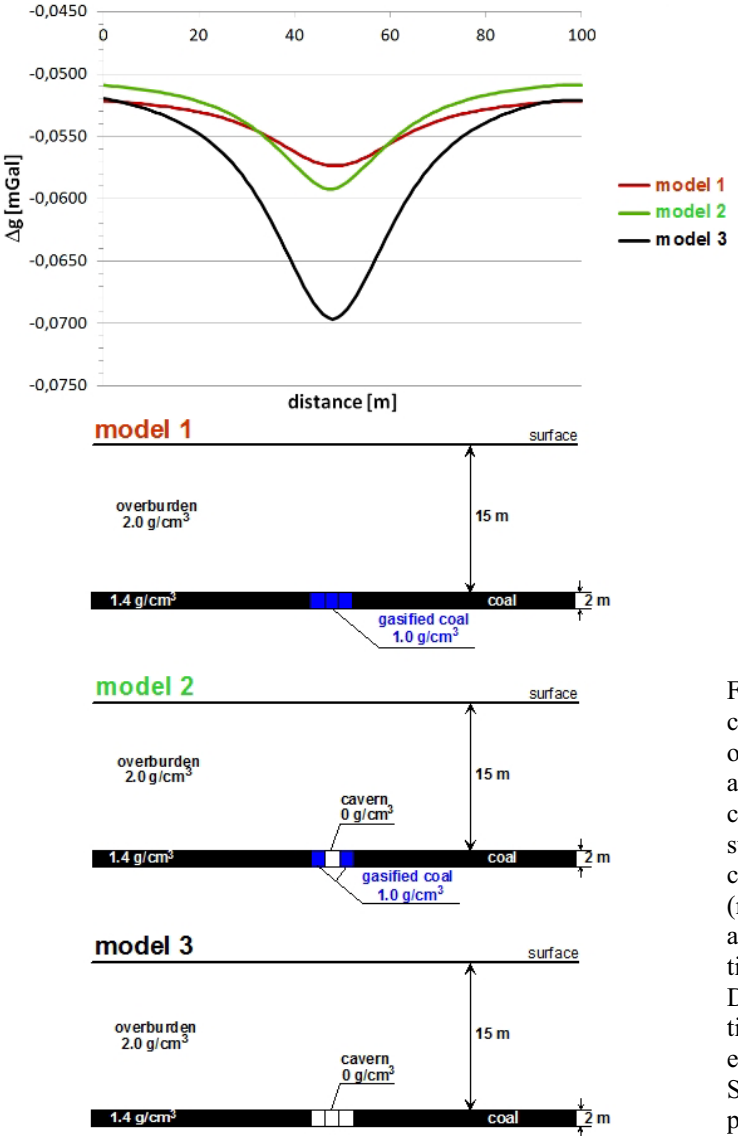

Fig. 4. Theoretical distribution of gravity field anomalies over a coal seam in the stages of gasification process (models 1, 2, 3) and a computational models. Detailed description of all models is given in Section 6 of the paper.

In model 1, which represents only the area of gasified coal, a local decrease in the value of gravity reaches its maximum amplitude of approx. 0.0055 mGal. It is the value that is nearly equal to the value of an error in a single read-out of CG-5 gravimeter. Formation of a cavern within the gasification zone only slightly increases the value of the amplitude of anomalies to the level of approx. 0.0083 mGal in model 2. A significant change occurs only after all the mass in all the gasification area disappears as a result of its conversion into gas, which is represented in model 3. This reflects the situation when the whole gasification zone turns into a cavern of height equal to the thickness of the seam. In that case, the value of amplitude of anomalies reaches 0.0178 mGal and it is a value significantly exceeding the value of a field measurement error for a standard land gravimeter.

7. RESULTS OF THE MEASUREMENTS AND THEIR INTERPRETATION

Table 3 contains the lowest and the highest values of gravity in Bouguer reduction Δg in the databases for given measurement series. It is apparent that maximum amplitudes of changes in relative values of gravity – anomalies in column 2 are by approximately an order of magnitude higher than the maximum values of the error of determining them showed in column 4. This allows, despite low numerical values, conducting both qualitative and quantitative interpretation of the data.

Table 3

Changes in relative values of gravity in Bouguer reduction Δg in databases for the measurement series

Series	Range of changes in relative values Δg [mGal]	MSE of single measurement μ_0 [mGal]	MSE of determining value of anomaly in Bouguer reduction v_0 [mGal]
1	2	3	4
I	–0.0123-0.0125	± 0.0028	± 0.0036
II	–0.0042- 0.0178	± 0.0021	± 0.0029
II – I	–0.0163- 0.0158	± 0.0028	± 0.0036

In the obtained map of anomalies in Bouguer reduction for data of measurement series I (Fig. 5) we can see three areas of anomalously lowered value of relative gravity. The first one is located in the northern corner of the test site with the centre of the anomaly in points 11-12. The second one is near the junction of the flues and north of the place with the maximum in point 40. The third one is in the eastern corner with the centre in point 59.

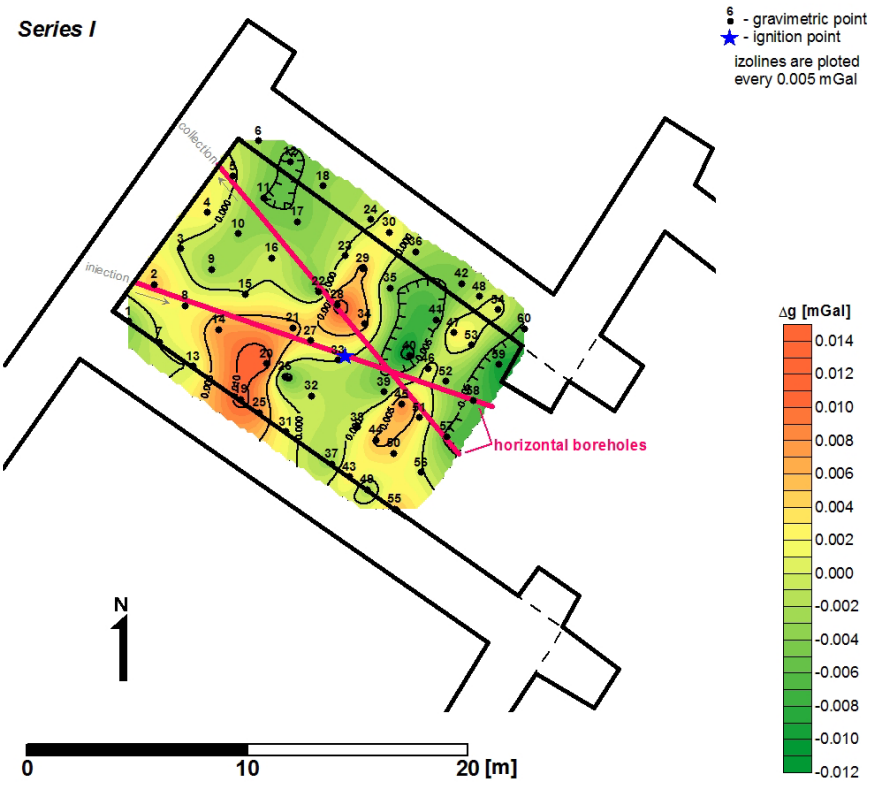

Fig. 5. Distribution of Bouguer anomaly before gasification – series I.

The highest amplitude of changes was observed for anomaly 2. In point 40, the relative value of gravity is negative, and it is –0.01226 mGal. There are also two positive anomalies in the distribution of the gravity field. They are located around points 19-20 and 28. The anomaly has the highest values, of 0.01248 mGal, in point 20. The genesis of the anomalies is most probably connected with the heterogeneity of geological layers forming the rock mass and in their density fluctuations. The distribution of Bouguer anomalies shows that the rock mass in the tested area is not homogenous. It causes local changes in the value of Bouguer anomaly of amplitude of ±0.005 mGal, similar to the values of measurement error.

Figure 6 shows distribution of relative values of gravity recorded in series II, *i.e.*, after termination the coal gasification process in the seam 24 days after series I. To visualise the data we used the same colour patterns for the values of gravity field to facilitate comparing measurement series.

Generally, in the map of anomalies in Bouguer reduction, made after termination of the experiment, we can see a slight increase in relative values

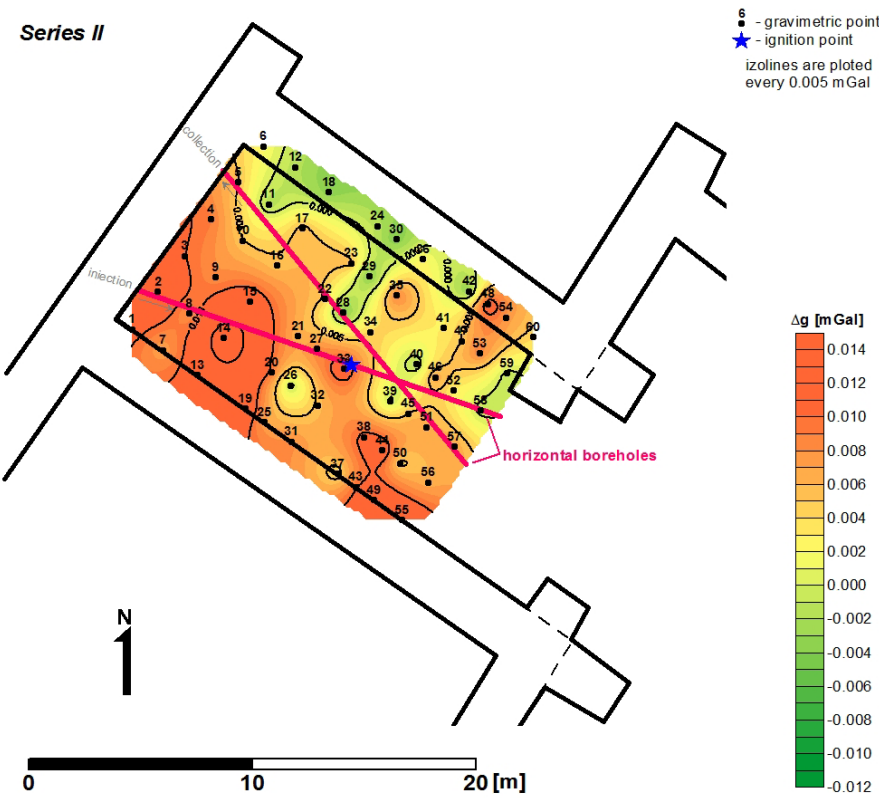

Fig. 6. Distribution of Bouguer anomaly after gasification – series II.

of gravity comparing with the data obtained in the measurement series made before gasification. In the image of isolines for series II, there is a new distinct negative anomaly spreading from the roadway bordering the block of gasified coal from the north towards its centre. The anomaly contains the points: 28, 29, and 30, which had apparently positive relative values (>0.003 mGal) in series I. In series II, in those points, relative values of gravity dropped below –0.004 mGal. The difference in values between series I and II is approx. 0.007 mGal in the area.

As far as the assessment of effects of coal gasification in a seam is concerned, the map of differential anomalies of gravity in Bouguer reduction is the most useful (Fig. 7).

Within the map we can distinguish two areas, marked A and B, where the difference in values of anomalies is negative. Area A is located in the vicinity of the junction of the flues and behind the place where gasification process is initiated in a seam. Its surface area is rather small, of approx. 3 m^2.

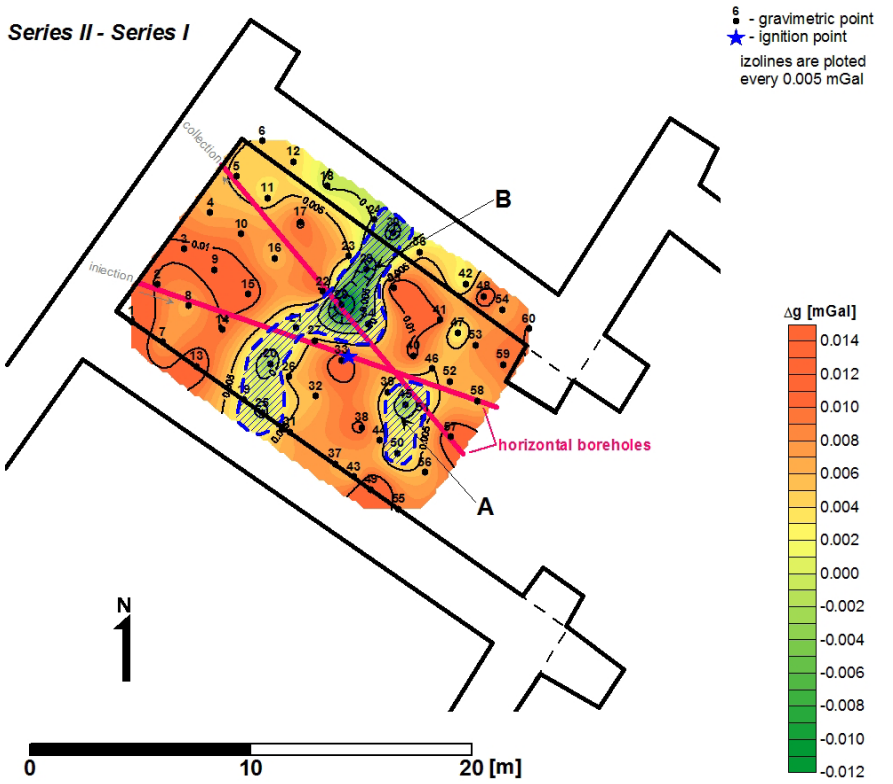

Fig. 7. Differential map of Bouguer anomaly (series II – series I) with interpretation.

The amplitude of differential anomaly in the centre of the anomalous area is 0.007 mGal. The area of differential anomaly B runs perpendicular towards the roadways bordering the gasified coal block, and covers its whole width. It has a much bigger surface area than anomalous area A. Relative amplitude of differential anomaly reaches its maximum value in the vicinity of an outlet. Its local decrease, in comparison with the values in the surrounding rock mass, is by 0.012 mGal.

The recorded anomaly in the vicinity of the place where the coal is ignited may mean that there is an area of transformed coal of relatively lower density. It is possible that the flow of gas within the seam was different than it was assumed due to a leakage in the roadway support. It could lead to a situation when the process of coal oxidation developed in two areas of the block to be gasified within the coal seam. While gases being the product of the process occurring within anomalous area A flowed properly along the flue to the receiving installation, the gases from the central part of anoma-

lous area B migrated towards the sidewalls of roadways surrounding the block of coal.

The interpretation of the results of gravimetric measurements is consistent with the simulations of the size of the coal gasification zone recreated basing on the amount of process gases received. Observations made in the roadways after extinguishing fire in the coal block confirm it too. In some places of the support there were visible leaks of tar – a by-product of the gasification. With the test borehole B1, whose location and log are given in Fig. 1, drilled in anomalous area A, a small cavern was detected of a height of 0.15 m at a depth of 15.4 m. In its surroundings there was only coal transformed during the gasification process. Generally, this is consistent with the image of a gasified coal seam described with model 2 in theoretical considerations.

8. SUMMARY

Results of the conducted tests confirm the initial assumptions that the microgravity method can be used for imaging and controlling the development of coal gasification process in a shallow seam. In the case described in the paper, the gasification experiment lasted too short to cover a bigger volume of coal. During the experiment in the seam, transformation of solid mass into gas occurred in a limited space. That is why coal probably underwent mainly chemical transformation in anomalous areas A and B. In those areas, only small caverns could be formed which could not have a significant influence on gravity field since their values are beyond measuring capabilities of land gravimeters. Anomaly A was detected in the place located behind the point of ignition. Test borehole drilled within the range of that anomaly revealed the presence of a small cavern at the depth of the coal seam. Anomaly B is located in front of this point. Furthermore, it transects both flues and the faces of the surrounding galleries. It can be assumed that the development of this undesired zone led to termination of the experiment untimely. This happened when in the gaseous products of combustion have increased the nitrogen content significantly (Table 1).

The data obtained in the tests confirmed model analyses made at the stage of designing the measurements. The final effect of gasifying a coal seam on changes in gravity field is well described by model 2, in which a local transformation zone is formed in the seam. The zone contains degasified coal with micro pores and small caverns in regions where the combustion took place. The zone, in the described experiment, is relatively small. That is why the amplitudes of changes in the field of differential Bouguer anomaly in anomalous areas are relatively small, yet similar to model 2 analysed prior to the tests. In the model we assumed that the cavern within the gasification

zone covers the whole thickness of the seam. In model analyses we *a priori* assumed the value of bulk density of 1.00 g/cm^3 for the gasified coal zone. In reality it can be smaller and in such a case quantitative changes in the distribution of differential anomalies will be bigger than the ones described with a theoretical model. This may explain the fact that within differential anomaly B the amplitude reaches a higher value than in theoretical models.

The tests described in the paper allow to conclude that in industrial applications of the gasification in the seam, where processing coal into gas will occur in areas of much larger volume, gravimetric anomalies will have similar and higher values to the ones described with model 3 for a 2-meter-thick seam completely transformed into gas. The amplitude of differential anomaly will increase with the thickness of coal deposit.

Acknowledgments. The results presented in this work have been obtained within the frames of the EU research project co-financed by the Research Fund for Coal and Steel and the Polish Ministry of Science and Higher Education UE project entitled "Hydrogen Oriented Underground Coal Gasification for Europe – Environmental and Safety Aspects" (HUGE2).

References

Bhutto, A.W., A.A. Bazmi, and G. Zahedi (2013), Underground coal gasification: From fundamentals to applications, *Prog. Energ. Combust. Sci.* **39**, 1, 189-214, DOI: 10.1016/j.pecs.2012.09.004.

Burton, E., J. Friedman, and R. Upadhye (2005), Best practices in underground coal gasification, Lawrence Livermore National Laboratory, Contract No. W-7405-Eng-48, Livermore, USA, http://www.purdue.edu/discoverypark/energy/pdfs/cctr/BestPracticesinUCG-draft.pdf.

Fajklewicz, Z. (1989), Application of microgravity method to detection of subsurface cavities and prediction of rock bursts. **In:** R.K. Verma (ed.), *Advances in Coal Geophysics: Proceedings*, AEG India, Hydebrad, 11-18.

Geotools (1999), Gravmodeler user's manual, Geotools Corporation, Austin, USA.

Gregg, D.W., and T.F. Edgar (1978), Underground coal gasification, *AIChE J.* **24**, 5, 753-781, DOI: 10.1002/aic.690240502.

Itakura, K., M. Wakamatsu, M. Sato, T. Goto, Y. Yoshida, M. Ohta, K. Shimada, A. Belov, and G. Ram (2010), Fundamental experiments for developing underground coal gasification (UCG) system, *Mem. Muroran Inst. Tech.* **59**, 51-54.

Jacoby, W., and P.L. Smilde (2009), *Gravity Interpretation. Fundamentals and Application of Gravity Inversion and Geological Interpretation*, Springer, Berlin Heidelberg.

Kotyrba, A., and K. Stańczyk (2013), Application of a GPR technique for the monitoring of simulated underground coal gasification in a large-scale model, *Near Surf. Geophys.* **11**, 5, 505-515, DOI: 10.3997/1873-0604. 2013030.

Parseliunas, E., P. Petroskevicius, R. Birvydiene, and R. Obuchovski (2011), Investigation of the automatic gravimeters Scintrex CG-5 and analysis of gravimetric measurements. **In:** *Proc. 8th Int. Conf. "Environmental Engineering"*, 19-20 May 2011, Vilnius Gediminas Technical University, Vilnius, Lithuania, 1416-1423.

Perkins, G., and V. Sahajwalla (2006), A numerical study of the effects of operating conditions and coal properties on cavity growth in underground coal gasification, *Energy Fuels* **20**, 2, 596-608, DOI: 10.1021/ef050242q.

Scintrex (2006), CG-5 Scintrex Autograv System. Operation manual, Scintrex Ltd., Ontario, Canada.

Shafirovich, E., and A. Varma (2009), Underground coal gasification: a brief review of current status, *Ind. Eng. Chem. Res.* **48**, 17, 7865-7875, DOI: 10.1021/ie801569r.

Stańczyk, K., A. Smoliński, K. Kapusta, M. Wiatowski, J. Świądrowski, A. Kotyrba, and J. Rogut (2010), Dynamic experimental simulation of hydrogen oriented underground gasification of lignite, *Fuel* **89**, 11, 3307-3314, DOI: 10.1016/j.fuel.2010.03.004.

Styles, P., R. McGrath, E. Thomas, and N.J. Cassidy (2005), The use of micro- gravity for cavity characterization in karstic terreains, *Quat. J. Eng. Geol. Hydrogeol.* **38**, 2, 155-169, DOI: 10.1144/1470-9236/04-035.

Su, F., T. Nakanowataru, K. Itakura, K. Ohga, and G. Deguchi (2013), Evaluation of structural changes in the coal specimen heating process and UCG model experiments for developing efficient UCG systems, *Energies* **6**, 5, 2386-2406, DOI: 10.3390/en6052386.

Talwani, M., J.L. Worzel, and M. Landisman (1959), Rapid gravity computations for two-dimensional bodies with application to the Mendocino submarine fracture zone, *J. Geophys. Res.* **64**, 1, 49-59, DOI: 10.1029/JZ064i001 p00049.

Received 7 February 2014
Received in revised form 24 April 2014
Accepted 18 June 2014

DE GRUYTER OPEN

Acta Geophysica
vol. 63, no. 3, June 2015, pp. 652-678
DOI: 10.1515/acgeo-2015-0012

Prony Filtering of Seismic Data

Georgy MITROFANOV[1] and Viatcheslav PRIIMENKO[2]

[1]Trofimuk Institute of Petroleum Geology and Geophysics,
Siberian Branch of the Russian Academy of Sciences, Novosibirsk, Russia
e-mail: georgymitrofanov@rambler.ru

[2]Laboratory of Petroleum Engineering and Exploration,
North Fluminense State University Darcy Ribeiro, Macaé, RJ, Brazil
e-mail: slava@lenep.uenf.br (corresponding author)

A b s t r a c t

Prony filtering is a method of seismic data processing which can be used to solve various geological and production tasks, involving an analysis of target horizons characteristics and a prediction of possible productive zones. This method is based on decomposing the observed seismic signals by exponentially damped cosines at short-time intervals. As a result, a discrete Prony spectrum including values of four parameters (amplitude, damping factor, frequency, phase) can be created. This decomposition occurs at many short-time intervals moving along an observed trace. The combined Prony spectrum of the trace can be used to create images of the trace through a selection of some values of the parameters. These images created for all traces of a seismic section provide an opportunity for locating zones of frequency-dependent anomalous scattering and absorption of seismic energy. Subsequently, the zones can be correlated with target seismic horizons. Analysis and interpretation of these zones may promote understanding of the target horizons features and help to connect these features with the presence of possible reservoirs.

Key words: data and signal processing, stacks imaging, parameter estimation, attenuation, Prony transform.

1. INTRODUCTION

Gabor's (1946a, b, c) pioneering work on accurate spectral estimation of the short-time signals has been essential in many scientific and industrial applications. Over the last few decades, extensive research on digital spectral estimation has led to a significant development of modern technologies in this area (Grossmann and Morlet 1984, Marple 1987, Marks 2009). For example, a technology based on wavelet analysis allowing optimal results for the short-time signals has been developed (Chui 1992a, b). However, the use of these methods in the processing of field seismic data may have some limitations with the formal selection of orthogonal functions as their basis.

An alternative way to explore short signal and non-stationary processes is the use of the Prony method based on the functions that correspond to the nature of real seismic impulses. Data description using the sum of complex exponentials (Prony decomposition) was proposed by French engineer and mathematician Gaspard Riche more than two centuries ago (de Prony 1795). Although this method overlapped the discrete Fourier transform, which was developed later, it was forgotten until the 1960s. Renewed research interest in the Prony method can be explained by the development of powerful computers and the need to provide good spectral resolution in data processing when the form of the observed signal is well approximated by a decaying sinusoid.

Over the last four decades, new schemes for the Prony decomposition have been developed (see, *e.g.*, Osborne 1975, Kumaresan 1983, Marple 1987, Osborne and Smyth 1991, 1995, Beylkin and Monzón 2005, Bracale *et al*. 2007, Mitrofanov and Priimenko 2011, Fomel 2013, Hu *et al*. 2013). Some of these schemes are based on the least-squares method, nonlinear optimization or polynomial factorization. These schemes are directly related to the analysis of autoregressive models (AR-models) and high-speed operations. Other schemes use singular value decomposition method (SVD), which provides good results for a relatively high signal-to-noise ratio (SNR) of data (greater than 2). However, in cases of an extremely low SNR or a rapid decay of the observed signal, results obtained through the SVD method are unsatisfactory due to considerable difficulties in separating the singular values. Some aspects of stable estimation for noisy data and comparison with the properties of wavelet decomposition can be found in Berti *et al*. (2007) and Lobos *et al*. (2009). An overview of parameters estimation for approximation of exponential sums in experimental data can be found in Marple (1987), Kahn *et al*. (1992), Holmström and Petersson (2002), and Potts and Tasche (2010). Mitrofanov and Priimenko (2011) give an overview of several schemes for the Prony decomposition as well as its theoretical background.

Kovaljev and Telepnev's (1981) research is one of the first studies on the application of the Prony method and AR-models to processing and interpretation of seismic data (see also Kovaljev *et al*. 1992, Mitrofanov *et al*. 1993). The research showed that using damping factor as one of the parameters of Prony decomposition provides more accurate and detailed forecast of deep and lateral variations in reservoir properties, in particular, the anomalies of high pore pressure (Helle *et al*. 1993).

Prony filtering is one of the possible procedures which use the Prony decomposition. The decomposition establishes a discrete spectrum associated with a set of short-time intervals located along the analyzed trace. The spectrum contains calculated values of the four parameters: (i) amplitude, (ii) frequency, (iii) damping factor, and (iv) phase. Selection of some values of these parameters and creation of a seismic trace image by using different criteria is called the Prony filtering (Mitrofanov *et al*. 1998a, b, Gritsenko *et al*. 2001). It should be noted that if the selection is based on the frequency parameter only, the procedure could be considered as an analogue of the well-known band-pass filtering. But unlike the band-pass filtering, the Prony filtering allows to obtain a better resolution both in time and space domains, providing an opportunity to analyze a wave field in more detail. Furthermore, it provides a stable estimate of damped sinusoidal components of short signals. Usually, two of the four above-mentioned parameters, frequency and damping factor, form the basis for the selection of damped sinusoidal components. Images built from the selected damped sinusoidal components represent the final results in the form of common time sections. The procedure improves the resolution of short seismic signals and consequently helps to identify areas with anomalous values of seismic energy scattering (dispersion) related to the frequency-dependent effect.

Prony filtering tests have been performed on a large number of mathematical and physical models (Orlov *et al.* 1999, Brekhuntcov *et al.* 2001, Mitrofanov *et al.* 2003a, Mitrofanov and Priimenko 2013). Extensive research was required due to nonlinearity of the procedure. During the research, the several aspects were analyzed: seismic signal form influence, stability of the procedure for noise, signals resolution, *etc*. The investigations confirmed that Prony filtering was effective in analyzing reservoir structure, contouring of oil/gas production areas, and in determining productive reservoir properties (see Mitrofanov *et al.* 1999, 2001, 2003b, 2006). To some extent, these results were expected because the seismic signal is similar to the exponentially damped sinusoid, and the damping coefficient is related to the Q factor, which plays a significant role in the description of lithology, fluid content, and pressure variations.

2. PRONY FILTERING

The original Prony method aims to fit a deterministic exponential model to equally spaced data points, as discussed in details by Marple (1987) and Therrien (1992). Assuming a signal data $x[n]$ with N complex samples $x[1]$, $x[2], ..., x[N]$, the Prony method will fit the data with the sum of M complex exponential functions. For real data, the complex exponential functions can be written by means of exponentially damped cosines. In this case the number of components M is always even and our representation will have the following form

$$x[n] \cong \sum_{k=1}^{L} A_k \cdot e^{\alpha_k (n-1)\Delta} \cos\left(2\pi f_k (n-1)\Delta + \theta_k\right), \tag{1}$$

where $L = M/2$ and values of unknown real parameters: A_k is the amplitude, α_k is the damping factor, f_k is the harmonic frequency, θ_k is the phase, and Δ is the sampling interval.

The fitting of a designated signal is usually accomplished by minimizing the total squared error over the N data, *i.e.*, through the last square method. As a result, a set of four parameters $\{A_k, \alpha_k, f_k, \theta_k\}_{k=1}^{k=M}$ corresponding to the individual complex exponential functions or exponentially damped cosines becomes available. For a detailed description of the Prony method see, for example, Marple (1987), Potts and Tasche (2010), and Mitrofanov and Priimenko (2011).

2.1 Prony spectrum

Using an analogy to the discrete Fourier spectrum, we can call this set "the discrete Prony spectrum" $\Re_{\tau,T}(M)$, *i.e.*,

$$\Re_{\tau,T}(M) = \{A_k, \alpha_k, f_k, \theta_k\}_{k=1}^{k=M}, \tag{2}$$

where real parameters τ, T define a time interval where the Prony decomposition has been carried out. Here τ characterizes the position of the analyzed time interval and $T = (N-1)\Delta$ is its total width with the sampling interval Δ. Both parameters, τ and T, play an important role in the Prony filtering.

Thus, the discrete Fourier spectrum is a set of values of two variable parameters, amplitude and phase, and one fixed parameter, which is frequency, whereas the Prony spectrum is a set of values of four variable parameters. This is an important difference between the discrete Fourier and Prony transforms. Unlike the discrete Fourier transform, where the frequency samples are equal, the frequency in the case of the Prony transform can have arbitrary values and is one of the estimated parameters. Thus, in the discrete Prony spectrum (Eq. 1), there will be a non uniformly spaced frequency grid for

each signal. As a result, for some bands of frequencies the values of the Prony parameters will be absent, while the width of these bands may vary depending on the observed data. The major differences between Fourier and Prony approaches are summarized in Table 1.

Table 1

Comparison between Fourier and Prony approaches

Fourier Approach (FA)	Prony Approach (PA)
FA is a non-parametric method	PA is a parametric method
FA fit a sum of undamped complex exponentials (undamped cosines\sines) (orthogonal base)	PA fit a sum of damped complex exponentials (damped cosines\sines) (non orthogonal base)
FA computes amplitude, phase, and uniformly spaced frequency grid	PA computes amplitude, phase, damping coefficients, and non uniformly spaced frequency grid

Another important aspect in determining the possibility of using the Prony decomposition is a near-orthogonality of damped sine/cosine functions (see Appendix). This property allows us to use a small part of the decomposition components to determine the components of the signals that correspond to a small range of frequencies.

The transition of recorded continuous data, for instance, seismic traces, to the discrete Prony spectrum can be represented as follows:

$$x(t) \xrightarrow[\text{sampling}]{\text{data}} \{x[i]\}_{i=1}^{i=I} \xrightarrow[\text{by } \tau,T]{\text{selection}} \{x[n]\}_{n=1}^{n=N} \xrightarrow[\text{transform}]{\text{Prony}} \Re_{\tau,T}(M) \ . \qquad (3)$$

Here $\{x[i]\}_{i=1}^{i=I}$ is the total set of discrete data and $\{x[n]\}_{n=1}^{n=N}$, $N \le I$ is part of the data used for the Prony transform, *i.e.*, $\{x[n]\}_{n=1}^{n=N} \subseteq \{x[i]\}_{i=1}^{i=I}$. The discrete Prony spectrum $\Re_{\tau,T}(M)$ depends on the data selection parameters τ, T and on the order of approximation, M. The scheme (3) will serve as the basis for all our subsequent constructions.

The classical Prony method can be formulated in several ways. Some of these approaches were discussed in the introduction. However, the most important point is that we can describe the observed seismic data in the form (1) and estimate the number of damped cosines and their parameters.

Although the real seismic signals are similar to the exponentially damped sinusoid (Prony components), there are still some differences between them. In our research we analyzed numbers of discrete Prony spectra for various short-time seismic signals obtained though mathematical and physical modelling, as well as in field experiments.

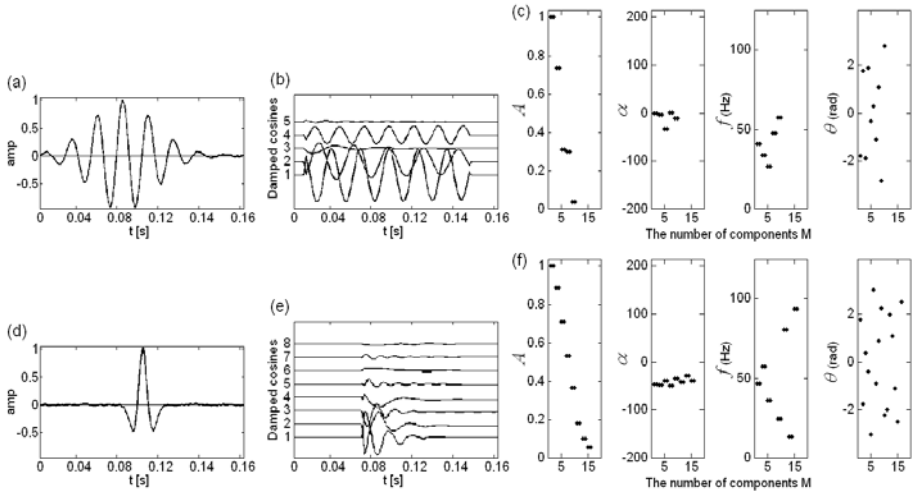

Fig. 1. Two types of signals: (a) and (d) – original signal, (b) and (e) – obtained damped cosines; (c) and (f) – corresponding Prony spectrum.

Usually, three or four pairs of complex harmonics, *i.e.*, $M \leq 8$, are sufficient for an acceptable approximation of the wavelet. However, for a more complete fitting we sometimes need to use up to 10 or 11 pairs of harmonics. In this case, two interesting features emerge. Firstly, the wider the signal in time domain, the smaller the number of harmonics needed. This fact is confirmed by comparing the Prony spectra for signals presented in Fig. 1. Secondly, the higher the decay of the observed signal, the wider the spread in the Prony parameters values into 4D space. For example, Ricker's wavelet is one of the pulses with a broad spectrum. Figure 1d shows the Ricker pulse with the predominant frequency 40 Hz. As can be seen here, sufficient approximation is achieved by means of eight Prony modes, *i.e.*, $M = 16$. Notably, the frequencies of corresponding components have a large spread (from 15 up to 100 Hz). In addition, there are several large variations in the values of the amplitude and the phase parameters.

Currently, many software tools have a common procedure for the Prony transform, which might be used for the analysis of seismic signals. However, in the case of field seismic data, there are several important features that complicate their analysis and processing: (i) the signal position is not accurately determined, (ii) seismic impulses are often too short (20-30 samples), (iii) for target objects a few reflected signals with completely different features are located within the same time interval, and (iv) the spectrum of noise can be close to that of the evaluated signal. All of these features were taken into account before applying the Prony filtering in practice.

2.2 Shifting time windows

Three major problems rise from an analysis of the results of the Prony transform used in field seismic data processing. "The first problem" related to seismic impulses is how to establish stable and well-defined parameters of Prony decomposition when arrival times for the impulses are not precisely defined. For this reason, various algorithms give different results depending on the shape of the seismic signal and the values of the signal-to-noise ratio.

"The second problem" is related to Prony's estimation of the four parameters for a full trace. Here we need to combine different Prony spectra corresponding to different time intervals. For this purpose, shifting time windows can be used. However, this problem is aggravated by the fact that in a real seismic experiment, we do not have enough information about the location of each of the analysed signals. Therefore, we must evaluate and analyse the Prony parameters for various time intervals, *i.e.*, we need to find the optimal sampling interval as well as τ and T (see, *e.g.*, Lee and Kim 2005, Bracale *et al.* 2007). Defining sampling intervals, τ and T, for a combined Prony spectrum of the full trace was an important element in the creation of Prony filtering algorithms, which can be applied to field seismic data. This aspect has only recently been discussed by researchers, see, *e.g.*, Lee and Kim (2005), Bracale *et al.* (2007), Mitrofanov and Priimenko (2011, 2013), Fomel (2013).

In order to understand the use of the discrete Prony spectrum in the selection of impulse components, *i.e.*, in the process of Prony filtering, we are going to examine a few examples. The selection procedure can be used to separate any of the individual components or a certain part of them for the observed wave field approximation, for the purpose of further interpretation. The selection depends on the seismic/geological tasks and the features of the Prony transform.

First of all, before we solve the two problems mentioned above, "the third problem" needs to be solved: How can we choose optimal parameters for the Prony decomposition? A solution to this problem was found by the analysis of experimental results of the Prony filtering obtained using the model and field seismic data. The most complete criteria for determining optimum parameters of the Prony decomposition and filtering are presented in Mitrofanov and Priimenko (2013). These principles allow us to determine time windows, frequency intervals and attenuation, which provide a stable separation of the signal being analyzed for a given frequency.

As an illustration, we are going to consider an example of the use of Prony spectrum estimation for a signal in the form of decaying sinusoids (see Fig. 2). The initial signal form is shown in red. In Figure 2, the Prony decomposition is performed using a shifting time window for the estimation

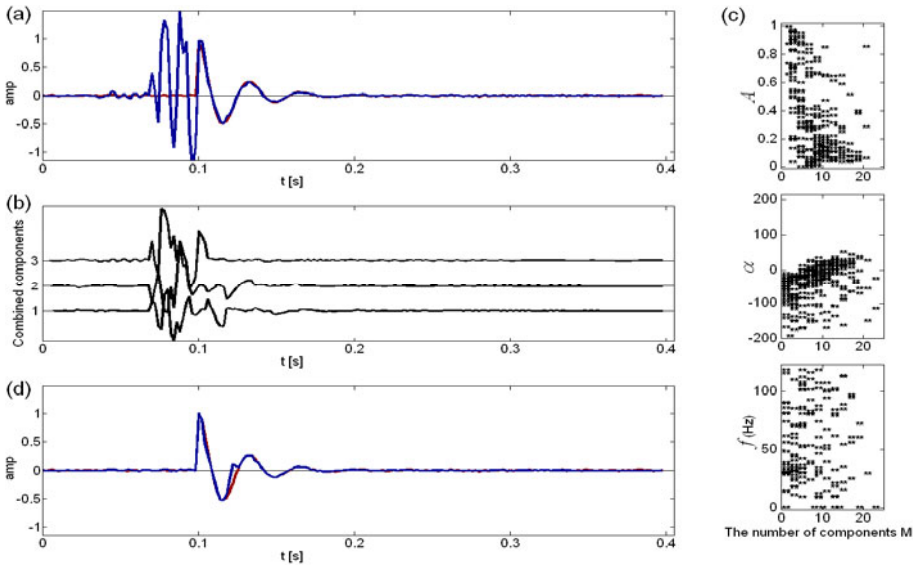

Fig. 2. Results of Prony filtering: (a) signal form estimate based on the combined Prony spectrum, (b) combined Prony components, (c) values of the Prony parameters (amplitude, attenuation, frequency) corresponding to all the calculated spectra, and (d) result based on special procedures. The estimation was performed using the shifting time windows (duration 0.094 s).

of the spectrum. This kind of determination of the Prony parameters is similar to the field seismic data processing when the exact location of the impulses is not known. A general approximation of observed data based on Prony spectra determined by the shifting time windows is shown in Fig. 2a in blue. As we can see, the approximation to the test signal is quite poor. Moreover, the combined Prony spectrum is very complex when the spectra of all shifting intervals are mixed (see Fig. 2c). The complexity of the combined spectrum leads to the irregular structure of the combined Prony components. Moreover, the components do not provide direct information about the original signal (see Fig. 2b). Both the complex combined Prony spectrum and the irregular structure of the Prony components result from the limited knowledge about the observed signal, including its time arrival. Therefore, we can neither accurately identify the signal nor determine the Prony parameters (or components).

Furthermore, as it was noted above, the discrete Prony spectrum of observed data may have a much broader set of parameters than the damped sine wave. The difference between seismic impulses and damped sine impulses hinders identification of seismic signals in the process of their separation by

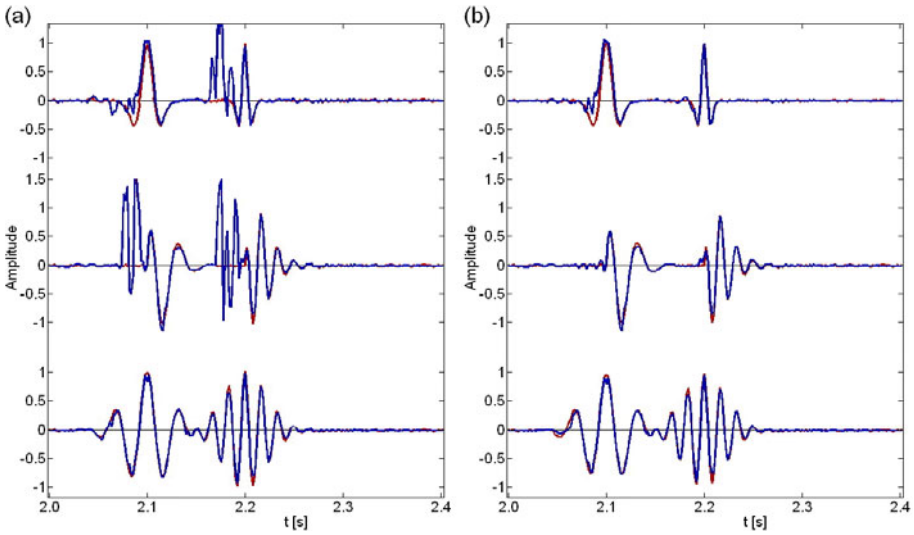

Fig. 3. Signal form fitting: (a) without and (b) with special procedures.

the Prony method. Therefore, it is necessary to set up special procedures to determine the Prony parameters.

The procedures are based on the algorithms which ensure the stability of the Prony decomposition for different types of signals resembling real seismic ones. The proposed special procedures can be summarized as follows: the discrete Prony spectra (Eq. 2), obtained at separated short intervals using the least-square method (Holmström and Petersson 2002), are joined together for the entire processed trace. They are joined in order to minimize the difference between the observed data and their approximated representation (Eq. 1). Some examples of the application of these procedures are given in Fig. 2d. The procedures were tested on several model data; see Mitrofanov and Priimenko (2013) for details.

The special procedures are most important when we have a set of signals in different shapes at one short time interval. In some cases we can have very unstable results, which do not allow us to define any specific characteristics for certain types of signals (see Fig. 3). For example, comparing the middle traces in Figs. 3a-b we can see that it is impossible to accurately detect the arrival time and signal forms in the middle trace in Fig. 3a.

2.3 Damping factor estimation

There is another important aspect of the application of Prony filtering. The separation of individual signals based on the fixed values of the Prony parameters is quite relevant, but in our opinion, it is also worth to examine the

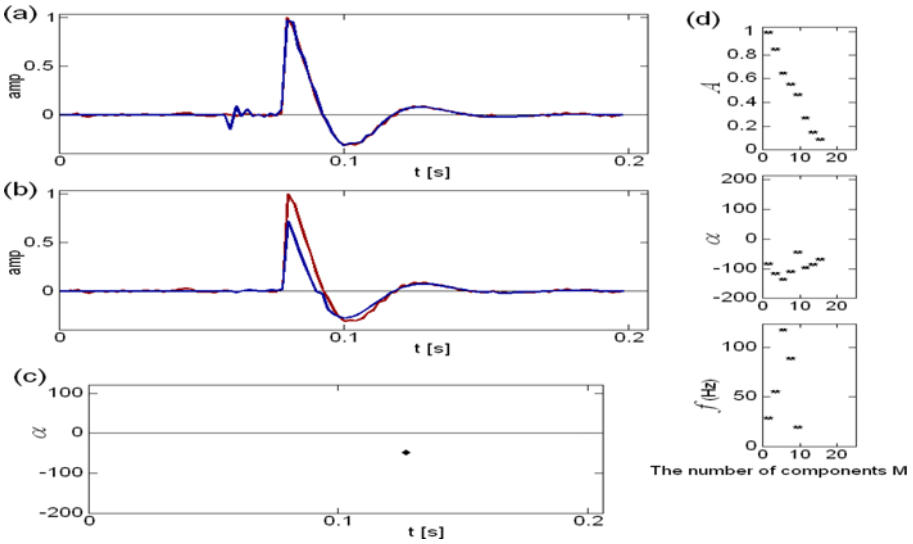

Fig. 4. Estimation of a decaying component and its damping factor based on the Prony filtering procedure.

changes of the damping factor as a function of frequency because they may provide very important information about rock properties.

Figure 4 shows some examples of synthetic signal estimation. The signal is represented as a damped sinusoid with the frequency $f = 20$ Hz and the damping factor $\alpha = -50$. Figure 4a shows the result of the signal approximation based on the Prony decomposition. For the estimation in Fig. 4, we did not use any information about the location of the impulse. The application of the special procedures, discussed in the previous section, allowed us to accurately determine the entire impulse. The initial signal is represented by the red curve, and its evaluation by the blue one. Figure 4d shows the complete set of the Prony parameters. Having selected the parameters through Prony filtering procedures, we succeeded in restoring the original waveform at the exact time and with the correct value of the damping factor; see Figs. 4b-c.

A more complex synthetic signal is shown in Fig. 5a (the red line). In this case, we had three damped sinusoids along the trace with the frequency $f = 20$ Hz and three different values of the damping factor $\alpha = -50, -75, -100$, respectively, for the first, second, and third sine wavelets.

The Prony decomposition for this model was carried out using shifting time windows and the special procedures. This approach resulted in sufficient accuracy of the full trace approximation (see the blue line in Fig. 5a). It should be noted that a more complex target signal represented by the three

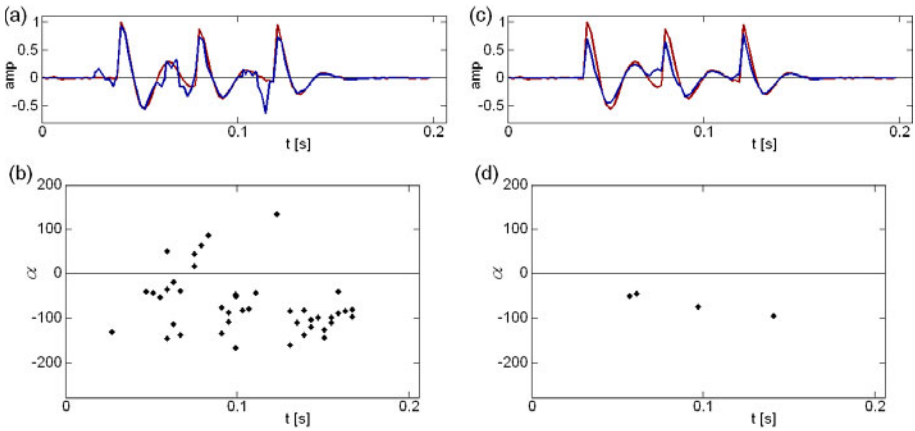

Fig. 5. Estimation of the decaying components and their damping factor for the three signals on the basis of the Prony filtering procedure: without (left column) and after (right column) filtering.

damped sinusoids leads to a wider range of Prony parameters and to a greater variation of damping factors (Fig. 5b). Prony filtering enabled us to determine the position of the impulses and their shapes more precisely (see the blue line in Fig. 5c). As a result, the damping factor was also identified more accurately (see the bottom part of Fig. 5d). Even if there was moderate noise in the trace, it was possible to determine the position of these impulses and their damping factors.

3. PRONY FILTERING TECHNOLOGY

We would like to briefly introduce the main elements of this technology. The Prony filtering method includes several steps.

The first step is the use of ordinary spectral analysis based on the Fourier transform in order to determine the basic frequencies of the observed seismic data and the width of their spectrum. The frequencies should be identified in three different parts of the frequency domain: lower, middle, and higher frequencies. This analysis is carried out through selection of the most stable frequencies for all studied signals belonging to several profiles in the investigated area. Usually, analysis is done at a time interval which is longer than the duration of the impulse response reflected from the target object. The interval may include reflected signals from several seismic horizons. Therefore, it should be stressed that the selected frequencies correspond to all these signals. Thus, a set of basic and high frequencies is prepared for the next step.

The second step is the selection of parameters for optimal Prony filtering. Selection depends on the task to be solved and the data features. This step is very important for the determination of Prony decomposition, its parameters, and how they are to be used to solve the problem. This stage is the most complex part of the method. It is also the most crucial step in the method application because it determines the efficiency of further data processing and the quality of subsequent interpretation. The optimal parameters are selected for the seismic data which correspond to the sequence of profiles from the investigated area and to the set of the frequencies defined during the first step. The process of optimal parameters selection is not formal. Some suggestions on the optimal parameters selection and its implementation have been given in Mitrofanov *et al.* (1999, 2001). Main principles of the selection as well as its application in the processing of data, obtained using mathematical and physical models, were discussed in Mitrofanov and Priimenko (2013). The results obtained show that the strategy provides an opportunity for the selection of optimal parameters, which ensure a higher resolution for the signals related to the target objects on each of the selected frequencies. This information helps us to identify more accurately signals associated with target horizons and correlate frequency-dependent variations, determined by the Prony filtering method, with the horizons features.

The third step is processing of the available seismic data, mapping and interpretation of zones with different frequency-dependent responses. This processing is based on the optimal parameters selected for the sequence of profiles used during the second step. As a result, we have a complete set of processed profiles filtered by the Prony method and responding to the selected frequencies. This set is the basis for analyzing and mapping areas with different frequency-dependent responses. At this stage, we need to use information about the target horizon picking. Usually, correct mapping and interpretation require the knowledge of: (i) the approximate duration of the time interval containing reflections from the target layers, and (ii) the possible top of the target horizon. If this information is available, we can accurately define short-time intervals to estimate Prony dynamic parameters on the basis of the Prony filtering results. These parameters are used to make maps which use various combinations of the Prony dynamic parameters. For instance, we can use the relationship between values of the dynamic parameters for different frequencies or time intervals. The choice of these combinations would depend on the data and the tasks to be solved.

It should be noted that the image of stack obtained after Prony filtering contains more information for the analysis than we could obtain by applying the standard procedures of band-pass filtering. The images of ordinary stacks constructed on a set of frequencies can be called “Prony stacks”. An analysis of Prony stacks corresponding to different frequencies gives additional in-

formation about the top, the structure of the studied reservoir and the anomalous zones of seismic energy scattering and absorption. For instance, a strong short response at high frequencies is a typical feature of a good reservoir cover. Moreover, we can observe variations of properties at different frequencies for thin layer objects. Meanwhile, a high resolution of Prony stacks allows us to study objects in detail, for example, areas of bed thinning into a sedimentary unit.

Thus, if we want to preserve all information about Prony filtering results for mapping, we need to use several dynamic parameters of signals. We recommend using three of them: (i) the mean value of interval energy, (ii) parameter of exponential decay, and (iii) degree of coherence between adjacent traces. The mean value of interval energy, which gives the most stable result, is the dynamic parameter we most often use in practice.

4. APPLICATIIONS OF THE PRONY FILTERING TECHNOLOGY

In our earlier papers, we explained some aspects of the application of Prony technology to synthetic and field seismic data analysis (Orlov *et al.* 1999, Brekhuntcov *et al.* 2001, Mitrofanov *et al.* 1999, 2001, 2003b, 2006). We demonstrated that Prony filtering helps to localize areas of seismic energy absorption and dispersion, which may be correlated, with some characteristics of the medium in the observed wave field. Usually, localizing such areas on the basis of high frequencies proves to be highly significant for further interpretation. Field seismic data processing confirms the effectiveness of the Prony algorithm for determining areas with anomalous absorption/dispersion, which may be associated with the presence of an oil/gas reservoir.

As an example of this possibility, we are going to examine the results shown in Fig. 6. They represent one of the first applications of the Prony technology to field seismic data. In this case, the total processing was applied to a stacked seismic data. Note that Prony filtering can be applied to both stacked and unstacked seismic data. However, most of our experiments on its application to field data were performed using stacked seismic data, as customers determined it. As a rule, the data were obtained in land seismic using explosive type of source and underwent standard data processing preceding the interpretive stage with maximum preservation of frequencies.

Figure 6a shows an initial time section. According Prony filtering technology (see Section 3), for each trace of this section of the analyzed time interval $[2.2, 2.4]$ s usual spectral analysis was performed. The results, in the form of amplitude spectra calculated in the range $[1, 100]$ Hz, are shown in Fig. 6b. It can be seen that the present data rate is of 10 to 65 Hz. These amplitude spectra allowed a choice of ten frequencies which manifest themselves in the most stable fashion on the data: 16, 21, 25, 32, 37, 41, 43, 53, 60, and 65 Hz. In practical use of the Prony filtering we usually select from

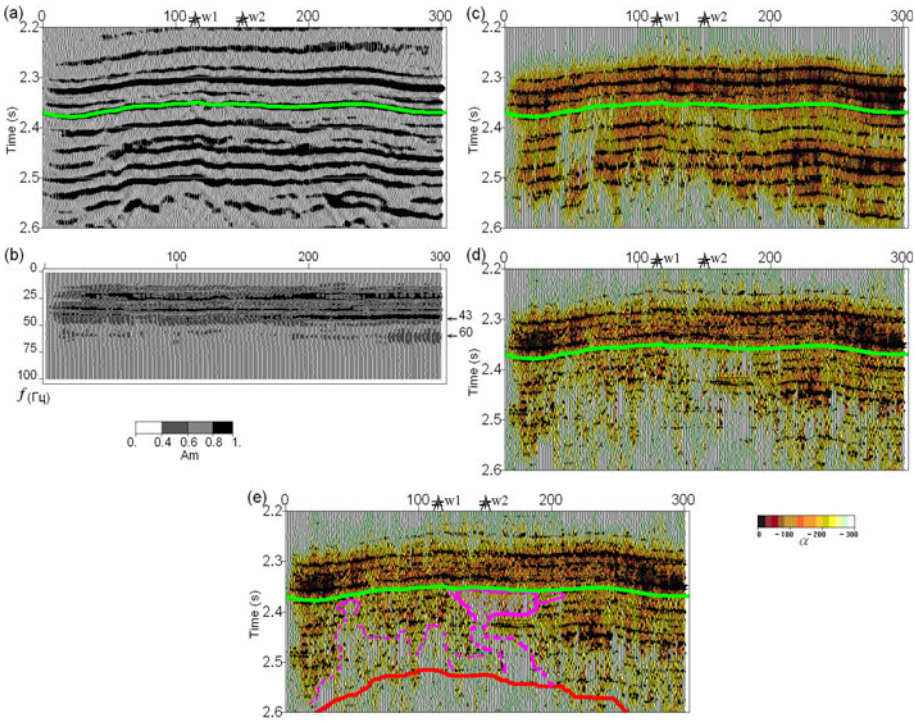

Fig. 6. Example of Prony filtering results and their interpretation.

eight to fifteen analyzed frequencies. For each of these frequencies Prony filtering is performed with optimal parameters. We do not present here the results of selecting the parameters for the selected frequencies. It is a chore and requires a significant sorting of values of parameters (see Mitrofanov and Priimenko 2013). We note only that in the initial stages such a selection takes a long time. To date, our technique requires a few hours to select final set of optimal parameters.

The analysis of the Prony filtering results performed for all of the frequencies has shown that frequencies up to 43 Hz are no significant frequency dependent effects. Such effects should be correlated with the target horizons, which in this case are located directly below the green line. In the transition to a higher frequency these effects appear more evidently. Perhaps this is due to the nonlinear increase of the absorption and dispersion depending on the frequency.

Figures 6c-d present images of the initial time section after Prony filtering on two frequencies, 43 and 60 Hz, correspondingly. The values of the damping factor determined by Prony filtering are given as background col-

ours in Figs. 6c-d. It is evident that a change in the frequency from 43 to 60 Hz makes it possible to identify a sufficiently large anomalous zone with increasing scattering and absorbing of seismic energy in the target horizon (under the green line). For the frequency of 65 Hz the results obtained are not sufficiently stable, and that is why they were not used for further interpretation.

The recognized anomalous zone is connected to one of the two wells located on the profile line. It must be noted that Prony filtering was used here in order to understand the cause of the significant difference in the production features of these wells. In spite of a relatively small distance between the wells (~800 m), the well W1 was dry and the well W2 had high production features (up to 500 m^3 of oil per day). The subsequent interpretation of the Prony filtering results enabled the geologists to create a model of the reservoir identifying the regions where hydrocarbon migration channels linking the mother rock of the Paleozoic strata to the trap are likely to be found (see Fig. 6e). The result shows that it is possible to use the Prony filtering method for the solution of geological problems.

Figure 6 also illustrates possibilities of Prony filtering for an analysis of thin-layer structures of the medium. A transition to high frequencies improves the resolution of the reflected signals situated in an area approximately 20 ms above the target horizon (green line in Fig. 6a). Here we can observe a non-stable reflection from an internal boundary. This reflection is tracked much better after Prony filtering with frequency 43 Hz (Fig. 6c) and 60 Hz (Fig. 6d).

A more explicit example of a similar analysis is represented in Fig. 7. Original data (Fig. 7a) belonged to another study area, where the target time interval was equal to [1.7, 2.0] s. As in the previous example, there were selected several frequencies (marked by pink lines) for which the optimal filtering parameters were selected. Figure 7b presents the results of filtering obtained for four such selected frequencies: 27, 40, 54, and 84 Hz. They provide the most expressive representation of change in the response of the medium depending on the frequency of propagating seismic signal. Again, the background colours related to the damping factor values are used for the Prony filtering results.

These results enabled us to improve the analysis of the structure of the reservoir (located just above Horizon C) and of the underlying horizons. According to the initial stack (Fig. 7a), Horizons C and B correspond to two strong reflections. However, on the basis of the Prony filtering results obtained on the frequency of 54 Hz (Fig. 7b), it was possible to clearly distinguish four reflections located between Horizons C and B. These reflections were confirmed by well data. In addition, it was possible to clarify how an error occurred while tracing Horizon A. First, this horizon was accurately

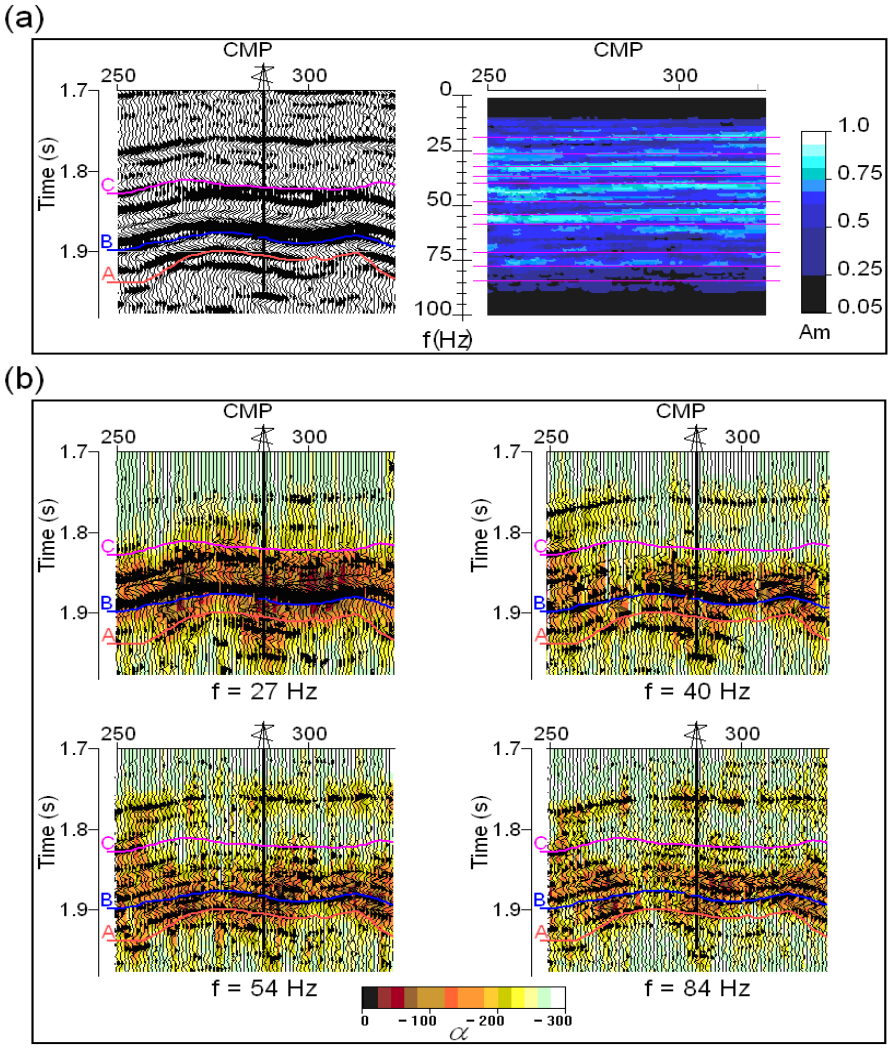

Fig. 7. Analysis of thin-layer structure based on the Prony filtering results.

identified by LOG-data of the well shown in Fig. 7. Then, the horizon line was lowered by 20 ms, which resulted in an error of about 40 m in the next well. This mistake was caused by a fault in the area around 260 CMP that can be seen on 84 Hz (Fig. 7b). It should be noted that some deterioration of the results on the frequency of 84 Hz is related to a sharp decrease in the SNR values for high frequencies.

This approach was used for a detailed study of target horizons. It also helped to choose better locations of exploration wells (Mitrofanov *et al.*

2006). However, for the field seismic data processing it would also be important to obtain a quantitative characteristic of possible anomalous zones and frequency variations observed in the results of Prony filtering. This estimate could be based on the mean value of interval energy and its combinations (Brekhuntcov *et al*. 2001). These combinations can be used to create anomalous zone maps as a basis for the study of oil/gas fields. Map interpretation can help to predict some of target horizon characteristics.

We are going to look at one of the first maps used to predict target horizons' productive features (see Fig. 8). This map was created for an analysis of one of the productive horizons. In the preparation of this map there were processed seismic data relating to 73 profiles of 2D survey, which covers an area of 1400 km^2. The target horizons refer in this case to a time range of [2.45, 2.7] s.

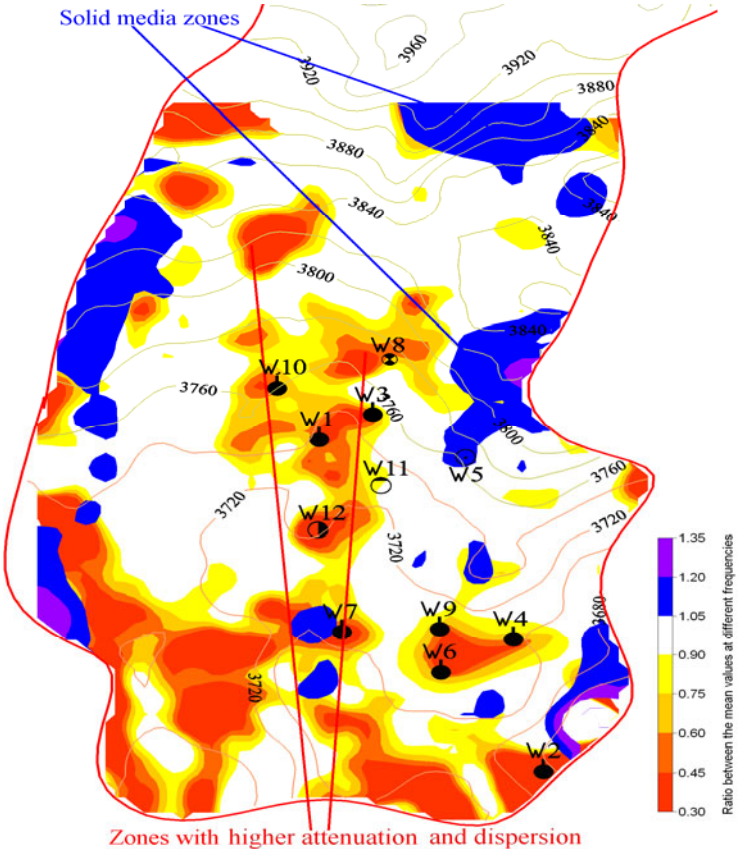

Fig. 8. Example of a map for target horizon features analysis created on the basis of the Prony filtering method. Thin lines show the depth isochrones for the top of target horizon.

The results presented above (Figs. 6 and 7) show that the Prony filtering allows us to study the response of the medium at a fixed frequency with a high enough resolution with respect to the time variable. This enables us to calculate the energy interval for a relatively narrow time intervals correlated with correlation lines of target horizons. So, for this example, the length of intervals for the energy of the time section, obtained by Prony filtering at a fixed frequency, was 25 ms (subsequent experiments performed in other areas have shown that the length may be reduced to 10-15 ms). Calculated values of energy can be used to draw the maps which characterize a change in the response of the medium along the analyzed horizon.

Their normalization with respect to the overlying horizons is important during the maps construction. In particular, the map of Fig. 8 was a result of relations between the two maps constructed using energies calculated for the intervals located directly above the productive horizon and along it. As the initial images, all 73 time sections were used (obtained for 60 Hz), which gave nearly 90% correlation with productivity of test wells. Therefore, there was a high level of confidence to the anomalous zones obtained as results of interpretation of the constructed maps.

Apart from the anomalous zones that characterize differences in attenuation and absorption of seismic energy at high frequencies (the regions with high attenuation and absorption are in bright red), the map shows zones where the medium is possibly consolidated (blue colour). The consolidation zones are related to intensification of response at high frequencies. The map shows a structural plan of the horizon, the position of the wells and their general production features obtained in the process of previous interpretation. In addition, it shows the anomalous zones determined by the Prony method. It is clear that the properties of the production wells are well correlated with the zones of high attenuation and absorption of seismic energy at high frequencies. At the same time, the structural plan of the horizon cannot guarantee the same production characteristics even for wells, which are relatively close to each other. For example, wells W10, W3, and W5 are almost at the same level, whereas well W11 is even more favourably located on the structural plan. Nonetheless, all the four wells have different production characteristics. The results obtained by the Prony filtering method also point to the differences. It is interesting to note that the position of well W12 was chosen based on the Prony filtering results. The well testing showed that the well was productive.

Thus, the use of the interval energy characteristics defined by the Prony filtering results made it possible to formalize the obtained results. However, these characteristics were neither linked to the well data, nor did they allow to interpret the results in terms of the well data. As a result, the maps of the dynamic Prony parameters were analyzed without taking into account the

well data, although an analysis of possible relations between these parameters and well data could be effective in a study of local reservoir characteristics which may be a key for a characterization of thin-layer objects.

Essentially, using the Prony filtering technology for target horizon analysis, we can construct maps based solely on filtration results for different frequencies. However, if there is some additional well information, it would be helpful to use it in full. It could be a way to create maps of production characteristics for target horizons on the basis of combined Prony parameters (Fedortsov *et al.* 2004) providing an opportunity to improve the quality and reliability of prediction features through the Prony method. The relationship between combined Prony parameters and well data can be traced in different ways.

As an example of this relationship we can consider the correlation between combined Prony parameters, built on the interval energy characteristics (C_p^{Pr}), and a generalized LOG-parameter, constructed on the basis of well logging results (C_p^{LOG}). This hyperbolic type of ratio between C_p^{Pr} and C_p^{LOG} is shown in Fig. 9. In this case, the correlation coefficient is 0.72. If

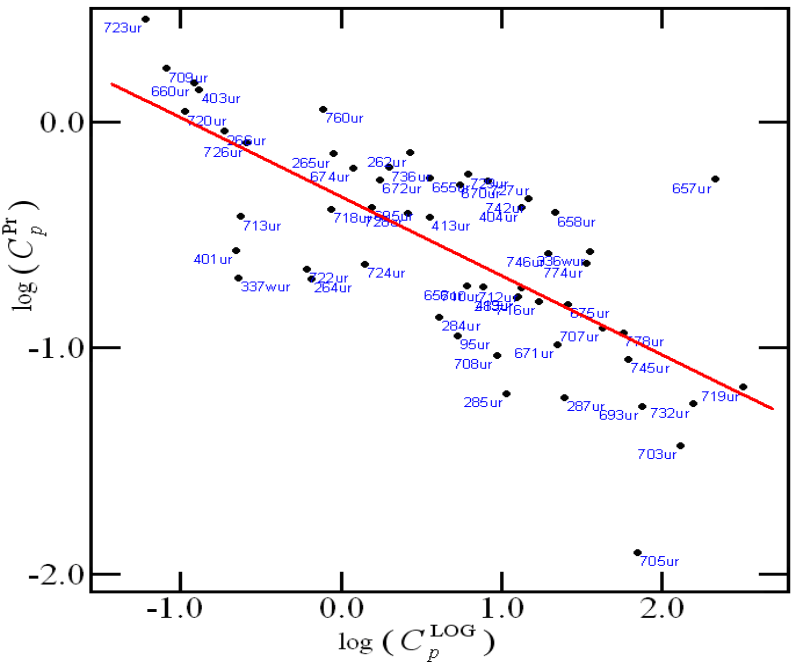

Fig. 9. Example of the ratio between a combined Prony parameter (C_p^{Pr}) and a generalized LOG-parameter (C_p^{LOG}).

only two wells (705 and 657) are removed from the plot, the coefficient value increases up to 0.83. Unfortunately, we had too little information to understand the difference between the features of these two wells and of the other ones. Prediction maps of target horizons production characteristics were created on the basis of this ratio. Then, the results were tested on a wider range of independent well data. The predictions proved to be precise for the entire studied area.

We suggest that the Prony filtering has a good potential for the analysis and localization of zones with different attenuation and dispersion characteristics of the studied medium. When these zones correlate with target horizons and tested wells, highly accurate characteristics of oil/gas reservoirs or carbonate bodies or fault zones can be determined. In addition, using an analysis of high-frequency response and tracing a relationship with the well data, the method can provide information about some properties of the rock which are not so easy to evaluate using surface seismic data. In this way, the method contributes to modern seismic data processing.

5. CONCLUSIONS

This article introduces a method for seismic data processing and discusses some examples of its application in geological and field tasks. The method is based on Prony decomposition and selection of components of this decomposition in order to obtain images of seismic data, which correspond to a narrow band of frequencies. Therefore, it can be called “Prony filtering”. Its closest analogue is the band-pass filtration. However, the method provides a higher resolution of signal images in terms of the time variable. Also, it allows us to obtain the damping factor corresponding to the frequency of filtering, which makes it possible to investigate changes in the damping factor as a function of frequency.

Using simple examples of signals, we have introduced the basics of the technology and discussed some examples of the aspects which are relevant for the application of this method to the processing of field seismic data. As we have seen, the results show a good stability of the algorithm for different waveforms and in the presence of other signals and noise. Also, we have discussed the main possibilities for the application of the method in practical tasks. We hope that this approach will be interesting for both, researchers and industrialists, and that the nonlinear Prony filtering method will become one of the instruments of geophysical spectral analysis.

Acknowledgments. This work was supported by Petrobras Institute for Research and Development – CENPES, RJ, Brazil, and National Institute of Science and Technology of Petroleum Geophysics – INCT-GP/CNPq/MCT, Brazil. The first author is especially thankful to North Fluminense

State University Darcy Ribeiro – UENF, RJ, Brazil, for providing support for him as a visiting researcher. We also thank Prof. Allen Howard, Jr., for stimulating discussions and Oksana Kitaeva, M.A. (TESOL), for editing the paper.

Appendix

About near-orthogonality of damped cosines

Consider the decomposition (1) of a vector $\mathbf{x}$ with respect to the basis of a finite-dimensional vector space

$$\mathbf{x} = \sum_{k=1}^{N} \alpha_k \mathbf{e}_k \ ,$$

where $\mathbf{x} = (x[1], x[2], \ldots, x[N])$, and

$$\mathbf{e}_k = \left(1 \cdot \cos\theta_k, e^{\alpha_k \Delta} \cdot \cos(2\pi f_k \Delta + \theta_k), \ldots, e^{\alpha_k (N-1)\Delta} \cdot \cos(2\pi f_k (N-1)\Delta + \theta_k)\right)$$

are the basis vectors. There is a similar representation for an infinite linear vector space in the case of continuous functions

$$x(t) = \sum_{k=1}^{\infty} \alpha_k h_k(t) \ ,$$

where

$$h_k(t) = e^{\alpha_k t} \cdot \cos(\omega_k t + \theta_k), \quad \omega_k = 2\pi f_k \ .$$

In the case of an approximate formulation of the problem, we can use finite expansion of the function $x(t)$

$$\tilde{x}(t) = \sum_{k=1}^{N} \alpha_k h_k(t) \ .$$

We assume that $\tilde{x}(t_k) = x(t_k)$ in points $t_k = (k-1)\Delta$. Then we can say that Eq. 1 gives a decomposition of the observed data on the elements of an infinite-space basis.

Now we study properties of h_k depending on $\mathbf{e}_k$. Let us consider the usual definition of the scalar product of two continuous functions defined on a finite interval $[0, T]$, $T > 0$, giving in the following form

$$\left(h_i(t), h_j(t)\right) = \int_0^T h_i(t), h_j(t)\, dt\,. \tag{A1}$$

Thus, to find the value of the scalar product between these basic functions it is necessary to calculate

$$I^{(1)} = \int_0^T \mathrm{e}^{(\alpha_i+\alpha_j)t} \cos(\omega_i t + \theta_i)\cdot\cos(\omega_j t + \theta_j)\, dt \tag{A2}$$

and

$$I_k^{(0)} = \int_0^T \mathrm{e}^{2\alpha_k t} \cos^2(\omega_k t + \theta_k)\, dt, \quad k = i, j\,, \tag{A3}$$

which are required for computing the norm of the corresponding functions.

Consider the Eq. A2. It is easy to show that

$$\int e^{\alpha t} \cos(bt + c)dt = e^{-\alpha c/b}\cdot(\alpha^2 + b^2)^{-1}\left[e^{-\alpha T/b}(\alpha\cdot\cos T + b\cdot\sin T) - \alpha\right].$$

Then, using

$$\cos(\omega_i t + \theta_i)\cdot\cos(\omega_j t + \theta_j) = \cos\left((\omega_i + \omega_j)t + (\theta_i + \theta_j)\right) + \cos\left((\omega_i - \omega_j)t + (\theta_i - \theta_j)\right)$$

and introducing the notations $\alpha = \alpha_i + \alpha_j$, $b^{\pm} = \omega_i \pm \omega_j$, $c^{\pm} = \theta_i \pm \theta_j$, we obtain

$$I^{(1)} = \frac{e^{-ac^+/b^+}}{\alpha^2 + (b^+)^2}\left[e^{\alpha T/b^+}(\alpha\cdot\cos T + b^+\cdot\sin T) - \alpha\right] +$$
$$+ \frac{e^{-ac^-/b^-}}{\alpha^2 + (b^-)^2}\left[e^{\alpha T/b^-}(\alpha\cdot\cos T + b^-\cdot\sin T) - \alpha\right],$$

which determines Eq. A1.

In a similar way we obtain the following expression for the integral A3

$$I_k^{(0)} = \frac{e^{-2a_k\theta_k/\omega_k}}{2(\alpha^2 + \omega_k^2)}\left[e^{\alpha_k T/\omega_k}(\alpha_k\cdot\cos T + \omega_k\cdot\sin T) - \alpha_k\right] + \frac{1}{4\alpha_k^2}\left[e^{2\alpha_k T} - 1\right],\ k = i, j\,.$$

These expressions allow us to calculate the cosine of the angle between the basis functions

$$\cos\left(h_i(t) \wedge h_j(t)\right) = \frac{\left(h_i(t), h_j(t)\right)}{\sqrt{\left(h_i(t), h_i(t)\right)\cdot\left(h_j(t), h_j(t)\right)}} = \frac{I^{(1)}}{\sqrt{I_i^{(0)}\cdot I_j^{(0)}}}\,. \tag{A4}$$

Formula A4 will be used for characterization of the basis vectors in the Prony decomposition of the Eq. 1 and for analyzing the degree of non-orthogonality of these vectors.

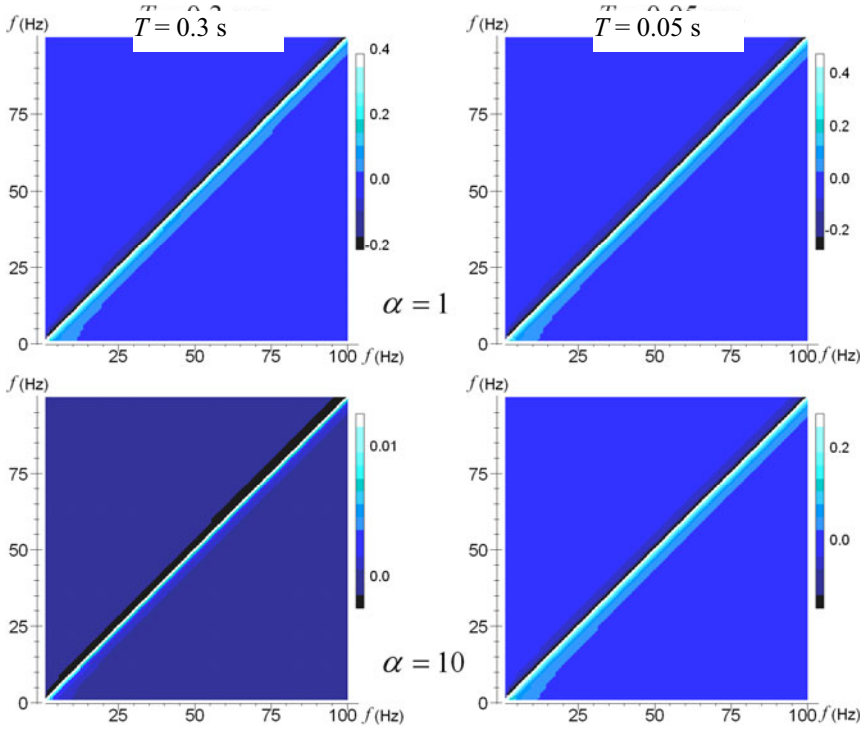

Fig. 10. Defining the cosine of the angle between the basis functions in the Prony expansion.

The analysis will be done for a particular case when $\alpha_i = \alpha_j \equiv \alpha$ and $\theta_i = \theta_j \equiv \theta$, *i.e.*, we consider $\mathbf{e}_k$ as a function of the frequency only. Examples of calculation of the cosine values are shown in Fig. 10. It was done for combinations of two values of the duration interval T (0.3 and 0.05 s) and two values of the damping parameter α (1 and 10) with $\theta = 0$. Formula A4 permits to consider any combinations of the frequency f during the cosine calculation. This made it possible to build a two-dimensional pictures, illustrating the dependence of the cosine function on the combinations of f_i, f_j. The colour scale shows that when the difference in the frequencies is less than 10 Hz, the cosine is very close to 0, *i.e.*, becomes near-orthogonal. These results indicate that the increasing value of α improves the orthogonality of the basis vectors, and a decreasing duration of interval T may increase the degree of non-orthogonality.

The obtained near-orthogonality of the basis vectors could be one of the reasons for good performing the Prony filtering based on the selection of the decomposition components. In addition, it allows a better understanding of

this selection and the impact on him of parameters such as the duration of interval T or α. This propery helps us to obtain a better signal resolution and use a few Prony modes.

References

Berti, E., V. Cardoso, J.A. González, and U. Sperhake (2007), Mining information from binary black hole mergers: A comparison of estimation methods for complex exponentials in noise, *Phys. Rev. D* **75**, 12, 124017, DOI: 10.1103/PhysRevD.75.124017.

Beylkin, G., and L. Monzón (2005), On approximation of functions by exponential sums, *Appl. Comput. Harmon. Anal.* **19**, 1, 17-48, DOI: 10.1016/j.acha.2005.01.003.

Bracale, A., P. Caramia, and G. Carpinelli (2007), Adaptive Prony method for waveform distortion detection in power systems, *Int. J. Elec. Power Energy Sys.* **29**, 5, 371-379, DOI: 10.1016/j.ijepes.2006.10.005.

Brekhuntcov, A., Yu. Ilein, A. Jedkov, and G. Mitrofanov (2001), Prediction of production features on Prony-filtration results. **In:** *EAGE 63rd Conference and Technical Exhibition, 11-15 June 2001, Amsterdam, Netherlands*, 345-348.

Chui, C.K. (1992a), *An Introduction to Wavelets,* Wavelet Analysis and its Applications. Vol. 1, Academic Press, San Diego, 264 pp.

Chui, C.K. (ed.) (1992b), *Wavelets: A Tutorial in Theory and Applications,* Wavelet Analysis and its Applications. Vol. 2, Academic Press, San Diego, 723 pp.

de Prony, G.R. (1795), Essai éxperimental et analytique: sur les lois de la dilatabilité de fluides élastique et sur celles de la force expansive de la vapeur de l'alkool, à différentes températures, *J. École Polytech. Flor. Plair.* **1**, 22, 24-76 (in French).

Fedortsov, V.K., E.V. Bazhanova, Yu.M. Ilein, and G.M. Mitrofanov (2004), Solution of some application tasks under studying of NGK reservoirs on the basis of wave fields decomposition by the Prony method, *Gornye Vedomosti* **3**, 81-85 (in Russian).

Fomel, S. (2013), Seismic data decomposition into spectral components using regularized nonstationary autoregression, *Geophysics* **78**, 6, O69-O76, DOI: 10.1190/geo2013-0221.1.

Gabor, D. (1946a), Theory of communication. Part 1: The analysis of information, *J. Inst. Elect. Eng.* **93**, 26, 429-441, DOI: 10.1049/ji-3-2.1946.0074.

Gabor, D. (1946b), Theory of communication. Part 2: The analysis of hearing, *J. Inst. Elect. Eng.* **93**, 26, 442-445, DOI: 10.1049/ji-3-2.1946.0075.

Gabor, D. (1946c), Theory of communication. Part 3: Frequency compression and expansion, *J. Inst. Elect. Eng.* **93**, 26, 445-457, DOI: 10.1049/ji-3-2.1946.0076.

Gritsenko, S.A., S. Fomel, and V.S. Cherniyak (2001), Filtering using Prony's method. **In:** *Geophysics. The Jubilee Volume "50th Khantymansiisk-geofizika"*, Euro-Asian Geophysical Society, Moscow, Russia, 24-26 (in Russian).

Grossmann, A., and J. Morlet (1984), Decomposition of Hardy functions into square integrable wavelets of constant shape, *SIAM J. Math. Anal.* **15**, 4, 723-736, DOI: 10.1137/0515056.

Helle, H.B., O.H. Inderhaug, V.P. Kovaljev, A.G. Madatov, and G.M. Mitrofanov (1993), Complex seismic decomposition – application to pore pressure prediction. **In:** *EAGE 55th Conference and Technical Exhibition, 7-11 June 1993, Stavanger, Norway*, 132-139, DOI: 10.3997/2214-4609.201411369.

Holmström, K., and J. Petersson (2002), A review of the parameter estimation problem of fitting positive exponential sums to empirical data, *Appl. Math. Comput.* **126**, 1, 31-61, DOI: 10.1016/S0096-3003(00)00138-7.

Hu, S.-L.J., W.-L.Yang, and H.-J. Li (2013), Signal decomposition and reconstruction using complex exponential models, *Mech. Syst. Signal Process.* **40**, 2, 421-438, DOI: 10.1016/j.ymssp.2013.06.037.

Kahn, M.H., M.S. Mackisack, M.R. Osborne, and G.K. Smyth (1992), On the consistency of Prony's method and related algorithms, *J. Comput. Graph. Stat.* **1**, 4, 329-349, DOI: 10.1080/10618600.1992.10474589.

Kovaljev, V.P., and G.F. Telepnev (1981), Method of implicit periodicity in study of dynamic problems of seismic waves, *Rep. Ukr. Acad. Sci.* **5**, 38-47 (in Russian).

Kovaljev, V.P., A.G. Madatov, and G.M. Mitrofanov (1992), Complex convolution decomposition (CCD) and new possibilities at detail investigation of attenuation. **In:** *EAGE 54th Conference and Technical Exhibition, 1-5 June 1992, Paris, France*, 267-275.

Kumaresan, R. (1983), On the zeros of the linear prediction-error filter for deterministic signals, *IEEE Trans. Acoust. Speech Sign. Process.* **31**, 1, 217-220, DOI: 10.1109/TASSP.1983.1164021.

Lee, J.-H., and H.-T. Kim (2005), Selection of sampling interval for least squares Prony method, *Electron. Lett.* **41**, 1, 47-49, DOI: 10.1049/el:20056678.

Lobos, T., J. Rezmer, P. Janik, H. Amaris, M. Alonso, and C. Álvarez (2009), Application of wavelets and Prony method for disturbance detection in fixed speed wind farms, *Int. J. Elec. Power Energy Sys.* **31**, 9, 429-436, DOI: 10.1016/j.ijepes.2009.03.019.

Marks, R.J., II (2009), *Handbook of Fourier Analysis & Its Applications*, Oxford University Press, New York, 800 pp.

Marple, S.L. Jr. (1987), *Digital Spectral Analysis with Applications*, Prentice-Hall, Englewood Cliffs.

Mitrofanov, G.M., and V.I. Priimenko (2011), Prony filtration of seismic data: theoretical background, *Rev. Bras. Geofis.* **29**, 4, 703-722.

Mitrofanov, G.M., and V.I. Priimenko (2013), Prony filtering of seismic data: mathematical and physical modelling, *Rev. Bras. Geofis.* **31**, 1, 151-168.

Mitrofanov, G.M., H.B. Helle, V.P. Kovaliev, and A.G. Madatov (1993), Complex seismic decomposition – theoretical aspects. **In:** *EAGE 55th Conference and Technical Exhibition, 7-11 June 1993, Stavanger, Norway*, 235-242.

Mitrofanov, G.M., T.V. Nefedkina, and L.Sh. Girshgorn (1998a), Aspects of Pronitransformation applying in seismic data processing, *Ann. Geophys.* **16**, Suppl. Part I, 156-161.

Mitrofanov, G.M., Z. Zhan, and J. Cai (1998b), Using the Proni transform in processing of Chinese seismic data. **In:** *SEG 68th Ann. Meeting, 13-18 September 1998, New Orleans, USA*, 1157-1159.

Mitrofanov, G.M., A.N. Bobryshev, and V.G. Savin (1999), Using Prony filtering for the identification of perspective zones in hydrocarbon deposits. **In:** *Proc. 3rd Scientific-Practical Conf.* "*Ways of Realization of Oil and Gas Potential of the KMAO", Khanty-Mansiysk, Russia*, 281-294 (in Russian).

Mitrofanov, G.M., T.V. Nefedkina, A.N. Bobryshev, V.G. Savin, and V.G. Popov (2001), Applying Prony filtering for seismic wave field analysis with the purpose of perspective zones determination in exploration of oil/gas reservoirs. **In:** *Geophysics. The Jubilee Volume "50th Khantymansiisk-geofizika"*, Euro-Asian Geophysical Society, Moscow, Russia, 92-100 (in Russian).

Mitrofanov, G., V. Priimenko, and D.M. Soares Filho (2003a), Development of the Proni filtering method. **In:** *8th Int. Congr. Brazilian Geophysical Society, August 2003, Rio de Janeiro, Brazil.*

Mitrofanov, G., V. Priimenko, D.M. Soares Filho, R.M. Misságia, M.H. Grochau, and R.G. Lima (2003b), Using the Proni filtration in geological and production tasks. **In:** *8th Int. Congr. Brazilian Geophysical Society, August 2003, Rio de Janeiro, Brazil.*

Mitrofanov, G., S. Smolin, and L. Slepokurova (2006), Determination of permeability zones and traps by means of the Proni filtration method. **In:** *68th EAGE Conference and Exhibition incorporating SPE EUROPEC 2006, Vienna, Austria*, DOI: 10.3997/2214-4609.201402075.

Orlov, Y.A., G.M. Mitrofanov, I.F. Rakhmenkulova, and T.V. Kurdujkova (1999), Testing the Proni filtering by model data. **In:** *EAGE 61st Conference and Technical Exhibition, 7-11 June 1999, Helsinki, Finland*, DOI: 10.3997/2214-4609.201407884.

Osborne, M.R. (1975), Some special nonlinear least squares problems, *SIAM J. Numer. Anal*. **12**, 4, 571-592, DOI: 10.1137/0712044.

Osborne, M.R., and G.K. Smyth (1991), A modified Prony algorithm for fitting functions defined by difference equations, *SIAM J. Sci. Stat. Comput*. **12**, 2, 362-382, DOI: 10.1137/0912020.

Osborne, M.R., and G.K. Smyth (1995) A modified Prony algorithm for exponential functional fitting, *SIAM J. Sci. Comput.* **16**, 1, 119-138, DOI: 10.1137/0916008.

Potts, D., and M. Tasche (2010), Parameter estimation for exponential sums by approximate Prony method, *Signal. Process.* **90**, 5, 1631-1642, DOI: 10.1016/j.sigpro.2009.11.012.

Therrien, C.W. (1992), *Discrete Random Signals and Statistical Signal Processing*, Prentice Hall, Englewood Cliffs, 727 pp.

Received 9 February 2014
Received in revised form 16 June 2014
Accepted 24 June 2014

DE GRUYTER OPEN

Acta Geophysica
vol. 63, no. 3, June 2015, pp. 679-697
DOI: 10.1515/acgeo-2015-0015

Earthquake-related Electric Field Changes Observed in the Ionosphere and Ground

Yingying FAN, Xuebin DU, Zhanghui AN, Jun LIU, Dacheng TAN, and Junying CHEN

Lanzhou Base of Institute of Earthquake Prediction, China Earthquake Administration, Lanzhou City, China; e-mail: fyy416@163.com

Lanzhou Institute of Seismology, China Earthquake Administration, Lanzhou City, China

A b s t r a c t

The changes of the ionospheric electric field before and after four huge earthquakes, which include the *Ms* 8.7 earthquake of 2004 and the *Ms* 8.5 earthquake of 2005 in Sumatra of Indonesia, the *Ms* 8.0 Wenchuan earthquake of 2008 in China, the *Ms* 8.8 earthquake of 2010 in Chile, and their strong aftershocks are studied in this paper. The significant results revealed that the power spectral density of low-frequency electric field below 20 Hz in the ionosphere, a kind of electromagnetic radiation phenomena, increased abnormally before and after the earthquakes and partially corresponded to the increased power spectral density of the low-frequency geoelectric field in time. This research preliminarily indicates that the low-frequency electromagnetic radiation during the imminent stages before such earthquakes could be detected by the observation of the ionospheric electric field. However, the spatial, temporal, and intensive complexities of the electric field anomalies in the ionosphere before earthquakes have come in sight also.

Key words: ionosphere, satellite, electric field, earthquake, changes.

1. INTRODUCTION

Recently, more and more attention is paid internationally to the application of electromagnetic observations in the earthquake (EQ) and volcano monitoring. Since the 1950s, the former Soviet Union, Japan, the United States, China, and other countries have carried out the ground electromagnetic observations and reported the electromagnetic precursory phenomena in the time and frequency domains before earthquakes (Varotsos *et al.* 1986, Varotsos and Lazaridou 1991, Michel and Zlotnicki 1998, Zlotnicki *et al.* 2001, Uyeda *et al.* 2002, Ma *et al.* 2004, Telesca *et al.* 2005, 2008, 2009, Enomoto *et al.* 2006, Telesca and Hattori 2007, Nagamoto *et al.* 2008, Tang *et al.* 2008, Fan *et al.* 2010, Liu *et al.* 2011). Furthermore, a lot of loading experiments and theoretical studies have been made on the mechanism of generation and propagation of the electromagnetic signals (Ogawa *et al.* 1985, Cress *et al.* 1987, Yamada *et al.* 1989, Enomoto and Hashimoto 1992, Varotsos *et al.* 1998, Huang and Ikeya 1998, Adler *et al.* 1999, Ishido and Pritchett 1999, Huang 2005). However, the long-term observation also reveals that the earthquake-related precursory anomalies recorded by ground stations displayed extremely complicated spatial, temporal, and intense distributions. For example, no anomalies appeared evenly in/near the epicentral areas of some strong or huge EQs, anomalies have not been repeatedly recorded before the equivalent-magnitude EQs, and even there were a lot of anomalies without any earthquake (no earthquake occurred near the station at which an electromagnetic anomaly has been recorded), as reported by Du (2011). These complicated phenomena cause great difficulties in identifying any earthquake-related information and determining an EQ forecasting statement.

Since the 1980s, the space-to-ground electromagnetic observation with the purpose of EQ monitoring and prediction has been carried out internationally (Parrot 1995, 2006a, b), and the electromagnetic phenomena in the ionosphere associated with EQs were reported (Liu *et al.* 2003, Pulinets *et al.* 2005, Zhang *et al.* 2012). This will set up a three-dimension- al electromagnetic observation system by integrating with the ground electromagnetic observations, which will perhaps help to overcome the afore- mentioned complicated problems of earthquake-related electromagnetic precursory anomalies. In 2004, France launched a special satellite, the Demeter (detection of electro-magnetic emissions transmitted from EQ regions), for the EQ electromagnetic monitoring. During the satellite's operation, a number of great EQs, with magnitude of above *Ms* 8.0, occurred globally, and a series of EQs above *Ms* 7.0 happened in Chinese mainland and surrounding areas. The electromagnetic precursory anomalies in the ionosphere deemed to be associated with the EQs are reported (Liu *et al.* 2003, 2011, Pulinets *et al.*

2005, Cussac *et al.* 2006, He *et al.* 2009, Fan *et al.* 2010, Zhang *et al.* 2012). This paper will study the changes of the ionospheric electric field observed by Demeter before and after the EQs, compare the ionospheric electric fields and the ground electric/magnetic field changes before the EQs occurred in Chinese mainland, and, accordingly, report some significant results obtained.

2. DATA AND METHOD

The satellite Demeter was launched into orbit on 29 June 2004, as a special seismic electromagnetic observation satellite, which had a circular sun-synchronous polar orbit with an inclination of 98.23° and a run altitude of 710 km (this altitude was changed to 665 km in mid-December 2005; Cussac *et al.* 2006, Parrot 2006a, b). During its operation, a series of EQs with the magnitude of above *Ms* 8.0 occurred globally, such as the *Ms* 8.7 EQ (2004), *Ms* 8.5 EQ (2005), the *Ms* 8.5 and 8.3 EQs (2007) in Sumatra, Indonesia, the *Ms* 8.0 EQ (2008) in Wenchuan, China, and the *Ms* 8.8 EQ (2010) in Chile as well as the *Ms* 7.3 EQ (2008) in Yutian, China. This paper focuses on the ionospheric electric field changes observed by the ICE (Instrument Capteur Electrique; Berthelier *et al.* 2006) electric field instrument before the great EQs. The ICE electric field instrument measured the three electrical field components. The Demeter satellite adopts the "survey" mode to record the electric field data with the sampling frequency of 39.0625. Considering that the earthquake-related electromagnetic field has the characteristics of "the field distribution and propagation", the observation data of the Demeter's orbits within the latitude and longitude of $20° \times 20°$ range above the epicenters are selected. Under normal circumstances, the satellite runs through 2 to 3 half orbits every day within the above-mentioned range, and thus the electric field observation data of a number of days before and after the EQs may constitutes the time series that consists of many half-orbits according to time order, which is referred to as "successive orbit" in this paper.

The *Ms* 8.0 Wenchuan EQ and the *Ms* 7.3 Yutian EQ happened in the eastern and western edges of the Qinghai-Tibet Plateau, respectively, with a distance of about 2000 km between their epicenters. The ground electric stations, with the solid non-polarized electrodes made in China, are distributed in the northern, northeastern, and eastern edges of the Qinghai-Tibet Plateau. The station measures the three components of the geoelectric field below 0.005 Hz, along the NS, EW, and oblique directions, respectively; its electrode spacing is 90~300 m and they are buried below 2 m depth (Qian *et al.* 2004, Du *et al.* 2006). Fan *et al.* (2010) and Liu *et al.* (2011) studied the electric/magnetic response observed on the ground before the two EQs. Referring to the ground electric/magnetic changes, this paper reports a compar-

ative research on the ionospheric electric field changes observed by the Demeter before and after the two great EQs.

Due to the high sampling rate of the Demeter's ionospheric electric field observations, it is not suitable to analyze the waveform changes of the electric field in time domain. Fan *et al.* (2010) and Liu *et al.* (2011) applied the maximum entropy method (MEM) to conduct research on the time-varying power spectral density (PSD) of the electric/magnetic field observed by the ground electromagnetic stations, approaching to the occurrence date of the Wenchuan EQ and other strong EQs in the Qinghai-Tibet Plateau and its edge. The significant information of the time-varying PSD changes corresponding to the EQs has been obtained. This paper applies the method to process the electric field observation data in the ionosphere observed by Demeter, which is conductive to the comparative analysis for the ionospheric and ground electric field changes before EQs.

3. IONOSPHERIC ELECTRIC FIELD CHANGES BEFORE GREAT EQS

3.1 Ionospheric and ground electric fields before the Wenchuan *Ms* 8.0 EQ

3.1.1 Ionospheric electric field (continual orbit)

Here, the so-called continual orbit means all orbits of Demeter over the selected area within the required time. The Wenchuan *Ms* 8.0 EQ, in Sichuan, China, occurred on 12 May 2008 (LZT), with its epicenter located at N31.01°, E103.38°. The observational data of the ionosperic electric field of the Demeter's orbits, the Up-orbit observation data (night orbits) in the range of N20°-40° and E90°-110° and in the period from 1 January to 23 June 2008 are selected.

Figure 1 shows the time-varying PSD changes of the ionospheric electric field of the three components: *X*, *Y*, and *Z* (the abscissa is the date, the vertical axis is the frequency, and the color is amplitude of PSD; the date and EQs in the figure are marked in UT). The data are observed by the Demeter above the Wenchuan and analyzed through the MEM method. Three EQs with the magnitude $Ms \geq 6.9$ occurred in the selected range of the Demeter's orbit from 1 January to 23 June 2008, which were the *Ms* 6.9 Gaize EQ in Tibet on 9 January, the *Ms* 7.3 Yutian EQ in Xinjiang on 20 March, and the *Ms* 8.0 Wenchuan EQ on 12 May, in China. It can be seen from Fig. 1a that discontinuous PSD increase of frequency $f < 3$ Hz appeared in the three components of ionosphere electric field from 8 January 2008, which disappeared around 10 February 2008. These changes corresponded to the time of occurrence of the *Ms* 6.9 Gaize EQ and its strong aftershocks. From Fig. 1b, the PSD increase of $f < 3$ Hz in the *Y*-component on 19 March, correspond-

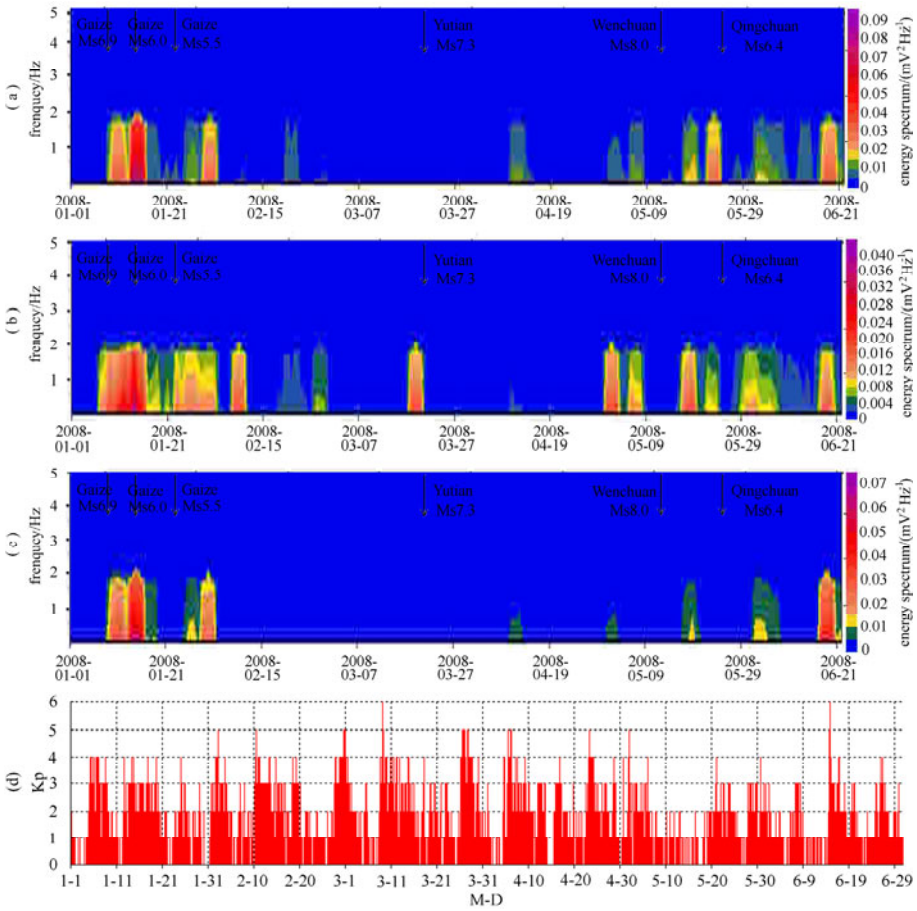

Fig. 1. Time-varing electric field PSD of Demeter's Up Orbit above Wenchuan and the *Kp* index in the corresponding period (d). Note: (a)-(c) are diagrams for *X*-, *Y*-, and *Z*-components.

ingly, at 22:00 of 20 March (at 6:33 of 21 March LZT), the *Ms* 7.3 EQ happened in Yutian county, Xinjiang. And then, since the occurrence of the Yutian EQ till the end of April, the PSD of the three electric field components has kept relatively calm (Fig. 1a-c) and during the time interval no EQ with the magnitude of $Ms \geq 6$ happened globally, except for the *Ms* 6.1 EQ occurred in the south Taiwan sea, China. In early May 2008, the *X*- and *Y*-components had the PSD increase, of which the most significant one was the PSD increase of the *Y*-component, and this corresponded to the time of occurrence of the Wenchuan *Ms* 8.0 EQ on 12 May 2008 and its aftershocks. However, the PSD increase starting before the occurrence of the Wenchuan

great EQ did not disappear until 23 June, and consequently a series of *Ms* 5.0~6.4 strong aftershocks, such as the *Ms* 6.4 Qingchuan EQ and others, occurred in the Wenchuan and its vicinity from June to July 2008. Therefore, the increased PSDs were perhaps related to these strong aftershocks.

Figure 1d shows the geomagnetic *Kp* indexes from January to June 2008. According to the analysis, the *Kp* indexes are less than 4 during the time interval of the PSD increase when approaching the date of occurrence of these EQs; however, as for the corresponding magnetic storms of $Kp = 6$ on 9 March and 14 June, no PSD increase appeared in the ionospheric electric field. Thus, the above-mentioned PSD increase should not be caused by magnetic activity.

From January to June 2008, in addition to the aforementioned EQs, 11 other EQs with the magnitude $Ms > 7.0$ occurred globally; the greater EQs corresponding to the time interval of the aforementioned PSD increase were the Sumatra *Ms* 7.7/7.6 EQs on 20 and 25 February and the Okhotsk *Ms* 7.6 EQ on 5 July, which were far from the selected orbit range.

3.1.2 Comparisons between the ionospheric and ground electric field changes

The Wenchuan *Ms* 8.0 EQ occurred in the eastern edge of the Qinghai-Tibet Plateau. Dozens of electromagnetic stations of the China Earthquake Administration (CEA) are distributed along the eastern, northeastern and northern edges. Two ground geo-electromagnetic stations, namely, SHN and TIA, co-established by Lanzhou Institute of Seismology (CEA-LIS) and Clermont-Ferrand Geophysical observatory of French Academy of Sciences (CNRS-OPGC) are distributed near the Tianzhu fault, China Gansu, which is located in the Northeastern Tibetan Plateau. These stations are dozens of kilometers to 1000 km from the epicenter of the great Wenchuan EQ. Fan *et al.* (2010) applied the MEM method to process the ground electric field data observed by SHN (683 km from the epicenter), TIA (669 km), and Chengdu station (CDU, 35 km). Among the stations, the electrode-ranging region of stations SHN and TIA are the herdsmen's pastures, which are open and flat, without the low-frequency electromagnetic interference like plants and large electrical equipments within dozens of kilometers around. The electromagnetic environment is very favorable. Geologically, the two stations are located in the Haiyuan-Liupanshan mountain fracture zone. According to a long-term observation of EQ precursor, if the geo-electromagnetism, underground flow and crustal deformation stations are located nearby such active fracture zone, the imminent anomalies at these stations are easy to be observed immediately before EQs (Du *et al.* 1993, 1997, 2000). Furthermore, the rock experiments showed the medium stress in this position is sensitive to disturbed stress (Kusunose *et al.* 1980).

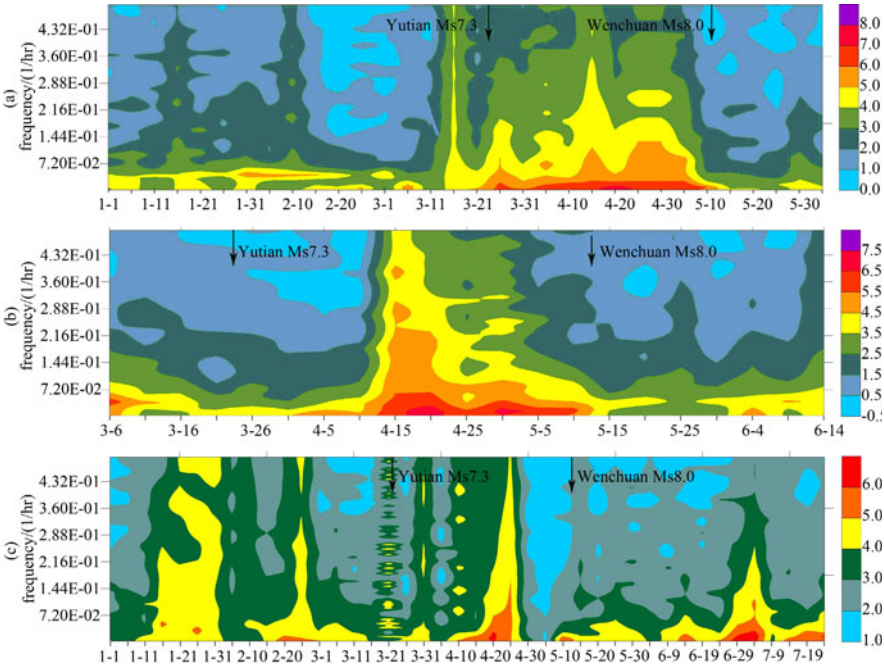

Fig. 2. MEM time-frequency diagrams for the N_1S_1 channel of SHN (a), the N_1S_1 channel of TIA (b), and the EW channel of CDU (c) stations. Note: Color values are Lg(PSD).

Figure 2 shows the time-varying PSD of the geoelectric field data of the N_1S_1 channel of station SHN, the N_1S_1 channel of station TIA, and the EW channel of station CDU (the date in the figure is in local time), which are processed by using the MEM method. In the calculation of PSD, every 5-day continuous observation data constitutes a time series and is used to calculate the PSD changes with frequency. A number of 5-day calculation results constitute the time-frequency color drawings as shown in Fig. 2. Figure 2a shows the geoelectric field PSD calculated by the hourly average values of 10-s sampling observational data of SHN station from January to May 2008. By compared the PSD changes before 16 March with those from 17 March till the occurrence of the Wenchuan EQ in the figure, the PSD in the latter time interval is significantly increased while obviously decreased immediately after the great EQ. From the overall changes, before the occurrence of the Wenchuan EQ, the geoelectric field PSD of N_1S_1 channel of station SHN had an increase of 1 to 3 orders of magnitude while it decreased when approaching the date of occurrence of the great EQ. In particular, from March 16 to 20 (local time) transient and significant increase of the $T < 3h$ electric field PSD occurred, which was corresponding to the occurrence time of the

Ms 7.3 Yutian EQ. Figure 2b shows the PSD changes of the geoelectric field calculated by the hourly average values of 10-ssampling data of station TIA from March to June 2008. It can be seen that from 15 April to the occurrence of the Wenchuan EQ, there was a significant PSD increase in N_1S_1 channel of station TIA, larger than the PSD at any time, which reached the maximum and then gradually decreased, returning to the value level before 15 April, immediately after the Wenchuan EQ. Figure 2c shows the PSD changes calculated by the hourly average values of minute-sampling data of station CDU from January to July 2008. Before the Wenchuan EQ, the PSD of the electric field in the EW channel of CDU increased overtly, which showed the following aspects:

(i) From 16 January to the occurrence of the EQ (nearly 4 months), the PSD of each low-frequency had fluctuating changes, while they were relatively stable after the EQ. This may be caused by the great affects from the focal preparation of the EQ due to the small distance between the station and the epicenter.

(ii) Roughly from 10 April, the PSD of low-frequency geoelectric field (particularly period $T < 3h$ components) obviously increased as compared to those in the past 40 days, with the maximum increase reaching 3 orders of magnitude; then since 30 April (12 days before the great EQ), the PSD decreased to the minimum.

(iii) Around the occurrence time of the Yutian *Ms* 7.3 EQ (local time, 21-25 March), the PSD alternately increased and reduced, which showed a remote relevance between the PSD changes and the epicenter of the *Ms* 7.3 EQ.

It can be seen from the comparison between Figs. 2 and 1 that:

(i) Roughly from 15 January to 1 March, before the *Ms* 8.0 Wenchuan EQ, CDU station that was nearest to the epicenter had a prominent PSD increase of the near-DC component geoelectric field; and during this period of time, the three components of ionospheric electric field also had the PSD significant increase with the 0 ~ a few Hz frequency, both of which corresponded in time.

(ii) On the eve of the Yutian *Ms* 7.3 EQ, in the period of geoelectric field PSD increase of SHN station (calculated by the data of 16 to 20 March, local time), the ionospheric electric field *Y*-component had an obvious PSD increase of 0 ~ a few Hz on 20 March, basically consistent with the ground electric field PSD increase in time.

(iii) During the period from 30 April to the occurrence of the Wenchuan EQ, the *X*- and *Y*-components of the ionospheric electric field had the PSD increase with 0 ~ a few Hz frequency, but the three ground stations had no such phenomena.

3.1.3 Ionospheric electric field (Demeter's revisit orbits)

Figure 3 shows the time-frequency PSD of the ionospheric electric field of the Demeter's revisited orbits above the Wenchuan EQ. The revisited period of was 16 days before the end of June 2008 and that was about 14 days after this. The time when the revisited orbits run above Wenchuan was 14:50:30 UT, roughly in the range of N20°-40° and E100.8°-105.4° and with the operating altitude of 660 km. The data of a total of 90 half-orbits in the period from 1 January 2006 to 31 December 2009 are selected. Within 90 days of running 90 half orbits, only on 5 April 2006, $Kp > 4$ and $|Dst| < 40$. It can be seen from the figure that the significant PSD increase of electric field ($f \leq 2$ Hz) appeared above Wenchuan from May to June 2006, June to November 2007, May to September 2008, and from July to October 2009. During these periods, a series of strong EQs and great EQs happened in the Qinghai-Tibet Plateau and its surrounding areas as well as in Indonesia. Nevertheless, the PSD increase of the ionospheric electric field observed by the revisited orbits behaved complicatedly, on the whole. It is difficult to analyze the correspondence in time between the EQs and the PSD increases, and no significant anomaly appeared before the Wenchuan EQ.

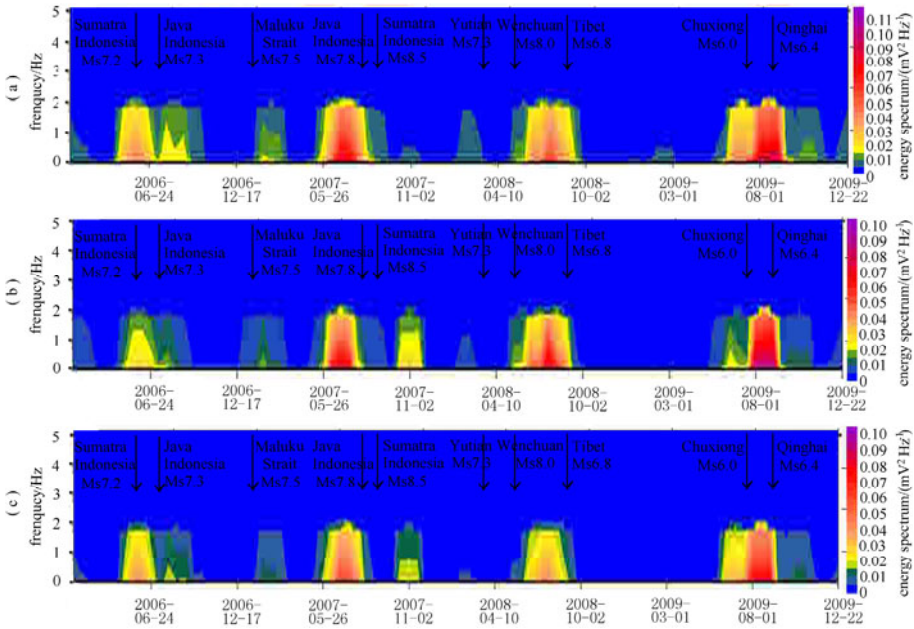

Fig. 3. PSD time-frequency diagram of electric field of the Demeter's revisit orbits above Wenchuan. Note: (a)-(c) represent the *X*-, *Y*-, and *Z*-components, respectively.

3.2 Ionospheric electric field changes of the Sumatra *Ms* 8.7 and 8.5 EQs (continual orbit)

On 26 December 2004, an *Ms* 8.7 EQ happened in the sea west of Sumatra, and its epicenter was located at N3.9° and E95.9°. On 28 March 2005, an *Ms* 8.5 EQ occurred north of Sumatra, and its epicenter was located at N2.2° and E97.0°. The distance between the two epicenters is very short. The data of the Demeter's orbits in the range of S5°-N15° and E85°-105°, above Sumatra, are selected, and the data was from September 2004 to April 2005. Figure 4 shows the PSD changes with time of the ionospheric electric field, namely, the *X*-, *Y*-, and *Z*-components of the electric field (the EQs in the figure are marked in UT). The PSD of electric field is calculated by the MEM method. From September 2004 to April 2005, within the area below the selected the Demeter's orbits, three *Ms* ≥7.0 EQs happened, including the *Ms* 7.0 EQ on 1 January 2005 (N5.2°, E92.3°), the *Ms* 7.0 and 8.7 EQs which occurred in the sea west of Sumatra. In addition, an *Ms* 7.3 EQ happed in Sumatra (S2.3°, E104.1°) on 25 July 2004. In Figure 4, from early December 2004 to early February 2005, and from middle March to middle

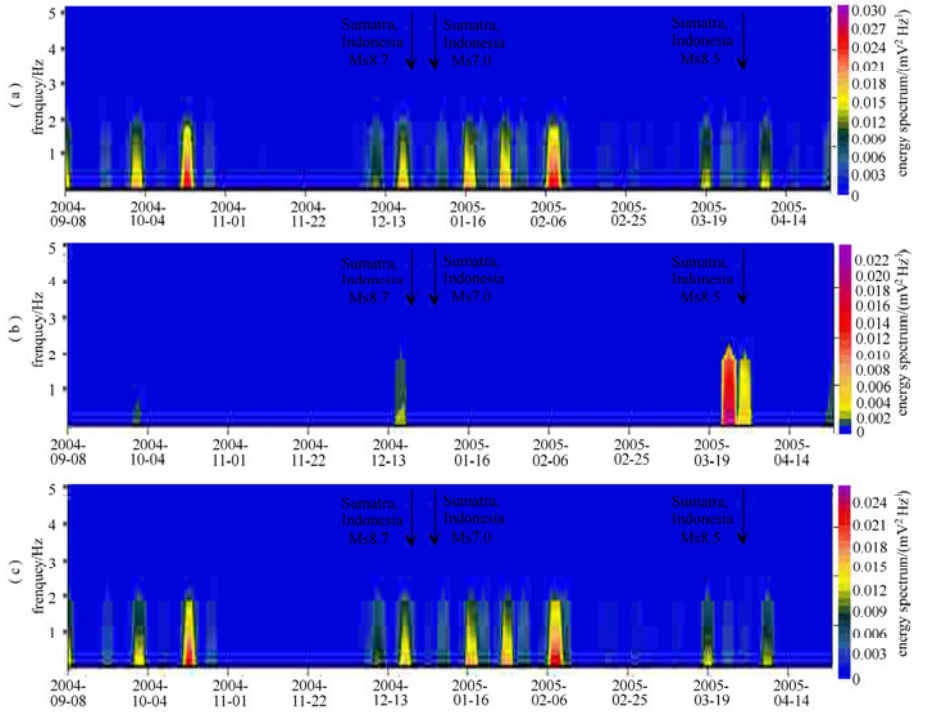

Fig. 4. PSD diagrams of the electric field of the Demeter's Up Orbit above the Sumatra EQs. Note: (a)-(c) represent the *X*-, *Y*-, and *Z*-components, respectively.

April 2005, the PSD of the ionospheric electric field of $f < 3$Hz increased, which was corresponding to the occurrence of the three EQs in Sumatra in time. Especially in the diagram of the *Y*-component of electric field, the increase phenomena of PSD obviously corresponded to the *Ms* 8.7 and 8.5 EQs. From September to October 2004, the *X*- and *Z*-components of the ionospheric electric field had the PSD increase, but no EQs above *Ms* 7.0 happened in the zone below the selected Demeter's orbits and its surrounding zone during the period of time before and after the PSD increase.

3.3 Ionospheric electric field changes of the Chile *Ms* 8.8 EQ

At 06:34:16 UT on 27 February 2010, an *Ms* 8.8 EQ occurred in Concepcion, Chile, with its epicenter located at S35.8°, W72.7°. Taking the epicenter of Chile EQ as the center, we selected the electric field data of Demeter's orbits in the rectangular range of S30°-S50° and W70°-W90°, and in the period of time from 1 September 2009 to 31 March 2010. Figure 5 shows the PSD changes of the three components of the ionospheric electric field of the

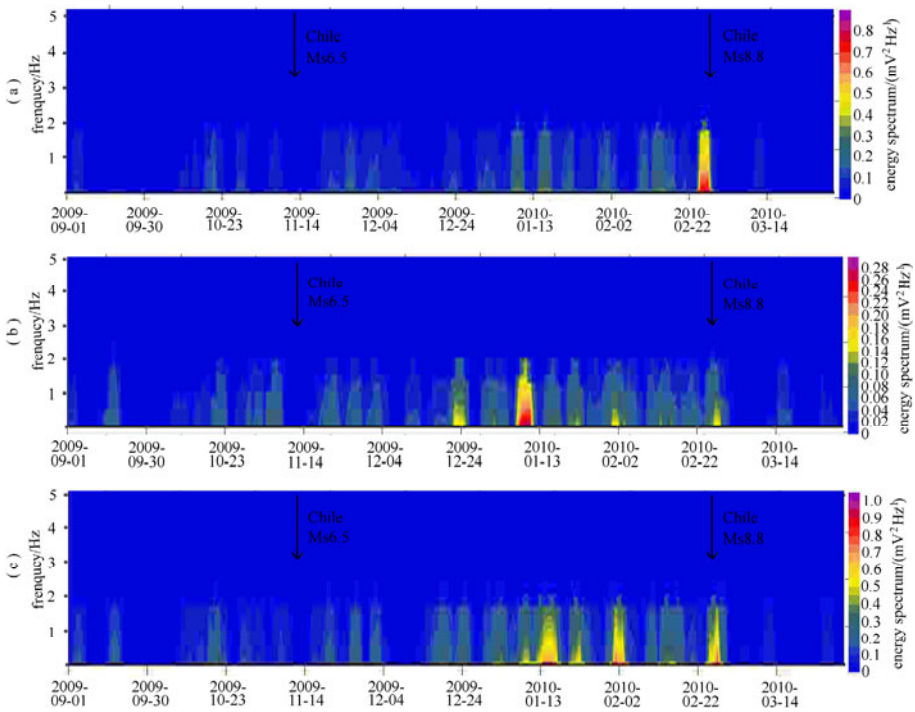

Fig. 5. PSD diagrams of the electric field of the Demeter (Up Orbits) above the Chile *Ms* 8.8 EQ from 1 September 2009 to 31 March 2010. Note: (a)-(c) represent the *X*-, *Y*-, and *Z*- components, respectively.

orbits above the epicenter of Chile EQ (the EQs in the figure are marked in UT). It can be seen from the figure that before the Chile *Ms* 8.8 EQ, the three components had significant PSD increases, which disappeared immediately after the EQ; among them, the PSD increase phenomena of *X*-component on the eve of the EQ was the most prominent. On 13 November 2009, a *Ms* 6.5 EQ (S19.3°, W70.3°) occurred in the coast offshore area of northern Chile and Fig. 5 shows that there was no PSD increase before the EQ as in the case of the *Ms* 8.8 EQ, perhaps due to its small magnitude.

3.4 Interim summaries

- The PSD increase of the low-frequency components appeared, below a few Hz and in the ionospheric electric field observed by the Demeter when approaching the date of the Wenchuan *Ms* 8.0 EQ. Their frequencies were below a few Hz and basically consistent with the PSD increase of the ground electric field in time.
- When approaching the date of such great EQs as the Wenchuan *Ms* 8.0 EQ, the Yutian *Ms* 7.3 EQ, and the Sumatra *Ms* 8.7/8.5 EQ, especially before the Chile *Ms* 8.8 EQ, the PSD of the ionospheric electric field observed by the Demeter had a significant increase in low-frequency components.
- The low-frequency PSD increase of the ionospheric electric field seems to correspond to those of the geoelectric field in the time immediately before the *Ms* 8.0 Wenchuan and *Ms* 7.3 Yutian EQs and their strong aftershocks.
- The phenomena of the PSD increase of the ionospheric electric field observed by the Demeter's revisited orbits are very complicated, so it is quite difficult to analyze the correspondence in time between the EQ and the PSD increase.

4. DISCUSSION ON REASONS OF THE GROUND AND IONOSPHERIC ELECTRIC FIELD CHANGES BEFORE EQS

According to the literature (Du *et al.* 2000, Du 2011), in the late preparation stage of strong EQs (several months to one-year scale before EQs), in the focal area and nearby, the amplitude and duration of apparent resistivity (AR, for short) anomalies show a non-linear relationship with an increase of EQ magnitude as follows: for the small-magnitude EQs, the amplitude of anomaly increase slowly, whereas the duration of anomaly grows rapidly; for the large-magnitude EQs, the situation is opposite. This relationship indicates the non-linear development of the micro-cracks within the underground medium within or nearby focal areas in the late preparation stage of strong EQs by the actual EQ cases, supporting the forecast of the IPE model that the mi-

cro-cracks are an avalanche development in the focal area (Mjachkin *et al.* 1975) and the inference that the micro fracture amount within the medium of focal area increases non-linearly in the late preparation stage (Kusunose *et al.* 1980). Du *et al.* (2007) has studied the AR anisotropic changes nearby epicentral areas of moderate and above EQs in the late EQ preparation stage, and came to the following conclusion: the primary reason for the anisotropic changes is due to the deformation of underground medium, which will conduct a micro-crack directional alignment or preponderant orientation effect in the process of medium deformation. From this point of view, in the later preparation stage of a strong EQ, the non-linearly and directionally aligned medium process of the micro cracks occurred really within the medium in the focal area or its vicinity. The DD model (Nur 1972, Scholz *et al.* 1973) emphasized the role of groundwater in the medium within a focal region, and other publications (Du *et al.* 2007, Du 2011) stressed the significant contribution of water to AR changes in the aforementioned medium process. These research of mechanism on AR changes before EQs reveals that in the later preparation stage of a strong EQ, two physical processes of medium may exist in a focal region and its vicinity, such as the non-linear development of the micro cracks within the medium, and their directional alignment or preponderant orientation effect. The reason for the electromagnetic radiation before an EQ could be also associated with these two physical processes. Therefore, it can be believed that in the later stage of an EQ preparation the physical processes occurred within the medium in the focal area or its vicinity, which caused the water migration due to the chaining effect of the micro cracks and made the conducting paths in the medium connected, and almost immediately induced the changes of the natural electric field due to the electronic and ionic conduction mechanism; in this process, such factors as simultaneous occurrence of "the mechanical to electrical conversion effect" and the water migration also excited the intensely low-frequency electromagnetic radiation.

A number of scholars have studied the possible reason why the low-frequency geo-electromagnetic signals might be propagated to the ionosphere from the underground electromagnetic radiation source (Molchanov *et al.* 1995, Shalimov and Gokhberg 1998, Huang 2002, Pulinets 2004, Sorokin *et al.* 2005). According to the calculations for the upward propagation of the electromagnetic waves by Molchanov *et al.* (1995), the high-frequency components in the wide-band electromagnetic waves caused by the EQ preparation are mostly absorbed when they propagated to the surface from the focal area; consequently, of the electromagnetic waves that can reach the earth surface, only electromagnetic waves with the frequency below 10-20 Hz can penetrate the atmosphere and be observed by the satellite.

This paper has processed and studied the ionospheric electric field data with the sampling frequency of 39.0625 Hz observed by Demeter; it was found that before an impending great EQs, only the PSD increase of the low-frequency components of electric field, a few Hz or even DC, appeared prominently, consistent with the results calculated by Molchanov *et al.* (1995). Supposing the PSD increase of the low-frequency ionospheric electric field that is corresponding to the EQs is spread to the earth surface from the focal region, and then propagated to the ionosphere, and taking the atmospheric conductivity $\sigma = 1 \times 10^{-4}$ s/m, relative permeability $\mu_r = 1$ and relative dielectric constant $\varepsilon_r = 1$, it can be estimated that the minimum propagation distance of the electric wave of 20 Hz to the atmosphere is 300 km, and that of the electric wave of 2 Hz is around 1000 km. The running altitude of the Demeter satellite is 710 km (which changes into 665 km in mid-December 2005), and the PSD increase of a few Hz components of the ionospheric electric field are the most prominent before the Wenchuan EQ, the Sumatra EQ, and the Chile EQ. Pulinets and Boyarchuk (2004) have discussed how the anomalous electric field generated in the seismogemnic area penetrates through the ionosphere and prompts the non-uniform plasma in the ionosphere, so it can be believed that the phenomena of the PSD increase corresponding to the EQs may be caused by the propagation of low-frequency electromagnetic wave from the ground to the ionosphere.

5. CONCLUSIONS

- The phenomena of the PSD increase of the low-frequency components (DC to a few Hz) in the ionospheric electric field observed by Demeter satellite appeared before the *Ms* 8.0 Wenchuan EQ and strong aftershocks, the *Ms* 7.3 Yutian EQ, the *Ms* 8.7/8.5 Sumatra EQs, and the *Ms* 8.8 Chile EQ; these were mainly the imminent anomalies, more significant for the short-distance and large-magnitude EQs.
- Before the occurrence of the *Ms* 8.0 Wenchuan EQ and the *Ms* 7.3 Yutian EQ, the PSD increase of near-DC components in the geoelectric field appears also in several ground electromagnetic stations in the northeastern and western edges of the Qinghai-Tibet Plateau, and agrees in time with the PSD increase of the low-frequency components in the ionospheric electric field. This shows a good correspondence between the ionospheric and ground electromagnetic phenomena before the two great EQs. In particular, when approaching the date of occurrence of the *Ms* 7.3 Yutian EQ, the SHN station recorded the significant PSD increase in the geoelectric field during the period of the PSD increase of the *Y*-component in the ionospheric electric field.

- It is rather difficult to analyze the PSD anomalies in the ionospheric electric field before EQs due to their complicated time, spatial, and intense distributions. There sometimes existed the confusing phenomena. For example, the prominent anomaly appeared before the long-distance great EQs while no anomaly before the short-distance EQs, and a small-amplitude anomaly appeared before the large-magnitude EQs or even no anomaly, while the prominent anomaly appeared before the small-magnitude EQs. This is similar to the results observed by the ground stations. Hence, it is very difficult to discern the earthquake-related anomaly in the ionospheric electric field observed by the Demeter's revisited orbits.

Acknowledgment. This work was supported by the Basic Scientific Research Special Fund of Institute of Earthquake Prediction (2012IESLZ06) and Natural Science Foundation of China (41374080). Thanks are extended to Demeter website (http://demeter.cnrs-orleans.fr/) for providing the ionospheric magnetic field data, and thanks are given to Professor Jacques Zlotnicki at France National Center for Scientific Research and Professor Mechel Parrot at the Orleans University in France.

References

Adler, P.M., J.L. Le Mouël, and J. Zlotnicki (1999), Electrokinetic and magnetic fields generated by flow through a fractured zone: A sensitivity study for La Fournaise volcano, *Geophys. Res. Lett.* **26**, 6, 795-798, DOI: 10.1029/1999GL900095.

Berthelier, J.J., M. Godefroy, F. Leblanc, M. Malingre, M. Menvielle, D. Lagoutte, J.Y. Brochot, F. Colin, F. Elie, C. Legendre, P. Zamora, D. Benoist, Y. Chapuis, J. Artru, and R. Pfaff (2006), ICE, the electric field experiment on DEMETER, *Planet. Space Sci.* **54**, 5, 456-471, DOI: 10.1016/j.pss.2005.10.016.

Cress, G.O., B.T. Brady, and G.A. Rowell (1987), Sources of electromagnetic radiation from fracture of rock samples in the laboratory, *Geophys. Res. Lett.* **14**, 4, 331-334, DOI: 10.1029/GL014i004p00331.

Cussac, T., M.A. Clair, P. Ultré-Guerard, F. Buisson, G. Lassalle-Balier, M. Ledu, C. Elisabelar, X. Passot, and N. Rey (2006), The Demeter microsatellite and ground segment, *Planet Space Sci.* **54**, 5, 413-427, DOI: 10.1016/j.pss.2005.10.013.

Du, X.B. (2011), Two types of changes in apparent resistivity in earthquake prediction, *Sci. China D* **54**, 1, 145-156, DOI: 10.1007/s11430-010-4031-y.

Du, X.B., H.Y. Zhao, and B.Z. Chen (1993), On the relation of imminent sudden change in earth resistivity to the active fault and earthquake generating stress field, *Acta Seismol. Sin.* **6**, 3, 663-673, DOI: 10.1007/BF02650405.

Du, X.B., Y.W. Liu, and M.K. Ni (1997), On the spatial characteristic of the short-term and imminent anomalies of underground water behaviors before strong earthquake, *Acta Seismol. Sin.* **10**, 4, 523-533, DOI: 10.1007/s11589-997-0062-7.

Du, X.B., S.Z. Xue, Z. Hao, and S.Z. Zhang (2000), On the relation of moderate-short term anomaly of earth resistivity to earthquake, *Acta Seismol. Sin.* **13**, 4, 393-403, DOI: 10.1007/s11589-000-0021-z.

Du, X.B., J.L. Xi, D.C. Tan, J.L. Zhao, J.D. Qian, Y.Q. Lu, J. Lu, Y.X. Tang, H.L. Kang, Y.F. Chen, and D.Z. Wang (2006), Specification for the construction of seismic station geoelectrical station. Part 2: Geoelectrical field observatory, DB/T 18.2-2006, The Seismology Trades Standard of the PRC, 2-5 (in Chinese).

Du, X.B., N. Li, Q. Ye, Z.H. Ma, and R. Yan (2007), A possible reason for the anisotropic changes in apparent resistivity near the focal region of strong earthquake, *Chinese J. Geophys.* **50**, 6, 1555-1565, DOI: 10.1002/cjg2.1175 (in Chinese).

Enomoto, Y., and H. Hashimoto (1992), Transient electrical activity accompanying rock under indentation loading, *Tectonophysics* **211**, 1-4, 337-344, DOI: 10.1016/0040-1951(92)90069-1.

Enomoto, Y., H. Hashimoto, N. Shirai, Y. Murakami, T. Mogi, M. Takada, and M. Kasahara (2006), Anomalous geoelectric signals possibly related to the 2000 Mt. Usu eruption and 2003 Tokachi-Oki earthquakes, *Phys. Chem. Earth* **31**, 4-9, 319-324, DOI: 10.1016/j.pce.2006.02.013.

Fan, Y.Y., X.B. Du, J. Zlotnicki, D.C. Tan, Z.H. An, J.Y. Chen, G.L. Zheng, J. Liu, and T. Xie (2010), The electromagnetic phenomena before the M_s8.0 Wenchuan earthquake, *Chinese J. Geophys.* **53**, 6, 997-1010, DOI: 10.1002/cjg2.1570.

He, Y.F., D.M. Yang, H.R. Chen, J.D. Qian, R. Zhu, and M. Parrot (2009), SNR changes of VLF radio signals detected onboard the DEMETER satellite and their possible relationship to the Wenchuan earthquake, *Sci. China D* **52**, 6, 754-763, DOI: 10.1007/s11430-009-0064-5.

Huang, Q.H. (2002), One possible generation mechanism of co-seismic electric signals, *Proc. Japan Acad. B* **78**, 7, 173-178, DOI: 10.2183/pjab.78.173.

Huang, Q.H. (2005), Controlled analogue experiments on propagation of seismic electromagnetic signals, *Chin. Sci. Bull*. **50**, 17, 1957-1961, DOI: 10.1360/982004-312.

Huang, Q.H., and M. Ikeya (1998), Seismic electromagnetic signals (SEMS) explained by a simulation experiment using electromagnetic waves, *Phys. Earth Planet. In.* **109**, 3-4, 107-114, DOI: 10.1016/S0031-9201(98)00135-6.

Ishido, T., and J.W. Pritchett (1999), Numerical simulation of electrokinetic potentials associated with subsurface fluid flow, *J. Geophys. Res*. **104**, B7, 15247-15259, DOI: 10.1029/1999JB900093.

Kusunose, K., I.K. Yamamoto, and T. Hirasawa (1980), Source process of microfracture in granite with reference to earthquake prediction, *Sci. Rep. Tohoku Univ. Geophys.* **26**, 3-4, 111-121.

Liu, J.Y., Y.I. Chen, Y.J. Chuo, and S.A. Pulinets (2003), A statistical study of ionospheric precursors of M > 5.0. **In:** *Proc. EGS-AGU-EUG Joint Assembly, 6-11 April 2003, Nice, France*, Abstr. no. 4780.

Liu, J., X.B. Du, J. Zlotnicki, Y.Y. Fan, Z.H. An, T. Xie, G.L. Zheng, D.C. Tan, and J.Y. Chen (2011), The changes of the ground and ionosphere electric/magnetic fields before several great earthquakes, *Chinese J. Geophys.* **54**, 11, 2885-2897, DOI: 10.3969/j.issn.0001-5733.2011.11.018.

Ma, Q.Z., Z.S. Feng, Z.P. Song, and W.G. Zhao (2004), Study on the variation characteristics of the geoelectric field preceding earthquakes, *Acta Seismol. Sin.* **17**, 3, 334-343, DOI: 10.1007/s11589-004-0055-8.

Michel, S., and J. Zlotnicki (1998), Self-potential and magnetic surveying of La Fournaise volcano (Réunion Island): Correlations with faulting, fluid circulation, and eruption, *J. Geophys. Res.* **103**, B8, 17845-17857, DOI: 10.1029/98JB00607.

Mjachkin, V.I., W.F. Brace, G.A. Sobolev, and J.H. Dieterich (1975), Two models for earthquake forerunners, *Pure Appl Geophys*. **113**, 1, 169-181, DOI: 10.1007/BF01592908.

Molchanov, O.A., M. Haykawa, and V.A. Rafalsky (1995), Penetration characteristics of electromagnetic emissions from an underground seismic source into the atmosphere, ionosphere, and magnetosphere, *J.Geophys. Res.* **100**, A2, 1691-1712, DOI: 10.1029/94JA02524.

Nagamoto, H., T. Fukushima, Y. Ida, Y. Matsudo, and M. Hayakawa (2008), Disturbances in VHF/UHF telemetry links as a possible effect of the 2003 Hokkaido Tokachi-oki earthquake, *Nat. Hazards Earth Syst. Sci*. **8**, 4, 813-817, DOI: 10.5194/nhess-8-813-2008.

Nur, A. (1972), Dilatancy, pore fluids, and premonitory variations of t_s/t_p travel times, *Bull. Seismol. Soc. Am.* **62**, 5, 1217-1222.

Ogawa, T., K. Oike, and T. Miura (1985), Electromagnetic radiations from rocks, *J. Geophys. Res*. **90**, D4, 6245-6249, DOI: 10.1029/JD090iD04p06245.

Parrot, M. (1995), Use of satellites to detect seismo-electromagnetic effects, *Adv. Space Res*. **15**, 11, 27-35, DOI: 10.1016/0273-1177(95)00072-M.

Parrot, M. (ed.) (2006a), First Results of the DEMETER Micro-satellite, *Planet. Space Sci.* **54**, 5.

Parrot, M. (2006b), Special issue of Planetary and Space Science'DEMETER', *Planet. Space Sci.* **54**, 5, 411-412, DOI: 10.1016/j.pss.2005.10.012.

Pulinets, S. (2004), Ionospheric precursors of earthquakes; Recent advances in theory and practica1 applications, *Terr Atmos. Ocean Sci*. **15**, 3, 413-435.

Pulinets, S., and K. Boyarchuk (2004), *Ionoshperic Precursors of Earthquakes*, Springer, Berlin, 315 pp.

Pulinets, S.A., A. Leyva Contreras, G. Bisiacchi-Giraldi, and L. Ciraolo (2005), Total electron content variations in the ionosphere before the Colima, Mexico, earthquake of 21 January 2003, *Geophys. Int.* **44**, 4, 369-377.

Qian, J.D., Z.W. Guo, J.L. Zhao, D.M. Yang, J.L. Xi, Y.F. Gao, J.P. Zhou, X.J. Mao, Z.B. Zheng, G.Z. Zhao, X. Zhou, S.L. Ma, X.B. Chen, J.J. Wang, Q.Z. Ma, D.C. Tan, Y.X. Tang, and T.Q. Yang (2004), Technical requirement for observational environment of seismic stations – Part 2: Electromagnetic observation, GB/T 19531.2-2004, The Standard of the PRC, 14-29 (in Chinese).

Scholz, C.H., L.R. Sykes, and Y.P. Aggrawal (1973), Earthquake prediction: A physical basis, *Science* **181**, 4102, 803-810, DOI: 10.1126/science.181.4102.803.

Shalimov, S., and M. Gokhberg (1998), Lithosphere-ionosphere coupling mechanism and its application to the earthquake in Iran on June 20, 1990. A review of ionospheric measurements and basic assumptions, *Phys. Earth Planet. In*. **105**, 3-4, 211-218, DOI: 10.1016/S0031-9201(97)00092-7.

Sorokin, V.M., V.M. Chmyrev, and A.K. Yaschenko (2005), Theoretical model of DC electric field formation in the ionosphere stimulated by seismic activity, *J. Atmos. Sol.-Terr. Phys.* **67**, 14, 1259-1268, DOI: 10.1016/j.jastp.2005.07.013.

Tang, J., Y. Zhan, L.F. Wang, J.L. Xu, G.Z. Zhao, X.B. Chen, Z.Y. Dong, Q.B. Xiao, J.J. Wang, J.T. Cai, and G.J. Xu (2008), Coseismic signal associated with aftershock of the Ms8.0 Wenchuan earthquake, *Seismol. Geol.* **30**, 3, 739-745, DOI: 10.3969/j.issn.0253-4967.2008.03.012.

Telesca, L., and K. Hattori (2007), Non-uniform scaling behavior in ultra-low-frequency (ULF) earthquake-related geomagnetic signals, *Physica A* **384**, 2, 522-428, DOI: 10.1016/j.physa.2007.05.040.

Telesca, L., G. Colangelo, and V. Lapenna (2005), Multifractal variability in geoelectrical signals and correlations with seismicity: a study case in southern Italy, *Nat. Hazards Earth Syst. Sci.* **5**, 5, 673-677, DOI: 10.5194/nhess-5-673-2005.

Telesca, L., V. Lapenna, M. Macchiato, and K. Hattori (2008), Investigating non-uniform scaling behavior in Ultra Low Frequency (ULF) earthquake-related geomagnetic signals, *Earth Planet. Sci. Lett.* **268**, 1-2, 219-224, DOI: 10.1016/j.epsl.2008.01.033.

Telesca, L., M. Lovallo, A. Ramirez-Rojas, and F. Angulo-Brown (2009), A nonlinear strategy to reveal seismic precursory signatures in earthquake-related self-potential signals, *Physica A* **388**, 10, 2036-2040, DOI: 10.1016/j.physa.2009.01.035.

Uyeda, S., M. Hayakawa, T. Nagao, O. Molchanov, K. Hattori, Y. Orihara, K. Gotoh, Y. Akinaga, and H. Tanaka (2002), Electric and magnetic phenomena observed before the volcano-seismic activity in 2000 in the Izu Island Region, Japan, *Proc. Natl. Acad. Sci. USA* **99**, 11, 7352-7355, DOI: 10.1073/pnas.072208499.

Varotsos, P., and M. Lazaridou (1991), Latest aspects of earthquake prediction in Greece based on seismic electric signals, *Tectonophysics* **188**, 3-4, 321-347, DOI: 10.1016/0040-1951(91)90462-2.

Varotsos, P., K. Alexopoulos, K. Nomicos, and M. Lazaridou (1986), Earthquake prediction and electric signals, *Nature* **322**, 6075, 120, DOI: 10.1038/322120a0.

Varotsos, P., N. Sarlis, M. Lazaridou, and P. Kapiris (1998), Transmission of stress induced electric signals in dielectric media, *J. Appl. Phys.* **83**, 1, 60-70, DOI: 10.1063/1.366702.

Yamada, I., K. Masuda, and H. Mizutani (1989), Electromagnetic and acoustic emission associated with rock fracture, *Phys. Earth Planet. In.* **57**, 1-2, 157-168, DOI: 10.1016/0031-9201(89)90225-2.

Zhang, X.M., H.R. Chen, J. Liu, X.H. Shen, Y.Q. Miao, X.B. Du, and J.D. Qian (2012), Ground-based and satellite DC-ULF electric field anomalies around Wenchuan M8.0 earthquake, *Adv. Space Res.* **50**, 1, 85-95, DOI: 10.1016/j.asr.2012.03.018.

Zlotnicki, J., J.L. Le Mouël, Y. Sasai, P. Yvetot, and M.H. Ardisson (2001), Self-potential changes associated with volcanic activity: Short-term signals associated with March 9, 1998 eruption on La Fournaise volcano (Réunion Island), *Ann. Geophys.* **44**, 2, 335-354, DOI: 10.4401/ag-3600.

Received 24 December 2013
Received in revised form 24 June 2014
Accepted 4 July 2014

DE GRUYTER OPEN

Acta Geophysica
vol. 63, no. 3, June 2015, pp. 698-714
DOI: 10.1515/acgeo-2015-0019

Seismic Wave Velocities in Deep Sediments in Poland: Borehole and Refraction Data Compilation

Marcin POLKOWSKI and Marek GRAD

Institute of Geophysics, Faculty of Physics, University of Warsaw, Warsaw, Poland
e-mail: marcin.polkowski@igf.fuw.edu.pl

A b s t r a c t

Sedimentary cover has significant influence on seismic wave travel times and knowing its structure is of great importance for studying deeper structures of the Earth. Seismic tomography is one of the methods that require good knowledge of seismic velocities in sediments and unfortunately by itself cannot provide detailed information about distribution of seismic velocities in sedimentary cover. This paper presents results of *P*-wave velocity analysis in the old Paleozoic sediments in area of Polish Lowland, Folded Area, and all sediments in complicated area of the Carpathian Mountains in Poland. Due to location on conjunction of three major tectonic units – the Precambrian East European Craton, the Paleozoic Platform of Central and Western Europe, and the Alpine orogen represented by the Carpathian Mountains the maximum depth of these sediments reaches up to 25 000 m in the Carpathian Mountains. Seismic velocities based on 492 deep boreholes with vertical seismic profiling and a total of 741 vertical seismic profiles taken from 29 seismic refraction profiles are analyzed separately for 14 geologically different units. For each unit, velocity *versus* depth relations are approximated by second or third order polynomials.

Key words: vertical seismic profiling, seismic refraction profiles, seismic velocity analysis, sedimentary cover, Poland.

1. INTRODUCTION

The structure of the sedimentary cover in the area of Poland is very complex due to complicated geological structure of three major tectonic units: the Precambrian East European Craton (EEC), the Paleozoic Platform of Central and Western Europe (PP), and the Alpine orogen represented by the Carpathian Mountains (Pożaryski *et al.* 1982, Znosko 1975, 1979; Berthelsen 1992, 1998). All these units differ in tectonic age, geological history and development, and require individual analysis on *P*-wave velocities. Such differentiated layer of sediments has great influence on seismic wave travel times and good knowledge of seismic velocity distribution is crucial for global and regional tomography.

The thickness of the sedimentary cover varies from 300 m in NE Poland to about 16 000 m in area of Trans European Suture Zone and 25 000 m in the Carpathians (Skorupa 1974, Czuba *et al.* 2002, Grad *et al.* 1990, 1991; Janik *et al.* 2011). The structure of sediments is well studied for layers of Tertiary and Quaternary, Cretaceous, Jurassic, Triassic, and Permian by over 100 000 geological boreholes from which over 1000 boreholes had vertical seismic profiling done (VSP; Grad and Polkowski 2012). Range of borehole surveying is limited to approximately 5000 m in depth (the deepest borehole in Poland, Kuźmina-1, has 7541 m depth; Moryc and Łydka 2000). Below that level other sources have to be introduced, such as deep seismic refraction. Poland is very well covered with seismic refraction profiles from multiple experiments:

- **POLONAISE'97** (Guterch *et al.* 1999): P1 (Jansen *et al.* 1999), P2 (Janik *et al.* 2002), P3 (Środa *et al.* 1999), P4 (Grad *et al.* 2003a), P5 (Czuba *et al.* 2001).
- **CELEBRATION 2000** (Guterch *et al.* 2003): CEL01 (Środa *et al.* 2006), CEL02 (Malinowski *et al.* 2005), CEL03 (Janik *et al.* 2005), CEL04 (Środa *et al.* 2006), CEL05 (Grad *et al.* 2006), CEL10 (Grad *et al.* 2009), CEL06, CEL11, CEL12, CEL13, CEL14, CEL21, CEL22, CEL23 (Janik *et al.* 2009).
- **SUDETES 2003** (Grad *et al.* 2003c): S01 (Grad *et al.* 2008), S02, S03, S06 (Majdański *et al.* 2006).
- other profiles: LT-2, LT-4 (Grad *et al.* 2005), LT-7 (Guterch *et al.* 1994), M07, M09 (Grad *et al.* 1991), TTZ (Grad *et al.* 1999).

Seismic refraction profiles provide detailed data about seismic velocities along profile down to 40-80 km depth, depending on profile length and type of seismic sources used. To allow combination of data from profiles with data from boreholes with VSP and to remain compatible with the result form previous analysis for shallower sediments, the "virtual boreholes" are introduced being vertical velocity to depth relations taken from 2D velocity mod-

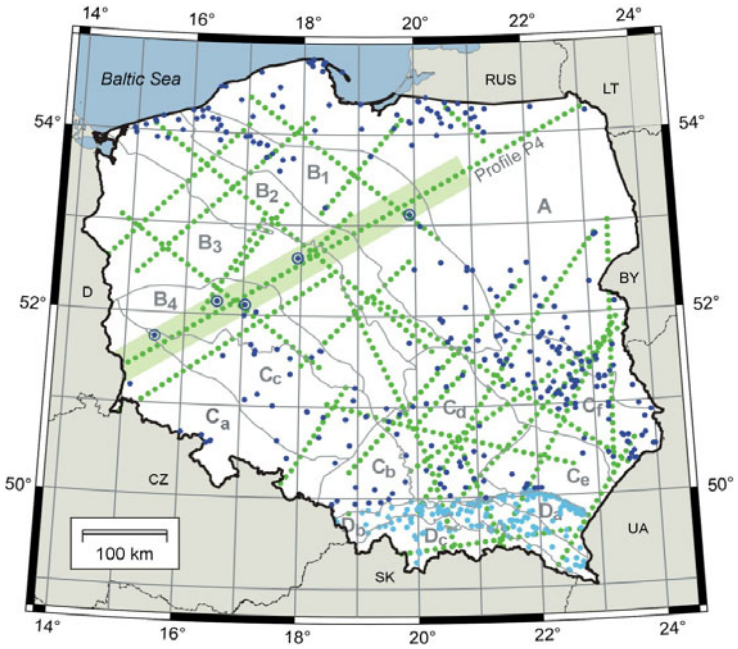

Fig. 1. Location map of boreholes used in this study on the background of the geological division of Poland (Sokołowski 1968). Dark blue dots symbolize boreholes reaching old Paleozoic outside the Carpathians, light blue dots symbolize boreholes in the Carpathians, green dots symbolize "virtual boreholes" (see text for explanation) from seismic refraction profiles, light green rectangle marks part of P4 profile from Fig. 2, blue circles marks boreholes locations shown in Fig. 2.

els for certain location among profile paths. "Virtual boreholes" can be calculated at any location on the profile and in this paper they are calculated for every 10th km of all profiles within the territory of Poland (Fig. 1). Data from "virtual boreholes" is later analyzed in the same manner as standard geological borehole with VSP (Grad and Polkowski 2012).

To keep the compatibility with previous analysis, the same division for regional and local units is taken (Sokołowski 1968). The area of Poland is divided into 4 regional units and a total of 14 local sub-units (Fig. 1) including: A – East European Craton, B – Polish Lowland (B_1 – marginal synclinorium, B_2 – Pomorze–Kujawy anticlinorium, B_3 – Szczecin–Łódź synclinorium, B_4 – northern fore-Sudetic monocline), C – Folded Area (C_a – Sudety Mts. and fore-Sudetic block, C_b – Upper Silesian block, C_c – southern fore-Sudetic monocline, C_d – Miechów synclinorium, Goleniów anticlinorium, Holy Cross anticlinorium; C_e – San elevation, C_f – Lublin synclinorium), D – Carpathians (D_a – Outer Carpathians, D_b – Silesian unit, D_c – Magura unit and Inner Carpathians).

Locations of boreholes providing velocity information for old Paleozoic sediments for East European Craton, Polish Lowland, and Folded Area, locations of boreholes providing velocity information for Carpathian sediments and locations of virtual boreholes taken for further analysis among the regional division are shown on the map in Fig. 1. As can be noted from this figure, the distribution of boreholes is not uniform. Especially, in units B_2 and B_3, where sedimentary cover is very thick, no boreholes reach the old Paleozoic sediments. Fortunately, this area is well covered with virtual boreholes due to high density of seismic profiles there.

The goal of this paper is to provide, together with previous results (Grad and Polkowski 2012), complete knowledge about velocity-depth relations for the whole area of Poland, individually for 14 separate units, for all sediments: Tertiary and Quaternary, Cretaceous, Jurassic, Triassic, Permian, old Paleozoic, and all Carpathian Sediments. All these relations can be used in the future for creating 3D model of *P*-wave velocities of entire crust in Poland, which is of great importance for studying deeper structures with different methods, including seismic tomography, surface wave inversion and receiver function. Additionally, it could be used for gravity, magnetic, and heat flow analysis.

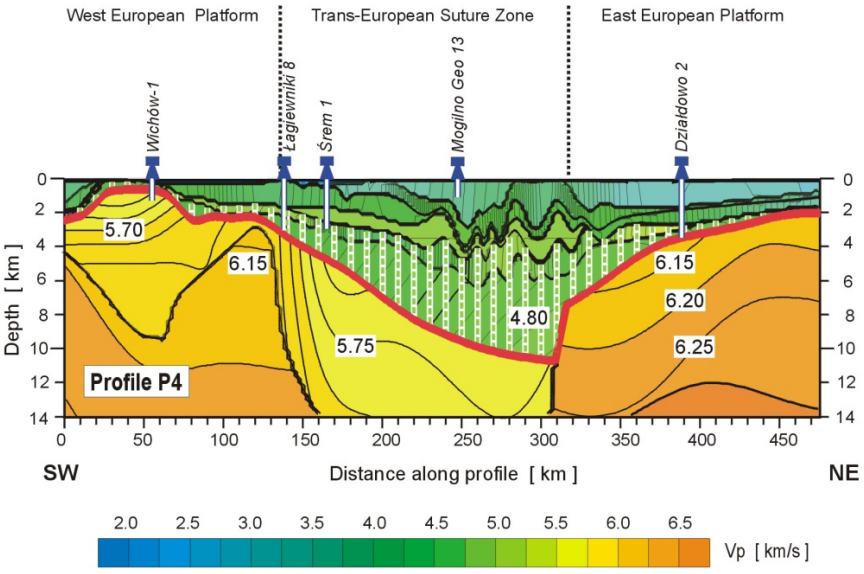

Fig. 2. Section of the upper crust beneath refraction seismic profile P4. Colors correspond to *P*-wave velocity; thick red line marks floor of sediments, white lines with borehole symbols show locations of boreholes (with depth range) located close to the profile line, green dashed lines show locations and ranges of "virtual boreholes" in the old Paleozoic sediments.

2. VSP AND REFRACTION DATA

For this study, a total of 833 554 m of vertical seismic profiles from 498 boreholes were analyzed, including 299 295 m of VSP in old Paleozoic sediments in the area of East European Craton, Polish Lowland, and Folded Area, and 534 259 m from the Carpathian Mountains (all sediments). Additionally, to cover areas and depths not reached by boreholes, 29 seismic refraction profiles were processed. To allow common processing for borehole VSP data and refraction data "virtual boreholes" are introduced. Figure 2

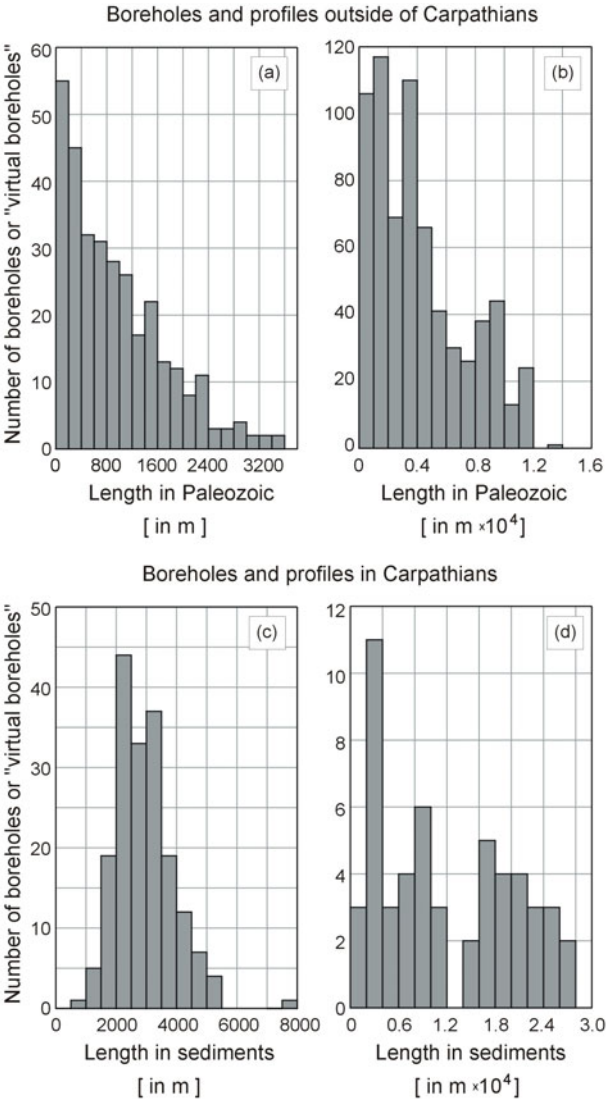

Fig. 3: (a) Distribution of borehole amount with length in the old Paleozoic sediments outside the Carpathians, $n = 316$, total length 299 295 m; (b) Distribution of "virtual borehole" amount with length in the old Paleozoic sediments outside the Carpathians, $n = 688$, total length 2 862 618 m; (c) Distribution of borehole amount with length in all Carpathian sediments, $n = 182$, total length 534 259 m; (d) Distribution of "virtual borehole" amount with length in Carpathian sediments, $n = 53$, total length 604 226 m.

presents part of refraction profile P4 with "virtual boreholes" in old Paleozoic sediments and locations with depth of geological boreholes located close to the profile path. To equalize importance of refraction and borehole data sets "virtual boreholes" are taken from profiles every 10th km 741 "virtual boreholes" are analyzed and provide 3 466 844 m of virtual VSP, including 604 226 m in the Carpathians. Figure 3 shows histograms of analyzed lengths of boreholes VSP for both standard and "virtual boreholes" separately outside the Carpathians and in the Carpathians.

Sediments in the Carpathians are well mixed, fractured, trusted, and folded, creating flysch deposits that are composed of different age rocks (Tertiary and Quaternary, Cretaceous, Jurassic). Structure of these deposits, and even older rocks, makes them very difficult to differentiate, so in this paper all Carpathian sediments are analyzed together.

To allow further analysis, all data were recalculated (interpolated) to provide velocity data with 1-m interval (Grad and Polkowski 2012) and classified to units A, B_1, B_2, B_3, B_4, C_a, C_b, C_c, C_d, C_e, C_f, D_a, D_b, D_c, and layers Tertiary and Quaternary, Cretaceous, Jurassic, Triassic, Permian, old Paleozoic, Carpathian Sediments.

3. VELOCITY–DEPTH ANALYSIS

In this paper, 17 velocity *versus* depth relations are provided, including 1 relation for the old Paleozoic sediments for the East European Craton (unit A), 4 relations for the old Paleozoic sediments in the Polish Lowland (units B_1, B_2, B_3, and B_4), 5 relations for the old Paleozoic sediments in the Folded Area (units C_a, C_b, C_c, C_d, C_e, and C_f), and 3 relations for all sediments in the Carpathians (units D_a, D_b, and D_c). Additionally, 3 relations for combined units $B_1 + B_2 + B_3$ (part of the Polish Lowland with deepest old Paleozoic sediments), $C_d + C_e + C_f$ (part of the Folded Area with deepest old Paleozoic sediments), and $D_a + D_b + D_c$ (whole Carpathians, all sediments) are presented. All relations are calculated using the same three step method (Grad and Polkowski 2012), here described briefly.

Firstly, from the whole data set containing information about depth, velocity and belongingness to layer and unit for both real and "virtual boreholes" values for requested unit and layer are selected (for example, old Paleozoic in unit B_1 or all sediments in unit D_a). In Figures 4 and 5 these are shown as thin blue (for real boreholes) and green (for "virtual boreholes") lines.

Secondly, moving averages of velocities are calculated with depth. Length of moving averages window is set to 50 m. This step is necessary to event weight of large amount of data at low depths with significantly smaller amount of data at greater depths. In Figures 4 and 5, the moving average is shown as a thick red line.

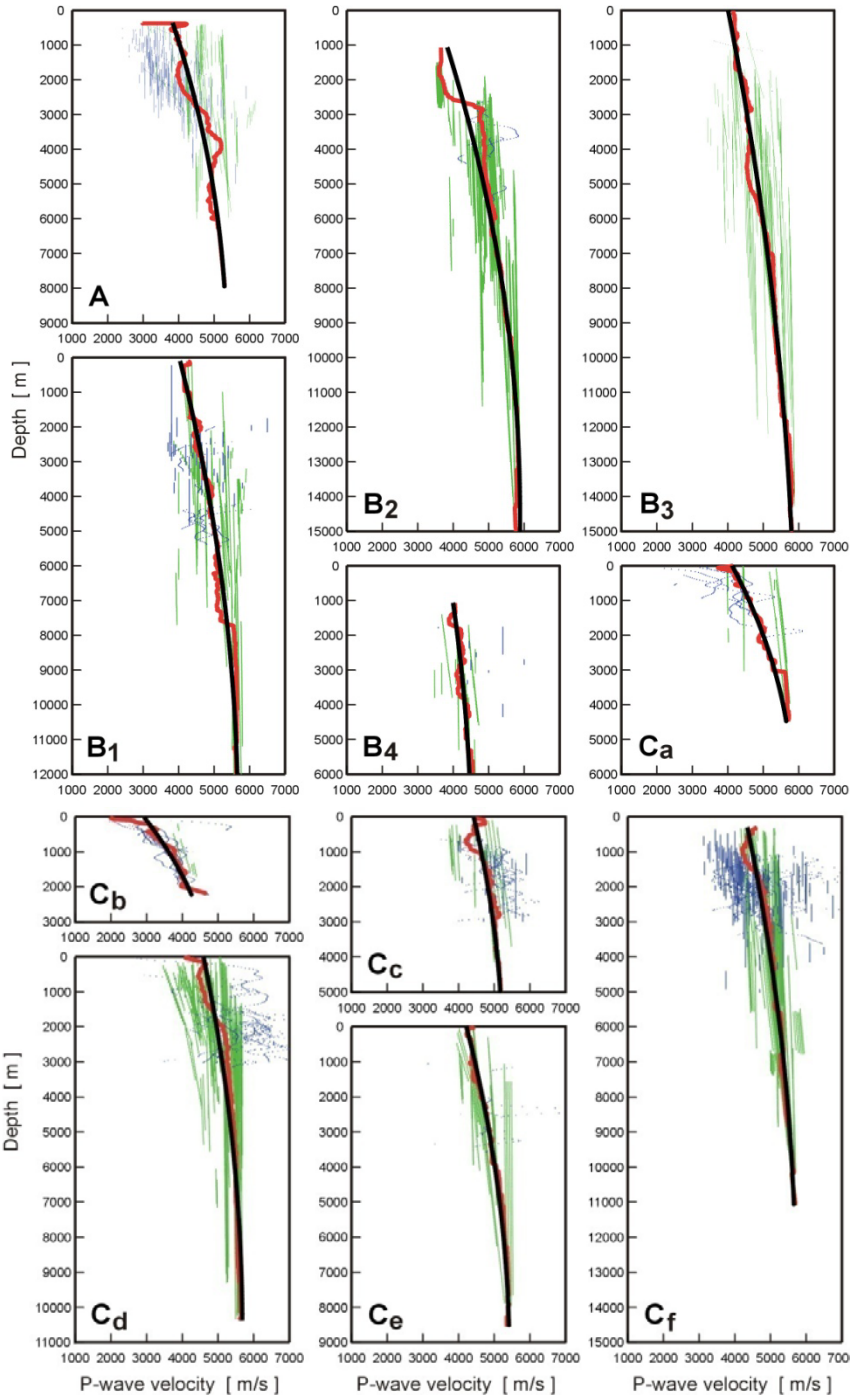

Fig. 4. Caption on next page.

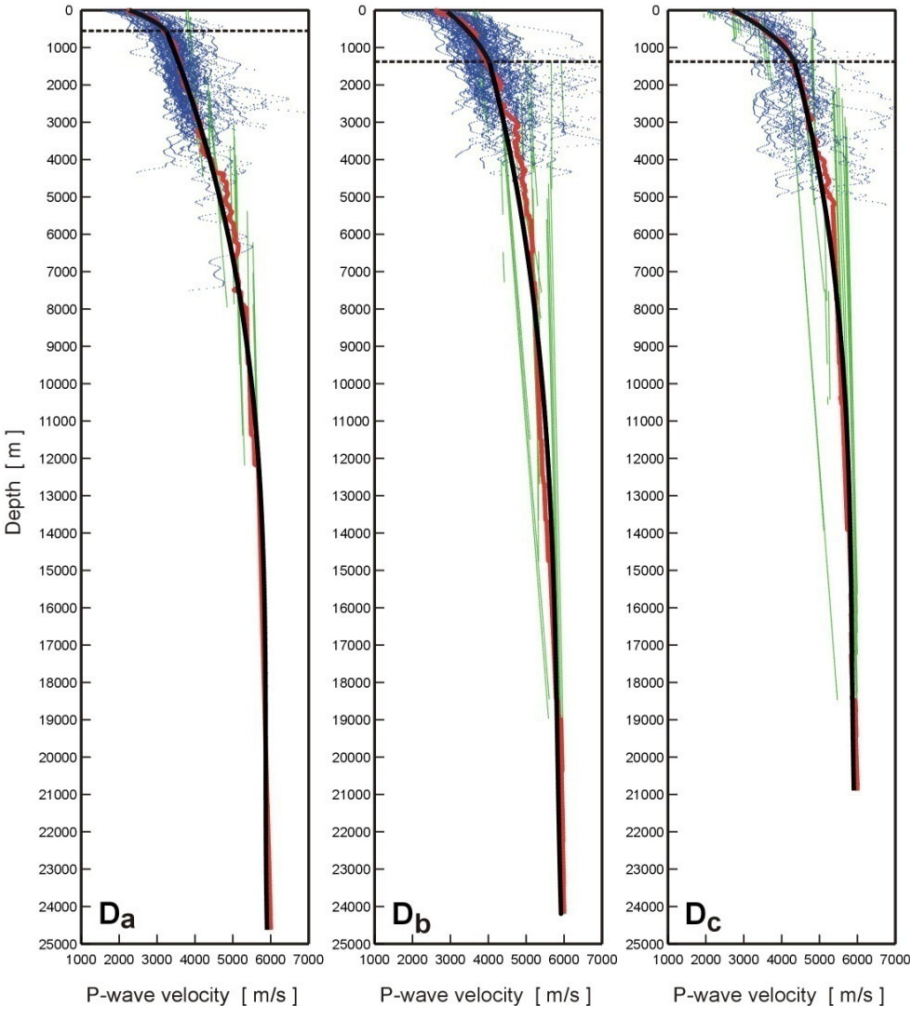

Fig. 5. *P*-wave seismic velocities for all Carpathian sediments. The dashed black line shows split between two polynomials range – see Table 1 for details. Other explanations as in Fig. 4.

Fig. 4. *P*-wave seismic velocities for the old Paleozoic sediments measured in boreholes (thin blue lines) and "virtual boreholes" (thin green lines) along with moving of velocities average with depth (thick red lines) and fitted polynomial (thick black lines). Polynomial coefficients are provided in Table 1. Division into geological units corresponds to Fig. 1. See text for more explanation.

Table 1

Velocity [m/s] – depth [m] formulas for sedimentary cover in Poland

Unit	Coefficients of $V(z) = a + bz + cz^2 + dz^3$	Depth range	Amount of data used
A	$a = (3713.91 \pm 8.17) \times 10^{0}$ $b = (3330.38 \pm 28.14) \times 10^{-4}$ $c = (-1696.92 \pm 20.49) \times 10^{-8}$	U: 370 m L: 7975 m	NB: 90 NR: 110 LB: 97818 m LR: 167039 m
B_1	$a = (4015.50 \pm 3.96) \times 10^{0}$ $b = (2454.40 \pm 10.69) \times 10^{-4}$ $c = (-908.10 \pm 6.05) \times 10^{-8}$	U: 113 m L: 12000 m	NB: 39 NR: 61 LB: 25827 m LR: 201183 m
B_2	$a = (3496.23 \pm 8.36) \times 10^{0}$ $b = (3276.80 \pm 18.12) \times 10^{-4}$ $c = (-1123.87 \pm 8.38) \times 10^{-8}$	U: 1074 m L: 15000 m	NB: 11 NR: 97 LB: 3455 m LR: 733880 m
B_3	$a = (4008.77 \pm 3.36) \times 10^{0}$ $b = (1926.90 \pm 7.71) \times 10^{-4}$ $c = (-492.01 \pm 3.72) \times 10^{-8}$	U: 17 m L: 15083 m	NB: 2 NR: 111 LB: 1070 m LR: 599516 m
B_4	$a = (3835.62 \pm 5.53) \times 10^{0}$ $b = (1597.08 \pm 20.18) \times 10^{-4}$ $c = (-939.99 \pm 15.95) \times 10^{-8}$	U: 1074 m L: 6299 m	NB: 10 NR: 41 LB: 2315 m LR: 39481 m
C_a	$a = (4124.86 \pm 6.49) \times 10^{0}$ $b = (5142.60 \pm 31.59) \times 10^{-4}$ $c = (-389.17 \pm 3.22) \times 10^{-7}$	U: 0 m L: 4486 m	NB: 8 NR: 18 LB: 6861 m LR: 28306 m
C_b	$a = (2917.78 \pm 12.24) \times 10^{0}$ $b = (777.71 \pm 7.78) \times 10^{-3}$ $c = (-798.76 \pm 10.38) \times 10^{-7}$	U: 24 m L: 2239 m	NB: 11 NR: 7 LB: 10199 m LR: 3530 m
C_c	$a = (4422.02 \pm 5.45) \times 10^{0}$ $b = (2309.69 \pm 24.60) \times 10^{-4}$ $c = (-1627.97 \pm 23.29) \times 10^{-8}$	U: 31 m L: 5200 m	NB: 22 NR: 26 LB: 19890 m LR: 56098 m
C_d	$a = (4592.94 \pm 4.85) \times 10^{0}$ $b = (2026.58 \pm 14.56) \times 10^{-4}$ $c = (-939.73 \pm 9.16) \times 10^{-8}$	U: 0 m L: 10382 m	NB: 27 NR: 100 LB: 16854 m LR: 531541 m
C_e	$a = (42180.95 \pm 29.76) \times 10^{-1}$ $b = (2520.55 \pm 10.14) \times 10^{-4}$ $c = (-1314.63 \pm 7.24) \times 10^{-8}$	U: 0 m L: 8557 m	NB: 13 NR: 26 LB: 1430 m LR: 105376 m

to be continued

Table 1 (continuation)

Unit	Coefficients of $V(z) = a + bz + cz^2 + dz^3$	Depth range	Amount of data used
C_f	$a = (4288.87 \pm 3.55) \times 10^{0}$ $b = (2077.59 \pm 9.96) \times 10^{-4}$ $c = (-762.90 \pm 5.89) \times 10^{-8}$	U: 310 m L: 11089 m	NB: 83 NR: 79 LB: 113576 m LR: 396668 m
D_a	$a = (2276.41 \pm 11.40) \times 10^{0}$ $b = (261.32 \pm 5.85) \times 10^{-2}$ $c = (-158.23 \pm 6.29) \times 10^{-5}$	U: 0 m L: 565 m	NB: 72 NR: 10 LB: 213734 m LR: 118150 m
	$a = (3016.23 \pm 4.35) \times 10^{0}$ $b = (4220.82 \pm 12.72) \times 10^{-4}$ $c = (-2088.78 \pm 9.98) \times 10^{-8}$ $d = (3454.46 \pm 22.16) \times 10^{-13}$	U: 566 m L: 24620 m	
D_b	$a = (2877.34 \pm 12.93) \times 10^{0}$ $b = (1191.07 \pm 29.85) \times 10^{-3}$ $c = (-261.42 \pm 14.45) \times 10^{-6}$	U: 0 m L: 1385 m	NB: 82 NR: 21 LB: 221191 m LR: 209400 m
	$a = (3648.06 \pm 6.53) \times 10^{0}$ $b = (2909.68 \pm 19.36) \times 10^{-4}$ $c = (-1361.34 \pm 15.41) \times 10^{-8}$ $d = (225.89 \pm 3.47) \times 10^{-12}$	U: 1386 m L: 24198 m	
D_c	$a = (2706.20 \pm 7.28) \times 10^{0}$ $b = (1871.75 \pm 16.80) \times 10^{-3}$ $c = (-501.60 \pm 8.13) \times 10^{-6}$	U: 0 m L: 1379 m	NB: 28 NR: 22 LB: 99334 m LR: 276676 m
	$a = (3936.66 \pm 5.38) \times 10^{0}$ $b = (3110.79 \pm 17.30) \times 10^{-4}$ $c = (-1729.00 \pm 15.07) \times 10^{-8}$ $d = (330.72 \pm 3.76) \times 10^{-12}$	U: 1380 m L: 20891 m	
B_1 B_2 B_3	$a = (3903.84 \pm 3.58) \times 10^{0}$ $b = (2330.96 \pm 8.24) \times 10^{-4}$ $c = (-688.49 \pm 3.97) \times 10^{-8}$	U: 17 m L: 15083 m	NB: 52 NR: 269 LB: 30352 m LR: 1534579 m
C_d C_e C_f	$a = (44291.22 \pm 30.41) \times 10^{-1}$ $b = (2015.43 \pm 8.73) \times 10^{-4}$ $c = (-792.44 \pm 5.25) \times 10^{-8}$	U: 0 m L: 11089 m	NB: 123 NR: 205 LB: 131860 m LR: 1033585 m
D_a D_b D_c	$a = (3797.94 \pm 5.63) \times 10^{0}$ $b = (2741.71 \pm 14.79) \times 10^{-4}$ $c = (-1233.88 \pm 10.76) \times 10^{-8}$ $d = (1925.83 \pm 22.79) \times 10^{-13}$	U: 1500 m L: 24620 m	NB: 182 NR: 53 LB: 534259 m LR: 604226 m

Explanations: U – upper depth limit of function domain, L – lower depth limit of function domain, NB – number of boreholes in the unit, NR – number of virtual boreholes in the unit, LB – total length of boreholes in the unit, LR – total length of virtual boreholes in the unit. Last 3 relations are given for combined units $B_1 + B_2 + B_3$ (part of the Polish Lowland with deepest old–Paleozoic sediments), $C_d + C_e + C_f$ (part of the Folded Area with deepest old Paleozoic sediments), and $D_a + D_b + D_c$ (whole Carpathians, all sediments).

Lastly, the final velocity *versus* depth formulas is calculated by fitting polynomials to moving averages. For the area of East European Craton, Polish Lowland, and Folded Area, second order polynomials are used. For the Carpathians where total thickness of sediments exceeds 20 000 m and all sediments are analyzed, two polynomials are introduced to better fit data at full depth range: second order for 500-1500 m of sub surface sediments, and third order for deeper sediments. Both polynomials are intersecting, so the overall result is a continuous function, but not a smooth function. In Figures 4 and 5 velocity *versus* depth result polynomials are shown as thick black lines. All polynomials and their coefficients are given in Table 1.

Note that depth values increase downward and zero corresponds to terrain level.

Figure 4 shows data and analysis results for the old Paleozoic sediments in the East European Craton, Polish Lowland, and Folded Area, while Fig. 5 shows the data and analysis results for the Carpathian sediments.

In areas of the East European Craton, the Polish Lowland, and the Folded Area *P*-wave seismic velocities in the old Paleozoic sediments increase slowly with depth, reaching up to 5500-6000 m/s at depths of 8000-11 000 m. Calculated moving averages are smooth and second order polynomials fit them very well. The largest velocity increase with depth can be observed in unit C_b, where the old Paleozoic sediments reach only the 2500 m depth.

In the Carpathians, where all the sediments are analyzed, a significant increase of velocity with depth, from about 2000 m/s at the surface to about 4500 m/s at 1000 m depth is observed. For deeper sediments, velocity increases slower with depth and for depths over 15 000 m the speed remains almost constant, not exceeding 6000 m/s.

4. SUMMARY AND CONCLUSION

Velocity *versus* depth formulas presented in this and previous paper (Grad and Polkowski 2012) provide full knowledge of *P*-wave velocities in the whole sedimentary cover in Poland. In this paper, VSP data was combined with seismic refraction profiles data to provide velocity *versus* depth relations for the old Paleozoic sediments in the area of East European Craton, Polish Lowland and Folded Area, and for all Carpathian sediments. Thickness of sediments in Poland reaches up to about 25 000 m, but *P*-wave velocities do not exceed 6000 m/s, making knowledge about seismic velocities in sediments very important.

To provide verification of the presented results, velocity *versus* depth relations for combined units $B_1 + B_2 + B_3$ (part of the Polish Lowland with deepest old Paleozoic sediments), $C_d + C_e + C_f$ (part of the Folded Area with deepest old Paleozoic sediments), and $D_a + D_b + D_c$ (whole Carpathians, all

sediments) were calculated and compared to similar studies from other deep sedimentary basins: the Baikal Southern Basin and the Southernwest Siberia (Suvorov and Mishen'kina 2005), the German Basin and the North Sea

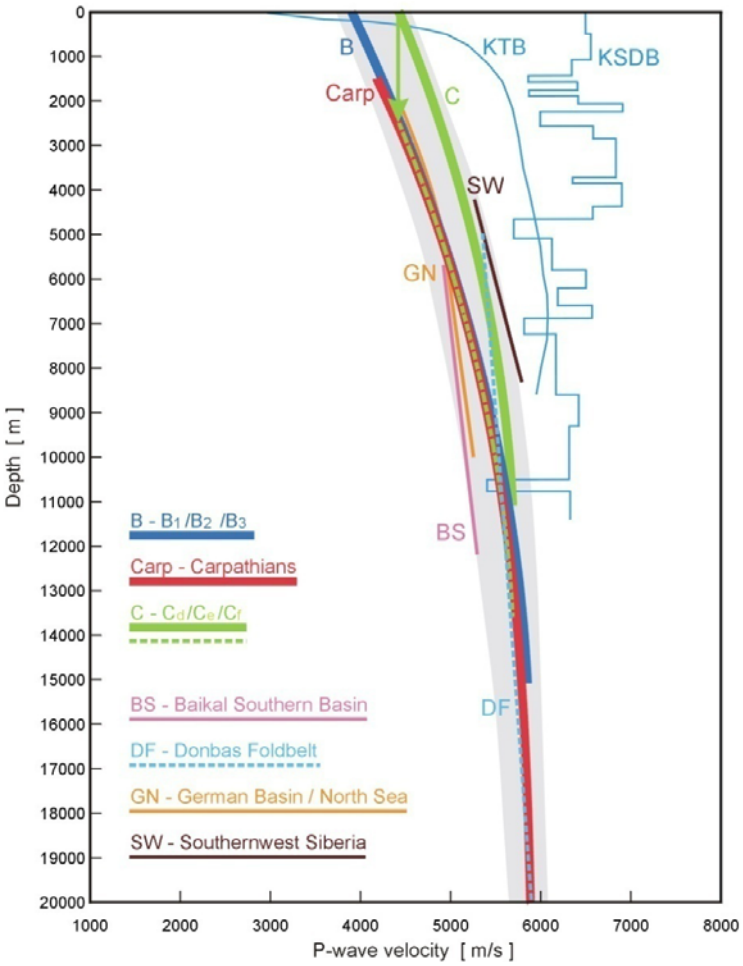

Fig. 6. Comparison of results for combined units $B_1 + B_2 + B_3$ (part of the Polish Lowland with deepest old Paleozoic sediments, thick blue line), $C_d + C_e + C_f$ (part of the Folded Area with deepest old Paleozoic sediments, thick green line), and $D_a + D_b + D_c$ (whole Carpathians, all sediments, thick red line) with similar studies from other deep sedimentary basins: the Baikal Southern Basin, and the Southernwest Siberia (Suvorov and Mishen'kina 2005), the German Basin and the North Sea Basin (Nielsen *et al.* 2005), the Donbas Foldbelt (Grad *et al.* 2003b), and two deep boreholes: Kola Superdeep Borehole (KSDB) in Kola Peninsula in north-eastern Russia and Kontinentales Tiefbohrprogramm Borehole (KTB) from Germany (Smithson *et al.* 2000).

Basin (Nielsen *et al.* 2005), and the Donbas Foldbelt (Grad *et al.* 2003b). All these results show some similarities: velocities are ±300 m/s with similar velocity gradients in the whole depth range. Additionally, two deep boreholes: Kola Superdeep Borehole (KSDB) in Kola Peninsula in northeastern Russia and Kontinentales Tiefbohrprogramm Borehole (KTB) from Germany (Smithson *et al.* 2000) are compared to results from this paper. The KSDB borehole is drilled through *ca*. 12 000 m of the Precambrian rocks including *ca.* 7000 m of the Proterozoic supracrustal rocks and *ca*. 5000 m of the Archean gneisses, while KTB is located in a terrain of Hercynian metamorphic rocks in southern Germany and reaches over 9000 m deep. Because of that, velocities in those boreholes are much bigger than velocities in the sediments in Poland. All comparisons are presented in Fig. 6.

Comparison of the velocity *versus* depth relations for combined units can lead to an interesting observation: the velocity-depth relation for part of the Folded Area ($C_d + C_e + C_f$) is shifted by *ca*. 2500 m in relation to two other combined units ($B_1 + B_2 + B_3$, $D_a + D_b + D_c$), which are almost identical. This shift might be a result of an uplift of this area in tectonic history. Material might have been deposited deeper and later, after it was compacted, the whole area might have been uplifted so now it has characteristic velocities for deeper sediments. Scherbaum (1982) made similar observation in Germany. This effect might also be a result of local anisotropy between vertical velocity (to which VPS measurements are sensitive) and horizontal velocity (measured by refraction). This could be a very interesting topic for further analysis.

Acknowledgments. The VSP data collected in the 1980s are from the Archives of the PBG Geophysical Exploration; more recent data are from the Central Geological Archives. The public domain GMT software (Wessel and Smith 1998, Wessel *et al.* 2013) has been used to produce map in Fig. 1. National Science Centre Poland provided financial support for this work by NCN grant DEC-2011/02/A/ST10/00284.

References

Berthelsen, A. (1992), From Precambrian to Variscan Europe. **In:** D. Blundell, R. Freeman, and S. Mueller (eds.), *A Continent Revealed – The European Geotraverse*, Cambridge University Press, Cambridge, 153-164.

Berthelsen, A. (1998), The Tornquist Zone northwest of the Carpathians: An intraplate pseudosuture, *GFF* **120**, 2, 223-230, DOI: 10.1080/11035899801202223.

Czuba, W., M. Grad, U. Luosto, G. Motuza, V. Nasedkin, and POLONAISE P5 Working Group (2001), Crustal structure of the East European Craton along the POLONAISE '97 P5 profile, *Acta Geophys. Pol.* **49**, 2, 145-168.

Czuba, W., M. Grad, U. Luosto, G. Motuza, V. Nasedkin, and POLONAISE P5 Working Group (2002), Upper crustal seismic structure of the Mazury complex and Mazowsze massif within East European Craton in NE Poland, *Tectonophysics* **360**, 1-4, 115-128, DOI: 10.1016/S0040-1951(02)00352-9.

Grad, M., and M. Polkowski (2012), Seismic wave velocities in the sedimentary cover of Poland: Borehole data compilation, *Acta Geophys.* **60**, 4, 985-1006, DOI: 10.2478/s11600-012-0022-z.

Grad, M., T. Trung Doan, and W. Klimkowski (1990), Seismic models of sedimentary cover of the Precambrian and Palaeozoic Platforms in Poland, *Kwart. Geol.* **34**, 2, 393-410 (in Polish).

Grad, M., T. Trung Doan, and W. Klimkowski (1991), Seismic models of sedimentary cover of the Precambrian and Paleozoic platforms in Poland, *Publs. Inst. Geophys. Pol. Acad. Sc.* **A-19**, 236, 125-145.

Grad, M., T. Janik, J. Yliniemi, A. Guterch, U. Luosto, T. Tiira, K. Komminaho, P. Środa, K. Höing, J. Makris, and C.E. Lund (1999), Crustal structure of the Mid-Polish Trough beneath the Teisseyre-Tornquist Zone seismic profile, *Tectonophysics* **314**, 1-3, 145-160, DOI: 10.1016/S0040-1951(99)00241-3.

Grad, M., S.L. Jensen, G.R. Keller, A. Guterch, H. Thybo, T. Janik, T. Tiira, J. Yliniemi, U. Luosto, G. Motuza, V. Nasedkin, W. Czuba, E. Gaczyński, P. Środa, K.C. Miller, M. Wilde-Piórko, K. Komminaho, J. Jacyna, and L. Korabliova (2003a), Crustal structure of the Trans-European suture zone region along POLONAISE'97 seismic profile P4, *J. Geophys. Res.* **108**, B11, 2541, DOI: 10.1029/2003JB002426.

Grad, M., D. Gryn, A. Guterch, T. Janik, R. Keller, R. Lang, S.B. Lyngsie, V. Omelchenko, V.I. Starostenko, R.A. Stephenson, S.M. Stovba, H. Thybo, and A. Tolkunov (2003b), DOBREfraction'99 – velocity model of the crust and upper mantle beneath the Donbas Foldbelt (East Ukraine), *Tectonophysics* **371**, 1-4, 81-110, DOI: 10.1016/S0040-1951(03)00211-7.

Grad, M., A. Špičák, G.R. Keller, A. Guterch, M. Brož, E. Hegedűs, and SUDETES 2003 Working Group (2003c), SUDETES 2003 seismic experiment, *Stud. Geophys. Geod.* **47**, 3, 681-689, DOI: 10.1023/A:1024732206210.

Grad, M., A. Guterch, and A. Polkowska-Purys (2005), Crustal structure of the Trans-European Suture Zone in Central Poland – reinterpretation of the LT-2, LT-4 and LT-5 deep seismic sounding profiles, *Geol. Quart.* **49**, 3, 243-252.

Grad, M., A. Guterch, G.R. Keller, T. Janik, E. Hegedűs, J. Vozár, A. Ślączka, T. Tiira, and J. Yliniemi (2006), Lithospheric structure beneath trans-Carpathian transect from Precambrian platform to Pannonian basin:

CELEBRATION 2000 seismic profile CEL05, *J. Geophys. Res.* **111**, B3, B03301, DOI: 10.1029/2005JB003647.

Grad, M., A. Guterch, S. Mazur, G.R. Keller, A. Špičák, P. Hrubcová, and W.H. Geissler (2008), Lithospheric structure of the Bohemian Massif and adjacent Variscan belt in central Europe based on profile S01 from the SUDETES 2003 experiment, *J. Geophys. Res.* **113**, B10, B10304, DOI: 10.1029/2007JB005497.

Grad, M., E. Brückl, M. Majdański, M. Behm, A. Guterch, CELEBRATION 2000 Working Group, and ALP 2002 Working Group (2009), Crustal structure of the Eastern Alps and their foreland: Seismic model beneath the CEL10/Alp04 profile and tectonic implications, *Geophys. J. Int.* **177**, 1, 279-295, DOI: 10.1111/j.1365-246X.2008.04074.x.

Guterch, A., M. Grad, T. Janik, R. Materzok, U. Luosto, J. Yliniemi, E. Lück, A. Schulze, and K. Förste (1994), Crustal structure of the transition zone between Precambrian and Variscan Europe from new seismic data along LT-7 profile (NW Poland and eastern Germany), *C. R. Acad. Sci. Paris II* **319**, 12, 1489-1496.

Guterch, A., M. Grad, H. Thybo, G.R. Keller, and POLONAISE Working Group (1999), POLONAISE '97 — an international seismic experiment between Precambrian and Variscan Europe in Poland, *Tectonophysics* **314**, 1-3, 101-121, DOI: 10.1016/S0040-1951(99)00239-5.

Guterch, A., M. Grad, G.R. Keller, K. Posgay, J. Vozár, A. Špičák, E. Brückl, Z. Hajnal, H. Thybo, O. Selvi, and CELEBRATION 2000 Experiment Team (2003), CELEBRATION 2000 seismic experiment, *Stud. Geophys. Geod.* **47**, 3. 659-669, DOI: 10.1023/A:1024728005301.

Janik, T., J. Yliniemi, M. Grad, H. Thybo, T. Tiira, and POLONAISE P2 Working Group (2002), Crustal structure across the TESZ along POLONAISE'97 seismic profile P2 in NW Poland, *Tectonophysics* **360**, 1-4, 129-152, DOI: 10.1016/S0040-1951(02)00353-0.

Janik, T., M. Grad, A. Guterch, R. Dadlez, J. Yliniemi, T. Tiira, G.R. Keller, E. Gaczyński, and CELEBRATION 2000 Working Group (2005), Lithospheric structure of the Trans-European Suture Zone along the TTZ-CEL03 seismic transect (from NW to SE Poland), *Tectonophysics* **411**, 1-4, 129-156, DOI: 10.1016/j.tecto.2005.09.005.

Janik, T., M. Grad, A. Guterch, and CELEBRATION 2000 Working Group (2009), Seismic structure of the lithosphere between the East European Craton and the Carpathians from the net of CELEBRATION 2000 profiles in SE Poland, *Geol. Quart.* **53**, 1, 141-158.

Janik, T., M. Grad, A. Guterch, J. Vozár, M. Bielik, A. Vozárova, E. Hegedűs, C.A. Kovács, I. Kovács, G.R. Keller, and CELEBRATION 2000 Working Group (2011), Crustal structure of the Western Carpathians and Pannonian Basin: Seismic models from CELEBRATION 2000 data and geological implications, *J. Geodyn.* **52**, 2, 97-113, DOI: 10.1016/j.jog.2010.12.002.

Jansen, S.L., T. Janik, H. Thybo, and POLONAISE Profile P1 Working Group (1999), Seismic structure of the Palaeozoic Platform along POLONAISE'97 profile P1 in northwestern Poland, *Tectonophysics* **314**, 1-3, 123-143, DOI: 10.1016/S0040-1951(99)00240-1.

Majdański, M., M. Grad, A. Guterch, and SUDETES 2003 Working Group (2006), 2-D seismic tomographic and ray tracing modelling of the crustal structure across the Sudetes Mountains basing on SUDETES 2003 experiment data, *Tectonophysics* **413**, 3-4, 249-269, DOI: 10.1016/j.tecto.2005.10.042.

Malinowski, M., A. Żelaźniewicz, M. Grad, A. Guterch, T. Janik, and CELEBRATION Working Group (2005), Seismic and geological structure of the crust in the transition from Baltica to Palaeozoic Europe in SE Poland – CELEBRATION 2000 experiment, profile CEL02, *Tectonophysics* **401**, 1-2, 55-77, DOI: 10.1016/j.tecto.2005.03.011.

Moryc, W., and K. Łydka (2000), Sedimentation and tectonics of the Upper Proterozoic-Lower Cambrian deposits of the southern Małopolska Massif (SE Poland), *Geol. Quart.* **44**, 1, 47-58.

Nielsen, L., H. Thybo, and M. Glendrup (2005), Seismic tomographic interpretation of Paleozoic sedimentary sequences in the southeastern North Sea, *Geophysics* **70**, 4, R45-R56, DOI: 10.1190/1.1996908.

Pożaryski, W., W. Brochwicz-Lewiński, and H. Tomczyk (1982), Sur la caractére hétérochronique de la Ligne Teisseyre-Tornquist, entre Europe centrale et orientale, *C. R. Acad. Sci. Paris II* **295**, 691-696 (in French).

Scherbaum, F. (1982), Seismic velocities in sedimentary rocks – indicators of subsidence and uplift?, *Geol. Rundsch.* **71**, 2, 519-536, DOI: 10.1007/BF01822381.

Skorupa, J. (1974), Seismic velocity map of Poland 1:500000, Wyd. Geol., Warszawa.

Smithson, S.B., F. Wenzel, Y.V. Ganchin, and I.B. Morozov (2000), Seismic results at Kola and KTB deep scientific boreholes: velocities, reflections, fluids, and crustal composition, *Tectonophysics* **329**, 1-4, 301-317, DOI: 10.1016/S0040-1951(00)00200-6.

Sokołowski, J. (1968), Geology and structure of the regional units of Poland from the point of view oil exploration. **In:** J. Biernat (ed.), *Surowce Mineralne*, Vol. 1, 7-58 (in Polish).

Suvorov, V.D., and Z.R. Mishen'kina (2005), Structure of sedimentary cover and basement beneath the South Basin of Lake Baikal inferred from seismic profiling, *Russ. Geol. Geophys.* **46**, 11, 1141-1149.

Środa, P., and POLONAISE Profile P3 Working Group (1999), P- and S-wave velocity model of the southwestern margin of the Precambrian East European Craton; POLONAISE'97, profile P3, *Tectonophysics* **314**, 1-3, 175-192, DOI: 10.1016/S0040-1951(99)00243-7.

Środa, P., W. Czuba, M. Grad, A. Guterch, A.K. Tokarski, T. Janik, M. Rauch, G.R. Keller, E. Hegedűs, J. Vozár, and CELEBRATION 2000 Working

Group (2006), Crustal and upper mantle structure of the Western Carpathians from CELEBRATION 2000 profiles CEL01 and CEL04: seismic models and geological implications, *Geophys. J. Int.* **167**, 2, 737-760, DOI: 10.1111/j.1365-246X.2006.03104.x.

Wessel, P., and W.H.F. Smith (1998), New, improved version of Generic Mapping Tools released, *Eos Trans. AGU* **79**, 47, 579, DOI: 10.1029/98EO00426.

Wessel, P., W.H.F. Smith, R. Scharroo, J. Luis, and F. Wobbe (2013), Generic Mapping Tools: Improved version released, *EOS Trans. AGU* **94**, 45, 409-420, DOI: 10.1002/2013EO450001.

Znosko, J. (1975), Tectonic units of Poland against the background of the tectonics of Europe, *Geol. Inst. Anniv. Bull.* **252**, 61-75.

Znosko, J. (1979), Teisseyre-Tornquist tectonic zone: some interpretative implications of recent geological and geophysical investigations, *Acta Geol. Pol.* **29**, 4, 365-382.

Received 11 July 2014
Received in revised form 24 September 2014
Accepted 26 September 2014

DE GRUYTER OPEN

Acta Geophysica
vol. 63, no. 3, June 2015, pp. 715-734
DOI: 10.2478/s11600-014-0259-9

Acoustic Reverse-time Migration using Optimal Staggered-grid Finite-difference Operator Based on Least Squares

Hongyong YAN[1], Lei YANG[1,2], and Hong LIU[1]

[1]Key Laboratory of Petroleum Resources Research, Institute of Geology and Geophysics, Chinese Academy of Sciences, Beijing, China;
e-mail: yanhongyong@163.com

[2]University of Chinese Academy of Sciences, Beijing, China

A b s t r a c t

Reverse-time migration (RTM) directly solves the two-way wave equation for wavefield propagation; therefore, how to solve the wave equation accurately and quickly is very important for RTM. The conventional staggered-grid finite-difference (SFD) operators are usually based on the Taylor-series expansion theory. If they are used to solve wave equation on a larger frequency content, a strong dispersion will occur, which directly affects the seismic image quality. In this paper, we propose an optimal SFD operator based on least squares to solve acoustic wave equation for prestack RTM, and obtain a new antidispersion RTM algorithm that can use short spatial difference operators. The synthetic and real data tests demonstrate that the least squares SFD (LSSFD) operator can mitigate the numerical dispersion, and the acoustic RTM using the LSSFD operator can effectively improve image quality comparing with that using the Taylor-series expansion SFD (TESFD) operator. Moreover, the LSSFD method can adopt a shorter spatial difference operator to reduce the computing cost.

Key words: migration; difference operator; image quality; least squares.

1. INTRODUCTION

Reverse-time migration (RTM) provides a superior way to image steeply dipping reflectors and complex subsurface structures in seismic exploration, because it is based on computing numerical solutions to a two-way wave equation (Baysal *et al*. 1983, McMechan 1983, Zhang and Zhang 2009, Pestana *et al*. 2012). The wave equation solutions are to describe the wavefield propagation features, and accurately image the subsurface structure with the wavefield information (Yan *et al*. 2013). The accuracy and efficiency of the RTM is strongly dependent on the algorithms used for numerical solutions of wave equation (Pestana and Stoffa 2009, Tessmer 2011). Therefore, how to solve the wave equation accurately and quickly is very important in RTM. At present, some ways have been used to solve wave equation, such as finite-difference (FD) methods, finite-element methods, and pseudo-spectral methods. But one of the most popular and easiest ways to implement numerical modeling and RTM based on the numerical solutions of wave equation is to use FD methods, including explicit methods and implicit methods, which mainly contain regular grid FD (Liu *et al*. 1998, Kosloff *et al*. 2010, Yan and Liu 2013) and staggered-grid FD (Virieux 1986, Pei 2004). These FD methods are flexible and efficient (Li *et al*. 2013). Furthermore, the staggered-grid FD methods have better accuracy and stability compared to the regular grid FD methods (Igel *et al*. 1992).

However, the numerical dispersion is an unavoidable weakness for FD methods (Pestana and Stoffa 2010), and it directly affects the image quality (Liu *et al*. 2008). To achieve higher accuracy and less dispersion, staggered-grid finite-difference (SFD) methods require higher-order SFD operators to compute the spatial derivatives, and the advantages of high-order SFD operators in solving the wave equation have been presented by many scholars (Dong *et al*. 2000, Pei 2004). The conventional classic coefficients of the higher-order SFD operator on spatial derivatives are usually determined by a Taylor-series expansion of spatial derivative term (Dong *et al*. 2000). If these difference operators are directly chosen to compute spatial derivatives on a relatively wider frequency band in solving the wave equation, a strong dispersion will still occur. To effectively solve this problem, some optimization methods for the coefficients of SFD operators have been proposed to improve the accuracy and efficiency for modeling and imaging, such as Newton method (Kindelan *et al*. 1990), implicit scheme (Liu and Sen 2009), time-space domain dispersion-relation-based method (Liu and Sen 2011), scaled binomial windows (Chu and Stoffa 2012), and simulated annealing algorithm (Zhang and Yao 2013). However, most of the optimization methods are too complicated to become widely implemented in seismic imaging. Liu (2013) proposed an easy way to obtain optimal finite-difference operator

based on least squares on a wide frequency zone, but his optimal finite-difference operator only applied to the second-order spatial derivatives for the regular grid. Yang *et al*. (2014) derived the difference coefficients for the first-order spatial derivatives by the dispersion relation and the least squares theory; however, these difference coefficients were only used for elastic modeling, and were not further extended to seismic imaging.

In this paper, we propose an optimal SFD operator based on least squares to perform wavefield forward and backward extrapolations for acoustic prestack RTM. We first introduce the least squares staggered-grid finite-difference (LSSFD) operator for solving the acoustic wave equation, then test the LSSFD operator by acoustic RTM with the synthetic and real data. Meanwhile, the numerical dispersion, modeling and imaging accuracy, and their computational efficiency are analyzed. Moreover, we compare the LSSFD operator with the conventional classic SFD operator based on Taylor-series expansion in the test application.

2. THEORY AND METHOD

2.1 Optimal staggered-grid finite-difference operator based on least squares

In this section, we introduce the optimal staggered-grid finite-difference operator and illustrate its basic formulation. We discuss the acoustic isotropic case, which is described by the 2D acoustic wave equation (Claerbout 1985)

$$\frac{\partial}{\partial x}\left(\frac{1}{\rho}\frac{\partial p}{\partial x}\right)+\frac{\partial}{\partial z}\left(\frac{1}{\rho}\frac{\partial p}{\partial z}\right)=\frac{1}{\rho v^2}\frac{\partial^2 p}{\partial t^2} \quad , \tag{1}$$

where x and z are the space coordinates, ρ is the density, v is the velocity, p represents the pressure, and t is the time.

In order to solve Eq. 1, the temporal derivative is usually calculated by the second-order finite-difference scheme, and the spatial derivatives are calculated by the high-order SFD schemes to improve the accuracy. The ($2M$)th-order SFD schemes for the first-order spatial derivative of the pressure $p(x,z)$ can be expressed as follows (Kindelan *et al*. 1990):

$$\frac{\partial p}{\partial x}\approx\frac{\delta p}{\delta x}=\frac{1}{\Delta x}\sum_{m=1}^{M}c_m\left[p\left(x+m\Delta x-0.5\Delta x,z\right)-p(x-m\Delta x+0.5\Delta x,z)\right] , \tag{2a}$$

$$\frac{\partial p}{\partial z}\approx\frac{\delta p}{\delta z}=\frac{1}{\Delta z}\sum_{m=1}^{M}c_m\left[p\left(x,z+m\Delta z-0.5\Delta z\right)-p(x,z-m\Delta z+0.5\Delta z)\right] , \tag{2b}$$

where Δx and Δz are the grid intervals, and c_m ($m=1,2,..,M$) are the SFD coefficients on spatial derivatives. Conventional classic SFD operator derives spatial high-order difference coefficients c_m by the Taylor-series ex-

pansion (Dong *et al*. 2000), so we call it Taylor-series expansion staggered-grid finite-difference (TESFD) when using these spatial difference coefficients to solve wave equations. In this paper, we adopt the least squares method proposed by Yang *et al*. (2014) to determine the optimal coefficients of high-order SFD operators on spatial derivatives.

We take the spatial derivative about the x direction as an example. Using the plane wave theory, we let

$$p\left(x+m\Delta x\right)=p_0 e^{\mathrm{i}k\left(x+m\Delta x\right)} \ , \tag{3}$$

where p_0 is a constant, $\mathrm{i}=\sqrt{-1}$, and k is the wavenumber. Substituting Eq. 3 into Eq. 2a, and simplifying it, we obtain

$$\beta \approx \sum_{m=1}^{M} c_m \sin\left[\left(2m-1\right)\beta\right] \ , \tag{4}$$

where $\beta = kh/2$, h is the grid size, $h=\Delta x$ and $0 \le \beta \le \pi/2$.

Because the left-hand side of Eq. 4 is the reserved item of the spatial derivative, and the right-hand side is the reserved item of the SFD schemes, we can construct a square error function based on dispersion relation (Yang *et al*. 2014)

$$E\left(c_1,c_2,\cdots c_M\right)=\int_0^b \left\{\beta-\sum_{m=1}^{M} c_m \sin\left[\left(2m-1\right)\beta\right]\right\}^2 d\beta \ , \tag{5}$$

where b is the upper limit of the integral. The quadratic function 5 represents the square error introduced by the SFD schemes over the given interval $[0, b]$ in solving spatial derivative, and we determine its minimum value with the least squares theory (Yang *et al*. 2014). According to the necessary condition of extremum, we get

$$\frac{\partial E\left(c_1,c_2,\cdots c_M\right)}{\partial c_m}=0 \ . \tag{6}$$

Substituting Eq. 5 into Eq. 6, we can obtain the optimal coefficients of high-order SFD operators by solving the following equations (see the Appendix A for more details):

$$\int_0^b \beta \sin\left[\left(2n-1\right)\beta\right]d\beta-\sum_{m=1}^{M} c_m\left\{\int_0^b \sin\left[\left(2n-1\right)\beta\right]\times\sin\left[\left(2m-1\right)\beta\right]d\beta\right\}=0 \ , \quad (n=1,2,3,...,M) \ . \tag{7}$$

2.2 The basic workflow of acoustic RTM

The acoustic prestack RTM used has three main parts: forward extrapolating the wavefield from the source, backward propagating the wavefield by reducing time from the recorded seismic data, and applying a proper imaging condition to construct an image where the reflection occurred (Zhang *et al*. 2010, Liu *et al*. 2011, Yan *et al*. 2013). In practice, the most important part of RTM is solving the wave equation for the forward and backward wavefields. We adopt the LSSFD operator presented in the previous section to solve the acoustic wave equation to improve the imaging accuracy for RTM. Moreover, there are some classes of imaging conditions that can be used to produce an image of the subsurface by propagating wavefields (Chattopadhyay and McMechan 2008). Here, we choose the source-normalized cross-correlation imaging condition (Leveille *et al*. 2011):

$$I(x,z)=\frac{\int s(x,z,t)\,r(x,z,t)\,dt}{\int |s(x,z,t)|^2\,dt+\sigma}\,, \tag{8}$$

where $I(x,z)$ is the migration result of the position (x,z), $s(x,z,t)$ is the forward extrapolated wavefield form the source, $r(x,z,t)$ is the backward propagated wavefield from the recorded seismic data, and σ is a small undefined and arbitrary damping factor.

Unfortunately, the imaging condition defined in Eq. 8 usually generates the low frequency noises (Liu *et al*. 2011). In this paper, we apply a Laplacian filter presented by Zhang and Sun (2009) to suppress the low frequency noises.

3. NUMERICAL RESULTS

3.1 Numerical dispersion analysis

According to Eq. 4, we define $\delta(\beta)$ as follows to describe the numerical dispersion of SFD:

$$\delta(\beta)=\frac{\sum_{m=1}^{M} c_m \sin\left[(2m-1)\beta\right]}{\beta}-1\,. \tag{9}$$

If $\delta(\beta)=0$, there is no numerical dispersion. If $\delta(\beta)$ is far from 0, a large numerical dispersion will occur. Figure 1 shows variations of $\delta(\beta)$ with β for different M by the TESFD and LSSFD of relative error of numerical dispersion relation, respectively. From Fig. 1, we can see that the LSSFD operator widens the frequency zone for the same dispersion and the same spatial difference operator length parameter M, compared to the TESFD operator.

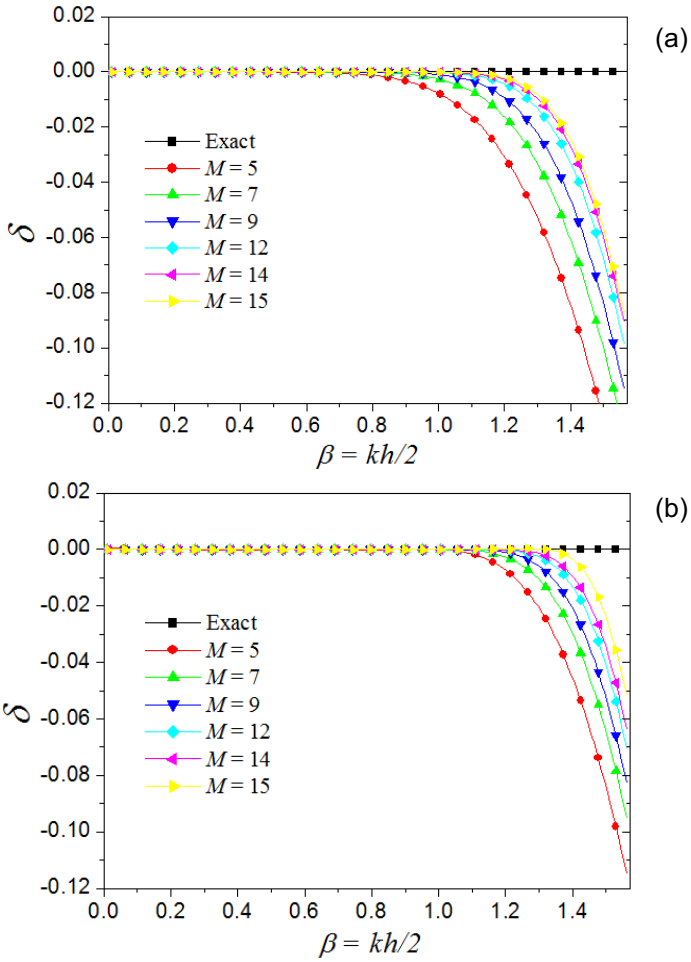

Fig. 1. Variations of $\delta(\beta)$ with β for different M by the TESFD operators and the LSSFD operators of a relative error of numerical dispersion relation, respectively: (a) by the TESFD, and (b) by the LSSFD.

From the comparison, the accuracy of the 10th-order LSSFD operator is much higher than that of the 10th-order TESFD operator, and even reaches that of the 18th-order TESFD operator because their relative error curves share almost the same position in Fig. 1. Namely, the accuracy of the LSSFD operators is much higher than that of the TESFD operators when using the same spatial difference operator length. Additionally, the length of LSSFD operator is shorter than that of TESFD operator under the same numerical accuracy.

3.2 Numerical modeling and RTM for fault model

We use a fault model with two horizontal and one dipping interfaces shown in Fig. 2 to demonstrate effects of numerical modeling and RTM. The model is discretized into 401 by 201 grid points, with a grid interval of 10 m. The velocity and the density for the first layer are 1600 m/s and 1700 kg^3m^{-3}, respectively, and for the second layer they are 2000 m/s and 1800 kg^3m^{-3}, respectively. We perform numerical modeling and prestack RTM using the SFD methods of 2nd-order accuracy in time and high-order accuracy in space. The source function is a Ricker wavelet with a peak frequency of 30 Hz. There are 73 sources in total, and the sources are placed at a horizontal interval of 50 m; the first source is located at (100 m, 90 m). Each source has 400 receivers, with a receiver interval of 10 m. The time step is 0.001 s with 3 s total propagation time.

Figure 3 shows the modeling acoustic seismograms for the fault model computed by the LSSFD and the TESFD operators, respectively, when the source is located at (2000 m, 60 m). Figure 4 is the records extracted from Fig. 3. Figure 5 shows the corresponding snapshots of the seismograms in Fig. 3 at $t = 1$ s. From Figs. 3, 4, and 5, we observe that the waveforms on both seismograms and snapshots computed by the 8th-order LSSFD operator and the 16th-order TESFD operator have very small numerical dispersion. However, the waveforms on both seismogram and snapshot computed by the 8th-order TESFD operator have obvious numerical dispersion and waveform distortion. By comparing these seismograms and snapshots, we can find that the acoustic modeling accuracy by the 8th-order LSSFD operator is much higher than that by the 8th-order TESFD operator, and even slightly higher than that by the 16th-order TESFD operator. Note that these accuracy analyses based on acoustic modeling are fully consistent with the theoretical analyses in the previous section.

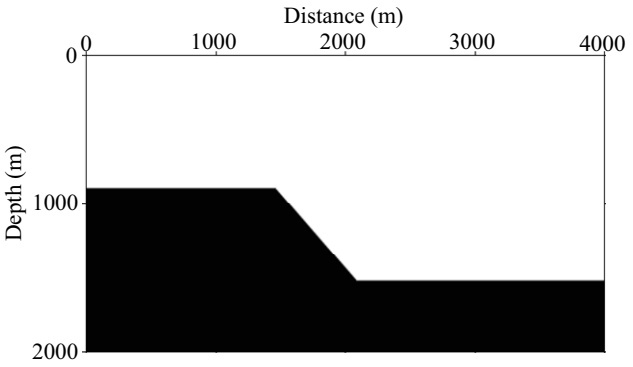

Fig. 2. The fault model.

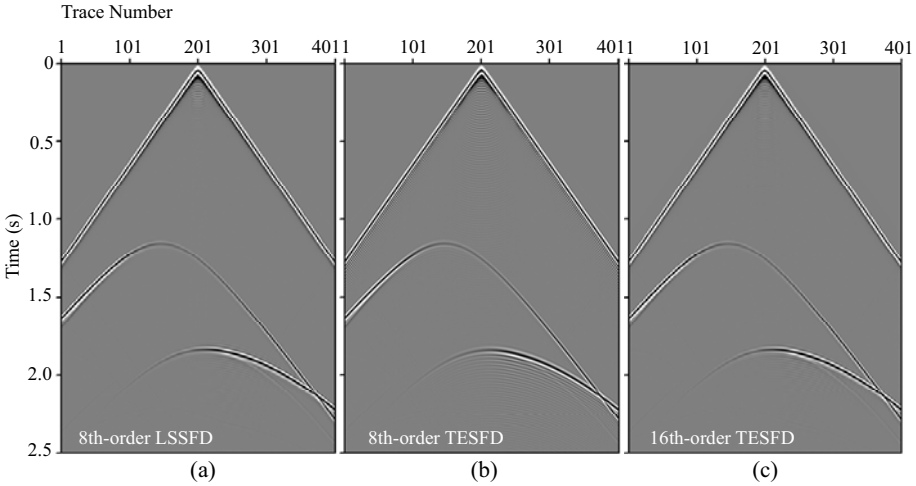

Fig. 3. Seismograms for the fault model computed by: (a) the 8th-order LSSFD operator, (b) the 8th-order TESFD operator, and (c) the 16th-order TESFD operator, respectively.

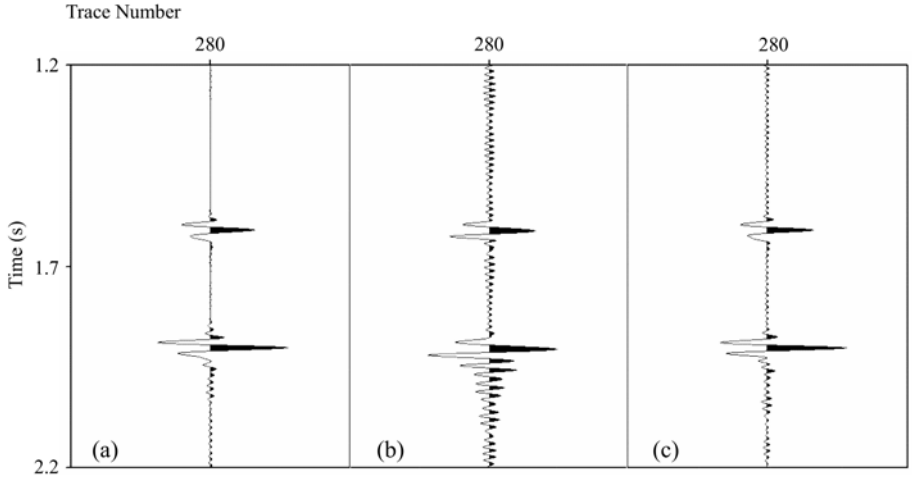

Fig. 4. Comparison of the records extracted from: (a) Fig. 3a, (b) Fig. 3b, and (c) Fig. 3c, respectively. Here, all the records are shown on the same amplitude scales.

Figure 6 shows a comparison of computing costs for different SFD operators with different spatial difference operator length in acoustic modeling. Obviously, the computing costs of the LSSFD operators are very close to that of the TESFD operators under the same spatial difference operator length.

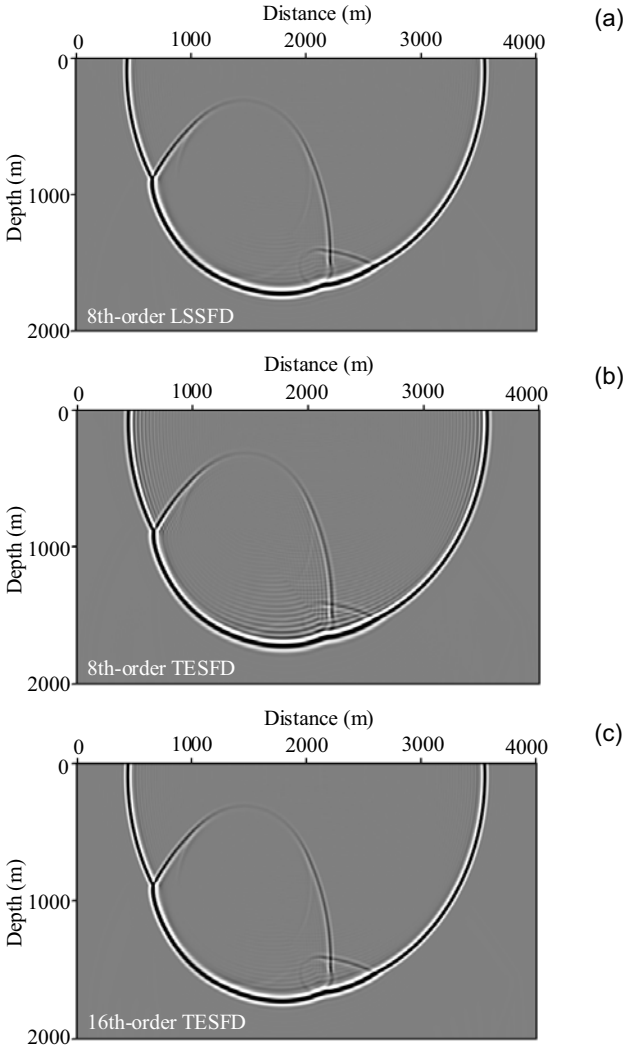

Fig. 5. Snapshots for the fault model computed by: (a) the 8th-order LSSFD operator, (b) the 8th-order TESFD operator, and (c) the 16th-order TESFD operator, respectively. Here, all the snapshots are shown on the same amplitude scales.

Therefore, the comparison shows that the solving of wave equation using LSSFD operator has hardly any extra computing costs in comparison with that using the TESFD operator. Obviously, the application of the LSSFD operator for RTM has the same conclusion in the computing costs.

Figure 7 shows the final RTM images using the 8th-order LSSFD operator, the 8th-order TESFD operator, and the 16th-order TESFD operator, re-

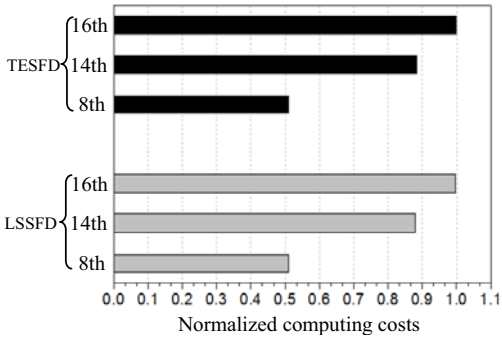

Fig. 6. Comparison of the computing costs for the TESFD and the LSSFD in acoustic modeling. The normalized computing costs of 8th-, 14th-, 16th-order TESFD operators and 8th-, 14th-, 16th-order LSSFD operators are shown in this figure.

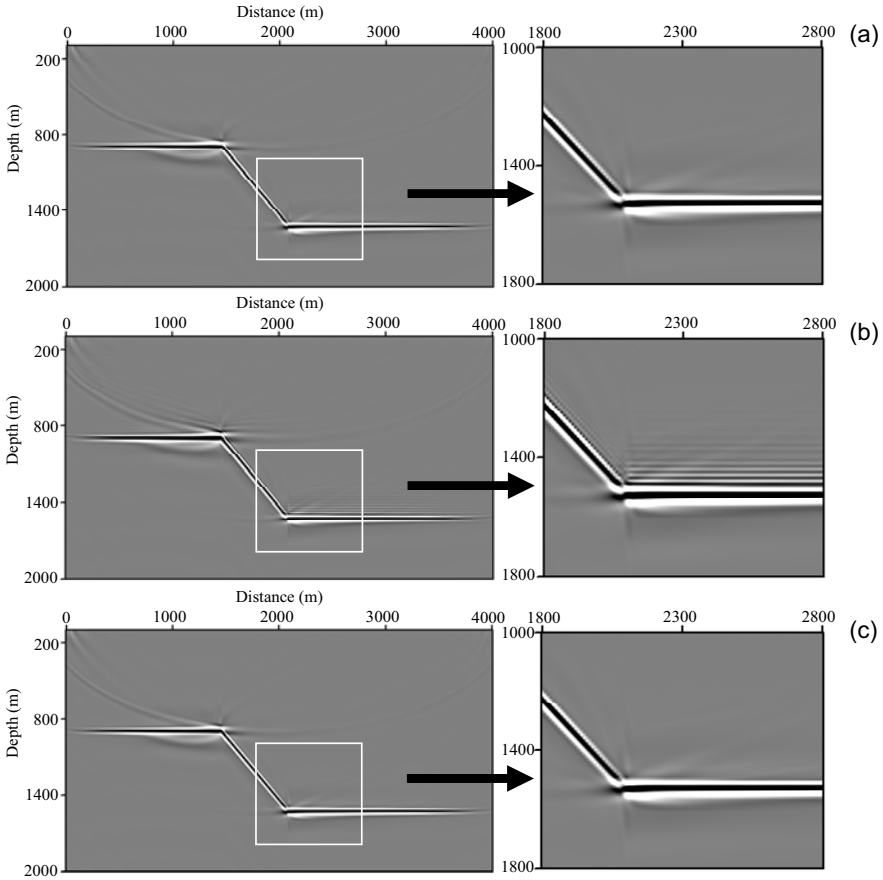

Fig. 7. The RTM images for the fault model by: (a) the 8th-order LSSFD operator, (b) the 8th-order TESFD operator, (c) the 16th-order TESFD operator, respectively.

spectively. From Fig. 7, we observe that the image using the 8th-order LSSFD operator is very clear and shows the structure of the real model. However, the image using the 8th-order TESFD operator has some artifacts along the reflector interfaces resulting from numerical dispersion effects in wave propagation. So the model test demonstrates the acoustic RTM using the LSSFD operator can obtain the better image than that using the TESFD operator under the same spatial difference operator length. Additionally, the image using the 16th-order TESFD operator is of less dispersion noise and very clear. By comparing Fig. 7a with c, we find that the LSSFD operator can adopt a shorter spatial difference operator in RTM while preserving the high imaging accuracy, compared to the TESFD operator.

3.3 RTM for salt model

To further examine the image quality, we test the RTM algorithms on the 2D Society of Exploration Geophysicists/European Association of Geoscientists and Engineers (SEG/EAGE) salt model. The salt model is discretized into 600 (in x) by 200 (in depth) grid points, with grid intervals of 20 m (in x) and 20 m (in depth). The P-wave velocity is illustrated in Fig. 8a, and Fig. 8b is

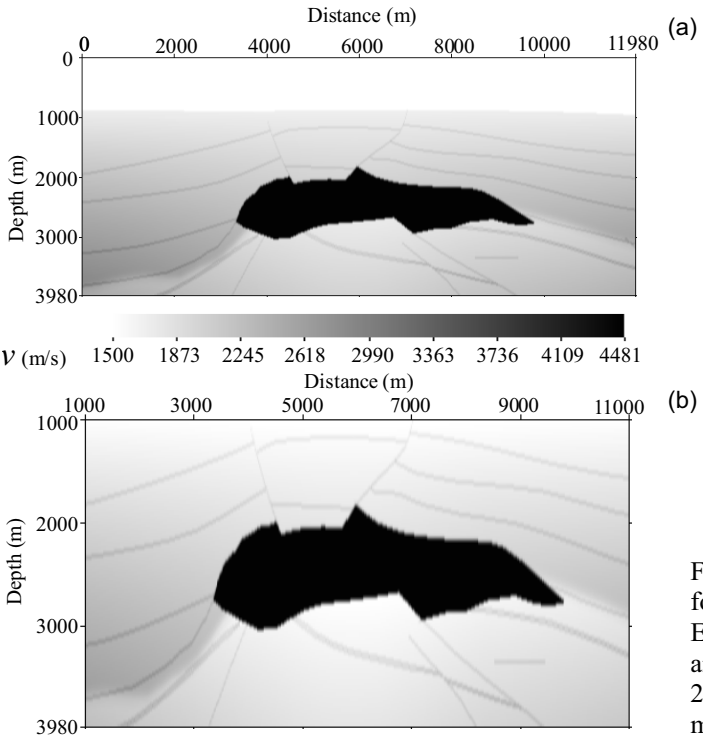

Fig. 8: (a) Velocity for the 2D SEG/EAGE salt model, and (b) zoom of the 2D SEG/EAGE salt model.

the zoom of Fig. 8a. The density is constant. We use the 8th-order LSSFD to generate synthetic data for 116 sources from location 200 to 11700 m with a source spacing of 100 m. The source function is a 30 Hz Ricker wavelet. The total record time is 8 s and the time step is 0.001 s. We perform the acoustic RTM using the TESFD and the LSSFD operators, respectively. Here, the true model velocity is taken as the migration velocity.

Figure 9 shows the final RTM images by the 6th-order LSSFD and the 6th-order TESFD operators, respectively. The image using the LSSFD operators is very clear and accurate by comparison with the true model (Fig. 8b). However, the image using the TESFD operator has some artifacts along the reflector interfaces and the boundary of the salt body, which result from the numerical dispersion. By comparing the images using two kinds of SFD operators, we observe that the image using the LSSFD operator has better image quality than that using the TESFD operator.

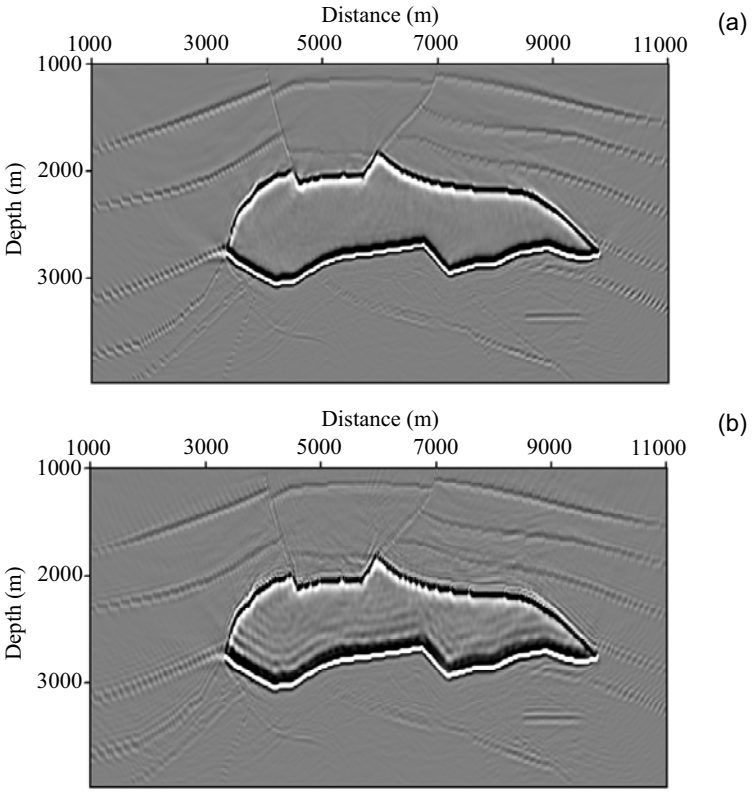

Fig. 9. The RTM images for the 2D SEG/EAGE salt model by: (a) the LSSFD operator, and (b) the TESFD operator, respectively.

4. REAL DATA APPLICATION

We use a real 2D seismic data from the northeast China to test RTM algorithms based on the LSSFD operator and the TESFD operator under the same spatial difference operator length (8th-order), respectively. The data consists of 100 shot gathers with a source interval of 100 m. For each shot gather, there are 159 traces with a trace interval of 50 m. The time sampling interval for receiver recording is 0.001 s. Figure 10 shows the common-shot gathers. Figure 11 is the migration velocity model for the real data test. Grid

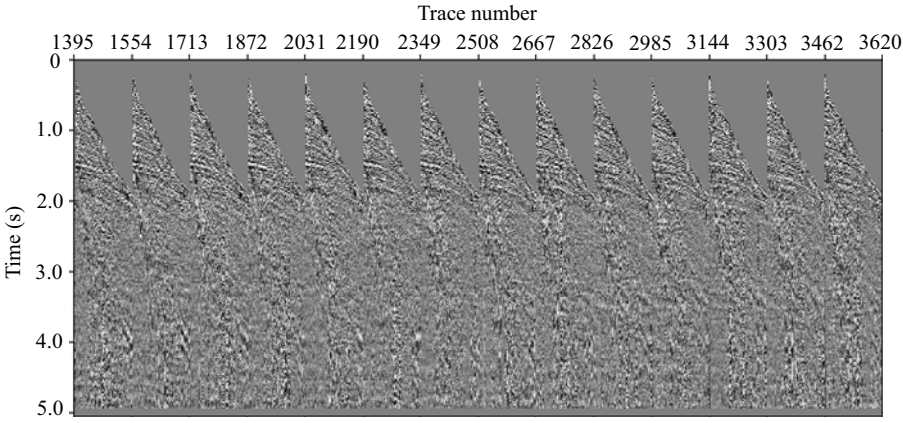

Fig. 10. The common-shot gathers (only fourteen shots are shown).

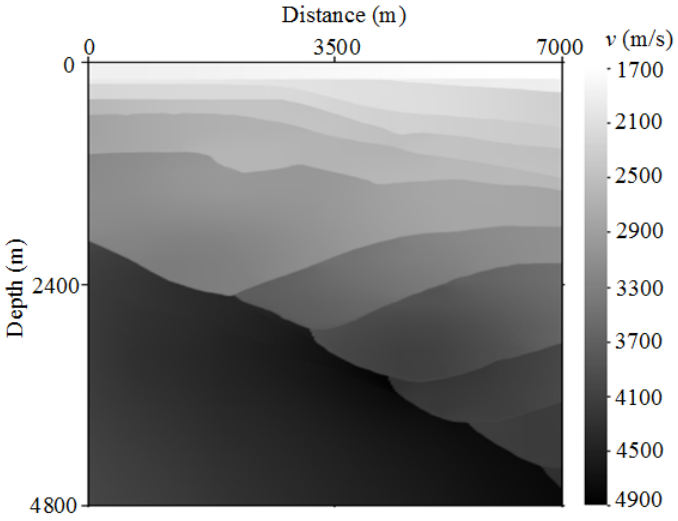

Fig. 11. The migration velocity model for the real data test.

intervals are 10 m (in x) and 10 m (in z). The RTM images obtained by the LSSFD operator and the TESFD operator are shown in Fig. 12, respectively. Figure 13 is the partial zoom of RTM sections in Fig. 12 (black boxes). Comparing these two images, the reflectors in the RTM image by the LSSFD operator are characterized by better focusing and balancing of amplitudes, and contain fewer artifacts compared to the RTM image by the TESFD operator. This suggests that the numerical dispersion affects the quality of the RTM image. The real data test shows that the RTM by the LSSFD operator produced a better image than that by the TESFD operator.

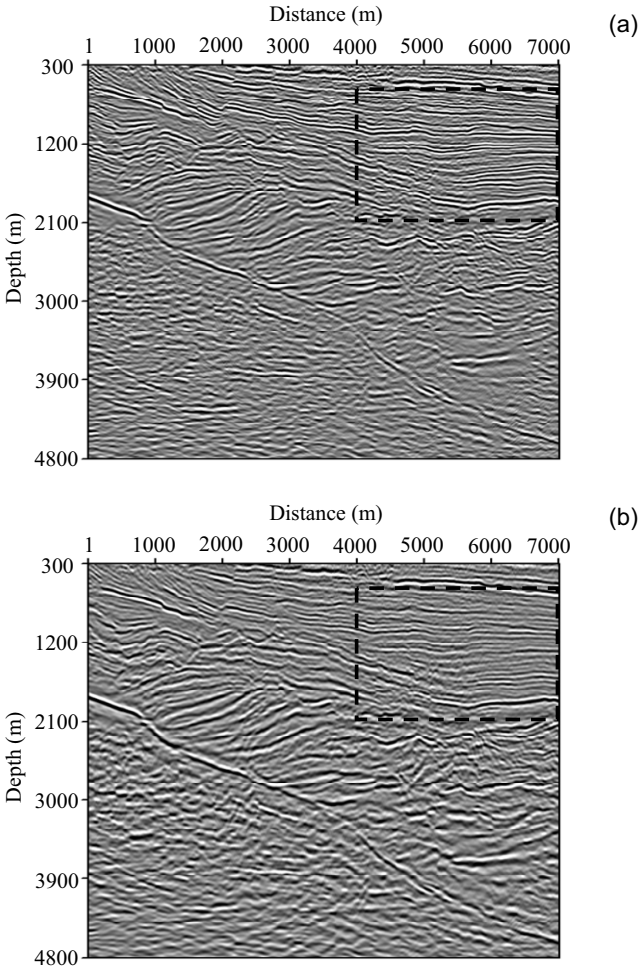

Fig. 12. The RTM images for the real data obtained by: (a) the LSSFD operator, and (b) the TESFD operator. The black boxes indicate the areas for zoom view.

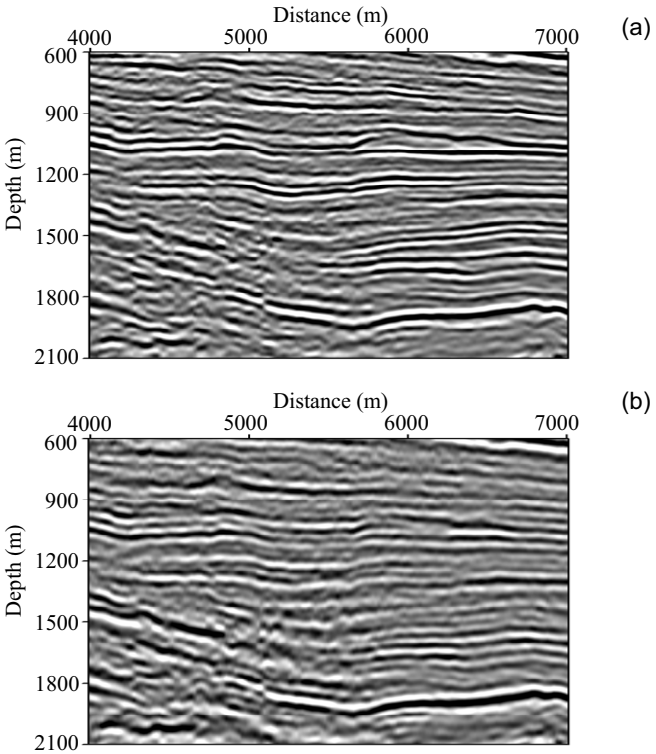

Fig. 13. The zoom views of the black boxes in Fig. 12: (a) the RTM image obtained by the LSSFD operator, and (b) the RTM image obtained by the TESFD operator.

5. CONCLUSIONS

We propose the LSSFD operator to perform wavefield forward and backward extrapolations for acoustic prestack RTM, and obtain a new antidispersion RTM algorithm that can use short spatial difference operator. The numerical results demonstrate that the LSSFD operator can effectively attenuate the numerical dispersion on the larger frequency zone, and the acoustic modeling accuracy by the LSSFD operators is much higher than that by the TESFD operators under the same spatial difference operator length. Moreover, the synthetic and real data tests demonstrate that the acoustic RTM using the LSSFD operator can effectively improve the image quality comparing with that using TESFD operator without extra computing costs. And the LSSFD method can adopt a shorter spatial difference operator to reduce the computing cost with preserving the modeling and imaging accuracy. Furthermore, the LSSFD operator can be easily extended to other RTM algorithms based on different wave equations.

Acknowledgements. This research is supported by the China Postdoctoral Science Foundation funded project under contract numbers 2012M520374, 2013T60169, the National High Technology Research and Development Program of China (‘‘863” Program) under contract number 2012AA061202, and China National Petroleum Corporation (the Scientific Research and Technology Development Project).

APPENDIX

The difference coefficients for the LSSFD operators

In this Appendix, we derive the difference coefficients for the LSSFD operators in detail, and list the values of the difference coefficients for LSSFD operators and TESFD operators, respectively.

Let

$$\varphi_m(\beta) = \sin\left[(2m-1)\beta\right]. \tag{A1}$$

So Eq. 5 can be rewritten as

$$E(c_1, c_2, \cdots c_M) = \int_0^b \left\{\beta - \sum_{m=1}^{M} c_m \varphi_m(\beta)\right\}^2 d\beta. \tag{A2}$$

Let

$$(\varphi_n, \varphi_m) = \int_0^b \varphi_n(\beta)\varphi_m(\beta)d\beta, \tag{A3}$$

$$(\beta, \varphi_m) = \int_0^b \beta\varphi_m(\beta)d\beta, \tag{A4}$$

where $n, m = 1, 2, \ldots, M$.

Substituting Eq. A2 into Eq. 6, and simplifying them by introducing Eqs. A3 and A4, we finally obtain

$$\begin{bmatrix} (\varphi_1,\varphi_1) & (\varphi_1,\varphi_2) & \cdots & (\varphi_1,\varphi_M) \\ (\varphi_2,\varphi_1) & (\varphi_2,\varphi_2) & \cdots & (\varphi_2,\varphi_M) \\ \vdots & & & \vdots \\ (\varphi_M,\varphi_1) & (\varphi_M,f_2) & \cdots & (\varphi_M,\varphi_M) \end{bmatrix} \begin{bmatrix} c_1 \\ c_2 \\ \vdots \\ c_M \end{bmatrix} = \begin{bmatrix} (\beta,\varphi_1) \\ (\beta,\varphi_2) \\ \vdots \\ (\beta,\varphi_M) \end{bmatrix}. \tag{A5}$$

We use Gaussian elimination to solve linear Eq. A5 for obtaining the difference coefficients for LSSFD operators (Yang *et al*. 2014), then apply the LSSFD operators to solve wave equation and perform RTM.

Tables A1 and A2 list the 4th, 6th, 8th, 10th, 12th, 14th, 16th, 18th, 20th, and 22nd-order SFD coefficients calculated by the Taylor-series expansion method and the least squares method, respectively.

Table A1

Difference coefficients of the TESFD operators (Liu and Sen 2009)

c_m	$M=2$	$M=3$	$M=4$	$M=5$	$M=6$
c_1	1.125000e+0	1.171875e+0	1.196289e+0	1.211243e+0	1.221336e+0
c_2	–4.166667e-2	–6.510417e-2	–7.975260e-2	–8.972168e-2	–9.693146e-2
c_3		4.687500e-2	9.570313e-3	1.384277e-2	1.744766e-2
c_4			–6.975446e-4	–1.765660e-3	–2.967290e-3
c_5				1.186795e-4	3.590054e-4
c_6					–2.184781e-5
c_m	$M=7$	$M=8$	$M=9$	$M=10$	$M=11$
c_1	1.228606e+0	1.234091e+0	1.238376e+0	1.241816e+0	1.244638e+0
c_2	–1.023839e-1	–1.066498e-1	–1.100779e-1	–1.128924e-1	–1.152443e-1
c_3	2.047677e-2	2.303637e-2	2.521784e-2	2.709417e-2	2.872242e-2
c_4	–4.178933e-3	–5.342386e-3	–6.433123e-3	–7.443453e-3	–8.373884e-3
c_5	6.894535e-4	1.077271e-3	1.496785e-3	1.929784e-3	2.363985e-3
c_6	–7.692250e-5	–1.664189e-4	–2.862801e-4	–4.306130e-4	–5.934385e-4
c_7	4.236515e-6	1.702171e-5	4.099395e-5	7.707717e-5	1.249670e-4
c_8		–8.523464e-7	–3.848877e-6	–1.021650e-5	–2.085870e-5
c_9			1.762665e-7	8.837806e-7	2.564127e-6
c_{10}				–3.723759e-8	–2.052722e-7
c_{11}					8.001648e-9

Table A2

Difference coefficients of the LSSFD operators (b = 1.02)

c_m	M = 2	M = 3	M = 4	M = 5	M = 6
c_1	1.188401e+0	1.216624e+0	1.230862e+0	1.239407e+0	1.245095e+0
c_2	–7.046382e-2	–9.197724e-2	–1.034123e-1	–1.105315e-1	–1.153979e-1
c_3		1.300041e-2	2.011671e-2	2.496329e-2	2.848442e-2
c_4			–3.245760e-3	–5.804879e-3	–7.899473e-3
c_5				9.358680e-4	1.898222e-3
c_6					–2.935304e-4
c_m	M = 7	M = 8	M = 9	M = 10	M = 11
c_1	1.249150e+0	1.252186e+0	1.254544e+0	1.256428e+0	1.257967e+0
c_2	–1.189375e-1	–1.216289e-1	–1.237449e-1	–1.254524e-1	–1.268598e-1
c_3	3.116091e-2	3.326513e-2	3.496337e-2	3.636307e-2	3.753689e-2
c_4	–9.623004e-3	–1.105777e-2	–1.226716e-2	–1.329873e-2	–1.418823e-2
c_5	2.812069e-3	3.647865e-3	4.401731e-3	5.078779e-3	5.686916e-3
c_6	–6.655106e-4	–1.066144e-3	–1.468116e-3	–1.857840e-3	–2.228932e-3
c_7	9.728191e-5	2.437491e-4	4.198223e-4	6.117512e-4	8.105434e-4
c_8		–3.351959e-5	–9.196027e-5	–1.694350e-4	–2.605010e-4
c_9			1.188808e-5	3.543912e-5	6.954928e-5
c_{10}				–4.311393e-6	–1.387702e-5
c_{11}					1.591802e-6

References

Baysal, E., D.D. Kosloff, and J.W.C. Sherwood (1983), Reverse time migration, *Geophysics* **48**, 11, 1514-1524, DOI: 10.1190/1.1441434.

Chattopadhyay, S., and G.A. McMechan (2008), Imaging conditions for prestack reverse-time migration, *Geophysics* **73**, 3, S81-S89, DOI: 10.1190/ 1.2903822.

Chu, C., and P.L. Stoffa (2012), Determination of finite-difference weights using scaled binomial windows, *Geophysics* **77**, 3, W17-W26, DOI: 10.1190/ geo2011-0336.1.

Claerbout, J.F. (1985), *Imaging the Earth's Interior*, Blackwell Scientific Publs., Oxford.

Dong, L.G., Z.T. Ma, J.Z. Cao, H.Z. Wang, J.H. Gao, B. Lei, and S.Y. Xu (2000), A staggered-grid high-order difference method of one-order elastic wave equation, *Chin. J. Geophys.* **43**, 3, 411-419 (in Chinese).

Igel, H., B. Riollet, and P. Mora (1992), Accuracy of staggered 3-D finite-difference grids for anisotropic wave propagation. **In:** *62th SEG Ann. Meeting, 25-29 October 1992, New Orleans, USA*, SEG-1992-1244, Society of Exploration Geophysicists, 1244-1246.

Kindelan, M., A. Kamel, and P. Sguazzero (1990), On the construction and efficiency of staggered numerical differentiators for the wave equation, *Geophysics* **55**, 1, 107-110, DOI: 10.1190/1.1442763.

Kosloff, D., R.C. Pestana, and H. Tal-Ezer (2010), Acoustic and elastic numerical wave simulations by recursive spatial derivative operators, *Geophysics* **75**, 6, T167-T174, DOI: 10.1190/1.3485217.

Leveille, J.P., I.F. Jones, Z.-Z. Zhou, B. Wang, and F. Liu (2011), Subsalt imaging for exploration, production, and development: A review, *Geophysics* **76**, 5, WB3-WB20, DOI: 10.1190/geo2011-0156.1.

Li, J., D. Yang, and F. Liu (2013), An efficient reverse time migration method using local nearly analytic discrete operator, *Geophysics* **78**, 1, S15-S23, DOI: 10.1190/geo2012-0247.1.

Liu, F., S.A. Morton, J.P. Leveille, and G. Zhang (2008), An anti-dispersion wave equation for modeling and reverse-time migration. **In:** *78th SEG Ann. Meeting, 9-14 November 2008, Las Vegas, USA*, SEG-2008-2277, Society of Exploration Geophysicists, 2277-2281.

Liu, F., G. Zhang, S.A. Morton, and J.P. Leveille (2011), An effective imaging condition for reverse-time migration using wavefield decomposition, *Geophysics* **76**, 1, S29-S39, DOI: 10.1190/1.3533914.

Liu, Y. (2013), Globally optimal finite-difference schemes based on least squares, *Geophysics* **78**, 4, T113-T132, DOI: 10.1190/geo2012-0480.1.

Liu, Y., and M.K. Sen (2009), An implicit staggered-grid finite-difference method for seismic modelling, *Geophys. J. Int.* **179**, 1, 459-474, DOI: 10.1111/j.1365-246X.2009.04305.x.

Liu, Y., and M.K. Sen (2011), Scalar wave equation modeling with time-space domain dispersion-relation-based staggered-grid finite-difference schemes, *Bull. Seismol. Soc. Am.* **101**, 1, 141-159, DOI: 10.1785/0120100041.

Liu, Y., C. Li, and Y. Mou (1998), Finite-difference numerical modeling of any even-order accuracy, *Oil Geophys. Prospect.* **33**, 1-10 (in Chinese).

McMechan, G.A. (1983), Migration by extrapolation of time-dependent boundary values, *Geophys. Prospect.* **31**, 3, 413-420, DOI: 10.1111/j.1365-2478.1983.tb01060.x.

Pei, Z. (2004), Numerical modeling using staggered-grid high order finite difference of elastic wave equation on arbitrary relief surface, *Oil Geophys. Prospect.* **39**, 629-634 (in Chinese).

Pestana, R.C., and P.L. Stoffa (2009), Rapid expansion method (REM) for time-stepping in reverse time migration (RTM). **In:** *79th SEG Ann. Meeting, 25-30 October 2009, Houston, USA*, SEG-2009-2819, Society of Exploration Geophysicists, 2819-2823.

Pestana, R.C., and P.L. Stoffa (2010), Time evolution of the wave equation using rapid expansion method, *Geophysics* **75**, 4, T121-T131, DOI: 10.1190/1.3449091.

Pestana, R.C., B. Ursin, and P.L. Stoffa (2012), Rapid expansion and pseudo spectral implementation for reverse time migration in VTI media, *J. Geophys. Eng.* **9**, 3, 291, DOI: 10.1088/1742-2132/9/3/291.

Tessmer, E. (2011), Using the rapid expansion method for accurate time-stepping in modeling and reverse-time migration, *Geophysics* **76**, 4, S177-S185, DOI: 10.1190/1.3587217.

Virieux, J. (1986), P-SV wave propagation in heterogeneous media: Velocity-stress finite-difference method, *Geophysics* **51**, 4, 889-901, DOI: 10.1190/1.1442147.

Yan, H., and Y. Liu (2013), Visco-acoustic prestack reverse-time migration based on the time-space domain adaptive high-order finite-difference method, *Geophys. Prospect.* **61**, 5, 941-954, DOI: 10.1111/1365-2478.12046.

Yan, H., Y. Liu, and H. Zhang (2013), Prestack reverse-time migration with a time-space domain adaptive high-order staggered-grid finite-difference method, *Explor. Geophys.* **44**, 2, 77-86, DOI: 10.1071/EG12047.

Yang, L., H. Yan, and H. Liu (2014), Least squares staggered-grid finite-difference for elastic wave modelling, *Explor. Geophys.* **45**, 4, 255-260, DOI: 10.1071/EG13087.

Zhang, J.-H., and Z.-X. Yao (2013), Optimized finite-difference operator for broadband seismic wave modeling, *Geophysics* **78**, 1, A13-A18, DOI: 10.1190/geo2012-0277.1.

Zhang, Y., and J. Sun (2009), Practical issues of reverse time migration: True amplitude gathers, noise removal and harmonic-source encoding, *First Break* **26,** 19-25.

Zhang, Y., and G. Zhang (2009), One-step extrapolation method for reverse time migration, *Geophysics* **74**, 4, A29-A33, DOI: 10.1190/1.3123476.

Zhang, Y., P. Zhang, and H. Zhang (2010), Compensating for visco-acoustic effects in reverse-time migration. **In:** *80th SEG Ann. Meeting, 17-22 October 2010, Denver, USA*, SEG-2010-3160, Society of Exploration Geophysicists, 3160-3164.

Received 19 January 2014
Received in revised form 18 April 2014
Accepted 6 May 2014

DE GRUYTER OPEN

Acta Geophysica
vol. 63, no. 3, June 2015, pp. 735-760
DOI: 10.1515/acgeo-2015-0003

NMR Parameters Determination through ACE Committee Machine with Genetic Implanted Fuzzy Logic and Genetic Implanted Neural Network

Mojtaba ASOODEH[1], Parisa BAGHERIPOUR[1], and Amin GHOLAMI[2]

[1]Department of Petroleum Engineering, Aligudarz Branch, Islamic Azad University, Aligudarz, Iran; e-mail: asoodeh.mojtaba@gmail.com

[2]Abadan Faculty of Petroleum Engineering, Petroleum University of Technology, Abadan, Iran

A b s t r a c t

Free fluid porosity and rock permeability, undoubtedly the most critical parameters of hydrocarbon reservoir, could be obtained by processing of nuclear magnetic resonance (NMR) log. Despite conventional well logs (CWLs), NMR logging is very expensive and time-consuming. Therefore, idea of synthesizing NMR log from CWLs would be of a great appeal among reservoir engineers. For this purpose, three optimization strategies are followed. Firstly, artificial neural network (ANN) is optimized by virtue of hybrid genetic algorithm-pattern search (GA-PS) technique, then fuzzy logic (FL) is optimized by means of GA-PS, and eventually an alternative condition expectation (ACE) model is constructed using the concept of committee machine to combine outputs of optimized and non-optimized FL and ANN models. Results indicated that optimization of traditional ANN and FL model using GA-PS technique significantly enhances their performances. Furthermore, the ACE committee of aforementioned models produces more accurate and reliable results compared with a singular model performing alone.

Keywords: NMR, rock physics, petrophysics, integrated intelligent systems.

1. INTRODUCTION

Nuclear magnetic resonance (NMR) log contains priceless information about the *in situ* characteristics of hydrocarbon-bearing intervals. Free fluid porosity and permeability are two invaluable parameters of reservoir formations which could be determined by interpreting transverse relaxation time data (T_2 distribution) of NMR log. NMR logging becomes impractical in cased-hole wells and where insufficient deal of money and time exists. However, invaluable information obtained from NMR log has tempted several researchers to devise quick, cheap, and practical methods of gaining NMR log parameters. Conventional well log data have been used by some researchers for synthesizing NMR log parameters through the use of intelligent systems (Mohaghegh 2000a, Malki and Baldwin 2002, Ogilvie *et al*. 2002, Labani *et al.* 2010). These methodologies enable reservoir engineers to extract free fluid porosity and permeability for both cased holes and open holes in a cheap and fast way. Since conventional well logs are cheap and available for almost all wells, many researchers are interested in extracting petrophysical, geomechanical, and geophysical properties from conventional well logs using intelligent systems (Kadkhodaie-Ilkhchi *et al*. 2009, Asoodeh and Bagheripour 2012a, 2013a; Asoodeh 2013, Bagheripour and Asoodeh 2013). A growing tendency among researchers has been emerged in recent years to utilized integrated approaches for enhancing accuracy of final prediction (Sharkey 1996, Chen and Lin 2006, Asoodeh *et al*. 2014a, b, Gholami *et al*. 2013, Asoodeh and Bagheripour 2013b). However, no optimization on individual intelligent systems has been done till now. In this study, artificial neural network (ANN) and fuzzy logic (FL) are optimized stochastically by means of hybrid genetic algorithm-pattern search (GA-PS) technique to estimate NMR log parameters. This strategy significantly enhances efficiencies of ANN and FL models. Owing to further increase in accuracy of final prediction, an alternative condition expectation (ACE) committee with GA-PS optimized FL and ANN models is constructed. This model is capable of satisfyingly improving accuracy of NMR log prediction using the concept of committee machine. Several papers have investigated performance of committee machine compared with individual intelligent systems performing alone (Asoodeh and Bagheripour 2013b, Afshar *et al*. 2014, Asoodeh and Kazemi 2013). The proposed strategy was applied in one of Iranian hydrocarbon fields with carbonate reservoir formations. A satisfying improvement was observed in accuracy of predicted NMR parameters, including free fluid porosity and permeability after three-step optimization approach.

2. METHODS

This study follows a three-step strategy for formulating conventional well logs to NMR log parameters. The first step is devoted to optimization of arti-

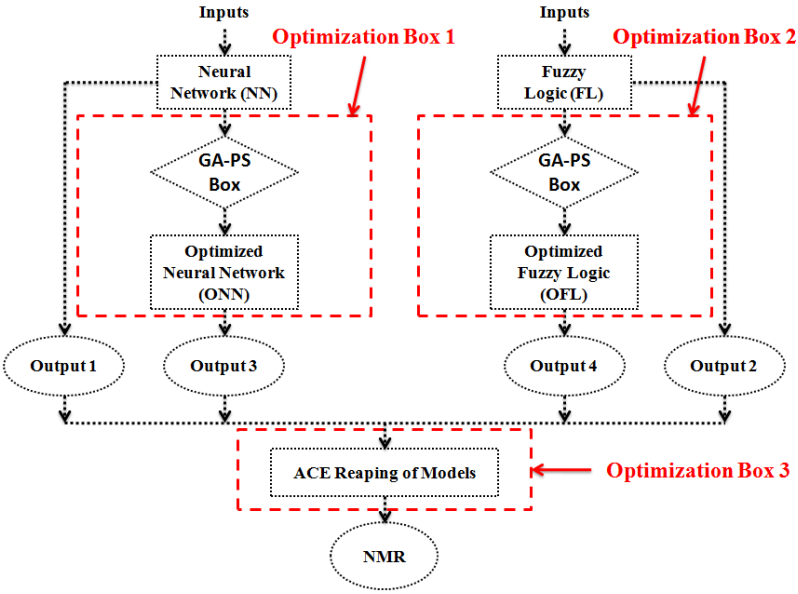

Fig. 1. General flowchart followed in this study.

ficial neural network (ANN) by means of hybrid genetic algorithm-pattern search (GA-PS) technique. Next, fuzzy logic (FL) model is optimized with GA-PS tool. Up to here, four models, including optimized FL, optimized ANN, non-optimized FL, and non-optimized ANN exist. In last stage of this study, an alternative condition expectation (ACE) committee of four models is constructed to combine their results. This step will reap benefits of all models and will enhance accuracy of final prediction. A flowchart of this study is provided in Fig. 1.

2.1 Artificial neural network

Artificial neural networks emulate the biological neural storage and analytical operations of brain through non-linear processing elements (neurons) connected by fixed (Lippmann 1987), variable (Barhen *et al*. 1989), or fuzzy (Gupta and Ding 1994) weights. Each neural network is made up of three layers (parallel arrangement of neurons): an input layer, one or more hidden layers depending on complexity of the problem, and an output layer. Back-propagation is a popular learning method for neural networks. It requires a set of input/output training data to gain knowledge from them and then applying that knowledge to new situations and problems. This method performs in a way that initial weights are randomly assigned to the neural network and its output is then calculated through random weights and biases.

Differences between neural network's outputs and desired outputs are evaluated and the obtained error is then propagated back to the neural network to adjust connection weights and biases. This process is conducted iteratively until network's output locates in close proximity of desired output.

2.2 Fuzzy logic

The basic theory of fuzzy logic was proposed by Zadeh in 1965 as an extension of traditional Boolean logic (Zadeh 1965). A fuzzy set is characterized by a membership function which assigns to each object a grade of membership ranging between zero and one (Zadeh 1965). The main part of fuzzy logic is the fuzzy inference system, which formulates inputs to an output. A fuzzy inference system consists of five major steps: fuzzification of input variables, application of fuzzy operators (AND, OR, and NOT) in the rule's antecedent, implication from the antecedent to the consequent, aggregation of consequent across the rules, and defuzzification. These steps have been discussed in a number of papers (Mohaghegh 2000c, Kadkhodaie-Ilkhchi *et al.* 2006). In the Takagi Sugeno fuzzy inference system (the most popular type of fuzzy inference system), membership functions are defined by subtractive clustering process, which divides the input-output data space into fuzzy clusters, each representing a specific part of the system behavior. Each membership function generates a set of fuzzy "if-then" rule for formulating inputs to output. The fuzzy system makes a sum of all "then" parts and uses a defuzzification method to give the final output.

2.3 Hybrid genetic algorithm-pattern search technique

Genetic algorithm is a stochastic global optimization tool which emulates the biological process of natural evolution for solving problems in widespread fields. It utilizes a specific terminology for optimization purpose, *i.e.*, the function meant to optimize is called fitness function, the probable solutions of the function are called chromosomes, involved parameters in a solution are called genes, and mathematical functions which provide a stochastic generation of new solutions are called genetic operations. Genetic algorithm starts with a population of randomly generated chromosomes and evolves toward better chromosomes by applying genetic operators. This strategy provides a stochastic search capability for genetic algorithm. Evolutionary process by use of genetic operations continues until it finds the best chromosome (or solution) in which global minimum of fitness function has been occurred. More description about genetic algorithm can be found in Mohaghegh (2000b).

In the pattern search technique, the algorithm searches a set of points, called a mesh, around the current point (the point computed at the previous

step of the algorithm). The mesh is formed by adding the current point to a scalar multiple of a set of vectors called a pattern. If the pattern search algorithm finds a point in the mesh that improves the objective function at the current point, the new point becomes the current point at the next step of the algorithm (MATLAB user's guide; Mathworks 2011).

2.4 Alternative condition expectation (ACE)

Alternating conditional expectation (ACE) is a nonparametric method, which was first established by Breiman and Friedman (1985). ACE is robust data driven technique widely utilized for identifying the complicated relationship between independent variables and response variable, especially in the situation when there are no prior assumptions of functional form for expressing relation between input/output data space. This method seeks the optimal transformations of response and a set of predictor variables, thereby the maximal multiple correlation between independent variables and the response variable is achieved. The optimal transformation is determined through minimizing the error variance between the transformed dependent variable and the sum of the transformed predicted variables. The value of error variance is minimized through employing of a series of single-function minimizations. Through iterative minimization of error variance, the optimal transformation of input and output is computed. Indeed, this method involved two operations for solving regression problems including conditional expectation and iterative minimization process. This technique gained increasing attention in both science and engineering fields due to its simplicity and its successful results in uncovering the nonlinearity relationship between dependent and independent variables (Malallah *et al*. 2006, Xue *et al*. 1996, Shokir 2007). For comprehensive study of ACE formulation principles, readers are referred to original paper of Breiman and Friedman (1985). In this study ACE is employed as nonlinear combiner to computing the contribution of different predictive models in overall prediction.

3. WHY OPTIMIZATION IS NEEDED?

3.1 For fuzzy logic

Subtracting clustering is an effective approach for determining the number of rules in Takagi Sugeno fuzzy model (Al-Jarrah and Halawani 2001), which reduces computation compared with mountain clustering (Bataineh *et al*. 2011). However, it has the flaw of being affected by constant clustering radius. It means, by use of subtractive clustering, no modification is done over spread of Gaussian membership functions and all extracted membership functions have the same variance value. Furthermore, subtractive clustering looks for cluster centers among the data points; however, the actual cluster

centers are not necessarily located at one of data points (Bagheripour and Asoodeh 2013). These shortcomings of subtractive clustering entail to propose an alternative for setting up fuzzy rules and clusters. Stochastic optimization capability of hybrid genetic algorithm-pattern search tool provides a powerful search engine which is capable of finding optimal values of cluster centers and spreads, regardless of the above-mentioned limitations of subtractive clustering.

3.2 For artificial neural network

As mentioned in Section 2.1, back-propagation algorithm is the widely-used method of determining connection weights. Performance of neural network is strongly dominated by initial weights and biases which are randomly assigned to it by back-propagation algorithm. It means, the final stage of convergence depends on where the back-propagation algorithm starts from. In other words, several runs of back-propagation algorithm with similar initial condition will converge to the same minimum. By change of the initial condition, final results of neural network might differ. Therefore, to find the optimal initial condition which leads to reaching global minimum, too many boring runs of back-propagation algorithm are needed. Nonetheless, during all these runs, neural network is highly at risk of trapping in local minima. Stochastic search capability of hybrid genetic algorithm-pattern search tool is independent of initial condition of its run. It will converge to global minimum regardless from where it starts (Conn *et al*. 1991). Therefore, the use of hybrid genetic algorithm-pattern search tool instead of back-propagation algorithm in the structure of neural network will improve the accuracy of modeling and eliminate the probability of sticking in local minima.

4. INPUTS-OUTPUTS DEPENDENCY

The first criterion in modeling by intelligent system is the quality of data. Therefore, low quality data should be removed before modeling. For this purpose, a quality control was done and bad hole intervals were removed by processing of well log data. Existence of logical relationship between inputs and outputs is another important criterion which should be kept in mind while modeling. Introducing some input parameters which have no dependency with outputs, makes the intelligent system confused and weakens the modeling. Outputs of this study are free fluid porosity and permeability. Free fluid porosity includes the pores containing fluids which are expected to flow. Permeability is defined as the capacity of a rock or sediment for fluid transmission, and is a measure of the relative ease of fluid flow under pressure gradients. Therefore, conventional well logs that have an underlying dependency with these two parameters are desired. Inputs for prediction of

free fluid porosity and permeability are the same. Because, behavioral physics of free fluid porosity and permeability are completely intertwined. Free fluid porosity increases as permeability increases and *vice versa*. Available well logs for this study were including DT, RHOB, NPHI, RT, PEF, GR, and Caliper. Caliper log was firstly used to identify bad hole intervals where standoff is higher than 1.5 inches in 8.5″ hole. Bad hole intervals were removed because they contain erroneous recordings. Photoelectric factor (PEF) is a litho-log which determines composition of reservoir rocks. NMR log is independent of lithology. Therefore, PEF was not used as input. Gamma ray (GR) is an indicator of shale content. However, in unconventional carbonate reservoirs, GR is contaminated by digenesis factors and is misleading. In this study, four conventional well logs, including sonic transit time (DT), bulk density (RHOB), neutron porosity (NPHI), and true formation resistivity (RT) were chosen as inputs. These are known appropriate in-

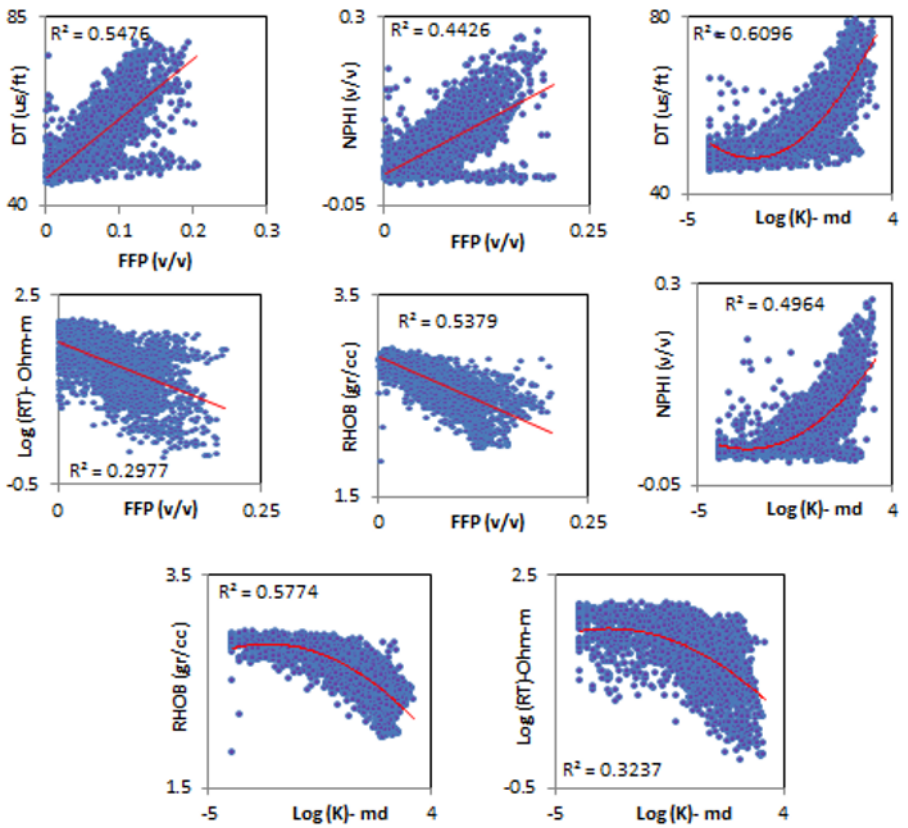

Fig. 2. Crossplots showing relationship between conventional well log data and NMR log parameters, including free fluid porosity and permeability.

put logs having logical relationship with outputs, because the first three logs are porosity logs and the last one is attributed to fluid flow pass (tortuosity) (Asoodeh and Bagheripour 2012a). Figure 2 shows the logical dependency of chosen conventional well log data and nuclear magnetic resonance log parameters using the concept of correlation coefficient. Appendix provides conversion factors from field units to SI units for permeability and sonic transit time. Conventional well logs and NMR logs which have been used for both training and testing of models are originated from Asmari formation. Asmari formation is composed of fossilifrous limestone, dolomitic limestone, argilious limestone, sandstone, and shale and constitutes the major reservoir rock for several carbonate oil fields of Iran.

5. MODELING, RESULTS, AND DISCUSSION

5.1 Optimization of artificial neural network

At the first stage, a three-layered structure of ANN was used for estimation of free fluid porosity and permeability from conventional well logs. This structure utilizes TANSIG and PURELIN transfer functions for its hidden and output neurons, correspondingly. TANSIG is mathematically equivalent to tangent hyperbolic function and PURELIN is a simple linear function of $f(x) = x$ (Asoodeh and Bagheripour 2012b). "Trainlm" training function was used for ANN to learn from training data (for more details about Trainlm refer to Hagan and Menhaj (1994)). To achieve optimal number of hidden neurons, different ANNs with different number of hidden neurons were constructed and performance of each was evaluated using mean square error function as shown in Fig. 3. Results showed that if seven and three nodes were inserted in the hidden layer of neural network for permeability and free fluid porosity, respectively, the highest performances are achieved. The constructed model was then evaluated by means of blind testing. A set of unseen well log data was used to assess performance of constructed ANN. Results showed that the correlation coefficient between predicted values using neural networks and NMR parameters was equal to 0.84 and 0.857 for permeability and free fluid porosity, respectively. Mean square error of prediction was equal to 0.73 [md^2] and 0.000501 for permeability and free fluid porosity, correspondingly. In the next stage, the neural network is optimized through the search capability of hybrid genetic algorithm-pattern search tool. This procedure is discussed in the following paragraphs.

Stochastic search capability of hybrid genetic algorithm-pattern search tool enables it to escape from local minima and converge to global minimum. This feature of hybrid genetic algorithm-pattern search tool could be employed to eliminate the flaw of neural networks which use back-propagation algorithm for finding their weights. To extract the optimum val-

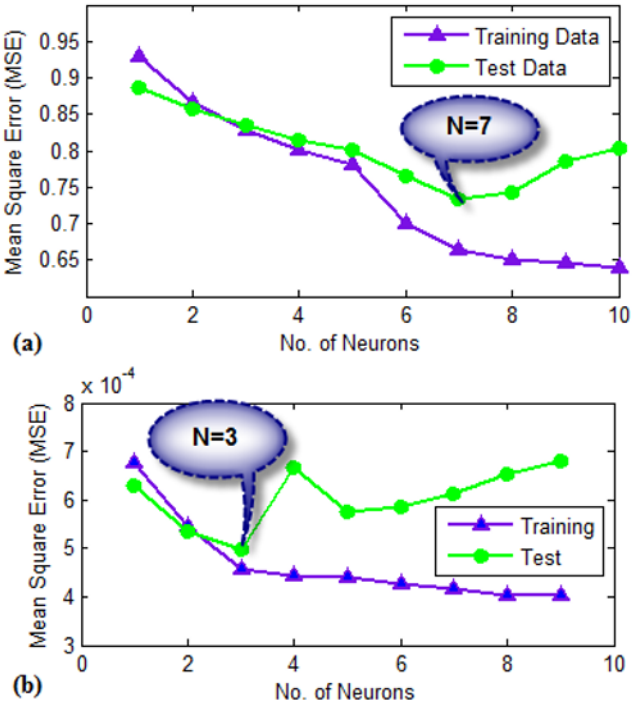

Fig. 3. Graph showing the mean square error (MSE) performance of back-propagation neural network in test data *versus* different number of nodes of hidden layer for: (a) permeability, and (b) free fluid porosity. Optimal models are achieved when 3 and 7 nodes are inserted in hidden layer of neural network for free fluid porosity and permeability, respectively.

ues of ANN's weights, the following mean square error function was introduced into hybrid genetic algorithm-pattern search tool:

$$MSE_{ONN} = \frac{1}{K}\sum_{\ell=1}^{k}\left(Output_{NMR\ell} - Output_{ONN\ell}\right)^2 , \qquad (1)$$

where O_{estNN} is ANN output. $Output_{ONN}$ is estimated values of nuclear magnetic resonance (NMR) log parameters from optimized neural network, $Output_{NMR}$ is the NMR log parameter, MSE_{ONN} is the mean square error function of optimized neural network, and k is the number of training data. The process of producing an output from neural network is discussed by Asoodeh and Bagheripour (2013c). Hybrid genetic algorithm-pattern search technique looks for optimum values of connection weights of ANN such that Eq. 1 converges to its global minimum. Blue lines of Fig. 4 indicate mean value of mean square error (MSE) for a population of chromosomes (solutions) dur-

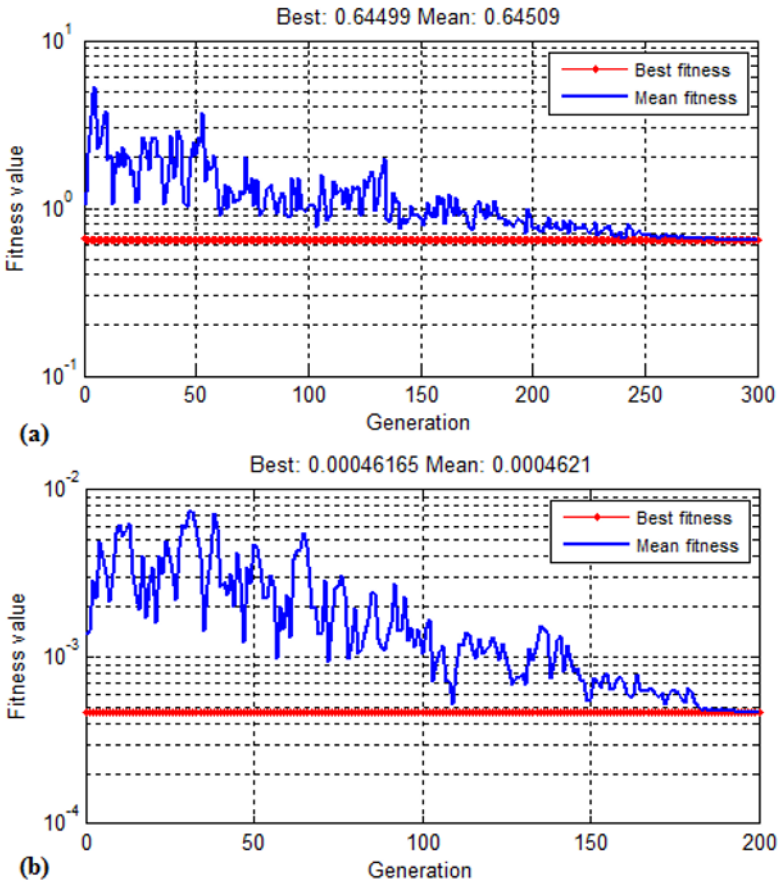

Fig. 4. Run of hybrid genetic algorithm-pattern search tool for stochastic optimization of neural network. This plot shows the best and mean fitness values of fitness functions after 300 generations for: (a) permeability and (b) free fluid porosity.

ing 300 generations for permeability model and 200 generations for free fluid porosity (FFP) models. The red lines in Fig. 4 show mean square error corresponding to best chromosomes. After stochastic optimization of neural network, performances of optimized models were evaluated by test data, *i.e.*, test data were introduced to optimized model and quality of estimation was assessed. Figure 5 indicates error distributions for optimized and non-optimized neural network models. It is obvious that stochastic optimization of neural networks led mean of error distributions to approach zero and standard deviation of error distributions to decrease. Furthermore, correlation coefficient of prediction has improved after stochastic optimization of neural networks.

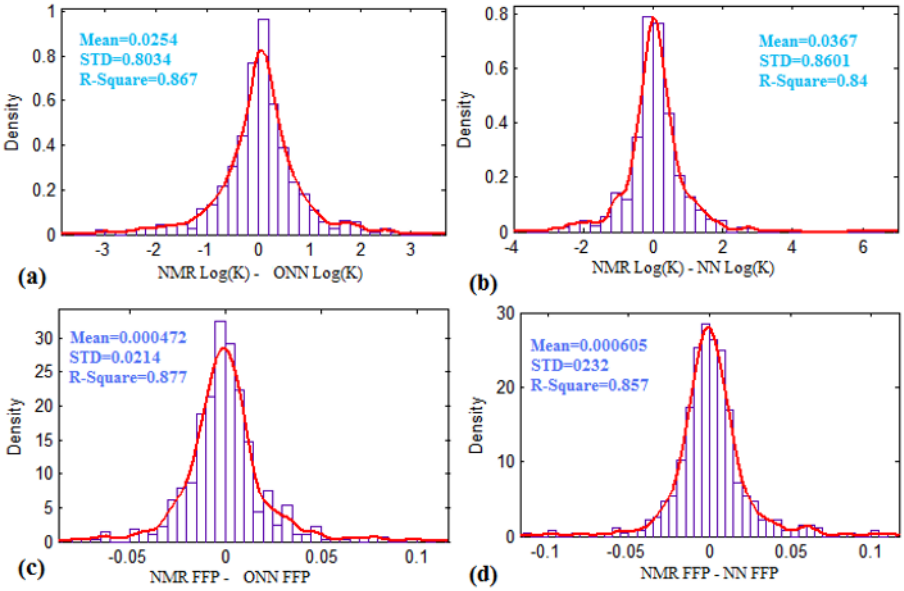

Fig. 5. Error distribution of: (a) optimized neural network for permeability, (b) non-optimized neural network for permeability, (c) optimized neural network for free fluid porosity, and (d) non-optimized neural network for free fluid porosity. In optimized models, the mean of error distributions approach zero and their standard deviation decrease. It means, optimized models performed better than non-optimized models.

5.2 Optimization of fuzzy logic

The next stage of this study was initiated with construction of fuzzy model for estimation of nuclear magnetic resonance (NMR) log parameters, including free fluid porosity and permeability from conventional well log data. To find optimum fuzzy model which best describes quantitative formulation between inputs and outputs, several fuzzy inference systems with various values of clustering radius were constructed. Fuzzy inference systems which have the lowest mean square error for the test data were chosen as optimal ones. Figure 6 indicates variations of mean square error for test and training data in conjugation with variation of number of rules for different clustering radii. This figure indicates fuzzy inference systems with clustering radii of 0.6 and 0.9 for permeability and free fluid porosity, respectively, can extract the best quantitative relationship between inputs and outputs. Furthermore, this figure shows that four and two linguistic rules can in turn handle the relationship between inputs and outputs for permeability and free fluid porosity models. Figure 7 shows the extracted Gaussian membership functions

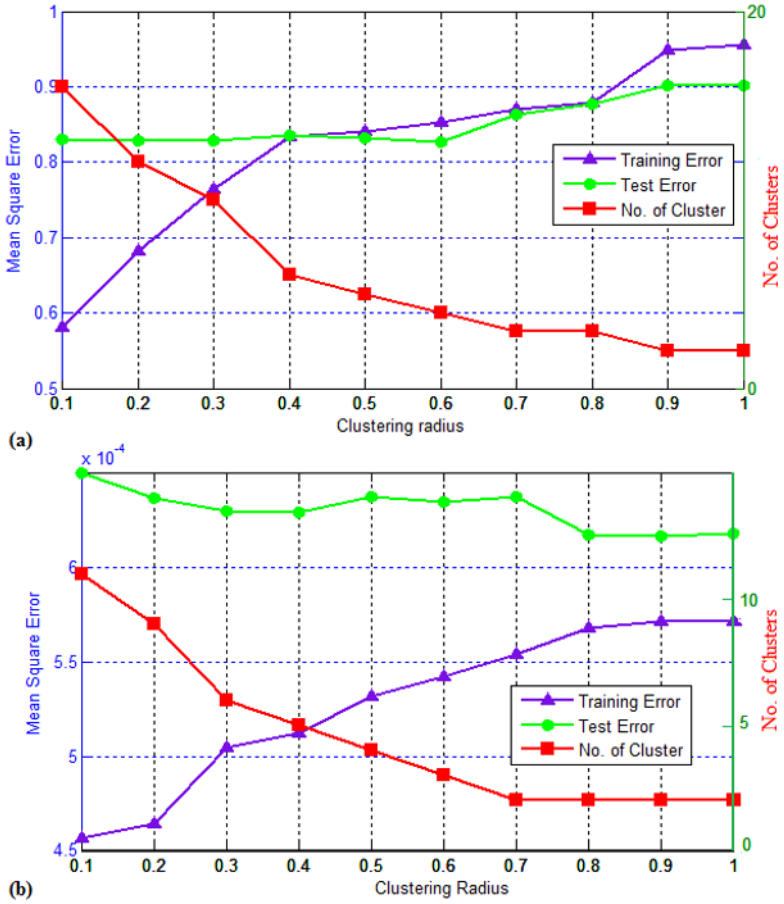

Fig. 6. Graphs showing the mean square error (MSE) performance of Takagi-Sugeno fuzzy inference system (TS-FIS) in test and training data in conjugation with number of rules *versus* clustering radius for: (a) permeability, and (b) free fluid porosity. Optimal models are achieved when 0.6 and 0.9 are chosen for clustering radius of permeability and free fluid porosity models, respectively.

corresponding to aforementioned linguistic rules. As this figure shows, the subtractive clustering implies no optimization over variances (spreads) of fuzzy clusters corresponding to each input. This flaw is eliminated in next step. Evaluating with test data, the results showed that correlation coefficient between fuzzy logic predicted free fluid porosity and NMR values was equal to 0.852. This value for permeability was equal to 0.845. Mean square errors of fuzzy logic predictions are equal to 0.000521 and 0.7201 [md^2] for free fluid porosity and permeability, correspondingly.

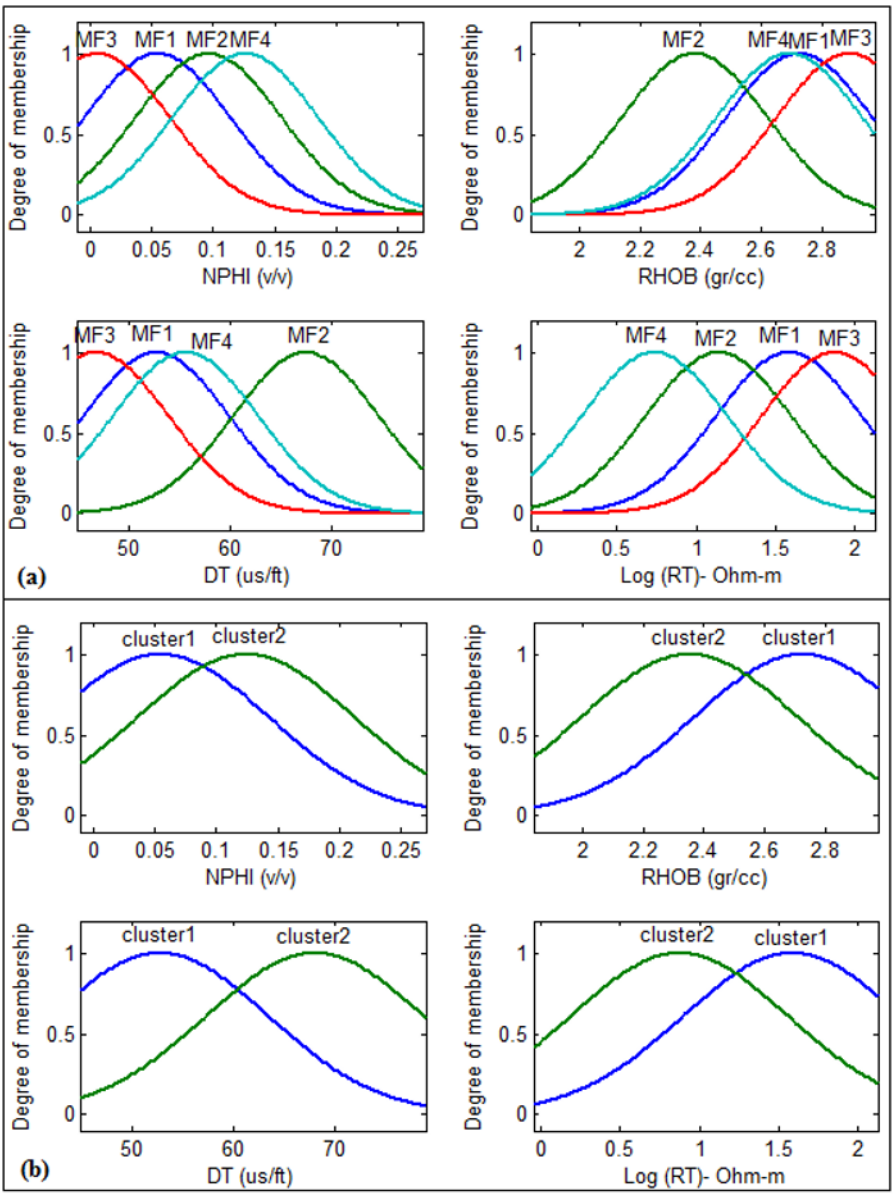

Fig. 7. TS-FIS generated Gaussian membership functions (fuzzy clusters) for the inputs of model meant to predict: (a) permeability, and (b) free fluid porosity.

Since conventional well log data, which constitute input data space, cover various ranges of data, all inputs were normalized to improve the performance of search capability of hybrid genetic algorithm-pattern search tool

for optimizing fuzzy logic model. Since this type of normalization does not destroy the consistency of input data, shape of membership functions will just be scaled and normalization would not have any effect in the overall shape of membership functions. Similar to ANN, a mean square error (MSE) function was used as fitness function of hybrid genetic algorithm-pattern search to find optimal membership functions such that MSE function reaches its global minimum. Stochastic search capability of hybrid genetic algorithm-pattern search tool makes it possible to optimize both mean and variance (spread) of input Gaussian membership functions along with optimization of output linear membership functions. Figure 8 shows results of hybrid genetic algorithm-pattern search runs for permeability and free fluid porosity. Extracted fuzzy Gaussian membership functions are illustrated in Fig. 9. A comparison between Figs. 7 and 9 shows that the proposed

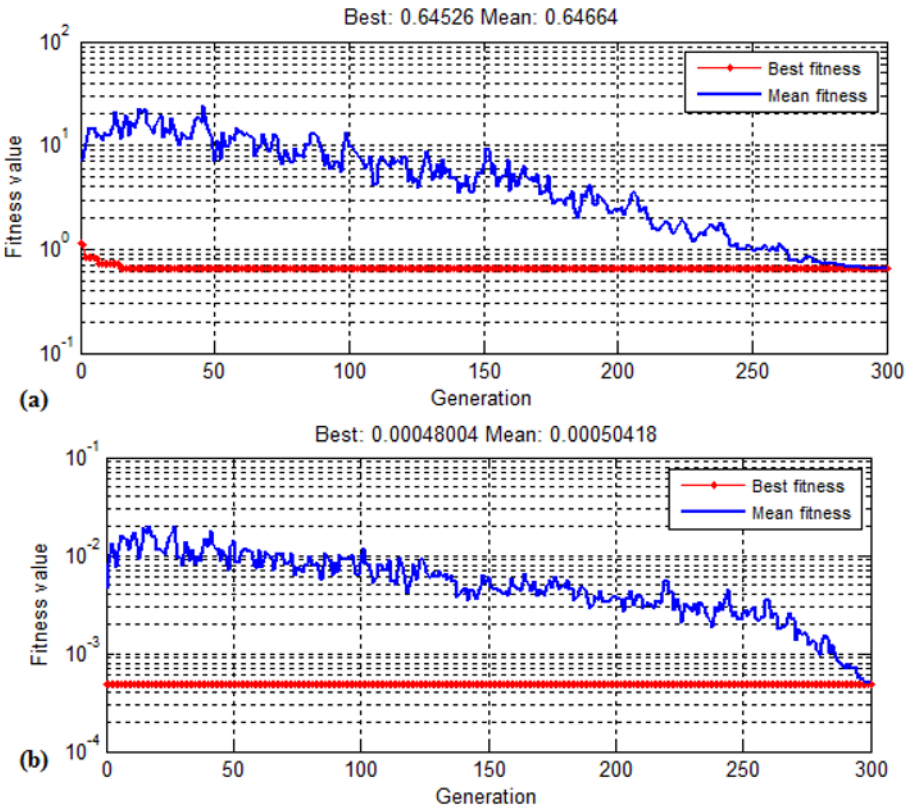

Fig. 8. Run of hybrid genetic algorithm-pattern search tool for stochastic optimization of fuzzy logic. This plot shows the best and mean fitness values of fitness functions after 300 generations for: (a) permeability, and (b) free fluid porosity.

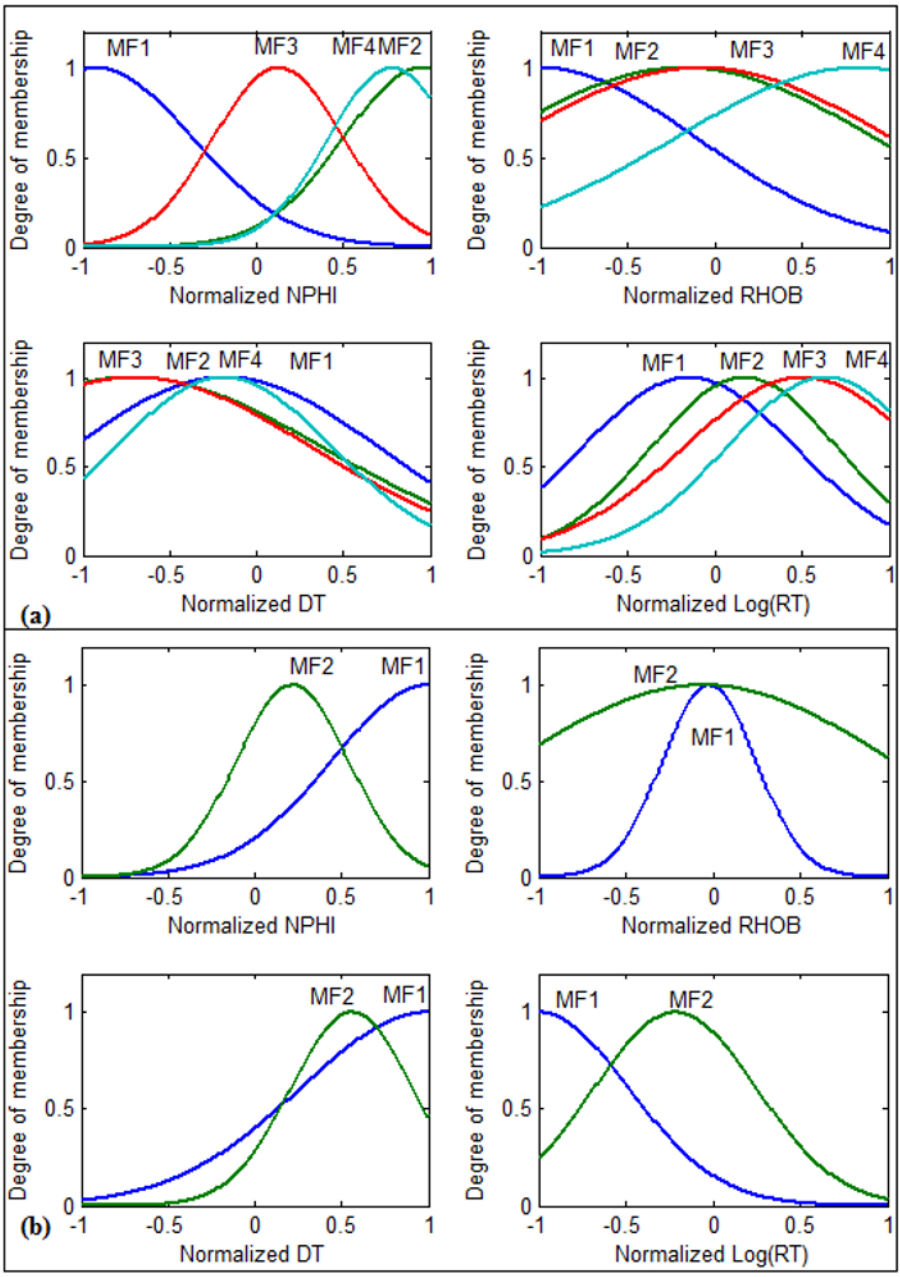

Fig. 9. Stochastically generated Gaussian membership functions (fuzzy clusters) for the inputs of model meant to predict: (a) permeability, and (b) free fluid porosity.

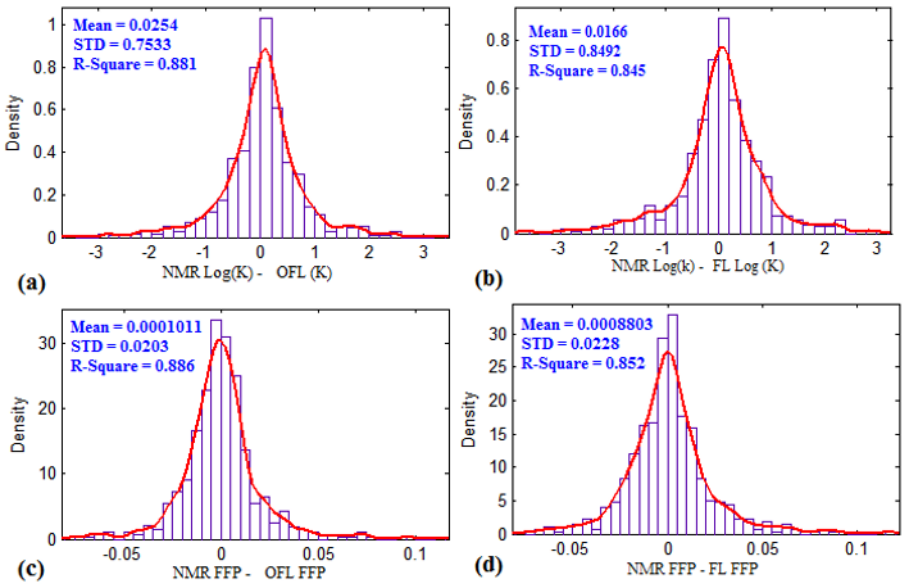

Fig. 10. Error distribution of: (a) optimized fuzzy model for permeability, (b) non-optimized fuzzy model for permeability, (c) optimized fuzzy model for free fluid porosity, and (d) non-optimized fuzzy model for free fluid porosity. In optimized models, mean of error distributions approach to zero and their standard deviation decrease. It means, optimized models performed better than non-optimized models.

model was capable of optimizing variances (spreads) of Gaussian membership function in addition to optimizing mean of Gaussian membership functions. Figure 10 illustrates error distributions of optimized and non-optimized fuzzy logic models. It is obvious that stochastic optimization of fuzzy logic models has reduced the absolute mean and standard deviation of error distributions. Furthermore, correlation coefficient of prediction improved after stochastic optimization of fuzzy logic models.

5.3 ACE committee of models

As mentioned previously, ACE is employed as a combiner to integrate outputs of different models and consequently reaping their benefits through constructing a more accurate model for estimating free fluid porosity and permeability. For this purpose, ACE transfers input parameters and target values into a desired space where maximum correlation exists between them. Thus, outputs of predictive models, including fuzzy logic, optimized fuzzy logic, neural network, and optimized neural network are employed as inputs of ACE and free fluid porosity and permeability are considered as ACE out-

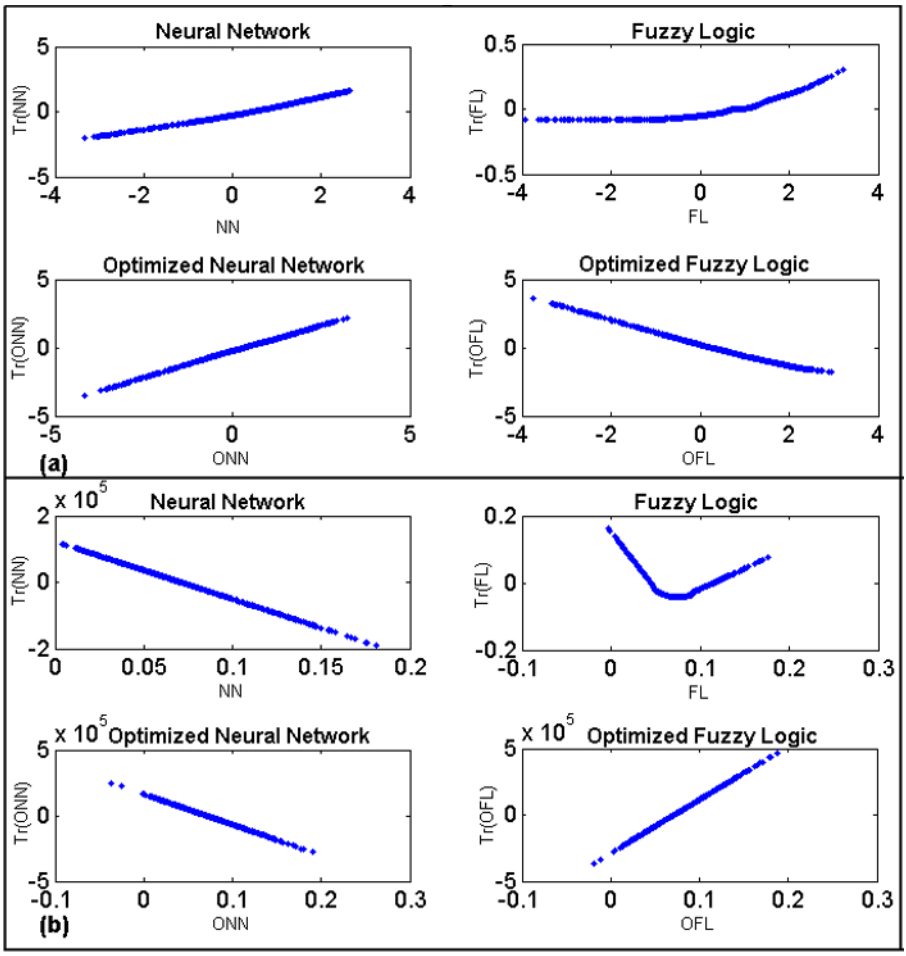

Fig. 11. Optimal transformation of input parameters which determined by ACE for: (a) permeability, and (b) free fluid porosity.

puts. Figure 11 demonstrates ACE extracted optimal transformation of input parameters for free fluid porosity and permeability, respectively. Although ACE algorithm approximates optimal transformations of input/output data space, it does not present a computational model for relating parameters and their optimal transformations. Hence, a simple polynomial function is fitted for making formulation between the parameters and their optimal transformations. The resulting polynomial functions with associated parameters for transforming neural network, optimized neural network, fuzzy logic, and optimized fuzzy logic are shown in Eqs. 2-9.

(a) Transformations for permeability modeling

$$\varphi^*(NN) = a_2(NN)^2 + a_1(NN) + a_0 \ , \tag{2}$$

where $a_2 = 0.034882108437520$, $a_1 = 0.0626864203614067$, and $a_0 = -0.28077401469906$.

$$\varphi^*(FL) = a_3(FL)^3 + a_2(FL)^2 + a_1(FL) + a_0 \ , \tag{3}$$

where $a_3 = 0.001772160478232$, $a_2 = 0.016384002242114$, $a_1 = 0.042023493356332$, and $a_0 = -0.050567771173985$.

$$\varphi^*(ONN) = a_1(ONN) + a_0 \ , \tag{4}$$

where $a_1 = 0.\ 756690942653011$, and $a_0 = -0.263928319591898$.

$$\varphi^*(OFL) = a_3(OFL)^3 + a_2(OFL)^2 + a_1(OFL) + a_0 \ , \tag{5}$$

where $a_3 = 0.007540599087205$, $a_2 = 0.034647276929447$, $a_1 = -0.871553938494339$, and $a_0 = 0.211074313346156$.

(b) Transformations for FFP modeling

$$\varphi^*(NN) = a_1(NN) + a_0 \ , \tag{6}$$

where $a_1 = -1735498.432421821$, and $a_0 = 122908.214346089$.

$$\varphi^*(FL) = a_4(FL)^4 + a_3(FL)^3 + a_2(FL)^2 + a_1(FL) + a_0 \ , \tag{7}$$

where $a_4 = -1179.828742552175$, $a_3 = 244.364360922208$, $a_2 = 18.984460901200$, $a_1 = -5.166180545100$, and $a_0 = -0.050567771173985$.

$$\varphi^*(ONN) = a_1(ONN) + a_0 \ , \tag{8}$$

where $a_1 = -2324155.414675274$, and $a_0 = 163629.816053569$.

$$\varphi^*(OFL) = a_1(OFL) + a_0 \ , \tag{9}$$

where $a_1 = 4013501.320037709$, and $a_0 = -286489.622011131$.

Summations of optimal transformation of input parameters are as follows:

$$\varphi^*(Log(K)) = \varphi^*(NN) + \varphi^*(FL) + \varphi^*(ONN) + \varphi^*(OFL) \ , \tag{10}$$

$$\varphi^*(FFP) = \varphi^*(NN) + \varphi^*(FL) + \varphi^*(ONN) + \varphi^*(OFL) \ . \tag{11}$$

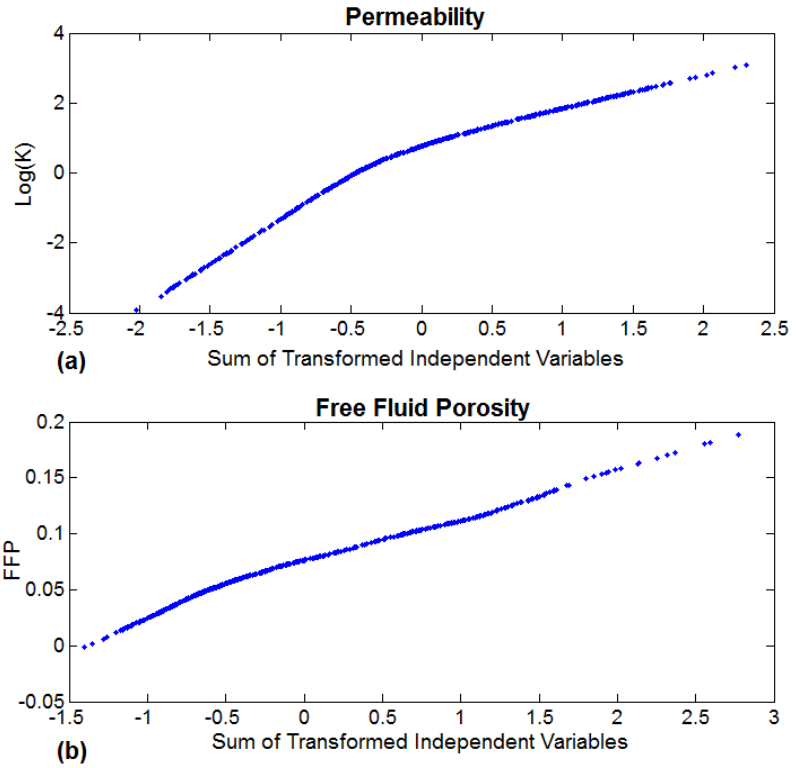

Fig. 12. Relation between sum of transformed independent variables and: (a) permeability, and (b) free fluid porosity determined by ACE.

Figure 12 shows the relationship between permeability and free fluid porosity and sum of optimal transformation of input parameters. A simple curve fitting can result in permeability and free fluid porosity through following equations.

$$Log(K) = a_3\left(\varphi^*(Log(K))\right)^3 + a_2\left(\varphi^*(Log(K))\right)^2 + a_1\left(\varphi^*(Log(K))\right) + a_0 \quad , \quad (12)$$

where $a_3 = 0.070938496352028$, $a_2 = -0.380116311467027$, $a_1 = 1.466278287151171$, and $a_0 = 0.727440481067394$.

$$FFP = a_3\left(\varphi^*(FFP)\right)^3 + a_2\left(\varphi^*(FFP)\right)^2 + a_1\left(\varphi^*(FFP)\right) + a_0 \quad , \quad (13)$$

where $a_3 = 0.003322744745387$, $a_2 = -0.007556364428498$, $a_1 = 0.040164861128829$, and $a_0 = 0.076864737700259$.

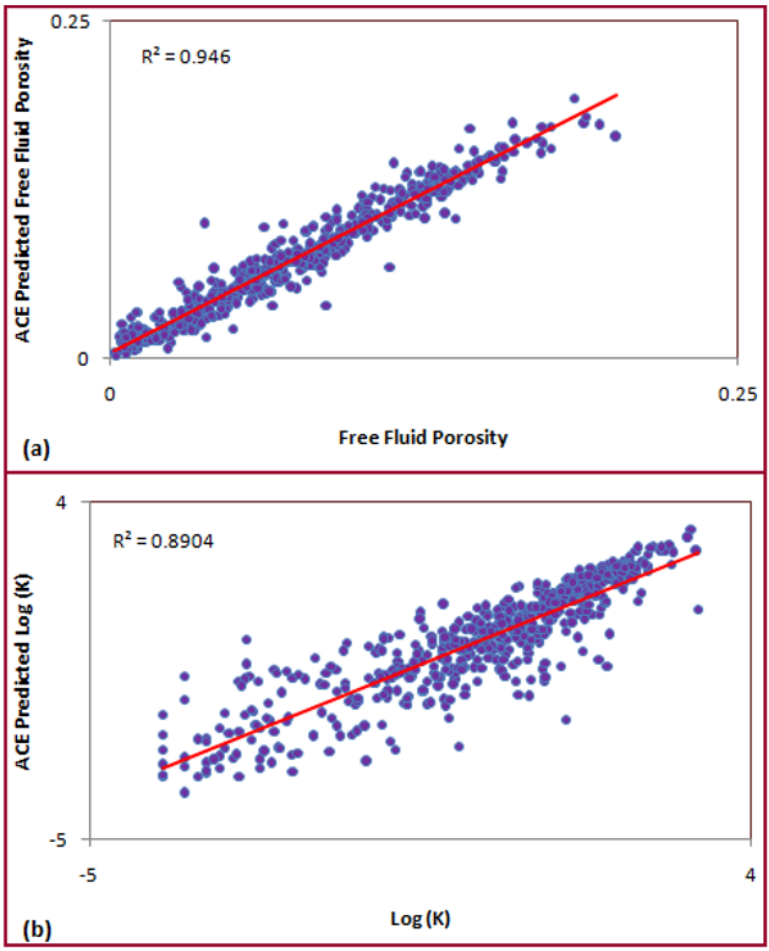

Fig. 13. Crossplots showing correlation coefficient between measured and predicted: (a) free fluid porosity, and (b) log (K).

After developing above formulation through the use of ACE method, performance of constructed model was assessed by means of test data. Figure 13 shows correlation coefficient between measured and predicted NMR parameters. This figure shows that the ACE model was capable of producing high accuracy results. For better illustration, results of ACE models are compared with individual models *viz*. neural network, fuzzy logic, optimized neural network, and optimized fuzzy logic in term of correlation coefficient and mean square error (Fig. 14). This figure shows that ACE is a good alternative for combining different models in order to enhance accuracy of final prediction.

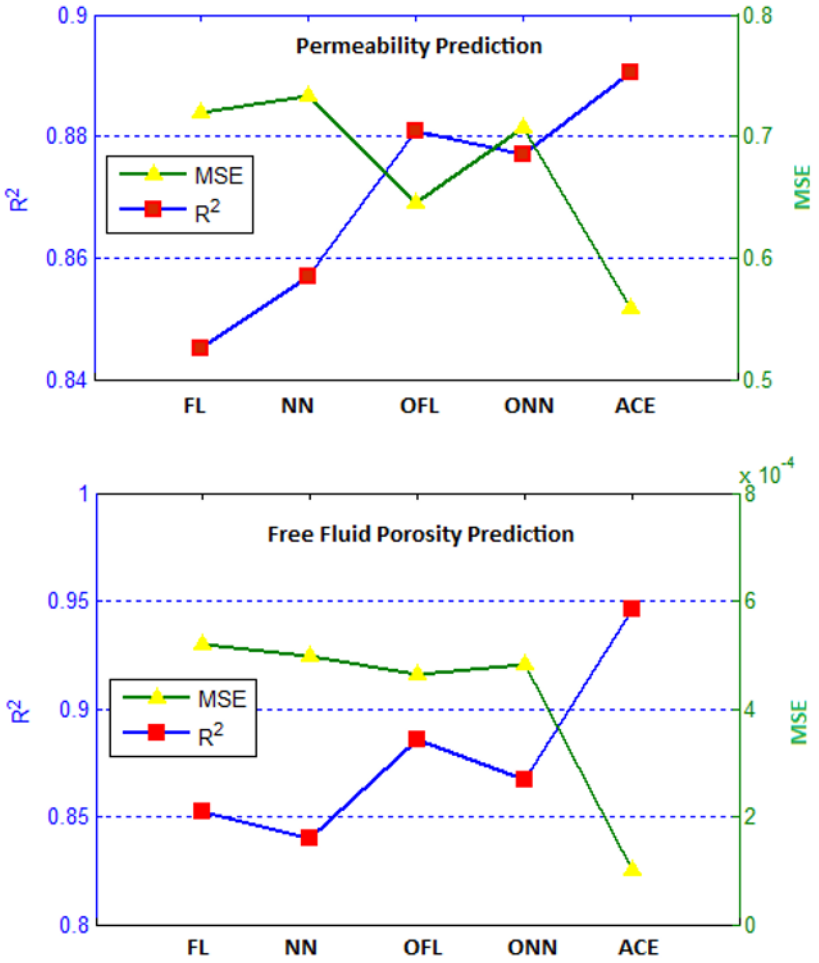

Fig. 14. A comparison between different models *versus* correlation coefficient and mean square error.

6. CONCLUSIONS

In this study, a stochastic optimization tool, called hybrid genetic algorithm-pattern search, was employed to strengthen fuzzy logic and artificial neural network. Strengthened models were then used to estimate nuclear magnetic resonance (NMR) log parameters, including free fluid porosity and rock permeability. At the final step of this study, an ACE committee with optimized and non-optimized models was constructed. Some noticeable points deduced from this study can be expressed as follows:

- In spite of complex behavior of carbonate reservoirs, neural network and fuzzy logic are able to extract the formulation between conventional well log data and NMR log parameters, including free fluid porosity and permeability.
- Performance of back-propagation neural network is greatly dominated by initial weights and biases which are randomly assigned to the neural network. Furthermore, the back-propagation algorithm is highly at risk of trapping in local minima.
- Fuzzy clustering is strongly governed by heterogeneity of training data. This flaw might result in non-smooth multi-dimensional formulation. Therefore, need of comprehensive training database is inevitable.
- Subtractive clustering has just some control on means of Gaussian membership functions, *i.e.*, no modification on variances (spread) of membership functions is done by it.
- Hybrid genetic algorithm-pattern search as a global optimization tool provides a stochastic search capability which is not affected by initial condition of algorithm run. It converges to global minimum regardless from where it starts.
- Extracting optimal weights and biases of neural network through the use of stochastic search of hybrid genetic algorithm-pattern search tool is more confident and efficient than the use of back-propagation algorithm.
- By extracting fuzzy formulation through the use hybrid genetic algorithm-pattern search tool, it is possible to have a control on both means and variances (spread) of Gaussian membership functions.
- Stochastically optimized fuzzy logic and neural network performed better than non-optimized ones.
- Convergence speed of hybrid genetic algorithm-pattern search is low. Substituting faster algorithms for future works are suggested.
- ACE committee machine with optimized and non-optimized models can significantly enhance accuracy of final prediction.
- In situations where there are multiple choices to solve a problem, by little additional computation it is possible to construct an ACE committee machine to improve precision of prediction.
- Implementation of the propounded strategy provides an accurate, quick and cost-effective way of estimating NMR log parameters, including free fluid porosity and rock permeability from conventional well log data for wells that have no NMR run.

Appendix

Conversion factors for transferring permeability and sonic transit time units from field units to SI units

Parameter	Conversion factor	
	Field units	SI units
Permeability	mili-darcy [md]	$= 9.86923\times10^{-4}$ μm^2
Sonic transit time	microsecond per foot [μs/ft]	$= 3.289474\times10^{-6}$ s/m

References

Afshar, M., A. Gholami, and M. Asoodeh (2014), Genetic optimization of neural network and fuzzy logic for oil bubble point pressure modeling, *Korean J. Chem. Eng.* **31**, 3, 496-502, DOI: 10.1007/s11814-013-0248-8.

Al-Jarrah, O.M., and A. Halawani (2001), Recognition of gestures in Arabic sign language using neuro-fuzzy systems, *Artif. Intell.* **133**, 1-2, 117-138, DOI: 10.1016/S0004-3702(01)00141-2.

Asoodeh, M. (2013), Prediction of Poisson's ratio from conventional well log data: A committee machine with intelligent systems approach, *Energ. Source. A* **35**, 10, 962-975, DOI: 10.1080/15567036.2011.557693.

Asoodeh, M., and P. Bagheripour (2012a), Prediction of compressional, shear, and stoneley wave velocities from conventional well log data using a committee machine with intelligent systems, *Rock Mech. Rock Eng.* **45**, 1, 45-63, DOI: 10.1007/s00603-011-0181-2.

Asoodeh, M., and P. Bagheripour (2012b), Estimation of bubble point pressure from PVT data using a power-law committee with intelligent systems, *J. Petrol. Sci. Eng.* **90-91**, 1-11, DOI: 10.1016/j.petrol.2012.04.021.

Asoodeh, M., and P. Bagheripour (2013a), Core porosity estimation through different training approaches for neural network: Back-propagation learning vs. genetic algorithm, *Int. J. Comput. Appl.* **63**, 5, 11-15, DOI: 10.5120/10461-5172.

Asoodeh, M., and P. Bagheripour (2013b), Fuzzy classifier based support vector regression framework for Poisson ratio determination, *J. Appl. Geophys.* **96**, 7-10, DOI: 10.1016/j.jappgeo.2013.06.006.

Asoodeh, M., and P. Bagheripour (2013c), Neuro-fuzzy reaping of shear wave velocity correlations derived by hybrid genetic algorithm-pattern search technique, *Cent. Eur. J. Geosci*. **5**, 2, 272-284, DOI: 10.2478/s13533-012-0129-4.

Asoodeh, M., and K. Kazemi (2013), Estimation of bubble point pressure: Using a genetic integration of empirical formulas, *Energ. Source. A* **35**, 12, 1102-1109, DOI: 10.1080/15567036.2011.574195.

Asoodeh, M., A. Gholami, and P. Bagheripour (2014a), Oil-CO_2 MMP determination in competition of neural network, support vector regression, and committee machine, *J. Disper. Sci. Technol*. **35**, 4, 564-571, DOI: 10.1080/01932691. 2013.803255.

Asoodeh, M., A. Gholami, and P. Bagheripour (2014b), Asphaltene precipitation of titration data modeling through committee machine with stochastically optimized fuzzy logic and optimized neural network, *Fluid Phase Equilibr*. **364**, 67-74, DOI: 10.1016/j.fluid.2013.12.016.

Bagheripour, P., and M. Asoodeh (2013), Fuzzy ruling between core porosity and petrophysical logs: Subtractive clustering vs. genetic algorithm-pattern search, *J. Appl. Geophys.* **99**, 35-41, DOI: 10.1016/j.jappgeo.2013.09.014.

Barhen, J., M. Zak, and S. Gulati (1989), Fast neural learning algorithms using networks with non-Lipschitizian dynamics. **In:** J.C. Rault (ed.), *Proceedings of Neuro-Nimes '89*, EC2 Press, Paris, 55-68.

Bataineh, K.M., M. Naji, and M. Saqer (2011), A comparison study between various fuzzy clustering algorithms, *Jordan J. Mech. Ind. Eng.* **5**, 4, 335-343.

Breiman, L., and J.H. Friedman (1985), Estimating optimal transformations for multiple regression and correlation*, J. Am. Stat. Assoc.* **80**, 391, 580-598, DOI: 10.1080/01621459.1985.10478157.

Chen, C.H., and Z.S. Lin (2006), A committee machine with empirical formulas for permeability prediction, *Comput. Geosci*. **32**, 4, 485-496, DOI: 10.1016/ j.cageo.2005.08.003.

Conn, A.R., N.I.M. Gould, and P. Toint (1991), A globally convergent augmented Lagrangian algorithm for optimization with general constraints and simple bounds, *SIAM J. Numer. Anal.* **28**, 2, 545-572, DOI: 10.1137/0728030.

Gholami, A., S. Moradi, and B. Dabir (2013), A power law committee scaling equation for quantitative estimation of asphaltene precipitation, *Int. J. Sci. Emerging Technol*. **6**, 5, 275-283.

Gupta, M.M., and H. Ding (1994), Foundations of fuzzy neural computations. **In:** F. Aminzadeh and M. Jamshidi (eds.), *Soft Computing: Fuzzy Logic, Neural Networks, and Distributed Artificial Intelligence*, Prentice Hall Inc., Upper Saddle River, 165-199.

Hagan, M.T., and M.B. Menhaj (1994), Training feedforward networks with the Marquardt algorithm, *IEEE Trans. Neural Netw.* **5**, 6, 989-993, DOI: 10.1109/72.329697.

Kadkhodaie-Ilkhchi, A., M.R. Rezaee, and S.A. Moallemi (2006), A fuzzy logic approach for the estimation of permeability and rock type from conventional well log data: An example from the Kangan reservoir in the Iran offshore gas field, *J. Geophys. Eng.* **3**, 4, 356-369, DOI: 10.1088/1742-2132/3/4/007.

Kadkhodaie-Ilkhchi, A., H. Rahimpour-Bonab, and M.R. Rezaee (2009), A committee machine with intelligent systems for estimation of total organic carbon content from petrophysical data: An example from Kangan and Dalan reservoirs in South Pars gas field, Iran, *Comput. Geosci.* **35**, 3, 459-474, DOI: 10.1016/j.cageo.2007.12.007.

Labani, M.M., A. Kadkhodaie-Ilkhchi, and K. Salahshoor (2010), Estimation of NMR log parameters from conventional well log data using a committee machine with intelligent systems: A case study from the Iranian part of the South Pars gas field, Persian Gulf Basin, *J. Petrol. Sci. Eng.* **72**, 1-2, 175-185, DOI: 10.1016/j.petrol.2010.03.015.

Lippmann, R.P. (1987), An introduction to computing with neural nets, *ASSP Mag. IEEE* **4**, 2, 4-22, DOI: 10.1109/MASSP.1987.1165576.

Malallah, A., R. Gharbi, and M. Algharaib (2006), Accurate estimation of the world crude oil PVT properties using graphical alternating conditional expectation, *Energy Fuels* **20**, 2, 688-698, DOI: 10.1021/ef0501750.

Malki, H.A., and J. Baldwin (2002), A neuro-fuzzy based oil/gas producibility estimation method. **In:** *Proc. Int. Jt. Conf. Neural Networks IJCNN 2002, Vol. 1, 12-17 May 2002, Honolulu, USA*, 896-901, DOI: 10.1109/IJCNN.2002.1005593.

Mathworks (2011), MATLAB user's guide. Fuzzy logic, neural network & GA and direct search toolboxes, Mathworks, Inc., CD-rom.

Mohaghegh, S. (2000a), Virtual-intelligence applications in petroleum engineering: Part 1 – Artificial neural networks, *J. Petrol. Technol.* **52**, 9, 64-73, DOI: 10.2118/58046-JPT.

Mohaghegh, S. (2000b), Virtual-intelligence applications in petroleum engineering: Part 2 – Evolutionary computing, *J. Petrol. Technol.* **52**, 10, 40-46, DOI: 10.2118/61925-JPT.

Mohaghegh, S. (2000c), Virtual-intelligence applications in petroleum engineering: Part 3 – Fuzzy logic, *J. Petrol. Technol.* **52**, 11, 82-87, DOI: 10.2118/62415-JPT.

Ogilvie, S.R., S. Cuddy, C. Lindsay, and A. Hurst (2002), Novel methods of permeability prediction from NMR tool data, Dialog, London Petrophysical Society, London, 1-14.

Sharkey, A.J.C. (1996), On combining artificial neural nets, *Connect. Sci.* **8**, 3-4, 299-314, DOI: 10.1080/095400996116785.

Shokir, E.M. (2007), CO_2-oil minimum miscibility pressure model for impure and pure CO_2 streams, *J. Petrol. Sci. Eng.* **58**, 1-2, 173-185, DOI: 10.1016/j.petrol.2006.12.001.

Xue, G., A. Datta-Gupta, P. Valko, and T. Blasingame (1996), Optimal transformations for multiple regression: application to permeability estimation from well logs, Paper No. SPE-35412, Society of Petroleum Engineers, Inc., Richardson, USA.

Zadeh, L.A. (1965), Fuzzy sets, *Inf. Control*. **8**, 3, 338-353, DOI: 10.1016/S0019-9958(65)90241-X.

Received 2 February 2014
Received in revised form 5 April 2014
Accepted 9 May 2014

DE GRUYTER OPEN

Acta Geophysica
vol. 63, no. 3, June 2015, pp. 761-775
DOI: 10.1515/acgeo-2015-0010

An Amplitude-normalized Pseudo Well-log Construction Method and its Application on AVO Inversion in a Well-absent Marine Area

Chunyan FAN[1], Yan SONG[1], Yuanyin ZHANG[1,2], and Zhenxue JIANG[1]

[1]China University of Petroleum – Beijing, Beijing, China

[2]Petroleum Exploration & Production Research Institute, SINOPEC, Beijing, China
e-mail: yuanyinshou@163.com (corresponding author)

A b s t r a c t

AVO inversion is hard to be efficiently applied in unexploited fields due to the insufficiency of well information. For the sake of AVO inversion in a well-absent area, the most conventional method is to construct pseudo well-logs by defining seismic processing velocity as the *P*-velocity and computing *S*-velocity and density using empirical formulas, yet the resolution of the corresponding earth models and final inverted results could be extremely low, and a rough formula could destroy the inversion thoroughly. To overcome this problem, an amplitude-normalized pseudo well-log construction method that reconstructs pseudo well-logs in accordance with computed *P*-wave reflection amplitudes and nearby drilling data is proposed in this paper. It enhances the inversion resolution efficiently with respect to the real elastic parameter relationships, so that the corresponding AVO inversion results are reasonably improved. In summary, the proposed method is successfully applied in the AVO inversion of a well-absent marine area, and could be valuable in the early phase, particularly of the offshore hydrocarbon exploration.

Key words: well-absent pre-stack seismic AVO inversion, marine exploration, reservoir appraisal, pseudo well-logs reconstruction.

1. INTRODUCTION

The pre-stack seismic AVO inversion is better for reservoir prediction than post-stack methods owing to its preservation of the AVO information and more elastic parameters (Connolly 1999, Zhang *et al.* 2011b), but it cannot be efficiently conducted if the well information is insufficient to accurately scale the wavelets and build constrained elastic models. Because the constrained models essentially represent initial predictions to construct inversion, and can lead to a better resolvability and link between the seismic data and the actual lithology (*e.g.*, from logging data and geological mapping), the inversion result of predicted sediment properties is actually a set of elastic volumes that deviate as little as possible from the initial predictions, while at the same time they are modeling the real geology as closely as possible (Hampson *et al.* 2001, 2005).

For a convenient application of AVO inversion method in a well-absent area, the most conventional way is to construct some pseudo well-logs by defining interval velocities obtained from 3D seismic processing stage, initially as the *P*-velocities, and then compute *S*-velocities and densities using empirical formulas. However, by this method the resolutions of corresponding earth models and final results directly inverted from seismic processing velocities could be extremely low, and using a rough formula for elastic parameters prediction could further destroy the inversion (Zhang *et al.* 2011b, Fan *et al*. 2013).

In this paper, in order to increase the resolution of well-absent AVO inversion results and hence retrieve reliable elastic parameters for reservoir description, we propose a new pseudo well-log construction method and apply it in an undrilled marine study area, where quite promising but not well-studied reef and turbidity sand reservoirs need to be appraised for further exploration.

2. GEOLOGICAL SETTING AND DATA SETS

As shown in Fig. 1, the study field is located in the northwestern segment of South China Sea. It lies offshore southern Hainan trending northwest-southeast with an areal extent of around 200 km^2; the nearest drilling site is about 60 km away from the study area, marked as well Y-1 on the index map. The water depth gradually increases from 1.2 s (around 600 m) in the northwest to 1.6 s (around 800 m) in the southeast, whereas a seabed pit can be distinctly seen in the southern segment.

The pre- and post-stack 3D seismic data quality is quite good for seismic stratigraphic interpretation and AVO analysis. The bin size of CMP gathers is 12.5×25 m, with a full fold of 140. As shown in Fig. 2, the seismic traces are characterized by a frequency content from 8 to 75 Hz with the predomi-

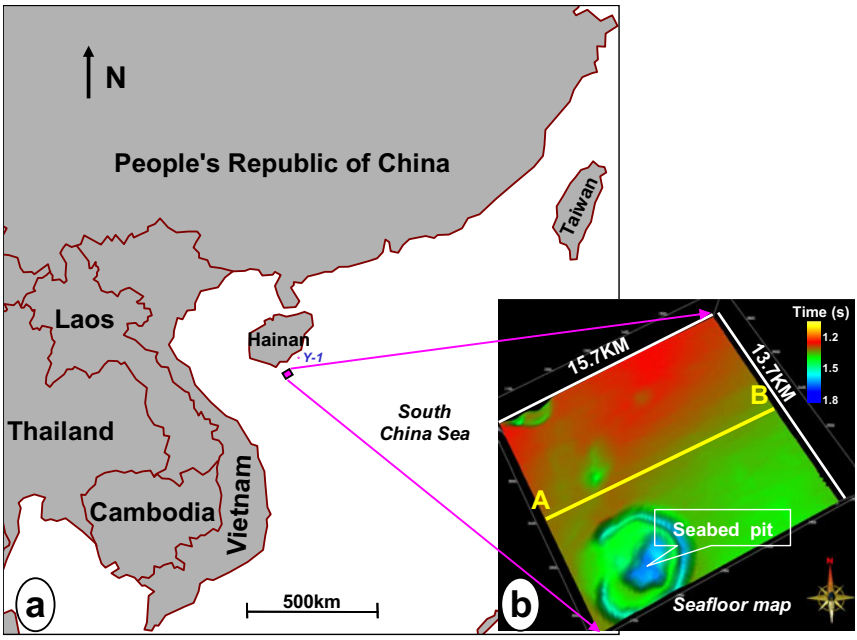

Fig. 1. Location of the study field, about 60 km away from Well Y-1 (a). Its seafloor map (b) shows that the water depth gradually increases from 1.2 s (around 600 m) in the northwest to 1.6 s (around 800 m) in the southeast, whereas an obvious seabed pit exists in the southern segment.

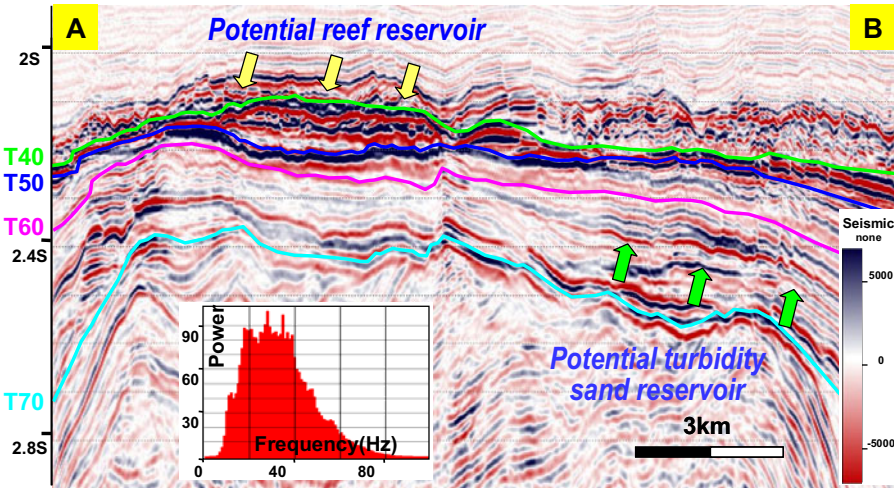

Fig. 2. The typical seismic section following line AB in Fig. 1b. Two sets of potential reservoirs, separately marked by yellow and green arrowheads, need to be finely described for further exploration.

nant frequency of 34 Hz. The main stratigraphy summarized from the nearest drilling area is listed in Table 1. It indicates that Meishan (T40 to T50) and Lingshui (T60 to T70) fm are the two target formations, prone to develop reservoirs in carbonate reef and turbidity sand units, respectively.

Table 1

Stratigraphy summarized from the nearest drilling location

System	Series	Formation	Horizontal
Neogene	Holocene Pleistocene Pliocene	Yinggehai	T20 T30 T40 T50 T60 T70 T80
	Miocene	Huangliu **Meishan** Sanya	
Oligocene	Oligocene Eocene	**Lingshui** Yacheng Lingtou	

The top and base units of two potential reservoir intervals can be clearly identified from the post-stack seismic reflection data by their very strong reflection amplitudes (Fig. 2); the time thickness distributions of Meishan and Lingshui formations (Fig. 3) have roughly revealed that both of the two sets of reservoirs lie in an area of large extent. Unfortunately, AVO inversion cannot be efficiently applied to retrieve valuable elastic parameters for reser-

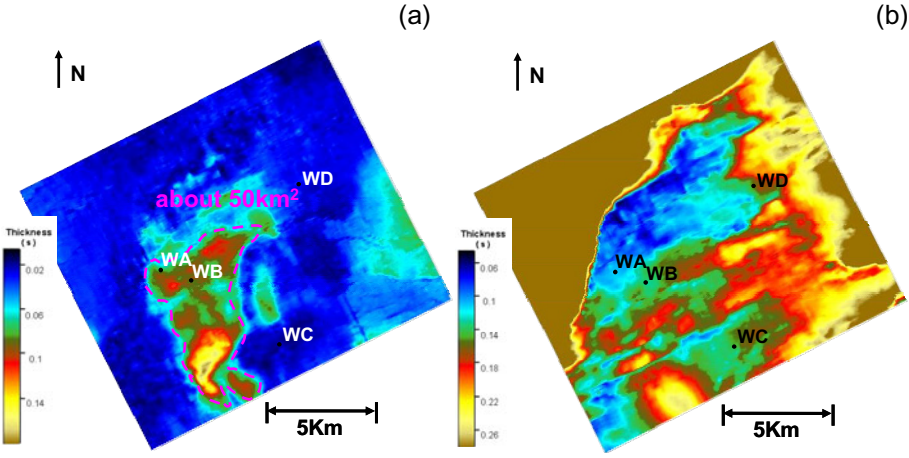

Fig. 3. The time thickness maps of Meishan (T40-T50) (a), and Lingshui (T60-T70) fm (b). WA, WB, WC, and WD are the four pseudo wells.

voir description since there is no well currently drilled in the study area. The drilling cost and risks in a marine environment, especially in deep waters, are actually a few times higher than that of land exploration. Therefore, it is crucial not only to perform a detailed reservoir assessment or cautious well-deployment but also to carry on an AVO study without well-logging data. On the contrary, the lack of the logging data in the early exploration phase also restricts the reservoir prediction accuracy. This common contradiction is essentially the key problem in the study area.

3. METHODS

Different from the conventional method by directly defining seismic processing velocity as the *P*-velocity and computing *S*-velocity and density using empirical formulas, the new method proposed in this paper reconstructs, at first, the pseudo well-logs incorporated with computed *P*-wave reflection amplitudes and an actual well-log data from the nearest drilling site. It then conducts pre-stack simultaneous AVO/AVA inversion for a high-quality description of elastic reservoir parameters. The *P*-wave data are computed from CRP (common reflection point) gathers by AVO inversion. As shown in Fig. 4, this method consists of three major approaches, including the initial pseudo well-logs construction, reconstruction, and AVO inversion.

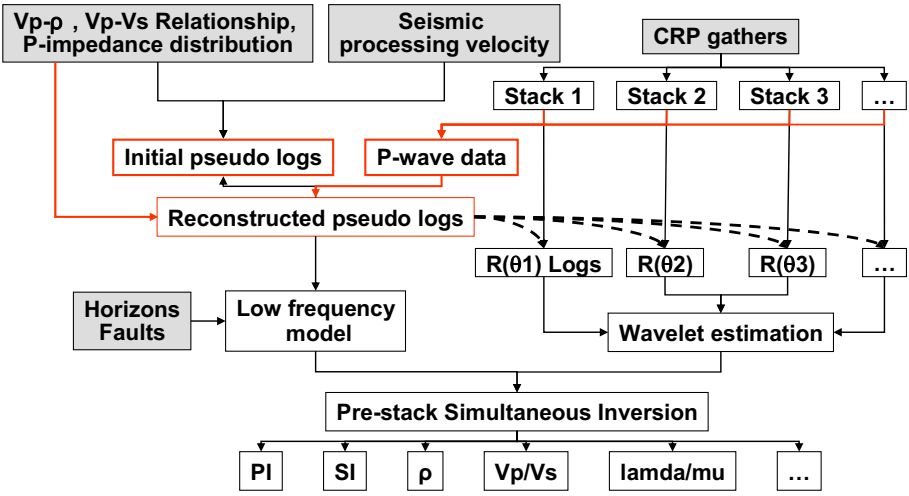

Fig. 4. The well-absent AVO inversion workflow based on amplitude-normalized pseudo well-logs construction method. The original data are marked by gray shades. The V_p-ρ and V_p-V_s relationships, as well as *P*-impedance distribution, are achieved from nearby drilling data. The *P*-wave data computed from CRP gathers by AVO inversion have a higher resolution, and are more beneficial for reservoir prediction and pseudo well-logs reconstruction.

3.1 Initial pseudo well-logs construction

The first step, constructing *P*-velocity for a pseudo well from interval velocity, is probably the same as in the conventional method. Although the interval velocities defined in 3D seismic processing stage could be carefully and densely picked, its dominant frequency (related to seismic velocity picking, often less than 5 Hz) is still inferior to that of seismic data (around 20-40 Hz), and far below that of logging data (often > 1000 Hz). Thus, the corresponding final inverted results are liable to have low resolutions and incorrect predictions.

Besides, as mentioned above, using a rough formula for elastic parameters prediction could destroy inversion thoroughly (Zhang *et al.* 2011b, Fan *et al*. 2013). Therefore, comparing to empirical formulas (for instance, Castagna's mud-rock line and Greenberg-Castagna's V_p-V_s relationship, *etc*.; Lamb *et al.* 1992), it is preferable to use the V_p-V_s and V_p-ρ relationships summarized from nearby drilling data to compute *S*-velocity and density, respectively.

3.2 Pseudo well-logs reconstruction

To reasonably improve the inversion resolution, the amplitude-preserved seismic data, drilling information and seismic processing velocity are integrated to reconstruct pseudo well-logs. The basic methodology is that the magnitudes and signs of seismic reflections are correlative with those of the subsurface layers if the stacked seismic data are amplitude-preserved. The reflectivity variations are also related to the changes of *P*-impedance (*PI*). The pseudo *PI* well-logs can therefore be reconstructed by converting full-stack seismic reflection to elastic parameters following the *PI* tendency.

3.2.1 P-wave data computation

As the full-stacked data have made a reluctant compromise to data resolution sacrificing due to the contamination of AVO effects no matter how much the SNR degree could be enhanced in the stacking process (Zhang *et al.* 2013), we compute the *P*-wave data from CRP gathers by AVO inversion to make a corroborating substitution, based on Eq. 1 (Gidlow 1992, Sun 1999):

$$R_{pp}(\theta) = (1+\tan^2\theta)R_p - 8\frac{V_s^2}{V_p^2}R_s \sin^2\theta - \left(\frac{1}{2}\tan^2\theta - 2\frac{V_s^2}{V_p^2}\sin^2\theta\right)\frac{\Delta\rho}{\rho}, \qquad (1)$$

where R_p and R_s are theoretical zero-offset *P*-wave reflectivity and *S*-wave reflectivity, respectively,

$$R_p = \frac{1}{2}\left(\frac{\Delta\rho}{\rho} + \frac{\Delta V_p}{V_p}\right), \quad R_s = \frac{1}{2}\left(\frac{\Delta\rho}{\rho} + \frac{\Delta V_s}{V_s}\right), \qquad (2)$$

and V_p, V_s, and ρ are the average *P*-wave velocity, *S*-wave velocity, and density of the reflection boundary, respectively. θ is the average of incidence and transmission angles, $R_{pp}(\theta)$ is the elastic reflectivity with ray-path of incident angle, $\Delta\rho/\rho$ is the density gradient, and V_s/V_p is the *S*-to-*P*-wave velocity ratio.

For solving the non-linear Eq. 1, the *P*-wave result is comparatively stable since the coefficient of R_p is usually bigger than that of R_s or $\Delta\rho/\rho$, and has nothing to do with V_p/V_s (Zhang *et al.* 2013). If we use seismic amplitudes of CRP gathers to substitute $R_{pp}(\theta)$, then the computed corresponding R_p results are the zero offset *P*-wave reflection data. Comparing to conventional full-stack data, the computed *P*-wave data have a higher resolution and are more beneficial for reservoir prediction (Zhang *et al.* 2013), inevitably for pseudo well-logs reconstruction.

3.2.2 P-impedance tendency computation

The *P*-impedance tendency (PI_0) is computed by the multiplication between seismic interval velocity and density, while density is computed from the statistical relationship of the nearest drilling data instead of any empirical formulas.

3.2.3 Pseudo well-logs reconstruction

The amplitude-normalized pseudo-well log reconstruction equation for each sample in each trace can be listed as follows:

$$\frac{x-0}{B-A}=\frac{PI-PI_0}{D-C}\ , \tag{3}$$

where PI is the reconstructed *P*-impedance, PI_0 is the *P*-impedance tendency, and x is the reflection amplitude for *P*-wave data in that sample. $[A,B]$ and $[C,D]$ are the distribution ranges of computed *P*-wave reflection amplitudes and recorded *P*-impedance values from the nearby drilling data, respectively. So,

$$PI=\frac{1}{B-A}\big((D-C)x+(B-A)PI_0\big)\ , \tag{4}$$

The density and *S*-impedance of pseudo well-logs can be computed from the statistical relationships from nearby drill well logs too.

3.3 AVO inversion conduction

With these reconstructed pseudo well-logs, the pre-stack simultaneous AVO/AVA inversion can be conducted to achieve a great number of elastic parameters such as PI, SI (*S*-impedance), V_p/V_s, Poisson ratio, $\lambda\rho$, and $\mu\rho$,

etc., for reservoir prediction. The reconstructed curves have higher dominant frequencies (same as that of seismic data), which could be definitely helpful for scaling wavelets and building initial models. The final AVO inverted results could therefore be improved.

4. COMPARISON OF RESULTS

Figure 5 shows the interval velocity profile defined in seismic processing stage of study area in the same line as in Fig. 2. It has been carefully and densely picked, with an interval of 100×100 m. Besides, the amplitude of CRP gathers analyzed in this study is well-preserved and qualified for *P*-wave data computation via AVO inversion because of the careful seismic data processing, including signal to noise ratio (SNR) enhancement, consistency and vertical resolution improvement, amplitude-preserved pre-stack migration, as well as data conditioning (Zhang *et al.* 2011a, b).

As shown in Fig. 6, comparing with conventional full-stack data (Fig. 6a), the inverted *P*-wave data from CRP gathers by AVO inversion (Fig. 6b) have a higher resolution with more clear and continuous events. The dominant frequency of inverted *P*-wave data is 39 Hz, while the counterpart of stack data is only 34 Hz on the whole section. This enhancement is even higher in some target zones, and crucial for pseudo well-logs reconstruction.

Figure 7 shows the comparison of seismic (a), synthetic (b), constructed *P*-impedance (*PI*) (c), and extracted wavelet (d) by conventional method for pseudo-well WC. The constructed pseudo *PI* log inevitably has a very low

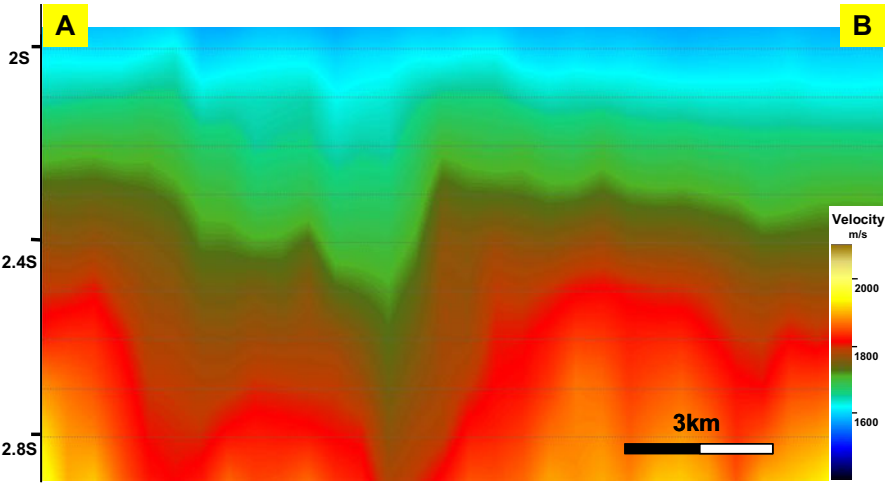

Fig. 5. The seismic processing velocity profile in the same line as in Fig. 2.

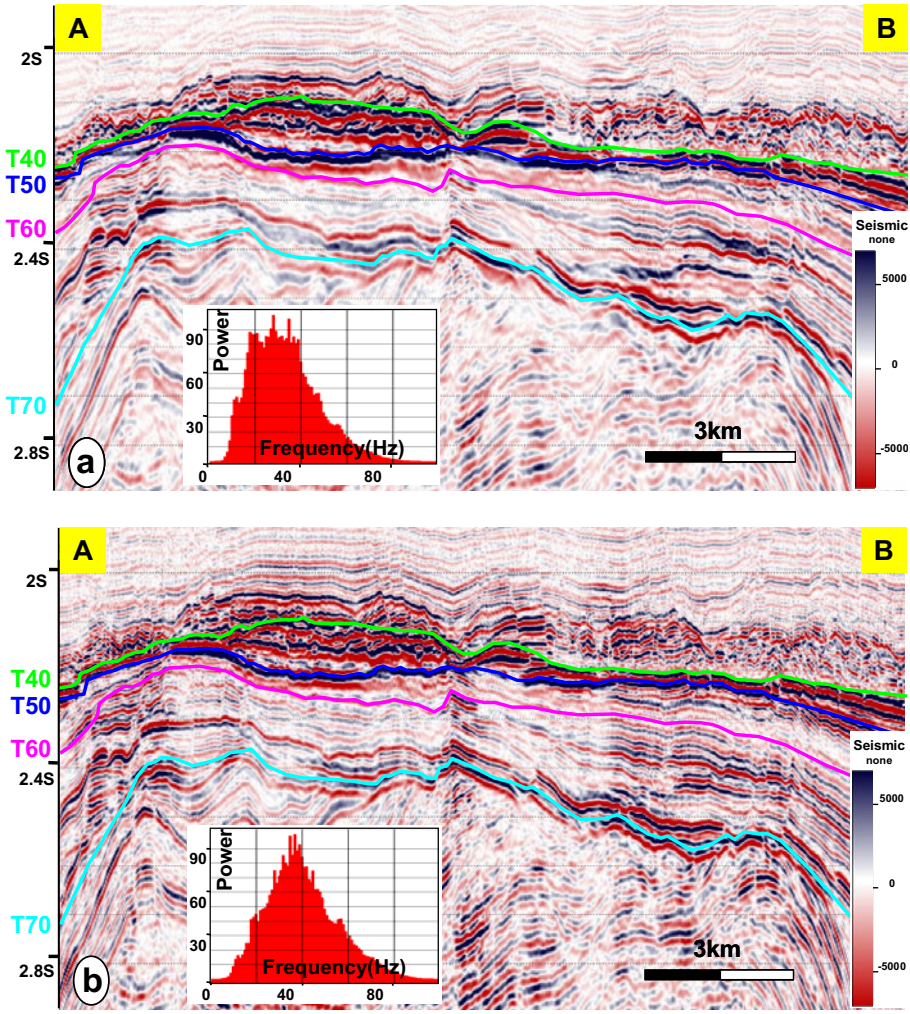

Fig. 6. Comparison between full-stack section (a) and inverted *P*-wave section (b) across the same profile as in Fig. 2. After the removal of AVO effects, seismic reflection events are more clear and continuous on the inverted *P*-wave section, and the dominant frequency is enhanced by 5 Hz compared with full-stack data across the whole section.

frequency bandwidth and definitely lost many details, thus the extracted wavelet energy has to be increased to compensate for the tiny reflection variations. Consequently, it is failed to produce a qualified correction between synthetic and seismic data. The extraction of reflection coefficients in

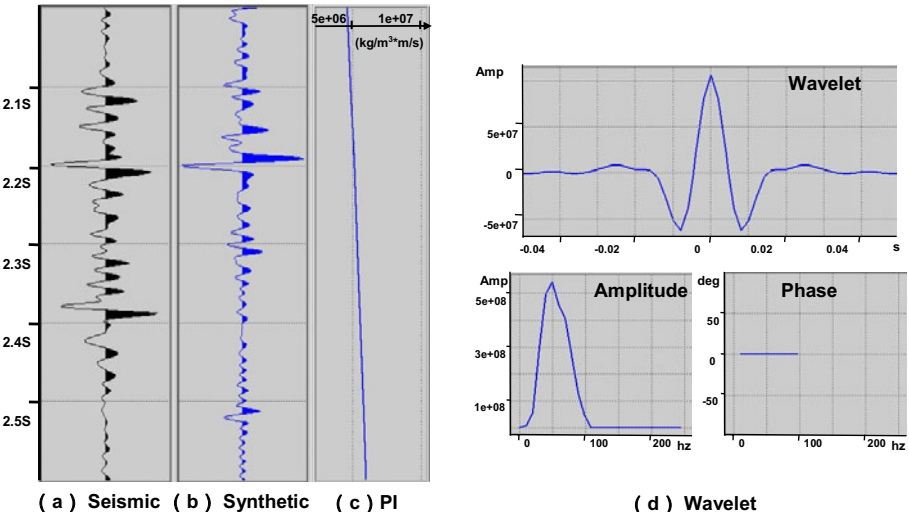

Fig. 7. The comparison of seismic (a), synthetic (b), constructed pseudo *P*-impedance (*PI*) (c), and extracted wavelet (d) by conventional method for pseudo-well WC. The constructed pseudo *PI* well-log with an extremely low dominant frequency has inevitably smoothed many details and irrationally boosted up the energy of extracted wavelets, which subsequently cause a bad-correlation between synthetic and seismic data.

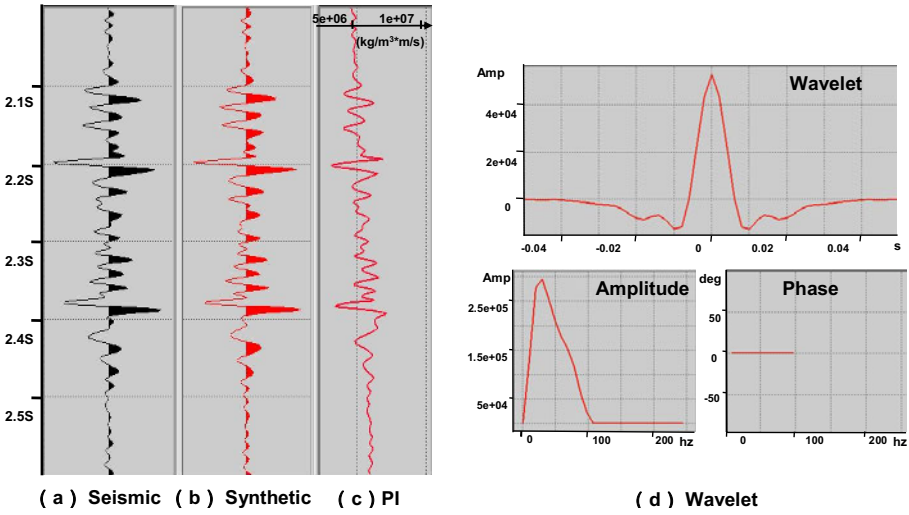

Fig. 8. The comparison of seismic (a), synthetic (b), reconstructed pseudo *P*-impedance (*PI*) (c), and extracted wavelet (d) by our proposed method for pseudo-well WC. The dominant frequency of pseudo well-log is higher than that of conventional counterpart (Fig. 7c).

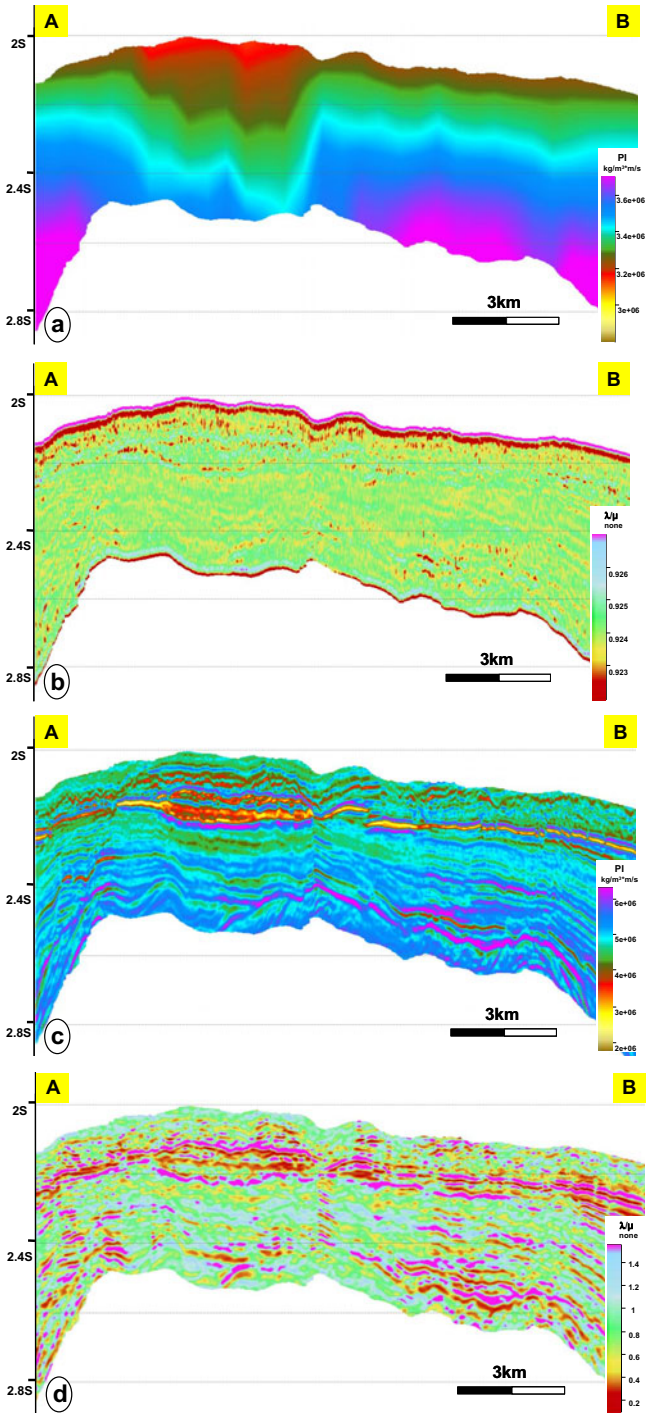

Fig. 9. Comparison between inverted *PI* and λ/μ results across the same line as in Fig. 2 based on conventional (a and b) and proposed (c and d) methods. The resolution of conventional result is much less than that of proposed competitor. Note that the conventional *PI* result is highly correlated to seismic processing velocity (Fig. 5), and both conventional *PI* and λ/μ results show very limited distributions of reservoirs, while the new results are more correlative to seismic reflections and are more beneficial for reservoir prediction.

the conventional pseudo well-logs directly from interval velocities is obviously not applicable. It is not difficult to forecast that the corresponding in vert resolution will not be qualified, and the computed results can hardly end up with good correlations to reservoir parameters. On the contrary, the reconstructed curve by the method we proposed has a higher dominant frequency (same as that of seismic data), as shown The extracted wavelet has produced a higher correlation rate made by correlating synthetic seismograms of reconstructed reflection coefficients and original seismic signals (Fig. 8a, b), which is quite essential to improve the inversion results. A further comparison will be illustrated in Fig. 9.

With these pseudo well-logs, the pre-stack simultaneous AVO/AVA inversion can be conducted to achieve a great number of elastic parameters, such as *PI*, *SI* (*S*-impedance), V_p/V_s, Poisson ratio, $\lambda\rho$, and $\mu\rho$, *etc*., for reservoir prediction. In particular, both the two sets of pseudo well-logs constructed from the conventional and proposed methods are employed to conduct pre-stack simultaneous AVO/AVA inversion. Figure 9 shows a comparison between the two sets of inverted *PI* and λ/μ results across the same line based on conventional (a and b) and new (c and d) methods, respectively. Obviously, the resolution of conventional result is much lower than that of proposed competitor, as indicated by these illustrations. In particular, the conventional *PI* result is highly correlated to seismic processing velocity (Fig. 5), and both conventional *PI* and λ/μ results have very limited value distributions. On the other hand, the new results by the proposed method are more correlative to seismic reflections and are definitely more beneficial for reservoir prediction.

5. APPLICATION IN RESERVOIR PREDICTION

Specifically, as shown in Fig. 10b, the cross-plot of λ/μ and *PI*, that is usually regarded as the best reservoir indicator, is employed for reef and sand reservoir discrimination by separately tracking appropriate data following the yellow and green polygons. The two polygons are similar to that of the nearest drilling place. Thus, the predicted reef (yellow) and sand reservoir (green) can be described, respectively, and elaborately plotted in Fig. 10a. The time thickness maps of predicted reef (Fig. 11b) and sand reservoirs (Fig. 11d) could also be further mapped by summing these qualified samples in a 3D area within two sets of formations, respectively. The two sets of reservoirs have been better delineated by the comparison with their corresponding formation thickness maps (Fig. 11a and c), and they are useful for further exploration of the reservoirs.

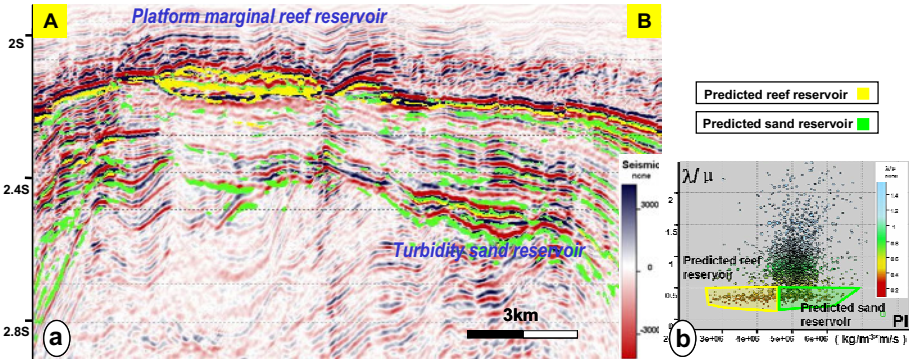

Fig. 10. The cross-plot of inverted *PI* and λ/μ attributes (b), and the predicted reservoir distributions in the same line as in Fig. 2 (a).

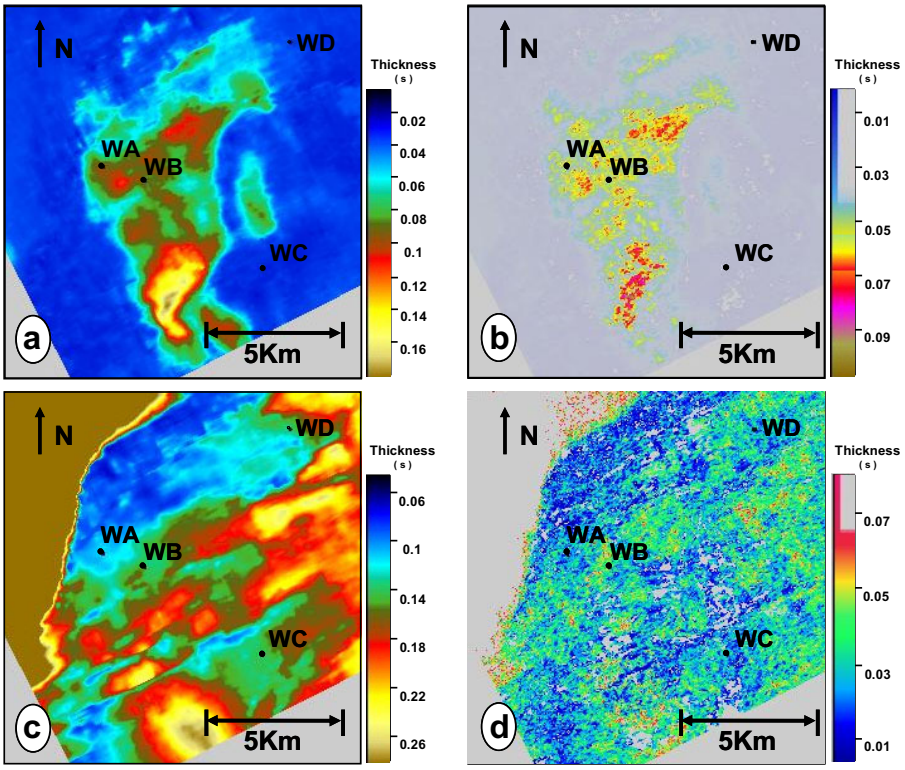

Fig. 11. The time thickness maps of Meishan (T40-T50) (a), and Lingshui (T60-T70) fm (c), the predicted reef (b), and turbidity sand (d) reservoir distributions in the two formations, respectively.

6. CONCLUSIONS

It is a common method to construct pseudo well-logs for AVO inversion in unexploited fields that are short of wells, especially in marine cases. But most of conventional methods by directly defining *P*-velocities from seismic processing and computing the *S*-velocity and density using empirical equations are not qualified to scale the extracted source wavelets and build constrained models. They tend to produce very low resolution AVO inversion results. On the contrary, the method we proposed, that reconstructs pseudo well-logs in accordance with reflection amplitudes of computed pure *P*-wave data from CRP gathers (AVO) and drilling information from a close area, is proven to be more beneficial for AVO inversion and more suitable for defining the reservoir prediction parameters. However, it should be noted, in particular, that the CRP data used in this method should have high quality.

Acknowledgments. The authors thank National Basic Research Program of China (Grant No. 2011CB201103), the National Science and Technology Major Project (Grant No. 2011ZX05004003), the Science Foundation of China University of Petroleum-Beijing (KYJJ2012-05-03), and Chinese Scholarship Council for financial support.

References

Connolly, P. (1999), Elastic impedance, *The Leading Edge* **18**, 4, 438-452, DOI: 10.1190/1.1438307.

Fan, C., Y. Song, Z. Jiang, Y. Zhang, and M. Sun (2013), Reservoir prediction in a well-absent area – a case study in a marine area. **In:** *75th EAGE Conference and Exhibition incorporating SPE EUROPEC 2013, 10-13 June 2013, London, UK*, Extended abstracts, DOI: 10.3997/2214-4609.20130877.

Gidlow, P.M., G.C. Smith, and P.J. Vail (1992), Hydrocarbon detection using fluid factor traces: A case history. **In:** *Joint SEG/EAEG Summer Research Workshop on "How Useful is Amplitude-Versus-Offset (AVO) Analysis?"*, Expanded abstracts, 78-89.

Hampson, D.P., J.S. Schuelke, and J.A. Quirein (2001), Use of multiattribute transforms to predict log properties from seismic data, *Geophysics* **66**, 1, 220-236, DOI: 10.1190/1.1444899.

Hampson, D.P., B.H. Russell, and B. Bankhead (2005), Simultaneous inversion of pre-stack seismic data. **In:** *75th Annual International Meeting SEG,* Expanded abstracts, Society of Exploration Geophysicists, 1633-1637.

Lamb, W.J., X.H. Zhu, G.A. McMechan, M.L. Greenberg, and J.P. Castagna (1992), Elastic wave propagation in composite media, *Geophysics* **57**, 9, 1155-1165, DOI: 10.1190/1.1443329.

Sun, Z. (1999), Seismic methods for heavy oil reservoir monitoring and characterization, Ph.D. Thesis, University of Calgary, Calgary, Canada.

Zhang, Y., Z. Sun, C. Fan, and H. Bai (2011a), Data conditioning for pre-stack inversion – a case study from Xingma area, Liaohe Oil field, China. **In:** *73rd EAGE Conference and Exhibition incorporating SPE EUROPEC 2011, 23-26 May 2011, Vienna, Austria*, Extended abstracts, DOI: 10.3997/2214-4609.20149593.

Zhang, Y., Z. Sam, H. Yang, H. Wang, J. Han, H. Gao, C. Luo, and B. Jing (2011b), Pre-stack inversion for caved carbonate reservoir prediction: A case study from Tarim Basin, China, *Pet. Sci.* **8**, 4, 415-421, DOI: 10.1007/s12182-011-0159-4.

Zhang, Y., Z. Sun, and C. Fan (2013), An iterative AVO inversion workflow for S-wave improvement. **In:** *75th EAGE Conference and Exhibition incorporating SPE EUROPEC 2013, 10-13 June 2013, London, UK*, Extended abstracts, DOI: 10.3997/2214-4609.20130268.

Received 29 July 2013
Received in revised form 15 April 2014
Accepted 9 June 2014

DE GRUYTER OPEN

Acta Geophysica
vol. 63, no. 3, June 2015, pp. 776-788
DOI: 10.1515/acgeo-2015-0009

Vibrator Data Denoising Based on Fractional Wavelet Transform

Jing ZHENG[1,2], Guowei ZHU[1,2], and Mingchu LIU[3]

[1]State Key Laboratory of Coal Resources and Safe Mining,
China University of Mining and Technology, Beijing, China,
e-mail: zhengjing8628@163.com

[2]College of Geoscience and Surveying Engineering,
China University of Mining and Technology, Beijing, China

[3] Pingxiang College, Pingxiang, China

A b s t r a c t

In this paper, a novel data denoising method is proposed for seismic exploration with a vibrator which produces a chirp-like signal. The method is based on fractional wavelet transform (FRWT), which is similar to the fractional Fourier transform (FRFT). It can represent signals in the fractional domain, and has the advantages of multi-resolution analysis as the wavelet transform (WT). The fractional wavelet transform can process the reflective chirp signal as pulse seismic signal and decompose it into multi-resolution domain to denoise. Compared with other methods, FRWT can offer wavelet transform for signal analysis in the time-fractional-frequency plane which is suitable for processing vibratory seismic data. It can not only achieve better denoising performance, but also improve the quality and continuity of the reflection syncphase axis.

Key words: seismic method, vibrator data, chirp signals, noise attenuation, fractional wavelet transform.

1. INTRODUCTION

The methods generally called vibratory seismic have been very important in seismic exploration. Many works focus on the research of highly efficient acquisition methods of vibroseis data, such as cascaded sweeps, slip-sweep acquisition, simultaneous shooting, and so on (Bagaini 2010). With the development of the exploration methods, the corresponding signal processing methods have been drawing more and more attention (Jeffryes 1996, Sallas *et al.* 1998, Meunier and Bianchi 2002), since the seismic noise shrinkage becomes more and more important, as the requirements of high-quality data for post-processing increase. Transform-based methods are the most popular. If the seismic data is spare in the transform domain, denoising goal can be achieved by eliminating the small coefficients which are considered to be noise. The vibratory seismic system produces a chirp-like signal, which makes it difficult to find an optimum transform domain in which seismic data can be sparsely represented.

To date, some of the recently developed signal processing methods are introduced into this field, *e.g.*, wavelet transform (WT), fractional Fourier transform (FRFT), Radon-Wigner transform, *etc*. However, they have different disadvantages for chirp-like signals processing. The WT, which enables a researcher to study features of the signal locally with a detail matched to their scale (Morlet *et al.* 1982), *i.e.*, broad features on a large scale and fine features on a small scale, may not able to offer the sparest representation of the signal. The FRFT, which can represent signal in the time fractional frequency domain, is a global transformation, so it limits the usage on the area of analyzing signal's localized characteristics (Miah and Sacchi 2011). The Radon-Wigner transform (Wood and Barry 1994) can analyze local property of chirp-like signals (Steeghs 1998), but it has cross-term problem with the quadratic time-frequency representation.

Mendlovic *et al.* (1997) first proposed the FRWT to analyze optical signals. Then, Huang and Suter (1998) proposed the fractional wave packet transform (FRWPT). Shi *et al*. (2012) proposed a novel fractional wavelet transform (NFRWT) based on fractional convolution theorem. There are some other works which define fractional wavelet transform based on the fractional splines (Unser and Blu 2000). In this work, the FRWT is introduced to suppress noise in the vibratory seismic system. As a generalization of WT, the FRWT combines the advantages of the wavelet transform and the FRFT; it is a linear transform without cross-term interference and is capable of providing multiresolution analysis and representing signals in the fractional domain. Thus, it is more suitable to analyze chirp-like signals.

The rest of the paper is organized as follows. In Section 2, we briefly introduce the characteristics of linear frequency modulation (LFM) signal

(chirp-like signal which is used as a vibratory source). In Section 3, we propose the FRWT by treating the wavelet transform as a filter defined in fractional domain. Then the FRWT is applied to analyze the reshaped vibratory seismic signal. The performance is analyzed and compared with other signal processing methods in Section 4. Finally, conclusions are provided in Section 5.

2. LINEAR FREQUENCY MODULATION SIGNAL

Linear frequency modulation (LFM) signal is a common kind of chirp-like signal, which is widely used in radar and vibratory seismic systems:

$$s_t(t) = A\,\mathrm{rect}\left(\frac{t}{T}\right)e^{j2\pi\left(f_0 t+\frac{1}{2}\beta t^2\right)} , \tag{1}$$

where f_0 is the carried frequency, A is the amplitude, $\beta = B/T$ is the frequency rate, B is the bandwidth, T is the pulse width, rect(w) is a rectangular pulse with width w. The waveform of the signal is shown in Fig. 1A.

Instantaneous frequency of the signal can be expressed as:

$$f(t) = \frac{1}{2\pi}\frac{d}{dt}\left(2\pi\left(f_0 t+\frac{1}{2}\beta t^2\right)\right) = f_0 + \beta t . \tag{2}$$

A linear relationship, as shown in Fig. 1B, exists between the instantaneous frequency and time.

The frequency spectrum of chirp signal can be written as:

$$S(f) = A\sqrt{\frac{\pi}{\beta}}\left\{\left[c(u_1)+c(u_2)\right]^2+\left[s(u_1)+s(u_2)\right]^2\right\}^{1/2} e^{j\theta(f)} , \tag{3}$$

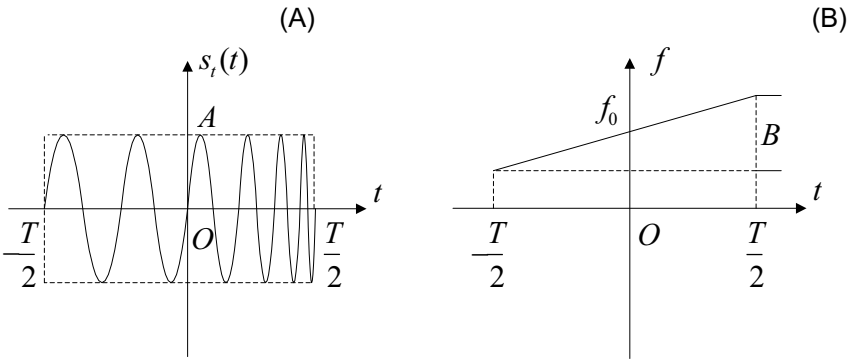

Fig. 1. Linear frequency modulation signals: (A) chirp waveform, and (B) instantaneous frequency.

where

$$\theta(f) = -\frac{2\pi^2}{\beta}\left(f - f_0\right)^2 + \arctan\left[\frac{s(u_1)+s(u_2)}{c(u_1)+c(u_2)}\right], \tag{4}$$

$$u_1 = \sqrt{D}\,\frac{1+2(f-f_0)/\Delta f}{\sqrt{2}}, \tag{5}$$

$$u_2 = \sqrt{D}\,\frac{1-2(f-f_0)/\Delta f}{\sqrt{2}}, \tag{6}$$

$$c(u) = \int_0^u \cos\left(\frac{\pi}{2}x^2\right)dx, \tag{7}$$

$$s(u) = \int_0^u \sin\left(\frac{\pi}{2}x^2\right)dx, \tag{8}$$

where $D = BT$, T is the width of pulse, and B is the width of spectrum.

3. THEORY

3.1 Fractional Fourier transform (FRFT)

Fractional Fourier transform (FRFT), which is widely used in non-stationary signal processing, is a generalized form of Fourier transform. FRFT can be considered as a rotation operator in the time-frequency plane.
The kernel of continuous FRFT is defined as:

$$K_\alpha(u,t) = \begin{cases} A_\alpha e^{j\pi\left[(t^2+u^2)\cot\alpha - 2ut\csc\alpha\right]}, & \alpha \neq n\pi \\ \delta\left[t-(-1)^n u\right], & \alpha = n\pi \end{cases}, \tag{9}$$

where α can be considered as an angle with the time axis,

$$A_\alpha = \sqrt{1 - j\cot\alpha}\ .$$

When $\alpha = \pi/2$ in Eq. 1 one obtains the traditional Fourier transform.
The FRFT and inverse FRFT (IFRFT) of the signal $x(t)$ are:

$$\begin{aligned} X_\alpha(u) &= \left\{F_\alpha[x(t)]\right\}(u) = \int_{-\infty}^{+\infty} K_\alpha(u,t)x(t)dt, \\ x(t) &= \left\{F_{-\alpha}[X_\alpha(u)\right\}(t) = \int_{-\infty}^{+\infty} K_{-\alpha}(t,u)X_\alpha(u)du, \end{aligned} \tag{10}$$

where $F_\alpha[\bullet]$ is the operator of FRFT.

The calculation of FRFT can be divided into the following three steps:

1. Multiplying LFM signal:

$$g(t) = e^{j\pi t^2 \cot\alpha} x(t) \ ;$$

2. Calculating FRFT of $g(t)$, the argument's scaling is included:

$$X'_\alpha(u) = \int_{-\infty}^{+\infty} e^{j2\pi ut \csc\alpha} g(t)dt \ ;$$

3. Multiplying LFM signal:

$$X_\alpha(u) = A_\alpha e^{j\pi u^2 \cot\alpha} X'_\alpha(u) \ .$$

It is obvious that the existing condition of FRFT is consistent with FFT. The algorithm only needs two chirp multiplications and one FFT calculation. It meets the analysis and synthesis requirements for the signal because the reversibility and periodicity have been demonstrated by Kraniauskas *et al.* (1998), Ozaktas *et al*. (1996), and Pei and Ding (2000).

3.2 Novel fractional wavelet transform (FRWT)

The FRFT has been widely used in signal procession field in recent years. However, the FRFT tells us the fractional frequencies which exist across the whole duration of the signal but not the frequencies which exist only at a particular time. It means that the FRFT is a global transform and it fails in obtaining local information of the signal, which is crucial for processing non-stationary signals. With the knowledge that the wavelet transform is a localized transformation and is efficient for transient signal processing, a generalized wavelet transform, called fractional wavelet transform, which can offer signal representation in the time-fractional-frequency plane, has been developed; it inherits both the advantages of multi-resolution analysis of the wavelet transform and the capability of the signal representation in the fractional domain which is similar to FRFT. A general deduction of FRWT can be found below.

The wavelet transform can be defined as a convolution in the time domain:

$$W(a,b) = \left\langle f(t), \varphi_{a,b}(t) \right\rangle = \int_0^\infty f(t)\varphi^*_{a,b}(t)dt = \int_0^\infty f(t)\frac{1}{\sqrt{a}}\varphi^*\left(\frac{t-b}{a}\right)dt = f(t) \otimes \left(\frac{1}{\sqrt{a}}\varphi^*\left(\frac{-t}{a}\right)\right), \quad (11)$$

where $\varphi(t)$ is the mother wavelet, a and b are the parameters which are used to control dilation and translation, respectively.

As we know, the fractional convolution can be expressed as:

$$f(t) \underset{\alpha}{\otimes} \left(h(t)\right) = A_\alpha e^{-j\pi t^2 \cot\alpha} \cdot \left[\left(f(t)e^{j\pi t^2 \cot\alpha}\right) \otimes \left(h(t)e^{j\pi t^2 \cot\alpha}\right)\right] = e^{-j\pi t^2 \cot\alpha} \cdot \left\langle f(\cdot)e^{j\pi(\cdot)^2 \cot\alpha}, h^*(t-\cdot)e^{-j\pi(t-\cdot)^2 \cot\alpha} \right\rangle . \quad (12)$$

The output in the fractional Fourier domain is:

$$F_\alpha\left[f(t)\underset{\alpha}{\otimes}\left(h(t)\right)\right]=F_\alpha(u)H(u\csc\alpha)e^{-j\pi\cot\alpha u^2}. \tag{13}$$

Applying the fractional convolution to the LFM signal which is introduced by vibratory seismic systems, we can find that the item of frequency modulation can be demodulated by a chirp signal. The chirp item in Eq. 13 is not necessary for the analysis. If we modify the convolution, we can get a simplified expression in the fractional Fourier domain without the chirp signal term:

$$F_\alpha\left[f(t)\underset{\alpha}{\otimes}\left(h(t)e^{-j\pi\cot\alpha t^2}\right)\right]=F_\alpha(u)H(u\csc\alpha) \tag{14}$$

extends the wavelet transform with the fractional convolution expressed as:

$$\begin{aligned}W_\alpha(a,b)&=f(t)\underset{\alpha}{\otimes}\left(\frac{1}{\sqrt{a}}\varphi^*\left(\frac{-t}{a}\right)e^{-j\pi u^2\cot\alpha}\right)=e^{-j\pi b^2\cot\alpha}\left\{\left(f(t)e^{j\pi u^2\cot\alpha}\right)\otimes\left(\frac{1}{\sqrt{a}}\varphi^*\left(\frac{-t}{a}\right)e^{-j\pi u^2\cot\alpha}e^{j\pi u^2\cot\alpha}\right)\right\}\\&=\int_{-\infty}^{\infty}f(t)e^{j\pi(t^2-b^2)\cot\alpha}\varphi_{a,b}^*(t)dt=\left\langle f(\cdot),\varphi_{a,b}(\cdot)e^{-j\pi(\cdot)^2\cot\alpha}e^{j\pi b^2\cot\alpha}\right\rangle=\left\langle f(\cdot),\varphi_{\alpha,a,b}(\cdot)\right\rangle.\end{aligned} \tag{15}$$

where $W_\alpha(a,b)$ expresses the fractional wavelet transform:

$$\varphi_{\alpha,a,b}(t)=\varphi_{a,b}(t)e^{-j\pi(t^2-b^2)\cot\alpha}.$$

The inverse transform can be calculated as follows:

$$f(t)=\frac{1}{C_{\alpha,\varphi}}\int_0^\infty\int_{-\infty}^{\infty}W_\alpha(a,b)\varphi_{\alpha,a,b}(t)db\frac{da}{a^2}, \tag{16}$$

where $C_{\alpha,\varphi}$ is a constant that depends on the wavelet used. The success of the reconstruction depends on this constant, called the admissibility constant; it should satisfy the following admissibility condition:

$$C_{\alpha,\varphi}=\int_0^\infty\frac{\left|\Psi(u\csc\alpha)\right|^2}{u}du<\infty, \tag{17}$$

where $\Psi(x)$ denotes the Fourier transform of $\varphi(t)$. The admissibility condition implies that $\Psi(0)=0$, which is $\int_{-\infty}^{\infty}\varphi(t)dt=0$. Consequently, continuous fractional wavelets must oscillate and behave as bandpass filters in the fractional Fourier domain. Whenever $\alpha=\pi/2$, the FRWT reduces to the classical wavelet transform.

4. EXPERIMENT

The wavelet transform is actually a differently scaled bandpass filter in frequency domain, as we can see from Section 3.3. If the signal's energy is well

concentrated in the frequency domain, the wavelet denoising methods is one of the most effective ways to suppress noise. As for the signals whose energy is not well concentrated in the frequency domain, *e.g.*, chirp signals, the signals' energy may be well focused in a certain fractional domain, so it is suitable for FRWT to process this kind of signals.

The computation of the fractional wavelet transform for the vibratory seismic signals can be done in the following steps:

(i) Multiply a chirp signal and do wavelet transform. The process of multiplying a chirp signal can help to modify the concentrated performance of the signal energy. After the wavelet transform, signals are decomposed into different fractional-frequency bands with different scales.

(ii) The denoising idea is to set zero for all coefficients that are less than thresholds.

(iii) The modified coefficients are used in an inverse transform to reconstruct the desired signal.

The thresholds in step (ii) are chosen according to Birge–Massart strategy (Birge and Massart 1997). The thresholds can be achieved as follows:

- Given the wavelet decomposition layer j, retain all the coefficients for $(j + 1)$ and higher layer.
- When the layer i satisfies the condition $1 \le i \le j$, keep n_i coefficients which have the largest absolute value; n_i is determined by: $n_j = M(j + 2 - i)^{\text{ALPHA}}$. Normally, ALPHA = 3 for denoising. A default value for M is $M = \text{prod}(s(1,:))$ which is the number of low frequency coefficients. Parameter s is the wavelet decomposition structure of the seismic data to be denoised.
- Take the absolute coefficient value of i-th layer, and arrange the coefficient value in a sequence $|c(k_i)|$ by decreasing order; $c(k_i)$ is the k-th coefficient on this layer. The threshold λ_i can then be calculated as $\lambda_i = |c(n_i)|$.

4.1 Velocity model with horizontal layer

We first assume a velocity model shown in Fig. 2. The paper focuses on the random noise attenuation. According to the stochastic process theory, we can employ Gaussian random noise to illustrate the random noise. In order to verify the performance, seismic data with different signal-to-noise ratio (SNR) is provided.

As the wavelet denoising method is widely used in seismic signal processing with convincing performance, we apply the wavelet method for comparison to verify the performance of the method proposed. The parameters of vibratory seismic system used in simulation are: 50 ~ 200 Hz linear sweep signal (chirp signal), 0.001 s time step, 0.16 ms waveform length, a total of 49 seismic traces with spacing of 10 m. The refraction syncphase ax-

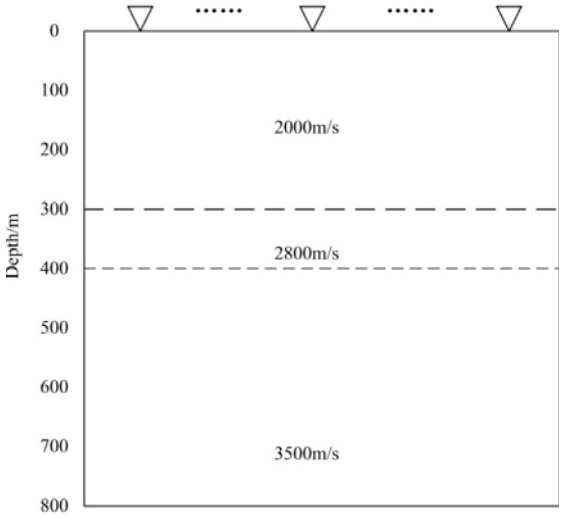

Fig. 2. Velocity model for numerical experiments.

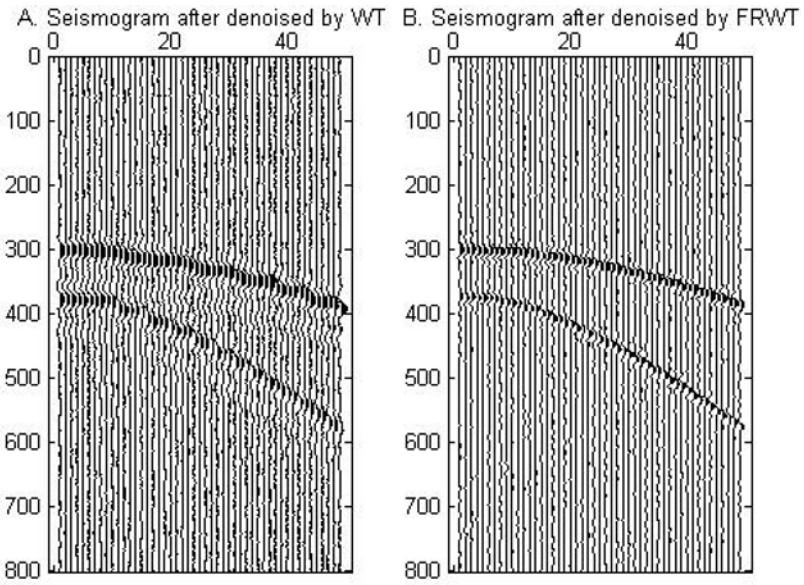

Fig. 3. Denosing performance comparison between WT and FRWT at SNR of 10 dB.

is from 300 and 400 m, respectively. We apply the WT and FRWT to denoise, as shown in Fig. 3 panels A and B, respectively. From both figures we can find that the noises are both removed effectively. The denoising per-

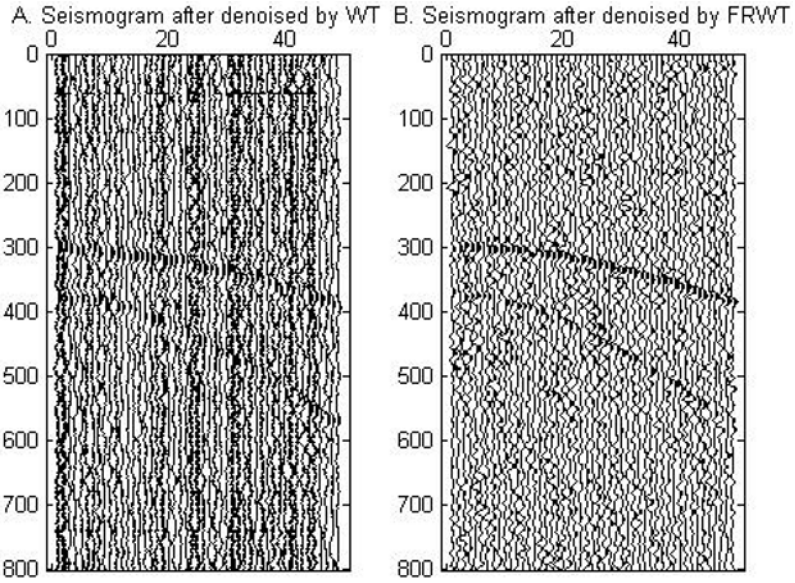

Fig. 4. Denoising performance comparison between WT and FRWT at SNR of –5 dB.

formance in Fig. 3B is better, since both quantity and continuity of syncphase axis are improved.

The parameters of the vibratory system used in Fig. 4 are the same as those in Fig. 3. We can find that with the increase of noise, the performance of the syncphase axis has decreased for both methods, WT and FRWT. However, the denoising performance in Fig. 4B efficient than that based on WT with the velocity model specified is still better than that in Fig. 4A. Thus, it is proved that the denoising method based on FRWT is more efficient than that based on WT with the velocity model specified.

4.2 Velocity model with inclined layer

To further analyse the performance of the proposed method, we also simulate a velocity model with an inclined layer. We assume a velocity model shown in Fig. 5. As in the previous model, only Gaussian random noise is addressed. Seismic data with different signal-to-noise ratio (SNR) is also provided.

The sampling parameters in Figs. 6 and 7 are the same as those in Figs. 3 and 4. The refraction syncphase axis at 400 m is inclined at 30 degrees. Comparing in Fig. 6 panel A with panel B, we can find that the denoising performance based on the FRWT method is better. Even at a SNR lower than 0 dB, the syncphase axis can be found with the FRWT method while it

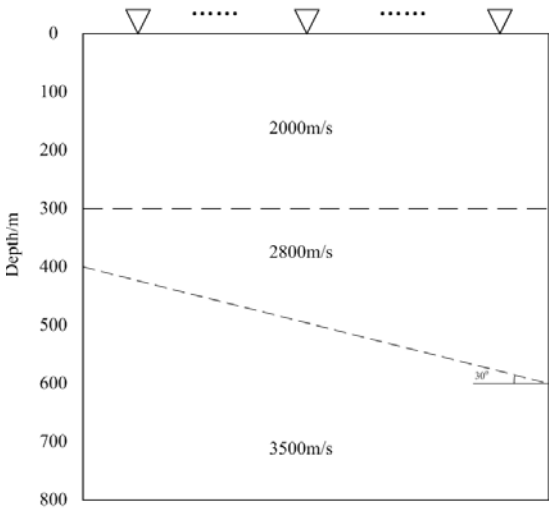

Fig. 5. Velocity model for numerical experiments.

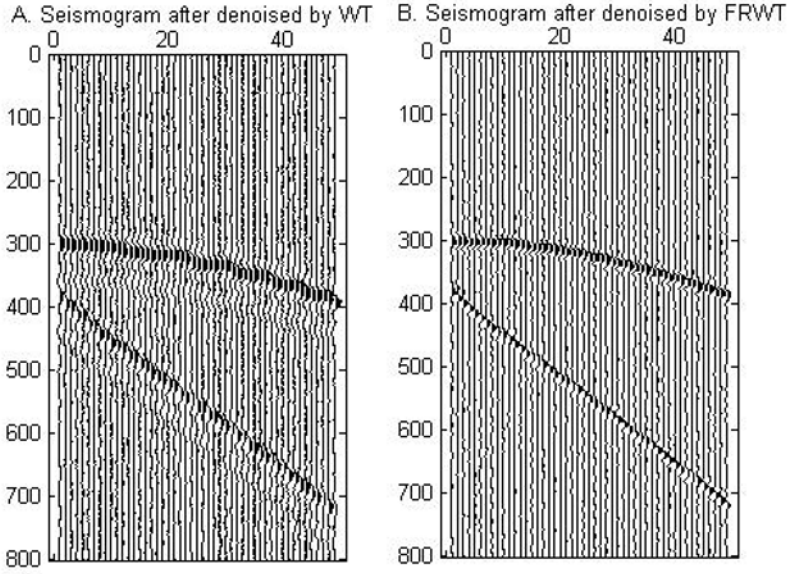

Fig. 6. Denoising performance comparison between WT and FRWT at SNR of 10 dB.

is not clear with WT method, as shown in Fig. 7. It is proved that the performance of denoising method based on FRWT is more efficient than that based WT method for the inclined layers with low SNR data.

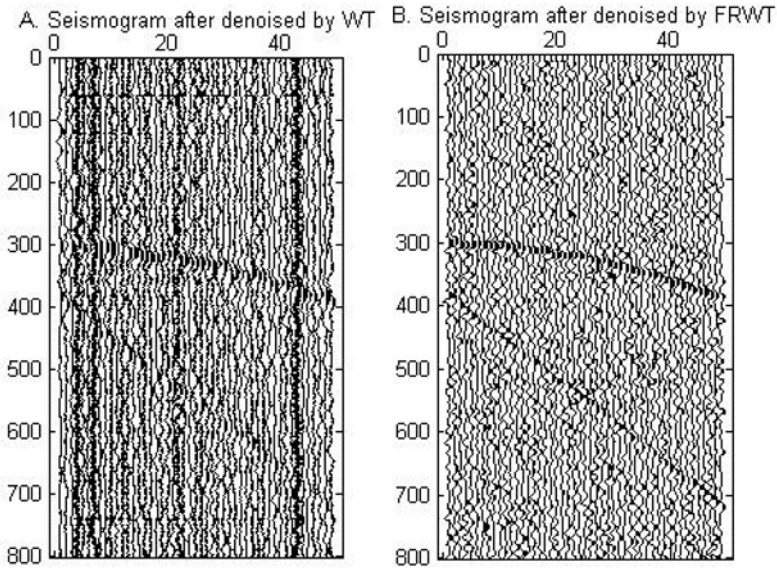

Fig. 7. Denoising performance comparison between WT and FRWT at SNR of –5 dB.

5. CONCLUSION

A novel method has been proposed for denoising seismic data in vibratory seismic systems based on the FRWT. This method can give better denoising performance, while the continuity of the syncphase axis in the seismic profile is maintained, which is very important to process the seismic data. The performance of the procedure is evaluated via simulation of seismic data with vibrator and pulse source. The results show that the FRWT is more efficient than traditional WT to suppress noise in vibratory seismic systems. Combining the special design of the seismic source, the quality and continuity of the syncphase axis in the seismic profile has been improved greatly.

Acknowledgments. We appreciate Suping Peng, the editor Zbigniew Wisniewski and reviewers for the guidance and help. We express our gratitude to State Key Laboratory for Coal Resources and Safe Mining, China University of Mining & Technology (No. SKLCRSM13KFB02), and the Fundamental Research Funds for the Central Universities.

References

Bagaini, C. (2010), Acquisition and processing of simultaneous vibroseis data, *Geophys. Prospect*. **58**, 1, 81-100, DOI: 10.1111/j.1365-2478.2009.00842.x.

Birgé, L., and P. Massart (1997), From model selection to adaptive estimation. **In:** D. Pollard, E. Torgersen, and G.L. Yang (eds.), *Festschrift for Lucien Le Cam. Research Papers in Probability and Statistics*, Springer, New York, 55-87, DOI: 10.1007/978-1-4612-1880-7_4.

Huang, Y., and B. Suter (1998), The fractional wave packet transform, *Multidim. Syst. Signal Process.* **9**, 4, 399-402, DOI: 10.1023/A:1008414608970.

Jeffryes, B.P. (1996), Far-field harmonic measurement for seismic vibrators. **In:** *66th SEG Annual Meeting, 10-15 November 1996, Denver, USA*, Expanded Abstracts, Society of Exploration Geophysicists, 60-63.

Kraniauskas, P., G. Cariolaro, and T. Erseghe (1998), Method for defining a class of fractional operations, *IEEE Trans. Signal Process.* **46**, 10, 2804-2807, DOI: 10.1109/78.720382.

Mendlovic, D., Z. Zalevsky, D. Mas, J. García, and C. Ferreira (1997), Fractional wavelet transform, *Appl. Optics* **36**, 20, 4801-4806, DOI: 10.1364/AO.36.004801.

Meunier, J., and T. Bianchi (2002), Harmonic noise reduction opens the way for array size reduction in vibroseis operations. **In:** *72nd SEG Annual Meeting, 6-11 October 2002, Salt Lake City, USA*, Expanded Abstracts, Society of Exploration Geophysicists, 70-73, DOI: 10.1190/1.1817354.

Miah, K.H., and M.D. Sacchi (2011), Fractional Fourier transform and its application in seismic signal processing. **In:** *Proc. 73rd EAGE Conference and Exhibition incorporating SPE EUROPEC 2011*, 1645-1649, DOI: 10.3997/2214-4609.20149189.

Morlet, J., G. Arens, E. Fourgeau, and D. Giard (1982), Wave propagation and sampling theory – Part II: Sampling theory and complex waves, *Geophysics* **47**, 2, 222-236, DOI: 10.1190/1.1441329.

Ozaktas, H.M., O. Arikan, M.A. Kutay, and G. Bozdagt (1996), Digital computation of the fractional Fourier transform, *IEEE Trans. Signal Process*. **44**, 9, 2141-2150, DOI: 10.1109/78.536672.

Pei, S.C., and J.J. Ding (2000), Closed-form discrete fractional and affine Fourier transforms, *IEEE Trans. Signal Process.* **48**, 5, 1338-1353, DOI: 10.1109/78.839981.

Sallas, J.J., D. Corrigan, and K.P. Allen (1998), High fidelity vibratory source seismic method with source separation, United States Patent: 5721710A.

Shi, J., N. Zhang, and X. Liu (2012), A novel fractional wavelet transform and its applications, *Sci. China Inf. Sci.* **55**, 6, 1270-1279, DOI: 10.1007/s11432-011-4320-x.

Steeghs, P. (1998), Wigner-Radon representations for 3-D seismic data analysis. **In:** *Proc. IEEE-SP Int. Symp. on Time-Frequency and Time-Scale Analysis, 6-9 October 1998, Pittsburgh, USA*, 433-436, DOI: 10.1109/TFSA.1998.721454.

Unser, M., and T. Blu (2000), Fractional splines and wavelets, *SIAM Rev*. **42**, 1, 43-67, DOI: 10.1137/S0036144598349435.

Wood, J.C., and D.T. Barry (1994), Linear signal synthesis using the Radon–Wigner transform, *IEEE Trans. Signal Process.* **42**, 8, 2105-2111, DOI: 10.1109/78.301845.

Received 15 June 2013
Received in revised form 5 February 2014
Accepted 9 June 2014

DE GRUYTER OPEN

Acta Geophysica
vol. 63, no. 3, June 2015, pp. 789-814
DOI: 10.1515/acgeo-2015-0013

Tight Reservoir Properties Derived by Nuclear Magnetic Resonance, Mercury Porosimetry and Computed Microtomography Laboratory Techniques. Case Study of Palaeozoic Clastic Rocks

Paulina I. KRAKOWSKA and Edyta PUSKARCZYK

Faculty of Geology Geophysics and Environmental Protection,
Department of Geophysics, AGH University of Science and Technology,
Kraków, Poland; e-mail: krakow@agh.edu.pl

A b s t r a c t

Results of the nuclear magnetic resonance (NMR) investigations, mercury porosimetry measurements (MP) and computed microtomography (micro-CT), applied to the tight Palaeozoic rocks from the depths lower than 3000 m, were presented to estimate their reservoir potential. NMR signal analysis and interpretation were performed. Based on NMR driven models, permeability and Free Fluid Index were calculated for data sets divided into homogeneous clusters. Computerized mercury porosimetry results visualization and processing provided useful information, as the automatically determined Swanson parameter is correlated with petrophysical properties of rocks. Micro-CT enriched the image of porous space in qualitative and quantitative ways. Homogeneity of pore space structure was discussed using micro-CT approach. Integration of the results in the frame of reservoir parameters from standard laboratory methods and the modern ones resulted in the improvement of methodology for determining the old, deep-seated, hard sedimentary rocks reservoir potential.

Key words: palaeozoic sedimentary rocks, nuclear magnetic resonance, mercury porosimetry, computed microtomography.

1. INTRODUCTION

Petrophysical properties of deep-seated, old rocks are now a new research target due to the recent increased interest in tight gas formations (Monk 2013, Czekański *et al*. 2012). Previously, Precambrian and Palaeozoic sedimentary rocks were the objects of scientific research regarding the analysis of the sedimentary basins and recognition of the lithosphere structure (Bakun-Czubarow 1984, Jaworowski and Mikołajewski 2007, Kotarba 2010). Methodology which has been applied so far for investigation of hydrocarbon-bearing formations was mainly focused on precise determination of water or hydrocarbon saturation by selection of the adequate geological and geophysical models, *e.g.*, in the Polish part of the Carpathian Foredeep (Zorski 2009, Zorski *et al*. 2011).

Precambrian and Palaeozoic sedimentary rocks may be analyzed from the point of their reservoir properties in prospecting for hydrocarbons, table and geothermal waters, and for estimation of the rock utility to the CO_2 storage (Kiersnowski *et al.* 2010, Semyrka *et al*. 2010, Such *et al.* 2010, Jarzyna *et al.* 2012, Xiao *et al.* 2014). Combination of laboratory measurements including nuclear magnetic resonance (NMR), mercury porosimetry (MP), and computed microtomography (micro-CT) leads to building up a detailed methodology in analyzing low porosity and low permeability rocks. Results obtained for selected rock samples are presented as an example of sophisticated approach to reservoir properties determination. An integration of the NMR and MP results using different permeability models (SDR, Coates, and clay-bound water) and fluid flow description was made. Information on pore space distribution was obtained from micro-CT experiments.

2. MATERIAL

Tight and hard rocks of the Cambrian, Silurian, Ordovician, Carboniferous, and Permian age, located at the depth range of 3007.2-4588.0 m in wells sited in the Polish territory were used as testing material (Table 1). Rock samples were selected from deep wells, complying with four conditions: (i) depth of the rock was greater than 3000 m, (ii) rocks were of Precambrian or Palaeozoic age, (iii) lithology was represented by sandstones and claystones or carbonates (limestones and dolomites), and (iv) it was possible to probe the core sample of 0.10 m length and a quarter of core volume, which was cut at half of core's diameter (Fig. 1).

Deep wells were located in the north, south-east, and central Poland in selected geological units built of old rock formation (Fig. 2). Samples were initially interpreted in the aspect of lithology and age. Several well recognized methods of laboratory investigation of core samples were applied to determine bulk density and specific density, total porosity and absolute per-

Table 1

Wells, depth, stratigraphy, and lithology of the studied rock samples

No.	Well	Year	Bottom depth [m]	Bottom stratigraphy	Sample depth [m]	Lithology	Age
869	H-IG1	1974	3520	Pt	3457	sandstone	Cm
870	O-IG1	1967	4298	Pt	4106	sandstone	Cm
871	P-IG1	1970	3930	Pt	3460	sandstone	Cm
872	S-IG1	1974	5120	Pt	3546	claystone	S
873	G-IG1	1972	3353.5	Cm	3012.3	sandstone	Cm
874	Ł-IG1	1975	5632	Cm	4588	sandstone	Cm
876	Si-IG1	1970	3010.3	Cm	3007.2	sandstone	Cm
877	T-IG5	1977	3850.5	Cm	3034	sandstone	O
878	Ż-IG1	1969	3276	Cm	3233	sandstone	Cm
879	L-IG1	1961	3310	O	3246.5	claystone	S
889	Br-1	1983	4065	C	3818	sandstone	C
892	C-IG2	1980	5020	P	4016	sandstone	P
894	Z-2	1976	4569.6	C	4498.6	sandstone	C
896	Op-PIG2	1991	3055	C	3045	sandstone	C

Explanations: No. – sample number, Year – drilling year, Age – age of the rock sample, Pt – Proterozoic, Cm – Cambrian, O – Ordovician, S – Silurian, C – Carboniferous, P – Permian.

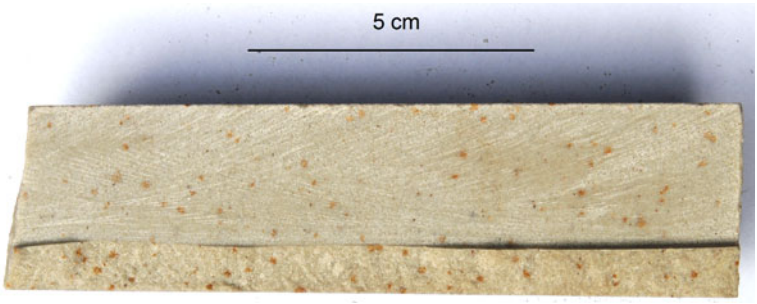

Fig. 1. Sandstone core sample No. 871, photo by M. Michna.

meability, *P*- and *S*-wave velocity, *etc.*, and special attention was paid to keep necessary preciseness and accuracy of measurements and determination of extreme values of measured parameters (Zalewska *et al*. 2011). The total porosity was determined on the basis of measurements carried out using two cooperative tools: pycnometer AccuPyc 1330 (specific density) and GeoPyc

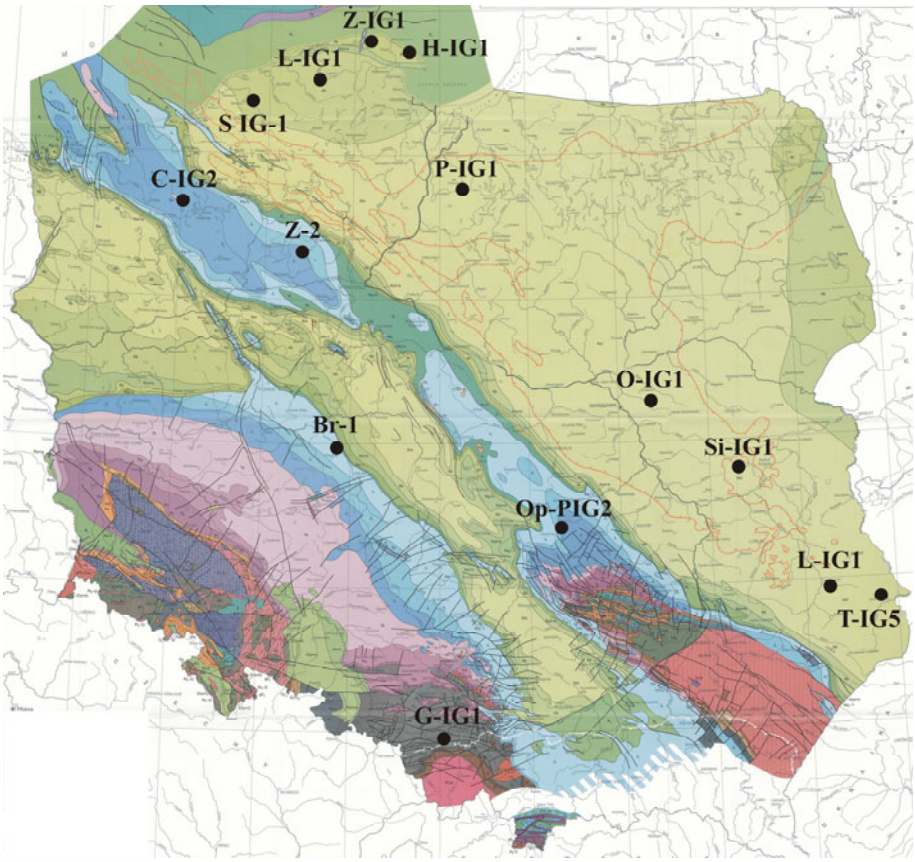

Fig. 2. Wells location on the geological map of Poland without Cenozoic deposits (Dadlez *et al.* 2000, modified); colours are related to stratigraphic units as follows: Proterozoic – red, Cambrian – dark green, Ordovician – dark violet, Silurian – dark blue, Devonian – brown, Carboniferous – grey, Permian – orange, Triassic – light violet, Jurassic – light blue, and Cretaceous – light green.

1360 (bulk density). An accuracy of porosity calculation was ± 1.5%. Permeability was measured using Gas Permeameter (Temco Co.) with resolution not exceeding the 0.01 mD.

Petrophysical properties of the selected rock samples (12 sandstones and 2 claystones) are presented in Table 2. Moderate variability of different parameters and rather small ranges of values of all presented variables are observed. For instance, bulk density of sandstones is in the range of 2.47-2.73 × 10^3 kg/m^3 and specific density varies in the range of 2.63-2.78 × 10^3 kg/m^3. Also, low total porosity (0.8-8.47%) and very low permeability (0.01-0.28 mD) are just going to show that special attention should be

paid to these rocks and strong relationships between various parameters may form the way to characterize such rocks with indirect methods.

Table 2

Petrophysical properties of studied rock samples

No.	$\delta_r \times 10^3$ [kg/m^3]	$\delta_b \times 10^3$ [kg/m^3]	Φ [%]	K [mD]	V_p [m/s]	V_s [m/s]	VC [wt%]	Φμ-CT [%]	Φmp [%]
869	2.65	2.57	3.18	0.05	5096	2591	6	1.7	0.83
870	2.68	2.55	4.79	0.01	4813	2615	5	2.5	0.74
871	2.63	2.61	0.80	0.01	4893	2729	0	0.5	0.29
872	2.71	2.62	3.15	0.01	5054	2751	17	3.7	0.77
873	2.71	2.66	1.76	0.02	4778	2772	11	1.6	0.37
874	2.64	2.61	1.22	0.28	5141	2497	1	1.7	0.24
876	2.69	2.57	4.41	0.06	4692	2260	15	2.6	0.18
877	2.66	2.57	3.25	0.01	5008	2705	2	3.9	0.82
878	2.70	2.47	8.47	0.01	4365	2454	16	2.1	1.21
879	2.74	2.73	1.50	0.01	5549	3140	33	0.4	0.13
889	2.78	2.69	3.36	0.07	4446	2522	41	0.9	0.17
892	2.70	2.66	1.31	0.03	4445	2494	4	0.9	0.26
894	2.67	2.6	2.46	0.01	5144	2647	3	1.3	4.43
896	2.70	2.72	1.50	0.01	5350	2598	21	0.4	0.09

Explanations: No. – sample number, δ_r – specific density, δ_b – bulk density, Φ – total porosity from laboratory measurements, K – absolute permeability from laboratory measurements, Vp – P-wave velocity, Vs – S-wave velocity, VC – clay minerals content from Roentgen analysis, Φμ-CT – porosity from computed microtomography, Φmp – porosity from mercury porosimetry.

3. METHODOLOGY

New technologies in laboratory investigations on rock plugs together with well-known verifiable techniques were the basis of detailed low porosity and low permeability rock analysis. Computed microtomography, NMR spectroscopy and mercury measurement confirmed the ability of detailed rock samples investigations to improve the precision of reservoir properties determination.

3.1 Nuclear magnetic resonance (NMR) measurements and interpretation

NMR technique applied in petrophysics and well-logging uses the effect of relaxation of protons in the hydrogen atoms in rock formation. Hydrogen oc-

curs in rocks in the form of water or hydrocarbons contained in rock pores, water bound in clay minerals and hydrogen included in hydroxyl groups in these minerals. The basic parameters observed in relaxation examination are: proton signal amplitude, spin-lattice relaxation time T_1 and spin-spin relaxation time T_2 (Andrew 1969). These parameters are the source of detailed information about porosity (total and effective), irreducible water saturation and permeability of reservoir rocks, pore space structure and type of liquid filling rock pores (Coates *et al*. 1999). In the multiphase systems, *e.g.*, rocks where media of diverse quality fill the complex rock pore space, the spin-spin relaxation curve can be presented as a sum of components characterized by the relaxation time T_2. The continuous distribution of relaxation times is directly related to distribution of pore sizes in the examined rock sample. Individually selected T_2 cut-offs included into interpretation of NMR signals improve the determination of bound water volume and moveable media in rock formation (Liu *et al.* 2007).

NMR measurements were performed using NMR Maran7 equipped with permanent magnet generating 0.186 T intensity field. Frequency of hydrogen nuclei precession was equal to 7.9 MHz. Measurements were carried out in the temperature of 35° C. Core samples (0.04 m in length and 0.0254 m in diameter) were saturated with brine (NaCl mineralization = 50 g/l). Before each measurement series, a control measurement on the standard reference was done. Standard reference (porosity = 15%) was saturated with brine (containing hydrogen and deuterium) of NaCl mineralization = 50 g/l. Spin-spin relaxation times were measured with pulse methods using the Carr–Purcell–Meiboom–Gill spin echo methodology.

Based on T_2 relaxation times distributions and standard T_2-cut-offs for clastic rocks (3 and 33 ms), which are known from literature, *e.g.*, Coates *et al*. (1999), Kenyon (1992), Kleinberg and Vinegarm (1996), Straley *et al.* (1997), total, effective and dynamic porosity was calculated. Cut-offs underline differences in porosity values related to water bound in clays or micropores ($T_2 < 3$ ms), capillary water ($T_2 > 3$ ms and $T_2 < 33$ ms) and large pores filled with free water ($T_2 > 33$ ms). Results of division into free, capillary and clay-bound water are shown in Table 3 and Fig. 3. Cumulated NMR signals normalized in relation to the maximum value were calculated and presented *versus* relaxation time T_2 to characterize the place of protons in the rock pore space (Fig. 4). Graphs of cumulated signals are used for qualitative description of the porous space in rocks. Three groups can be distinguished among the cumulated and normalized signals. Concave curves belong to the first group (*e.g.*, 872, 876) corresponding to the rocks in which smaller pores or fractures dominate. The course of convex curves is typical for the rocks (*e.g.*, 877) in which medium migration is performed in large-diameter pores or fractures. The third group consists of graphs of nearly con-

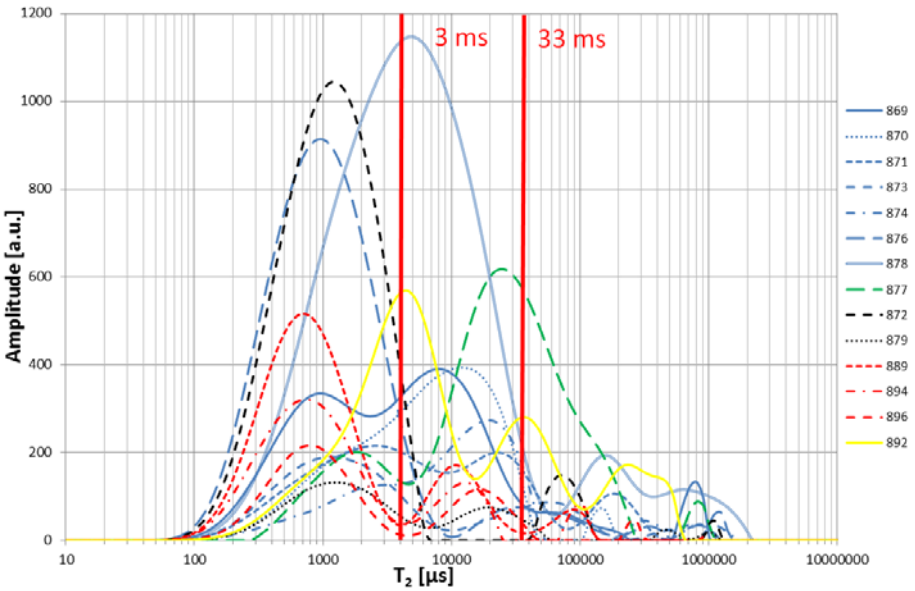

Fig. 3. T_2 distributions with division into clay-bound water, capillary water, and free fluid. Colours: Cambrian – blue, Ordovician – green, Silurian – black, Carboniferous – red, and Permian – yellow.

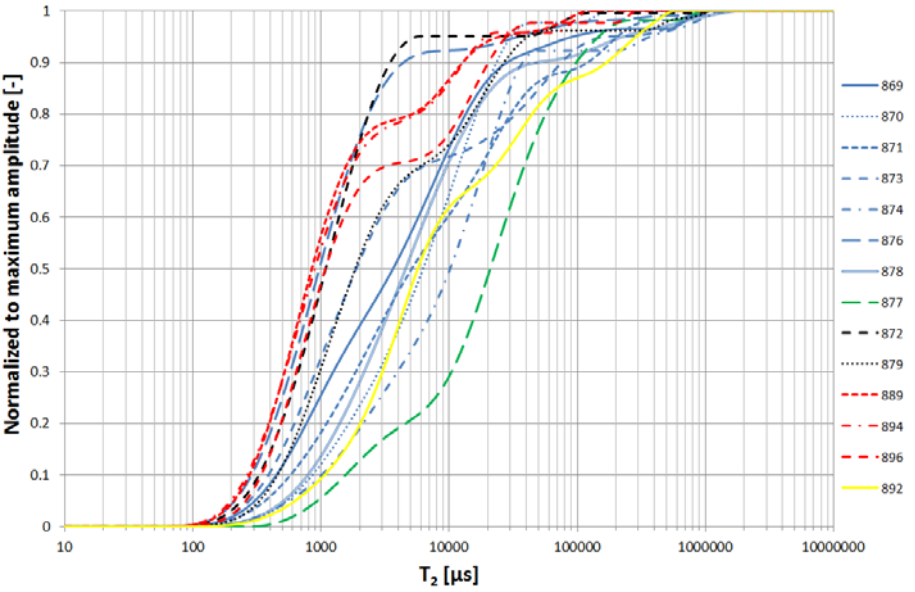

Fig. 4. Normalized cumulative NMR signal *versus* T_2 relaxation time. Colours as in Fig. 3.

Table 3

Results of the NMR interpretation using standard cut-offs

No.	$Kp1$ [%]	$Kp2$ [%]	$Kp3$ [%]	Φ_{NMR} [%]	$\Phi_{NMR,ef}$ [%]	S_w irr [%]	K [nD]	K_C [nD]	K_{SDR} [nD]	K_{WWZ} [nD]	FZI_C [μm]	FZI_{SDR} [μm]	FZI_{WWZ} [μm]	Class
869	3.31	3.02	0.65	6.98	3.67	47.42	50	191	9844	291808	0.06	0.43	2.32	2
870	1.86	3.56	0.26	5.68	3.82	32.75	10	49	15481	439030	0.03	0.50	2.68	2
871	0.95	0.91	0.45	2.31	1.36	41.13	10	20	285	5836	0.09	0.33	1.49	1
872	3.29	0.25	0.18	3.72	0.43	88.44	10	0.01	0.69	327	0.01	0.09	2.01	2
873	0.66	0.19	0.22	1.07	0.41	61.68	20	0.19	1.4	51	0.05	0.14	0.85	1
874	0.86	1.94	0.45	3.25	2.39	26.46	280	84	3738	86165	0.08	0.51	2.43	2
876	5.05	0.5	0.31	5.86	0.81	86.18	60	0.13	9	3034	0.02	0.13	2.35	2
877	0.84	2.22	1.76	4.82	3.98	17.43	10	8301	49596	121170	0.35	0.85	4.18	2
878	3.29	3.98	0.95	8.22	4.93	40.02	10	1009	44301	102515	0.09	0.57	2.76	2
879	0.7	0.33	0.09	1.12	0.42	62.50	10	0.02	1.34	57	0.02	0.13	0.86	1
889	1.23	0.27	0.07	1.57	0.34	78.34	70	0.00	0.28	46	0.01	0.08	1.08	1
892	0.8	1.08	0.64	2.52	1.72	31.75	30	101	973	18641	0.14	0.43	1.87	2
894	0.62	0.15	0.03	0.80	0.18	77.50	10	0.00	0.02	3	0.01	0.06	0.76	1
896	0.74	0.28	0.04	1.06	0.32	69.81	10	0.00	0.31	24	0.01	0.10	0.84	1

Explanations: $Kp1$ – irreducible water, $Kp2$ – capillary-bound water, $Kp3$ – moveable water, Φ_{NMR} – total porosity from NMR, $\Phi_{NMR,ef}$ – effective porosity from NMR, S_W irr – irreducible water saturation, K_C – permeability calculated from Coates model, K_{SDR} – permeability calculated from SDR model, K_{WWZ} – permeability calculated from clay-bound water model, FZI_C – flow zone index calculated using K_C, FZI_{SDR} – flow zone index calculated using K_{SDR}, FZI_{WWZ} – flow zone index calculated using K_{WWZ}, Class – classes from cluster analysis.

stant slope, *e.g.*, 870, 878, which illustrate behavior of hydrogen nuclei in the porous space consisting of diverse diameter pores. In analyzed data sets, domination of samples with high peak for T_2 about 3 ms (Fig. 3) and group of concave curves are observed (Fig. 4).

3.2 Permeability calculation and Fluid Flow Unit description

Permeability depends on the size of connecting pore throats between pores and the pore bodies. For hydrogen nuclei in porous media, the T_2 relaxation time is mainly influenced by the pore bodies. Basing on the division into free, capillary and clay-bound water, the permeability was calculated. Values of $Kp1$ (irreducible water: clay-bound water and water closed in micropores), $Kp2$ (capillary-bound water), and $Kp3$ (moveable water) was used for two well-known permeability models:

(1) Coates model:

$$K_{\mathrm{C}} = \left[\left(C\varphi_{\mathrm{NMR,ef}} \right)^2 \left(\frac{Kp3}{Kp1 + Kp2} \right) \right]^2 , \tag{1}$$

where $\Phi_{\mathrm{NMR,ef}}$ is the effective porosity from NMR [frac], $Kp3$ is the free fluid index [frac], $Kp1 + Kp2$ is the bulk volume index [frac], K is the permeability [mD], C is the empirical coefficient, equal 10 (Coates and Denoo 1981, Coates *et al.* 1999).

(2) SDR model:

$$K_{\mathrm{SDR}} = a\Phi_{\mathrm{NMR,ef}}{}^4 T_2^2 lm , \tag{2}$$

where T_2lm is the T_2 logarithmic mean [ms], a is the empirical coefficient, usually equal 4 (Kenyon 1992).

Coates and SDR models work better for the high porosity and permeability samples (Kleinberg and Vinegarm 1996, Straley *et al.* 1997, Puskarczyk 2011, Puskarczyk and Jarzyna 2012). It was decided to add a third permeability calculation model, relating to the clay-bound water:

(3) Clay-bound water model:

$$K_{WWZ} = \left(c\Phi_{\mathrm{NMR,ef}} \right)^4 \left(\frac{\Phi_{\mathrm{NMR}} - Kp1}{Kp1} \right)^2 , \tag{3}$$

where $Kp1$ is the clay-bound water [frac], c is the empirical coefficient, usually equal 10, Φ_{NMR} is the total porosity from NMR [frac].

This model excludes clay-bound water content but uses capillary-bound water. It is very important to take into account water closed in micropores in low porosity and low permeability samples.

Values of absolute permeability were estimated on the basis of NMR parameters (Table 3). The results of later calculations turned off to be more precise than other permeability values (Coates and Denoo 1981). Next, permeability values were used to estimate the flow zone index (FZI) values. Calculations were made on the basis of NMR parameters obtained from the interpretation (Table 3).

High correlation between effective porosity (NMR) and permeability calculated on the basis of NMR is observed (Fig. 5). There is no correlation between laboratory permeability measurement results (pink) and effective porosity (NMR). Higher determination coefficient (r^2) for clay-bound water model (WWZ) confirmed the sense of using this approach. Results of permeability calculation using WWZ model are the closest to laboratory measurements. The WWZ model reflects the clay-bound water contribution in the total water content, which is significant in this type of rocks.

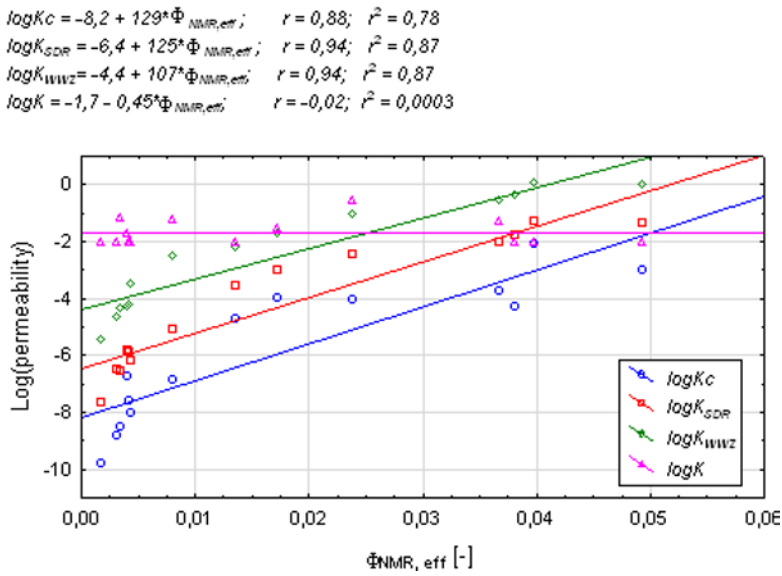

Fig. 5. Relationship between permeability *versus* porosity; permeability was calculated according to various formulas (symbols are explained in Table 3).

The NMR measurement provides information about effective porosity and irreducible water saturation. Permeability calculated from NMR is only estimation and logarithm of permeability *versus* porosity relationship could be different from linear. Flow zone index (FZI) was used to obtain Fluid Flow Unit characterization of investigated rocks (Amaefule *et al.* 1993). Flow zone index (FZI) includes indirect information on pore throats and also on pores and grains distributions. The FZI parameter changes according to geological features as texture and structure of the rock. A low value of FZI is related to high tortuosity and low permeability.

FZI was calculated for standard NMR interpretation results. Inspection of results revealed two groups of samples responding to two Fluid Flow Units with similar factors. For division, the cluster analysis was used. The purpose of cluster analysis is to assemble observations into relatively homogeneous groups. For the discussed data sets, cluster analysis was performed by *k*-means methods (MacQueen 1967). The *k*-mean clustering aim is to partition the observations into clusters, in which each observation belongs to the cluster with the nearest centroids. When the objects are assigned, the positions of centroids are recalculated. The procedure is repeated until the centroids movement is stopped. The members of clusters are at once alike and at the same time unlike members of other groups. There is no analytical solution to this problem, which is common to all areas of classification.

Cluster analysis was performed for each permeability model (1)-(3) (Table 3). Results of classification were the same. For further analysis, the WZ model (3) was chosen, because of the best fitting results. It was decided that this model provided the best permeability estimation for the analyzed data.

The first class comprised samples number 871, 873, 879, 889, 894, and 896 with FZI values less than 1.8 μm and the second one – samples number 869, 870, 872, 874, 876, 877, 878, and 892 with FZI above 1.8 μm (Fig. 6). The FZI cutoff was selected after statistical analysis (histograms, scatterplots, *etc*.) of the total FZI values from the whole data set. The highest value of determination coefficients r^2 of log permeability *versus* porosity function was obtained within both groups of data for WWZ model in comparison to other two models. The same relationship for the full data set achieved the highest correlation coefficient but authors decided to keep the division into two separate groups. The red group (FZI ≤ 1.8 μm) of effective porosity less than 1.5% (average 0.5%) and permeability less than 0.005 mD (average 0.001 mD) represented the Carboniferous and some Cambrian samples. The blue group (FZI > 1.8 μm) of higher porosity (average effective porosity equal to 2.7%) and permeability (average 0.38 mD) consisted mainly of the Cambrian samples. The Permian sample was classified in the red group and two Silurian samples in both groups.

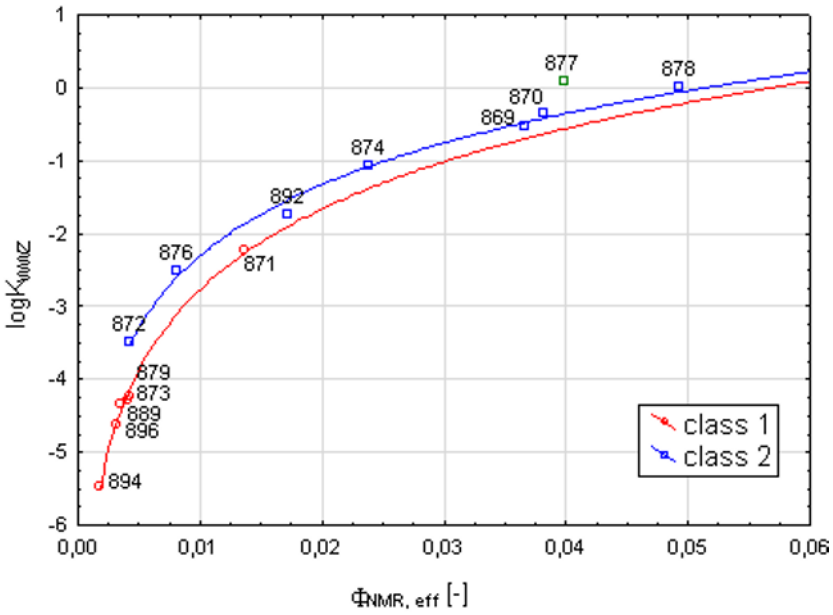

Fig. 6. Permeability *versus* porosity relationship according to FZI division; improved NMR interpretation using WWZ permeability calculation model.

3.3 Visualization and processing of mercury porosimetry results

Mercury porosimetry is a well-known and useful technique of porous space investigation and provides the following parameters: total intrusion volume, median pore diameter-volume, median pore diameter-area, average pore diameter, porosity, threshold pressure, characteristic length, and tortuosity (Pittman 1992, Vavra *et al.* 1992, Webb 2001). Mercury porosimetry measurements were performed using porosimeter AutoPore IV 9500.

Improved approach of presentation and processing of mercury porosimetry data was applied to obtain relationships between the reservoir parameters: effective porosity (Φmp), permeability (*K*), and other factors from NMR (Table 3) and Swanson parameter (Swanson 1980, Thomeer 1983). Computerized processing of cumulative volume of mercury *versus* pressure from porosimetry curves provided automatic coordinates for Swanson parameter calculation (Wojtanowski 2011) (Fig. 7).

Computerized processing of selected mercury porosimetry results revealed 3 porous systems in the majority of rocks. Each porous system was characterized by Thomeer hiperbola presented in pressure [psi] *versus* volume of mercury [mL/g] coordinate frame (Fig. 7), Swanson parameter (coordinates: *Spc versus Sbv*), threshold pressure or extrapolated displacement pressure (*Pd*), and total porosity of system (*Bv*). Swanson parameter coordinates are defined as bulk volume of mercury (*Bv)* and pore pressure (*Pc)* at the inflection point on the *Pc versus Bv* plot. Swanson parameter may be also defined as the apex at the plot of *Bv/Pc versus Bv* (Mao *et al.* 2013). Threshold pressure (*Pd*) and total porosity (*Bv*) of selected pore systems mean pressure at which mercury starts to intrude into pore system and bulk volume occupied by mercury, respectively. For each system, average pore diameter was also determined on the basis of mercury volume *versus* pore

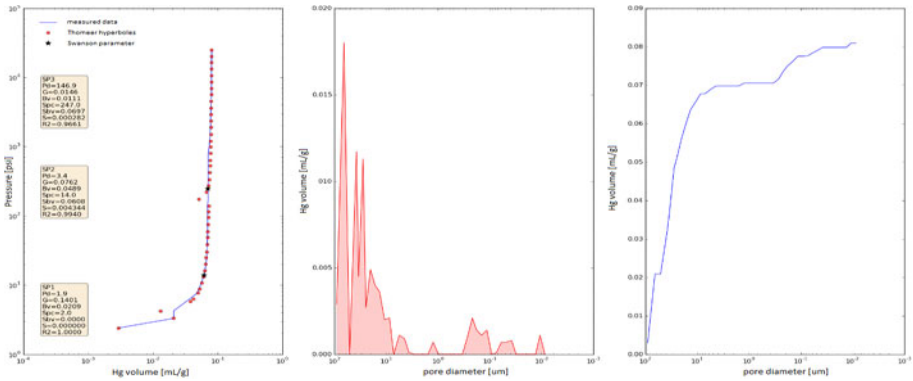

Fig. 7. Result of computerized processing of the mercury cumulative volume *versus* pressure for 892 sample; three pore systems were distinguished.

diameter plot. Relationships between selected variables turned out to be quite strong and useful in determining porosity and pore diameters. Swanson parameter was also well correlated with individual parameters, *i.e.*, threshold pressure and total porosity and also with the specific reservoir parameter calculated as the square root of permeability and porosity (Jarzyna and Puskarczyk 2010, Xiao *et al.* 2008). Presented plots and statistical formulas are the tools for calculating extreme values of porosity and determining low pore diameter range on the basis of computerized processing results. Also, results of porosimetry harmonize with NMR outcomes and micro-CT solutions.

Several examples of relationships between various parameters characterizing pore space of examined rocks are presented (Figs. 8-11) and discussed. Of great importance is the strong correlation between average pore diameters in pore systems and pressure values at which mercury intrudes into pore system. Results for various pore systems illustrated by different hyperbolas determined in automatic processing of mercury porosimetry outcomes matched to the same relationship (Fig. 8).

The definition of Swanson parameter pointed out its close relationship with bulk volume of mercury in pore system. Dispersion of data in Fig. 8 was caused by not fully precise hyperbola matching to the measured data. The first pore system assigned to the highest volume of intruded mercury revealed the best correlation (Fig. 9). Two other pore systems assigned to low bulk volumes of mercury (and low diameters of pores) cannot be distin-

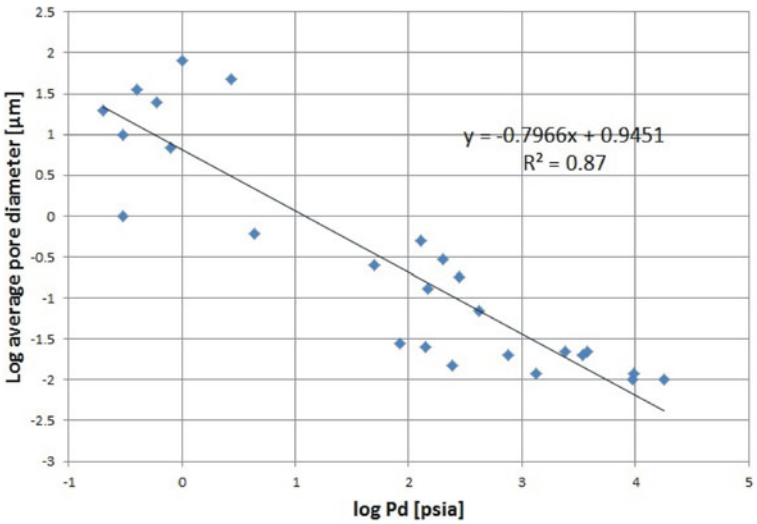

Fig. 8. Relationship between the average pore diameter in pore systems and the threshold pressure, *Pd*.

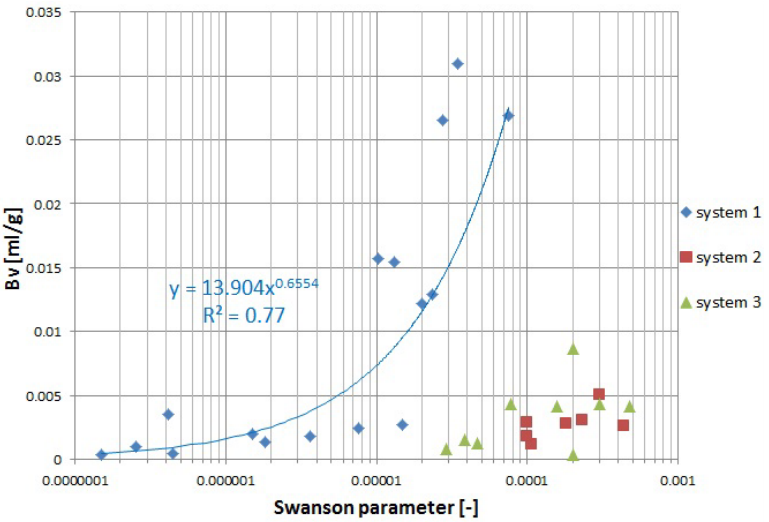

Fig. 9. Relationship between bulk volume occupied by mercury for each pore system *Bv* and the Swanson parameter.

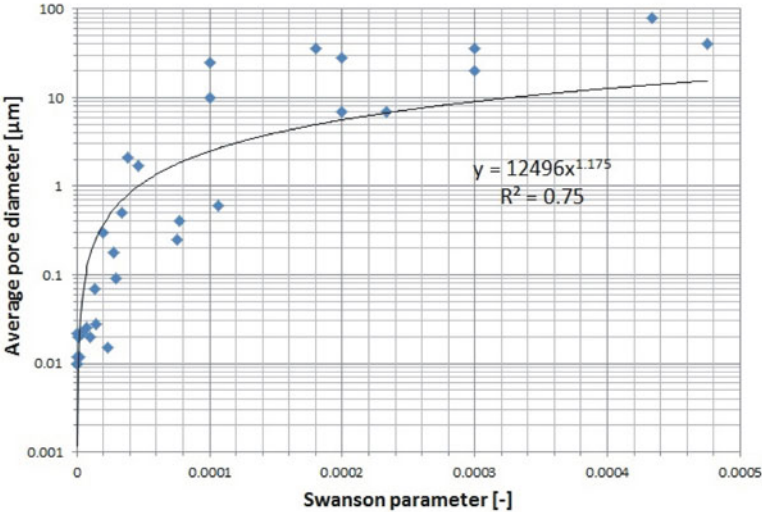

Fig. 10. Relationship between the average pore diameter in pore systems and the Swanson parameter.

guished. It means that the applied criteria for distinguishing the Thomeer hyperbolas did not work properly in each case. Swanson parameter well correlates also with average pore diameter in pore systems (Fig. 10). This relationship holds true for the full data set.

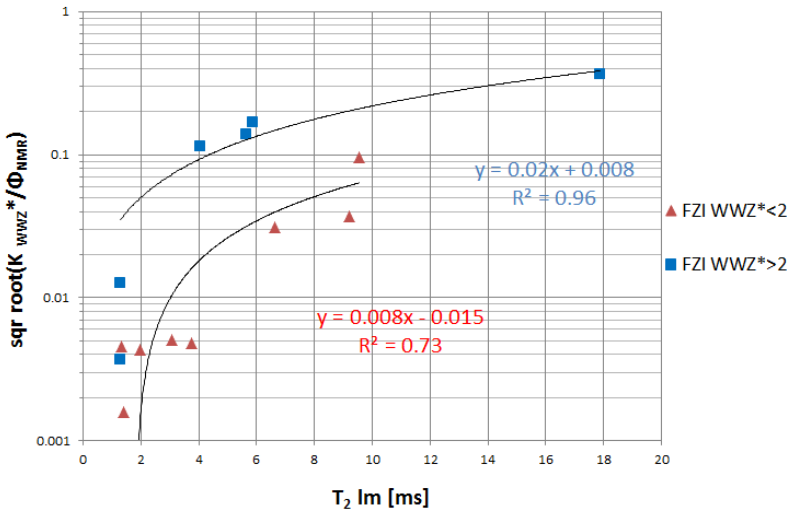

Fig. 11. Relationship between square root of the ratio of permeability calculated using WWZ model to the total porosity from NMR *versus* T_2 logarithmic mean, T_2lm.

An attempt to combine the NMR results with the MP results was made. Relationships between specific petrophysical parameter defined as square root of permeability and porosity ratio *versus* T_2 logarithmic mean showed high determination coefficients (Fig. 11). Samples were grouped in FZI_{WWZ} manner.

Similarity of cumulative NMR T_2 distributions and MP results is presented in Figs. 12-15. Analysis of the plots explains also the dispersion of data in the relationships presented above and sheds light into different ranges of amplitude of NMR distributions, different arrivals of signals and shows various pore systems revealed in porosimetry. From the whole group of cumulative T_2 distributions, only Cambrian samples indicate almost flat (constant gradient) run of the curves, which gives the information that pores of different diameters but still in the low range simultaneously took part in fluid flow. Figures 12-15 show that in low porosity and low permeability samples, the mercury volume increases stepwise (only three from the 14 samples: one Carboniferous and two Cambrian samples do not follow these ways). It means that the mercury had to force the narrow and complex pore throats or had to imbibe by the opening microfractures. For this group of samples, two pore systems were distinguished: one relating to the pore system and second to the fracture system. The rest of the analyzed samples are characterized with the cumulative T_2 distribution curves reflecting the pores' size in the range of irreducible water saturation and capillary-bound water saturation (subcapillary and capillary pore diameters).

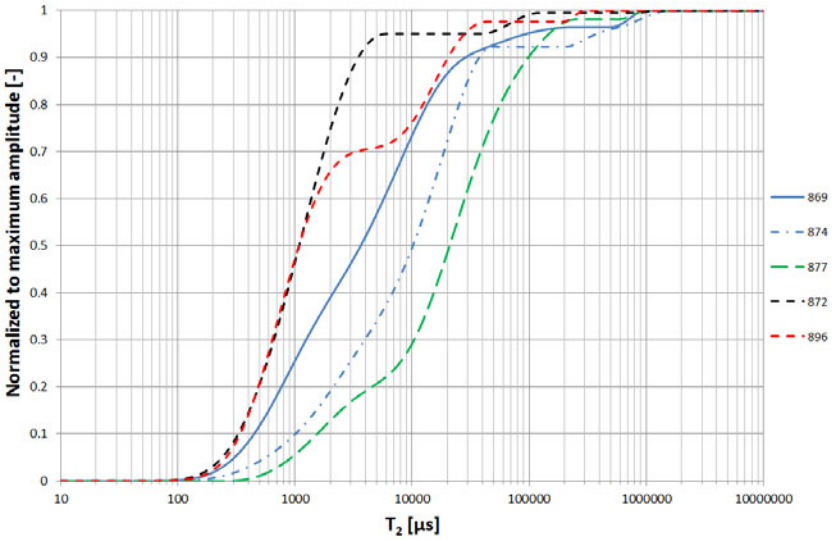

Fig. 12. Cumulative T_2 distributions of NMR signals for selected samples. Colours as in Fig. 3.

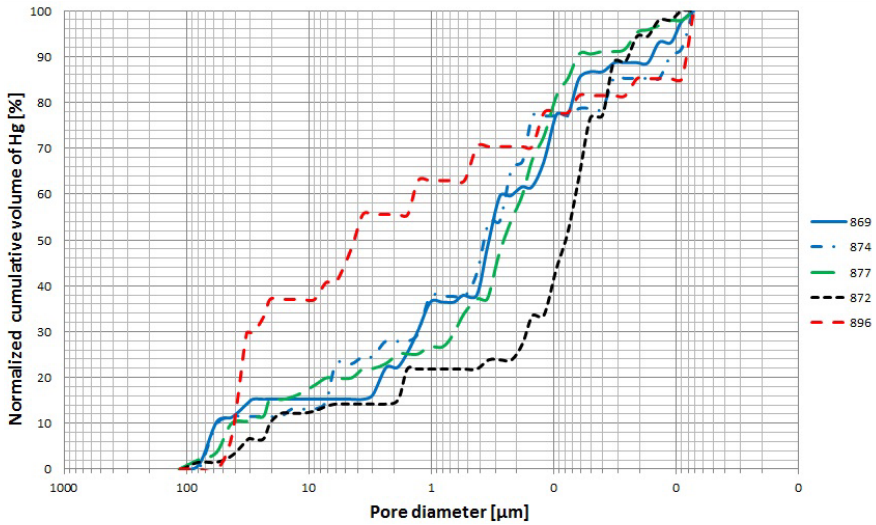

Fig. 13. Mercury porosimetry results for selected samples. Colours as in Fig. 3.

An influence of clay minerals volume was observed in the NMR and porosimetry cumulative curves behavior. Samples characterized with higher clay content have a convex run of the curve (sample No. 872, clay volume equal to 17%) while the concave curves pertain to low clay content samples

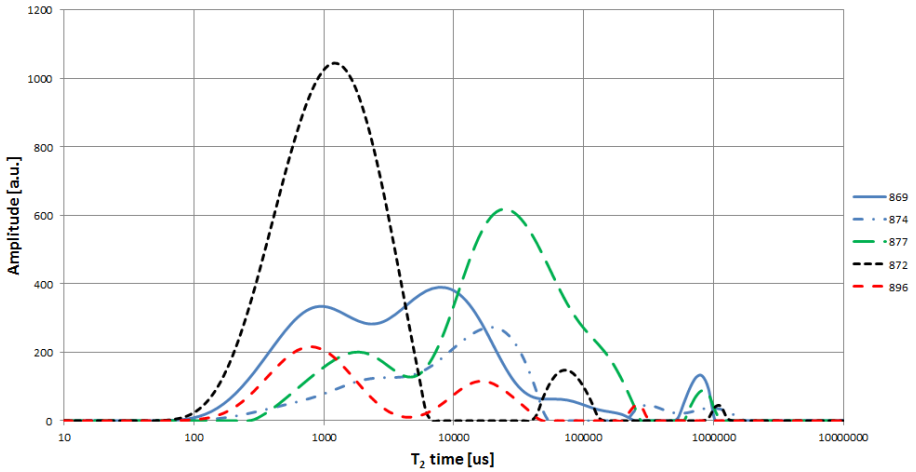

Fig. 14. T_2 distributions for selected samples. Colours as in Fig. 3.

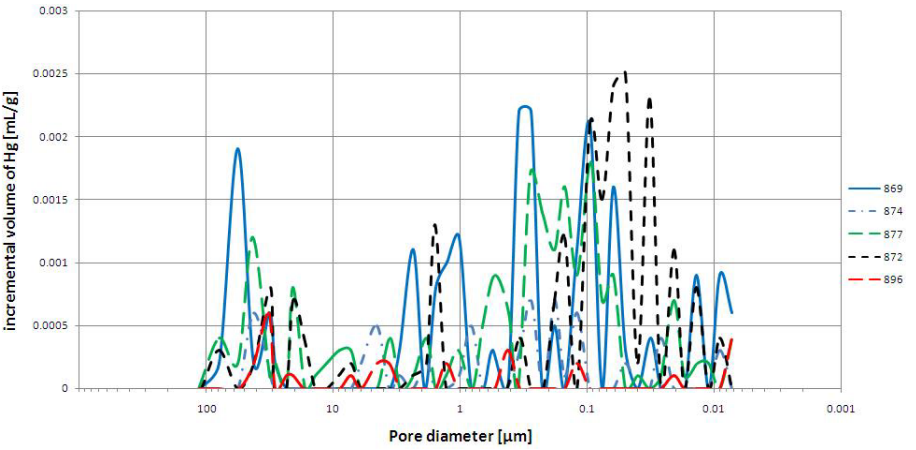

Fig. 15. Incremental volume of mercury *versus* pore diameter for selected samples. Colours as in Fig. 3.

(sample No. 896, clay volume equal to 21%) which is also reflected in incremental volume of mercury (Fig. 14).

Joint analysis of NMR curves and MP plots gave the data set for calculating a relationship between pore diameter and T_2 time. Immediate comparison of T_2 distributions (Fig. 14) and incremental volume of mercury (Fig. 15) is rather difficult, but detailed inspection of the sequences of maxima on both plots enables mutual assigning of pore diameter and T_2 time distribution.

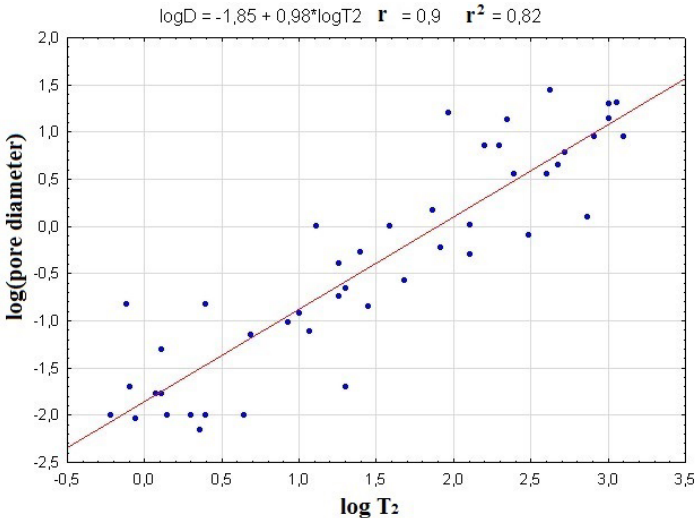

Fig. 16. Relationship between logarithm of pore diameter and logarithm of transverse relaxation time, T_2.

On the basis of the data collected, the correlation relation between the relaxation time T_2 and the pore diameter was calculated. Despite of complicated pore and fracture systems in analysed samples, the correlation coefficient was high ($r = 0.9$). Linear regression (Fig. 16) was observed for logarithm value of pore diameter and T_2 time (determination coefficient equal $r^2 = 0.82$). The equation obtained can be used for pore size estimation based on NMR measurements.

3.4 Computed microtomography (micro-CT, μ-CT)

Computed microtomography is one of the modern, non-destructive research methods allowing to investigate the object using X-rays and present the pore space image of the examined sample (Zalewska *et al*. 2010, Bielecki *et al.* 2012, Dohnalik 2013). Processing of the 3D μ-CT image provides the information about porosity, number and length of the pore channels, their connections, directions of fluid flow, and structure. Results of μ-CT enable also permeability modelling (Arns *et al.* 2005, Bielecki 2011). The measurements were performed using Benchtop CT160 microtomograph. The results of the 3D visualization of the pore space were obtained using AVIZO software and were illustrated in the video form, colouring pore space in green and rock matrix in grey. MAVI software allowed determination of the qualitative petrophysical information which was presented graphically (Figs. 17 and 18) and numerically (Figs. 19-22).

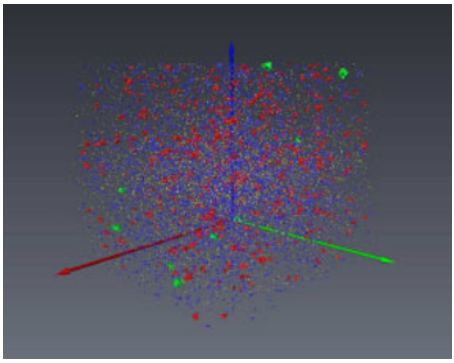

Fig. 17. Microtomographic characteristics, sample No. 871.

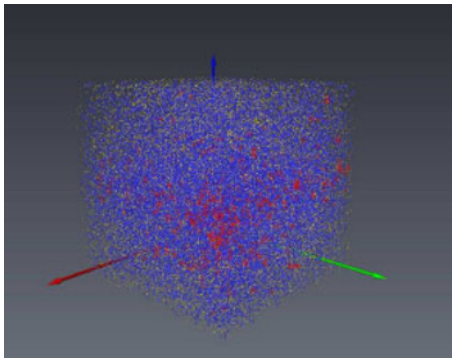

Fig. 18. Microtomographic characteristics, sample No. 876.

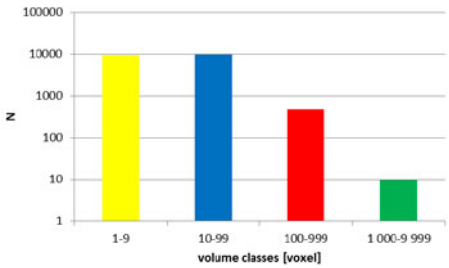

Fig. 19. Number of porosity subgroups (*N*) refers to volume class, sample No. 871.

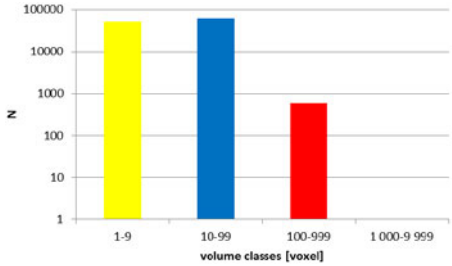

Fig. 20. Number of porosity subgroups (*N*) refers to volume class, sample No. 876.

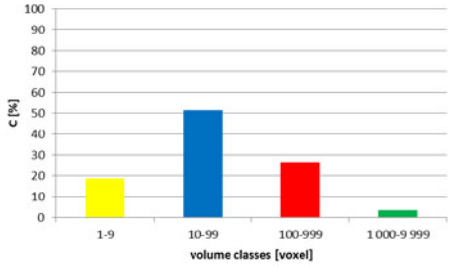

Fig. 21. Volume class percentage (*C*) referring to class volume, sample No. 871.

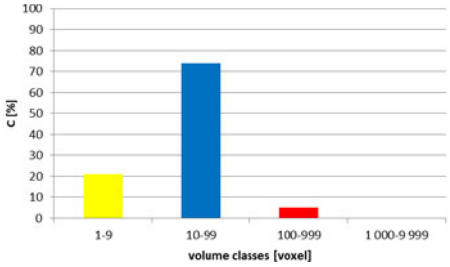

Fig. 22. Volume class percentage (*C*) referring to class volume, sample No. 876.

The results of porosity determination were based on the pore space division into subgroups. Each subgroup consists of the pores connected with each other but not communicated with pores from other subgroups. Subgroups are divided into classes regarding their volume. Volume class unit is voxel. In the presented results 1 voxel [v] is equal to $5.8 \times 5.8 \times 5.8 =$

195 μm^3 and is the smallest volume which could be detected using Benchtop CT160 microtomograph and available samples. Spatial visualization of the pore space is made at the beginning. The visualized sample is cuboid with the size 950 × 950 × 400 v, measured in the *X*, *Y*, and *Z* directions. The subsample size is equal to 1/4 of the whole sample size (475 × 475 × 400 v). The effect of the further analysis is the distinction of the six volume classes of the subgroups in the whole visualized pore space (Table 4).

Table 4

Description of classes

Class volume	I	II	III	IV	V	VI
Number of voxels	1-9	10-99	100-999	1 000-9 999	10 000-99 999	> 100 000
Maximum number of μm^3	1 755	19 305	194 805	1 949 805	19 499 805	> 19 500 000

Figures 17 and 18 visualize the distribution of the pores classes, where each volume classes correspond to the one colour, *i.e.*, I – yellow, II – blue, III – red, IV – green, V – white, and VI – violet. Graphs in two versions are presented in Figs. 19-22. The first group (Figs. 19 and 20) presents the number of subgroups in particular volume class what refers to class splitting. The second group (Figs. 21 and 22) presents the volume of class contribution in the total pore space volume in percentage. The micro-CT results are presented for two sandstone samples: 871 and 876 (Figs. 17-22) showing the difference in the pore network (Figs. 17 and 18). Sample No. 876 revealed higher porosity than sample No. 871. Pore space distributions are different in these two samples. Red subgroups (100-999 v) are concentrated in one part of the sample No. 876 and sample No. 871 occurs to be more homogenous. Sample No. 876 is more porous but less homogenous. Porosity calculated from computed microtomography for sample No. 871 is equal to $\Phi\mu$-CT = 0.5% and for sample No. 876 $\Phi\mu$-CT = 2.6%. Porosity from computed microtomography, $\Phi\mu$-CT, was lower than porosity calculated from standard laboratory measurements (Table 2).

Comparison of the subgroup numbers in the particular volume class (Table 5) provides information that the most diverse pore space is in the Cambrian and Ordovician samples. The Permian sample is characterized by irregular pores distribution. Within the subgroups with the smallest volume (class I and II), one subgroup belongs to class V. The Carboniferous samples are mainly composed of subgroups from classes I and II.

Table 5

Number of subgroups in the volume classes

No.	I	II	III	IV	V	VI
869	27406	23253	1581	124	7	–
870	22395	74821	2212	75	–	–
871	9310	9718	478	10	–	–
872	62183	92182	3576	12	–	–
873	54450	53489	134	–	–	–
874	50781	51647	922	6	–	–
876	51326	60826	598	–	–	–
877	62615	82790	2982	200	8	–
878	42818	33726	692	31	8	2
879	25623	13042	–	–	–	–
889	54036	44096	127	–	1	–
892	17009	37397	84	1	–	–
894	95853	91307	553	9	–	–
896	16435	12912	47	–	–	–

Another important issue is related to fluid flow capability. Analyzed samples are in general impermeable or having permeability less than 0.01 mD (it was confirmed by micro-CT images in voxel resolution). Micro-CT analysis proved that there is no connection between pores subgroup from the opposite walls of the analyzed sample (cuboid). It means there is no fluid flow capability. Only 3 from the 14 samples indicated pore connections between the opposite walls. These samples, one Cambrian (No. 878) and one Ordovician (No. 877), are composed of subgroups from higher classes (class V and VI). One Cambrian sample (No. 876) consisting of subgroups I-III reached also the opposite walls connection.

Fractures and microfractures can be observed in the microtomographic images, as in Fig. 23. The qualitative estimation of complexity of pore space structure plays an important role in rock susceptibility to hydraulic fracturing. Thanks to microtomographic image, the initial evaluation of pore space homogeneity can be realized. From the whole data set, the Cambrian samples are characterized by the most uniformly distributed pores, which may indicate the controlled fracturing process but on the other hand difficulties in the fracturing itself.

High resolution of computed tomography, its ability to detect pores in micro and nano scale and determine mutual connections between them is crucial in the case of analyzing tight formations. Micro-CT results are useful

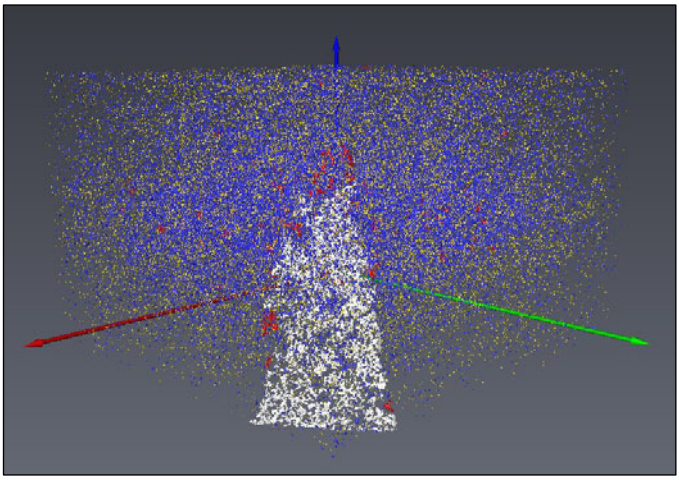

Fig. 23. Microtomographic image of the Carboniferous sandstone, microfractures marked in white; sample No. 889.

for estimation of fluid flow capability in pore space, mainly because the fluid flow is realized in macro- and mezopores (natural and after fracturing) (Montaron 2008). Nowadays, computed tomography offers measurement also in nano scale, which could be more useful in tight formation analysis than the one proposed there.

4. DISCUSSION AND CONCLUSIONS

Combination of the results from various methods with different physical background turned out to be an effective tool in examination of hard, low-porosity, and low-permeability old formations. Signals from various methods provided different porosity values and by joining them together new characteristics of the reservoir properties of investigated rocks were revealed. Differences in porosity values obtained from NMR, MP, and micro-CT were visible. Porosity from NMR was generally higher than from the other methods because of receiving the signal from the all pores and fractures systems in the pore samples. Porosity from micro-CT is lower and connected with the tool resolution. MP results indicated the microfracturing process occurring in the samples during the measurements.

The most justified method from the point of physical background in porosity determination is the NMR measurement. In the analyzed case, the micro-CT takes into account pores larger than $5.8 \times 5.8 \times 5.8\ \mu m^3$, which, in the case of tight formations, underestimates the porosity value but is crucial to estimate the fluid flow capability. Porosimetry together with micro-CT give the information about the pores distribution. However, porosimetry is the de-

structive method and the influence of mercury injection on core sample should be taken into account (overestimated effective porosity). Standard porosity measurements (pycnometer) meet requirement as a reference measurement of total porosity.

The NMR signals and T_2 relaxation time distributions, cumulated curves of effective porosity and pore geometry distributions related to components of the rock porous space. Also graphs of cumulated pore specific surface were used for qualitative description of the porous space in rocks. Permeability calculated from NMR interpretation parameters is more accurate than standard laboratory measurements for low porosity, low permeability reservoirs in analyzed case, and available equipment. The cluster analysis and FZI approach lead to more precise information about fluid flow abilities. In addition to giving standard parameters like effective porosity, average pore diameter or tortuosity, the MP may be also analyzed in terms of hydraulic properties. Swanson parameter is defined at the point in which mercury fills the connected pores responsible for the permeability and starts to squeeze into blind pores. Integration of NMR and MP results enabled getting the information on pore diameter and extrapolation of the relationship to lower pores.

Microtomography allowed analyzing the pore space structure: pores orientation in pore space formation, microfractures presence and their directions, porosity values and distribution. Micro-CT images informed about the pore space parameters graphically and numerically. 3D investigations in micro-CT explained the complexity of pore space in tight rocks.

A new approach to combine the results of various methods for the effective analysis of tight, low porosity, and low permeability rocks is needed with the aim of not omitting the potential of tight reservoirs.

Acknowledgments. The authors express their gratitude to Polish Ministry of the Environment and Polish Geological Institute – National Research Institute, Warsaw, Poland, for the data. Laboratory measurements apart from mercury porosimetry were done in the Oil and Gas Institute, Kraków, Poland. Mercury porosimetry measurements were done in AGH UST, Faculty of Geology Geophysics and Environment Protection, Department of Fossil Fuels by Roman Semyrka, Ph.D. eng.

The project was founded by the National Science Centre on the basis of decision DEC-2011/03/N/ST10/05354, No. AGH 18.18.140.244.

Research was also financially supported by AGH UST FGGEP grant No. 15.11.140.053 for Ph.D. students in 2011 and statutory funds at AGH UST FGGEP, Kraków, Poland.

References

Amaefule, J.O., M. Altunbay, D. Tiab, D.G. Kersey, and D.K. Keelan (1993), Enhanced reservoir description: using core and log data to identify hydraulic (flow) units and predict permeability in uncored intervals/wells. **In:** *SPE Ann. Technical Conference and Exhibition, 3-6 October 1993, Houston, USA*, SPE 26436-MS, 205-220, DOI: 10.2118/26436-MS.

Andrew, E.R. (1969), *Nuclear Magnetic Resonance*, Cambridge University Press, Cambridge.

Arns, C.H., F. Bauget, A. Ghous, A. Sakellariou, T.J. Senden, A.P. Sheppard, R.M. Sok, W.V. Pinczewski, J.C. Kelly, and M.A. Knackstedt (2005), Digital core laboratory: Petrophysical analysis from 3d imaging of reservoir core fragments, *Petrophysics* **46**, 4, 260-277.

Bakun-Czubarow, N. (1984), Petrology and elements of geochemistry.**In:** J. Leliwa-Kopystyński and R. Teisseyre (eds.), *Constitution of the Earth's Interior. Vol. 1*, Physics and Evolution of the Earth's Interior, PWN – Polish Scientific Publ., Warszawa, Elsevier, Amsterdam, 326-357.

Bielecki, J. (2011), Investigation of complex structures by means of computed tomography method, Ph.D. Thesis, Institute of Nuclear Physics, Polish Academy of Sciences, Poland.

Bielecki, J., S. Bożek, E. Dutkiewicz, R. Hajduk, J. Jarzyna, J. Lekki, T. Pieprzyca, Z. Stachura, Z. Szklarz, and W.M. Kwiatek (2012), Preliminary investigations of elemental content, microporosity, and specific surface area of porous rocks using PIXE and X-ray microtomography techniques, *Acta Phys. Pol.* **121**, 2, 474-479.

Coates, G., and S. Denoo (1981), The producibility answer product, *The Tech. Rev.* **29**, 2, 54-63.

Coates, G.R., L. Xiao, and M.G. Prammer (1999), *NMR logging. Principles and Applications*, Haliburton Energy Services, Huston, 234 pp.

Czekański, E., and Group in POGC Co. (2012), Carboniferous – prospects of new hydrocarbon reservoirs discoveries, *Sci. Works Oil and Gas Inst.***182** (in Polish).

Dadlez, R., S. Marek, and J. Pokorski (2000), Geological map of Poland without Cainozoic deposits, scale 1:1 000 000, Polish Geological Institute, Warsaw, Poland.

Dohnalik, M. (2013), Improving the ability of determining reservoir rocks parameters using X-ray computed microtomography, Ph.D. Thesis, AGH University of Science and Technology, Kraków, Poland.

Jarzyna, J., and E. Puskarczyk (2010), Nuclear magnetic resonance (NMR) and mercury porosimetry measurements for permeability determination. **In:** G. Christofides *et al.* (eds.), *Proc. 19th Congress of the Carpathian-Balkan Geological Association, 23-26 September 2010, Thessaloniki, Greece*, Scientific Annals, School of Geology, Sp. Vol. 99, 371-376.

Jarzyna, J.A., P.I. Krakowska, and E. Puskarczyk (2012), Tight Precambrian and Paleozoic reservoirs in the light of petrophysical analysis. **In:** *Proc. 74th EAGE Conference and Exhibition incorporating EUROPEC 2012, 4-7 June 2012, Copenhagen, Denmark*, DOI: 10.3997/2214-4609.20148228.

Jaworowski, K., and Z. Mikołajewski (2007), Oil- and gas-bearing sediments of the Main Dolomite (Ca2) in the Międzychód region: a depositional model and the problem of the boundary between the second and third depositional sequences in the Polish Zechstein Basin, *Prz. Geol.* **55**, 12/1, 1017-1024 (in Polish).

Liu, Z.H., C.C. Zhou, L.H. Zhang, D.J. Dai, C.L. Li, L. Zhang, G.Q. Liu, and Y.J. Shi (2007), An innovative method to evaluate formation pore structure using NMR logging data. **In:** *Proc. SPWLA 48th Annual Logging Symposium, 3-6 June 2007, Austin, USA*, SPWLA-2007-S.

MacQueen, J.B. (1967), Some methods for classification and analysis of multivariate observations. **In:** *Proc. 5th Berkeley Symp. Mathematical Statistics and Probability*, University of California Press, Berkeley, 281-297.

Mao, Z.-Q., L. Xiao, Z.-N. Wang, Y. Jin, X.-G. Liu, and B. Xie (2013), Estimation of permeability by integrating nuclear magnetic resonance (NMR) logs with mercury injection capillary pressure (MICP) data in tight gas sands, *Appl. Magn. Reson.* **44**, 4, 449-468, DOI: 10.1007/s00723-012-0384-z.

Monk, D. (2013), Unconventional reservoir sweet spots from geophysics (editorial), *Oilfield Rev.* **Winter 2013/2014**, 1.

Montaron, B. (2008), Connectivity theory – a new approach to modeling "non-Archie" rocks. **In:** *Proc. SPWLA 49th Annual Logging Symposium, 25-28 May 2008, Edinburgh, Scotland*, SPWLA-2008-GGGG.

Pittman, E.D. (1992), Relationship of porosity and permeability to various parameters derived from mercury injection-capillary pressure curves for sandstone, *AAPG Bull.* **76**, 2, 191-198.

Puskarczyk, E. (2011), Assessment of reservoir properties of rock through nuclear magnetic resonance phenomenon application, Ph.D. Thesis, AGH University of Science and Technology, Kraków, Poland (in Polish).

Puskarczyk, E. and J. Jarzyna (2012), New method of NMR signals fitting using 'Distribution' program. **In:** *Proc. 74th EAGE Conference and Exhibition incorporating EUROPEC 2012, 4-7 June 2012, Copenhagen, Denmark*, DOI: 10.3997/2214-4609.20148554.

Semyrka, G., J. Jarzyna, R. Semyrka, M. Kaźmierczuk, and L. Pikulski (2010), Reservoir parameters of lithostratigraphic successions of the lower Paleozoic strata in the Polish part of the Baltic region based on laboratory studies and well logs, *Geol. Quart.* **54**, 2, 227-240.

Straley, Ch., D. Rossini, H. Vinegar, P. Tutunjian, and Ch. Morriss (1997), Core analysis by low-field NMR, *The Log Analyst* **38**, 2, 84-94.

Such, P., G. Leśniak, and M. Słota (2010), Quantitative porosity and permeability characterization of potential Rotliegend tight gas reservoir, *Prz. Geol.* **58**, 4, 345-351 (in Polish).

Swanson, B.F. (1981), A simple correlation between permeabilities and mercury capillary pressures, *J. Petrol. Technol.* **33**, 12, 2498-2504, DOI: 10.2118/8234-PA.

Thomeer, J.H. (1983), Air permeability as a function of three pore-network parameters, *J. Petrol. Technol.* **35**, 4, 809-814, DOI: 10.2118/10922-PA.

Vavra, C.L., J.G. Kaldi, and R.M. Sneider (1992), Geological applications of capillary pressure: A review, *AAPG Bull.* **76**, 6, 840-850.

Webb, P.A. (2001), An introduction to the physical characterization of materials by mercury intrusion porosimetry with emphasis on reduction and presentation of experimental data, Micrometrics Instrument Corp., Norcross, USA.

Wojtanowski, K. (2011), Algorithm and application program to processing and interpretation of capillary pressure data, M.Sc. Thesis, AGH University of Science and Technology, FGGEP, Kraków, Poland.

Xiao, L., Z.Q. Mao, Z.X. Xiao, and C. Zhang (2008), A new method to evaluate pore structure consecutively using NMR and capillary pressure data. **In:** *Proc. SPWLA 49th Annual Logging Symposium, 25-28 May 2008, Edinburgh, Scotland*, SPWLA-2008-AA.

Xiao, L., X.-P. Liu, C.-C. Zou, X.-X. Hu, Z.-Q. Mao, Y.-J. Shi, H.-P. Guo, and G.-R. Li (2014), Comparative study of models for predicting permeability from nuclear magnetic resonance (NMR) logs in two Chinese tight sandstone reservoirs, *Acta Geophys.* **62**, 1, 116-141, DOI: 10.2478/s11600-013-0165-6.

Zalewska, J., M. Dohnalik, J. Kaczmarczyk, A. Poszytek, G. Sikora, D. Cebulski, M. Masłowski, and E. Biały (2010), X-ray computed microtomography in examination of carbonate rocks, *Sci. Works Oil and Gas Inst.* **171**, 1-263 (in Polish).

Zalewska, J., M. Dohnalik, G. Łykowska, and J. Kiernicki (2011), Laboratory of the rocks and reservoir fluids geophysical parameters, Report no. 37/11/2011, Oil and Gas Institute, Kraków, Poland (in Polish).

Zorski, T. (2009), Recent improvements in interpretation methodology applied in GeoWin SATUN application, *AGH Geologia* **35**, 2/1, 549-557.

Zorski, T., A. Ossowski, J. Środoń, and T. Kawiak (2011), Evaluation of mineral composition and petrophysical parameters by the integration of core analysis data and wireline well log data: the Carpathian Foredeep case study, *Clay Minerals* **46**, 1, 25-45, DOI: 10.1180/claymin.2011.046.1.25.

Received 4 May 2014
Accepted 18 June 2014

DE GRUYTER OPEN

Acta Geophysica
vol. 63, no. 3, June 2015, pp. 815-842
DOI: 10.1515/acgeo-2015-0014

Wave Propagation Modeling and Amplitude-Variation-with-Offset Response in a Fractured Coalbed

Qing-Xi LIN[1], Su-Ping PENG[1], Wen-Feng DU[1], Su-Zhen SHI[1], and Jing-Wei GOU[2]

[1]State Key Laboratory of Coal Resources and Mine Safety, China University of Mining & Technology (Beijing), Beijing, China; e-mail: psp@cumtb.edu.cn

[2]Geophysical Prospecting Institute, China National Administration of Coal Geology, Zhuozhou, China

Abstract

Coalbed methane can be detected employing the amplitude-variation-with-offset technique. However, there are two issues in applying this technique to a coalbed: strong azimuthal anisotropy resulting from high-density fractures, and the seismic response being composed of many or several individual reflections within the coalbed. To overcome these difficulties, we present an exact solution for reflections in extensive dilatancy anisotropy media. First, we build a three-layer model and simulate the wave propagation in this model. Then we derive an exact *P*- and converted *S*-wave reflection coefficient equation based on boundary conditions. Finally, substituting given model parameters into the exact equation, we obtain the variation in the reflection coefficient with incidence angle. The results show that the fracture factors, wavelet frequency and thickness of the coalbed have different effects on the reflection coefficient. Furthermore, we create a synthetic seismogram by forward calculation, and the result fits well with results of the exact equation.

Key words: extensive dilatancy anisotropy, amplitude-variation-with-offset response, wave propagation for wave field modeling, reflection coefficient.

1. INTRODUCTION

In recent decades, coalbed methane (CBM) has become one of the most important future fuel resources in many countries. It has been claimed that the worldwide resources of methane trapped in coal are greater than the total reserves of all known conventional gas fields (Bachu and Bell 2001). Because of its extensive presence in coalbeds, not only can CBM be explored as a clean energy in industrial production, but it is also a hazard in traditional mining. Coal and methane outbursts, which threaten the lives of coal miners, may occur when a coal mining operation breaks into CBM that has accumulated in natural or manmade voids (Hu and McMechan 2007). Therefore, the detection of CBM plays an important role in exploring fuel resources and ensuring the safety of coal miners.

As a direct hydrocarbon-detection technique, the amplitude variation with offset (AVO) technique has been used in the oil and gas industry for more than 20 years. With seismic prestack data, the technique can be employed to predict reservoir properties and the fluid content. The theoretical basis of the AVO technique is the Zoeppritz equation, which was first proposed by Zoeppritz (1919). Zoeppritz calculated the reflection and transmission coefficients of plane waves generated by an incidence wave at a flat interface separating two homogeneous half-spaces. Because the complexity of the problem obscures any physical insight into the AVO signature, simplified or approximate equations have been discussed in the literature (*e.g.*, Aki and Richards 1980, Bortfeld 1961, Shuey 1985). The equations describe the physical phenomenon that provides a possibility of direct hydrocarbon detection. Ostrander (1984) first introduced a practical application of the AVO effect, showing that the presence of gas causes amplitudes to increase with offset. Rutherford and Williams (1989) classified the AVO anomalies relating various AVO phenomena to their geologic and geophysical origins and established a consistent and theoretical AVO-anomaly interpretation system. Castagna *et al*. (1998) discussed the Rutherford and Williams' classification and proposed a fourth class of sand (class IV). Furthermore, many researchers have studied the AVO research of anisotropic media and obtained a lot of useful conclusions on the detection of cracks and fluid (*e.g.*, Wright 1987, Chen 1995, Bakulin *et al*. 2000a, b). And now, the AVO technique has drawn substantial attention within the oil industry, eventually becoming a commercial tool.

Although the AVO technique has matured sufficiently to be used in finding oil and gas, it cannot be used directly in CBM detection for three main reasons. First, CBM is a form of natural gas that commonly exists in coalbeds. Unlike traditional natural gas that accumulates in a free state, CBM is stored in deeply buried coal seams by a process called "adsorption"

in a near-liquid state and lines the inside of pores within the coal (called the matrix). Coal is a porous medium with a dual-pore system comprising microcracks and cleats and micropores. Furthermore, the high-density vertical cracks and fractures contained in a coalbed result in strong seismic anisotropy. Shuck *et al*. (1996) and Ramos and Davis (1997) studied the multicomponent characterization of a CBM reservoir and demonstrated moderate to strong anisotropy of 30-50%, which is higher than the anisotropy of other sedimentary rocks (10-20%). As the theoretical basis of AVO technology, Zoeppritz equation is mainly applied to isotropy and weak anisotropy. In strongly anisotropic environments, where the anisotropic properties are possibly induced by aligned fractures, fillings or other factors, conventional AVO analysis could be distorted significantly and inaccurate. Second, the coalbed is considered to be a thin bed. The seismic response recorded at the surface is composed of many or several individual reflections, including reflections from the top and bottom of the coal seam, converted wave reflections, and multiple reflections (Gochioco 1991, Meissner and Meixner 1969). Third, in the coal industry, the seismic data acquisition requirements (such as sampling, offsets, noise types, *etc*.) are very different from oil detection. In addition, coal seams can produce distinct reflections because of the exceptionally large impedance contrast with respect to roof and floor rocks. Therefore, AVO analysis is not suitable for CBM detection. We need build a new model suitable for a coalbed instead of applying the conventional AVO to CBM detection directly.

A few researchers have transferred AVO technique to CBM exploration. Ramos and Davis (1997) characterized fractured reservoirs and applied the AVO technique to CBM exploration of the Cedar Hill Field. Peng *et al*. (2006) compared the strengths and weaknesses of the AVO technique for CBM reservoirs with those of the AVO technique for gas sand reservoirs and detected rich methane within coal seams. However, the reflection coefficients of the coalbed that are more important for describing AVO responses have not been calculated using a set of exact formulae. Wave propagation should be analyzed to investigate the characteristics of elastic wave propagation in a fractured coalbed. A formula can then be derived to calculate the reflection coefficients.

In this study, we analyzed the fractured coalbed with strong anisotropy. We consider the coalbed to be an extensive dilatancy anisotropic (EDA) medium, which is typically produced by a system of vertical cracks. We used Cheng's (1993) model and the Kelvin–Christoffel equations to estimate the elastic parameters of the EDA medium and compute the wave velocity, respectively. A three-layer medium model (the EDA medium spread between two isotropic layers) was then designed with the cracks along the 90° azimuth. The elastic wave propagation was simulated at azimuthal angles of 0°

and 90°. We derived an exact formula from the Zoeppritz equation to calculate the reflection coefficients with high precision. When the physical parameters of the coalbed are estimated for the model, the change in *P*- and converted *S*-wave reflection coefficients with different fracture factors can be analyzed.

2. THEORETICAL ASPECTS

2.1 Anisotropy of the coalbed

It is widely known that anisotropy pervades most rocks in the Earth's crust. Coal is an unusual reservoir rock that has an impermeable and isotropic matrix together with a fabric of natural fractures known as cleats or cracks that most likely causes the observed anisotropy. It is important to model the coalbed with layers of elastic anisotropy when we describe the wave propagation through a fractured coalbed.

Crampin (1989) classified anisotropy into 10 groups according to the symmetry of the medium produced by the wave driving force. One class of anisotropy, EDA, was firstly proposed by Crampin (1984). He pointed out that stress-induced cracks would be open in the direction of maximum stress and closed in the direction of minimum stress. Stress-aligned near-parallel near-vertical cracks are thus formed. EDA is used frequently to describe a system of parallel and vertically aligned penny-shaped cracks embedded in an isotropic matrix, and has hexagonal symmetry with a horizontal axis of symmetry, parallel to the minimum horizontal compressional stress.

Generally, coalbeds are equivalent to EDA media because the aligned cracks contained by coalbeds are always distributed parallel to each other. A sketch of an EDA model is shown in Fig. 1. Research on the layout and anisotropy of EDA media helps clarify the factors affecting CBM.

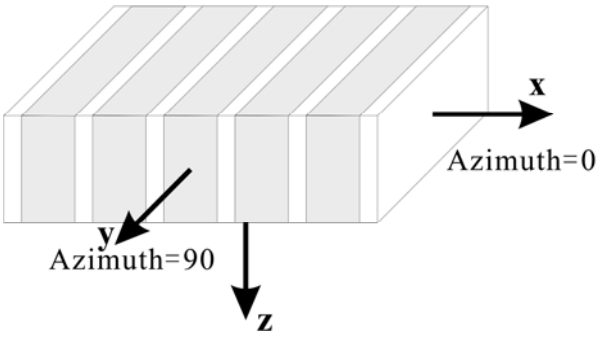

Fig. 1. Sketch of an EDA model.

2.2 Computation of the stiffness tensor

The effective anisotropic stiffness tensor is a mathematical expression of anisotropy and is important in describing fractured rocks. Coal has a much higher fracture density than other sedimentary rocks. High fracture density leads to stronger anisotropy. In consideration of the strong anisotropy, it is important to choose a parameterization model to compute the stiffness tensor of anisotropic coal. There are two models commonly used to describe the fracture density of coal: the Hudson (1981) and the Cheng (1993) models.

The widely accepted model for fracture-induced anisotropy is that of Hudson (1980, 1981). This model mainly uses Eshelby's (1957) technique for calculating the elastic constants of cracked solids and the effects on seismic waves of scattering at penny-shaped ellipsoidal fractures or inclusions.

Hudson's theory computes the stiffness tensor from the background rock moduli, crack density, aspect ratio, and physical parameters of material inside cracks. The crack density is defined as:

$$\varepsilon = Na^3 / V \ , \tag{1}$$

where N is the number of cracks of radius a in a volume V. The Hudson second-order expression for the stiffness matrix $\mathbf{C}^*$ is:

$$\mathbf{C}^* = \mathbf{C}^0 + \mathbf{C}^1 + \mathbf{C}^2 \ , \tag{2}$$

where $\mathbf{C}^0$ is the stiffness tensor of the host rock (isotropic background rock). The first-order term $\mathbf{C}^1$ accounts for single scattering and the second-order term $\mathbf{C}^2$ gives the crack-crack interactions. Both $\mathbf{C}^1$ and $\mathbf{C}^2$ are perturbations of the isotropic stiffness tensor $\mathbf{C}^0$ of the uncracked solid.

Hudson's second-order formulation has been used by Crampin (1984) and other researchers to model anisotropy of seismic waves propagating through EDA cracks. However, it has been found that Hudson's approximation is inaccurate for high crack densities. This is because the second-order terms can dominate the first-order terms at higher crack densities and the effective moduli increases with increasing crack density, as shown in Fig. 2a. Generally, it is assumed that this model works when the crack density is less than 0.1.

To overcome the existing limits, Cheng's (1993) idea was to extend Hudson's theory to high crack density and reformulate the expansion as a Padé series. The problem of divergence at higher crack densities can be avoided using this Padé-approximation-based expansion. The improved formulation for calculating the stiffness tensor is expressed as:

$$\mathbf{C}^* = \mathbf{C}^0 (1 - \mathbf{A}\varepsilon) \big/ (1 + \mathbf{B}\varepsilon) \ , \tag{3}$$

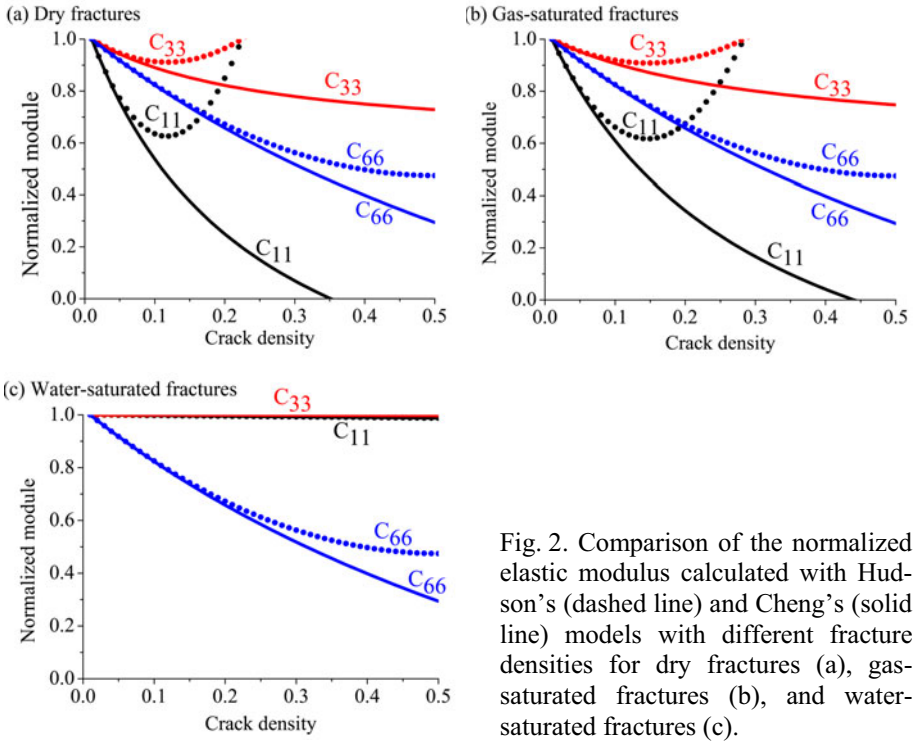

Fig. 2. Comparison of the normalized elastic modulus calculated with Hudson's (dashed line) and Cheng's (solid line) models with different fracture densities for dry fractures (a), gas-saturated fractures (b), and water-saturated fractures (c).

where ε is the crack density. Padé coefficient matrixes **A** and **B** are defined as:

$$\mathbf{A} = -\mathbf{C}^1 \big/ \left(\mathbf{C}^0 \varepsilon\right) - \mathbf{B} \ , \quad \mathbf{B} = -\mathbf{C}^2 \big/ \left(\mathbf{C}^1 \varepsilon\right) \ . \tag{4}$$

We computed the elastic constants for the anisotropic layers using Hudson's and Cheng's theories for the properties of the fractured layer. Figure 2 shows the elastic constants C_{11}, C_{33}, and C_{66} against crack density of the coalbed with dry, gas-saturated, and water-saturated cracks. The dashed lines and solid lines were calculated by Hudson's second-order formulation and Cheng's expansion, respectively. The background *P*- and *S*-wave velocities of the coalbed were, respectively, $v_{p0} = 2200$ m/s and $v_{s0} = 1100$ m/s, and the density was $\rho_0 = 1390$ kg/m^3. The average aspect ratio of cracks was 0.002. The bulk moduli of the gas and water that filled the fractures were 2 and 2250 MPa, respectively. The azimuth of the cracks is 90° (shown in Fig. 1). From Fig. 2, we see that Hudson's expansion becomes physical for water-saturated cracks but unphysical for dry and gas-saturated cracks when the crack density is beyond 0.1. Meanwhile, Cheng's formulation agrees well for coal over a large range of crack densities of up to 0.35.

2.3 Wave propagation in EDA media

In the isotropic media, velocity of *P* and *S* waves do not vary with direction of propagation. The polarization directions are mutually orthogonal to each other. A *P* wave is polarized along its propagation direction. The polarization direction of an *S* wave is orthogonal to the propagation direction.

In EDA media, wave propagation adds some new challenges. First, shear wave splitting can occur when a polarized shear wave enters an EDA medium and splits into two polarized shear waves: *SV* and *SH*. One of the shear waves is faster than the other owing to the cracks in the medium. Second, a qualifier *quasi* is always written in front of "*P* wave" and "*S* wave" because the longitudinal wave or shear wave is not polarized normal to either the slowness or propagation directions for EDA media. Third, the wave velocity is dependent on propagation and polarization directions.

According to the above, the derivation of wave velocities and that of polarization vectors are two necessary elements in studying wave propagation in EDA media. In this paper, we calculated the seismic wave velocities and associated polarization vectors from the solution of Kelvin–Christoffel equations for an arbitrary propagation direction (Appendix A). As described in Appendix A, crack-induced anisotropy has an important effect on wave velocity.

3. EXACT SOLUTION FOR REFLECTIONS IN EDA MEDIA

To study the AVO response in a fractured coalbed, we need to establish a geological model and present solutions to the reflection problem. A coalbed is well known to be a layer of sedimentary rock buried between overlaying and underlying strata. The AVO response of the coalbed, which is always considered as a thin bed, is composed of many reflections. Wave propagation in layered isotropic media has been studied by many researchers (*e.g.*, Du 1996), and an exact formula has been derived for calculating reflection coefficients. However, strong anisotropy is presented by the quite large crack density of the coalbed and the isotropic model is unable to provide accurate results. Therefore, we have to build an anisotropic model.

A three-layer model was established and is shown in Fig. 3b. The top and bottom layers are isotropic, while the middle layer is an EDA medium. To simplify the calculation, wave propagation is only simulated at azimuthal angles of 0° and 90°. In Figure 3b, the symmetry axis of cracks is parallel to the x direction. The $[x,z]$-plane is referred to as the "symmetry-axis plane", and the $[y,z]$-plane where waves do not experience any anisotropy is the so-called "isotropy plane" (Rüger 1997). We define that a plane wave propagates in the $[x,z]$-plane and $[y,z]$-plane when the azimuthal angles are 0° and 90°, respectively.

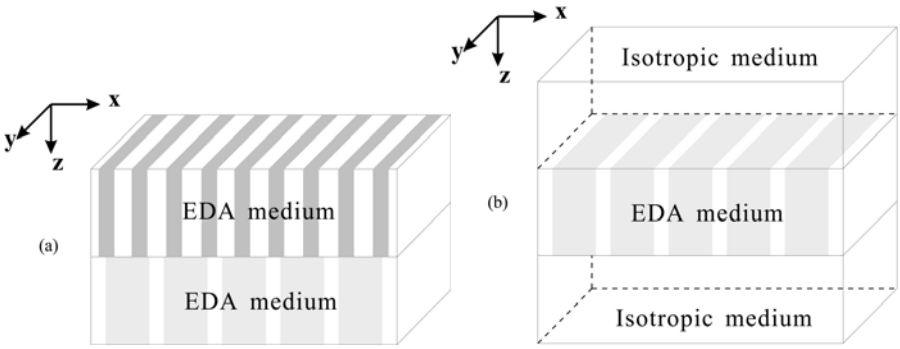

Fig. 3. Geological models of the coalbed: (a) a two-layer model with two EDA media, and (b) a three-layer model with two isotropic media and an EDA medium.

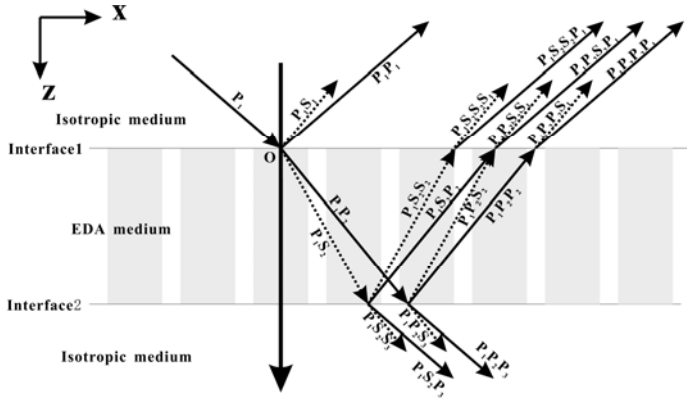

Fig. 4. Wave paths of plane elastic waves propagating in the fractured coalbed.

In Appendix B, a different model (upper and lower layers are both an anisotropic medium) is established (Fig. 3a). One can illustrate the characteristics of the wave motion and obtain the reflection coefficients at the interface. Then, as an extension of the above studies, an exact solution for reflections was obtained for the three-layer model (Fig. 3b).

First, we will study the wave propagation in the three-layer model for an azimuthal angle of 0°. When a plane *P* wave is incident at interface 1 (shown in Fig. 4), it is reflected on the upper and lower boundaries of the coalbed. The observed reflection is a composite of the reflections from the top and bottom of the coalbed and all multiple and converted waves reflections within the coalbed. However, in the highly attenuated layer the influence of the attenuation is the highest for the multiple reflections. For this reason, we de-

cided to neglect their presence in our study. Figure 4 shows all the reflections and transmissions when waves propagate into the fractured coalbed.

In Figure 4, there are 10 reflected waves in the upper isotropic layer when waves pass through the fractured coalbed: reflected P waves P_1P_1, $P_1S_2S_2P_1$, $P_1S_2P_2P_1$, $P_1P_2S_2P_1$, and $P_1P_2P_2P_1$, and converted S waves P_1S_1, $P_1S_2S_2S_1$, $P_1S_2P_2S_1$, $P_1P_2S_2S_1$, and $P_1P_2P_2S_1$. Note that waves $P_1S_2P_2P_1$ and $P_1S_2P_2S_1$ are not shown in Fig. 4, as their propagation paths coincide with those of $P_1P_2S_2P_1$ and $P_1P_2S_2S_1$.

To explain the wave paths in Fig. 4, we apply a finite difference method to simulate the elastic wave propagating in the three-layer model. This method has fourth-order accuracy in space and second-order accuracy in time. In the numerical example, the thickness of each layer is 100 m. The P-wave velocities, S-wave velocities, and densities in the top and bottom layers are $v_{p1} = v_{p3} = 3710$ m/s, $v_{s1} = v_{s3} = 1990$ m/s, and $\rho_1 = \rho_3 = 2.6$ g/cm^3, respectively, whereas in the middle layer, the background parameters are $v_{p2} = 2200$ m/s, $v_{s2} = 1100$ m/s, and $\rho_2 = 1.39$ g/cm^3. The crack density is 0.3 and the aspect ratio of the dry crack is 0.002. The azimuth of the cracks is 90°. The grid intervals are $\Delta x = \Delta z = 1$ m. The time sampling interval is $\Delta t = 0.1$ ms. The P-wave source with a frequency of 150 Hz is located at the center of the model. In this experiment, we use the classical perfectly matched layer (Komatitsch and Tromp 2003) as the absorbing boundary condition to eliminate reflections at the artificial boundaries. Figure 5 shows snapshots of elastic wavefields at different times. Some wave types shown in Fig. 4 are observed in these snapshots. Note that the snapshot time is stopped at 120 ms, because the conventional finite difference grids may become unstable after seismic waves run for long distances and a long time.

Next, the exact formula for reflection coefficients needs to be derived. As shown in Fig. 4, the propagation directions of all P waves are parallel to each other in the upper isotropic layer. Thus, these P waves have the same polarization, horizontal slowness, and vertical slowness, similar to the case for the S waves propagating in the upper isotropic layer. The displacement vector of any of the mentioned waves at interface 1 can be expressed as:

$$\mathrm{u}_{pm} = \left(f_p, h_p\right) A_{pm} \exp\left[i\omega\left(px + r_p z - t\right)\right] \exp\left(i\phi_{pm}\right), \quad m = 1, 2, ..., 5 \ , \tag{5}$$

$$\mathrm{u}_{sn} = \left(f_s, h_s\right) A_{sn} \exp\left[i\omega\left(px + r_s z - t\right)\right] \exp\left(i\phi_{sn}\right), \quad n = 1, 2, ..., 5 \ , \tag{6}$$

where the subscript $m = 1, 2, \ldots, 5$ corresponds to the P waves P_1P_1, $P_1S_2S_2P_1$, $P_1S_2P_2P_1$, $P_1P_2S_2P_1$, and $P_1P_2P_2P_1$, $n = 1, 2, \ldots, 5$ corresponds to the converted S waves P_1S_1, $P_1S_2S_2S_1$, $P_1S_2P_2S_1$, $P_1P_2S_2S_1$, and $P_1P_2P_2S_1$, (f_p, h_p) and (f_s, h_s) are unit polarization vectors of P and S waves, p is hori-

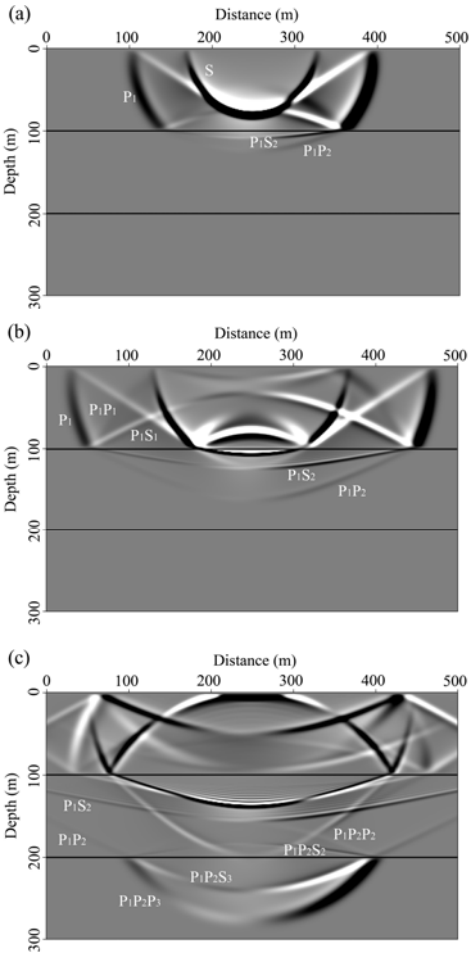

Fig. 5. Snapshots of the *X*-component at different times in the dry fractured coalbed model: (a) *X*-component snapshot at t = 60 ms, showing the incident *P* and *S* waves, and the transmitting *P* wave and converted *S* wave from the *P* wave on the coalbed roof; (b) *X*-component snapshot at t = 80 ms, showing the reflected *P* wave and converted *S* wave on the coalbed roof; (c) *X*-component snapshot at t = 120 ms, showing the reflected *P* wave and converted *S* wave from P_1P_2 on the coalbed floor, as well as transmitted waves.

zontal slowness, r_p and r_s are values of the vertical slowness of *P* and *S* waves, and φ_{pm} and φ_{sn} are the initial wavefront phases of *P* and *S* waves.

Assuming that the phase of the P_1 wave on arrival at interface 1 is zero, we obtain:

$$\phi_{p1} = \phi_{s1} = 0 \ . \tag{7}$$

The initial wavefront phases of other waves are constrained by the travel time delay. As an example, the initial phase of $P_1P_2P_2P_1$ (*i.e.*, φ_{p5}) can be calculated in the next step.

Figure 6 shows the ray paths of *P*-waves P_1, P_1P_2, $P_1P_2P_2$, and $P_1P_2P_2P_1$. The incidence angle of wave P_1 is θ_1 while the transmission angle is θ_2.

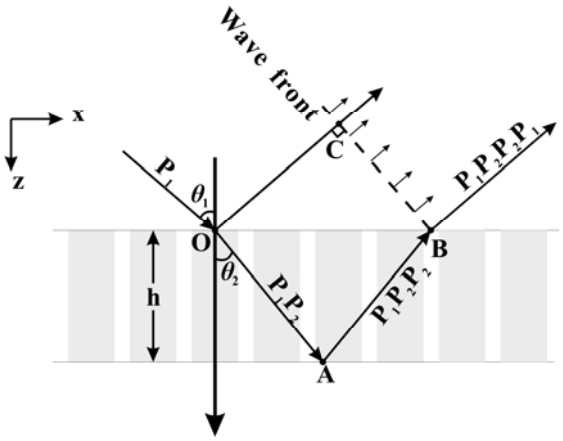

Fig. 6. Ray paths of *P* waves.

The thickness of the coalbed is h. The delay time Δt_{OC} can be calculated according to:

$$\Delta t_{OC} = \overline{OC}/v_1 = (\overline{OB}\sin\theta_1)/v_1 = \left(2h\sin^2\theta_2\right)/\left(v_2\cos\theta_2\right) , \tag{8}$$

where v_1 is the velocity of the *P* wave propagating in the upper isotropic layer, and v_2 is the velocity of *P* waves P_1P_2 and $P_1P_2P_2$. Δt_{OAB} is calculated as:

$$\Delta t_{OAB} = \Delta t_{OA} + \Delta t_{AB} = 2\overline{OA}/v_2 = 2h/\left(v_2\cos\theta_2\right) . \tag{9}$$

The travel time delay between reflected *P* waves is given by:

$$\Delta t = \Delta t_{OAB} - \Delta t_{OC} = 2h/\left(v_2\cos\theta_2\right) - \left(2h\sin^2\theta_2\right)/\left(v_2\cos\theta_2\right) = \left(2h\cos\theta_2\right)/v_2 . \tag{10}$$

The phase difference (*i.e.*, the initial phase of $P_1P_2P_2P_1$) is given by:

$$\phi_{p5} = \omega\Delta t = \omega\left(2h\cos\theta_2\right)/v_2 . \tag{11}$$

The initial phase of other waves can be calculated in the same way.

The amplitude of the reflection is governed by the transmission and reflection coefficients of the top and bottom interfaces. Equations 5 and 6 can be written as:

$$\mathrm{u}_{pm} = \left(f_p, h_p\right) A_p R_{pm} \exp\left[i\omega\left(px + r_p z - t\right)\right]\exp\left(i\phi_{pm}\right), \quad m = 1,2,...,5 , \tag{12}$$

$$\mathrm{u}_{sn} = \left(f_s, h_s\right) A_p R_{sn} \exp\left[i\omega\left(px + r_s z - t\right)\right]\exp\left(i\phi_{sn}\right), \quad n = 1,2,...,5 , \tag{13}$$

where A_p is the amplitude of incident wave P_1. When $m = n = 1$, we have:

$$R_{p1} = R_{p1p1} \ , \quad R_{s1} = R_{p1s1} \ , \tag{14}$$

where R_{p1p1} denotes the *P*-wave reflection coefficient of the P_1 wave at interface 1, R_{p1s1} denotes the *S*-wave reflection coefficient of P_1 at interface 1. When $m = n = 2$, we have:

$$R_{p2} = T_{p1s2} R_{p1s2s2} T_{p1s2s2p1} \ , \quad R_{s2} = T_{p1s2} R_{p1s2s2} T_{p1s2s2s1} \ , \tag{15}$$

where T_{p1s2} denotes the *S*-wave transmission coefficient of P_1 at interface 1, R_{p1s2s2} denotes the *S*-wave reflection coefficient of P_1S_2 at interface 2, $T_{p1s2s2p1}$ denotes the *P*-wave transmission coefficient of $P_1S_2S_2$ at interface 1, and $T_{p1s2s2s1}$ denotes the *S*-wave transmission coefficient of $P_1S_2S_2$ at interface 1. These reflection and transmission coefficients can be calculated using Eq. B14 derived in Appendix B.

Similarly, we have:

$$R_{p3} = T_{p1s2} R_{p1s2p2} T_{p1s2p2p1} \ , \quad R_{s3} = T_{p1s2} R_{p1s2p2} T_{p1s2p2s1} \ , \tag{16}$$

$$R_{p4} = T_{p1p2} R_{p1p2s2} T_{p1p2s2p1} \ , \quad R_{s4} = T_{p1p2} R_{p1p2s2} T_{p1p2s2s1} \ , \tag{17}$$

$$R_{p5} = T_{p1p2} R_{p1p2p2} T_{p1p2p2p1} \ , \quad R_{s5} = T_{p1p2} R_{p1p2p2} T_{p1p2p2s1} \ . \tag{18}$$

We assume that the depth of interface 1 is zero. Each wave propagating in the upper isotropic layer, except for incident wave *P*1, contributes to the total reflected waveform so that the composite reflection of the *P* wave is given by:

$$\mathbf{u}_{\mathbf{p}\Sigma} = \sum_{m=1}^{5} \mathbf{u}_{\mathbf{p}m} = \left(f_p, h_p\right) A_p \sum_{m=1}^{5} \left[R_{pm} \exp\left(i\varphi_{pm}\right) \right] \exp\left[i\omega(px - t) \right] . \tag{19}$$

Using Euler's formula, we can simplify Eq. 19 as:

$$\mathbf{u}_{\mathbf{p}\Sigma} = \left(f_p, h_p\right) A_p R_p \exp\left(i\phi_p\right) \exp\left[i\omega(px - t) \right] , \tag{20}$$

where

$$R_p = \sqrt{M_p^2 + N_p^2} \ , \quad \phi_p = \tan^{-1} \frac{M_p}{N_p} ,$$

$$M_p = \sum_{m=1}^{5} \left(R_{pm} \cos\varphi_{pm} \right) , \quad N_p = \sum_{m=1}^{5} \left(R_{pm} \sin\varphi_{pm} \right) . \tag{21}$$

The amplitude and initial phase of composite reflected *P* waves are A_pR_p and ϕ_p, respectively. R_p is the *P*-wave reflection coefficient.

Similarly, we add the displacements of *S* waves and obtain:

$$\mathbf{u}_{\mathbf{s}\Sigma} = \sum_{n=1}^{5} \mathbf{u}_{\mathbf{s}n} = \left(f_s, h_s\right) A_p R_s \exp\left(i\phi_s\right) \exp\left[i\omega(px - t) \right] , \tag{22}$$

where

$$R_s = \sqrt{M_s^2 + N_s^2}\,, \quad \phi_s = \tan^{-1}\frac{M_s}{N_s}\,,$$
$$M_s = \sum_{n=1}^{5}\left(R_{sn}\cos\varphi_{sn}\right), \quad N_s = \sum_{n=1}^{5}\left(R_{sn}\sin\varphi_{sn}\right)\,. \tag{23}$$

The amplitude and initial phase of composite reflected S waves are $A_P R_s$ and ϕ_s, respectively. R_s is the converted S-wave reflection coefficient.

The same derivation is applied to the solution for reflection coefficients when a wave propagates in the $[y,z]$-plane (azimuth of 90°).

The exact solution for reflections has been derived in Appendix B. In the next steps, forward modeling can be employed to compute the reflection coefficients and an accurate AVO response can be obtained.

4. AVO RESPONSE IN A FRACTURED COALBED

The AVO response refers to the variation of the seismic wave amplitude or reflection coefficient with offset or incidence angle. The exact formulation has been derived for calculating the reflection coefficient in a three-layer model as discussed above. In this section, we substitute various physical parameters into the equation and analyze the variation in the reflection coefficient with the incidence angle of the P wave. The physical parameters of the three-layer model are listed in Table 1. The values of crack density, crack aspect ratio, bulk modulus of the crack filler, wavelet frequency, and thickness of the coalbed, which are all listed in the table, can be used to analyze the characteristics of the AVO response.

Table 1

Physical parameters of the three-layer model

Layer	Background parameters			Crack density	Crack aspect ratio	Crack filler	Wavelet frequency [Hz]	Thickness [m]
	v_p [m/s]	v_s [m/s]	ρ [g/cm^3]					
Top layer	3710	1990	2.60					100
Coalbed	2200	1100	1.39	0.15 0.20 0.25 0.30 0.35	0.001 0.002 0.003	dry gas water	40 50 60 70 80	3 5 7 9 11
Bottom layer	3710	1990	2.60					100

Note: The bulk moduli of gas and water that fill the fractures are 2 and 2250 MPa.

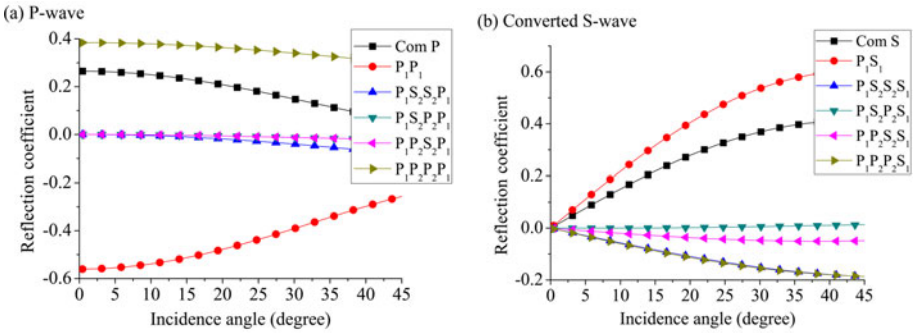

Fig. 7. Effect of a single wave on the reflection response of the composite wave.

We first discuss the characteristics of the variation of reflection coefficients at an azimuthal angle of 0°. From Section 3, we know that the reflection coefficient is a composite of the reflections from the top and bottom of the coalbed in the three-layer model. Thus, we need to analyze the effect of each single wave on the reflection coefficient of the composite wave. Figure 7 shows the *P*-wave and converted *S*-wave reflection coefficients evaluated at interface 1 with gas-saturated fractures. The crack density is set to 0.3, the average aspect ratio of cracks is 0.002, the wavelet frequency is 60 Hz, and the thickness of the coalbed is 7 m.

In Figure 7a, the reflection coefficients of *P* waves P_1P_1 and $P_1P_2P_2P_1$ decrease but those of other single waves increase as the incidence angle increases. It is obvious that the *P* waves P_1P_1 and $P_1P_2P_2P_1$ have considerable influence on the reflection coefficient of the composite *P* wave. Therefore, the reflection coefficient of the composite *P* wave (shown as "Com *P*") decreases with an increasing incidence angle. In Figure 7b, the *S*-wave reflection coefficients of all converted *S* waves appear to have an increasing trend. Additionally, the converted wave P_1S_1 has notably affects in the reflection coefficient of the composite *S* wave (shown as "Com *S*"). From the discussion above, we conclude that the reflection from the top of the coalbed strongly affects the reflection coefficients of composite waves.

Next, we consider factors, such as the crack density, crack aspect ratio (thickness over length, namely, minor/major axis of ellipsoid), bulk modulus of the crack filler, wavelet frequency and thickness of the coalbed that affect the AVO response. First, we vary the crack density from 0.15 to 0.35 at intervals of 0.05. The average aspect ratio of cracks is 0.002, the crack filler is gas, the wavelet frequency is 60 Hz, and the thickness of the coalbed is 7 m. Figure 8 shows the effect of crack density on the reflection coefficient.

In Figure 8a, both the intercept and slope of the *P*-wave reflection coefficient curves increase with increasing crack density. The reflection coeffi-

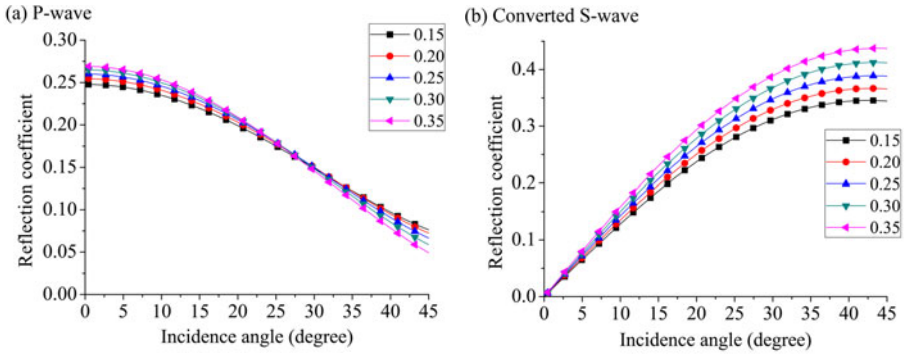

Fig. 8. Effect of crack density on the wave reflection coefficient.

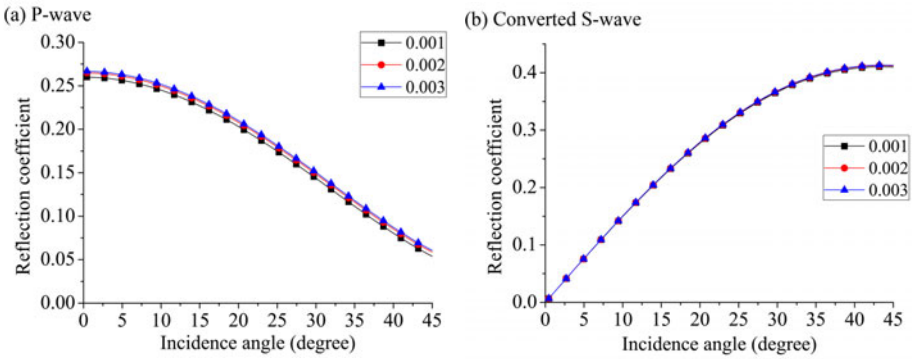

Fig. 9. Effect of the crack aspect ratio on the wave reflection coefficient.

cient curves resulting from different crack densities tend to equal each other when the incidence angle is about 27°. When the incidence angle is larger than 27°, the reflection coefficient decreases with increasing crack density. Figure 8b shows that the reflection coefficient of the converted *S* wave increases with increasing crack density.

The average aspect ratio of cracks affects the stiffness tensor of the coalbed, as well as the reflection coefficient. Figure 9 shows the effect of the crack aspect ratio, which varies from 0.001 to 0.003 in intervals of 0.05, on the reflection coefficient. The crack density is 0.3 and the other parameters are the same as above.

In general, the crack aspect ratio has little effect on the reflection coefficient. For the *P* wave, the intercept of the reflection coefficient curve increases with increasing crack aspect ratio, but the slope does not substantially change. For the converted *S* wave, there is a fractional change in the reflection coefficient.

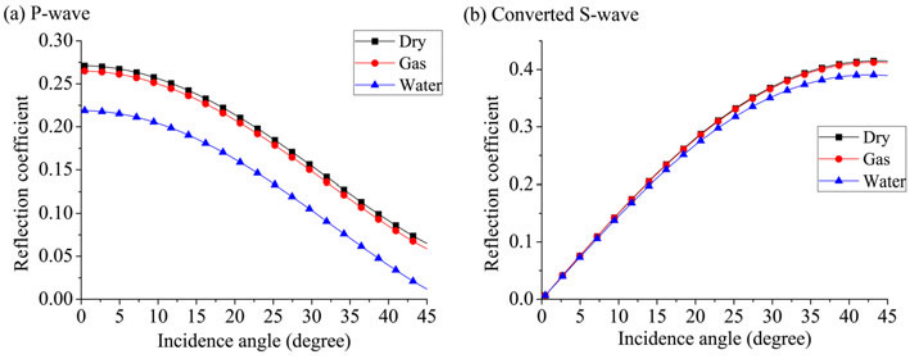

Fig. 10. Effect of the crack filler on the wave reflection coefficient.

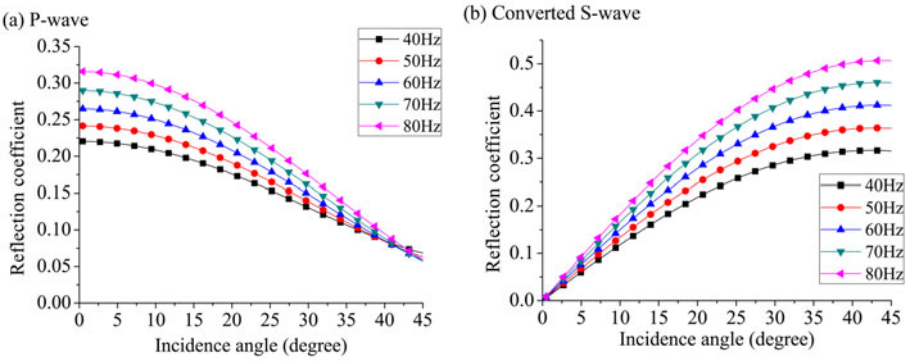

Fig. 11. Effect of wavelet frequency on the wave reflection coefficient.

In the next section we will discuss the effect on the reflection coefficient induced by the dry, gas or water saturated cracks. Figure 10 shows the incidence angle against the wave reflection coefficient for dry, gas-saturated, and water-saturated cracks. The bulk moduli were listed in Table 1. The crack density is 0.3, the average aspect ratio of cracks is 0.002, the wavelet frequency is 60 Hz, and the thickness of the coalbed is 7 m.

In Figure 10a, the reflection of the *P* wave is smaller when the crack is filled with gas or water than dry cracks. This is especially visible in the case of the water-saturated cracks. The same change is observed for the converted *S* wave in Fig. 10b. The wave reflection coefficient is little affected by the gas saturated cracks but strongly affected by the water saturated cracks.

Next, we will study the change of the wavelet frequency from 40 to 80 Hz at 10-Hz intervals. The crack filler is gas and the other parameters are the same as previously. The wave reflection coefficient changes are shown in Fig. 11.

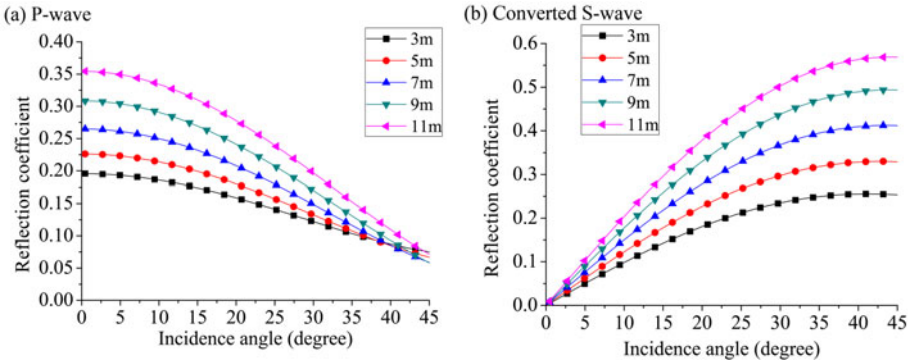

Fig. 12. Effect of the coalbed thickness on the wave reflection coefficient.

For the *P* wave, the intercept and slope of the reflection coefficient curves increase with increasing wavelet frequency. When the incidence angle is between 40° and 45°, the reflection coefficients calculated for different wavelet frequencies are approximately equal. For the converted *S* wave, the reflection coefficient increases with increasing wavelet frequency.

Finally, we investigate the effect of the coalbed thickness on the reflection coefficient. The thickness is set from 3 to 11 m at 2-m intervals, and the results are shown in Fig. 12.

The changes in the wave reflection coefficient curves seen in Fig. 12 are similar to those seen in Fig. 11. The reflection coefficient increases with increasing coalbed thickness. When the incidence angle is between 40° and 45°, the *P*-wave reflection coefficients calculated for different coalbed thicknesses are approximately equal.

After discussing the changes in the reflection coefficient for an azimuthal angle of 0°, we consider the simulation of the wave propagation at an azimuthal angle of 90°. Figure 13 shows the effect of the crack density, crack aspect ratio, crack filler, wavelet frequency, and thickness of the coalbed on the *P*-wave reflection coefficient at the azimuth of 90° (parallel to the cracks system).

In Figure 13a-c, there is no change in the *P*-wave reflection coefficient. Hence, a crack does not affect the reflection coefficient when the azimuthal angle is parallel to the cracks. In Figure 13d-e, the *P*-wave reflection coefficient increases with increasing wavelet frequency and coalbed thickness. As the incidence angle tends to 45°, the reflection coefficients become approximately equal. Therefore, when wave propagation is simulated at an azimuthal angle of 90°, only background isotropic parameters of the coalbed affect the reflection coefficient. This result is similar to that of Zhang *et al*. (1997) computed using a three-layer isotropic model.

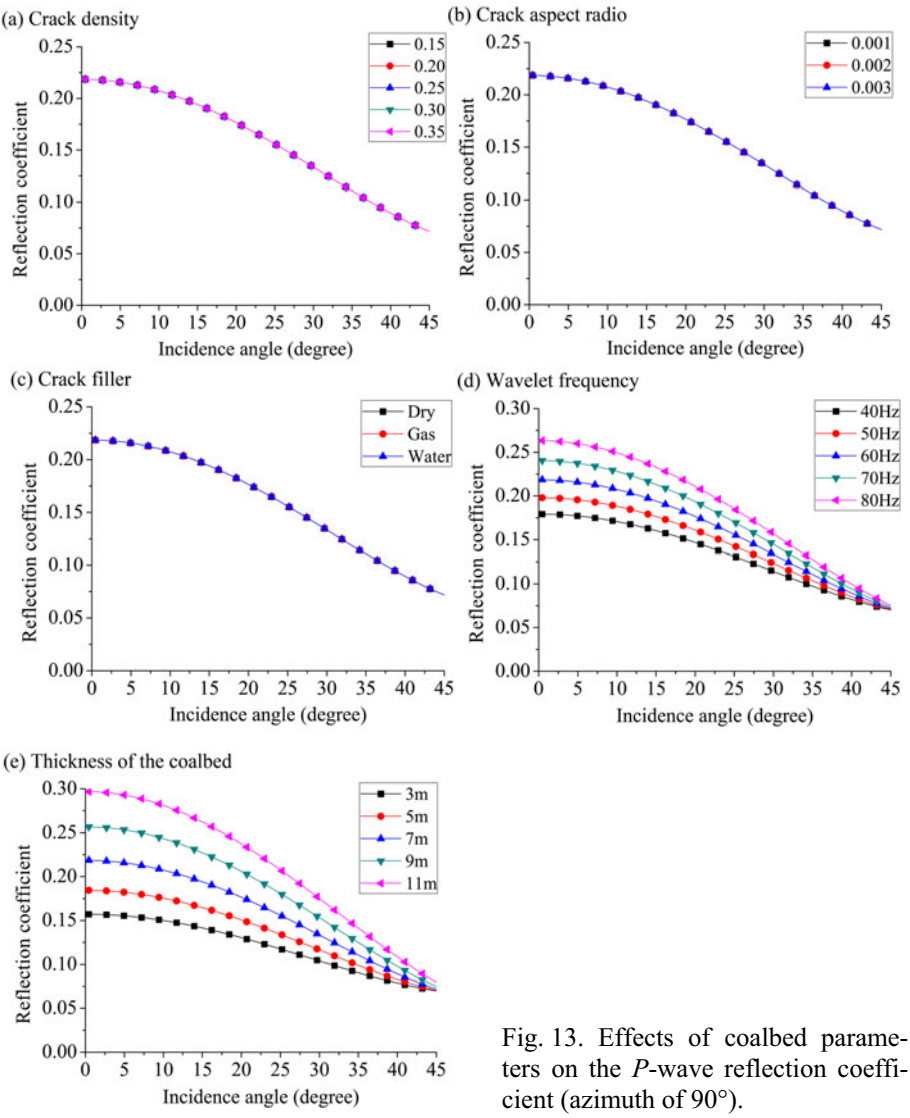

Fig. 13. Effects of coalbed parameters on the *P*-wave reflection coefficient (azimuth of 90°).

To investigate the seismic amplitude variation with the offset, we simulated a two-dimensional survey line at a 5-m receiver spacing at the surface. The *P*-wave source of the Ricker wavelet with a dominant frequency of 60 Hz is located at the starting point of the survey line. The time sampling interval is 0.5 ms. We use three-layer model for an azimuthal angle of 0° and a gas-saturated crack and the same other parameters as in the previous example. Figure 14 shows the synthetic common shot gather for the *P* and

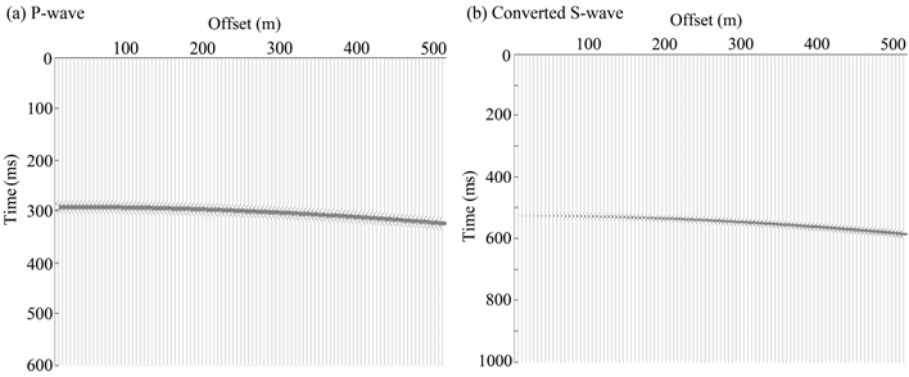

Fig. 14. Common shot gather.

converted *PS* waves. The offset varies from 0 to 500 m at intervals of 5 m. The synthetic seismogram shows the same general trend in the AVO response as observed in the previous example.

The seismic amplitude obtained by forward modeling has been used to interpret variations in physical parameters of the fracture and coalbed. In practice, by comparing real seismic records from a coalfield with the synthetic seismogram, we can inverse some parameters of the coalbed according to the amplitude. This has important significance in detecting CBM.

5. CONCLUSION

In this paper, we built a three-layer model to describe AVO responses in an anisotropic coalbed. The top and bottom layers were isotropic, while the middle layer was a fractured coalbed considered as an EDA medium. Using the model, we simulated wave propagation and discussed individual reflections from the top and bottom of the coalbed. Employing Cheng's theory, Kelvin–Christoffel equations and boundary conditions, an exact formula to calculate the reflection coefficient was derived. We modelled reflection coefficients of the *P* and converted *PS* waves for the azimuths 0° and 90°. We demonstrated that the reflection coefficient of the *P* wave increases while the converted *PS* wave decreases with the increasing incidence angle.

The crack density, crack aspect ratio, crack filler, wavelet frequency, and thickness of the coalbed have some effect on the reflection coefficient at an azimuthal angle of 0°. The results show that the intercept and slope of *P*-wave reflection coefficient curves increase with increasing crack density, wavelet frequency, and coalbed thickness. In a certain range of the incidence angle, *P*-wave reflection coefficients are approximately equal. For the converted *S* wave, there is also an increasing tendency for the reflection coefficient. Additionally, the reflection coefficients are considerably affected by

gas-saturated and water-saturated cracks. The crack aspect ratio has little effect on the reflection coefficient. When the azimuthal angle of fracture is parallel to the cracks, the differences in fracture parameters do not affect the reflected AVO signature, and the coalbed can be considered an isotropic medium.

To analyze the variation in seismic amplitude, we created a synthetic seismogram by forward calculation. The information of the amplitude was used to detect changes of cracks in the coalbed. In particular, AVO curves were notably different for gas-saturated cracks and water-saturated cracks in a coalbed. This finding can be applied to CBM detection. Although there will be some possible obstacles like data quality, effect from the stress, temperature, *etc*., our study shows that in the presence of the methane filled coal fractures we can expect changes in the amplitudes which can be possibly in the future inverted for the density of the fractures and may be for the methane content.

Acknowledgments. We greatly appreciate the support of the National 973 Program of China (2009CB219603, 2010CB226800, 2009CB724601), National Natural Science Foundation of China (Major Program) (50490271, 40672104), National Natural Science Foundation of China (General Program) (40874071), Joint Fund of Coal (U1261203), the National Science and Technology Pillar Program in the Eleventh Five-year Plan Period (2012BAB13B01, 2012BAC10B03), and the China Geological Survey Project (1212011220798, 1212011220188).

Appendices

A. Elastic wave equation and Kelvin–Christoffel equation for anisotropic media

As the theoretical basis of wave mechanics, the elastic wave equation has been widely used to describe seismic wave propagation in isotropic and anisotropic media. In anisotropic media, the strain produced by a stress of any kind is proportional to the stress. Hook's law explains the stress-strain relationship and can be written using matrix notation as (Carcione 2007):

$$\boldsymbol{\sigma} = \mathbf{C} \cdot \mathbf{e} \ , \tag{A1}$$

where $\boldsymbol{\sigma}$ is the stress tensor, $\mathbf{e}$ is the strain tensor, and $\mathbf{C}$ is the stiffness tensor of 6×6 matrices. From Newton's second law, which describes the dynamic

process among the stress, strain, and displacement, we get the general equation of motion in the absence of body forces

$$\rho \frac{\partial^2}{\partial t^2}\mathbf{u} = \nabla \cdot \boldsymbol{\sigma} \ , \tag{A2}$$

where ρ is the density, $\mathbf{u}$ is the displacement vector, and ∇ using the matrix representation is given by (Auld 1990)

$$\nabla = \begin{bmatrix} \partial_x & 0 & 0 & 0 & \partial_z & \partial_y \\ 0 & \partial_y & 0 & \partial_z & 0 & \partial_x \\ 0 & 0 & \partial_z & \partial_y & \partial_x & 0 \end{bmatrix}. \tag{A3}$$

Equation A2 can be written in another form according to the relationship among the stress, strain and displacement

$$\rho \frac{\partial^2}{\partial t^2}\mathbf{u} = \nabla \cdot \mathrm{C} \cdot \nabla^{\mathrm{T}} \cdot \mathbf{u} \ . \tag{A4}$$

Equation A4 is the anisotropic elastic wave equation.

A general wave solution for the displacement vector is written as (Ali and Jakobsen 2011)

$$\mathbf{u} = \mathbf{P} A_0 e^{i(\mathbf{k}\cdot\mathbf{x}-\omega t)} \ , \tag{A5}$$

where

$$\mathbf{k} = k\left(l_x, l_y, l_z\right) \ . \tag{A6}$$

Here $\mathbf{u} = (u_x, u_y, u_z)^T$ is the displacement vector, $\mathbf{P} = (p_x, p_y, p_z)^T$ is the polarization vector, A_0 is the wave amplitude, $\mathbf{k}$ is the wave-number vector and l_x, l_y, and l_z are the direction cosines. The spatial differential operator in Eq. A3 can be replaced by

$$\nabla \to ik \begin{bmatrix} l_x & 0 & 0 & 0 & l_z & l_y \\ 0 & l_y & 0 & l_z & 0 & l_x \\ 0 & 0 & l_z & l_y & l_x & 0 \end{bmatrix} = ik\mathbf{L} \ . \tag{A7}$$

Substitution of Eqs. A5-A7 into Eq. A4 gives the Kelvin–Christoffel equation (Musgrave 1970)

$$\begin{bmatrix} \Gamma_{11} - \rho v^2 & \Gamma_{12} & \Gamma_{13} \\ \Gamma_{21} & \Gamma_{22} - \rho v^2 & \Gamma_{23} \\ \Gamma_{31} & \Gamma_{32} & \Gamma_{33} - \rho v^2 \end{bmatrix} \begin{bmatrix} p_x \\ p_y \\ p_z \end{bmatrix} = 0 \, , \tag{A8}$$

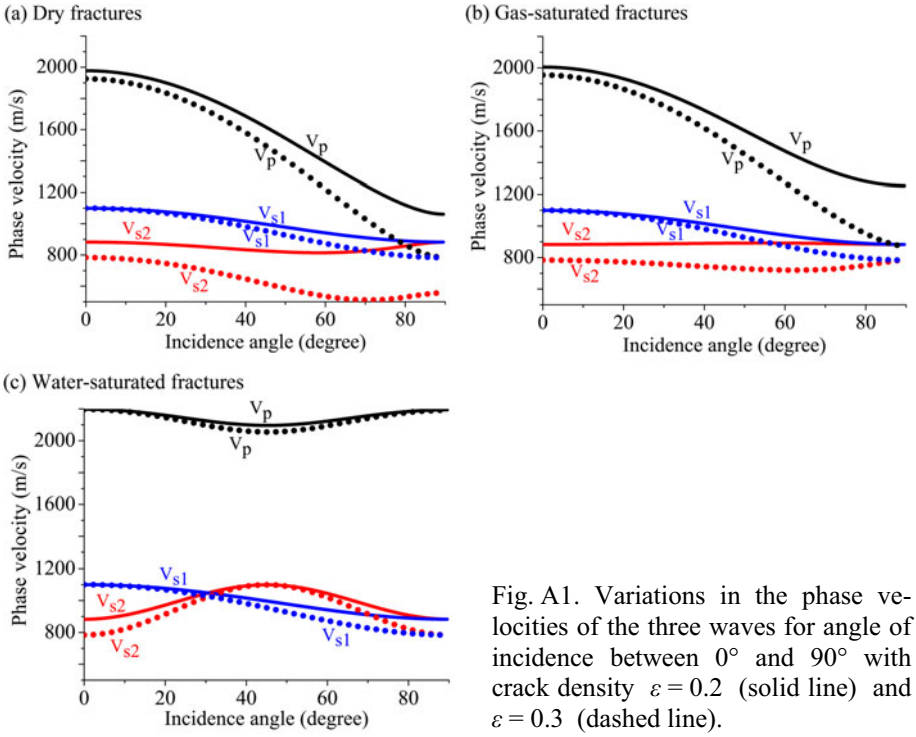

Fig. A1. Variations in the phase velocities of the three waves for angle of incidence between 0° and 90° with crack density $\varepsilon = 0.2$ (solid line) and $\varepsilon = 0.3$ (dashed line).

where

$$\mathbf{\Gamma} = \begin{bmatrix} \Gamma_{11} & \Gamma_{12} & \Gamma_{13} \\ \Gamma_{21} & \Gamma_{22} & \Gamma_{23} \\ \Gamma_{31} & \Gamma_{32} & \Gamma_{33} \end{bmatrix} = \mathbf{L} \cdot \mathbf{C} \cdot \mathbf{L}^T \tag{A9}$$

is the Christoffel matrix. Because the polarization vector is nonzero, Eq. A8 has a nonzero solution, *i.e.*,

$$\det(\mathbf{\Gamma} - \rho v^2 \mathbf{I}_3) = 0 \ . \tag{A10}$$

After solving Eqs. 9 and 10, we can obtain the wave velocity v and polarization vector **P**. Figure A1 shows the vertical sections of the *P*-, *SV*-, and *SH*-wave phase velocities for gas-saturated, water-saturated, and dry cracks. The background parameters are the same as in Fig. 2 except that the crack density is taken as 0.2 and 0.3. From Fig. A1, it is obvious that the crack filler strongly affects the velocities of *P*, *SV*, and *SH* waves. Additionally, the three wave velocities reduce as the crack density increases.

B. Reflection of a plane wave in a two-layer anisotropic model

The two-layer model is shown in Fig. 3a. Two homogeneous anisotropic half-spaces (EDA1 and EDA2) are separated by a horizontal interface. A plane *P*-wave incident on the interface generates three plane waves with mutually orthogonal polarization directions: *P*, *SV*, and *SH* waves. When the incident *P*-wave travels in the $[x,z]$-plane, we need to consider the coupling of *P* and *SV* waves at the interface. However, the third wave type, the *SH* wave, is polarized perpendicular to the $[x,z]$-plane and is not excited by incident *P* and *SV* waves. Additionally, it is decoupled from the *P* and *SV* waves. Thus, we only need to solve the transmission and reflection coefficients of the *P* and *SV* waves due to the continuity requirements at the plane horizontal interface in the $[x,z]$-plane (azimuth of 0°). The wave propagation in the $[y,z]$-plane (azimuth of 90°) can be described in the same way. Figure B1 shows the plane wave propagation in the two-layer model for an azimuthal angle of 0°. The plane *P*-wave *P* incident at the interface generates four waves: reflected PP_1 and PS_1 waves, and transmitted PP_2 and PS_2 waves.

Next, we begin to derive the exact solution for reflection and transmission coefficients as a function of the incidence angle. Boundary conditions have to be applied to solve for the reflection and transmission coefficients. We assume that the stiffness tensors of $\text{EDA}^{(1)}$ and $\text{EDA}^{(2)}$ are $\mathbf{C}^{(1)}$ and $\mathbf{C}^{(2)}$ for an azimuthal angle of 0°. Using Cheng's theory (1993) mentioned above, elastic stiffness tensors can be computed from the known background velocity, crack density, crack aspect ratio, and crack filler. The stress-strain relationship, explained by Hooke's law in Appendix A, can then be written as

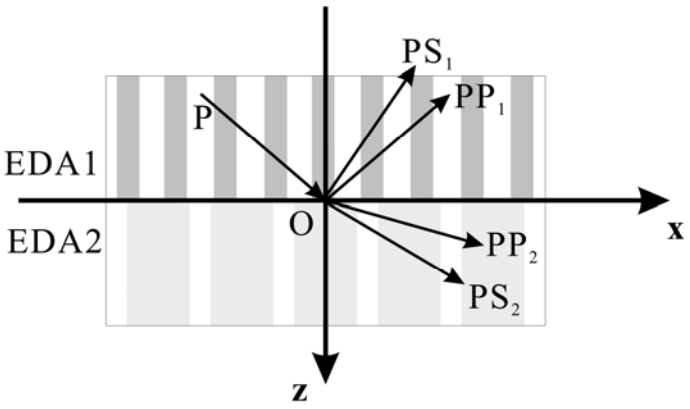

Fig. B1. Wave propagation in the two-layer model.

$$\begin{bmatrix} \sigma_{xx}^{(j)} \\ \sigma_{yy}^{(j)} \\ \sigma_{zz}^{(j)} \\ \sigma_{yz}^{(j)} \\ \sigma_{xz}^{(j)} \\ \sigma_{xy}^{(j)} \end{bmatrix} = \begin{bmatrix} c_{11}^{(j)} & c_{13}^{(j)} & c_{13}^{(j)} & 0 & 0 & 0 \\ c_{13}^{(j)} & c_{22}^{(j)} & c_{23}^{(j)} & 0 & 0 & 0 \\ c_{13}^{(j)} & c_{23}^{(j)} & c_{33}^{(j)} & 0 & 0 & 0 \\ 0 & 0 & 0 & c_{44}^{(j)} & 0 & 0 \\ 0 & 0 & 0 & 0 & c_{55}^{(j)} & 0 \\ 0 & 0 & 0 & 0 & 0 & c_{55}^{(j)} \end{bmatrix} \begin{bmatrix} e_{xx}^{(j)} \\ e_{yy}^{(j)} \\ e_{zz}^{(j)} \\ e_{yz}^{(j)} \\ e_{xz}^{(j)} \\ e_{xy}^{(j)} \end{bmatrix}, \quad (j = 1, 2) , \tag{B1}$$

where $\mathrm{C}^{(j)} = [c_{mn}^{(j)}]$ $(m,\ n = 1, 2, ..., 6)$ is the stiffness tensor of EDA$^{(j)}$, $\boldsymbol{\sigma}^{(j)} = [\sigma_{xx}^{(j)}, \sigma_{yy}^{(j)}, \sigma_{zz}^{(j)}, \sigma_{yz}^{(j)}, \sigma_{xz}^{(j)}, \sigma_{xy}^{(j)}]^T$ is the stress tensor of EDA$^{(j)}$, and $\mathbf{e}^{(j)} = [e_{xx}^{(j)}, e_{yy}^{(j)}, e_{zz}^{(j)}, e_{yz}^{(j)}, e_{xz}^{(j)}, e_{xy}^{(j)}]^T$ is the strain tensor of EDA$^{(j)}$.

Meanwhile, the strain–displacement relationship can be expressed as

$$e_{xx}^{(j)} = \frac{\partial u_x^{(j)}}{\partial x}, \quad e_{yy}^{(j)} = \frac{\partial u_y^{(j)}}{\partial y}, \quad e_{zz}^{(j)} = \frac{\partial u_z^{(j)}}{\partial z} ,$$

$$e_{yz}^{(j)} = \frac{\partial u_z^{(j)}}{\partial y} + \frac{\partial u_y^{(j)}}{\partial z}, \quad e_{xz}^{(j)} = \frac{\partial u_z^{(j)}}{\partial x} + \frac{\partial u_x^{(j)}}{\partial z}, \quad e_{xy}^{(j)} = \frac{\partial u_x^{(j)}}{\partial y} + \frac{\partial u_y^{(j)}}{\partial x} \quad (j = 1, 2) , \tag{B2}$$

where $u_x^{(j)}$, $u_y^{(j)}$, and $u_z^{(j)}$ are components of the displacement vector $\mathbf{u}^{(j)}$ in the directions of x, y, and z. The continuity of stress at the reflecting horizon yields (assuming that the depth of the interface is zero; *i.e.*, $z = 0$)

$$\sigma_{zz}^{(1)} = \sigma_{zz}^{(2)} , \quad \sigma_{zx}^{(1)} = \sigma_{zx}^{(2)} . \tag{B3}$$

Substituting Eq. B2 into B1, we have

$$\sigma_{zz}^{(j)} = c_{13}^{(j)} \frac{\partial u_x^{(j)}}{\partial x} + c_{33}^{(j)} \frac{\partial u_z^{(j)}}{\partial z} , \quad \sigma_{xz}^{(j)} = c_{66}^{(j)} \left(\frac{\partial u_z^{(j)}}{\partial x} + \frac{\partial u_x^{(j)}}{\partial z} \right) . \tag{B4}$$

Substituting Eq. (B4) into (B3), we have

$$c_{13}^{(1)} \frac{\partial u_x^{(1)}}{\partial x} + c_{33}^{(1)} \frac{\partial u_z^{(1)}}{\partial z} = c_{13}^{(2)} \frac{\partial u_x^{(2)}}{\partial x} + c_{33}^{(2)} \frac{\partial u_z^{(2)}}{\partial z} ,$$

$$c_{66}^{(1)} \left(\frac{\partial u_z^{(1)}}{\partial x} + \frac{\partial u_x^{(1)}}{\partial z} \right) = c_{66}^{(2)} \left(\frac{\partial u_z^{(2)}}{\partial x} + \frac{\partial u_x^{(2)}}{\partial z} \right) . \tag{B5}$$

Equation A5 is a function of the displacement vector of a plane wave. In the $[x, z]$-plane, the displacement vector $\mathbf{u}$ has the form

$$\mathbf{u}_k = \left(f_k, h_k \right) A_k \exp\left[i\omega \left(p_k x + r_k z - t \right) \right], \quad k = 1, 2, ..., 5 , \tag{B6}$$

where $\mathbf{P}_k = (f_k, h_k)$ is the unit polarization vector, A_k is the wave amplitude, p_k is horizontal slowness with respect to the x-axis, and r_k is vertical slowness with respect to the z-axis. $k = 1, 2, \ldots, 5$ denote the incident P-wave P, reflected P-wave PP_1, reflected converted S-wave PS_1, transmitted P-wave PP_2, and transmitted converted S-wave PS_2, respectively.

At the top of the interface, the total displacement of waves propagating in EDA$^{(1)}$ is written as

$$\begin{aligned} u_x^{(1)} &= \sum_{k=1}^{3} f_k A_k \exp\left[i\omega(p_k x + r_k z - t)\right], \\ u_z^{(1)} &= \sum_{k=1}^{3} h_k A_k \exp\left[i\omega(p_k x + r_k z - t)\right]. \end{aligned} \tag{B7}$$

Similarly, the total displacement at the bottom of the interface is written as

$$\begin{aligned} u_x^{(2)} &= \sum_{k=4}^{2} f_k A_k \exp\left[i\omega(p_k x + r_k z - t)\right], \\ u_z^{(2)} &= \sum_{k=4}^{2} h_k A_k \exp\left[i\omega(p_k x + r_k z - t)\right]. \end{aligned} \tag{B8}$$

From the boundary condition, which describes the continuity of displacement, we obtain

$$\sum_{k=1}^{3} f_k A_k \exp\left[i\omega(p_k x - t)\right] = \sum_{k=4}^{2} f_k A_k \exp\left[i\omega(p_k x - t)\right], \tag{B9}$$

$$\sum_{k=1}^{3} h_k A_k \exp\left[i\omega(p_k x + r_k z - t)\right] = \sum_{k=4}^{2} h_k A_k \exp\left[i\omega(p_k x + r_k z - t)\right]. \tag{B10}$$

From the solution of the Kelvin–Christoffel equation and Snell's law, we conclude that the horizontal slowness shown in Fig. B1 is the same for all waves. Letting $p_k = p$, Eqs. B9 and B10 can be reduced to

$$\sum_{k=1}^{3} f_k A_k = \sum_{k=4}^{2} f_k A_k, \quad \sum_{k=1}^{3} h_k A_k = \sum_{k=4}^{2} h_k A_k. \tag{B11}$$

Solving Eqs. B5 and B11, we have

$$\mathrm{M}(A_2, A_3, A_4, A_5)^T = \mathrm{N}(A_1), \tag{B12}$$

where M and N are 4×4 matrices that contain the elements of the stiffness matrix, polarization and slownesses. It is well known that the reflection and transmission coefficients are defined as

$$R_{pp} = \frac{A_2}{A_1}, \quad R_{ps} = \frac{A_3}{A_1}, \quad T_{pp} = \frac{A_4}{A_1}, \quad T_{ps} = \frac{A_5}{A_1}. \tag{B13}$$

Equation B12 can then be written as

$$\left(R_{pp}, R_{ps}, T_{pp}, T_{ps}\right) = \mathrm{M}^{-1}\mathrm{N} \ . \tag{B14}$$

Equation B14 represents the exact solution for reflection and transmission coefficients at an interface of EDA media.

References

Aki, K., and P.G. Richards (1980), *Quantitative Seismology*, W.H. Freeman & Co, New York.

Ali, A., and M. Jakobsen (2011), Seismic characterization of reservoirs with multiple fracture sets using velocity and attenuation anisotropy data, *J. Appl. Geophys.* **75**, 3, 590-602, DOI: 10.1016/j.jappgeo.2011.09.003.

Auld, B.A. (1990), *Acoustic Fields and Waves in Solids*, Krieger Publ. Malabar.

Bachu, S., and S. Bell (2001), Stress regime in the Cretaceous succession of the Alberta basin: A predictor for coal bed methane producibility. **In:** *Rock the Foundation Convention, 18-22 June 2001*, Canadian Society of Petroleum Geologists, Calgary, Canada, 003-1-003-5.

Bakulin, A., V. Grechka, and I. Tsvankin (2000a), Estimation of fracture parameters from reflection seismic data – Part I: HTI model due to a single fracture set, *Geophysics* **65**, 6, 1788-1802, DOI: 10.1190/1.1444863.

Bakulin, A., V. Grechka, and I. Tsvankin (2000b), Estimation of fracture parameters from reflection seismic data – Part II: Fractured models with orthorhombic symmetry, *Geophysics* **65**, 6, 1803-1817, DOI: 10.1190/1.1444864.

Bortfeld, R. (1961), Approximations to the reflection and transmission coefficients of plane longitudinal and transverse waves, *Geophys. Prospect.* **9**, 4, 485-502, DOI: 10.1111/j.1365-2478.1961.tb01670.x.

Carcione, J.M. (2007), Wave Fields in Real Media: Wave Propagation in Anisotropic, Anelastic, Porous and Electromagnetic Media, Elsevier, Amsterdam.

Castagna, J.P., H.W. Swan, and D.J. Foster (1998), Framework for AVO gradient and intercept interpretation, *Geophysics* **63**, 3, 948-956, DOI: 10.1190/1.1444406.

Chen, W. (1995), AVO in azimuthally anisotropic media fracture detection using P-wave data and a seismic study of naturally fractured tight gas reservoirs, Department of Geophysics, School of Earth Sciences, Stanford University, USA.

Cheng, C.H. (1993), Crack models for a transversely isotropic medium, *J. Geophys. Res.* **98**, B1, 675-684, DOI: 10.1029/92JB02118.

Crampin, S. (1984), Effective anisotropic elastic constants for wave propagation through cracked solids, *Geophys. J. Int.* **76**, 1, 135-145, DOI: 10.1111/j.1365-246X.1984.tb05029.x.

Crampin, S. (1989), Suggestions for a consistent terminology for seismic anisotropy, *Geophys. Prospect*. **37**, 7, 753-770, DOI: 10.1111/j.1365-2478.1989.tb02232.x.

Du, S.T. (1996), *Seismic Wave Dynamics*, China University of Petroleum Press, Dongying, China (in Chinese).

Eshelby, J.D. (1957), The determination of the elastic field of an ellipsoidal inclusion, and related problems, *Proc. Roy. Soc. London A* **241**, 1226, 376-396, DOI: 10.1098/rspa.1957.0133.

Gochioco, L.M. (1991), Tuning effect and interference reflections from thin beds and coal seams, *Geophysics* **56**, 8, 1288-1295, DOI: 10.1190/1.1443151.

Hu, Y.R., and G.A. McMechan (2007), Imaging mining hazards within coalbeds using prestack wave equation migration of in-seam seismic survey data: A feasibility study with synthetic data, *J. Appl. Geophys.* **63**, 1, 24-34, DOI: 10.1016/j.jappgeo.2007.03.002.

Hudson, J.A. (1980), Overall properties of a cracked solid, *Math. Proc. Cambridge Philos. Soc.* **88**, 2, 371-384, DOI: 10.1017/S0305004100057674.

Hudson, J.A. (1981), Wave speeds and attenuation of elastic waves in materials containing cracks, *Geophys. J. Int.* **64**, 1, 133-150, DOI: 10.1111/j.1365-246X.1981.tb02662.x.

Komatitsch, D., and J. Tromp (2003), A perfectly matched layer absorbing boundary condition for the second-order seismic wave equation, *Geophys. J. Int.* **154**, 1, 146-153, DOI: 10.1046/j.1365-246X.2003.01950.x.

Meissner, R., and E. Meixner (1969), Deformation of seismic wavelets by thin layers and layered boundaries, *Geophys. Prospect.* **17**, 1, 1-27, DOI: 10.1111/j.1365-2478.1969.tb02069.x.

Musgrave, M.J.P. (1970), *Crystal Acoustics: Introduction to the Study of Elastic Waves and Vibrations in Crystals*, Holden-Day, San Francisco.

Ostrander, W.J. (1984), Plane-wave reflection coefficients for gas sands at nonnormal angles of incidence, *Geophysics* **49**, 10, 1637-1648, DOI: 10.1190/1.1441571.

Peng, S.P., H.J. Chen, R.Z. Yang, Y.F. Gao, and X.P. Chen (2006), Factors facilitating or limiting the use of AVO for coal-bed methane, *Geophysics* **71**, 4, C49-C56, DOI: 10.1190/1.2217137.

Ramos, A.C.B., and T.L. Davis (1997), 3-D AVO analysis and modeling applied to fracture detection in coalbed methane reservoirs, *Geophysics* **62**, 6, 1683-1695, DOI: 10.1190/1.1444268.

Rüger, A. (1997), P-wave reflection coefficients for transversely isotropic models with vertical and horizontal axis of symmetry, *Geophysics* **62**, 3, 713-722, DOI: 10.1190/1.1444181.

Rutherford, S.R., and R.H. Williams (1989), Amplitude-versus-offset variations in gas sands, *Geophysics* **54**, 6, 680-688, DOI: 10.1190/1.1442696.

Shuck, E.L., T.L. Davis, and R.D. Benson (1996), Multicomponent 3-D characterization of a coalbed methane reservoir, *Geophysics* **61**, 2, 315-330, DOI: 10.1190/1.1443961.

Shuey, R.T. (1985), A simplification of the Zoeppritz equations, *Geophysics* **50**, 4, 609-614, DOI: 10.1190/1.1441936.

Wright, J. (1987), The effects of transverse isotropy on reflection amplitude versus offset, *Geophysics* **52**, 4, 564-567, DOI: 10.1190/1.1442325.

Zhang, A.M., Y. Wang, and S.Z. Zhao (1997), Study on the AVO model and AVO character of coal seams with different thickness, *J. China Univ. Min. Technol.* **26**, 3, 36-41 (in Chinese).

Zoeppritz, K. (1919), Erdbebenwellen VII B. On the reflection and penetration of seismic waves through unstable layers, *Nachr. Gesellsch. Wissensch. Göttingen, Math.-Physik. Kl.* **1919**, 66-84.

Received 11 December 2013
Received in revised form 7 May 2014
Accepted 24 June 2014

DE GRUYTER OPEN

Acta Geophysica
vol. 63, no. 3, June 2015, pp. 843-862
DOI: 10.1515/acgeo-2015-0021

Preliminary Results of Anthropogenic Seismicity Monitoring in the Region of Song Tranh 2 Reservoir, Central Vietnam

Jan WISZNIOWSKI[1], Nguyen Van GIANG[2], Beata PLESIEWICZ[1], Grzegorz LIZUREK[1], Dinh Quoc VAN[2], Le Quang KHOI[2], and Stanisław LASOCKI[1]

[1]Institute of Geophysics, Polish Academy of Sciences, Warsaw, Poland
e-mail: jwisz@igf.edu.pl (corresponding author)

[2]Institute of Geophysics, Vietnam Academy of Science and Technology, Hanoi, Vietnam; e-mail: giangnv@igp-vast.vn

A b s t r a c t

Song Tranh 2 hydropower plant and the reservoir containing backed up water are located in the Quang Nam province (Central Vietnam). The region experiences unusual seismic activity related to the reservoir impoundment, with earthquakes of magnitude up to 4.7. In result of cooperation between the Institute of Geophysics, Vietnam Academy of Sciences and Technology and the Institute of Geophysics, Polish Academy of Sciences a seismic network has been built to facilitate seismic monitoring of the Song Tranh 2 area. The network, operating since August 2013, consists of 10 seismic stations. Here we show that the network is sufficient for advanced data processing. The first results of monitoring of the earthquake activity in Song Tranh 2 area in the period between 2012 and 2014, especially the completeness of catalogs, study and comparisons between water level and the seismic activity suggest direct connection between reservoir exploitation and anthropogenic seismicity.

Key words: reservoir induced seismicity, seismic network, source parameters, focal mechanism, completeness of catalogs.

1. INTRODUCTION

Earthquakes can be caused by natural processes (tectonic movement, volcanic activity, *etc*.) or by human technological activity. The earthquakes associated with human activity are called Induced Seismicity (IS). Under certain suitable geological conditions, technological operations can trigger or induce earthquakes. Induced seismicity includes cases such as seismicity associated with an impoundment of surface water reservoirs, underground mining, large-scale surface quarrying, high-pressure fluid injection for geothermal power generation and a conventional and unconventional hydrocarbon exploitation, underground storage of fluids, removal of underground fluids, and underground explosions.

Association of earthquakes with impounding of artificial water reservoirs was for the first time pointed out by Carder (1945) for lake Mead in the United States. The number of reported cases of reservoir-induced earthquakes has steadily grown since then (Gupta 1992). The largest reservoir impoundment-triggered earthquakes exceeded magnitude 6. Occurrence of a damaging 6.3 magnitude earthquake at Koyna dam, India was in December 1967. Hoa Binh province, Northern Vietnam, is a case of reservoir triggered seismicity where in 1989 an earthquake of magnitude 4.9 took place (Gupta 2011).

Simpson (1976) and Gupta (1985) found that, in some locations, the Reservoir Induced Seismicity (RIS) occurs early after reservoir impoundment, whereas in other places the earthquake excitation occurs a number of years after the lake began to be filled. Based on such observations, Simpson (1986) and Simpson *et al.* (1988) have classified RIS into two types: rapid response type and delayed response type. The rapid response may be associated with changes in elastic stress due to the load of the reservoir. Examples of such a response (Simpson *et al.* 1988) are lakes Monticello, Manic 3, Nurek, Kariba, and Tehri (Choudhury *et al*. 2013). In contrast with the rapid response RIS phenomenon, in the delayed response RIS events occur relatively later after the reservoir filling. Some examples are Aswan, Koyna, and Oroville (Simpson *et al.* 1988). In such reservoirs the pore pressure at hypocentral depths can rise slowly, with the diffusion of water from the lake. In the delayed response class a number of water level changes can take place before the earthquake activity is enhanced. In some places, like Koyna and lake Mead, the rapid and the delayed response appeared.

The present paper considers the case of reservoir triggered seismicity in the Song Tranh 2 (STH2) reservoir region, located in the Quang Nam province in Central Vietnam. The largest earthquake, of magnitude 4.7, which occurred on 15 November 2012, was felt by people and damaged structures

of buildings in the surrounding areas. Currently a constant seismic activity is observed in the STH2 region.

On 4 April 2013, there was concluded an Agreement for Research Co-operation between the Institute of Geophysics, Vietnam Academy of Science and Technology (IGP VAST) and the Institute of Geophysics, Polish Academy of Sciences (IGP PAS). The purpose of this Agreement for Research Co-operation is to provide a framework for promotion of co-operative research between IGP VAST and IGP PAS in the field of RIS research. This includes, in particular, the installation of seismic stations, seismic monitoring and processing, analyzing and interpreting the seismological data of reservoir STH2 area in Bac Tra My district and surrounding areas in Quang Nam province in Central Vietnam. Special emphasis is focused on investigation of the focal mechanism of events and seismic hazard estimation. The first results of the monitoring campaign are presented below together with a preliminary interpretation of the observed seismic pattern.

2. SEISMIC ACTIVITY CAUSED BY FILLING OF THE SONG TRANH 2 RESERVOIR

The natural seismic activity of the STH2 region is very low. From the earthquake sources such as operational history, international data, as well as recorded by seismic stations in Central Vietnam, it has been found that, in the period from 1775 to 1992, only 13 events in this area have been found in both historical and instrumental world seismological data. Out of these 13, there was only one earthquake in 1715 which was located near the hydropower reservoir (Fig. 1) and its magnitude was about 4.7 (Thuy *et al.* 2003).

The filling of STH2 reservoir started in November 2010. The reservoir volume is 740 million m^3 and its height is 196 m. The water level began to increase slowly from about 153 m in early January 2011 to about 159.4 m on 17 February 2011 and then it was reduced to approximately 140 m on 20 July 2011. Filling of reservoir was recommenced on 20 August 2011. On 27 October 2011 the maximum water level of 175 m was reached. The water level around 175 m was kept until February 2012, when it was quickly reduced to the level of 157.64 m, because of some technical problems unconnected with seismicity. In May 2012 it was further decreased to 139.3 m. After that, it was kept close to 140 m to the end of September 2013. Fig. 2 shows the relationship between the reservoir water level variation and earthquakes.

During the period from the end of 2010, the analysis of seismic data recorded by 2 Vietnam national seismic stations, located in Binh Dinh and Hue (about 120-160 km from SH2), indicated several earthquakes whose epicenters were located in the province of Quang Nam (Fig. 1). Up to the beginning of 2011, the seismic activity in this area increased significantly. From

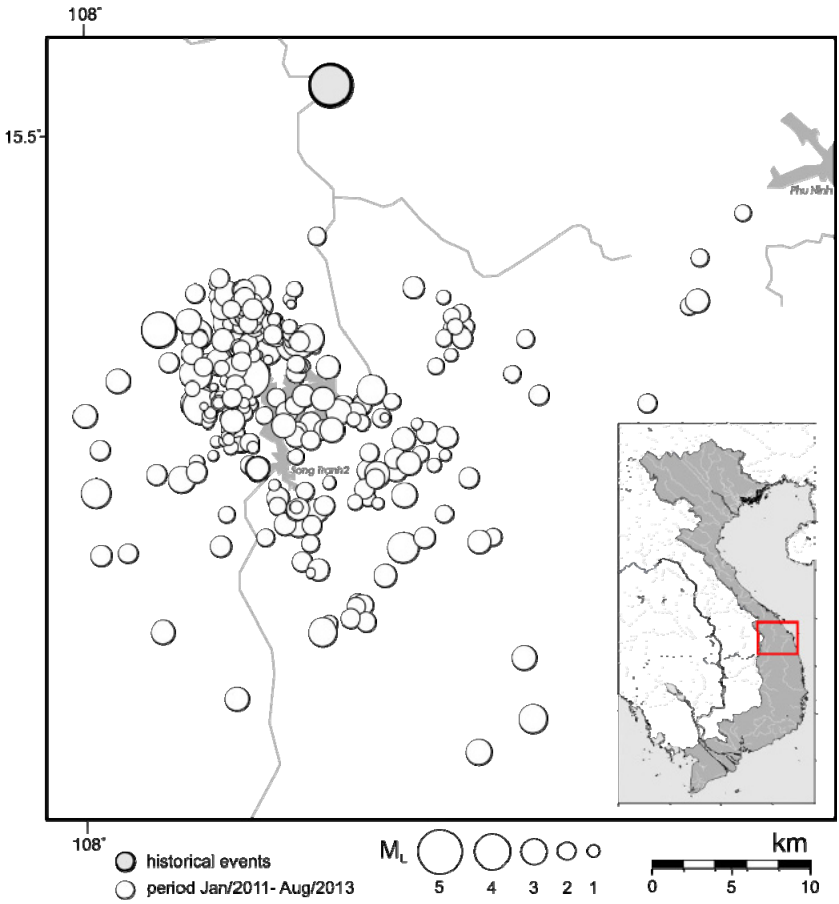

Fig. 1. Location of historical events and events from the period January 2011 – August 2013 grouped around the STH2 reservoir.

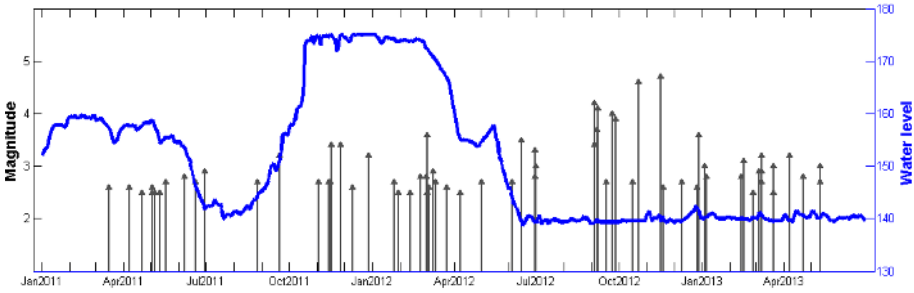

Fig. 2. The water level in the STH2 reservoir and seismic activity around the region with events with magnitude higher than 2.5 in the period from January 2011 to July 2013.

March 2011 also stronger events began to occur (Fig. 2). Two strongest took place on 22 October and 15 November 2012, and their magnitudes were $M_L = 4.6$ and 4.7, respectively. They were felt by people and caused minor damage to housing in the area.

3. GEOLOGY AND TECTONICS OF THE SONG TRANH 2 REGION

The STH2 dam and reservoir are located in Bac Tra My district in Quang Nam province, central part of Vietnam (Fig. 3). It is one of a few dams planned to be set up on the river Tranh. Geographic coordinates of the dam are: 108.1472°E and 15.3336°N.

The central and south Vietnamese continental margin forms the transition from the continental Indochina Block to the East Sea underlain partially by oceanic crust (Fyhn *et al.* 2009, Nam 1995). STH2 reservoir is located on boundary zone between Truongson and Kontum structural blocks. The first constitutes NW-SE trending Paleozoic fold system the latter is the uplifted Archean massif.

Target area constitute SE end of NW-SE trending left-lateral Cenozoic Ailao Shan-Red river shear zone. Tectonics of the area is dominated by system of W-E trending thrusts, with tectonic transport to the south: the Tam Ky-Phuoc Son, Tra Bong, and Hung Nhuong – Ta Vi (Fig. 3). STH2 is underlain by gneiss metamorphic complex Kham Duc – Nui Vu of Hung Nhuong – Ta Vi thrust.

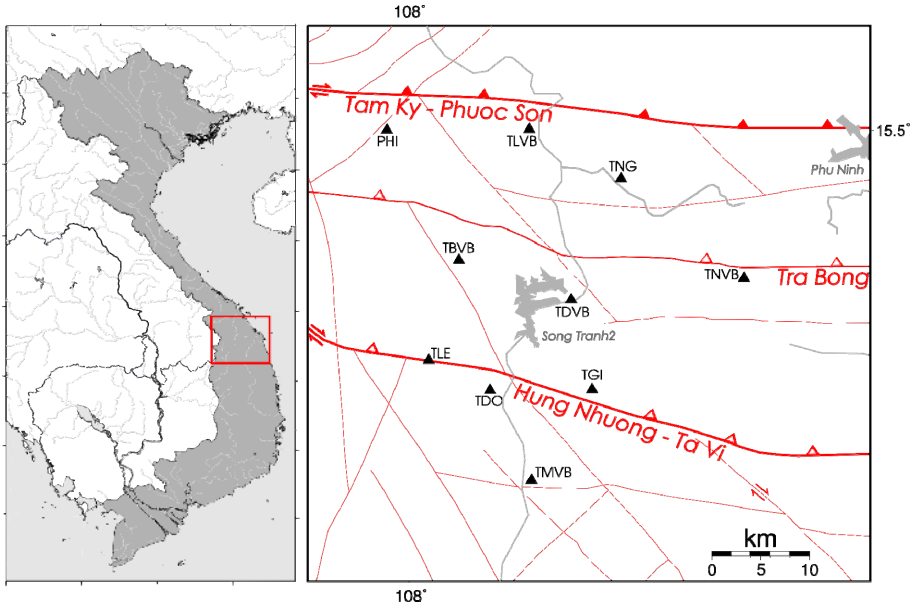

Fig. 3. Tectonic setting of the STH2 reservoir area.

There were reports of only several tremors since 17th century in the area of central Vietnam, which indicates that the whole region can be recently regarded as of moderately seismic activity (Phach and Chinh 1995).

4. SEISMIC MONITORING OF THE SONG TRANH 2 REGION

The recording of seismicity in STH2 area has had three phases:

Phase I – from January 2011 to October 2012

At the beginning of the reservoir filling, the STH2 area was monitored by two seismic stations located in Binh Dinh and Hue, away from the reservoir. Therefore, they were capable of recording earthquakes from the STH2 region with magnitudes from about 2.0 up. From January 2011 to September 2012, these two stations recorded more than 100 earthquakes in the Bac Tra My and surroundings, having magnitude $M = 1.8 \div 4.2$ (Fig. 2 and 9). Basic parameters of the stations in Binh Dinh and Hue are presented in Table 1.

Table 1

Seismic stations in phase I

No.	Station name	Code	Coordinates		Elevation [m]	Logger / seismometer
			φ [°N]	λ [°E]		
1	Binh Dinh	BDVB	13.8645	109.1111	61	Q330HRS / STS-2
2	Hue	HUBV	16.4155	107.5689	20	Q330 / Trillium-40

Phase II – from October 2012 to August 2013

Phase II began when IGP VAST deployed a five station seismograph network in the vast STH2 region. There were stations in Tra Doc, Tra Bui, Tra Nu, Tra Mai, and Tien Lanh (Table 2). The stations were equipped with Guralp seismometers and the SAMTAC logger and one Trillium-40 seismometer with the Q330 logger (Tra Doc station). The network made it possible to record events with magnitude less than 2.0 and to determine earthquake parameters such as epicentral locations more accurately.

Phase III – from August 2013 – new joint seismic network

In August 2013 a team from IGP VAST together with a team from IGP PAS installed 10 seismic stations. The integrated seismic network was called VERIS (ViEtnam Reservoir Induced Seismicity). Stations provided by IGP PAS were equipped with short-period seismometers Lennartz LE-3DLite (1 s), whereas station provided by IGP VAST were equipped with long-

Table 2

Seismic stations of VERIS network (stage III)

No.	Station name	Code	Coordinates		Elevation [m]	Logger / Seismometer
			φ [°N]	λ [°E]		
1	Tien Ngoc	TNG	15.4472	108.2038	97	NDL / LE-3Dlite
2	Tra Don	TDO	15.2432	108.0849	185	NDL / LE-3Dlite
3	Tra Leng	TLE	15.2722	108.0225	192	NDL / LE-3Dlite
4	Tra Giac	TGI	15.2400	108.1756	328	NDL / LE-3Dlite
5	Phuoc Hiep	PHI	15.4954	107.9776	56	NDL / LE-3Dlite
6	Tra Doc	TDVB	15.3342	108.1634	113	Guralp CMG-6TD (Q330 / Trillium-40)
7	Tra Bui	TBVB	15.3667	108.0503	224	Guralp CMG-6TD (SAMTAC / Guralp)
8	Tra Nu	TNVB	15.3564	108.3268	126	Guralp CMG-6TD (SAMTAC / Guralp)
9	Tra Mai	TMVB	15.1480	108.1202	202	Guralp CMG-6TD (SAMTAC / Guralp)
10	Tien Lanh	TLVB	15.4958	108.1200	325	Guralp CMG-6TD (SAMTAC / Guralp)

Note: seismometers and recorders used in phase II are in brackets.

period seismometers Guralp CMG-6TD (30 s). Signals from Lennartz seismometers were recorded by Net Data Logger (NDL), which served in the project with sampling rate of 100 sps and dynamics 132 dB. Seismometers Guralp have on-board digitizer of 130 dB dynamics. Seismic signal is sampled with a frequency of 100 sps. Both systems are appropriate to measure local and regional seismicity, as in such a case most of seismic waves' power is in the range of a few Hz, whereas Guralp stations are more suitable for the largest events in the STH2 region because their frequency band includes more low frequencies. The responses of both recording systems are presented in Fig. 4. Seismometers Lennartz LE-3DLite were installed in new stations, whereas Guralp stations replaced the previously working equipment (Table 2).

Positions of new five stations are determined by the location of the previous seismic events. They supplement earlier five stations and provide moderately complete azimuthal coverage (Fig. 10). It allows for more accurate moment tensor estimation.

The final choice of stations was preceded by ground-penetrating radar (GPR) measurements (Giang *et al.* 2010). The goal of this study was to find

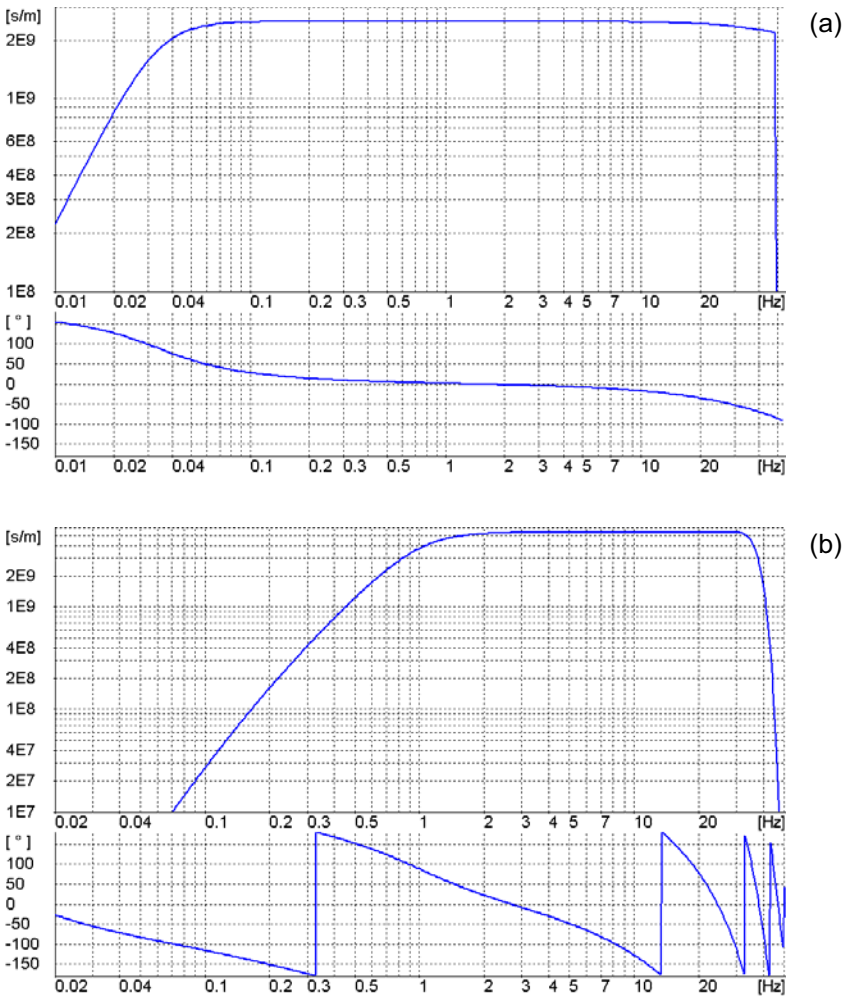

Fig. 4. The frequency-amplitude-phase response of: (a) the Guralp CMG-6TD seismometer, and (b) the Lennartz LE-3Dlite seismometer with the NDL recorder.

the location and foundations of stations on the bedrock. The GPR measurement helped assess the cohesiveness of the substratum, whether the rock is fissured or separated from the bedrock. Good foundation of seismic stations allows reducing the noise and improving detection of seismic events. It was important, because stations had to be located into residential places for security sake. The Power Spectral Densities (PSD) of seismic noises are presented in Fig. 5. We did not notice differences in noise between day and night and between Dry and Wet Seasons.

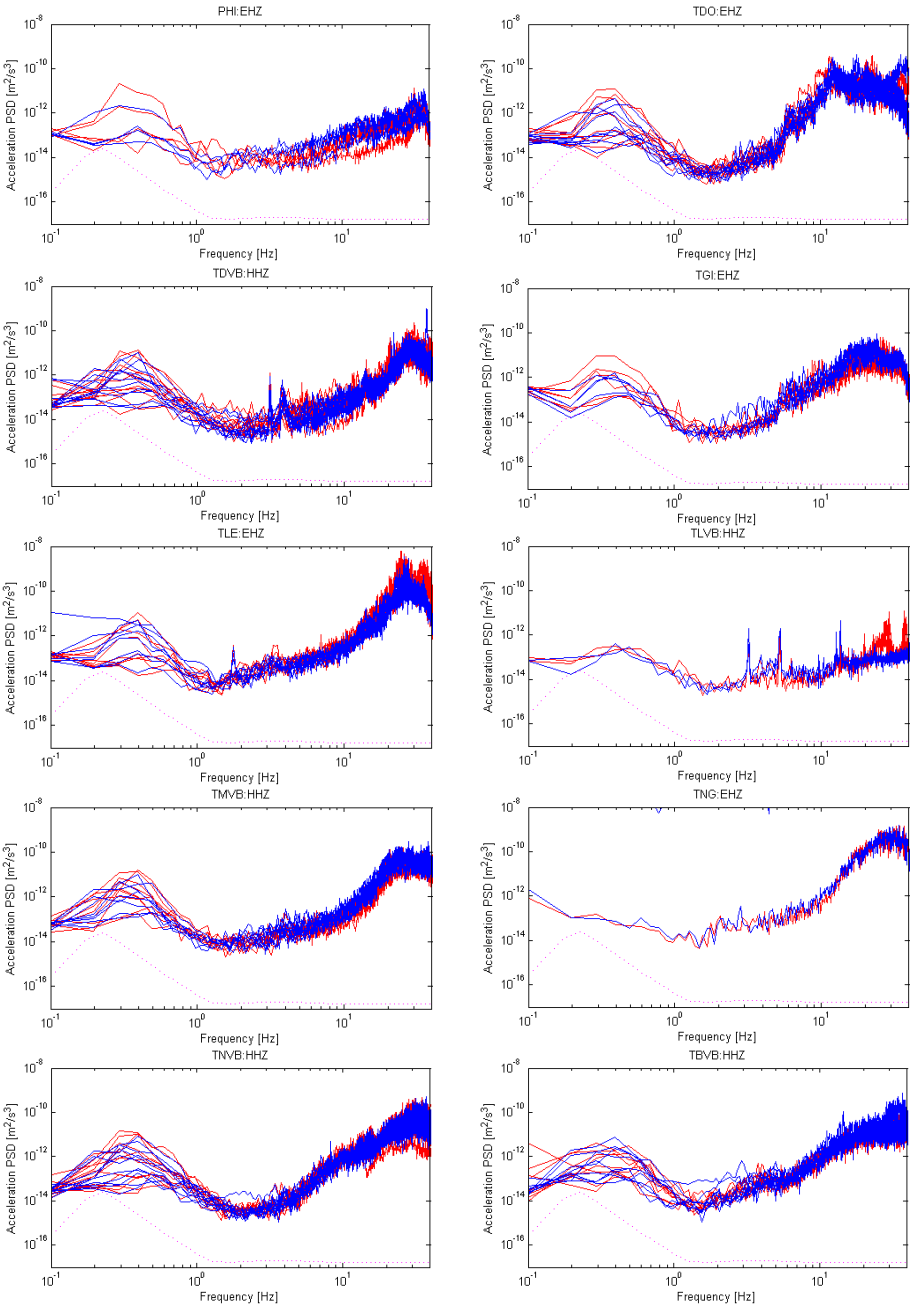

Fig. 5. The Power Spectral Densities (PSD) of seismic noise in STH2 network stations. In most of the stations the PSD is taken from both Dry and Wet Seasons. Red lines describe PSD in day whereas blue ones show noise in night. The dotted line is the PSD of Peterson's (1982) Low Noise Model.

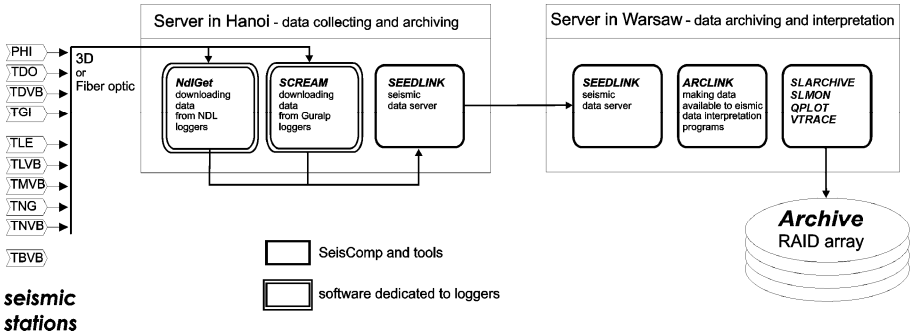

Fig. 6. Acquisition and archive system with data flow.

Seismic stations are connected to IGP VAST in Hanoi either by fiber optic or by 3G connections in Virtual Personal Network. Seismic data are transmitted on-line and stored both in Hanoi and Warsaw (Fig. 6). The system based on SeisComP (www.seiscomp3.org/wiki/doc) software is applied for collecting and archiving the data. Additional components like modules for communication with the stations have been added to adapt the system to the project requirements.

Data from Guralp stations is downloaded by SCREAM program and then transmitted to SeisComP, which is running at the same server. Data from NDLs is copied by FTP every two minutes to the same SeisComP. Seismic data from server in Hanoi is transmitted to Warsaw where waveforms are stored on a RAID matrix. The whole system combines earlier solutions (Lizurek *et al.* 2013, Trojanowski *et al.* 2015). It allows visualizing data in real time, saving and studying them as well as monitoring and controlling the data acquisition system.

Since 24 August 2013, seismic bulletins and catalogs for STH2 region are based on VERIS network. LocSAT application with the IASP91 travel-time tables provides estimates of the origin time, epicentral location, and depth from an iterative least-squares inversion of travel time, slowness, and/or azimuth (Bratt and Bache 1988, Bratt and Nagy 1991).

5. THE EXAMPLES OF FOCAL MECHANISMS OF EVENTS FROM SONG TRANH 2 REGION

Moment tensor estimates for STH2 earthquakes recorded by the VERIS network have been obtained from inversion of the *P*-wave amplitudes in time domain (Wiejacz 1992, Awad and Kwiatek 2005) using FOCI 3.0 software (Kwiatek 2013). The registered first onsets were of direct *P* wave according to the velocity model of the STH2 area. The velocity determined for the direct waves was 5.9 km/s upon the velocity model from Table 3 (Son 1995).

Table 3
Velocity model for Song Tranh 2 region

Depth [km]	*P*-wave velocity [km/s]
0-17	5.9
17-33	6.7
33-97	8.0

The direct waves were recorded on 8 stations of VERIS network. The input parameters were the amplitude and polarity of the first *P*-wave displacement pulses. According to Fitch *et al.* (1980) the recorded displacement for the vertical component of the *P*-wave phase is:

$$U_z^P(x,t) = \frac{1}{4\pi\rho\alpha^3 r}\left[\overline{\gamma}M\dot{s}\left(t-\frac{r}{\alpha}\right)\overline{\gamma}\right]l_z \ , \tag{1}$$

where ρ is the average density, r is the source-receiver distance, α is the average velocity of *P* wave, M is the seismic moment, l_z is the cosine of the incidence angle, and $\overline{\gamma}$ is the take-off angle. The Source Time Function (STF) was based on the Haskell's source model (Haskell 1953):

$$\dot{s} = \begin{matrix} 1/T, & 0 < t < T, \\ 0, & \text{elsewhere}, \end{matrix} \tag{2}$$

where T is the rupture time.

Moment tensor is obtained by solving of a set of N equations of type 1, where N is the number of stations that recorded the event. Six independent components of moment tensor require minimum six equations, and in the presented case we could use eight. All, full moment tensors, only deviatoric, and only DC solutions were calculated. L2 norm was used to determine a solution misfit (Wiejacz 1992, Awad and Kwiatek 2005). The results of inversion are presented in Table 4 and in Fig. 7. The azimuthal coverage was sparse and the number of available recordings was at the limit of the methodological requirements, which obviously influenced the inversion results. Nevertheless, those first two focal mechanism solutions provide a preliminary insight into tectonic properties of earthquake generation in the vicinity of STH2.

Additionally, the fault plane solutions were also calculated with use of HASH software. In this approach only polarities of *P*-wave onsets are used for constraining the fault plane orientations. All of the polarities have equal weight and the algorithm used in this technique uses a grid-search to deter-

Table 4

Seismic moment, moment magnitude, and nodal planes of the two studied events

Event	Seismic moment [Nm]	M_W	MT nodal plane A	MT nodal plane B	Fault plane nodal plane A	Fault plane nodal plane B
3 Sep 2013	5.01×10^{13}	3.1	33°/55°/–82°	200°/36°/–101°	6°/76°/–138°	263°/50°/–19°
31 Oct 2013	2.85×10^{12}	2.2	190°/78°/72°	69°/22°/147°	298°/78°/–143°	199°/54°/–15°

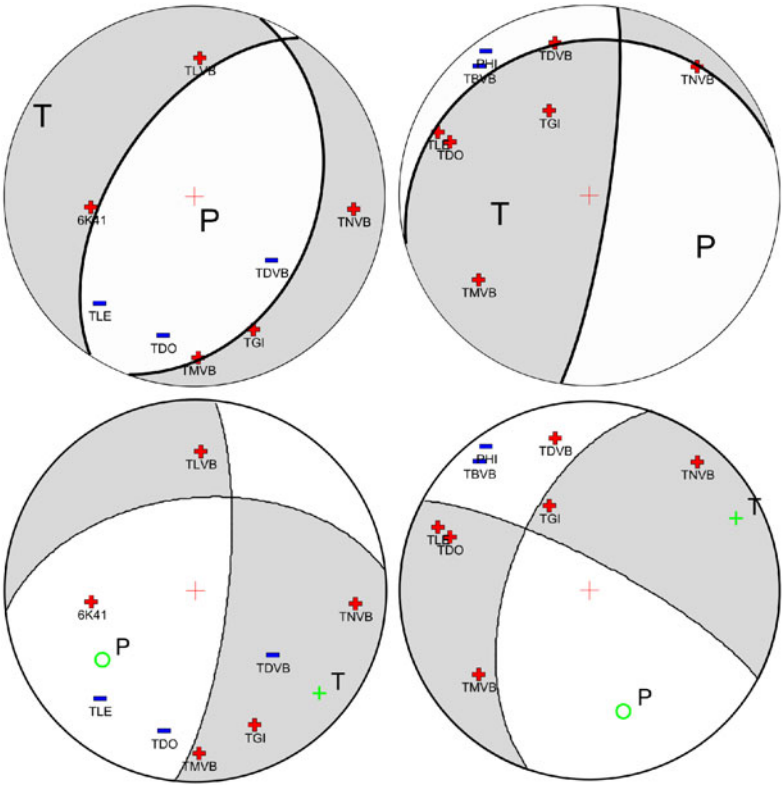

Fig. 7. Mechanism of two events from STH2 region. From left to right: M_L 3.2 on 3 September 2013 and M_L 1.8 on 31 October 2013. The codes and signs denote the station location and polarization on focal sphere. The upper row shows the results from the MT and the lower row the optimal results of fault plane solution.

mine *P*-wave polarity first-motion focal mechanisms. For each earthquake, a set of acceptable mechanisms is found. The spread of the acceptable mechanisms determines the uncertainty and the assigned solution quality. The al-

gorithm allows for minimum 7 *P*-wave onsets and there is up to 2 wrong polarity picks allowed for the search of optimal solution. The set of acceptable mechanisms takes into account the uncertainty in polarity measurements, event location, and takeoff angle (Hardebeck and Shearer 2002).

A comparison of obtained results is shown in Fig. 7. It is clearly visible that the MT inversion results (upper row of Fig. 7) better constrained the nodal planes according to polarities of the stations. Both methods suffer from poor azimuthal coverage and the quality of solutions. In both methods the uncertainty of fault plane orientations is high, with about 50 degrees of uncertainty of strike and rake, and about 15 degrees of uncertainty of dip. Taking the above issues into account, the MT inversion seems a more reasonable approximation of the mechanisms from the available data. Despite all above-mentioned limitations, the obtained mechanisms are valuable information about the seismic process in the Song Tranh 2 reservoir area.

Source mechanism of the 3 September 2013 event reveals normal faulting with strike azimuth NNE-SSE and moderate dip angle of about 40-50 degrees (Fig. 7). Nodal plane orientations are parallel to the Tra Bong thrusting movement direction, but perpendicular to the strike of this main discontinuity. In the area of the event location, the main discontinuities are not in agreement with the nodal planes orientation. Moreover, the principal stress regime indicates strike-slip faulting, while the inversion results indicate the normal faulting. The tension axis orientation is similar to the main strike slip stress pattern in this area, but the polarities and amplitudes of the first *P*-wave pulses determine the focal mechanism results as a normal fault. The quality of the solution is limited by the number of stations available and their azimuthal coverage. There were only 8 stations with good signal to noise ratio, which were used in inversion. The azimuthal coverage was good in the southern half of the focal sphere, but only one station was available in the northern half of the focal sphere.

The source mechanism obtained for the 31 October 2013 event suggests reverse faulting with strike almost N-S or W-E. The second nodal plane orientation is almost similar to the Hung Nhuong – Ta Vi thrust, but the main regime of this area is strike-slip, which is not in agreement with the obtained focal mechanism. Once again, the station azimuthal coverage was not sufficient, especially in SW quadrant of the focal sphere, where not even a single station was available, while 6 out of 8 available stations were covering the NW quadrant.

Due to the limited number of stations, the results should be treated as the fault plane solution, rather than the full MT. The obtained results are not sufficient yet for any general conclusions about the stress or tectonic regime of the process leading to the seismicity of the STH2 reservoir vicinity. Nevertheless the focal mechanism solution show that the seismic process in the

STH2 dam vicinity cannot be interpreted as purely tectonic. Both locations and mechanisms of the events indicate that the stress changes followed the dam impoundment may play a role in the seismogenic process.

6. COMPLETENESS OF CATALOGS FOR THE VERIS NETWORK

Completeness magnitude (M_C) of earthquake catalogs is the lowest magnitude at which all the earthquakes are detected in selected space and time volume. The completeness of catalogs has been estimated based on shape of frequency-magnitude distribution (FMD) of detected events in the selected region as well as by other techniques (Mignan and Woessner 2012): maximum curvature (MAXC) (Wyss *et al.* 1999, Wiemer and Wyss 2000), entire magnitude range (EMR) (Woessner and Wiemer 2005), and study of the *b*-value stability of Gutenberg–Richter (Gutenberg and Richter 1944) model as a function of cut off magnitude (MBS) (Cao and Gao 2002).

The MAXC method estimates M_C as the point of the maximum curvature by computing the maximum value of the first derivative of the frequency-magnitude curve (cumulated FMD). In practice, this matches the group of magnitudes with the highest frequency of events in the FMD. This technique requires fewer events than other techniques to reach a stable result; however, it underestimates sometimes the M_C value (Wiemer and Wyss 2000, Woessner and Wiemer 2005). Some modifications of this method are provided by Leptokaropoulos *et al.* (2013).

In EMR technique the entire observed magnitude range is used to estimate the M_C. Woessner and Wiemer (2005) proposed a model consisting of two parts: the Gutenberg–Richter law for the complete part, and the cumulative normal distribution for the incomplete part of the FMD. They tested also log-normal and Weibull distributions.

Cao and Gao (2002) estimated M_C using the stability of the *b*-value as a function of cut-off magnitude M_{Co}, named as MBS by Woessner and Wiemer (2005). The M_C is defined as the magnitude for which the changes in *b*-value (Δb) is smaller than 0.03. It is based on the assumption that estimation of *b* increases for $M_{Co} < M_C$ and remains constant for $M_{Co} > M_C$. This method does not produce good results in case of high variability of the FMD. Woessner and Wiemer (2005) used the *b*-value uncertainty δb according to formula (Shi and Bolt 1982).

$$\delta b = 2.3 b^2 \sqrt{\frac{\sum_{i=1}^{N} \left(M_i - \langle M \rangle \right)^2}{N(N-1)}} , \tag{3}$$

where $\langle M \rangle$ is the mean magnitude and N is the number of events.

Table 5

Estimates of completeness magnitude (M_C) for events from the period 2013-2014

Technique	M_C
MAXC	0.8
EMR	1.1
M_{min}	0.12

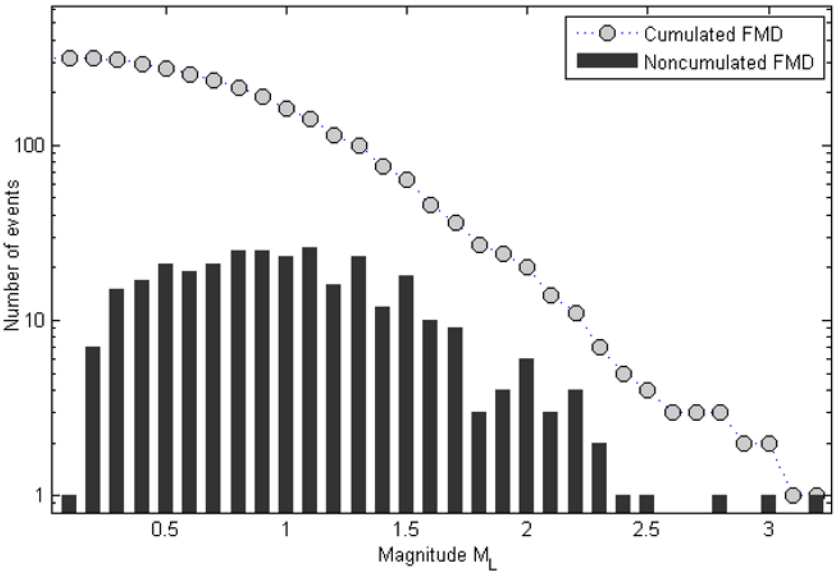

Fig. 8. FMD of events recoded in STH2 region in the period 2013-2014.

In the period from August 2013 to May 2014, the VERIS seismic network in central Vietnam recorded about 2000 earthquakes, from which approximately 350 were located. The values of M_C calculated by different methods and minimum magnitude observed (M_{min}) are presented in Table 5. Based on these values and on the shape of FMD of events recorded in the years 2013-2014 (Fig. 8) M_C is assumed to be 1.1.

7. SEISMIC ACTIVITY

When installing the VERIS network, the lake level was 140 m. Afterwards it began to increase with one sharp decline to the level of 149 m in November 2013. The level of water reached about 165.6 m at the beginning of 2014.

In the period from August 2013 to May 2014 about 2000 seismic events were detected; 359 of them were localized and magnitudes were calculated (Fig. 9a and 10). Figure 9a shows that in the consecutive phases the monitoring capacity increased, because of detection of smaller events. However, such events were not recorded in the beginning of seismic activity. Taking into consideration only events of magnitude $M \geq 2$ (Fig. 9b), there had not been noticed grown of seismic activity with the last increase of water level. A comparison of the seismic activity and the lake level does not suggest any straightforward correlation between these two parameters.

The network recorded also single small events close to the Phu Ninh reservoir northeast of the STH2 and weak seismicity in the whole area a few dozen kilometers away from the STH2 (Fig. 10).

In the period from 24 August 2013 to May 2014, earthquakes grouped in two locations: in the northern part of the reservoir, near the Tra Bong thrust, and to the south, aligned more or less parallel to the Hung Nhuong – Ta Vi thrust. This grouping is not indicated by locations of earthquakes recorded from January 2011 to July 2013, because of bigger error of their localization. Some earthquakes located next to the second reservoir (Phu Ninh), about 30 km away from STH2 reservoir, were also captured (Fig. 10).

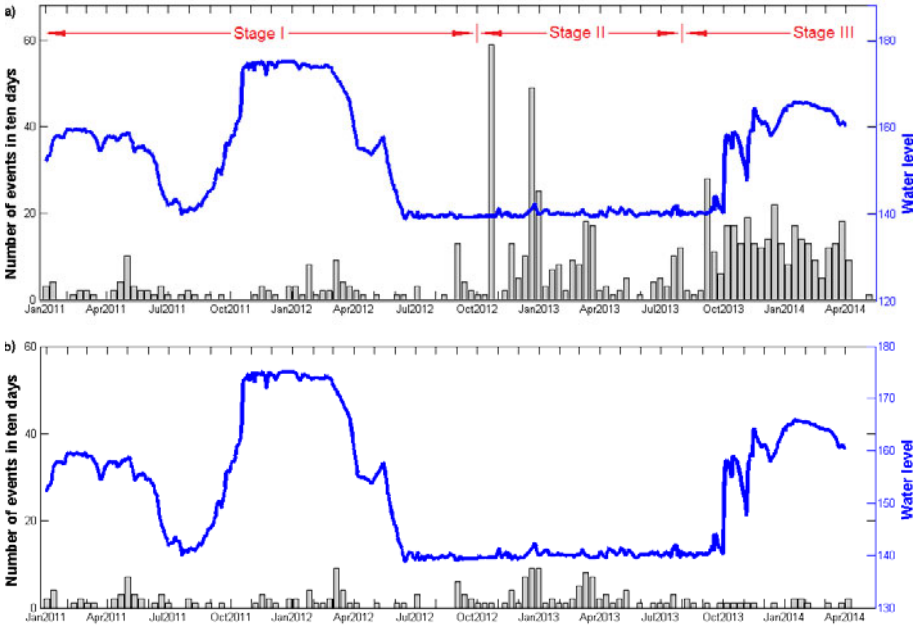

Fig. 9. The lake level of STH2 reservoir and seismic activity in the period January 2011 – May 2014 and: (a) the numbers of all localized events in 10 day periods, and (b) the numbers of events of magnitude ≥ 2 in 10 day periods.

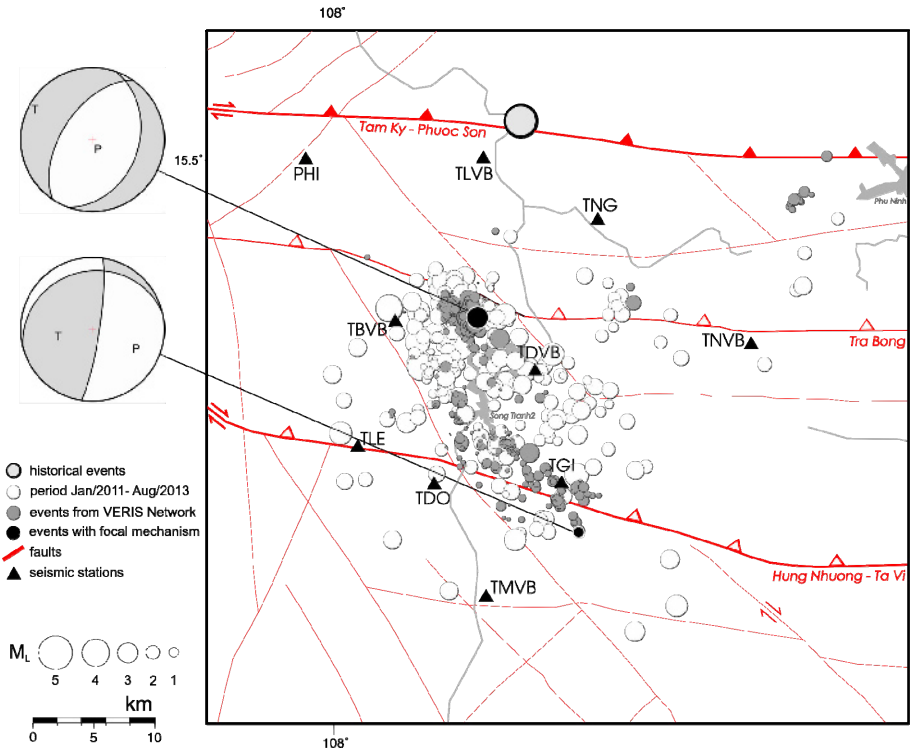

Fig. 10. Location of historical events and events from the period 2011-2014 grouped around the STH2 reservoir.

8. CONCLUSIONS

The installment of VERIS network increased significantly the earthquake detection and location capacity in the region of Song Tranh 2 reservoir. It also made it possible to calculate focal mechanisms and other source parameters. Unfortunately, the most intense seismic activity occurred earlier, when only two remote stations recorded seismic events. In order to monitor the whole development of seismicity triggered by reservoir impoundment, the monitoring should start before the beginning of filling the reservoir.

The fact that seismicity was practically absent in the studied region before the reservoir impoundment indicates that the earthquakes occurring since the impoundment are the effect of reservoir exploitation. More precise epicenter location facilitated by the VERIS network monitoring shows that earthquakes are grouped between the Tra Bong thrust and secondary faults of the Hung Nhuong – Ta Vi thrust. Analyses of mechanisms should soon provide better insight into the seismogenesis of the observed activity.

So far no immediate correlation of the seismic activity with the lake level has been ascertained.

Acknowledgments. This work was done in the framework of the project IS-EPOS: Digital Research Space of Induced Seismicity for EPOS Purposes (POIG.02.03.00-14-090/13-00), funded by the National Centre for Research and Development in the Operational Program Innovative Economy in the years 2013-2015.

This work was partially supported within statutory activities No. 3841/E-41/S/2015 of the Ministry of Science and Higher Education of Poland.

This research was carried out under financial supports of Ministry of Science and Technology of Vietnam, and Vietnam Academy of Science and Technology.

References

Awad, H., and G. Kwiatek (2005), Focal mechanism of earthquakes from June 1987 swarm in Aswan, Egypt, calculated by the moment tensor inversion, *Acta Geophys. Pol*. **53**, 3, 275-291.

Bratt, S.R., and T.C. Bache (1988), Locating events with a sparse network of regional arrays, *Bull. Seismol. Soc. Am.* **78**, 2, 780-798.

Bratt, S.R., and W. Nagy (1991), *The LocSAT program*, Science Applications International Corporation, San Diego.

Cao, A.M., and S.S. Gao (2002), Temporal variation of seismic b-values beneath northeastern Japan island arc, *Geophys. Res. Lett.* **29**, 9, 48-1-48-3, DOI: 10.1029/2001GL013775.

Carder, D.S. (1945), Seismic investigations in the Boulder Dam area, 1940-1944, and the influence of reservoir loading on local earthquake activity, *Bull. Seismol. Soc. Am.* **35**, 4, 175-192.

Choudhury, S., P.K. Gautam, and A. Paul (2013), Seismicity and reservoir induced crustal motion study around the Tehri Dam, India, *Acta Geophys.* **61**, 4, 923-934, DOI: 10.2478/s11600-013-0125-1.

Fitch, T.J., D.W. McCowan, and M.W. Shields (1980), Estimation of the seismic moment tensor from teleseismic body wave data with applications to intraplate and mantle earthquakes, *J. Geophys. Res.* **85**, B7, 3817-3828, DOI: 10.1029/JB085iB07p03817.

Fyhn, M.B.W., L.O. Boldreel, and L.H. Nielsen (2009), Geological development of the Central and South Vietnamese margin: Implications for the establishment of the South China Sea, Indochinese escape tectonics and Cenozoic volcanism, *Tectonophysics* **478**, 3-4, 184-214, DOI: 10.1016/ j.tecto.2009. 08.002.

Giang, N.V., G. Marquis, and L.H. Minh (2010), EM and GPR investigations of contaminant spread around the Hoc Mon waste site, Vietnam, *Acta Geophys*. **58**, 6, 1040-1055, DOI: 10.2478/s11600-010-0023-8.

Gupta, H.K. (1985), The present status of reservoir induced seismicity investigations with special emphasis on Koyna earthquakes, *Tectonophysics* **118**, 3-4, 257-279, DOI: 10.1016/0040-1951(85)90125-8.

Gupta, H.K. (1992), *Reservoir – Induced Earthquakes*, Developments in Geotechnical Engineering, Vol. 64, Elsevier Science Publ., Amsterdam.

Gupta, H.K. (2011), Artificial water reservoir triggered earthquakes. **In:** H.K. Gupta (ed.) *Encyclopedia of Solid Earth Geophysics*, Springer, Dordrecht, 15-24, DOI: 10.1007/978-90-481-8702-7_15.

Gutenberg, B., and C.F. Richter (1944), Frequency of earthquakes in California, *Bull. Seismol. Soc. Am.* **34**, 4, 184-188.

Hardebeck, J.L., and P.M. Shearer (2002), A new method for determining first-motion focal mechanisms, *Bull. Seismol. Soc. Am*. **92**, 6, 2264-2276, DOI: 10.1785/0120010200.

Haskell, N.A. (1953), The dispersion of surface waves on multilayered media, *Bull. Seismol. Soc. Am*. **43**, 1, 17-34.

Kwiatek, G. (2013), FOCI 3.0 software, http://induced.pl/foci (in Polish).

Leptokaropoulos, K.M., V.G. Karakostas, E.E. Papadimitriou, A.K. Adamaki, O. Tan, and S. İnan (2013), A homogeneous earthquake catalog for Western Turkey and magnitude of completeness determination, *Bull. Seismol. Soc. Am.* **103**, 5, 2739-2751, DOI: 10.1785/0120120174.

Lizurek, G., B. Plesiewicz, P. Wiejacz, J. Wiszniowski, and J. Trojanowski (2013), Seismic event near Jarocin (Poland), *Acta Geophys.* **61**, 1, 26-36, DOI: 10.2478/s11600-012-0052-6.

Mignan, A., and J. Woessner (2012), Estimating the magnitude of completeness for earthquake catalogs, Community Online Resource for Statistical Seismicity Analysis, http://www.corssa.org.

Nam, T.N. (1995), The geology of Vietnam: A brief summary and problems, *Geosci. Rep. Shizuoka Univ.* **22**, 1-10, DOI: 10.14945/00000334.

Peterson, J. (1982), GDSN enhancement studies final report, ARPA Order No. 4295, USGS Albuquerque Seismological Laboratory, Albuquerque, USA.

Phach, P.V., and V.V Chinh (1995), Report on structure/tectonic for Cenozoic and relationship with seismicity on territory of Vietnam, Archives of the Institute of Geophysics, VAST, Hanoi, Vietnam (in Vietnamese).

Shi, Y., and B.A. Bolt (1982), The standard error of the magnitude-frequency b-value, *Bull. Seismol. Soc. Am.* **72**, 5, 1677-1687.

Simpson, D.W. (1976), Seismicity changes associated with reservoir loading, *Eng. Geol.* **10**, 2-4, 123-150, DOI: 10.1016/0013-7952(76)90016-8.

Simpson, D.W. (1986), Triggered earthquakes, *Ann. Rev. Earth Planet. Sci.* **14**, 21-42, DOI: 10.1146/annurev.ea.14.050186.000321.

Simpson, D.W., W.S. Leith, and C.H. Scholz (1988), Two types of reservoir-induced seismicity, *Bull. Seismol. Soc. Am*. **78**, 6, 2025-2040.

Son, L.T. (1995), The approximation of seismic velocity model for Vietnam territory. **In:** *Proc. Fourth National Conference on Physics, 5-8 October 1993, Hanoi, Vietnam*, 651-655 (in Vietnamese, abstract in English).

Thuy, N.N., P.V. Phach, V.V. Chinh, L.H. Minh, P.D. Nguyen, P.Q. Hung, and N.A. Duong (2003), Report on estimation of the seismic design for the Song Tranh 2 hydropower construction*,* Archives of the Institute of Geophysics, VAST, Hanoi, Vietnam (in Vietnamese).

Trojanowski, J., B. Plesiewicz, and J. Wiszniowski (2015), Seismic monitoring of Poland – description and results of temporary seismic project with mobile seismic network, *Acta Geophys*. **63**, 1, 17-44, DOI: 10.2478/s11600-014-0255-0.

Wiejacz, P. (1992), Calculation of seismic moment tensor for mine tremors from the Legnica–Głogów Copper Basin, *Acta Geophys. Pol.* **40**, 2, 103-122.

Wiemer, S., and M. Wyss (2000), Minimum magnitude of completeness in earthquake catalogs: Examples from Alaska, the Western United States, and Japan, *Bull. Seismol. Soc. Am*. **90**, 4, 859-869, DOI: 10.1785/0119990114.

Woessner, J., and S. Wiemer (2005), Assessing the quality of earthquake catalogues: Estimating the magnitude of completeness and its uncertainty, *Bull. Seismol. Soc. Am*. **95**, 2, 684-698, DOI: 10.1785/0120040007.

Wyss, M., A. Hasegawa, S. Wiemer, and N. Umino (1999), Quantitative mapping of precursory seismic quiescence before the 1989, M7.1 off-Sanriku earthquake, Japan, *Ann. Geofis*. **42**, 5, 851-869.

Received 15 December 2014
Received in revised form 20 February 2015
Accepted 10 March 2015

DE GRUYTER OPEN

Acta Geophysica
vol. 63, no. 3, June 2015, pp. 863-883
DOI: 10.1515/acgeo-2015-0001

Effect of the North Atlantic Oscillation on the Thermal Characteristics of Lakes in Poland

Dariusz WRZESIŃSKI, Adam CHOIŃSKI, and Mariusz PTAK

Institute of Physical Geography and Environmental Planning,
Adam Mickiewicz University, Poznań, Poland;
e-mails: darwrze@amu.edu.pl, choinski@amu.edu.pl,
marp114@wp.pl (corresponding author)

A b s t r a c t

This paper presents the effect of the North Atlantic Oscillation (NAO) on the thermal characteristics of lakes in Poland. In the analysis, the use was made of monthly air temperatures recorded at fifteen meteorological stations, water temperatures of twelve lakes, and Hurrell's winter NAO indices. Over the study period (1971-2010), there was a marked increase in the temperatures of both, air and lake waters. Depending on the NAO phase, water temperatures were observed to depart from mean values, being markedly higher than average (even by 1°C) in the positive winter NAO phase. The differences in water temperatures were statistically significant in the winter-spring season. In turn, in the negative NAO_{DJFM} phase lake water temperatures in winter and spring were markedly lower than average (in March even by 1.0°C). The unique response of some lakes depends on their morphometric parameters, including their mean depth.

Key words: global warming, climate change, water temperature, macroscale atmospheric circulation.

1. INTRODUCTION

The pattern of processes and phenomena occurring in lakes results from global range-factors (air circulation, radiation level), local conditions in their

catchments (use pattern, hypsometry, *etc*.), and their individual morphometric parameters (area, depth, *etc*.). Of fundamental importance are the first ones, but what make even neighbouring water bodies different are their morphometric characteristics. Thus, in order to establish regularities controlling the functioning of a lake ecosystem, it is necessary to identify all the factors listed, both global ones and those unique to individual lakes.

In the case of Europe, hydrometeorological conditions are heavily influenced by one of the macro-scale types of circulation, *viz.* the North Atlantic Oscillation (NAO). It is a bi-polar type of circulation with centres located over Iceland and the Azores. The period in which the difference in pressure between the Azores High and the Icelandic Low is big is termed a positive NAO phase, or mode. This generates strong winds over Europe from the south-west and the transport of humid and warm air masses, mainly to the northern regions of the continent. A negative NAO phase is characterised by a clearly weaker Icelandic low and a shallower Azores High. The air masses that flow to Europe are then dry and cool and come from the north-east. As a result, precipitation is lower in northern Europe and markedly higher on the Iberian Peninsula. The NAO affects climatic conditions the strongest in winter, but also in the other seasons high values of its index are accompanied by higher-than-average air temperatures in western Europe (Carleton 1988, Rogers 1997, Trigo *et al.* 2002). It also determines climatic conditions in Poland by causing an increase in temperature in the cold season of the year (Marsz and Styszyńska 2001, Przybylak *et al*. 2003) and influencing radiation and humidity conditions (Bryś and Bryś 2002), precipitation (Styszyńska 2001, Wibig 2001), as well as the duration and thickness of snow cover (Falarz 2007). With reference to lakes, the NAO's effect is visible in their patterns of thermal conditions and ice phenomena. The NAO-related rise in the temperature of lake waters (Livingstone and Dokulil 2001, Straile *et al*. 2003, Gerten and Adrian 2002) has such consequences as, *e.g.*, an earlier disappearance of ice cover in the years with a positive winter NAO index (D'Odorico *et al.* 2002, Wrzesiński *et al*. 2013). In turn, changes in the heat balance of lakes brought about by the NAO transform the conditions of biological life in those ecosystems (Straile and Adrian 2000, Ottersen *et al*. 2001).

The principal goal of this paper is to compare the range of changes in the water temperature of the lakes under study in the individual winter NAO phases with the average values, as well as their spatial and temporal patterns. An attempt is also made to account for the observed differences in terms of both, a global factor in the form of changes in air temperature as well as local factors and morphometric features of the lakes. Thus, the authors seek to explain whether macro-scale factors controlling the thermal conditions of the lakes are modified by their individual features, and if so, to what extent.

2. MATERIAL AND METHODS

In the research use was made of standard measurements of lake water temperature at a depth of 0.4 m performed once a day at 7:00 (GMT +1) over the 40-year study period by the Institute of Meteorology and Water Management. Owing to frequent reorganisations of the observation network, the longest observation series cover a relatively small number of lakes, their greater density being found in the north-eastern part of Poland (the Mazurian Lakeland). However, since the distribution of a decided majority of Polish lakes is a product of the Last Pleistocene Glaciation (which embraced the north of the country), the bodies found in this location can be regarded as representative of the lakes in Poland. Also used were air temperature data (monthly means) from fifteen stations found in Internet climatic databases (http://www7.ncdc.noaa.gov/CDO/dataproduct, www.tutiempo.net). The morphometric characteristics of the lakes are presented in Table 1, while their location and that of the meteorological stations is given in Fig. 1.

In this paper use was made of the winter NAO index (NAO_{DJFM}) worked out by Hurrell (1995; http://www.cgd.ucar.edu/cas/jhurrell/nao.stat.winter.html). It is a normalised mean difference in atmospheric pressure in the December-March period (DJFM) between Lisbon at one end of the continent and Stykkisholmur and Reykjavik at the other. The term "a positive NAO phase" (NAO+) should be understood as the years in which the difference in pressure between the Azores High and the Icelandic Low is big, and the

Table 1

Morphometric data of the studied lakes (after Choiński 2006)

No.	Lake	Area [ha]	Volume [thous. m^3]	Depth average [m]	Altitude [m a.s.l.]	Mictic type
1	Charzykowskie	1 336	134 533.2	9.8	120	stratified
2	Gardno	2 337.5	30 950.5	1.3	0.3	unstratified
3	Hańcza	291.5	120 364.1	38.7	227.3	stratified
4	Jamno	2 231.5	31 528	1.4	0.1	unstratified
5	Jeziorak	3 152.5	141 594.2	4.1	99.2	stratified
6	Lubie	1 487.5	169 880.5	11.6	95.4	stratified
7	Łebsko	7 080	117 521	1.6	0.2	unstratified
8	Mikołajskie	424	55 739.7	11.2	115.7	stratified
9	Selmęt Wielki	1 207.5	99 463.9	7.8	120.7	stratified
10	Sępoleńskie	157.5	7 501.6	4.8	112.8	stratified
11	Sławskie	822.5	42 664.8	5.2	56.9	stratified
12	Studzieniczne	244	22 073.6	8.7	123.4	stratified

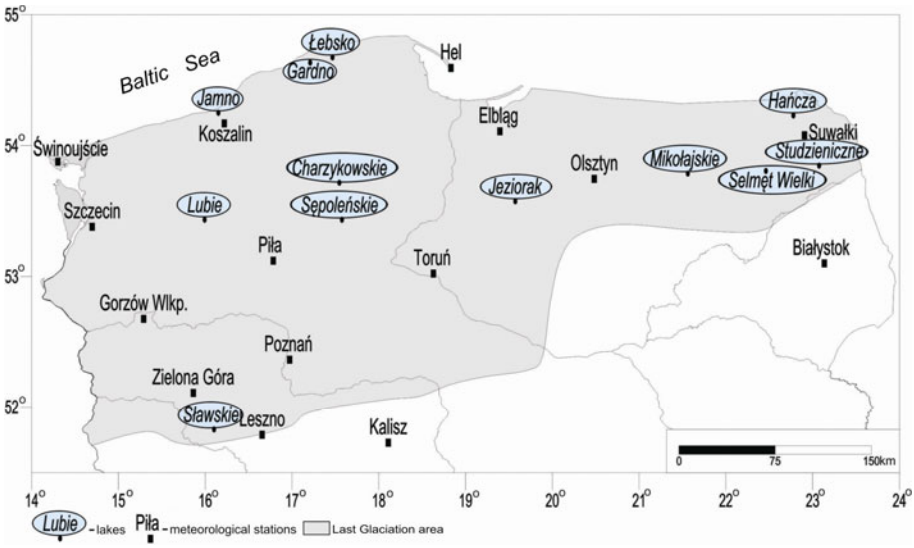

Fig. 1. Location of the limnological and meteorological stations.

NAO_{DJFM} index values exceed 2.52. In turn, a negative NAO phase (NAO–) means the years in which the Icelandic Low is clearly weaker, the Azores High shallower, and the NAO_{DJFM} values under –0.63. Those values roughly correspond to the first and third quartiles from the entire set of NAO_{DJFM} indices for the years 1971-2010.

To determine the relationship between changes in the temperature of lake water and the intensity of the North Atlantic Oscillation, Pearson's coefficient of linear correlation (r) was calculated, the correlation holding between the monthly, seasonal, and annual water temperatures on the one hand and Hurrell's winter NAO_{DJFM} index on the other. Changes in the thermal characteristics of the lakes in the two NAO_{DJFM} modes were established on the basis of differences in water temperatures in the positive and the negative mode against means from the years 1971-2010. Average monthly, seasonal and annual temperatures were calculated for years with high (NAO+) and low (NAO–) values of the winter NAO index. The statistical significance of those differences was examined using the T-test for independent samples. The hypothesis tested each time was $H_0{:}\mu_1 = \mu_2$ about the equality of expected values against $H_1{:}\mu_1 \neq \mu_2$. The rejection of the hypothesis allows the conclusion that there are significant differences between the mean temperatures observed in the various NAO_{DJFM} phases and the average magnitudes. The T-statistic has Student's distribution, with $n_1 + n_2 - 2$ degrees of freedom:

$$T = \frac{\overline{X_1} - \overline{X_2}}{S_{\overline{X_1} - \overline{X_2}}}, \tag{1}$$

where $S_{\overline{X_1} - \overline{X_2}}$ equals

$$S_{\overline{X_1} - \overline{X_2}} = \sqrt{\frac{(n_1 - 1)S_1^2 + (n_2 - 1)S_2^2}{n_1 + n_2 - 2}\left(\frac{1}{n_1} + \frac{1}{n_2}\right)}, \tag{2}$$

where n_1 and n_2 are the sample sizes, S_1^2 and S_2^2 are the sample variances, and $\overline{X_1} - \overline{X_2}$ are the sample means.

Spatial differences in the observed temperature changes are presented in a tabular and a graphic form. The graphics was prepared using the Surfer 10 program (GoldenSoftware), and in the construction of isoline maps the kriging procedure was employed.

3. RESULTS AND DISCUSSION

3.1 Preliminary results

The distribution of air temperatures obtained in the study period (1971-2010) for the fifteen weather stations shows annual means to decrease from west to east, which is connected with a stronger impact of the continental climate in the east of Poland, as observed by Ewert (1973). The highest mean annual air temperature was recorded in Szczecin (8.95°C) and Zielona Góra (8.81°C), and the lowest in Suwałki (6.57°C) and Białystok (7.10°C). At all the stations the mean annual air temperature can be observed to be rising. The increase was the highest in Gorzów Wielkopolski, Koszalin, and Piła, at 0.37°C per decade. In the annual cycle, the steepest rise in temperature can be noted in April, in Zielona Góra and Gorzów, by 0.96°C and 0.93°C, respectively.

Also mean annual temperatures of lake waters calculated for the same period were different. The highest values were recorded in Lake Sławskie (10.8°C), and the lowest in Lake Hańcza (8.5°C). The differences in their monthly temperatures were the widest in spring months: in April and May the water in Lake Sławskie was by more than 5.1°C warmer than in Hańcza.

Over the multi-year period under study, the mean annual water temperatures displayed an upward tendency in all the lakes. The highest increases per decade were recorded for lakes Lubie (0.55°C) and Selmęt Wielki (0.43°C), and the lowest for Jamno (0.25°C) and Hańcza (0.26°C). In the annual cycle, the warming of lake waters is especially readily visible in spring (April, May) and summer (July, August). The highest rises in the mean monthly water temperatures per decade were noted for lakes Lubie (in

May by 1.02°C, in July by 0.76°C, and in April by 0.73°C), Sławskie (in May by 0.79°C), and Selmęt Wielki (in April by 0.70°C). These results support the observations of changes in the thermal characteristics of lakes in Poland made so far. When analysing changes in the temperatures of surface water of lakes in the period 1961-2005, Skowron (2011) found them to show an upward tendency (on average, by 0.2°C per decade). The steepest increase was observed between March and May (0.02-0.05°C per year).

3.2 NAO – *T*-test correlation

In this paper correlations were examined of monthly, seasonal, and annual water and air temperatures with the winter NAO index (NAO_{DJFM}). The results obtained corroborate earlier findings, both in the case of polymictic lakes (Girjatowcz 2011) and those displaying summer stratification (Livingstone 1993, Gerten and Adrian 2001).

The strongest effect of the North Atlantic Oscillation on the thermal characteristics of lake waters can be observed in winter and spring months (from January to April). The calculated correlation coefficients are high and statistically significant ($p < 0.05$). Similar results were obtained for mean temperatures of lake waters in the winter and spring seasons. Only two lakes, Hańcza and Lubie, showed no significant correlation with the NAO_{DJFM} index. There was a less statistically significant correlation between annual temperatures and the NAO_{DJFM} index, but in five lakes (Charzykowskie, Gardno, Jeziorak, Łebsko, and Sępoleńskie) the correlation coefficient was significant at $p = 0.05$ (Table 2). Even stronger correlations were observed between air temperatures and NAO_{DJFM} (Table 3).

In the next stage of the research, it was established how the temperatures of lake waters and air in years with high and low values of the NAO_{DJFM} index departed from average values (Tables 4-7). Spatial differences in changes in the temperature of air and lake waters in the winter-spring period (January-April) under the influence of NAO and for the entire year are presented in Figs. 2 and 3.

Lake water temperatures grow markedly in the positive NAO_{DJFM} phase and go down in the negative one, especially in the period of the strongest impact of the North Atlantic Oscillation, *i.e.*, in winter and spring. In the positive NAO_{DJFM} phase in those periods, water temperatures are distinctly higher than average. The most statistically significant differences in water temperatures occur from January to March (an increase from 0.6°C to 1°C, $p < 0.05$) in lakes situated in the central, longitudinal belt of the study area. The differences decrease both, to the west (the smallest increase in temperature in the positive the NAO phase, 0.2-0.3°C, observed in Lake Lubie), and to the east (in Lakes Hańcza, 0.1°C, and Studzieniczne, 0.3°C). In April the differences are also high, from 0.6°C in the central part to 1°C in the east

Table 2

Coefficient of correlation of monthly, seasonal, and annual lake water temperatures with the winter NAO_{DJFM} index

Period / Lake	Nov	Dec	Jan	Feb	Mar	Apr	May	Jun	Jul	Aug	Sep	Oct	Year	Winter	Spring	Summer	Autumn
Charzykowskie	–0.25	0.06	**0.48**	**0.44**	***0.51***	**0.43**	**0.36**	0.04	0.07	0.14	0.09	0.13	**0.38**	**0.39**	***0.51***	0.11	0.04
Gardno	–0.28	0.15	***0.61***	***0.50***	***0.58***	**0.35**	**0.39**	0.08	0.06	–0.07	0.13	0.09	**0.42**	***0.60***	***0.55***	0.04	0.03
Hańcza	–0.21	–0.01	**0.33**	0.22	**0.32**	0.18	0.22	0.06	0.02	0.15	0.29	–0.05	0.21	0.20	0.26	0.09	–0.04
Jamno	**–0.37**	0.18	***0.62***	**0.49**	***0.50***	0.26	**0.31**	0.19	–0.03	0.02	0.26	0.08	**0.42**	***0.61***	**0.47**	0.07	0.09
Jeziorak	–0.12	0.00	***0.52***	**0.39**	**0.48**	**0.37**	0.26	0.13	0.09	0.11	0.10	0.12	**0.35**	**0.37**	**0.47**	0.16	0.11
Lubie	–0.17	–0.08	**0.37**	**0.40**	**0.36**	0.13	0.29	0.15	0.07	0.06	0.00	0.02	0.19	0.24	0.30	0.13	–0.01
Łebsko	–0.26	0.15	***0.58***	**0.47**	***0.59***	**0.31**	**0.37**	0.00	0.00	–0.09	0.19	0.08	**0.44**	***0.61***	***0.57***	–0.03	0.10
Mikołajskie	–0.20	–0.09	**0.48**	***0.57***	***0.52***	**0.47**	0.22	0.01	0.04	–0.12	0.10	0.10	0.27	0.30	**0.45**	–0.02	0.06
Selmęt Wielki	–0.28	–0.08	**0.42**	**0.46**	**0.48**	**0.43**	0.21	–0.01	–0.03	–0.10	0.09	0.05	0.20	0.30	**0.41**	–0.06	0.03
Sępoleńskie	–0.24	–0.03	***0.61***	***0.65***	***0.65***	**0.46**	**0.32**	0.01	0.05	0.09	0.09	0.13	**0.40**	***0.53***	***0.59***	0.07	0.07
Sławskie	–0.29	0.06	***0.56***	**0.46**	***0.51***	0.27	0.25	0.03	0.00	0.08	0.06	0.05	0.29	***0.49***	**0.43**	0.04	0.01
Studzieniczne	**–0.31**	–0.05	**0.32**	**0.33**	**0.41**	**0.48**	0.20	0.01	–0.06	–0.18	0.07	0.08	0.18	0.24	**0.42**	–0.10	0.04

Explanations: bold – difference at $p < 0.05$ significance level; bold, underlining – difference at $p < 0.01$; bold, italics – difference at $p < 0.001$.

Table 3

Coefficient of correlation of monthly, seasonal, and annual air temperatures with the winter NAO_{DJFM} index

Period / Station	Nov	Dec	Jan	Feb	Mar	Apr	May	Jun	Jul	Aug	Sep	Oct	Year	Winter	Spring	Summer	Autumn
Białystok	**–0.35**	**0.38**	***0.65***	**0.43**	**0.48**	0.25	–0.07	–0.02	–0.05	–0.10	0.24	0.18	***0.52***	***0.69***	**0.37**	–0.08	0.01
Elbląg	**–0.34**	**0.42**	***0.64***	**0.46**	**0.47**	0.25	0.15	0.03	0.00	–0.12	0.18	0.09	***0.55***	***0.70***	**0.46**	–0.04	0.00
Gorzów Wlkp.	**–0.30**	**0.43**	***0.66***	**0.41**	**0.47**	0.13	0.25	0.03	0.07	0.09	0.18	–0.01	***0.54***	***0.69***	**0.42**	0.09	–0.03
Hel	**–0.29**	**0.42**	***0.66***	***0.51***	***0.57***	**0.36**	0.30	0.19	0.02	-0.07	0.19	0.12	***0.57***	***0.71***	***0.55***	0.05	0.05
Kalisz	**–0.35**	**0.38**	***0.64***	**0.43**	**0.45**	0.19	0.16	0.01	0.09	0.17	0.23	0.11	***0.56***	***0.68***	**0.43**	0.12	0.04
Koszalin	**–0.29**	**0.45**	***0.64***	**0.46**	***0.51***	0.22	**0.32**	0.16	0.05	–0.09	0.17	0.03	***0.56***	***0.69***	***0.51***	0.05	0.01
Leszno	**–0.32**	**0.40**	***0.64***	**0.39**	**0.46**	0.19	0.18	0.01	0.08	0.13	0.25	0.08	***0.58***	***0.68***	**0.44**	0.10	0.03
Olsztyn	**–0.34**	**0.41**	***0.64***	**0.44**	**0.48**	0.24	0.05	0.00	0.01	–0.04	0.21	0.14	***0.55***	***0.70***	**0.42**	–0.01	0.02
Piła	**–0.32**	**0.41**	***0.64***	**0.42**	**0.48**	0.22	0.24	0.05	0.04	0.01	0.18	0.04	***0.53***	***0.68***	**0.47**	0.05	-0.02
Poznań	**–0.34**	**0.41**	***0.65***	**0.40**	**0.47**	0.18	0.20	–0.03	0.03	0.05	0.20	0.03	***0.52***	***0.68***	**0.44**	0.02	-0.02
Suwałki	**–0.36**	**0.37**	***0.64***	**0.44**	***0.50***	0.26	–0.06	–0.01	–0.04	-0.12	0.20	0.13	***0.50***	***0.69***	**0.40**	–0.07	0.00
Świnoujście	**–0.27**	**0.44**	***0.67***	**0.49**	***0.56***	0.28	**0.33**	0.17	–0.03	-0.01	0.15	0.01	***0.59***	***0.71***	***0.54***	0.04	0.00
Szczecin	**–0.25**	**0.46**	***0.66***	**0.45**	***0.56***	0.29	**0.36**	0.16	0.10	0.08	0.23	0.07	***0.66***	***0.70***	***0.60***	0.16	0.05
Toruń	**–0.35**	**0.40**	***0.64***	**0.44**	**0.45**	0.24	0.15	0.03	0.08	0.08	0.22	0.10	***0.56***	***0.69***	**0.44**	0.10	0.00
Zielona Góra	**–0.31**	**0.42**	***0.65***	**0.38**	**0.42**	0.11	0.23	–0.06	0.02	0.11	0.17	0.03	**0.49**	***0.67***	**0.39**	0.03	0.00

Explanations: bold – difference at $p < 0.05$ significance level; bold, underlining – difference at $p < 0.01$; bold, italics – difference at $p < 0.001$.

Table 4

Departures of air temperatures from average values in the positive NAO_{DJFM} phase

Period / Station	Nov	Dec	Jan	Feb	Mar	Apr	May	Jun	Jul	Aug	Sep	Oct	Year	Winter	Spring	Summer	Autumn
Białystok	–0.52	1.41	**3.13**	2.14	**1.74**	0.87	0.37	0.24	–0.17	0.17	–0.11	0.30	**0.80**	**2.23**	**0.99**	0.08	–0.22
Elbląg	–0.23	1.30	**2.80**	1.93	**1.56**	0.94	0.57	0.41	0.09	0.02	–0.16	0.16	**0.78**	**2.01**	**1.02**	0.17	–0.23
Gorzów Wlkp.	–0.21	1.07	**2.49**	1.58	**1.41**	0.69	0.64	0.43	0.32	0.29	–0.26	0.03	**0.71**	**1.71**	**0.91**	0.34	–0.26
Hel	–0.06	1.00	**2.25**	1.71	**1.57**	**0.88**	0.82	0.61	0.17	0.00	–0.16	0.13	**0.74**	**1.65**	**1.09**	0.26	–0.15
Kalisz	–0.30	0.97	**2.54**	1.78	1.33	0.80	0.61	0.37	0.37	0.57	–0.14	0.30	**0.77**	**1.76**	**0.91**	0.44	–0.16
Koszalin	0.01	1.17	**2.55**	1.80	**1.60**	1.00	0.79	0.47	0.09	–0.08	–0.14	0.09	**0.78**	**1.84**	**1.13**	0.16	–0.17
Leszno	–0.27	0.96	**2.47**	1.62	1.23	0.75	0.54	0.34	0.38	0.44	–0.05	0.18	**0.72**	**1.69**	**0.84**	0.39	–0.18
Olsztyn	–0.31	1.37	**2.87**	2.02	**1.64**	0.90	0.43	0.32	0.07	0.24	–0.15	0.26	**0.80**	**2.09**	**0.99**	0.21	–0.19
Piła	–0.20	1.07	**2.69**	1.73	**1.48**	0.79	0.65	0.47	0.19	0.18	–0.17	0.05	**0.74**	**1.83**	**0.97**	0.28	–0.26
Poznań	–0.25	1.06	**2.55**	1.68	**1.38**	0.78	0.61	0.31	0.16	0.25	–0.20	0.09	**0.70**	**1.77**	**0.92**	0.24	–0.25
Suwałki	–0.47	1.44	**3.10**	2.23	**1.88**	0.91	0.39	0.28	–0.03	0.10	–0.17	0.24	**0.82**	**2.26**	**1.06**	0.12	–0.24
Świnoujście	0.01	1.02	**2.35**	1.75	**1.66**	**0.91**	0.71	0.48	0.07	0.00	–0.26	0.07	**0.73**	**1.71**	**1.09**	0.18	–0.21
Szczecin	–0.04	1.10	**2.58**	1.84	**1.63**	0.88	0.82	0.51	0.31	0.19	–0.14	0.15	**0.82**	**1.84**	**1.11**	0.34	–0.16
Toruń	–0.39	1.16	**2.78**	1.88	**1.49**	0.83	0.60	0.46	0.26	0.33	–0.16	0.18	**0.78**	**1.94**	**0.97**	0.35	–0.26
Zielona Góra	–0.16	1.09	**2.31**	1.56	1.32	0.76	0.72	0.38	0.38	0.44	–0.29	0.23	**0.73**	**1.65**	**0.94**	0.40	–0.20

Explanations: bold – difference at $p < 0.05$ significance level; underlining – difference at $p < 0.01$ significance level.

Table 5

Departures of air temperatures from average values in the negative NAO_{DJFM} phase

Period / Station	Nov	Dec	Jan	Feb	Mar	Apr	May	Jun	Jul	Aug	Sep	Oct	Year	Winter	Spring	Summer	Autumn
Białystok	1.03	–0.81	**–3.86**	–1.89	–1.59	–0.17	0.44	0.09	0.01	0.15	–0.51	0.08	–0.59	**–2.19**	–0.44	0.08	0.05
Elbląg	1.08	–0.99	**–3.54**	–1.75	–1.50	–0.08	–0.09	–0.01	–0.04	0.15	–0.46	0.29	–0.58	**–2.09**	–0.56	0.03	0.12
Gorzów Wlkp.	0.87	–0.94	**–3.53**	–1.52	–1.40	0.14	–0.23	–0.17	0.01	–0.18	–0.41	0.47	–0.58	**–2.00**	–0.49	–0.11	0.20
Hel	0.85	–0.76	**–2.67**	–1.45	**–1.36**	–0.21	–0.37	–0.26	–0.04	–0.07	–0.45	0.26	–0.55	**–1.63**	–0.65	–0.12	0.05
Kalisz	1.00	–0.68	**–3.65**	–1.56	–1.40	0.02	–0.07	–0.14	–0.04	–0.31	–0.51	0.25	–0.60	**–1.96**	–0.48	–0.16	0.10
Koszalin	1.02	–0.95	**–3.06**	–1.60	**–1.41**	0.03	–0.52	–0.36	–0.08	0.05	–0.38	0.39	–0.58	**–1.87**	–0.63	–0.13	0.12
Leszno	0.79	–0.72	**–3.63**	–1.51	–1.34	0.06	–0.15	–0.12	0.02	–0.20	–0.48	0.23	–0.59	**–1.95**	–0.47	–0.10	0.11
Olsztyn	1.08	–1.00	**–3.66**	–1.78	–1.51	–0.05	0.23	0.03	–0.01	0.08	–0.49	0.24	–0.58	**–2.15**	–0.44	0.03	0.09
Piła	0.87	–0.89	**–3.55**	–1.65	–1.42	–0.02	–0.28	–0.07	0.02	–0.05	–0.43	0.34	–0.60	**–2.03**	–0.57	–0.03	0.15
Poznań	0.94	–0.81	**–3.57**	–1.47	–1.34	0.07	–0.17	–0.04	0.11	–0.09	–0.44	0.39	–0.54	**–1.95**	–0.48	–0.01	0.18
Suwałki	1.16	–0.83	**–3.70**	–2.04	**–1.79**	–0.31	0.45	0.06	–0.06	0.14	–0.50	0.21	–0.61	**–2.19**	–0.55	0.05	0.09
Świnoujście	0.91	–0.93	**–3.10**	–1.67	**–1.45**	–0.09	–0.50	–0.37	0.20	–0.06	–0.30	0.47	–0.58	**–1.90**	–0.68	–0.08	0.17
Szczecin	0.86	–1.09	**–3.55**	–1.70	**–1.63**	–0.09	–0.56	–0.34	–0.05	–0.16	–0.43	0.33	**–0.71**	**–2.11**	–0.76	–0.18	0.11
Toruń	0.99	–0.90	**–3.79**	–1.77	–1.41	0.01	–0.10	–0.08	–0.10	–0.17	–0.55	0.24	–0.64	**–2.15**	–0.50	–0.12	0.10
Zielona Góra	0.97	–0.83	**–3.40**	–1.37	–1.36	0.22	–0.12	–0.02	0.31	–0.22	–0.46	0.50	–0.49	**–1.87**	–0.42	0.02	0.18

Explanations: bold – difference at $p < 0.05$ significance level; underlining – difference at $p < 0.01$ significance level.

Table 6

Departures of water temperatures from average values in the negative NAO_{DJFM} phase

Lake \ Period	Nov	Dec	Jan	Feb	Mar	Apr	May	Jun	Jul	Aug	Sep	Oct	Year	Winter	Spring	Summer	Autumn
Charzykowskie	0.40	0.16	**–0.64**	–0.38	–0.71	–0.53	–0.39	0.14	0.11	–0.31	–0.23	0.10	–0.19	–0.29	–0.55	–0.02	0.07
Gardno	0.61	–0.02	**–0.79**	–0.66	**–0.98**	–0.52	–0.51	–0.36	–0.10	–0.06	–0.35	0.21	–0.29	–0.49	**–0.67**	–0.17	0.03
Hańcza	0.22	0.09	–0.48	–0.15	–0.35	–0.22	–0.49	0.12	0.11	–0.27	–0.40	0.15	–0.14	–0.18	–0.35	–0.01	0.04
Jamno	0.70	–0.10	**–0.90**	**–0.80**	**–1.10**	–0.60	–0.70	0.60	0.04	–0.50	–0.70	–0.20	–0.41	–0.59	**–0.80**	–0.30	–0.06
Jeziorak	0.48	0.33	–0.57	–0.35	–0.82	–0.51	–0.19	–0.17	–0.15	–0.37	–0.29	0.02	–0.22	–0.20	–0.51	–0.23	–0.07
Lubie	0.43	0.42	–0.22	–0.20	–0.33	0.06	–0.30	–0.22	0.00	–0.05	–0.12	0.28	–0.02	0.00	–0.19	–0.09	0.17
Łebsko	0.63	–0.05	**–0.76**	–0.60	**–1.06**	–0.20	–0.39	0.04	0.05	0.04	–0.32	0.28	–0.19	–0.47	–0.55	0.05	0.01
Mikołajskie	0.37	0.43	–0.43	–0.30	–0.62	–0.73	–0.25	0.16	–0.10	–0.01	–0.40	–0.02	–0.16	–0.10	–0.53	0.02	–0.10
Selmęt Wielki	0.55	0.36	–0.37	–0.37	–0.67	–0.83	–0.25	0.01	0.12	0.06	–0.17	0.14	–0.12	–0.13	–0.58	0.07	0.05
Sępoleńskie	0.59	0.26	–0.56	–0.58	**–1.08**	–0.64	–0.35	–0.04	0.07	–0.30	–0.24	0.08	–0.23	–0.30	**–0.69**	–0.09	0.01
Sławskie	0.80	0.17	**–0.84**	–0.68	–0.85	–0.29	–0.25	–0.13	0.28	–0.08	–0.04	0.32	–0.13	–0.45	–0.46	0.02	0.21
Studzieniczne	0.54	0.16	–0.31	–0.18	–0.43	–0.95	–0.15	–0.01	0.05	0.06	–0.26	–0.03	–0.13	–0.11	–0.51	0.03	–0.03

Explanations: bold – difference at $p < 0.05$ significance level.

Table 7

Departures of water temperatures from average values in the positive NAO_{DJFM} phase

Period / Lake	Nov	Dec	Jan	Feb	Mar	Apr	May	Jun	Jul	Aug	Sep	Oct	Year	Winter	Spring	Summer	Autumn
Charzykowskie	–0.08	0.42	0.65	0.57	0.78	0.81	1.23	0.48	0.42	0.40	–0.27	0.06	**0.46**	**0.54**	**0.94**	0.44	–0.11
Gardno	–0.03	0.54	**0.84**	0.73	**1.20**	0.75	1.08	0.14	0.04	–0.08	–0.43	0.03	0.40	**0.71**	**1.01**	0.03	–0.27
Hańcza	–0.29	–0.04	0.21	0.18	0.46	0.39	1.06	0.58	0.26	0.44	0.17	–0.38	0.25	0.12	0.64	0.43	–0.24
Jamno	–0.10	0.45	0.90	0.80	1.18	0.40	1.03	0.19	–0.32	–0.18	0.02	0.06	0.37	**0.70**	**0.90**	–0.10	–0.09
Jeziorak	0.28	0.59	**0.83**	0.57	0.92	0.70	0.99	0.89	0.37	0.67	–0.10	0.08	**0.56**	**0.66**	**0.87**	0.64	–0.03
Lubie	0.18	0.21	0.38	0.34	0.71	0.55	1.11	0.94	0.45	0.38	–0.42	–0.12	0.39	0.31	0.79	0.59	–0.10
Łebsko	–0.03	0.54	**0.93**	0.63	**1.18**	0.73	**0.99**	0.42	0.10	0.05	–0.12	0.05	**0.46**	**0.70**	**0.97**	0.19	–0.11
Mikołajskie	–0.12	0.31	**0.62**	**0.55**	**0.71**	**1.01**	1.01	0.43	0.11	0.05	–0.24	–0.04	0.37	0.49	**0.91**	0.20	–0.13
Selmęt Wielki	–0.12	0.41	**0.68**	**0.59**	0.69	0.93	0.98	0.27	–0.08	0.07	–0.25	–0.04	0.34	**0.56**	0.86	0.09	–0.09
Sępoleńskie	0.03	0.32	**0.76**	**0.71**	**0.88**	0.75	1.16	0.52	0.27	0.31	–0.25	0.10	**0.46**	**0.60**	**0.93**	0.36	–0.02
Sławskie	0.06	0.45	0.65	0.58	**0.87**	0.38	0.83	0.40	0.25	0.35	–0.29	0.06	0.38	**0.56**	0.70	0.34	–0.09
Studzieniczne	–0.35	0.22	0.37	0.34	0.55	**1.05**	1.03	0.33	–0.25	–0.13	–0.34	–0.11	0.23	0.31	**0.88**	–0.02	–0.13

Explanations: bold – difference at $p < 0.05$ significance level; underlining – difference at $p < 0.01$ significance level.

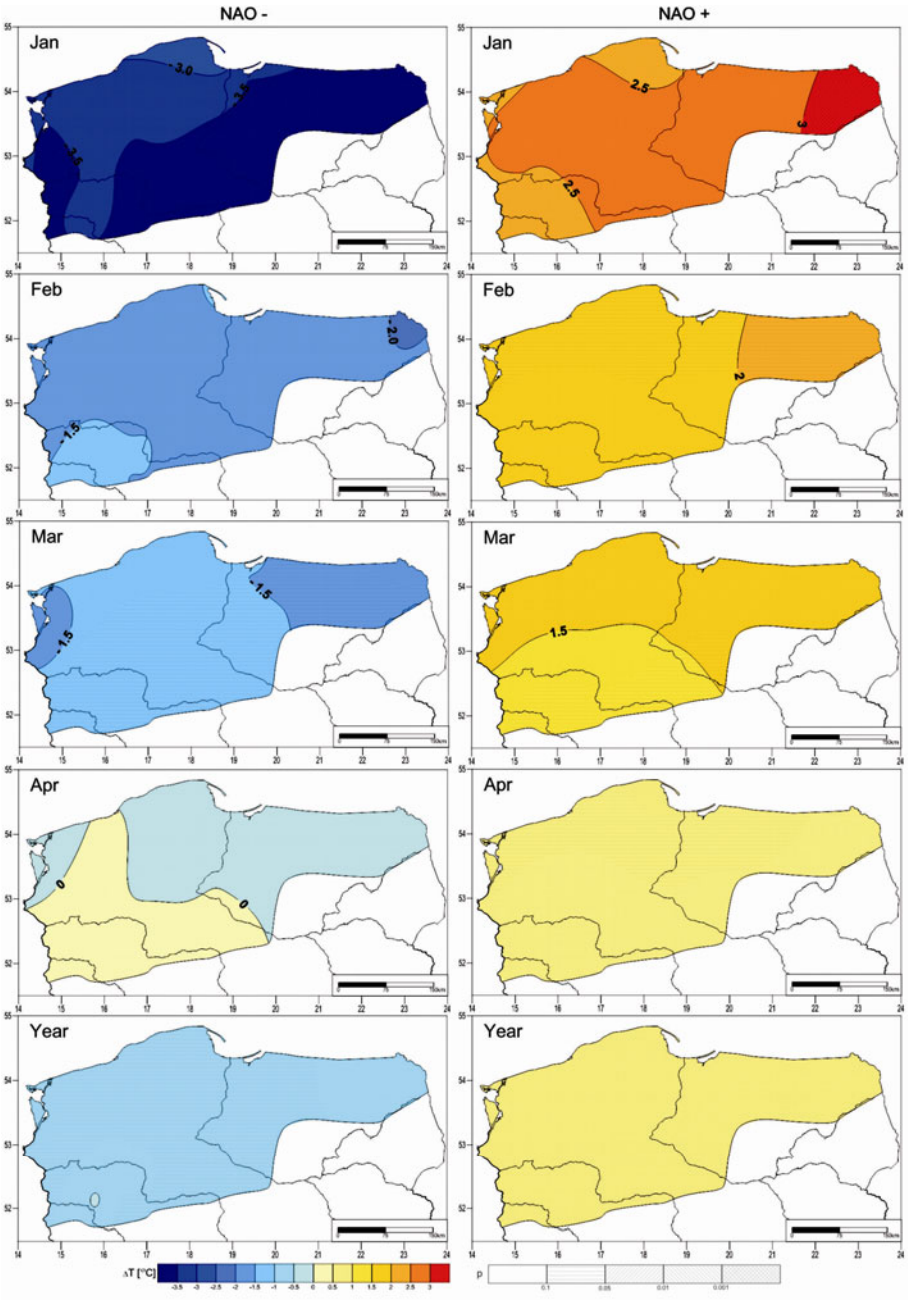

Fig. 2. Departures of selected monthly and annual air temperatures (ΔT) in the two NAO_{DJFM} phases from the 1971-2010 means, and their statistical significance (p).

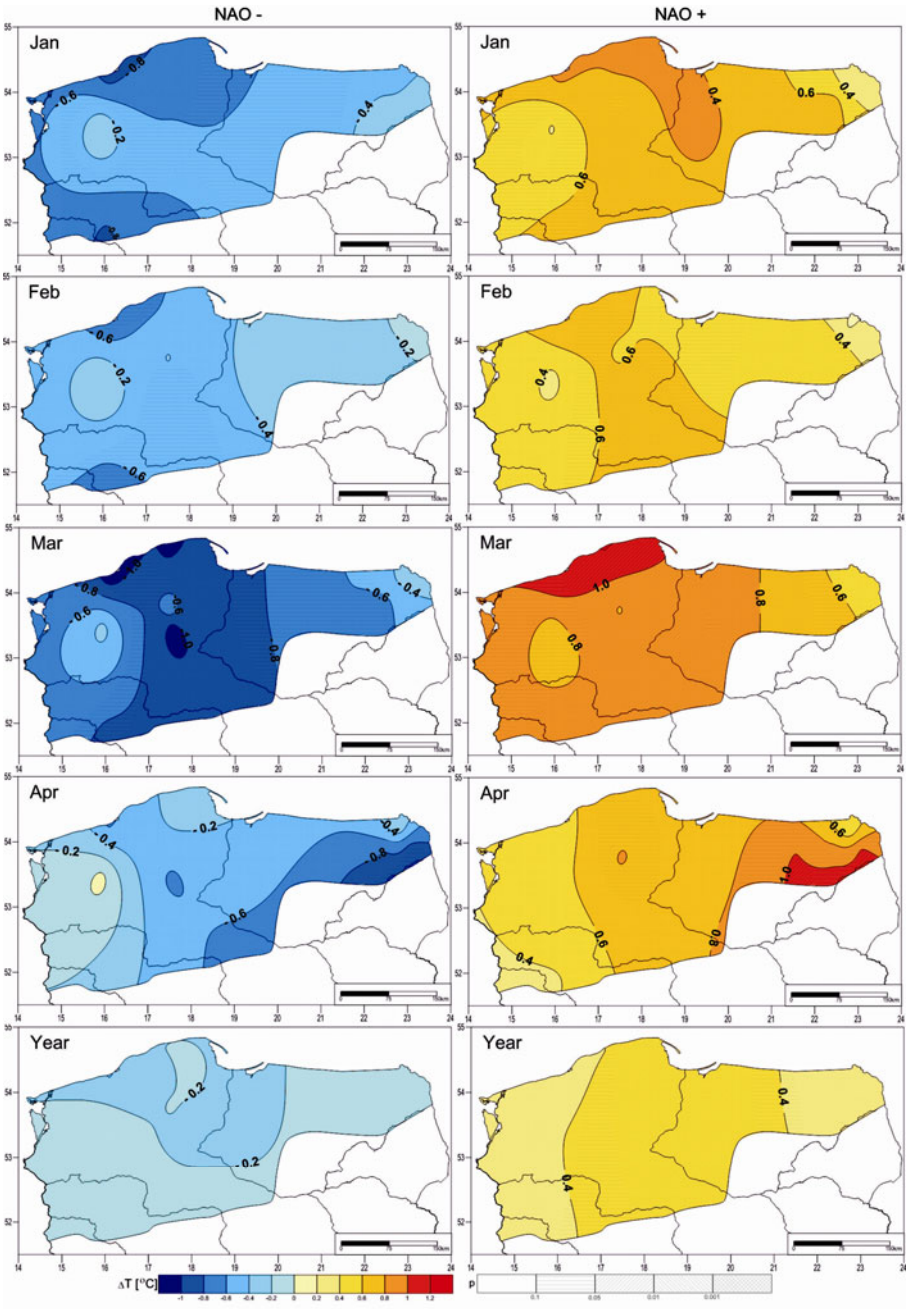

Fig. 3. Departures of selected monthly and annual temperatures of lake waters (ΔT) in the two NAO_{DJFM} phases from the 1971-2010 means, and their statistical significance (p).

(with the exception of Hańcza). Even wider differences in the water temperatures of all the lakes, in excess of 1°C, can be noted in May, but they are usually statistically insignificant, at $p > 0.05$. In the positive NAO_{DJFM} phase there is a similar spatial pattern of departures from the average in lake water temperatures in the winter-spring season. Winter temperatures exceed then the average by more than 0.6°C, and in spring by more than 0.8°C, and the differences are statistically significant ($p < 0.05$). The intensity of the North Atlantic Oscillation in the winter season has no effect on the temperature of lake waters in the remaining seasons of the year, *i.e.*, in summer and autumn. However, the elevated water temperatures in winter and spring cause annual temperatures of lake waters to be higher than average in this NAO_{DJFM} phase, too. Also in the case of this variable the greatest increase in water temperature (0.5°C) is recorded in the lakes located in the central part of the study area, and the observed differences are statistically significant ($p < 0.05$).

The situation is different in the negative NAO_{DJFM} phase. The temperature of lake waters in the winter-spring season is markedly lower than average. In January the greatest drops in temperature amount to 0.8°C, in February to 0.6°C, and in March even to more than 1.0°C. As in the case of temperature changes in the positive NAO_{DJFM} phase, spatial differences in the observed departures from the average show the greatest drop in water temperature to occur in lakes situated in the central and southern parts of the study area (Fig. 3). In the negative NAO_{DJFM} phase, water temperatures in winter, spring, and the entire year are lower than average by 0.4°C, more than 0.6°C, and 0.2°C, respectively. However, the observed differences are statistically insignificant ($p > 0.05$).

3.3 Effect of lake morphometry and location

The causes of the observed changes in lake water temperatures in the different NAO_{DJFM} modes should be sought, for obvious reasons, in changes in air temperatures. Departures of air temperature from the average are even wider than of lake waters. In the positive NAO_{DJFM} phase, they can exceed the average by more than 3°C in January, more than 2°C in February, and 1.5°C in March. Worth noting are smaller spatial differences in the observed departures of air temperatures, with a characteristic increase to the east. In the negative NAO_{DJFM} phase, air temperatures are much lower than average: more than 3.5°C in January, 2°C in February, and 1.5°C in March.

As follows from a comparison of changes in lake water temperatures with those in air temperatures, they concern not only the magnitude of differences in water and air temperatures, but also their temporal and spatial variability. This is due to differences in the heat balance of the lakes, which depend on their morphometry and location. There is a marked lag in the response of water temperature to changes in air temperature, hence the greatest

changes in water temperature can be observed later, from March to May. Besides, individual features of the lakes cause wider spatial differences in water temperature changes in the two NAO_{DJFM} phases.

To establish which bodies responded the strongest to air temperature, coefficients of the correlation between monthly, seasonal, and annual differences in air temperatures were calculated for the fifteen weather stations and the twelve lakes studied. Irrespective of the NAO_{DJFM} mode, the strongest connections were recorded for Lakes Gardno, Łebsko, and Jamno. Changes in their water temperature were very strongly correlated with those in air temperature recorded not only at the nearest stations, but also, though less distinctly, at the remaining stations ($p < 0.001$).

In turn, the weakest correlation links in the positive NAO_{DJFM} phase were found for Lakes Hańcza and Lubie, and in the negative phase, for Lubie, Mikołajskie, Selmęt Wielki, and Studzieniczne. As a rule, for those lakes the coefficients of the correlation between changes in water temperature and those in air temperature were low at most of the weather stations under study. They also had the lowest coefficients of the correlation between the winter NAO_{DJFM} index and the annual and winter water temperatures.

The reasons for the above unique features should be sought in their location and morphometric features. There are many works highlighting the connection between thermal characteristics of lakes and their local and individual features (Edmundson and Mazumder 2002, Nowlin *et al*. 2004, Houser 2006, Šporka *et al*. 2006, Wang *et al*. 2012, Novikmec *et al*. 2013). An analysis of the coefficients of the correlation between the morphometric parameters of the lakes (area, geographical latitude and longitude, mean depth, exposure, elevation a.s.l.) and changes in their temperatures in the two NAO_{DJFM} modes showed their mean depth to have the greatest effect on changes in the temperature of their waters. In the positive NAO_{DJFM} phase, there is a statistically significant dependence between the departures of lake water temperature from the average and the mean depth of a lake (Fig. 4). As

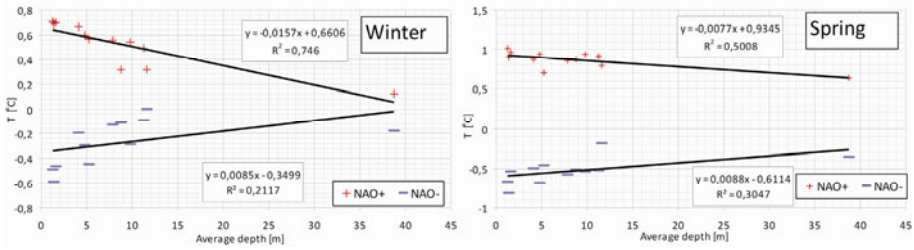

Fig. 4. Departures of the water temperature of the lakes from the average in the winter and spring seasons in the positive (NAO+) and the negative (NAO–) NAO_{DJFM} phase depending on their mean depth.

the mean depth increases, the observed differences in temperatures in winter ($r = –0.864$, $p < 0.01$) and spring ($r = –0.708$, $p < 0.01$) keep narrowing.

In the negative NAO_{DJFM} phase, the coefficients of the correlation between the departures of temperatures from the average and the morphometric parameters of the lakes are lower and statistically less significant.

The most susceptible to changes in water temperature are polymictic lakes (Gardno, Łebsko, and Jamno), with small mean depths and water masses mixing many times during the year. All three lakes have specific hydrological systems, heavily dependent on local characteristics, as emphasised by Cieśliński and Major (2012). Even so, their direct connection with the Baltic Sea (inflows of marine waters with their different physicochemical properties) and other elements (contact of the shorelines with peatlands, considerable thicknesses of sediments) are not decisive factors in modifying the thermal characteristics of those lakes.

In turn, in the case of Hańcza and Lubie, the lack of a strong correlation between the temperature of their waters and air in the positive NAO_{DJFM} phase can be explained by their great mean depth – the greatest among all the water bodies under study. It should be stressed that Hańcza is the deepest lake in the entire Central European Lowland. Because of those features, both water bodies have a great ability to accumulate heat, as pointed out by, *e.g.*, Choiński (2007), who established that large and deeper lakes emitted heat much longer than shallower ones. Besides, the great depths of the two bodies make possible their more substantial alimentation by groundwater, the temperature of which can differ from that of lake waters. The basins of Lubie and Hańcza penetrate into Quaternary water-bearing formations, which can be even up to 40 m thick. Groundwater alimentation affects the thermal characteristics of those lakes – its intensity can cause a change in the heat balance of a lake and affect the thickness of its ice cover (Choiński and Ptak 2012). Thus, both water bodies can be said to display a sort of thermal inertia with respect to atmospheric conditions.

4. CONCLUSIONS

The research has proved the North Atlantic Oscillation to have a big influence on the temperature of both, air and lake waters in the study area. The analysis of data from the fifteen weather stations confirmed the strong effect of its intensity on the mean annual temperature of air and those of the winter and spring seasons, the correlations observed being statistically significant (Table 3). In turn, the analysis of the temperatures of the twelve lakes under study showed the NAO to have a significant impact on the annual water temperature in six of them. Its influence was greater in winter (statistically

significant relations were noted for seven lakes) and in spring (here the relationship was found for ten lakes, Table 2).

Air temperatures tended to depart from the mean values more considerably in a positive NAO phase. This was observed at all the stations, both in the case of annual mean temperatures and those of the winter and spring seasons (Table 4). In a negative NAO phase the greatest departures from the means occurred in winter (all stations, Table 5). As to the temperatures of water, in a negative NAO phase their departures from the means were significant in only three cases in spring (Table 6). In a positive NAO phase significant differences in annual temperatures were recorded in four of the lakes, and in the winter and spring seasons, in eight of them (Table 7).

Lake water temperatures in the winter and spring seasons are markedly higher than average in the positive NAO_{DJFM} phase, and lower in the negative phase; the observed differences can even reach 1.0°C. Those changes in the temperature of lake waters in the two NAO_{DJFM} phases are caused by changes in air temperatures, which are even wider in those periods. Still, the spatial pattern of differences in air temperature changes, with their characteristic rise to the east, is different from that of lake water temperatures. The observed changes concern not only the magnitude of differences in water and air temperatures, but also their temporal and spatial variability. This follows from differences in the heat balance of the lakes, which depends on their morphometry and location. Water temperatures of some lakes do not show a close dependence on climatic conditions connected with NAO intensity. A weaker impact of the macro-scale climatic factors results from the location and morphometry of those lakes. As the conducted analysis has shown, an important parameter controlling the response of the thermal characteristics of lake waters to changes in air temperature is the mean depth of a lake. Lakes with the greatest mean depths, and hence the largest heat resources, are the most "resistant" to changes in air temperature, while those more sensitive to changes in thermal conditions are polymictic lakes characterised by the smallest mean depths.

The observed increase in lake water temperatures caused, among other things, by an intensive North Atlantic Oscillation can lead to a gradual transformation of lacustrine ecosystems. The transformation can affect both, their physico-chemical processes and phenomena as well as living conditions in a water environment different from those obtaining so far. This can lead to changes in the water-mass circulation pattern, in the trophic type of lakes, and in the species composition of their flora and fauna. In the future, an interesting issue to examine seems to be the effect of other macro-scale types of circulation (AO, ENSO) on the thermal characteristics of lakes in Poland, and in Europe.

References

Bryś, K., and T. Bryś (2002), Effect of the North Atlantic Oscillation on changes in humidity, radiation, dynamic and evaporation conditions in Wrocław-Swojc in the years 1946-2000. **In:** A.A. Marsz and A. Styszyńska (eds), *Oscylacja Północnego Atlantyku i jej rola w kształtowaniu zmienności warunków klimatycznych i hydrologicznych Polski*, Wyd. Uczelniane Akademii Morskiej, Gdynia, 147-162 (in Polish).

Carleton, A.M. (1988), Meridional transport of eddy sensible heat in winters marked by extremes of the North Atlantic oscillation, 1948/49-1979/80, *J. Climate* **1**, 2, 212-223, DOI: 10.1175/1520-0442(1988)001<0212:MTOESH>2.0.CO;2.

Choiński, A. (2006), *Catalogue of Polish Lakes*, Wyd. Nauk. UAM, Poznań (in Polish).

Choiński, A. (2007), *Physical Limnology of Poland*, Wyd. Nauk. UAM, Poznań (in Polish).

Choiński, A., and M. Ptak (2012), Variation in the ice cover thickness on Lake Samołęskie as a result of underground water supply, *Limnol. Rev.* **12**, 3, 133-138, DOI: 10.2478/v10194-012-0053-5.

Cieśliński, R., and M. Major (2012), Differences in the abiotic parameters of water in coastal lakes in the light of the EU water framework directive: An example of the Polish southern Baltic coast, *Acta Geophys.* **60**, 4, 1159-1179, DOI: 10.2478/s11600-012-0018-8.

D'Odorico, P., J.C. Yoo, and S. Jaeger (2002), Changing seasons: An effect of the North Atlantic Oscillation? *J. Climate* **15**, 4, 435-445, DOI: 10.1175/1520-0442(2002)015<0435:CSAEOT>2.0.CO;2.

Edmundson, J.A., and A. Mazumder (2002), Regional and hierarchical perspectives of thermal regimes in subarctic, Alaskan lakes, *Freshwater Biol.* **47**, 1, 1-17, DOI: 10.1046/j.1365-2427.2002.00775.x.

Ewert, A. (1973), The issue of the thermal continentality of climate in Poland and Europe against the continentality of the globe, *Prace Stud. Inst. Geogr. UW* 211, Klimatol. 6, 17-27 (in Polish).

Falarz, M. (2007), Snow cover variability in Poland in relation to the macro- and mesoscale atmospheric circulation in the twentieth century, *Int. J. Climatol.* **27**, 15, 2069-2081, DOI: 10.1002/joc.1505.

Gerten, D., and R. Adrian (2001), Differences in the persistency of the North Atlantic Oscillation signal among lakes, *Limnol. Oceanogr.* **46**, 2, 448-455, DOI: 10.4319/lo.2001.46.2.0448.

Gerten, D., and R. Adrian (2002), Effects of climate warming, North Atlantic Oscillation and El Niño-Southern Oscillation on thermal conditions and plankton dynamics in northern hemispheric lakes (review), *The Sci. World J.* **2**, 586-606, DOI: 10.1100/tsw.2002.141.

Girjatowicz, J.P. (2011), Effects of the North Atlantic Oscillation on water temperature in southern Baltic coastal lakes, *Ann. Limnol. Int. J. Limnol*. **47**, 1, 73-84, DOI: 10.1051/limn/2010031.

Houser, J.N. (2006), Water color affects the stratification, surface temperature, heat content, and mean epilimnetic irradiance of small lakes, *Can. J. Fish. Aquat. Sci.* **63**, 11, 2447-2455, DOI: 10.1139/f06-131.

Hurrell, J.W. (1995), Decadal trends in the North Atlantic Oscillation: Regional temperatures and precipitation, *Science* **269**, 5224, 676-679, DOI: 10.1126/science.269.5224.676.

Livingstone, D.M. (1993), Temporal structure in the deep-water temperature of four Swiss lakes: A short-term climatic change indicator? *Verh. Internat. Verein. Limnol*. **25**, 75-81.

Livingstone, D.M., and M.T. Dokulil (2001), Eighty years of spatially coherent Austrian lake surface temperatures and their relationship to regional air temperature and the North Atlantic Oscillation, *Limnol. Oceanogr.* **46**, 5, 1220-1227, DOI: 10.4319/lo.2001.46.5.1220.

Marsz, A., and A. Styszyńska (2001), *North Atlantic Oscillation and Air Temperature in Poland*, Wyższa Szkoła Morska, Gdynia, 107 pp. (in Polish).

Novikmec, M., M. Svitok, D. Kočický, F. Šporka, and P. Bitušík (2013), Surface water temperature and ice cover of Tatra Mountains lakes depend on altitude, topographic shading, and bathymetry, *Arct. Antarct. Alp. Res.* **45**, 1, 77-87, DOI: 10.1657/1938-4246-45.1.77.

Nowlin, W.H., J.M. Davies, R.N. Nordin, and A. Mazumder (2004), Effects of water level fluctuation and short-term climate variation on thermal and stratification regimes of a British Columbia reservoir and lake, *Lake Reserv. Manage*. **20**, 2, 91-109, DOI: 10.1080/07438140409354354.

Ottersen, G., B. Planque, A. Belgrano, E. Post, P.C. Reid, and N.C. Stenseth (2001), Ecological effects of the North Atlantic Oscillation, *Oecologia* **128**, 1, 1-14, DOI: 10.1007/s004420100655.

Przybylak, R., G. Wójcik, and K. Marciniak (2003), Influence of the North Atlantic and Arctic Oscillations on the thermal conditions in the cold season in Poland from 16th to the 20th centuries, *Prz. Geof.* **48**, 1-2, 61-74 (in Polish).

Rogers, J.C. (1997), North Atlantic storm track variability and its association to the North Atlantic Oscillation and climate variability of northern Europe, *J. Climate* **10**, 7, 1635-1647, DOI: 10.1175/1520-0442(1997)010<1635:NASTVA>2.0.CO;2.

Skowron, R. (2011), *The Differentation and the Changeability of Choin Elements of the Thermal Regime of Water in Lakes on Polish Lowland*, Wyd. Nauk. UMK, Toruń, 346 pp. (in Polish).

Straile, D., and R. Adrian (2000), The North Atlantic Oscillation and plankton dynamics in two European lakes – two variations on a general theme, *Glob. Change Biol.* **6**, 6, 663-670, DOI: 10.1046/j.1365-2486.2000.00350.x.

Straile, D., K. Jöhnk, and H. Rossknecht (2003), Complex effects of winter warming on the physicochemical characteristics of a deep lake, *Limnol. Oceanogr.* **48**, 4, 1432-1438, DOI: 10.4319/lo.2003.48.4.1432.

Styszyńska, A. (2001), North Atlantic Oscillation and precipitation on the territory of Poland, *Prace Stud. Geogr.* **29**, 232-241 (in Polish).

Šporka, F., D.M. Livingstone, E. Stuchlík, J. Turek, and J. Galas (2006), Water temperatures and ice cover in lakes of the Tatra Mountains, *Biologia* **61**, 18, S77-S90, DOI: 10.2478/s11756-006-0121-x.

Trigo, R.M., T.J. Osborn, and J.M. Corte-Real (2002), The North Atlantic Oscillation influence on Europe: climate impacts and associated physical mechanisms, *Climate Res.* **20**, 1, 9-17, DOI: 10.3354/cr020009.

Wang, S., X. Qian, B.P. Han, L.C. Luo, and D.P. Hamilton (2012), Effects of local climate and hydrological conditions on the thermal regime of a reservoir at Tropic of Cancer, in southern China, *Water Res.* **46**, 8, 2591-2604, DOI: 10.1016/j.watres.2012.02.014.

Wibig, J. (2001), *Impact of the Atmospheric Circulation on Spatial Distributions of Air Temperature and Precipitation Anomalies in Europe*, Wyd. Uniw. Łódz., 208 pp. (in Polish).

Wrzesiński, D., M. Ptak, and A. Baczyńska (2013), Effect of the North Atlantic Oscillation on ice phenomena on selected lakes in Poland over the years 1961-2010, *Quaest. Geogr.* **32**, 3, 119-128, DOI: 10.2478/quageo-2013-0020.

Received 15 March 2014
Received in revised form 26 August 2014
Accepted 27 August 2014

DE GRUYTER OPEN

Acta Geophysica
vol. 63, no. 3, June 2015, pp. 884-899
DOI: 10.1515/acgeo-2015-0018

Ionospheric Time-delay over Akure Using Global Positioning System Observations

Olawale S. BOLAJI[1], Patrick A. IZANG[2,3], Olakunle R. OLADOSU[2,3], Femi KOYA[4], Rufus S. FAYOSE[5,6], and Akeem B. RABIU[3,6]

[1]Department of Physics, University of Lagos, Akoka, Nigeria
e-mail: oloriebimpjch2002@yahoo.co.uk

[2]African Regional Centre for Space Science Technology Education (English), Obafemi Awolowo University, Ile Ife, Nigeria

[3]National Space Research and Development Agency (NASRDA), Abuja, Nigeria

[4]Department of Mechanical Engineering, Obafemi Awolowo University, Ile Ife, Nigeria

[5]Department of Physics, Adekunle Ajasin University, Akungba-Akoko, Nigeria

[6]Space Physics Laboratory, Department of Physics, Federal University of Technology, Akure, Nigeria

A b s t r a c t

Ionospheric time delay ($V\Delta t$) variability using Global Positioning System (GPS) data over Akure (7.15°N, 5.12°E), Nigeria, has been studied. The observed variability of $V\Delta t$ in comparison to older results of vertical total electron content (TEC) across similar regions has shown equivalent signatures. Higher monthly mean values of $V\Delta t$ ($MV\Delta t$) were observed during daytime as compared to nighttime (pre- and post-midnight) hours in all months. The highest $MV\Delta t$ observed in September during daytime hours range between ~6 and ~21 ns (~1.80 and ~6.30 m) and at post-midnight, they are in the range of ~1 to ~6 ns (~0.3 to ~1.80 m). The possible mechanisms responsible for this variability were discussed. Seasonal $V\Delta t$ were investigated as well.

Keywords: ionosphere, Global Positioning System, time delay, total electron content.

1. INTRODUCTION

Navigation systems have witnessed tremendous improvements in the past four decades. One of such areas of achievements is the invention of Global Positioning System (GPS) by the Department of Defence (DoD), United States of America (USA), in the 1990s. GPS positioning (P), velocity (V), and time (T) accuracy from the GPS receiver records are strongly affected by the ionosphere activities. Our major concern regarding this work is about the GPS radio wave signal propagation within the ionosphere and not the troposphere. Bolaji (2012) restricted the review of the atmospheric propagation on the GPS signal to geometric effects. From the geometric effect, he reported that signal absorption effects are not important because the restriction assumed that all changes in the medium are smaller within one wavelength of signal (in the case of GPS, this is about 20 cm). Electromagnetic (EM) wave interactions with the ionosphere are well understood from the previous works of Ginzburg (1970), Chen (1984), Davies (1990), McNamara (1991), Hofmann-Wellenhof *et al*. (2012), and Odijk (2002). They reported that when EM wave propagates in free space, its velocity is approximately equal to the velocity of light (3.0×10^8 m/s), so that the refractive index is equal to 1. However, when EM wave propagates in the ionosphere, its velocity change; this is due to its interaction with particles present within the ionospheric medium. Therefore, GPS signals traversing through ionospheric medium to the receiving point are expected to propagate along a straight and geometric line, but, in a refractive medium like ionosphere, they bend due to refraction. In this scenario, the wave could be in phase (advance) and the refractive index will be smaller than 1; otherwise, if the wave is in group (delay), the refractive index is larger than 1. This indicates that, in the ionosphere, the phase of the wave is advancing (< 1) and its group is delayed (> 1). Ratcliffe (1975) suggested that the ionospheric refractive index is not constant, so that it existed with varying densities of charged particles because it is an inhomogeneous medium. Apart from being an inhomogeneous medium, its anisotropy characteristic explains why the GPS waves are circularly polarized by Faraday rotation phenomenon (Hall *et al*. 1996).

Besides inhomogeneous and anisotropic phenomena, the ionosphere is a dispersive medium, that is, the phase velocity of a wave is a function of its frequency. All these inhomogeneous, anisotropic, and dispersive phenomena are well-represented in the Appleton-Hatree formula (Eq. 1) when the absorption effects due to collisions between the electrons are ignored.

$$n_{\varphi,j}^{ip} \pm = \sqrt{1 - \frac{X_j}{1 - \frac{Y_{T,j}^2}{2(1-X_j)} \pm \sqrt{\frac{Y_{T,j}^4}{4(1-X_j)^2} + Y_{L,j}^2}}}\,, \tag{1}$$

where $X_j = f_p^2 / f_j^2$, $Y_{T,j}$, and $Y_{L,j}$ are the transversal and longitudinal components of Y_j. $Y_j = f_g/f_j$, f_j is the GPS signal frequency and f_g is the gyro frequency. So, $Y_{T,j} = Y_j |\sin\theta|$ and $Y_{L,j} = Y_j |\cos\theta|$, θ being the angle between Y_j and $Y_{L,j}$. This is also applicable to Y_j and $Y_{T,j}$. The frequency f_p known as the electron plasma frequency is the natural frequency of oscillation for a slab of neutral plasma after the electrons have been displaced from the ions and are able to move freely. This is computed as follows:

$$f_p = \sqrt{AN_e} \tag{2}$$

where

$$A = \frac{e^2}{4\pi^2 m_e \varepsilon_0} \approx 80.6 \text{ m}^3/\text{s}^2 \ .$$

N_e denotes the free electron density in m^{-3}. The value for A in Eq. 2 was obtained from the natural constants $e = 1.60218 \times 10^{-19}$ coulomb for the electron charge, $m_e = 9.10939 \times 10^{-31}$ kg for the electron mass and $\varepsilon_0 = 8.85419 \times 10^{-12}$ farad/meter for the permittivity of free space.

The inhomogeneity of the ionosphere is reflected in the free electron density (N_e), which is not a constant, but is a function of place and time. The dispersive nature of the ionosphere is recognized from its dependence on the frequency of the wave. The anisotropic part is a function of f_g. The double-refraction is reflected by the ± sign, which means that either a plus or minus sign can be used, depending on the polarization of the wave. A positive sign corresponds to the left-handed circularly polarized wave (the extraordinary wave) and a negative sign indicates a right-handed circularly polarized wave (the ordinary wave). For GPS estimates, ordinary wave having minus sign is significant.

By comparing the phase and group propagation effects using the ionospheric first order, higher orders and total electron content (TEC), the GPS time delay observation can be made. In summary, the first-order phase effect is equal in magnitude but opposite in sign to the first-order group effect. The second and third order phase effects posses opposite signs compared to their corresponding group effect counterparts, but they do not have the same magnitude. The second order phase effect is half the second order group effect, while the third order phase effect is one third of the third order group effect. The fourth order phase and group effects are the same. From the first order ionospheric delay, which is a function of the integral term $\int N_e dp$, it is equivalent to the TEC, which is the number of free electrons in a tube of 1-meter square cross section along the geometric line from the receiver to satellite. The tube of 1-meter square cross section along the geo-

metric line is a function of the signal bend due to ionospheric refraction, which represents the area (distance covered) where the ionospheric delay occurs. TEC is often expressed in total electron content units (TECU) and 1 TECU = 10^{16} electron/m^2. Using this definition of TEC, the first-order delay can be rewritten as:

$$i_{g,j}^{(1)} = \frac{A}{2f_j^2}\text{TEC} \quad \text{where} \quad \text{A} \approx 80.6\ \text{m}^3/\text{s}^2 \ . \tag{3}$$

Therefore, the first order delay is equivalent to the distance covered (DC_d) around the tube where the ionospheric delay occurs:

$$i_{g,j}^{(1)} = DC_d \tag{4}$$

and

$$DC_d = \Delta t\, C \ . \tag{5}$$

From Eq. 5, Δt is the time delay experienced by the GPS signal when traversing through the ionosphere and C is the speed of light.

Interestingly, the TEC estimates (Eq. 3), which were originally aimed at correcting the ionospheric error due to electron density population from the GPS radio signal when travelling through the ionosphere could provide an extraordinary ionospheric research regarding ionospheric time delay. Therefore, the variability of vertical time delay over the Nigeria ionosphere, its influences on terrestrial applications and possible mechanisms responsible for its variability will be investigated.

2. MATERIALS AND METHODOLOGY

Records from Global Positioning System (GPS) receiver located at the Federal University of Technology (FUT), Akure, Nigeria (geographic latitude 7.15°N, geographic longitude 5.12°E) are employed. Data-set from 5 months (January, March, August, September, and October) during the year 2010 were analyzed. The remaining months are not available because they are associated with larger data gap due to inconsistent power supply. Despite this shortcoming, the available data accommodate all seasons. The Solar Influences Data Analysis Center (SIDC 2013) classified year 2010 as an ascending phase of solar activity with an annual sunspot number of 16.5. This classification results from comparing annual sunspot numbers of previous years 2008 and 2009. The years 2008 and 2009 have an annual sunspot numbers of 2.9 and 3.2, respectively. Estimates of the uncorrected slant total electron content (S_uTEC) measured at every 1 minute interval from records of GPS receiver at FUT, Akure, Nigeria, were corrected for satellite differential delay (b_s), receiver differential delay (b_R) and the receiver inter-channel bias (b_{RX}). These corrected S_uTEC values were then converted to vertical to-

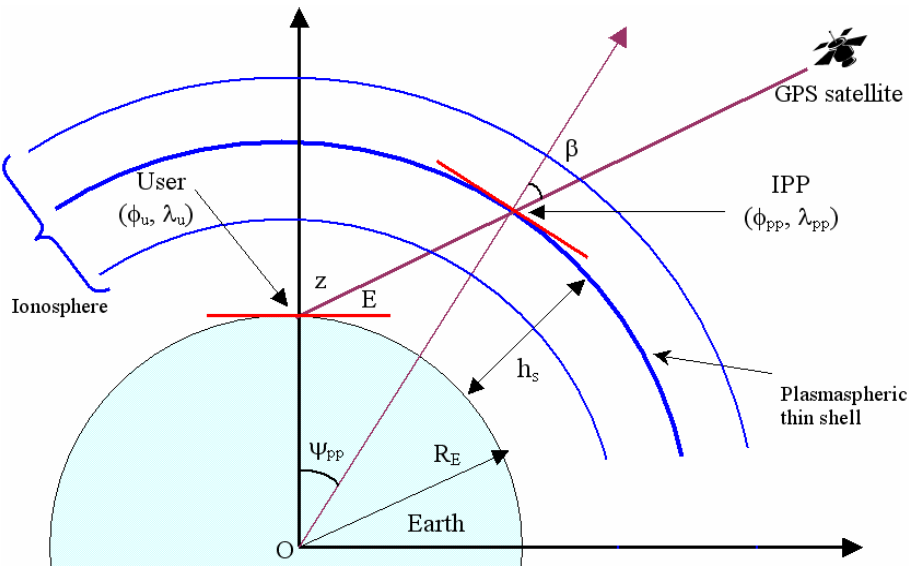

Fig. 1. The vertical total electron content (V_cTEC) deduced from slant total electron content (S_uTEC) using thin shell approximation with an ionospheric height (h_s) of 350 km.

tal electron content (V_cTEC) using thin shell approximation with an ionospheric height of 350 km. Figure 1 shows graphical representation of these analyses and the mathematical expressions for it are as follows:

$$V_c\text{TEC} = S_u\text{TEC} - \left[b_R + b_S + b_{RX}\right] / S(E) \ , \tag{6}$$

where $S(E)$ is the obliquity factor with zenith angle (z) at the Ionospheric Pierce Point (IPP), E is the elevation angle of the satellites in degrees, and V_cTEC is the vertical TEC at the IPP. The $S(E)$ is defined by Mannucci *et al.* (1993) and Langley *et al.* (2002) as:

$$S(E) = \frac{1}{\cos(z)} = \left\{1 - \left(\frac{R_E \times \cos(E)}{R_E + h_S}\right)^2\right\}^{-0.5} \ , \tag{7}$$

where R_E is the mean radius of the Earth, measured in kilometers [km], and h_s is the height of the ionosphere from the surface of the Earth (~350 km). These analyses from Eqs. 6 and 7 were put together in C-programming language developed by S.G. Krishna (ISR 2009). This software was used to compute V_cTEC values for each month under investigation. This same procedure was employed by Bolaji *et al.* (2012, 2013) to compute V_cTEC. The time convention for these analyses is in universal time (UT), but, in this pa-

per, local time (LT) will be used and Nigeria is 1 hour ahead of Greenwich Mean Time (GMT). Therefore, 12:00 UT is 13:00 LT in Nigeria. Now, substituting TEC and $i_{g,j}^{(1)}$ in Eq. 3, with V_cTEC in Eq. 6 and DC_d with Eq. 4, in that order, result to

$$\Delta t = \frac{A}{2Cf_j^2} V_c \mathrm{TEC} \ . \tag{8}$$

All meanings of terms from the above equations remained unchanged. The vertical Δt ($V\Delta t$) on each hour of a day over the 5 months were deduced. For each month, mean values of $V\Delta t$ (M$V\Delta t$) are estimated. Eleman (1973) classified months according to the Lloyd's seasonal pattern of three seasons: December Solstice (January, February, November, December), Equinoctial Season (March, April, September, October), and June Solstice (May, June, July, August). Since each month under investigation in this study falls within the Lloyd's seasonal pattern, each month will represent each season. That is, March, September, and October will represent Equinox Season. The month of August will represent June Solstice (Summer Season) and December will represent December Solstice (Winter Season). The seasonal variations of $V\Delta t$ ($SSV\Delta t$) for all the months under investigation are estimated by finding the average of the M$V\Delta t$ under a particular season.

3. RESULTS AND DISCUSSIONS

3.1 Variability of the ionospheric monthly vertical time delay (M$V\Delta t$)

For clearer representation of monthly mean hourly values of $V\Delta t$ (M$V\Delta t$) during daytime, pre-, and post-midnight hours, September with highest magnitudes of M$V\Delta t$ was divided into daytime (07:00-18:00 LT), pre-midnight (19:00-24:00 LT), and post-midnight (00:01-06:00 LT) hours (Fig. 1). In Figure 1, the top panel shows daytime M$V\Delta t$ variability, the bottom left-hand panel shows pre-midnight M$V\Delta t$ variability, and the bottom right-hand panel shows post-midnight M$V\Delta t$ variability. The magnitudes of M$V\Delta t$ were as well estimated over all hours for January, March, August, and October (Figs. 2-5). Figures 2-6 show September, January, March, August, and October M$V\Delta t$ variability with bar-charts coloured in blue, in that order. The M$V\Delta t$ magnitudes measured in nano seconds [ns] are plotted on the y axis, with local time (LT) on the x axis. Figure 7 shows the monthly mean variability of total electron content (TEC) on all hours. The September, January, March, August, and October variability of TEC is in dotted black lines with a downward-pointing triangle, red lines with a square, green lines with a diamond, blue lines with a five-pointed star, and magenta lines with a right-hand pointing triangle, in that order.

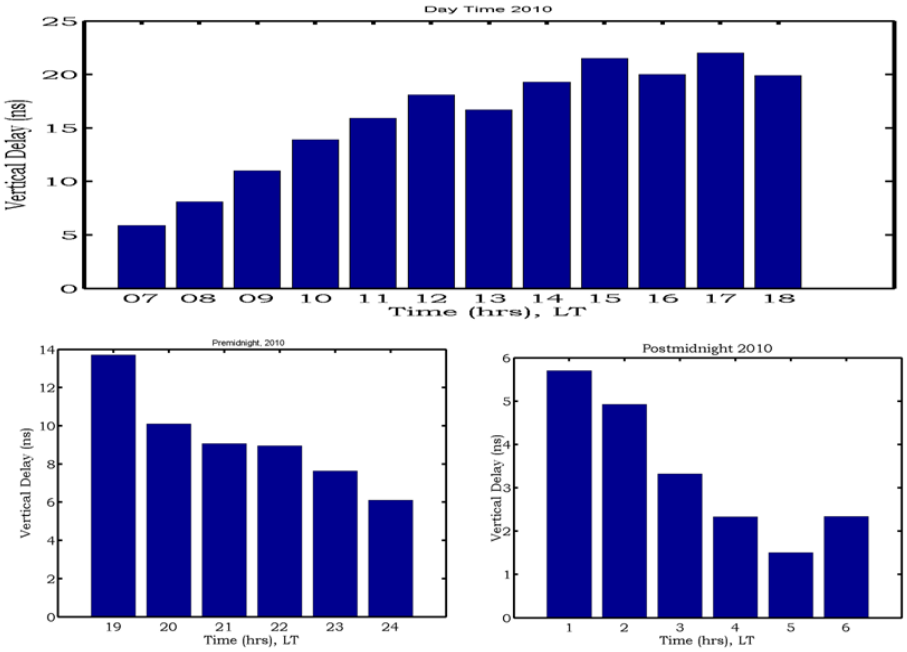

Fig. 2. Variability of the ionospheric monthly vertical time delay in September.

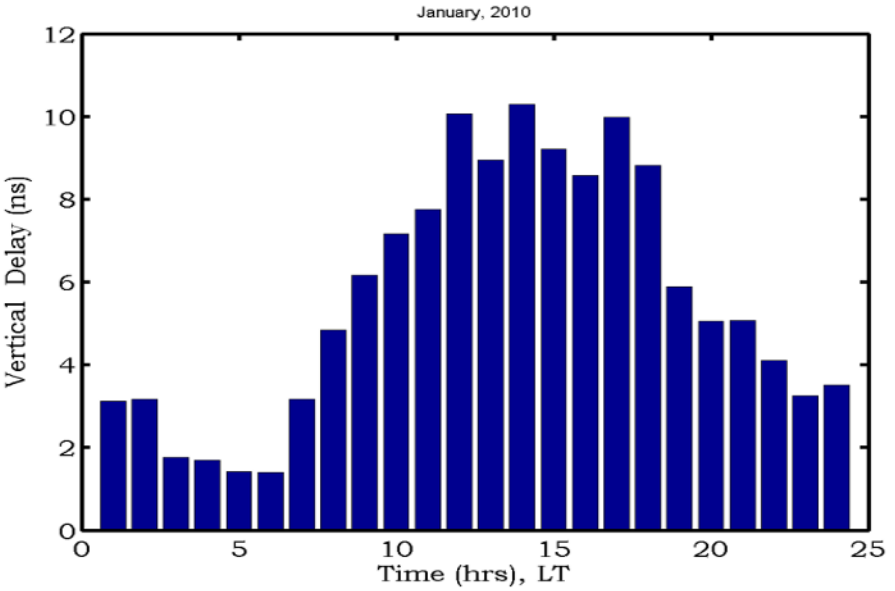

Fig. 3. Variability of the ionospheric monthly vertical time delay in January.

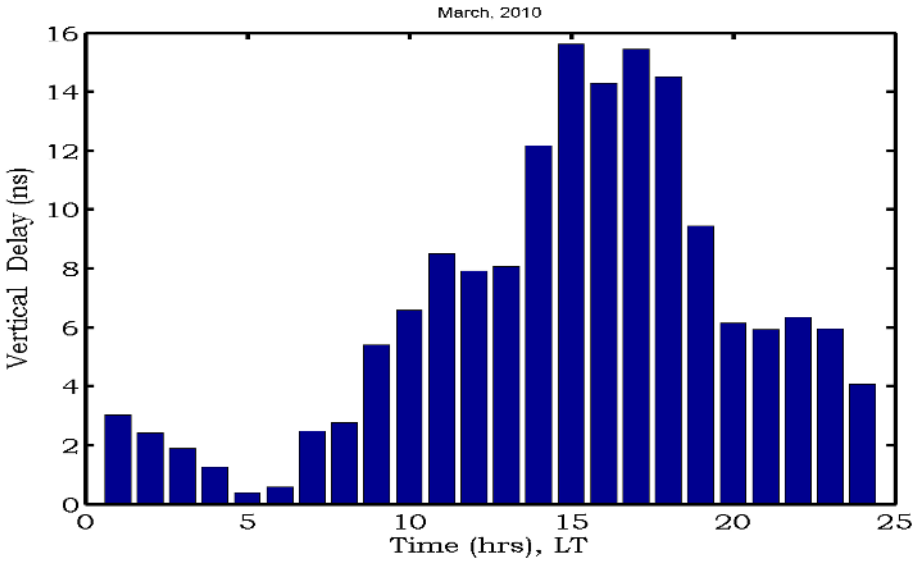

Fig. 4. Variability of the ionospheric monthly vertical time delay in March.

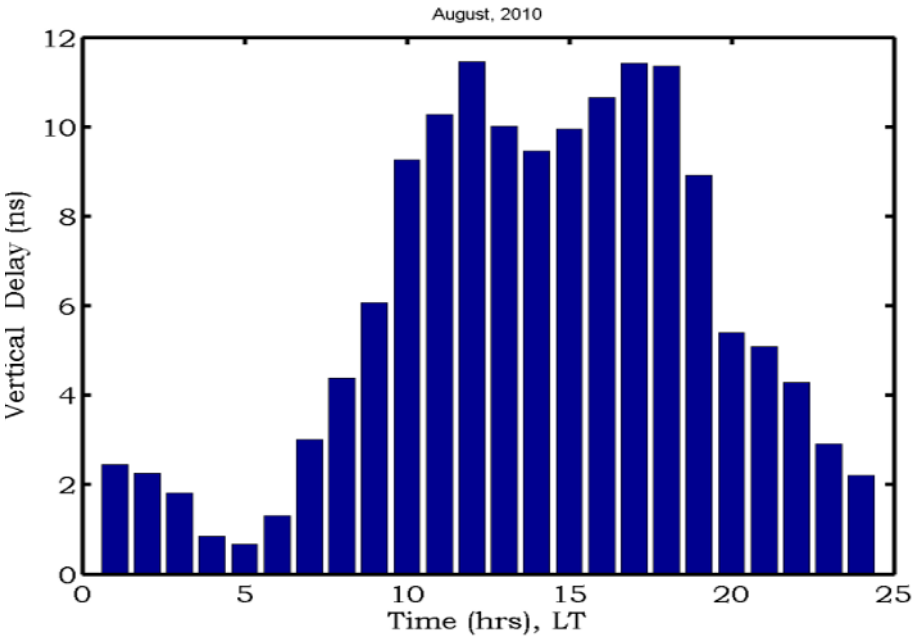

Fig. 5. Variability of the ionospheric monthly vertical time delay in August.

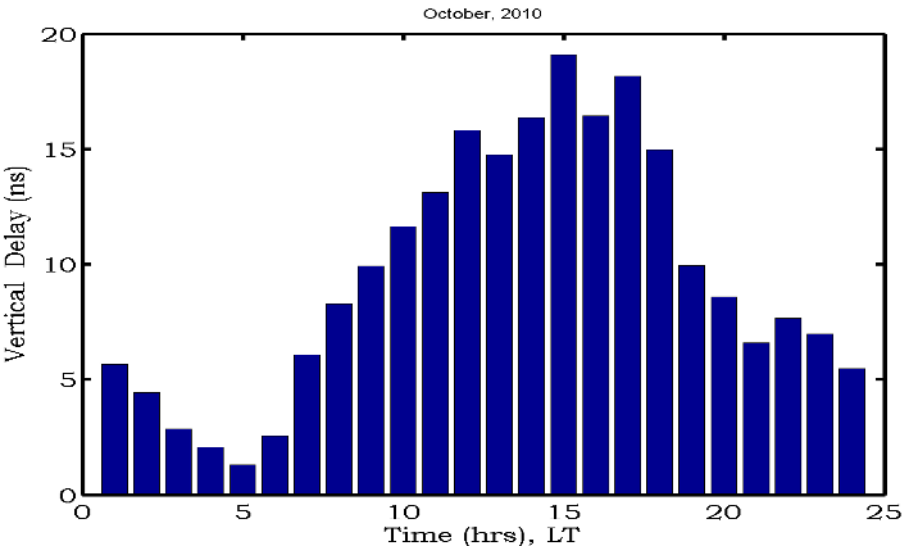

Fig. 6. Variability of the ionospheric monthly vertical time delay in October.

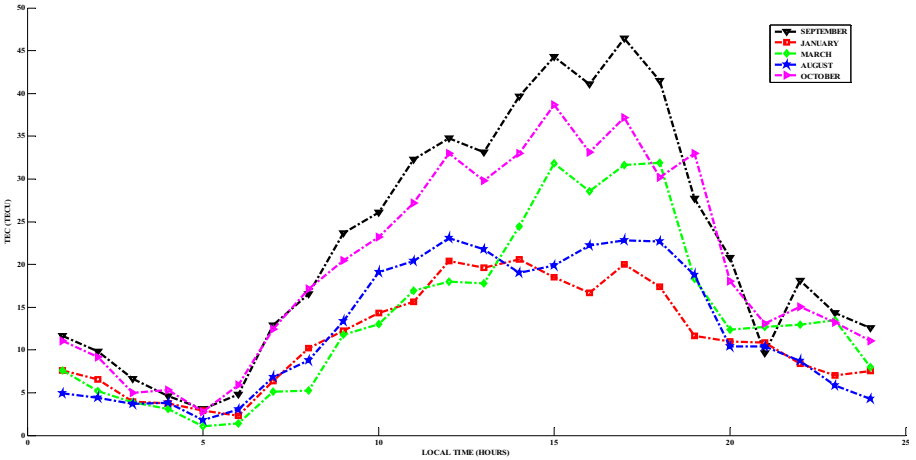

Fig. 7. Monthly mean hourly values of TEC over Akure.

Generally, all months under investigation shown in Figs. 2-6, exhibit highest, higher and low M$V\Delta t$ magnitudes during daytime, pre-, and post-midnight periods, respectively. As can be observed from Fig. 2 (September), during daytime, pre-, and post-midnight hours, M$V\Delta t$ magnitudes range from ~6 to ~21 ns (~1.80 to ~6.30 m), ~6 to ~14 ns (~1.80 to ~4.20 m), and ~1 to ~6 ns (~0.3 to ~1.80 m), in that order. Although, in other months: January,

March, August, and October, similar variability patterns were observed; compare with September. However, they have varying M$V\Delta t$ magnitudes during daytime, pre-, and post-midnight periods. Apart from the highest M$V\Delta t$ magnitudes observed in September, January has lowest magnitudes of M$V\Delta t$, in the range of ~4 to ~10 ns (~1.20 to ~3.0 m) on all hours. In January, during daytime hours, the M$V\Delta t$ magnitude is the highest, with a value of ~10 ns (~3.0 m) around 14:00 LT; during pre-midnight hours, the highest value is ~6 ns (~1.80 m) around 19:00 LT; and during post-midnight hours, between 01:00 and 02:00 LT, the highest value is ~4 ns (~1.20 m). Interestingly, during the period between 17:00 and 18:00 LT, M$V\Delta t$ variability was observed to increase slightly across all months.

These observations are similar to the works of Skinner (1966), Olatunji (1967), Bolaji *et al*. (2012, 2013) at Zaria, Ibadan, and Ilorin, respectively. They reported highest magnitudes of total electron content (TEC) over Nigeria during daytime hours using a Global Positioning System (GPS) facility. They reported that the range in maximums during daytime TEC in all months is greater that the range in minimums observed at nighttimes: pre- and post-midnight. They attributed this greater magnitude of TEC during daytime to greater solar ionization in-place, when the ionization loss rate is smaller. In addition to the similar highest magnitudes of TEC and M$V\Delta t$ observed during daytime hours, they also have similar variability patterns. For example, the variability patterns of TEC (Fig. 7) and M$V\Delta t$ (Figs. 2-6) are characterized with low pre-sunrise magnitudes, high daytime magnitudes, and moderate post sunset magnitudes. Also, during daytime hours, Skinner (1966), Olatunji (1967), and Bolaji *et al*. (2012, 2013) reported that the variability of TEC magnitudes was the highest in all months over all hours during daytime period. From this work, similar highest magnitudes of M$V\Delta t$ were as well observed over all hours in all months during daytime hours. Although TEC is measured in total electron content units (TECU) but M$V\Delta t$ is measured in nano seconds.

The slight increments observed in M$V\Delta t$ around 17:00 and 18:00 LT in all months were similar to the report of Koster (1972), Tyagi *et al*. (1982), Janve *et al*. (1979), Dabas *et al*. (2003), and Bolaji *et al*. (2012) on TEC magnitude variability. They suggested that such a scenario of slight increment of TEC magnitude during 17:00 and 18:00 LT could be due to evening renewal of fountain effect, which results from strong upward reversal of F-region EXB drift at equatorial latitudes and development of large pre-reversal enhancement (PRE) velocity.

Higher and lowest magnitude of M$V\Delta t$ observed during pre- and post-midnight hours, respectively, could be due to higher ionization loss rate. Skinner (1966), Olatunji (1967), and Bolaji *et al*. (2012, 2013) observed similar results from their TEC magnitudes during pre- and post-midnight hours.

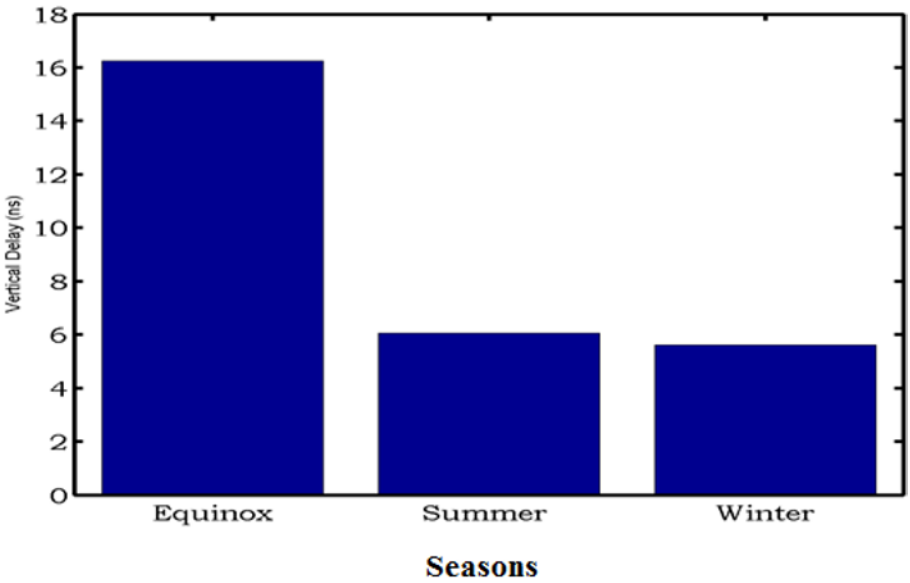

Fig. 8. Seasonal variation of ionospheric time delay in 2010.

The TEC magnitudes they observed are minimal (~4-5 TECU) during post-midnight hours and appreciable (of ~11-12 TECU) during pre-midnight hours. Apart from these similarities, the comparison is also evident from Eq. 8, which shows convincingly that there is a strong proportionality between ionospheric TEC and $V\Delta t$ parameters. Hence, this work reveals that the higher the magnitude of $V\Delta t$, the higher the magnitude of TEC, hence, otherwise. This indicates that the higher the level of electron contents in the ionosphere, the longer the delay in time of the GPS signal in the ionosphere before getting to the ground based receiver. Therefore, mechanisms responsible for TEC variability could as well directly influence the M$V\Delta t$ variability.

The estimated average value of $V\Delta t$ in the year 2010 is 10 ns using the method of Bhattacharya *et al*. (2009). Our analysis has shown that for a factor of 1 ns for 30 cm in range (altitude), the average range error for the year 2010 is ± 3 m in Akure. Then, on assumption that the GPS receiver is at an altitude of 100 m a.s.l., there could be an equivalent reading of 97 m altitude recorded on the GPS. From our results, maximum daytime and post-midnight $V\Delta t$ was ~21 and ~6 ns, in that order, which is equivalent to 6.30 and 1.80 m, respectively. These indicate that the convenient period when GPS could be best utilized is during post-midnight hours. Bhattacharya *et al*. (2009) investigated ionospheric time delay during disturbed period in the year 2005, a year of minimum solar activity. They observed that during the

main phase of the storm on 24 August 2005, the ionospheric time delay has a maximum value of 36.87 ns (11.061 m). This value is higher than the maximum value of 48 ns (14.4 m) observed in April when there was no storm. This value (48 ns) was as well higher than the maximum value (21 ns) we got from our investigation. Hence, we suggest that these differences could result from the sunspot number. Although the years 2005 and 2010 are both classified as low solar activity years. However, the SIDC archives show that the years 2005 and 2010 had annual sunspot number of 29.8 and 16.5, respectively. They also observed reduction from 12 to 7 in the observable satellites. The consequence could lead to data loss, cycle slip, and satellite geometry disturbances. Therefore, during a severe storm period with higher disturbed storm-time (*Dst*) magnitudes that could spread from hours to days, $V\Delta t$ could be between 60 and 100 ns. This will greatly affect the positioning estimate of the GPS, for example, if a severe storm period occurs when an aircraft is landing in Lagos airport, which is about 150 m a.s.l. The GPS facility monitoring the landing could have an equivalent altitude reading of 250 m. This could lead to airplane crash, if the pilot had no experience about stormy period. Also, military operations could be greatly affected, as the position error of about 1 m could alter the exact landing position of a missile on a target. This could lead to damaging of wrong facilities, infrastructures, and loss of lives.

3.2 Seasonal variability of vertical time delay ($SSV\Delta t$)

The seasonal variations of $V\Delta t$ ($SSV\Delta t$) for all the months under investigation are shown with bar charts and their magnitudes coloured blue in Fig. 6. The highest $SSV\Delta t$ was observed during equinoctial season with a value of ~16 ns. The value of $SSV\Delta t$ was higher and lowest in summer (~6 ns) and winter (~5 ns) seasons, respectively. This clearly shows a semi-annual variation in $SSV\Delta t$, highest value of $SSV\Delta t$ in equinoctial months (March, September, October), moderate values in summer month (August), and lower values in winter month (December). In general, our previous results and observations have shown that there is a proportionality in quantities between TEC and $V\Delta t$ variability (Eq. 8). Therefore, the mechanism responsible for seasonal TEC could be responsible for $SSV\Delta t$ as well.

Danilov and Lastovicka (2001) and Bhattacharya *et al*. (2009) have reported highest ionization value in the ionosphere regarding equinoctial season during disturbed periods. They attributed these highest values during equinoctial months to the down welling of thermospheric gas without any significant change in atom to molecule ratio, which is mainly caused by storm-induced thermospheric winds. But this study was carried out when there was no disturbed activity; hence, storm-induced thermospheric wind

might not be responsible for the highest $SSV\Delta t$ observed in this study during equinoctial months. Since the ionosphere is made up of neutral oxygen (O) and nitrogen gases N_2 (Risbeth and Setty 1961), the seasonal variability in $SSV\Delta t$ could be attributed to the changes in the ratio of atomic oxygen and molecular nitrogen gases concentration in the F2 layer, and possibly affects the F2 layer topside. Risbeth and Setty (1961) have also reported that irrespective of the solar extreme ultraviolet (SEU) radiation magnitude, the absorptions of SEU radiation in the ionosphere are always the highest during equinoctial months. This could be responsible for highest $SSV\Delta t$ during equinoctial months.

Previous works by Bhuyan and Borah (2007) regarding seasonal variability of TEC have also shown higher TEC magnitude during winter season as compared to summer season. They reported that this higher magnitude during winter season is due to weaker recombination of particles in the atmosphere. However, our results have shown higher magnitudes of $SSV\Delta t$ during summer season as compared to winter season. In this scenario, the recombination of particles in the atmosphere could be slightly higher. This could lead to lower $SSV\Delta t$ in winter as compared to summer season.

The semi-annual variations of TEC have been reported by Olatunji (1967), Bailey *et al*. (2000), Wu *et al*. (2004), Rama Rao *et al*. (2006), Liu *et al*. (2008), Lee *et al*. (2010), and Bolaji *et al*. (2012, 2013). They reported that semi-annual variation results from interaction between the magnetic field geometry and noon solar zenith angle, which is a significant factor in the increment and production of ionization during equinoctial months. Risbeth and Setty (1961) and Bhuyan and Borah (2007) have also shown that the semi-annual effect at the low latitude is caused by semi-annual changes in the neutral composition of the atmosphere.

4. CONCLUSIONS

The higher values of $V\Delta t$ irrespective of months and seasons are equivalent to higher values of TEC in a similar region. Therefore, our results have shown significant equivalency in terms of magnitude signature between $V\Delta t$ and TEC. Hence, mechanisms responsible for $V\Delta t$ could be responsible for TEC. We therefore conclude that telecommunications, geodetic and navigation systems will experience lesser error at night over Nigeria due to minimal $V\Delta t$ values observed. Hence, users of GPS applications like the military, security agencies, and aviation sector could take advantage of this period for operations and better services.

Acknowledgements. Authors acknowledged the kind gesture of the Air Force Research Laboratory (AFRL), USA, through its principal investigator (PI) Dr. Keith Grooves, that donated a Unit of Global Positioning Sys-

tem (GPS) to our Space Physics Laboratory, Department of Physics, Federal University of Technology, Akure, Nigeria. This GPS Unit was donated under the Scintillation Network Decision Aid (SCINDA) project of AFRL during the campaign of the International Heliophysical Year (IHY) in 2005 under the auspices of the United Nations (UN).

References

Bailey, G.J., Y.Z. Su, and K.I. Oyama (2000), Yearly variations in the low-latitude topside ionosphere, *Ann. Geophys*. **18**, 7, 789-798, DOI: 10.1007/s00585-000-0789-0.

Battacharya, S., P.K. Purohit, and A.K. Gwal (2009), Ionospheric time delay variations in the equatorial anomaly region during low solar activity using GPS, *Indian J. Radio Space Phys.* **38**, 5, 266-274.

Bhuyan, P.K., and R.R. Borah (2007), TEC derived from GPS network in India and comparison with the IRI, *Adv. Space Res.* **39**, 5, 830-840, DOI: 10.1016/j.asr.2006.12.042.

Bolaji, O.S. (2012), Variability of total electron content and magnetic field intensity at Ilorin, Ph.D. Thesis, University of Ilorin, Nigeria.

Bolaji, O.S., J.O. Adeniyi, S.M. Radicella, and P.H. Doherty (2012), Variability of total electron content over an equatorial West African station during low solar activity, *Radio Sci.* **47**, 1, RS1001, DOI: 10.1029/2011RS004812.

Bolaji, O.S., J.O. Adeniyi, I.A. Adimula, S.M. Radicella, and P.H. Doherty (2013), Total electron content and magnetic field intensity over Ilorin, Nigeria, *J. Atmos. Sol.-Terr. Phys*. **98**, 1-11, DOI: 10.1016/j.jastp.2013.02.011.

Chen, F.F. (1984), *Introduction to Plasma Physics and Controlled Fusion. Volume 1: Plasma Physics*, 2nd ed., Plenum Press, New York, 421 pp.

Dabas, R.S., L. Singh, D.R. Lakshmi, P. Subramanyam, P. Chopra, and S.C. Garg (2003), Evolution and dynamics of equatorial plasma bubbles: Relationships to ExB drift, postsunset total electron content enhancements, and equatorial electrojet strength, *Radio Sci.* **38**, 4, 1075, DOI: 10.1029/2001RS002586.

Danilov, A.D., and J. Lastovicka (2001), Effects of geomagnetic storms on the ionosphere and atmosphere, *Int. J. Geomagn. Aeronom.* **2**, 3, 209-224.

Davies, K. (1990), *Ionospheric Radio*, IEE electromagnetic waves series, Vol. 31, Peter Peregrinus Ltd., London, 580 pp.

Eleman, F. (1973), The geomagnetic field. **In:** A. Egeland,, Ø. Holter, and A. Omholt (eds.), *Cosmical Geophysics*, Chp. 3, Scandinavian University Books, Oslo, 45-62.

Ginzburg, V.L. (1970), *The Propagation of Electromagnetic Waves in Plasmas*, 2nd ed., Pergamon Press, Oxford.

Hall, M.P.M., L.W. Barclay, and M.T. Hewitt (eds.) (1996), *Propagation of Radiowaves*, IEE Press, London, 446 pp.

Hofmann-Wellenhof, B., H. Lichtenegger, and J. Collins (2012), *Global Positioning System: Theory and Practice*, 5th rev. ed., Springer Verlag, Wien, 382 pp., DOI: 10.1007/978-3-7091-6199-9.

ISR (2009), Global Positioning System total electron content analysis application user's manual, Institute for Scientific Research, Boston College, Chestnut Hill, USA.

Janve, A.V., R.K. Rai, M.R. Deshpande, R.G. Rastogi, A.R. Jain, M. Singh, and H.S. Gurm (1979), On the nighttime enhancements in ionospheric total content at low latitudes, *Ann. Geophys*. **35**, 159-165.

Koster, J.R. (1972), Equatorial scintillation, *Planet. Space Sci.* **20**, 12, 1999-2014, DOI: 10.1016/0032-0633(72)90056-6.

Langley, R., M. Fedrizzi, E. Paula, M. Santos, and A. Komjathy (2002), Mapping the low latitude ionosphere with GPS, *GPS World* **13**, 2, 41-46.

Lee, C.C., Y.J. Chuo, and F.D. Chu (2010), Climatology of total electron content near the dip equator under geomagnetic quiet-conditions, *J. Atmos. Sol.-Terr. Phys.* **72**, 2-3, 207-212, DOI: 10.1016/j.jastp.2009.11.011.

Liu, C., M.L. Zhang, W. Wan, L. Liu, and B. Ning (2008), Modeling M(3000)F2 based on empirical orthogonal function analysis method, *Radio Sci.* **43**, 1, RS1003, DOI: 10.1029/2007RS003694.

Mannucci, A.J., B.D. Wilson, and C.D. Edwards (1993), A new method for monitoring the Earth's ionospheric total electron content using the GPS global network. **In:** *Proc. 6th Int. Tech. Meet. Satellite Division of the Institute of Navigation, 22-24 September 1993, Salt Lake City, USA*, ION GPS-93, 1323-1332.

McNamara, L.F. (1991), *The Ionosphere: Communications, Surveillance, and Direction Finding*, Orbit – a foundation series, Krieger Publ. Co., Malibar.

Odijk, D. (2002), *Fast Precise GPS Positioning in the Presence of Ionospheric Delay*, Publications on geodesy, Vol. 52, Netherlands Geodetic Commission, Delft, 242 pp.

Olatunji, E.O. (1967), The total columnar electron content of the equatorial ionosphere, *J. Atmos. Terr. Phys.* **29**, 3, 277-285, DOI: 10.1016/0021-9169(67)90197-3.

Rama Rao, P.V.S., S. Gopi Krishna, K. Niranjan, and D. Prasad (2006), Temporal and spatial variations in TEC using simultaneous measurements from the Indian GPS network of receivers during low solar activity period of 2004-2005, *Ann. Geophys*. **24**, 12, 3279-3292, DOI: 10.5194/angeo-24-3279-2006.

Ratcliffe, J.A. (1975), The early ionosphere investigations of Appleton and his colleagues, *Phil. Trans. Roy. Soc. London A* **280**, 1293, 3-9, DOI: 10.1098/rsta.1975.0088.

Rishbeth, H., and C.S.G.K. Setty (1961), The F-layer at sunrise, *J. Atmos. Terr. Phys.* **20**, 4, 263-276, DOI: 10.1016/0021-9169(61)90205-7.

SIDC (2013), Solar Influences Data Analysis Center, archive at http://sidc.oma.be/sunspot-data (assesses 14 July 2013).

Skinner, N.J. (1966), Measurements of total electron content near the magnetic equator, *Planet. Space Sci.* **14**, 11, 1123-1129, DOI: 10.1016/0032-0633(66)90026-2.

Tyagi, T.R., K.C. Yeh, A. Tauriainen, and H. Soicher (1982), The electron content and its variations at Natal, Brazil, *J. Geophys. Res*. **87**, A4, 2525-2532, DOI: 10.1029/JA087iA04p02525.

Wu, C.C., C.D. Fry, J.Y. Liu, K. Liou, and C.L. Tseng (2004), Annual TEC variation in the equatorial anomaly region during the solar minimum: September 1996 – August 1997, *J. Atmos. Sol.-Terr. Phys.* **66**, 3-4, 199-207, DOI: 10.1016/j.jastp.2003.09.017.

Received 4 May 2014
Received in revised form 24 October 2014
Accepted 26 November 2014

DE GRUYTER OPEN

Acta Geophysica
vol. 63, no. 3, June 2015, pp. 900-921
DOI: 10.1515/acgeo-2015-0024

Comparison of Early Evolutions of Mimas and Enceladus

Leszek CZECHOWSKI and Piotr WITEK

Institute of Geophysics, University of Warsaw, Warszawa, Poland
e-mail: lczecho@op.pl (corresponding author)

A b s t r a c t

Thermal history of Mimas and Enceladus is investigated from the beginning of accretion to 400 Myr. The numerical model of convection combined with the parameterized theory is used. The following heat sources are included: short lived and long lived radioactive isotopes, accretion, serpentinization, and phase changes. The heat transfer processes are: conduction, solid state convection, and liquid state convection. We find that temperature of Mimas' interior was significantly lower than that of Enceladus. If Mimas accreted 1.8 Myr after CAI then the internal melting and differentiation did not occur at all. Comparison of thermal models of Mimas and Enceladus indicates that conditions favorable for the start of tidal heating lasted for a short time (~10^7 yr) in Mimas and for ~10^8 yr in Enceladus. This could explain the Mimas–Enceladus paradox. In fact, in view of the chronology based on cometary impact rate, one cannot discard a possibility that also Mimas was for some time active and it has the interior differentiated on porous core and icy mantle.

Key words: medium-sized satellites, thermal evolution, differentiation, Mimas–Enceladus paradox.

1. INTRODUCTION

Enceladus and Mimas are two smallest medium-sized satellites (MIS) of Saturn. The group consists of 6 spherical satellites: Mimas, Enceladus, Tethys, Dione, Rhea, and Iapetus. They are built of mixtures of rocks and

ices. The rocky component is believed to be of chondritic composition. The main component of ices is frozen H_2O but some admixture of ammonia and other volatiles is expected (*e.g.*, Peale 2003).

Since the flyby of the Voyager probe it is known that Mimas has a heavily cratered surface devoid of features that would indicate recent endogenic activity. The majority of craters are generally thought to form during the Late Heavy Bombardment Epoch. Lineaments visible on the surface of this satellite are thought to be a result of the impact that created the Herschel crater, although freezing expansion cannot be ruled out *a priori* (Jaumann *et al.* 2009). The density of Mimas (1147 $\mathrm{kg\,m^{-3}}$) is much lower than that of Enceladus (1609 $\mathrm{kg\,m^{-3}}$). This indicates that ices constitute important part of this body and the rock content is lower in Mimas than in Enceladus, which in turn suggests lower heating rate due to radiogenic isotopes. The shape of Mimas determined by the Cassini probe might suggest internal mass concentration (due to differentiation and formation of the core). The small deviation from the hydrostatic ellipsoid shape limits what can be inferred about the interior (Thomas 2010). The significant radial porosity gradient, as hypothesized by Eluszkiewicz (1990), is now thought to be short-lived (Leliwa-Kopystyński and Kossacki 2000).

Mimas has a relatively large eccentricity ($e = 0.02$) which is thought to be primordial (*e.g.*, Matson *et al.* 2009); however, it could also be explained by the passage of the satellite through mean motion resonances with either Enceladus or Dione (Meyer and Wisdom 2008). To sustain the primordial eccentricity, the Mimas' interior must have been cold and rigid through most of its history (McKinnon and Barr 2007). Calculations of Multhaup and Spohn (2007) indicate that partial melting and differentiation of Mimas is possible only if some ammonia is present and the nebula ambient temperature is around 250 K. However, they did not consider the heat of short-lived radioactive isotopes, like ^{26}Al. Moreover, Muro and Nimmo (2011) calculated that initial temperatures exceeding 220 K lead to runaway dissipation scenario and fast eccentricity damping. Charnoz *et al.* (2009) suggested that during the Late Heavy Bombardment (LHB) Mimas could have experienced catastrophic disruption and reassembled thereafter; in contrast, survival of Enceladus is much more probable in each considered model.

Data concerning interiors of the MIS are very scarce. The most direct data are measurements of gravitational field and magnetic field of the satellites. From these data one can obtain mass distribution and distribution of electric conductivity (high conductivity means a probable existence of liquid water); see, *e.g.*, Bobojć and Drożyner (2011), Essa (2007), Kriegel *et al.* (2009). However, even these data are rather limited. The best situation is for Enceladus because of several close flybys and determination of chemistry of the plumes over the South Polar Terrain (SPT).

A few papers considered early thermal evolution of Enceladus. First models, like Ellsworth and Schubert's (1983), do not include short-lived isotopes (SLI). They found that the heating from long-lived radioactive isotopes (LLI) was not intensive enough for melting the interior but it was large enough to support solid state convection for 3.3 billion years. This convection could prevent extensive melting.

Schubert *et al.* (2007) investigated first 20 Myr of Enceladus' history. They have found that the interior of Enceladus experienced early differentiation due to melting of ice from radiogenic heating (mainly ^{26}Al). At 10 to 20 Myr after formation, Enceladus had hot rocky core of 165 km size. However, this conclusion depends on time of accretion. If Enceladus accreted 3.5 Myr after the formation of Calcium-aluminum-rich inclusions (CAI), its interior would not melt, unless the initial temperature was high. If the temperature was 200 K at the time of Enceladus' formation, then differentiation occurred even for low content of ^{26}Al, but it would not be complete. Their model included short-lived isotopes and phase transitions, but they did not consider heat of serpentinization and finite time of accretion.

Malamud and Prialnik (2013) in their recent paper compare the early evolution of Mimas and Enceladus. The aim of our paper is similar but those authors used different methods and models. Models in both papers include the same sources of heating, *i.e.*, serpentinization, short-lived and long-lived isotopes, and gravitational energy. The main difference of their models comparing to ours is different rheology of the satellites' interior. Malamud and Prialnik (2013) assume matrix composed of rock. The flow of water through a porous rocky medium is the main process responsible for the mass transport. Water (and other liquids or gases) could flow throughout the matrix. Convection in porous media is possible but its properties are essentially different (especially efficiency of the heat transport); see Czechowski and Kossacki (2012). Of course, the sponge like model of Malamud and Prialnik (2013) includes neither solid state convection nor liquid state convection as the heat transport mechanism. The accretion is assumed to be instantaneous.

The results of Malamud and Prialnik (2013) confirm that if Enceladus accreted early (before decay of SLI) then it could be melted and differentiated into a rocky inner core and a thin icy crust. The melting of the interior led also to serpentinization of the interior. If Enceladus accreted after decay of SLI, then the melting (and serpentinization) in Enceladus could start only if ammonia was present in the ice. Malamud and Prialnik (2013) suggest that the present differences between Enceladus and Mimas could be a result of serpentinization of Enceladus during its early evolution, and the lack of this process in Mimas.

We investigate a few scenarios of Mimas and Enceladus evolutions that could lead to the present state of these satellites: dead Mimas and active

Enceladus. We include heating from SLI and LLI as well as the heat of accretion and serpentinization. The accretion is not instantaneous, convection is considered also during accretion of the satellites. Moreover, two regimes of convection are included: liquid state convection (LSC) and solid state convection (SSC).

The paper is organized as follows. The heat sources and basic properties of MIS interior are described in Section 2. Section 3 treats about the model of convection and numerical model used for our calculations. The results are presented and discussed in Section 4. Conclusions are in the last section.

2. HEAT SOURCES AND PROPERTIES OF MIS

2.1 Heat sources

We consider the following heat sources: decay of short-lived radioactive isotopes (*i.e.*, ^{26}Al, ^{60}Fe, ^{53}Mn), decay of long-lived radioactive isotopes (*i.e.*, ^{40}K, ^{232}Th, ^{238}U, ^{235}U), heat of serpentinization, and the heat of accretion. The latent heat of freezing/melting of ice component is also included. The tidal heating is not included because we consider only the period before the tidal heating became important. The gravitational energy released during differentiation and/or contraction is negligible for Enceladus (*e.g.*, Malamud and Prialnik 2013).

The initial radiogenic heat rates generated by a given isotope just after the formation of CAI are given in Table 1. For any given time t the heat rate is

$$Q(t) = f_m \sum_{i=1}^{7} Q_{0i} \exp\left(-C_i t\right) , \tag{1}$$

Table 1

Data concerning radioactive isotopes considered in the paper*

Isotope	Half life $t_{1/2}$ [My]	Initial rate of heating per unit mass of element [W kg^{-1}]	Isotopic concentration ppb [10^{-9}]	Half life $t_{1/2}$ [s]	Decay constant C_i [s^{-1}]	Initial rate of heating per unit mass of silicate Q_{0i} [W kg^{-1}]
^{238}U	4468	9.47E-05	26.2	1.409E+17	4.916E-18	2.48E-12
^{235}U	703.81	5.69E-04	8.2	2.221E+16	3.120E-17	4.66E-12
^{232}Th	14030	2.64E-05	53.8	4.427E+17	1.565E-18	1.42E-12
^{40}K	1277	2.92E-05	1104	4.029E+16	1.720E-17	3.22E-11
^{26}AL	0.716	3.41E-01	600	2.259E+13	3.067E-14	2.05E-07
^{60}Fe	1.5	7.10E-02	200	4.733E+13	1.464E-14	1.42E-08
^{53}Mn	3.7	2.70E-02	25.7	1.167E+14	5.936E-15	6.94E-10

*)after Robuchon *et al.* (2010) and Czechowski (2012)

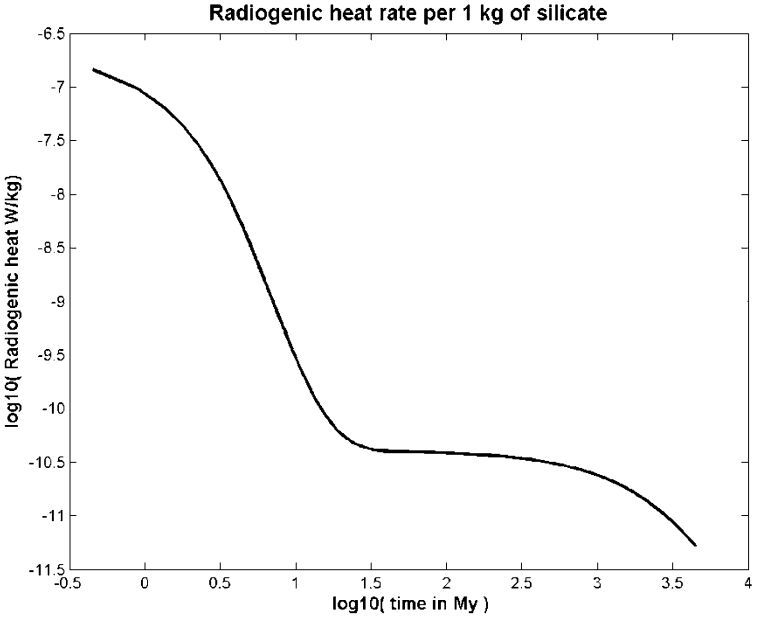

Fig. 1. Total radiogenic heat rate (in W per 1 kg of silicates of chondritic composition) *versus* time (from the origin of CAI). See Table 1 for isotopic composition.

where f_{m} is the silicate mass fraction in the satellite and time t is measured from the formation of CAI (Fig. 1).

The heat of accretion results from kinetic energy of the falling matter. The temperature increase resulting from this process could be calculated from the formula (*e.g.*, Multhaup and Spohn 2007):

$$T_{ac} = \left(\frac{4}{3} c_p\right) \xi \, \pi \, G \, \rho \, r^2(t) \left(1 + \frac{1}{2e_s}\right) + T_{\mathrm{nebula}} \,, \tag{2}$$

where $G = 6.67 \times 10^{-11}\ \mathrm{N\,m^2\,kg^{-2}}$ is the gravity constant, ρ is the density, $r(t)$ is the current radius of accreting body, and c_p is the specific heat. We adopt also here $\xi = 0.4$, and the Safronov number $e_S = 2$ after Multhaup and Spohn (2007). The surface temperature of both satellites and the nebula temperature are assumed to be the same, namely $T_s = T_{\mathrm{nebula}} = 75$ K.

After Abramov and Mojzsis (2011) we consider the following reaction of serpentinization:

$$\mathrm{Mg_2SiO_4\,(forsterite) + MgSiO_3\,(enstatite) + 2H_2O \rightarrow Mg_3Si_2O_5(OH)_4\,(antigorite)} \tag{3}$$

This reaction releases 241 000 J/kg of serpentine produced. The density of serpentine is 2470 kg m^{-3}. Moreover, we assume that silicates contain also 20% of nonreactive rock of 3630 kg m^{-3} density (Abramov and Mojzsis 2011). Malamud and Prialnik (2013) considered also reaction for olivine containing 80% Mg and 20% Fe:

$$Fe_{0.4}Mg_{1.6}SiO_4 + 1.23H_2O \rightarrow 0.5Mg_3SiO_5(OH)_4 + 0.1Mg(OH)_2 + 0.1.33F_3O_4 + 0.133H_2$$

The energy release is similar to Eq. 3. Note that we are interested mainly in energy release, and other details of reactions are not especially important.

2.2 Rheology

The volume percentage of rocky component in Enceladus is approximately 40%. It means that rheological properties of its undifferentiated interior are determined by the icy component; according to the Roscoe's theory (*e.g.*, Roscoe 1952, Schubert *et al.* 1986, Czechowski 2006a), the silicate particles form interconnecting matrix only if silicates concentration is at least 60% by volume. The rheology of icy satellites is typical for inner planets. The uppermost layer ("lithosphere") is probably elastic for small deformation and brittle for large deformations. The medium below the lithosphere is also solid but for very slow geologic processes it behaves like a viscous fluid with effective viscosity $\eta(T)$.

There are no observational data concerning the viscosity of the solid interior of MIS. Therefore we should investigate the problem for some range of viscosity. We started from the formula:

$$\eta(T) = \eta_x \sigma^{(1-i)} \exp\left(E/RT\right), \tag{4}$$

where η_x is a constant, σ is the second invariant of the deviatoric stress tensor, i is the power law index ($i = 1$ corresponds to a Newtonian fluid), E is the activation energy of the dominant mechanism of deformation, and R = 8.314 J K^{-1} mole^{-1} is the universal gas constant (McKinnon 1998, Goldsby and Kohlstedt 1997, Durham *et al*. 1998, Forni *et al.* 1991). Parameters η_x, E, and i depend on many factors; *e.g.*, size of ice crystals, content of gases, size of mineral grains, *etc.*, most of them being essentially unknown. Durham *et al.* (1998) give two extreme values of E: 43 kJ mole^{-1} (for water ice I below 195 K) and 107.5 kJ mole^{-1} (for NH_3 $2H_2O$). These values correspond to E/R of 5172 and 12 930 K, respectively. Rheology of both materials is highly nonlinear. Fortunately, non-Newtonian flow could be simulated by Newtonian flow with lower E (Christensen 1984, Dumoulin *et al.* 1999); therefore we assume that $i = 1$ (*i.e.*, Newtonian flow) but we use E =

50 kJ mole^{-1}. More complicated rheology is not necessary for our calculation (see also: Davaille and Jaupart 1993, Grasset and Parmentier 1998).

The viscosity η_m for the melting temperature T_m, and the activation energy E are used as parameters of our model; η_m is equal to

$$\eta_m = \eta(T_m) = \eta_x \exp(E/RT_m) . \tag{5}$$

2.3 Two regimes of convection

Two types of large scale motion in the MIS interior are considered in the present paper: solid state thermal convection (SSC), and thermal convection in liquid (LSC – liquid state convection) – Fig. 2. The SSC could develop in the upper solid layer (mantle), while LSC operates in the molten part.

The SSC is a very slow convection observed in media that are solid (from microscopic point of view) but behave like liquid in specific conditions. A few mechanisms of creep are possible, *e.g.*, Herring–Nabarro creep and/or Cobble creep. The very large value of the Prandtl number *Pr* is characteristic for SSC (*e.g.*, Czechowski 1993, p. 176):

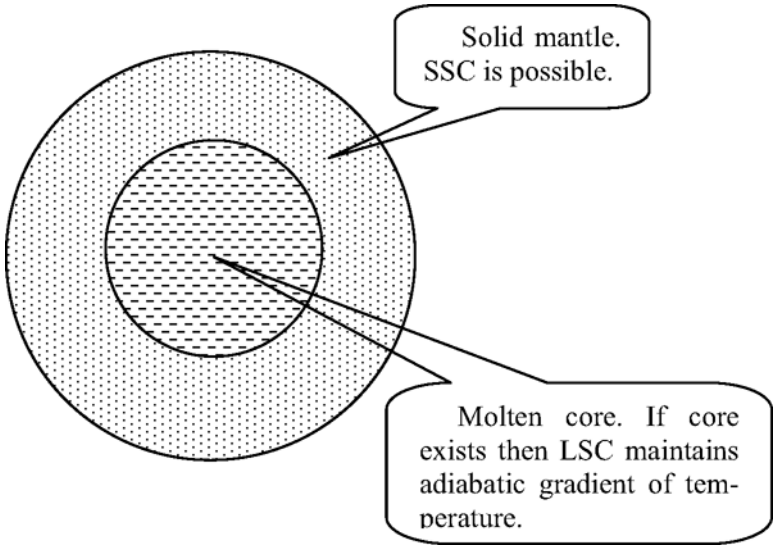

Fig. 2. Scheme of structure of modeled satellites. Two possible regions are considered: molten core and solid mantle. In the molten core (if it exists at all) adiabatic gradient is maintained by liquid state convection (LSC) for most of the considered time. In the solid mantle, solid state convection (SSC) is possible if Rayleigh number *Ra* is high enough.

$$Pr = \eta / \rho\kappa \,, \tag{6}$$

where η [Pa s] denotes the apparent viscosity, κ [$m^2 s^{-1}$] is the thermal diffusivity, and ρ [$kg\,m^{-3}$] is the density. For solid state convection, $Pr = O(10^{18})$. It means that inertial terms in the equation of motion (*e.g.*, Coriolis force) could be neglected.

Because mantle in MIS is heated mainly from below (from melted core) we use the following definition of the Rayleigh number Ra (*e.g.*, Czechowski 1993, p. 175; Schubert *et al.* 2001, p. 270):

$$Ra = r\, g_r\, a c_p \Delta T d^3 \big/ \left(\kappa h_r\right), \tag{7}$$

where g is the average gravity in the considered layer [$m\,s^{-2}$], α is the coefficient of thermal volume expansion [K^{-1}], c_p is the average specific heat [$J\,kg^{-1}\,K^{-1}$], $\kappa = k/(\rho c_p)$ is the average value of coefficient of temperature diffusion, k is the average thermal conductivity [$W\,m^{-1}\,K^{-1}$], ΔT is the temperature difference [K] across the considered layer, and $\eta(T)$ is the effective (temperature dependent) viscosity [Pa s]. Viscosity η is evaluated for the average temperature $T_{\rm av}$ in the considered region. Other non-constant parameters are also averaged over the considered region.

In the above equation, $\Delta T = T_{\rm m} - T_s$ where T_s is the surface temperature and $T_{\rm m}$ is the temperature of the molten region (or the temperature in the center of the satellite). Convection starts if the Rayleigh number exceeds its critical value $Ra_{\rm cr}$. This value depends on situation, but usually $Ra_{\rm cr} = O(1000)$, (see, *e.g.*, Czechowski 1993, p. 180 for more detailed discussion), so we choose $Ra_{\rm cr} = 1000$.

LSC could take place in a molten region only. The Prandtl number is $Pr = O(1)$. It means that inertial forces like the Coriolis force could be important for this motion (*e.g.*, Czechowski 2012). It is a dominant form of heat transfer in the molten core. Our preliminary calculations indicate that differentiation occurs when LSC is coming to the end. Therefore, for most of time LSC convection is heated from inside (the grains with radioactive isotopes are suspended in liquid), so we use $Ra_{\rm in}$ defined as follows:

$$Ra_{\rm in} = \alpha_m \rho_m^2 g h^5 Q(t) \big/ \left(k_m \kappa_m \eta_m\right), \tag{8}$$

where subscript m denotes that given parameter is calculated for molten region of the satellite. Note that liquid water contains suspended solid, so these values are not the same as for water. The $\kappa_m = k_m/(\rho_m c_{pm})$ is the average value of coefficient of temperature diffusion, and k_m is the average thermal conductivity [$W\,m^{-1}\,K^{-1}$].

3. NUMERICAL MODEL

3.1 Basic equations of the model

In our calculations we use numerical model developed by Czechowski (2012). Its short description only is given here. For details see Czechowski (2012, 2014). The model is based on parameterized theory of convection combined with 1-dimensional equation of the heat transfer in spherical coordinates

$$\rho c_p \frac{\partial T(r,t)}{\partial t} = \mathrm{div}\left(k(r,T)\,\mathrm{grad}T(r,t)\right) + Q(r,T) \ , \tag{9}$$

where r is the radial distance (spherical coordinate), ρ is the density [kg m^{-3}], c_p [J kg^{1} K^{-1}] is the specific heat, Q [W kg^{-1}] is the heating rate, and k [W m^{-1} K^{-1}] is the thermal conductivity. Note that $Q(r,t)$ includes sources and sinks of the heat. The heat of accretion is included as initial temperature of the accreted layer. Note that Eq. 9 is solved in time dependent region $[0, R(t)]$. During accretion the radius $R(t)$ increases in time according to the formula: $R(t) = a\,t$ for $t_{\mathrm{ini}} < t < t_{\mathrm{ac}}$, and $R(t) = R_{\mathrm{sat}}$ for $t > t_{\mathrm{ac}}$, *i.e.*, after the accretion (see, *e.g.*, Merk *et al.* 2002), where t_{ini} denotes the beginning of accretion and t_{ac} denotes the duration of this process.

If the Rayleigh number in the considered layer exceeds its critical value Ra_{cr} then convection starts. It leads to effective heat transfer. The full description of convection is given by a velocity field and temperature distribution. However, we are interested in convection as a process of heat transport only. For SSC heat transport can be described by dimensionless Nusselt number Nu. We use the following definition of Nu (*e.g.*, Czechowski 1993, p. 185):

$$Nu = \left(\text{True total surface heat flow}\right)/\left(\text{Total heat flow without convection}\right) \ . \tag{10}$$

The heat transport by SSC is modeled simply by multiplying the coefficient of the heat conduction in the considered layer, *i.e.*:

$$k_{\mathrm{conv}} = Nu\,k \ . \tag{11}$$

This approach is used successfully in parameterized theory of convection for SSC in planets and satellites (*e.g.*, Sharpe and Peltier 1978, Peltier and Jarvis 1982, Czechowski 2006b).

The method needs some formula for Nu. We tried here a few different sets of formulas. Our preliminary results indicate that SSC in a relatively small satellite is not as dominant heat transfer mode as for large MIS like Rhea. Therefore, for our purposes the simplest approach seems to be better suited. After Turcotte and Schubert (2002, p. 273) we use

$$Nu = 1.04\ \left(Ra/Ra_{\mathrm{crit}}\right)^{1/3} \ . \tag{12}$$

Parameterization of LSC is even simpler. *Ra* in molten region is very high (usually higher than 10^{16}). The LSC could be very intensive, resulting in almost adiabatic temperature gradient given by

$$\frac{dT}{dr} = \frac{g\alpha_m T}{c_{pm}}, \tag{13}$$

where α_m and c_{pm} are thermal expansion coefficient and specific heat in the molten region, g is the local gravity. In Enceladus and Mimas the adiabatic gradient is low and therefore the LSC region is almost isothermal.

3.2 Gravitational differentiation and LSC

The melting of ice allows for differentiation of the satellite. Then silicate grains sink in the molten core. However, we have also the opposite process: mixing by LSC. The interaction of these processes was considered by Czechowski (2014). His calculations indicate that convection is strong enough for mixing grains of ~1 mm size and consequently not allowing for core formation (of course, with the exception of largest grains) for more than 100 Myr, *i.e.*, even after the decay of most of the SLI. Convection eventually slows down and stops when the Rayleigh number drops below its critical value. Then the bulk of the core is formed. Note also that the convection and sinking process itself are strong factors separating grains according to their size, so one can expect the size of grains (and pores) to increase with depth. The relatively cold core (temperature is close to the melting point of water) of loosely packed grains with water between them is a result of this differentiation. At that time, there is no mechanism of removing the water. The chemical processing of solidification of the grains is possible but due to low temperature is rather slow. However, the concentration of silicates with radioactive elements allows for increasing the temperature in time.

The rheology of the core could be a crucial factor for tidal heating. Because the grains are mostly not glued, tidal deformations and efficient dissipation of energy are possible. In Enceladus the later evolution of core could be a result of strong tidal heating that could lead to removing water from the pores and even to dehydratation (if temperature exceed 800 K). That processes could lead eventually to rigid core of large density and of relatively small size (Schubert *et al.* 2007). However, another option is also possible: the core still contains large amount of water and serpetinized silicates of low density (*e.g.*, Malamud and Prialnik 2013). Calculation of Czechowski (2014) and interpretation of gravity data from Cassini (Taubner *et al.* 2014) indicate rather low density core of Enceladus. It means that the second option is more probable. The hypothetical core of Mimas is probably unchanged since its origin.

4. RESULTS AND DISCUSSION

4.1 Example of evolution

Figure 3 presents an example of thermal evolution of Mimas for the following values of parameters: η_m is 10^{14} Pa s, $c_{hyd} = 240\,000$ J kg^{-1}, $E = 5 \times 10^4$ J mole^{-1}, $t_{ac} = 0.1$ Myr, $k_{sil} = 4.2$ W m^{-1} K^{-1}, $t_{ini} = 1.8$ Myr. The vertical axis gives distance from the center of satellite (r/R_{sat}). The horizontal axis gives $\log_{10}$(time in Myr). Note that initially the isotherms are going up following increasing radius of the accreting body. For the first several millions of years the temperature increases fast because of high concentration of radioactive elements (SLI). The maximum is reached in a few millions of years and subsequently isotherms corresponding to high temperature (let's say 260 K) move down.

In the presented case there was no melting. However, for lower t_{ini}, or for Enceladus, the melting is possible. Contrary to expectation, the molten region does not follow the isotherms. The matter reaches the melting temperature in a few Myr but the melting occurs after the next 2-3 Myr. The melting triggers serpentinization that supplies additional thermal energy. The radius of molten region reaches its maximum value only after ~100 Myr. It is also the time of stopping LSC and forming the core.

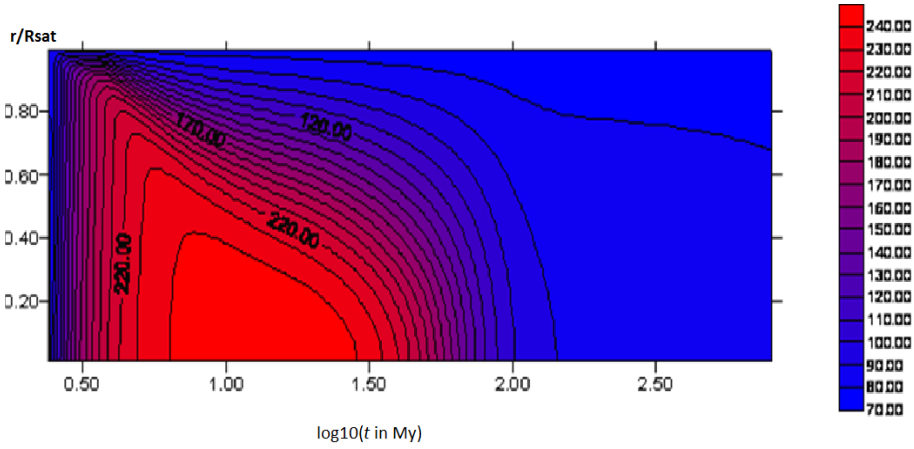

Fig. 3. Thermal evolution of Mimas for the following values of parameters: η_m of 10^{14} Pa s, $c_{hyd} = 240\,000$ J kg^{-1}, $E = 5 \times 10^4$ J mole^{-1}, $t_{ac} = 0.1$ Myr, k_si $= 4.2$ W m^{-1} K^{-1}, $t_{ini} = 1.8$ Myr. Vertical axis gives distance from the center of the satellite (r/R_{sat}). Horizontal axis gives $\log_{10}$(time in Myr). Note that initially the isotherms are going up following increasing radius of the accreting body. For the first Myr's the temperature increases fast because of high concentration of the radioactive elements. The maximum is reached in a few millions of years and subsequently isotherms corresponding to high temperature (say 220 K) move down.

4.2 Role of different parameters in evolution

We performed calculations for Mimas and Enceladus for different values of the parameters: t_{ini} (time of starting accretion), t_{ac} (duration of accretion), η_m (viscosity at melting temperature), k_{sil} (thermal conductivity of the silicate grains), and E (activation energy). The comparisons in Fig. 4 are done for

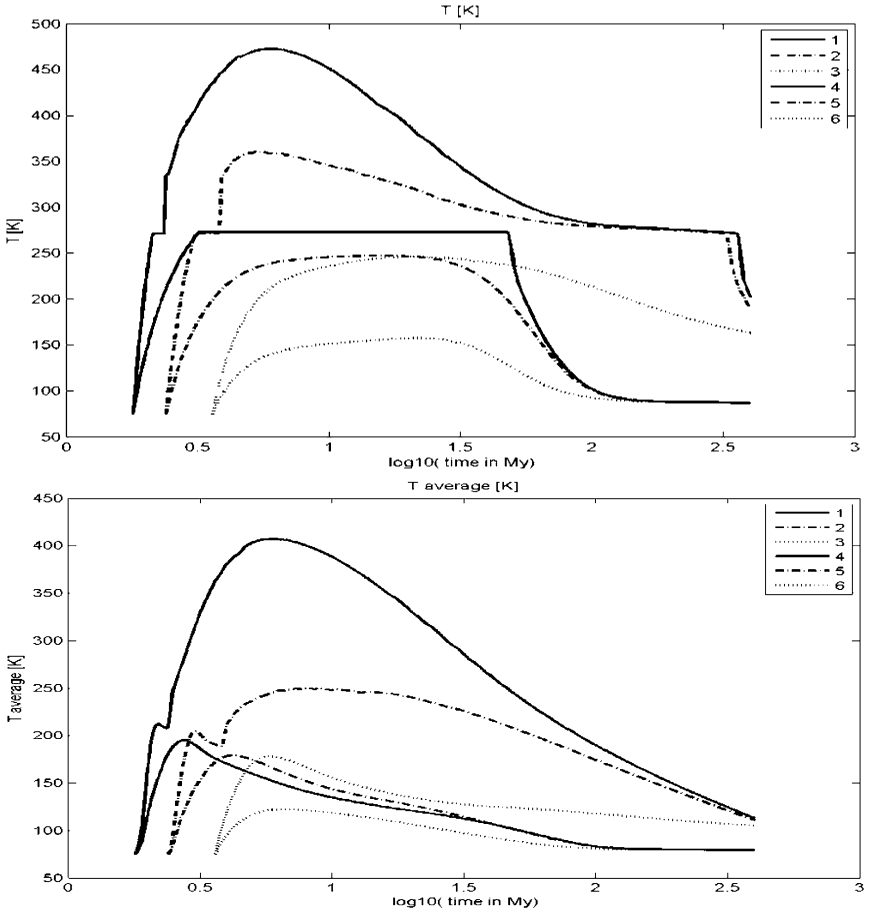

Fig. 4. Comparison of temperature in the center T_{max} (upper panel) and average temperature T_{ave} (lower panel) for Enceladus and Mimas. Parameters: viscosity η_m of 10^{14} Pa s, $c_{hyd} = 240\,000$ J kg^{-1}, $E = 5 \times 10^4$ J mole^{-1}, $t_{ac} = 0.1$ Myr, $k_{sil} = 4.2$ W m^{-1} K^{-1}, $t_{ini} = 1.8$, 2.4, 3.6 Myr for lines 1 (and 4), 2 (and 5), 3 (and 6), respectively. Initial temperatures of both satellites are the same; note common point at $t = t_{ini}$ (leftmost). All lines for Mimas are below the corresponding lines for Enceladus indicating lower temperature in smaller Mimas. Note also that all lines for Mimas for large time converge for substantially lower temperature than the lines for Enceladus.

the globally average temperature T_{av} (weighted average) and maximum temperature T_{max} (*i.e.*, temperature in the center of a given body). The following values of parameters are chosen: viscosity η_m of 10^{14} Pa s, c_{hyd} = 240 000 J kg^{-1}, $E = 5 \times 10^4$ J mole^{-1}, $t_{ac} = 0.1$ Myr, $k_{sil} = 4.2$ W m^{-1} K^{-1}, t_{ini} = 1.8, 2.4, 3.6 Myr for lines 1 (and 4), 2 (and 5), 3 (and 6), respectively. Initial temperatures of both satellites are the same (note common point at $t = t_{ini}$ (leftmost)). All lines for Mimas are below the corresponding lines for Enceladus, indicating lower temperature in smaller Mimas. Note also that all lines for Mimas for large time t converge to a substantially lower level than the lines for Enceladus.

Figures 5-10 present the role of other parameters. For Figure 5, the thermal conductivity $k_{sil} = 2.5$ W m^{-1} K^{-1}. Figures 6 and 7 give evolution of T_{ave} for Enceladus and Mimas for different values of the parameters of viscosity: η_m is 10^{16} Pa s and $E = 3 \times 10^4$ J mole^{-1}. Figure 8 presents T_{ave} for longer duration of accretion, $t_{ac} = 1$ Myr. The energy of serpentinization is negligible for models presented in Fig. 9. Figure 10 shows evolution of the satellite with 10% of ammonia in volatiles.

Note that all the parameters discussed are important for thermal evolution. However, differences of the results are not dramatic.

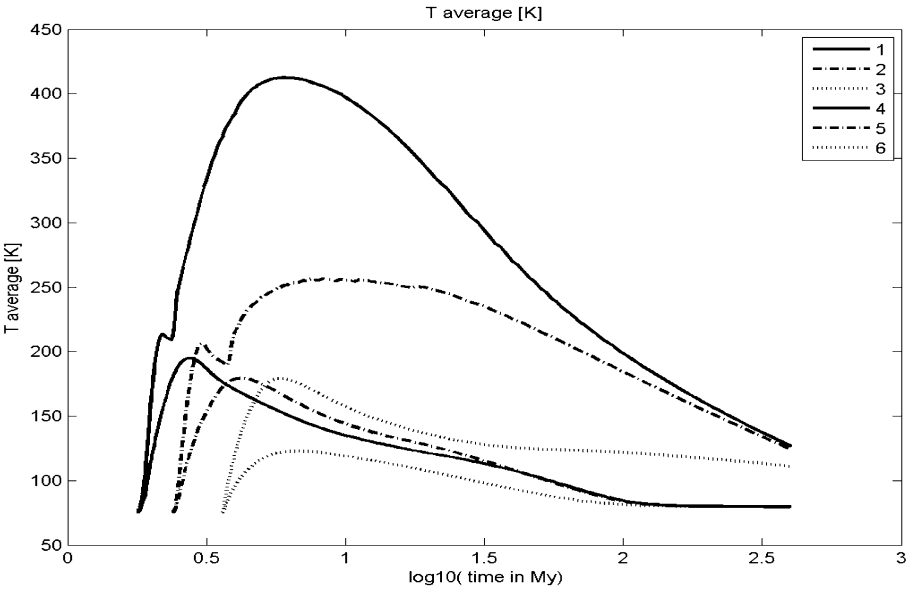

Fig. 5. Comparison of average temperature T_{ave} for Enceladus and Mimas. Thermal conductivity of silicates is $k_{sil} = 2.5$ W m^{-1} K^{-1}. The rest as for Fig. 4.

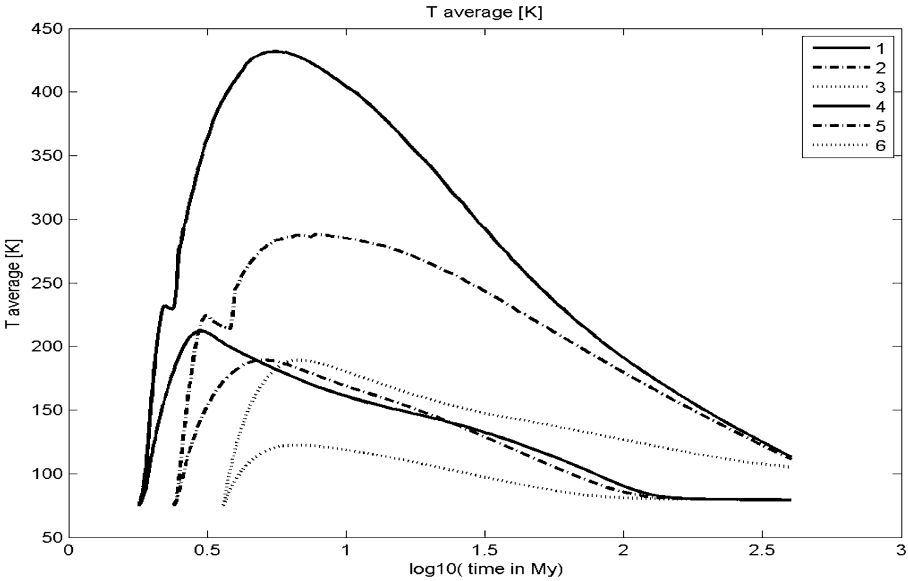

Fig. 6. Comparison of average temperature T_{ave} for Enceladus and Mimas. Viscosity at melting temperature η_m is 10^{16} Pa s. The rest as for Fig. 4.

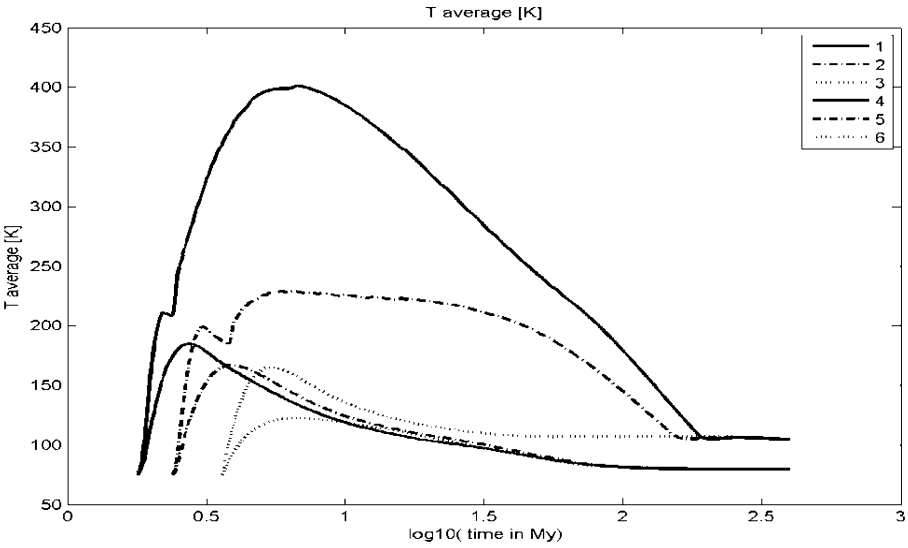

Fig. 7. Comparison of average temperature T_{ave} for Enceladus and Mimas. Activation energy is $E = 3 \times 10^4$ J mole^{-1}. The rest as for Fig. 4.

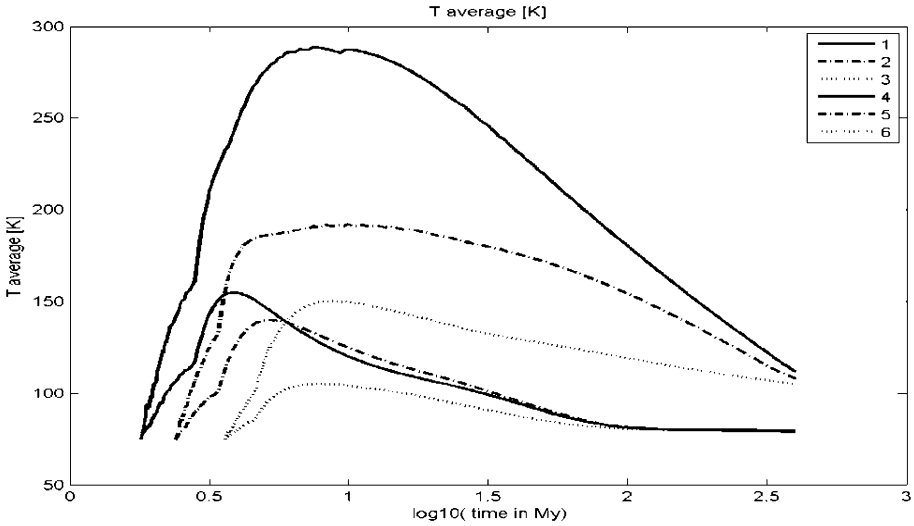

Fig. 8. Comparison of average temperature T_{ave} for Enceladus and Mimas. Duration of accretion is t_{ac} = 1 Myr. The rest as for Fig. 4.

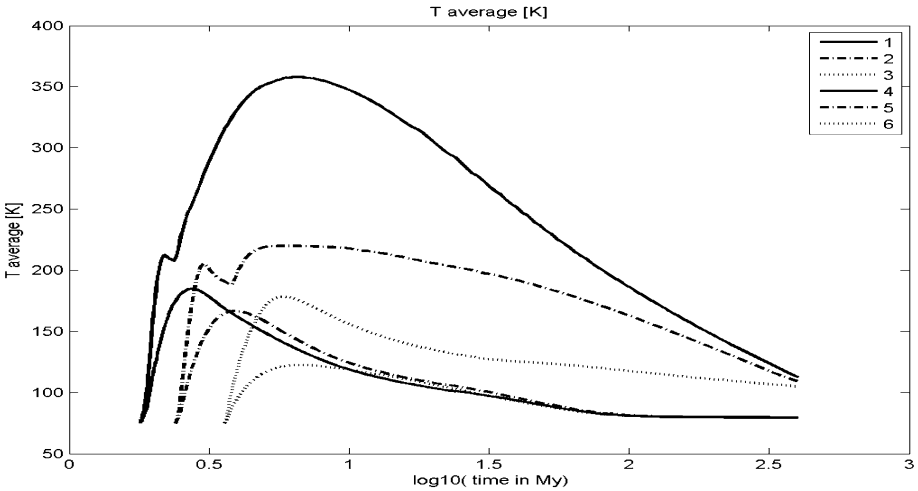

Fig. 9. Comparison of average temperature T_{ave} for Enceladus and Mimas. Energy of serpentinization c_{hyd} = 0 J kg^{-1}. The rest as for Fig. 4.

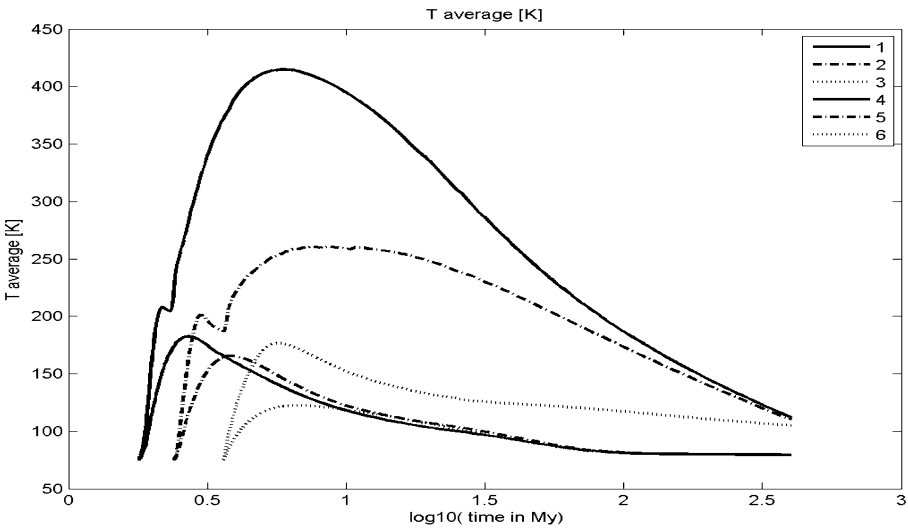

Fig. 10. Comparison of average temperature T_{ave} for Enceladus and Mimas. Ammonia content is 10% of ice component. The rest as for Fig. 4.

4.3 Mimas–Enceladus paradox

Mimas and Enceladus are similar in size and mass and they both are in orbit-orbit resonances with other MIS. However, their endogenic activities are different. Mimas is geologically dead for billions of years while Enceladus is presently active. Its activity is a result of tidal heating. For tidal heating in a satellite Poirier *et al.* (1983) gave the formula:

$$q_{t\,\mathrm{av}} = 63 r\, r^4 n^5 e^2 \,/ (38 m Q) \ , \tag{14}$$

where ρ is the density [kg m^{-3}], r [m] is the satellite's radius, n [rad s^{-1}] is the mean orbital motion, e is the eccentricity of the satellite's orbit, Q is the dimensionless dissipation factor, and μ [Pa] is the shear modulus of the satellite's interior. Equation 14 is derived for a homogeneous body; therefore, for a non-uniform body, the effective values of μ and Q should be used. The ratio of tidal heating $q_{t\,\mathrm{av}}$ to total average heating q_{av} is known as the dimensionless number $C = q_{t\,\mathrm{av}} / q_{\mathrm{av}}$.

Equation 14 was successfully used for Io (*e.g.*, Peale *et al.* 1979). Unfortunately, the direct use of Eq. 14 to Enceladus and Mimas leads to an apparent paradox. Assuming that rheological properties of these satellites are similar (*i.e.*, values of μ and Q are the same) the products $\theta = \rho r^4 n^5 e^2$ could be treated as a measure of tidal heating. One can find that θ for active Enceladus is 31 times lower than θ for dead Mimas. This paradox indicates that a more advanced model is necessary.

Czechowski (2006a, 2009) explained Mimas-Enceladus paradox as a result of nonlinear behavior of the system of equations describing the tidal heating, heat transfer, and rheological properties of the interior. He adopted the parameterized theory of convection for specific situation of MIS of Saturn. His model included not only temperature dependent Q and μ but also possible bifurcations. The system allows for a few steady state solutions for thermal state of a given satellite. Eventually Czechowski (2006a) stated that:

- Each of the satellites has a low temperature solution that usually corresponds to low tidal heating. This state is referred to as the basic thermal state. For the smallest of MIS (*i.e.*, Mimas or Enceladus) the temperature of this solution is very low; consequently, these satellites cannot be active in their basic states.
- Some of the satellites have also one or two additional solutions with higher temperatures and with higher rates of tidal heating than for the basic state. These additional solutions correspond to thermal states that are referred here as excited states.

The basic solution always exists and corresponds to the lowest possible temperature. The existence of excited states with high temperature does not guarantee an endogenic activity of a given satellite. It means only that the given satellite could be in one of a few thermal states; the satellite could be in its basic state even if exited states exist.

For starting efficient tidal heating it is necessary that:

1. temperature of interior is high enough for effective dissipation of tidal stresses,
2. the orbit has a significant eccentricity.

Moreover, for long lasted tidal heating it is necessary that:

3. there occurs an orbit-orbit resonance that could keep the non-zero eccentricity.

All conditions must be fulfilled simultaneously. Presently, Mimas fulfills conditions 2 and 3. If its temperature were high enough then the tidal heating could be high and Mimas could be active. The initial temperature of the satellite could be a factor deciding upon the path of evolution.

Generally, with the exception of a short time (approximately 1-4 Myr after CAI), Mimas was always substantially colder than Enceladus. We do not know the critical temperature necessary for starting process of effective tidal heating in Mimas, but evidently the high temperature is important. We do not know when condition 3 was fulfilled, *i.e.*, when Mimas–Tethys and Enceladus–Dione resonances were established. Note, however, that condition 1 could be satisfied in Mimas, only if it accreted early. This leads us to additional condition: $t_{\mathrm{ini}} < 1.8$ Myr for Mimas. However even if this additional condition was satisfied and Mimas was (for some time) hot enough for

efficient tidal dissipation, the duration of this "launch window" was dramatically shorter (~10 Myr) for Mimas than for Enceladus (~100 Myr). Probably the Mimas–Tethys resonance was established too late to change the path of evolution of Mimas.

Taking into account early thermal history of both satellites, the present situation can hardly be treated as a paradox. The Mimas should be very "lucky" if time of resonance and time of high temperature were at the moment when Mimas was hot.

4.4 Chronology and activity of Mimas and Enceladus

Mimas is classified as a dead satellite according to Rothery (1992). It means that there was no substantial endogenic activity since Heavy Bombardment Epoch (HBE). Note however that the assessment of age depends on the assumed model of flux of meteorites. Using the lunar-like flux, cratered plains of Enceladus are 4.2 Gyr old and only 1.7 Gyr old, if cometary impact rate is used for calculation (Zahnle *et al.* 2003, Spencer *et al.* 2009). Saturated by craters, the surface of Mimas is probably older than 4 Gyr according to "lunar" chronology, but only ~2 Gyr if cometary impact rate is appropriate. If "short", "cometary" chronology is correct then we do not have data concerning 2.5 Gyr of Mimas history. During that time, the satellite could be active but the older lithosphere was destroyed.

5. CONCLUSIONS

- We compared thermal evolution for Enceladus and Mimas for several parameters: η_m, c_{hyd}, E, t_{ac}, k_{sil}, and t_{ini}. All of these parameters are significant but the time of accretion t_{ini} is the most important (see also Czechowski 2014).
- The Mimas–Enceladus paradox is probably the result of short time when Mimas was hot enough. This conclusion does not contradict the results of Malamud and Prialnik (2013) about the role of serpentinization. However, we indicate that the role of serpentinization is not critical. The paradox could exist even if serpentization of the matter had occurred before accretion.
- If "short", "cometary" chronology is correct, then Mimas could have been active for some time.

Acknowledgements. This work was partially supported by the National Research Centre (grant 2011/01/B/ST10/06653). Computer resources of Interdisciplinary Centre for Mathematical and Computational Modeling of Warsaw University are also used in the research. We are also grateful for Dr. Anna Łosiak for her suggestions.

References

Abramov, O., and S.J. Mojzsis (2011), Abodes for life in carbonaceous asteroids? *Icarus* **213**, 1, 273-279, DOI: 10.1016/j.icarus.2011.03.003.

Bobojć, A., and A. Drożyner (2011), GOCE satellite orbit in the aspect of selected gravitational perturbations, *Acta Geophys.* **59**, 2, 428-452, DOI: 10.2478/s11600-010-0052-3.

Charnoz, S., A. Morbidelli, L. Dones, and J. Salmon (2009), Did Saturn's rings form during the Late Heavy Bombardment? *Icarus* **199**, 2, 413-428, DOI: 10.1016/j.icarus.2008.10.019.

Christensen, U. (1984), Convection with pressure- and temperature-dependent non-Newtonian rheology, *Geophys. J. Int.* **77**, 2, 343-384, DOI: 10.1111/j.1365-246X.1984.tb01939.x.

Czechowski, L. (1993), Theoretical approach to mantle convection. **In:** R. Teisseyre, L. Czechowski, and J. Leliwa-Kopystyński (eds.), *Dynamics of the Earth's Evolution*, PWN – Polish Scientific Publ., Warszawa, Elsevier, Amsterdam, 161-271.

Czechowski, L. (2006a), Parameterized model of convection driven by tidal and radiogenic heating, *Adv. Space Res.* **38**, 4, 788-793, DOI: 10.1016/j.asr.2005.12.013.

Czechowski, L. (2006b), Two models of parameterized convection for medium-sized icy satellites of Saturn, *Acta Geophys.* **54**, 3, 280-302, DOI 10.2478/s11600-006-0021-z.

Czechowski, L. (2009), Uniform parameterized theory of convection in medium sized icy satellites of Saturn, *Acta Geophys*. **57**, 2, 548-566, DOI: 10.2478/s11600-008-0084-0.

Czechowski, L. (2012), Thermal history and large scale differentiation of the Saturn's satellite Rhea, *Acta Geophys*. **60**, 4, 1192-1212, DOI: 10.2478/s11600-012-0041-9.

Czechowski, L. (2014), Some remarks on the early evolution of Enceladus, *Planet. Space Sci.* **104**, 185-199, DOI: 10.1016/j.pss.2014.09.010.

Czechowski, L., and K.J. Kossacki (2012), Thermal convection in the porous methane-soaked regolith in Titan: finite amplitude convection, *Icarus* **217**, 1, 130-143, DOI: 10.1016/j.icarus.2011.10.006.

Davaille, A., and C. Jaupart (1993), Transient high-Rayleigh-number thermal convection with large viscosity variations, *J. Fluid Mech.* **253**, 141-166, DOI: 10.1017/S0022112093001740.

Dumoulin, C., M.-P. Doin, and L. Fleitout (1999), Heat transport in stagnant lid convection with temperature- and pressure-dependent Newtonian or non-Newtonian rheology, *J. Geophys. Res.* **104**, B6, 12759-12777, DOI: 10.1029/1999JB900110.

Durham, W.B., S.H. Kirby, and L.A. Stern (1998), Rheology of planetary ices. **In:** B. Schmitt, C. de Bergh, and M. Festou (eds.), *Solar System Ices*, Kluwer Academic Publ., Dordrecht, 63-78, DOI: 10.1007/978-94-011-5252-5_3.

Ellsworth, K., and G. Schubert (1983), Saturn's icy satellites: Thermal and structural models, *Icarus* **54**, 3, 490-510, DOI: 10.1016/0019-1035(83)90242-7.

Eluszkiewicz, J. (1990), Compaction and internal structure of Mimas, *Icarus* **84**, 1, 215-225, DOI: 10.1016/0019-1035(90)90167-8.

Essa, K.S. (2007), A simple formula for shape and depth determination from residual gravity anomalies, *Acta Geophys*. **55**, 2, 182-190, DOI: 10.2478/s11600-007-0003-9.

Forni, O., A. Coradini, and C. Federico (1991), Convection and lithospheric strength in Dione, an icy satellite of Saturn, *Icarus* **94**, 1, 232-245, DOI: 10.1016/0019-1035(91)90153-K.

Goldsby, D.L., and D.L. Kohlstedt (1997), Grain boundary sliding in fine-grained Ice – I, *Scripta. Mater.* **37**, 9, 1399-1406, DOI: 10.1016/S1359-6462(97)00246-7.

Grasset, O., and E.M. Parmentier (1998), Thermal convection in a volumetrically heated, infinite Prandtl number fluid with strongly temperature-dependent viscosity: Implications for planetary evolution, *J. Geophys. Res.* **103**, B8, 18171-18181, DOI: 10.1029/98JB01492.

Jaumann, R., R.N. Clark, F. Nimmo, A.R. Hendrix, B.J. Buratti, T. Denk, J.M. Moore, P.M. Schenk, S.J. Ostro, and R. Srama (2009), Icy satellites: Geological evolution and surface processes. **In:** M.K. Dougherty L.W. Esposito, and S.M. Krimigis (eds.), *Saturn from Cassini-Huygens*, Springer Science+Business Media, Dordrecht, 637-681, DOI: 10.1007/978-1-4020-9217-6_20.

Kriegel, H., S. Simon, J. Müller, U. Motschmann, J. Saur, K.-H. Glassmeier, and M.K. Dougherty (2009), The plasma interaction of Enceladus: 3D hybrid simulations and comparison with Cassini MAG data, *Planet. Space Sci.* **57**, 14-15, 2113-2122, DOI: 10.1016/j.pss.2009.09.025.

Leliwa-Kopystyński, J., and K.J. Kossacki (2000), Evolution of porosity in small icy bodies, *Planet. Space Sci.* **48**, 7-8, 727-745, DOI: 10.1016/S0032-0633(00)00038-6.

Malamud, U., and D. Prialnik (2013), Modeling serpentinization: Applied to the early evolution of Enceladus and Mimas, *Icarus* **225**, 1, 763-774, DOI: 10.1016/j.icarus.2013.04.024.

Matson, D.L., J.C. Castillo-Rogez, G. Schubert, C. Sotin, and W.B. McKinnon (2009), The thermal evolution and internal structure of Saturn's mid-sized icy satellites. **In:** M.K. Dougherty, L.W. Esposito, and S.M. Krimigis (eds.), *Saturn from Cassini-Huygens*, Springer Science+Business Media, Dordrecht, 577-612, DOI: 10.1007/978-1-4020-9217-6_18.

McKinnon, W.B. (1998), Geodynamics of icy satellites. **In:** B. Schmitt, C. de Bergh, and M. Festou (eds.), *Solar System Ices*, Kluwer Academic Publ., Dordrecht, 525-550, DOI: 10.1007/978-94-011-5252-5_22.

McKinnon, W.B., and A.C. Barr (2007), The Mimas paradox revisited plus crustal spreading on Enceladus? *LPI Contrib*. **1357**, 91-92.

Merk, R., D. Breuer, and T. Spohn (2002), Numerical modeling of ^{26}Al-induced radioactive melting of asteroids concerning accretion, *Icarus* **159**, 1, 183-191, DOI: 10.1006/icar.2002.6872.

Meyer, J., and J. Wisdom (2008), Tidal evolution of Mimas, Enceladus, and Dione, *Icarus* **193**, 1, 213-223, DOI: 10.1016/j.icarus.2007.09.008.

Multhaup, K., and T. Spohn (2007), Stagnant lid convection in the mid-sized icy satellite of Saturn, *Icarus* **186**, 2, 420-435, DOI: 10.1016/j.icarus.2006.09.001.

Muro, G.D., and F. Nimmo (2011), Modeling the coupled thermal and orbital evolution of Mimas, *LPI Contrib.* **1608**, 1560.

Peale, S.J. (2003), Tidally induced volcanism, *Celest. Mech. Dyn. Astr*. **87**, 1-2, 129-155, DOI: 10.1023/A:1026187917994.

Peale, S.J., P. Cassen, and R.T. Reynolds (1979), Melting of Io by tidal dissipation, *Science* **203**, 4383, 892-894, DOI: 10.1126/science.203.4383.892.

Peltier, W.R., and G.T. Jarvis (1982), Whole mantle convection and the thermal evolution of the Earth, *Phys. Earth Planet. In.* **29**, 3-4, 281-304, DOI: 10.1016/0031-9201(82)90018-8.

Poirier, J.P., L. Boloh, and P. Chambon (1983), Tidal dissipation in small viscoelastic ice moons: The case of Enceladus, *Icarus* **55**, 2, 218-230, DOI: 10.1016/0019-1035(83)90076-3.

Robuchon, G., G. Choblet, G. Tobie, O. Čadek, C. Sotin, and O. Grasset (2010), Coupling of thermal evolution and despinning of early Iapetus, *Icarus* **207**, 2, 959-971, DOI: 10.1016/j.icarus.2009.12.002.

Roscoe, R. (1952), The viscosity of suspensions of rigid spheres, *British J. Appl. Phys*. **3**, 8, 267-269, DOI: 10.1088/0508-3443/3/8/306.

Rothery, D.A. (1992), *Satellites of the Outer Planets: Worlds in Their Own Right*, Clarendon Press, Oxford, 208 pp.

Schubert, G., T. Spohn, and R.T. Reynolds (1986), Thermal histories, compositions and internal structures of the moons of the solar system. **In:** J.A. Burns and M.S. Matthews (eds.), *Satellites*, University of Arizona Press, Tucson, 224-292.

Schubert, G., D.L. Turcotte, and P. Olson (2001), *Mantle Convection in the Earth and Planets*, Cambridge Univ. Press, Cambridge, 956 pp.

Schubert, G., J.D. Anderson, B.J. Travis, and J. Palguta (2007), Enceladus: Present internal structure and differentiation by early and long-term radiogenic heating, *Icarus* **188**, 2, 345-355, DOI: 10.1016/j.icarus.2006.12.012.

Sharpe, H.N., and W.R. Peltier (1978), Parameterized mantle convection and the Earth's thermal history, *Geophys. Res. Lett*. **5**, 9, 737-740, DOI: 10.1029/GL005i009p00737.

Spencer, J.R., A.C. Barr, L.W. Esposito, P. Helfenstein, A.P. Ingersoll, R. Jaumann, C.P. McKay, F. Nimmo, and J.H. Waite (2009), Enceladus: An active cryovolcanic satellite. **In:** M.K. Dougherty, L.W. Esposito, and S.M. Krimigis (eds.), *Saturn from Cassini-Huygens*, Springer Science+Business Media, Dordrecht, 683-724, DOI: 10.1007/978-1-4020-9217-6_21.

Taubner, R.S., J.J. Leitner, M.G. Firneis, and R. Hirzenberger (2014), Including Cassini's gravity measurements from the flybys E9, E12, E19 into interior structure models of Enceladus. **In:** *Proc. European Planetary Science Congress, 7-12 September 2014, Cascais, Portugal*, EPSC Abstracts, 2014-676.

Thomas, P.C. (2010), Sizes, shapes, and derived properties of the Saturnian satellites after the Cassini nominal mission, *Icarus* **208**, 1, 395-401, DOI: 10.1016/j.icarus.2010.01.025.

Turcotte, D.L., and G. Schubert (2002), *Geodynamics*, 2nd ed., Cambridge University Press, Cambridge, 465 pp.

Zahnle, K., P. Schenk, H. Levison, and L. Dones (2003), Cratering rates in the outer Solar System, *Icarus* **163**, 2, 263-289, DOI: 10.1016/S0019-1035(03)00048-4.

Received 19 November 2013
Received in revised form 7 January 2015
Accepted 19 January 2015